Army Science Conference Proceedings

20 - 22 June 1978
Volume III
Principal Authors N thru Z

Deputy Chief of Staff for Research,
Development & Acquisition
Department of the Army

DEPARTMENT OF THE ARMY
OFFICE OF THE ADJUTANT GENERAL AND THE ADJUTANT GENERAL CENTER
WASHINGTON, D.C. 20314

HQDA Ltr 70-78-7

DRXRO-SO (M) (31 Aug 78) 15 September 1978

Expires 15 September 1979

SUBJECT: 1978 Army Science Conference, Volume III

SEE DISTRIBUTION

1. Inclosed for your information and use is Volume III of the 1978 Army Science Conference Proceedings. This volume contains the unclassified papers by principal authors N through Z which were presented at the conference, 20-22 June 1978, U. S. Military Academy, West Point, New York.

2. Volumes I, II and IV of the Proceedings are being distributed separately.

3. Chiefs of Army Staff Agencies, major commanders, and heads of laboratories on the distribution list will insure that this volume is placed in the organization's Technical Library where it will be available for reference.

4. The expiration date does not apply to the 1978 Army Science Conference Proceedings which should be retained for reference purposes.

BY ORDER OF THE SECRETARY OF THE ARMY:

C. F. Briggs

C. F. BRIGGS
Colonel, AGC
Acting The Adjutant General

1 Incl
Vol III, 1978 Army Science
Conference Proceedings

DISTRIBUTION:
Director of Army Research
Office of the Surgeon General
Office, Chief of Engineers, ATTN: DAEN-RDZ-A
Office, Chief of Engineers, ATTN: DAEN-ZC
Office, Chief of Engineers, ATTN: DAEN-MCZ-S
Office, Chief of Engineers, ATTN: DAEN-CWM-R
The Army Library, ATTN: ANRAL-RS
COMMANDERS
US Army Materiel Development & Readiness Command, ATTN: DRCLDC
US Army Armament Research & Development Command
US Army Aviation Research & Development Command
US Army Armament Materiel Readiness Command
US Army Communications Research & Development Command
US Army Electronics Research & Development Command
US Army Mobility Equipment Research & Development Command
US Army Missile Research & Development Command
US Army Natick Research & Development Command
US Army Tank-Automotive Research & Development Command
US Army Communications & Electronics Materiel Readiness Command
US Army Missile Materiel Readiness Command
US Army Tank-Automotive Materiel Readiness Command
US Army Troop Support & Aviation Materiel Readiness Command
US Army Test & Evaluation Command
US Army Computer Systems Command
US Army Forces Command
US Army Ballistic Missile Defense Systems Command
US Army Training & Doctrine Command
US Army Intelligence & Security Command
US Army Electronics Materiel Readiness Activity
US Army Aircraft Development Test Activity
US Army Foreign Science & Technology Center
US Army Materiels & Mechanics Research Center
US Army Cold Regions Test Center
US Army Tropic Test Center
US Army Ballistic Missile Advanced Technology Center
US Army Operational Test & Evaluation Agency
US Army Environmental Hygiene Agency
US Army Medical Research & Development Command
US Army Health Services Command
US Army Institute of Surgical Research
US Army Aeromedical Research Laboratory
US Army Medical Bioengineering R&D Laboratory
US Army Research Institute of Environmental Medicine
US Army Medical Research Institute of Infectious Diseases
US Army Tripler Medical Center
US Army Institute of Dental Research

SUBJECT: 1978 Army Science Conference, Volume III

US Army Research Institute for the Behavioral & Social Sciences
Walter Reed Army Institute of Research
Walter Reed Army Medical Center
Dwight D. Eisenhower Army Medical Center
Brooke Army Medical Center
Fitzsimons Army Medical Center
Madigan Army Medical Center
Letterman Army Institute of Research
Armed Forces Institute of Pathology
US Army Research Office
US Army Research & Standardization Group (Europe)
US Army Aberdeen Proving Ground
US Army Dugway Proving Ground
US Army Yuma Proving Ground
US Army Electronics Proving Ground
US Army White Sands Missile Range
US Army Watervliet Arsenal
US Army Rock Island Arsenal
US Army Signal Center & Fort Gordon
US Army Combat Surveillance & Target Acquisition Laboratory
US Army Atmospheric Sciences Laboratory
Redstone Scientific Information Center, ATTN: Chief, Documents
Harry Diamond Laboratories
Chemical Systems Laboratory
Fort Huachuca
Los Alamos Scientific Laboratory
JS Army Engineer Waterways Experiment Station
JS Army Cold Regions Research & Engineering Laboratory
JS Army Engineer Topographic Laboratories
IS Army Coastal Engineering Research Center
IS Army Construction Engineering Research Laboratory
ECTORS
S Army Human Engineering Laboratory
S Army Materiel Systems Analysis Activity
S Army Ballistic Research Laboratory
S Army Logistics Center
S Army Concepts Analysis Agency
S Army Applied Technology Laboratory
S Army Acquisition Information Systems Agency
S Army Research & Technology Laboratories (USARTL), Ames Research Ctr
Applied Technology Laboratory, USARTL, Fort Eustis, VA
Structures Laboratory, USARTL, Langley Research Center, Hampton, VA
Propulsion Laboratory, USARTL, Lewis Research Center, Cleveland, OH
wrence Livermore Laboratory

Large Caliber Weapons Laboratory
Night Vision & Optics Laboratory
Benet Weapons Laboratory

PROJECT MANAGERS

Army Tactical Data Systems (ARTADS), Fort Monmouth
Remotely Monitored Battlefield Sensor Systems (REMBASS), Fort Monmouth
Army Tactical Communications Systems (ATACS), Fort Monmouth

SUPERINTENDENT

US Army Military Academy, ATTN: Technical Library
US Army Military Academy, ATTN: Acquisition Branch

COPIES FURNISHED:

Office, Under Secretary of Defense for Research & Engineering
Office, Deputy Director for Science & Technology, Defense Nuclear Agency
Chairman, Defense Science Board
Defense Advanced Research Projects Agency
National Security Agency
Institute for Defense Analysis
Defense Communication Engineering Center
Defense Communication Agency
Defense Science Board
Assistant Chief of Staff for Intelligence
Scientific Advisor, Code RD, HQ US Marine Corps
HQ, National Aeronautics & Space Administration (Code W)
National Bureau of Standards
National Science Foundation
National Academy of Sciences
National Institutes of Health
Office of Naval Research (Code 230)
Office of Naval Research (Code 102)
US Naval Research Laboratory (Code 2627)
Director, Naval Research Laboratory
Air Force Office of Scientific Research
Air Force Systems Command
Air Force Institute of Technology
Southwest Research Institute
Director, Mathematics Research Ctr, University of Wisconsin, Madison
Commandant:
National War College
Industrial College of the Armed Forces
Academy of Health Sciences
National Defense University
US Army Field Artillery School
US Army Reserve Components Personnel & Administration Center

P R O C E E D I N G S

O F T H E

1978 ARMY SCIENCE CONFERENCE

UNITED STATES MILITARY ACADEMY, WEST POINT, N.Y.

20 - 22 JUNE 1978

V O L U M E III

Principal Authors N through Z

All experiments involving live animals that are reported in the Proceedings were performed in accordance with the principles of laboratory animal care as promulgated by the National Society of Medical Research

TABLE OF CONTENTS

PROCEEDINGS OF THE 1978 ARMY SCIENCE CONFERENCE

AD-A056470

DEVELOPMENT OF A SYSTEMATIC METHODOLOGY FOR THE APPLICATION OF JUDGMENTAL DATA TO THE ASSESSMENT OF TRAINING DEVICE CONCEPTS

MARSHALL A. NARVA, Ph.D.
U.S. ARMY RESEARCH INSTITUTE FOR THE BEHAVIORAL AND SOCIAL SCIENCES
5001 EISENHOWER AVENUE
ALEXANDRIA, VIRGINIA 22333

Concurrency of development of the training subsystem is rapidly becoming a key concept in the development of new materiel systems. The development of the training subsystem must occur concurrently with that of the prime system, in order to meet the objective of having a total system operational when it is fielded. This requires that the development of the training subsystem commence early in the life cycle of the prime system, i.e., in the conceptual stage. Towards this end a number of activities concerned with concurrent training development have been outlined in such documents as DA Pamphlet 11-25, the Life Cycle System Management Model (13). These activities include the identification of requirements for training devices. Once a decision has been made that a training device is required (and there is an increasing impetus towards utilization of training devices), the training device concept or alternative concepts must be evaluated.

Due to the time constraints pushing in from the deadlines associated with the ongoing system development, the training developer must make decisions or judgments early on in the process, when information available from the prime system development may be sketchy. While the development of the training device concept must commence as soon as possible in order to meet the required deadlines, particularly on long lead-time items, "bending of metal" for prototypes cannot begin before the design freeze of the pertinent segment of the prime system. Therefore, assessment of training device concepts becomes more dependent upon the use of analytical as opposed to empirical assessment techniques. Also, the rising costs associated with the development of such devices gives rise to an increased requirement for development of a systematic methodology for the assessment of such concepts.

One methodological tool, or decision aid, which has been developed to assist in making such judgments is known as TRAINVICE. The original model was developed for the Army Research Institute and was based upon an extensive literature review and analytical work by a team of experienced behavioral scientists (15, 16, 17). A revision of this model based upon experience gained in its utilization and which we may call TRAINVICE II, is being developed with the aims of increasing the practicality and flexibility of its application and making the methodology more amenable to utilization by a wider spectrum of users (9). This paper will concentrate on the rationale for TRAINVICE II and the difficulties involved in the development of a practical model which provides for incorporation of the variable experience and personal judgmental factors of the training developer or analyst vis-a-vis available recommendations or guidance.

TRAINVICE II

Essentially the model provides a framework for asking three questions concerning a training device concept. As given in Figure 1, these are, "What," "Why," and "How." These three questions are asked for each unit of behavior that is being trained by the device. A training device represents a cluster of activities, which become better defined as the concept becomes better defined. This may take the form of definition at the task, subtask, or skill/knowledge level, which represents the component physical and mental activities involved. Such a model as this is best utilized when information is available to the finest meaningful level of detail, as the required judgments can be made more accurately. However, an attempt is being made to have the model accommodate information at a more molar level in order to initiate analysis as early as possible in the development cycle. (A corollary requirement is imposed upon the meteriel developer to make detailed information available as soon as possible to meet the needs of the training developer.)

In order to answer the question of "what" is to be represented in the training device, two judgments are required. The first deals with the requirement for the unit of activity to be represented in the device, while the second ascertains if that unit is covered. These two judgments together have as their objective the determination that the spectrum of activities covered neither exceeds that which is necessary nor leaves out any that should be covered.

The "why" question component deals with a more detailed "defense" of the reason for including the unit of activity which was deemed to be necessary in the previous judgment and which is indeed included, or is to be included, in the device. This assessment is

WHAT

Coverage Requirement

Should this unit of activity be represented in the device?

Coverage

Is this unit of activity represented in the device?

WHY

Training Criticality

What level of proficiency is required in this unit of activity?

Training Difficulty

How difficult will it be to train for this unit of activity?

HOW

Physical Characteristics

How well do the physical characteristics of the device involved in training for this unit of activity meet the perceived requirements and applicable guidelines?

Functional Characteristics

How well do the functional characteristics of the device involved in training for this unit of activity meet the applicable guidelines?

Figure 1. Judgments made in TRAINVICE II

performed relative to two aspects; Training Criticality, which relates to the degree of proficiency required at the end of the training, and Training Difficulty, which considers the degree of difficulty to be expected in training to reach the desired level of proficiency. When these factors are assessed quantitatively, these judgments in essence give a weighting to each required unit of activity covered by the device. It should be noted that the decisions concerning "what" may have to wait upon or be changed by feedback from the decisions concerning "why" an activity unit should be included in the device, depending upon the stage of development of the device concept.

The first two questions dealt with an assessment of the spectrum of activities to be covered by the device, and not with how these activities were to be taught or conveyed by the device; the last question "how" deals with this aspect. The "how" question considers two aspects; do the physical characteristics of the device follow available guidelines of "good practice" and do they fit the perceived requirements of the training device developer, and are these physical characteristics utilized in keeping with available guidelines for "good practice"; are their functional characteristics such as to make for good training?

The assumption is being made that the potential for transfer of training will increase as a function of the degree to which the required activities, physical and mental, are represented in the device and the degree to which the training device follows "good" practice in training in these activities. In addition, each of the activity units is appropriately weighted by the degree of skill required and the degree of difficulty involved.

At this point it may be well to discuss the utilization of the model for both prescriptive and predictive purposes. It is hoped that such a model as TRAINVICE II can be utilized for both purposes, in keeping with the objective of utilization as early as possible in the development cycle. A prescriptive utilization would be for the a priori formulation of the training device concept; predictive utilization would be the application of the model to an existing training device concept or prototype to predict the effectiveness of transfer of training which is to be expected through use of the device. When information is incomplete, due to the stage of development of the prime system or the training subsystem, the prescriptive mode takes on added importance. This aspect will be touched upon as we now go through the model in more detail.

Coverage requirement analysis. The first judgment to be made is whether each of the skills (or knowledges) subsumed under the

training objective should or should not be included in the training situation. Depending upon the stage of development of the training device, this analysis may help to delineate the range of skills to be represented in the device (the prescriptive mode), as well as assessing the range of skills represented in a device (the predictive mode). The judgments may be recorded simply in the form of a checklist, or, if a quantitative prediction is to be attempted, through the use of 1 or 0, to indicate a requirement for a skill/knowledge, or lack of a requirement, respectively. This analysis is a "gate" only; it determines if the skill should be represented in the training.

Coverage Analysis. The second judgment is made by comparing the skills which have been judged to be required to be included in the training with those that indeed are included in the training device concept. This judgment may not be possible to make in the prescriptive mode, before a training device concept is formulated; however, it could take the form of a checklist to be utilized as the concept takes form, to ensure that all the required skills are included. In the predictive mode, when an existing concept is being assessed, a "1" may be assigned rather that a checkmark, and a "0" utilized, rather than a lack of a checkmark, in order to feed into the overall index of predicted training device effectiveness which will be subsequently derived.

If the coverage requirement rating is "1" and the coverage rating is "0," this would indicate that training in this skill is lacking and steps should be taken to include it or the device will suffer in its overall rating. On the other hand, if the coverage requirement rating is "0" and the coverage rating is "1," this would indicate that unnecessary training is being provided and should be eliminated from the device, or its overall rating will also suffer.

Training Criticality Analysis. For each of the skills that have been judged to be necessary to be represented in the training situation and are indeed represented, a judgment is made as to the degree of proficiency required in that skill at the end of training. In the predictive mode, for the assessment of an existing concept, the following rating scale, adapted from Demaree (3), is used:

1 Should have limited knowledge of subject or skill
2 Should have received complete briefing on subject or skill
3 Should have understanding of subject or skill to be performed
4 Should have complete understanding of subject, or be highly skilled

In making this judgment, the analyst must take into account the nature of the skill and the degree to which the training will be supplemented by subsequent on-the-job training.

This rating could also be used in a prescriptive mode, in making decisions concerning which of the skills is to be represented; in working back to the coverage requirement decision.

Training Difficulty Analysis. In addition to assessing the level of proficiency required for each of the required skills, a judgment is made of the degree of difficulty which is to be expected in attaining that level of proficiency, for the particular skill and trainee population involved. In the predictive mode, the following rating scale, adapted from that of Rankin (11), is used:

1 Minimal or none
2 Some
3 Much
4 Substantial

The various factors which must be considered by the analyst in making this decision are not explicitly delineated or extracted for judgment, but must be integrated into the judgmental process. These factors are the required level of proficiency, the level of skill existing in the trainee, and the inherent level of difficulty of the activity per se. The analyst must rely upon his own experience or knowledge concerning the difficulty involved in training the various skills or rely on others who do have the experience, or attempt to extrapolate from available knowledge concerning related skills.

As was the case for training criticality, this rating may be used in a prescriptive mode, in making decisions concerning which of the skills are to be represented; in working back to the coverage requirement decision.

Physical Characteristics Analysis. Having considered what skills are covered by the training device concept, and why, we now turn to a consideration of how these skills are to be taught. The first judgment in this respect is that concerning the physical characteristics of the device.

A training device may be considered to be a mosaic of specific elements, be they displays, controls, inputs, outputs, or cue-response pairs. These elements may be likened to the simulation elements proposed by Smode (12), with the configuration and operation of the training device determining the spatial placement and temporal

sequencing of the elements. As Matheny (8) has pointed out, the assumption may be made that it is perceptual equivalence that results in positive transfer from the training to the operational situation, and it is the adequacy of these simulation elements in terms of perceptual or psychological equivalency, not physical equivalency, which must be judged. The total training device, and indeed each of the elements embedded in that mosaic, may be considered to lie within a space defined by the dimensions of fidelity and abstraction. Levels of abstraction range from the real world to mathematical models representing dynamics taking place in that world, they are analogies of the real world, while fidelity varies as to the comprehensiveness and level of detail to which the external world is represented (5, 10). In order to deal with the multiplicity of degrees of abstraction and fidelity with which training devices may clothe themselves, it was deemed necessary to translate the specific simulation elements into generic characteristics. This brings the number of specific possible forms that each element may assume into manageable proportions and provides for a common base upon which to make the required judgments concerning the stimuli and responses, or physical characteristics of the training device. Such a listing has been taken from that given in the TECEP technique of Braby, et al (2), and is shown as Figure 2.

The analyst must make a judgment as to what generic characteristics are required and rate the existing generic characteristics against this criterion. In order to make this judgment, he must draw upon his own perceived requirements for each of the elements, or turn to others, either directly or through reference to available guidelines, or both. Some guidance may be gleamed from the literature. However, a simplified version of the Aagard and Braby guidelines which is utilized in the ISD model (1, 14) appeared most suitable and has been adapted for use with the TRAINVICE II model to give some guidance to the analyst in making the judgments concerning the physical characteristics, in conjunction with his own perception of the requirements. However, these guidelines were intended for utilization in instructional system development and instructional delivery system or media selection, and not for scrutiny of specific aspects of a training device. The development of more specific guidelines is needed. These guidelines deal for the most part with functional aspects of the training situation, such as the sequencing of learning events. However, selected guidelines may be extracted as being applicable to the design of specific elements of the training device or situation.

The procedure followed in performing the physical characteristics analysis is shown in Figure 3. For most effective utilization of the model, task information down to the skill/knowledge

STIMULUS CAPABILITIES

Visual Form

1. Visual Alphanumeric
2. Visual Pictorial, Plane
3. Visual Line, Plane
4. Visual Object, Solid
5. Visual Environment

Visual Movement

6. Visual Still
7. Visual Limited Movement
8. Visual Full Movement
9. Visual Cyclic Movement

Visual Spectrum

10. Black and White
11. Gray Scale
12. Color

Scale

13. Exact Scale
14. Proportional Scale

Audio

15. Voice Sound Range
16. Full Sound Range
17. Ambient Sounds

Other

18. Tactile Cues
19. Internal Stimulus Motion Cues
20. External Stimulus Motion Cues

TRAINEE RESPONSE MODES

21. Covert Response
22. Multiple Choice
23. Pre-programmed Verbal
24. Free-Style Written
25. Decision Indicator
26. Voice
27. Fine Movement Manipulative
28. Broad Movement Manipulative
29. Tracking
30. Procedural Manipulative

Figure 2. Generic Characteristics List

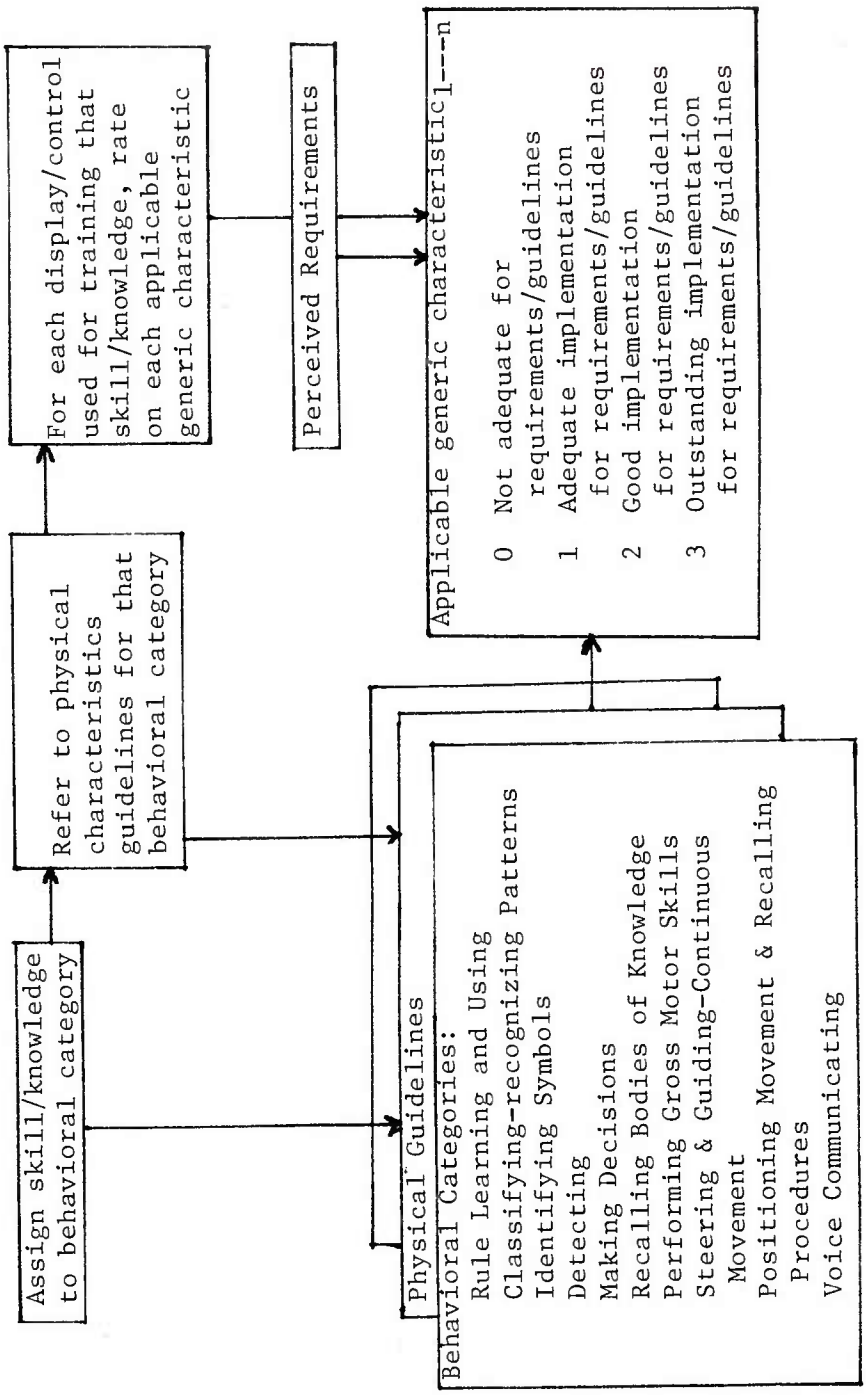

Figure 3. Physical Characteristics Analysis

level should be available. The reason for this is that the guidelines are accessed through means of behavioral categories; there is a different set of guidelines for each of the behavioral categories, and the skill/knowledge involved must be translated into a behavioral category. If an analysis is done at the subtask level, more than one behavioral category may be involved and more guidelines must be considered. Also, for each of the skills, information concerning the displays and controls involved in implementation of that skill should be available, as it is the generic characteristics of these controls and displays which are to be assessed. In the predictive mode, each of the generic characteristics associated with each of the displays or controls (or cues and responses) is rated using the scale shown in Figure 3. Therefore, each of the displays or controls, or physical characteristics, receives a physical characteristics score which is the total of the ratings given on the applicable generic characteristics. In addition, the maximum rating is given for each of the applicable parameters in order to provide a base for assessment of the device in the index subsequently calculated. The pattern of these ratings may serve to "highlight" the various physical characteristics of the device, both those that are outstanding and those that need change. In addition, each of the characteristics may require a justification in order to control for the introduction of unneeded features. In order to derive the Physical Characteristics rating for the skill involved, the ratings given on each of the displays or controls are added to give the total for that skill. Therefore, the presence of a "0" rating does not eliminate that skill from the total rating but does serve to downgrade the total rating for the skill and subsequently for the device.

If information concerning the specific characteristics of the displays or controls involved is not available due to the stage of development, the ratings may fall back to a prescriptive mode, in which the desired generic characteristics, possibly through use as a checklist, are chosen, in lieu of performing an assessment of existing generic characteristics. This is a similar procedure to that utilized in the TECEP technique of Braby et al (2). The TECEP technique gives recommendations as to which delivery system, including generic classes of training devices, permit the application of the learning guidelines for each of the behavioral categories; recommendations based upon the pattern of matching of the generic characteristics inherent in the various delivery systems and those judged necessary by the analyst. Jorgensen (6, 7) has utilized a similar matrix approach in which the generic characteristics judged as being required are matched against various media, of which training devices are one class, in order to select training media most suitable for training various tasks. However, these procedures are intended for the selection of or comparison

of various media or instructional delivery systems rather than the scrutiny of a training device per se or comparison of training devices.

Functional Characteristics Analysis. While the physical characteristics analysis is concerned with the analysis of the elements of the training device per se, the functional characteristics analysis is concerned with how these elements are utilized. The operation of the device is compared against guidelines to ascertain to what extent "good" training practices are followed. Once again, these guidelines are those extracted from the ISD model (14).

The procedure followed in performing the functional characteristics analysis is shown in Figure 4. As with the physical characteristics analysis, each of the skills is translated into a behavioral category, which dictates which set of guidelines is to be utilized. The set of guidelines is consulted as the functional, dynamic characteristics of the elements involved in training for that skill are considered. In the predictive mode, each of the guidelines judged to be pertinent to the particular situation involved is rated, using the scale shown in Figure 4. A judgment is made to the extent that that guideline is implemented by the functioning of the cluster of elements used to implement training for that skill. In order to derive a Functional Characteristics rating for the skill, the ratings are added to give the total for that skill. Therefore, the presence of a "0" rating does not eliminate that skill from the total device rating, but does serve to downgrade the rating for the skill, and subsequently of the device, and may also serve to "flag" some aspect that needs to be corrected. In addition the number of applicable guidelines are multiplied by "3," the highest possible rating, to give a baseline against which the derived rating may be compared in the subsequent device index.

If sufficient information is not available to make the required ratings, the procedure may revert to the prescriptive mode, in which the applicable guidelines are selected, and utilized as a checklist for the development of the training device concept. If the analysis must be performed at the subtask level, then more guidelines must be sorted out and consulted, as a larger unit of activity is involved, which may encompass more than one behavioral category.

Derivation of Index of Predicted Training Device Effectiveness. In the predictive utilization of the model, an index is derived. This index follows a procedure discussed by Gagne, Foster and Crowley (4). While not based on one of their formulas directly, it is in keeping with their conclusion that the most useful and

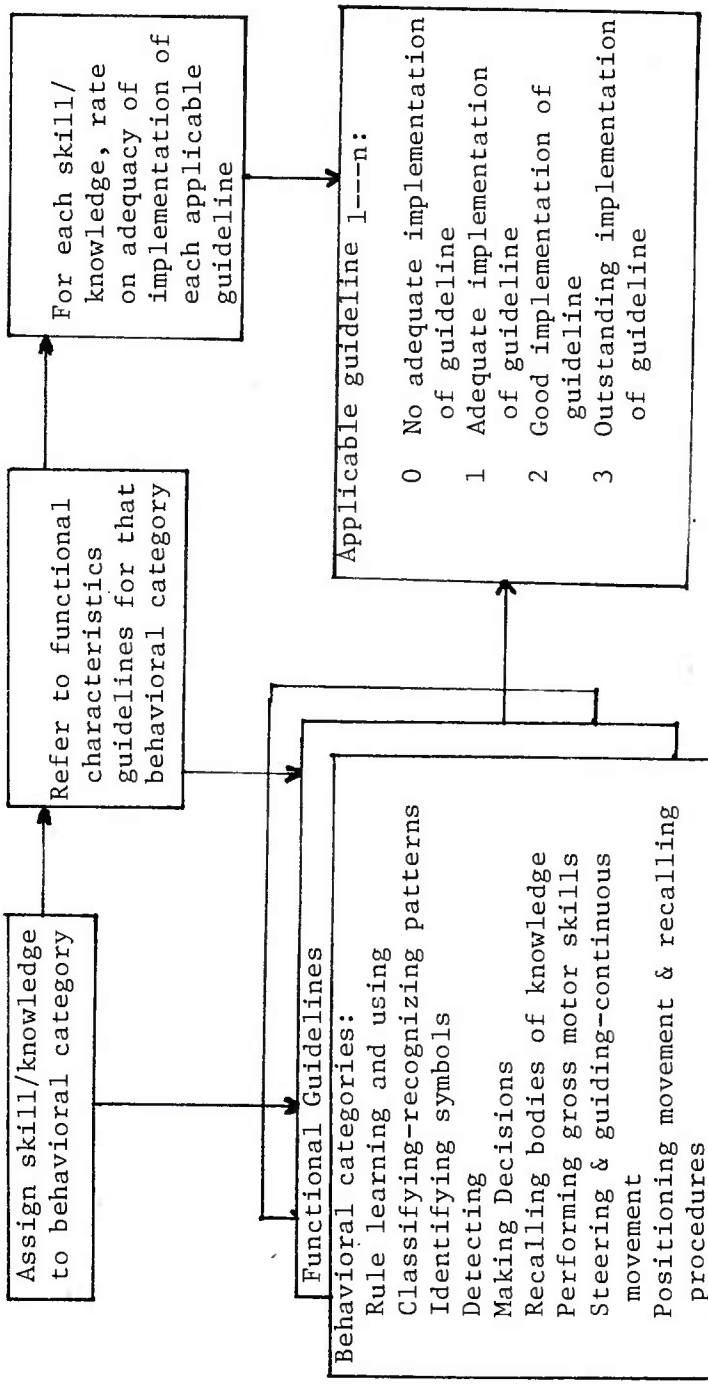

Figure 4. Functional Characteristics Analysis

practical type of formulation is that based on percentage of maximum possible transfer. It assumes that if the device were to follow perfectly all of the guidelines, as judged necessary by the analyst, that maximum transfer, which could be attributed to the device, would be the result. This forms the baseline against which the device under evaluation is compared. This score is weighted by the Coverage Requirement, Coverage, Training Criticality and Training Difficulty scores derived for that skill. The derived score for each skill is compared with the score representing maximum expected transfer. (If a "0" rating is given for either the Coverage Requirement or Coverage Analysis, the total score for that skill is reduced to "0" and makes no contribution to the derived index for the device.) To derive the score for the total device, each of the skill scores is added. Therefore, the index of predicted training device effectiveness is as follows:

$$\frac{\Sigma(CR \times C \times Ci \times D \times (PC + FC))i}{\Sigma(CR \times C \times Ci \times D \times (PC_{max} + FC_{max}))i}$$

where:

CR	Coverage Requirement Score
C	Coverage Score
Ci	Training Criticality Score
D	Training Difficulty Score
PC	Physical Characteristics Score
FC	Functional Characteristics Score
PC_{max}	Maximum Possible Physical Characteristics Score
FC_{max}	Maximum Possible Functional Characteristics Score for each skill.

This equation will yield an index ranging from 0 to 1. The larger the index, the larger the number of required skills represented and the higher were the ratings given on the Device Characteristics Analyses; therefore, presumably the greater the potential for transfer of training.

Conclusions

(1) Due to the increased emphasis on the concurrent development of training subsystems, the increased impetus towards the utilization of training devices, and the rising costs associated with the development of such devices, there is a need for the development of a systematic analytical methodology for the assessment of training device concepts which may be applied early in the development cycle of the materiel system.

(2) Such a methodology must permit the integration of the variable judgmental processes of the training developer and available guidance.

(3) A model has been described which provides a framework for the application of judgmental data concerning aspects of the training situation which have been hypothesized as having an impact upon the effectiveness of transfer from the training to the operational situation. Judgments are made concerning coverage of required skills, the weighting to be assigned to these skills from the aspects of training criticality and difficulty, and the effectiveness with which the physical and functional characteristics of the training situation follow guidelines of good practice.

(4) In order to apply such a methodology as early as possible in the development cycle, a prescriptive mode of utilization, concerned with assisting in the formulation of training device concepts, is provided for.

(5) There is a need for the development of more specific guidelines which may be applied to the assessment of training device concepts.

References

1. Aagard, A., and Braby, R. Learning guidelines and algorithms for types of training objectives. TAEG Report No. 23, U.S. Navy, Training Analysis and Evaluation Group, Orlando, FL, March 1976.
2. Braby, R., Henry, J., Parrish, W., and Swope, W. A technique for choosing cost-effective instructional delivery systems. TAEG Report No. 16, U.S. Navy, Training Analysis and Evaluation Group, Orlando, FL, April 1975.
3. Demaree, R. Development of training equipment planning information. ASD Technical Report 61-533, U.S. Air Force, Aerospace Medical Laboratory, Wright-Patterson Air Force Base, OH, October 1961.
4. Gagne, R., Foster, H., and Crowley, M. The measurement of transfer of training. Psychol. Bulletin, 1948, 45, 97-130.
5. Haythorn, W. W. Information systems simulation and modeling. Paper presented at First Congress on the Information System Sciences, Hot Springs, VA, November 19, 1962. (cited in Obermayer (10)).
6. Jorgensen, C. A methodology and analysis for cost-effective training in the AN/TSQ-73 Missile Minder. Army Research

Institute for the Behavioral and Social Sciences, Ft Bliss Field Unit, El Paso, TX, September 28, 1976.

7. Jorgensen, C. A method for cost training effectiveness analysis. Paper presented at Military Operations Research Symposium, Monterey, CA, 13-15 December 1977.
8. Matheny, G. Training simulator characteristics: Research problems, methods, and performance measurements. Proceedings, Aircrew Performance in Army Aviation, U.S. Army, Office of the Chief of Research, Development and Acquisition, July 1974.
9. Narva, M. Formative utilization of a model for the prediction of the effectiveness of training devices. Paper presented at Army Operations Research Symposium, Ft Lee, VA, 12 October 1977.
10. Obermayer, R. Simulation, models, and games: Sources of Measurement. Human Factors, 1964, 6, 607-619.
11. Rankin, W. Task description and analysis for training system design. Technical Memo 74-2, U.S. Navy, Training Analysis and Evaluation Group, Orlando, FL, January 1975.
12. Smode, A. Human factors inputs to the training device design process. Technical Report NAVTRADEVCEN 69-C-0298-1, Naval Training Device Center, Orlando, FL, September 1971.
13. U.S. Army, Life cycle system management model for Army Systems, DA Pam 11-25, May 1975.
14. U.S. Army, Interservice procedures for instructional system development. TRADOC Pam 350-30, U.S. Army Training and Doctrine Command, Ft Monroe, VA, August 1975.
15. Wheaton, G., Rose, A., Fingerman, P., Korotkin, A., and Holding, D. Evaluation of the effectiveness of training devices: Literature review and preliminary model. Research Memorandum 76-6, U.S. Army Research Institute for the Behavioral and Social Sciences, Arlington, VA, April 1976a.
16. Wheaton, G., Fingerman, P., Rose, A., and Leonard, R. Evaluation of the effectiveness of training devices: Elaboration and application of the predictive model. Research Memorandum 76-16, U.S. Army Research Institute for the Behavioral and Social Sciences, Arlington, VA, July 1976b.
17. Wheaton, G., Rose, A., Fingerman, P., Leonard, R., and Boycan, G. Evaluation of the effectiveness of training devices: Validation of the predictive model. ARI Technical Report TR-76-A2, U.S. Army Research Institute for the Behavioral and Social Sciences, Arlington, VA, October 1976c.

AD-A056471

EVALUATION OF DUAL-TEXTURE GRADIENT CAMOUFLAGE PATTERN

*MAJ TIMOTHY R. O'NEILL
MAJ JAMES M. BRUSITUS
CPT DAVID L. TAYLOR
CPT WILLIAM F. JOHNSMEYER
US MILITARY ACADEMY
WEST POINT, NEW YORK 10996

Recent trends in tactical doctrine for United States ground forces suggest the inevitability of "fighting outnumbered" in the unitial stages of the next war - a position of inferiority which increases as never before the need for the most effective training, doctrine and equipment. The battlefield of the 1980's will present new challenges for ground forces, and require a variety of passive and active counter-surveillance measures to allow tactical units to operate in an environment which combines not only very high weapon lethality but also improved target acquisition means. Maintaining favorable exchange ratios -- a fundamental supposition of the Active Defense -- will require the doctrine, training and hardware to counteract precision-guided munitions, protect headquarters units vital to battlefield control and communications, and insure initial advantage in tactical engagements. These advantages are unattainable without extremely effective countersurveillance measures.

Present measures include improved paints and coatings, lightweight multipurpose nets, thermal image suppression devices, and a standard concealment pattern. This pattern has been in use for several years, and has been applied successfully in a variety of units. The US Army (MERADCOM) pattern is a four-color standard pattern system which is designed to be supplemented with natural and artificial garnish for maximum concealment effect. This presents special problems in the Active Defense tactical scheme.

Nets and garnish-- including natural vegetation -- require set-up times which are generally proportional to the size and signature of the vehicle being camouflaged. Certain critical systems, however -- notably the XM1, MICV and Improved TOW Vehicle -- require not only the most astute camouflage measures, but also must meet the

requirement of rapid and frequent tactical movement. Without this mobility, such vehicles will rapidly become casualties in the intensely lethal battle areas. Complex net and disruptor kits, particularly those which require careful erection at the battle site and any more than a few seconds to store following the engagement and before further movement, will probably be discarded or simply remain stowed in most engagements. There is no value in deploying such measures if they will not be effective or are too much trouble to use under fire.

The Dual-Texture Gradient (Dual-Tex) pattern was designed by members of the Department of Behavioral Sciences and Leadership, US Military Academy, to fill the need for a practical, effective camouflage pattern measure which reduces the requirement for elaborate garnish kits. The Dual-Tex pattern uses two patterns: a macropattern of large light and dark areas which is indistinguishable from the standard US Army measure at long distances, and a micropattern of higher texture which resulves on closer observation or under optical enhancement and retains its texture and color match with the background. This effect is obtained by using color "bits" grouped together on a square grid; the large light-and-dark areas of the macropattern conform to the US Army pattern, the squares form a separate pattern within the macropattern. The observer perceives the macropattern at long range, at which its effect is comparable to that of the standard measure; at closer range (approximately 2000-1500 meters) the micropattern resolves, and the concealment value of the smaller pattern continues to provide concealment after the standard pattern has begun to form a signature of its own, easily observable without extensive garnish. (See figure 1.)

The pattern was developed for exploratory test using in-house US Military Academy resources. The research was conducted in two phases from September 1976 to June 1977; the first phase was a laboratory simulation, the second was an extension of the original objectives in a field environment.

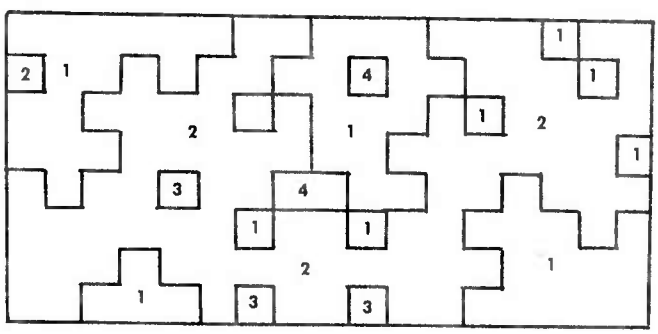

Figure 1:
Dual-Tex Pattern.
(Colors coded by number)

*O'NEILL, BRUSITUS, TAYLOR & JOHNSMEYER

Phase I: Summary of Laboratory Simulation

Objective. This preliminary phase was conducted to provide a rough comparison of the Dual-Tex pattern with the standard US Army pattern measure and a control (solid green) target in a controlled environment.

Method. Subjects viewed a series of 35mm color slides, phased at decreasing ranges, of targets placed in a woodline; the pattern measure was varied by subject group; Group A viewed the US Army pattern, Group B the Dual-Tex measure, Group C viewed a solid forest green control target. The dependent variable was in each case the distance from the target upon detection and at identification of the target shape.

Approximately 260 male cadets were used as subjects; each subject was presented only one target condition. The test targets were 4' x 8' panels; the stimulus photographs were phased at decreasing range intervals of 25 feet, from 675 to 75 feet. Subjects viewed the most distant first, least distant last, so that the apparent range of observation decreased uniformly. Distance from the target was expressed for scoring purposes as a slide number from 1 to 22.

The experiment was conducted in two parts -- a summer trial and a winter trial. Photographs were prepared in an open field with summer vegetation for the first and in a similar snow-covered field for the second. In the winter trials a fourth target was added, using an adaptation of the Swedish Army Pattern.

Results and Analysis. The results of summer and winter trials are summarized below, expressed as mean number of slides by group elapsed before detection (located a target of some kind) and identification (matched the target shape to one of four alternatives printed on a comparison card):

*Summer Trial	DETECTION	IDENTIFICATION	N
Group A (US Army Pattern)	11.97	14.22	38
Group B (Dual-Tex Pattern)	15.33	17.72	38
Group C (Control)	12.68	13.97	40

Groups A and C did not differ significantly in mean detection or identification scores; Group B (Dual-Tex) differed from Groups A and C in the predicted direction and beyond the .01 level of significance.

**Winter Trial:

	DETECTION	IDENTIFICATION	N
Group A (US Army Pattern)	10.95	11.59	44
Group B (Dual-Tex Pattern)	18.15	19.35	34
Group C (Swedish Pattern)	12.63	16.80	30
Group D (Control)	18.96	20.28	28

Group B differed significantly ($p < .05$) from Groups A and C, and in the predicted direction. Groups B and D, however, did not differ significantly, apparently due to special problems in the selection of the test site and the specific positions chosen for the targets.

The conclusions drawn from the initial laboratory phase were:

1. That the Dual-Texture Gradient pattern appeared to offer the potential for significant improvement over present measures in a variety of environments, and
2. That the Dual-Texture Gradient pattern required field validation.

*In the summer trial, group means were tested for significance by t-test.
**In the winter phase, group mean differences were tested by t-test; difference in means for groups A and D by Scheffé post-hoc comparison test.

Phase II: Field Evaluation

A field validation test was conducted by a research team from West Point, assisted by the US Army Human Engineering Laboratory, during May 1977 at Aberdeen Proving Ground, MD.

Objective. This phase was conducted in order to compare the standard US Army and Dual-Tex measures in a field environment, using an appropriate subject group representative of observers in a combat environment.

Method.

General. Selected subjects viewed a pattern-painted M113 target vehicle through the commander's sight of a Soviet T62 Main Battle Tank. One group viewed the target painted in the US Army pattern, the other the Dual-Tex pattern. Time to detection and correct or incorrect detection of the target type were recorded for each

subject.

Test Site. The experiment was conducted near Phillips Army Airfield, Aberdeen Proving Ground, Maryland. The site consisted of an open area several kilometers in length and approximately .8 km across, oriented approximately SW to NE and bounded on the SE by a hard-surface and a dirt road. The entire area was bordered by shrubs and low hardwood forest on all sides. The target vehicle was placed near the edge of a tree line at a distance of 926 meters from the observer vehicle. The distance of 926 meters represented the best compromise of the desired distance -- 1000 -- 1200 meters -- and the location of a slight prominence at the chosen range which provided excellent observation of the target area.

Subjects. Ten aviation warrant officers from assault helicopter units stationed at various posts were used; these were experienced pilots and trained observers who were on temporary duty with the US Army Human Engineering Laboratories. In addition, twenty-eight enlisted artillery observers from the 82d Airborne Division Artillery participated in the trials. All subjects were experienced observers and were trained in vehicle recognition. The ten pilots were used in both experimental conditions; the other subjects viewed only one pattern each.

Target Preparation. The target vehicle was viewed in two conditions: the US Army pattern and the Dual-Tex pattern. Natural garnish was applied in each case to the front, commander's station and ventilator dome. The garnish was placed in these locations because the test controllers believed that the glare would create an overwhelming signature.

Test Procedures.

1. Each subject was positioned in the commander's station of the T62 observer vehicle, standing on the turret floor and facing towards the TKN3 commander's sight; the controller was seated in the gunner's position where he could observe the subject and the gunner's azimuth indicator.

2. Each subject was briefed by the controller on the use of the TKN-3 sight; the turret was deflected to the left of the target area so that the sight was aimed at a prepositioned orange panel downrange. The subject was coached by the controller in adjusting the distance between the binocular eyepieces for comfort and focusing the diopters for clear observation.

3. The subject was briefed on the procedures for the test itself:

The height choke reticle in the lower portion of the field of view of the sight was used as the reference point for identification; the range markings 8 - 30 (representing 800 to 3000 meters) were used for this purpose. The subject was instructed to search for any military target, type unspecified, which would be located somewhere between the 8 and 30 range lines of the choke reticle. After explaining the procedures, the controller asked the subject to be seated on the turret floor while the commander's sight was being re-layed in the target area.

Using the gunner's azimuth indicator, the controller laid the main gun roughly on the target. He then looked through the commander's sight to make final adjustments and insure that the lay of the sight was correct and note the reticle number which was at the center of mass of the target. This was necessary because the turret traverse was somewhat erratic on the observer tank and the commander's sight could not be aligned properly using the main turret azimuth indicator. This method proved to be an additional control measure because a different range line was used to indicate center of mass for each subject. This eliminated the chance of subjects detecting the target because they had overheard a correct detection or by having a previous subject tell them the correct range line number.

The controller then re-engaged the infrared filters and quickly reviewed the procedures and asked for any questions the subject might have. When the subject was ready to begin, he took a comfortable position at the sight; the controller removed the filter and started his timer at the same moment.

When the subject said "stop," the controller stopped the timer and asked the subject to verify the target by supplying the reticle number at center of mass. If the number was incorrect, the controller checked the sight to insure that the cupola had not slipped during the search. If the detection was incorrect, the procedure was begun again and the time restarted. If no correct detection occurred within 60 seconds, the attempt was terminated.

When and if correct detection occurred, the controller asked the subject what the target appeared to be. The identification (such as "APC," "vehicle," etc.) was noted and the subject released.

After completion of the exercise, selected subjects (the warrant officers who had viewed both pattern conditions) were individually briefed on the nature of the experiment and their subjective comments were recorded with respect to comparative effectiveness of the US Army and Dual-Tex patterns. These comments were not

recorded for the other subjects, since they only saw the target in one of the two conditions and had no basis for comparison.

Results and Analysis.

Mean time-to-detection was computed for both test conditions; in cases of no detection within 60 seconds, a detection score of 60 was recorded; this was a conservative measure which allowed inclusion of all scores at the cost of inducing skewness in the sample distributions. In the sample groups, there were 9 such cases for the Dual-Tex condition and 3 for the US Army pattern; consequently, this tended to bias in favor of the US Army pattern. The experimenters accepted this bias as unavoidable.

The population parameters for observing the target patterns at a range of 926 meters were estimated. The mean score parameters estimated are listed below:

μ_{1D} - US Army Pattern Detection Mean Score.
μ_{2D} - Dual-Tex Pattern Detection Mean Score.

Observed target detection means, standard deviations and sample sizes are shown below:

	Mean (seconds)	Standard Deviation	n
US Army Pattern	22.32	20.88	23
Dual-Tex Pattern	40.35	19.74	25

Observed target detection means were t-tested; mean detection scores differed in the predicted direction beyond the .01 level of significance.

The simple difference in mean time to detect may, however, be misleading in certain practical aspects. The writers consider the likelihood of an enemy observer in a vehicle having leisure to observe one area of expected enemy activity for up to 60 seconds at 1000 meters without grave risk rather low (see discussion in paragraph below); for this reason, an observed-time hypothesis was used to show comparative effectiveness of the two patterns over time of exposure. The prediction specifies a critical span of exposure time during which the Dual-Tex pattern should demonstrate improvement over the US Army measure; common sense dictates that as exposure time approaches zero, probability of detection will likewise approach zero, and that, given sufficient exposure time, virtually all observers will detect. The rough prediction is shown

below:

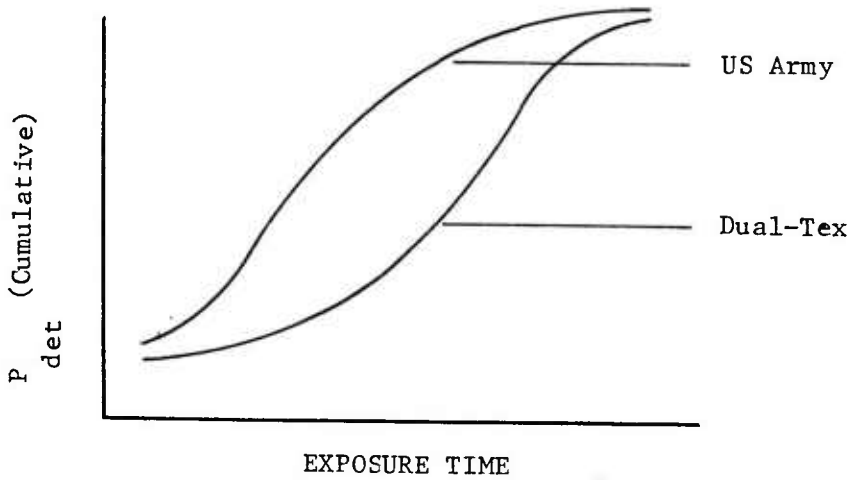

Figure 2

The observed probabilities of detection versus time are shown below:

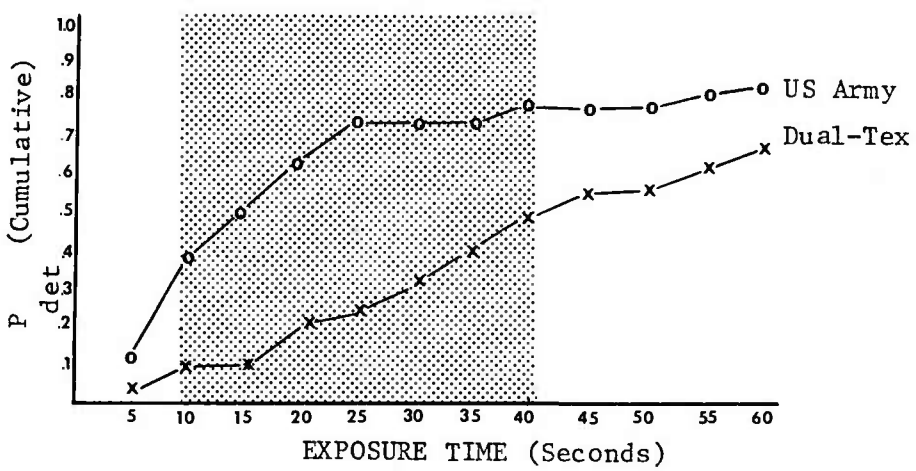

Figure 3

TABLE 1

SUMMARY OF PEARSON CHI-SQUARE TESTS OF ASSOCIATION FOR HYPOTHESES:

$H_0 : p(A_j, B_k) = p(A_j)p(B_k)$

$H_1 : p(A_j, B_k) \neq p(A_j)p(B_k)$

Time (seconds)	Chi-square Value	df	Result
5	.37	1	Accept H_0
10	4.93	1	Reject H_0 *
15	9.28	1	Reject H_0 **
20	6.68	1	Reject H_0 **
25	8.35	1	Reject H_0 **
30	5.49	1	Reject H_0 *
35	4.31	1	Reject H_0 *
40	4.53	1	Reject H_0 *
45	2.55	1	Accept H_0
50	2.55	1	Accept H_0
55	1.97	1	Accept H_0
60	2.25	1	Accept H_0

Where:

A=pattern attribute (US Army or Dual-Tex)
B=detection attribute (detection or no detection)
$p(A_j)$ = probability of occurance of event A_j

$p(B_k)$ =probability of occurance of event B_k

$p(A_j, B_k)$ = probability of occurance of the joint event (A_j, B_k)

* $p < .05$; ** $p < .01$.

Hypotheses of independence of camouflage pattern and target detection distributions at a specific point in exposure time elapsed were evaluated using the Pearson chi-square test for association. The hypotheses and results are listed at Table 1.

Discussion.

Since the Dual-Tex pattern is designed to fill a specific tactical requirement, the demonstration of higher performance without discussion of tactical impact is not of significant interest. The analysis of detection probability against exposure time, however, allows some speculation on the contribution of the experimental pattern in a modern combat environment. The shaded portion of figure 3 shows the time span in which a significant difference between Dual-Tex and the US Army pattern can be demonstrated.* This encompasses the exposure times 10 - 40 seconds; a period which probably brackets the most reasonable time required for an enemy to acquire, engage and destroy a target at the 1000-meter range tested. Hence the writers suggest that the demonstrated exposure times at which Dual-Tex offers a clear advantage are those of the most critical tactical significance. The 1000-meter range zone is generally accepted as the most likely engagement range for United States units in the European theater.

The subjective comments of the subjects who viewed both pattern conditions were uniformly favorable. These subjects were the attack helicopter pilots; since they were trained observers and gunners with considerable experience in target detection and engagement, they were considered the most credible source for qualitative critique. They were enthusiastic in their evaluation of the Dual-Tex pattern; two commented that, had they not been used to the procedure and prepared for the general target size and shape from the previous afternoon's iteration with the US Army pattern, they would not have seen the experimental pattern at all.

*The elegant consistency of the curves suggests that, had the sample size been sufficiently large, significance might have been demonstrated for the entire time range. However, the upper time span difference would, as discussion indicates, be relatively unimportant.

The writers prepared the site for test and photographed the target vehicle at various distances. At the time the photographs were taken the sun angle was most favorable for pattern effectiveness (this was at 1430, the same time that the artillery observer group which viewed the US Army pattern was tested). Under these conditions the target was almost indistinguishable despite the close range and very modest garnish. (See photographs below.) The reader will appreciate the difficulty the subjects experienced viewing the target from 926 meters, through low-magnification optics and under less favorable light conditions.

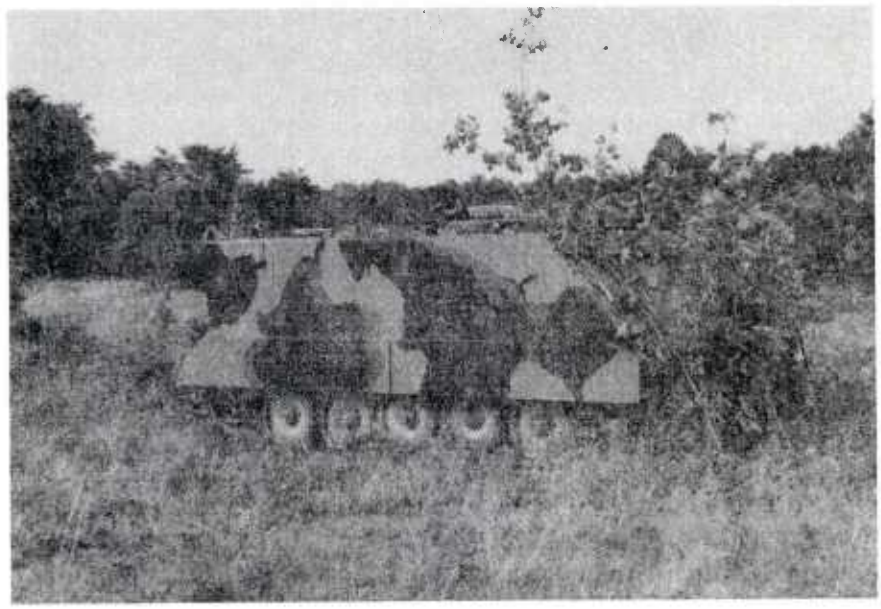

Photograph 1: US Army Pattern test vehicle.

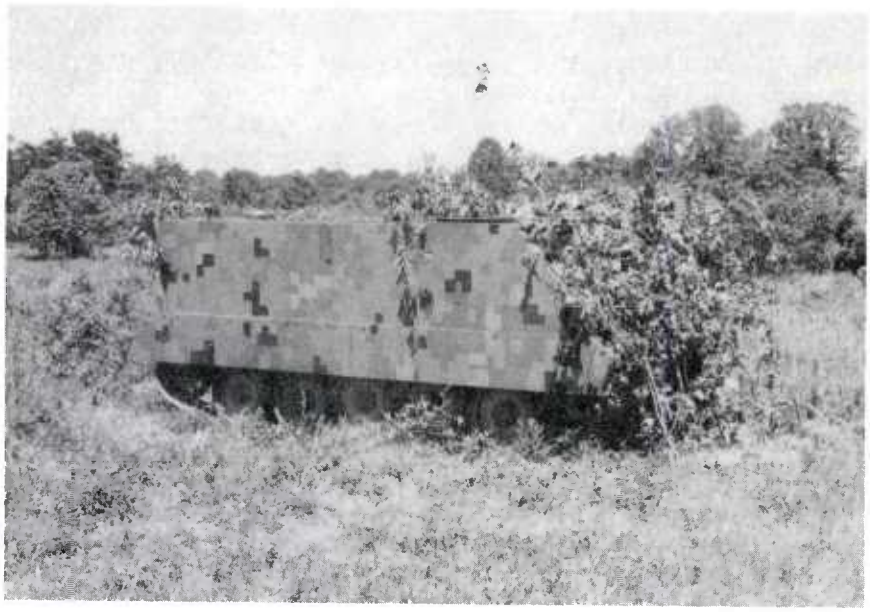

Photograph 2: Dual-Tex Pattern test vehicle.

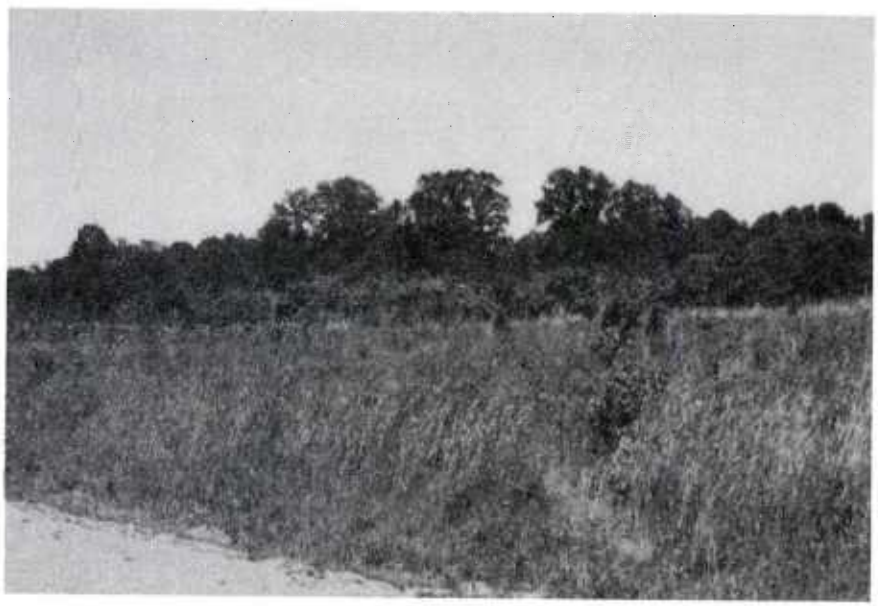

Photograph 3: Dual-Tex test vehicle at 75 m.

It is necessary to note at this point that the subjects' performance was to an extent at the mercy of the Soviet TKN-3 commander's sight. This is a panoramic sight of relatively low magnification; the example on the T62 used in the test did not speak well of Soviet optics in general. A particularly troublesome factor was the thickness and complexity of the stadia reticle. A US M60A1 had been positioned alongside the T62 for comparison purposes, and the reticle scribing on the US vehicle's sights was petite by comparison; the Soviet reticle actually blocked the observer's view. The writers are all familiar with the M48A3, M60A1 and M551 (and in one case the M60A2 and M60A1E3) sights, and were experienced tank commanders, and found this characteristic of the T62 sights bothersome. This is presumably considered an acceptable tradeoff given the close engagement ranges suggested by threat doctrine. The writers conclude that the crudeness of the sight also influenced the test results. However, the effect of the poor sight was uniform for both pattern conditions, and the objective of the test was to simulate enemy, not friendly, ability to detect targets. In this respect the objectives were admirably fulfilled.

Conclusions.

1. That the Dual-Tex pattern demonstrated a significant improvement in concealment effect over the standard US Army pattern under the field conditions tested.

2. That the exposure times in which significant improvement was demonstrated and the simulated engagement range match those conditions which may be tactically significant.

References. For further information consult:

O'Neill, et al. Dual-Tex: Evaluation of Dual-Texture Gradient Pattern. United States Military Academy, April 1977.

O'Neill, et al. Investigation of Psychometric Correlates of Camouflaged Target Detection and Identification. United States Military Academy, May 1977.

O'Neill, Brusitus, Taylor and Johnsmeyer. Dual-Tex II: Field Evaluation of Dual-Texture Gradient Pattern. United States Military Academy, July 1977.

AD-A056472

MOLECULAR STUDIES OF THE MECHANISM OF SHOCK INITIATION OF SOLID EXPLOSIVES

*F.J. OWENS, PhD, J. SHARMA, PhD
D.A. WIEGAND, PhD
ENERGETIC MATERIALS DIVISION, LARGE CALIBER WEAPON SYSTEMS LABORATORY, ARMAMENT RESEARCH AND DEVELOPMENT COMMAND
DOVER, NEW JERSEY 07801

INTRODUCTION: Although it has been long known that certain materials, when subjected to the stimuli of shock or heat, undergo rapid exothermic reaction having wide military and civilian technological application, there exists almost no understanding on the molecular or atomic level of the explosive phenomena. Such a situation is detrimental to the progress of explosive technology. A fundamental understanding establishing the relationship between the molecular or atomic parameters such as the electronic and vibrational energies, and such macroscopic behavior as explosive yield and sensitivity would have a significant impact on the use of explosives. The possibility of constructing new explosive formulations by modification on the molecular level could be envisioned. New methods of initiation could be developed, giving the user more precise control.

There has been a considerable amount of research on the effects of shock pulses on explosives, but the approach has emphasized a continuum mechanics model of the explosive, viewing the explosive as a fluid rather than an array of quantum particles capable of chemical interaction. Although useful in predicting many explosive properties, the approach has lead to no fundamental understanding of the explosive process.

Only very recently has there been discussion of possible microscopic mechanisms which address the question of how a shock impulse can initiate rapid exothermic chemical reactions that lead to detonation.(1) One plausible proposal envisions the shock wave breaking molecular bonds of the constituent molecules of the con-

densed explosive producing radicals, highly reactive molecular fragments with net unpaired electron spin.(1) Since this process is endothermic, the necessary exothermic reactions are viewed as occurring between the secondary products that are produced. Detonation would be achieved when a sufficient number of these products are available so that the released energy can cause further reaction and the process can become self-sustaining. It has also been proposed that there are localized regions of high concentration of decomposed products called "hot spots".(2) These hot spots are thought to occur when the rate of production of heat from the exothermic secondary reactions in this localized region exceeds the rate at which heat can be conducted away from the site.

Although it is well known that a shock pulse can break the bonds between the constituent molecules of the solid, there is prior to this work, no evidence that a shock wave can break an intra molecular bond of an explosive molecule. Since such a possibility would have important implications concerning the microscopic mechanism of explosive initiation, experiments were undertaken to study shocked explosives with a number of techniques which would yield information on the atomic or molecular level. The specific objectives were to; determine if a shock pulse could break an intra molecular bond of the component molecules of a solid explosive; to identify the specific bonds broken, and to specify the decomposition products and determine if radicals are produced.

EXPERIMENTAL APPROACH: Solid samples of ammonium nitrate, (AN), 1,3,5, trinitro-1,3,5, triazacyclohexane, (RDX) and trinitrotoluene, (TNT), all explosives used in various military formulations, were subjected to shock pulses of peak pressure and duration just less than necessary to cause detonation. The samples were shocked in such a way that they could be recovered and studied by various microscopic techniques. The apparatus to shock and recover the samples is shown in Figure 1. It consists of four one inch diameter cylinderical pieces of brass. The first hollow piece contains the explosive charge which when detonated imparts a shock to the second solid piece, called a spacer. The height of the pulse is controlled by varying the thickness of the spacer. The relationship of the spacer thickness to the peak pressure of the pulse was determined by placing a Manganin gauge after the spacer and detonating the charge with a number of different spacer thicknesses. The results show that the peak pulse pressure varies smoothly with the spacer thickness. The pulse width of 2μS was relatively independent of the spacer thickness. The shape of the pulse displayed on an oscilloscope connected to the Manganin gauge was approximately a right triangle. The third piece of the

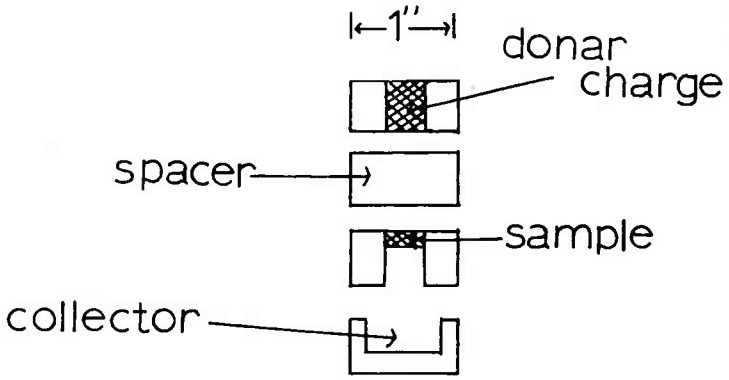

FIGURE 1. Apparatus used to shock and recover samples of solid explosive

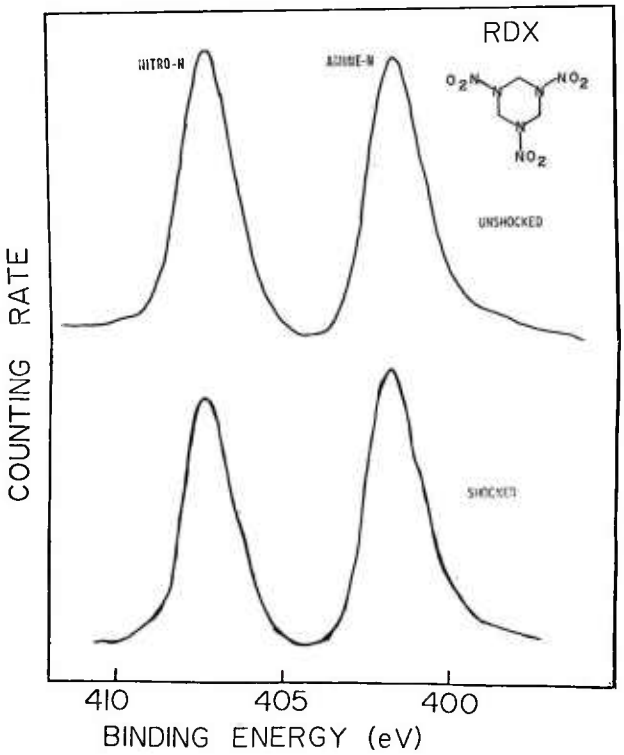

FIGURE 2. XPS spectra of 1s level of nitro and ring nitrogen in shocked and unshocked RDX.

device contained the sample in the form of a 100 mg pellet pressed to about 98% of the crystal density. The shocked sample was collected in the last stage of the device. The assembled device was contained in a rig which prevented the collector and the spacer from separating during shock, thus insuring that the sample was not contaminated by decomposition products of the detonated charge.

The recovered shocked samples were studied by a number of experimental techniques including, x-ray photo-electron spectroscopy, (XPS); electron paramagnetic resonance (EPR); Raman spectroscopy, optical absorption spectroscopy and x-ray diffraction. The x-ray photoelectron studies utilized a Varian IEE-15 system using Mg K radiation. Typically, the XPS data were recorded at room temperature in a vacuum of 10^{-6} torr. The EPR studies employed a Varian E-3 spectrometer operating at 9.2 Ghz. EPR measurements were made both at 77°K and 300°K. The Raman spectra were obtained using a Coderg T800 symmetrically mounted triple monochromator. The slit width could be set as low as 240 um corresponding to a spectral resolution of 1.0 cm^{-1}. A Coherent Radiation Argon-Ion Laser, with output at 488.0 nm with 60 mW of power was the excitation source. The detection system consisted of a cooled S25 phototube with photon counting circuitry. Optical absorption measurements were made with a Carey 14R spectrophotometer. X-ray diffraction studies utilized a Norelco unit which allowed the sample to be rotated about an axis perpendicular to the beam. The samples of explosives used were purified by numerous recrystallizations from solution.

RESULTS: A. XPS Studies of Shocked Explosives. In the XPS experiment a sample is subjected to a beam of x-rays which cause electrons to be emitted from the energy levels of the atoms or ions which make up the material. The energy of the emitted electrons will only have certain discrete values related to the energy levels from which they originated. In the XPS experiments, the energy and the number of emitted electrons is measured. In order to understand the XPS results on shocked RDX it is necessary to refer to the structure of the molecule shown in Figure 2. In terms of their position on the molecule, two kinds of nitrogen atoms can be identified; a nitrogen atom in the ring and a nitrogen atom in the nitro group (NO_2). The 1s level of each of these nitrogens has different energies and yields in the XPS data two distinct peaks. The peak at 407.5 eV is due to electrons from the nitrogen of the NO_2 group, while the peak at 402 eV arises from the 1s electrons of the ring nitrogen. When the same peaks are examined in the shocked RDX, as shown in Figure 2, it was found that the peak at 407.5 eV had decreased with respect to the peak at 402. This result clearly indicates that the effect of the shock was to rupture the N-N bond holding the nitro group to the ring,

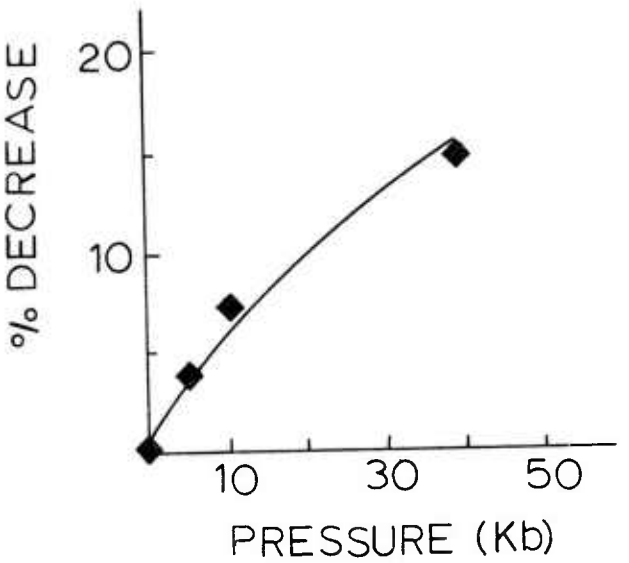

FIGURE 3. Percent change of nitro XPS peak relative to ring peak versus maximum pressure of shock pulse for RDX.

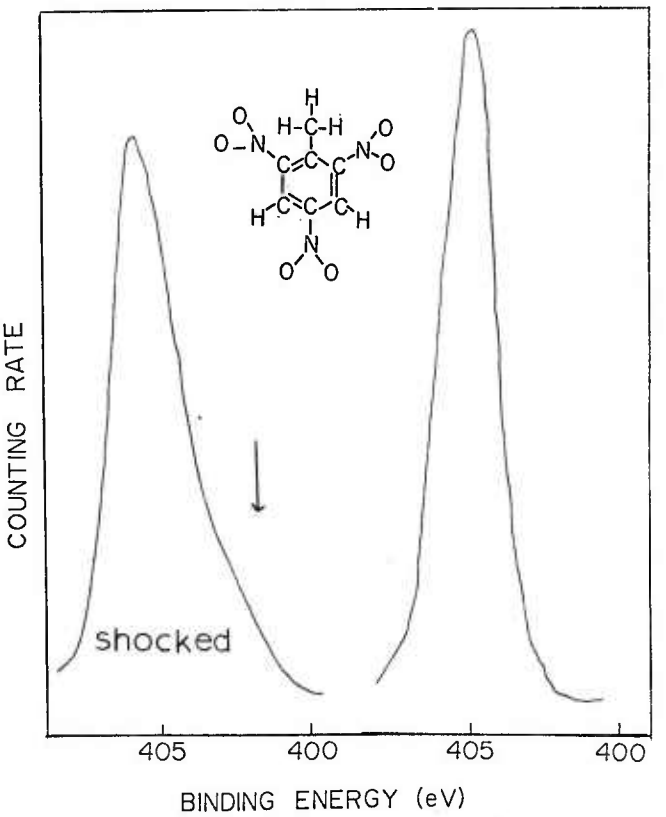

FIGURE 4. XPS spectrum of the nitrogen 1s level in shocked and unshocked TNT.

in effect removing the NO_2 from the ring. The magnitude of this relative change was measured as a function of the peak pulse pressure. In Figure 3 is plotted the percent decrease of the 407.5 eV peak relative to the 402 eV peak versus the peak pulse pressure as measured by the Manganin Gauge. In the most severely shocked sample representing a peak pulse pressure of 40 Kb a 14.0% decrease in the nitro peak was observed.

In TNT there is no nitrogen in the ring and only one nitrogen peak is observed in the XPS spectrum due to the nitro group. The 1s level of this nitrogen gives a peak at 405 eV. This peak is shown in Figure 4 for the shocked and the unshocked sample of TNT. The data shows that in the shocked sample, a new peak is occuring on the low binding energy side of the 405 eV peak. A similar low energy shoulder is observed on the carbon 1s peak. One possible effect consistent with the above data is an increase in the bonding between the hydrogen of a CH or CH_3 group and an oxygen of an adjacent NO_2 group of the TNT molecule. It is known that the first step in the photolytic decomposition of molecules like TNT is the so-called "insertion reaction" involving an exchange of the position of a hydrogen with an oxygen of the adjacent nitro group.(3) However, the results obtained here due to shock do not seem to be consistent with this type of an interaction. Such an effect would not result in both the carbon and the nitrogen shifting to lower binding energy as observed here. The effect of the shock appears to be to increase the bonding between the hydrogen and the oxygen without an exchange of the positions of the two atoms. This could be due to distortion of lattice which forces the CH_3 and NO_2 closer together. Evidence for shock induced distortion will be presented below.

In ammonium nitrate, the effects of the shock were studied by monitoring the 1s electron from the nitrogen of the ammonium ion and the nitrate ion. The peak associated with the nitrogen of the nitrate ion occurs at 407.5 eV and that of the ammonium ion occurs at 402.5 eV. In the shocked AN the intensity of the 402.5 eV peak has been reduced compared to the 407.5 eV peak. This clearly indicates that a dominant effect is a breakup of the NH_4^+ ion compared to the NO_3^- ion. This result does not preclude the possibility of decomposition of the NO_3^- ion. It does indicate that the NH_4^+ is more susceptible to shock decomposition. The results indicate a 3% decrease in the size of nitrogen 1s peak of the NH_4^+ ion relative to the nitrogen 1s peak from the nitrate ion for shock of 20 Kb peak pressure, as measured by the Manganin Gauge after the spacer.

B. Paramagnetic Resonance Studies of Shocked Explosives. The electron paramagnetic resonance experiment investigates the interaction of an atom, ion or molecule having a net magnetic moment with an applied dc magnetic field. The applied dc magnetic field splits the ground state level of the system into a number of energy levels labeled by the possible projections of the spin angular momentum with respect to the applied magnetic field. The sample in the magnetic field is subjected to microwave radiation of energy $h\nu$. When the dc magnetic field is such that the separation between the spin states is equal to $h\nu$, a transition is induced between the states and microwave energy is absorbed by the sample. The resonance condition occurs when,

$$h\nu = g\beta H \qquad (1)$$

where β is the Bohr magneton, g is a constant and H is the magnitude of the applied magnetic field. Because a radical has a net unpaired electron spin and therefore a net magnetic moment, paramagnetic resonance provides a powerful method of detecting trapped radicals. Samples of RDX, TNT and AN, examined at $77^{o}K$ and $300^{o}K$ showed no evidence of paramagnetic absorption prior to shocking. However, when the samples were subjected to shocks in the 20 to 40 Kb peak pulse range, large paramagnetic absorptions were detected indicating that the shock had produced paramagnetic species.

In RDX and TNT a broad resonance centered about the g value of 2.0023 was observed at $300^{o}K$. Since in single crystals the splitting between the spin states, $g\beta H$ is dependent on the orientation of the dc magnetic field in the lattice, the spectra of a powder, which is essentially a large number of small randomly oriented single crystals will consist of a superposition of resonances arising from all possible orientations of the magnetic field in the lattice. Unfortunately, this often obscures some of the rich character such as hyperfine structure which enables identification of the species. However, in some cases, it is possible to interpret EPR spectra in powders if some structure is in evidence. In the case of RDX unfortunately, this was not possible, however, some observations can be made concerning the causes of the EPR spectra. In RDX the XPS studies clearly point to the existence of the NO_2 as a product of the decomposition. This molecule is paramagnetic having a g value close to the value 2.0023, as observed here, and unlike most radicals can be detected at $300^{o}K$.(4) This suggests that some part of the EPR spectrum in the shocked material may be associated with the NO_2 radical. In the case of TNT it is not possible to make any conclusion concerning the nature of the EPR spectrum at this time.

The EPR spectrum obtained in shocked ammonium nitrate unlike the RDX spectra displays considerable structure which could

help in the identification of the species giving rise to the spectra. Since uv irradiation of ammonium nitrate powders produces a less complex spectra it was decided to compare this spectra with the results from shock in order to assist in the identification of the shock induced spectra. An EPR spectra obtained in ammonium nitrate photolyzed with uv light of 250 nm from a Hanovia light source, appears to correspond in both magnetic field value and line separation to the resonances in the spectra produced by shock suggesting that the spectra in the shocked sample arises from the same species as in the photolyzed sample. The spectra in the photolyzed sample actually consists of two distinct spectra. The large line at the center overlaps a smaller resonance with similar intensity to the outer resonances. This triplet spectrum arises from an unpaired electron interacting equally with a nucleus of spin one and has been assigned to the NO_3^{2-} radical.(5) However, more recent studies indicate that this spectrum is more likely a NO_2 radical.(6) Therefore, it is possible by this comparison to tentatively assign part of the spectra produced by the shock pulse in NH_4NO_3 to an NO_2 radical. Interestingly, Russian workers observed an IR absorption band in shocked KNO_3 which they attributed to a mode of the NO_2 radical.(7)

C. Laser Raman Studies of Shocked Explosives. In the Raman experiment a coherent laser beam typically of wavelength around 488 nm is incident on a sample, stimulating a transition from a vibrational state, n, of some species to a higher level. This excited state then decays to the n+1 level and a quantum $h\nu$ of light is emitted. The spectral distribution and the intensity of the emitted light is measured. The difference in wavelength between the stimulating light and the emitted light corresponds to the vibrational energy $h\nu$ of the species under study. In these studies Raman spectroscopy was used to look for evidence of bond breaking and decomposition by comparing relative intensities of Raman emitted light in shocked and unshocked material. A reduction in the concentration of one constituent of the lattice should result in a corresponding reduction in the intensity of the associated Raman spectra of the species. The Raman spectra of solids like TNT and RDX are quite complex. In RDX, for example, 41 Raman lines are observed in the condensed phase.(8) Generally, the Raman spectra arises from two distinct kinds of vibrations, those associated with the normal modes of vibration of the lattice, typically occuring below 200 cm^{-1}, and vibrations associated with internal modes of the molecules which make up the crystal. Because of the complicated crystal structure of TNT and RDX, detailed assignments of Raman lines in the lattice mode region have not been made, however, some assignments are available in the internal mode region.(8,9) A line at 1274 cm^{-1} is

associated with the symmetric stretch mode of the NO_2 group and a 1313 cm^{-1} line arises from the N-N stretch mode.(8) There appears to be a decrease in the magnitude of the N-N stretch mode intensity relative to the other Raman lines in the shocked sample. This result seems to be consistent with the XPS data indicating a breaking of the N-N bond. The effect is small and considering the difference between the background scattering in the shocked and unshocked samples, presumably due to a difference in particle size, must be considered tentative. In TNT a similar change in relative intensities of Raman lines in shocked and unshocked samples was observed. Unfortunately, the specific vibrations giving rise to these lines are not known and all that can be said is that the data indicates some change in bonding in the TNT molecule.

Considerably more is known about the vibrational structure and Raman spectra of ammonium nitrate.(10) The character of the observed Raman data in ammonium nitrate varies somewhat with temperature and pressure because of the numerous phase transitions that exist in the material. As the temperature is raised these phase transitions are characterized by successively greater rotational freedom of the NH_4^+ and NO_3^- ions. The results reported here are confined to phase III which exists above 305°K and at atmospheric pressure. Typical of the results obtained in the shocked samples is a decrease in the intensity of the symmetric stretch mode at 1044 cm^{-1} of the NO_3^- ion suggestive of a break up of the ion. In the region below 350 cm^{-1} where the normal modes of the lattice are observed, some effects of the shock were detected. An intriguing possibility is suggested by an examination of part of the lattice mode spectra in the shocked and the unshocked sample. The mode at 165 cm^{-1} is associated with a translational motion of the NH_4^+ ion and the mode at 143 cm^{-1} is due to a rotation of the NO_3^- (10). Taking into account the difference in the background between the shocked and the unshocked samples, the peak associated with the rotational mode at 143 cm^{-1} has decreased significantly with respect to the peak at 165 cm^{-1}. A possible explanation of this with interesting implications is that some of the NO_3^- ions that are not decomposed have obtained a higher degree of rotational freedom. Decreases in intensity and increases in line widths of rotational modes occur in Raman spectra with the onset of fluctuations associated with phase transitions in which the new phase is characterized by an increase in the rotational degree of freedom of a molecular anion. For example, in $NaNO_2$ which undergoes a phase change at 437°K involving an onset of motional tumbling of the NO_2^- a large increase in the line width is observed as the transition is approached from below the transition temperature.(11) In AN there

is a phase transition at 356°K which, among other things, involves an increase in the freedom of rotation of the NO_3^-. There is no doubt that a 40 Kb shock pulse will cause the temperature to rise above 356°K, particularly in powders causing the AN to go into the new phase. The data suggests that all of the NO_3^- ions do not return to a lower degree of rotational freedom after the shock wave has passed.

D. Optical Absorption Studies of Shocked Explosives. In an effort to understand the shock induced changes in explosives, the electronic structure of the shocked explosives was investigated by optical absorption techniques. Shocked and unshocked RDX and AN were dissolved in high purity distilled water and the resultant optical absorption spectra compared. The absorptions in unshocked RDX consists of two bands at 237.5 nm and 195 nm. In the shocked material, no new absorptions were observed at wavelengths greater than 300 nm. Thus, it seems probable that no new species were produced which remained in solution and absorb in the visable region of the spectra. The results for RDX confirm the XPS results that the nitroso derivative of RDX is not formed since this compound should absorb on the long wavelength side of 320 nm.(12) The shocked spectra did show a slight decrease of the maximum at 195 nm relative to the maximum at 237.5 nm. Although specific optical transitions have been proposed to account for these absorptions in RDX based on molecular orbital calculations of dimethylnitramine, which may be viewed as a "building block of RDX", no definitive identification of these absorptions is available.(13) It is thus not possible at this time to make detailed observations from the optical absorption spectra as to how the RDX molecule was altered by the shock. It is interesting to note that the photo decomposition of RDX in aqueous solutions as detected by optical absorption differs from the results of shock induced decomposition in the solid state with subsequent dissolving.(12) With continued exposure to uv light, the band at 237.5 nm decreases and the absorption at shorter wavelength increases. These differences could be due to solid state versus solution effects.

In an unshocked AN dissolved in water, two absorptions are detected at 300 nm and 200 nm which are associated with the NO_3^- ion. (15) The NH_4^+ ion does not absorb in the accessible wavelength region of the spectrometer. Small changes were observed in the optical absorption on the long wavelength side of the 200 nm absorption but it is not yet possible to associate these changes with decomposition products of AN. The optical absorption studies of the shocked explosives do, however, indicate that the molecules of the material have been affected by the shock pulse.

E. X-Ray Diffraction Studies of Shocked Explosives. Standard powder diffraction patterns were taken of shocked and unshocked RDX and AN. Experimental conditions limited the range of measurements of 2θ to a maximum of 60° (θ is the Bragg angle). The general approach was to compare the diffraction from shocked with unshocked samples and both with calculated diffraction patterns. Several deductions can be made from the experimental results and these are discussed below.

The data indicates that the crystal structure is not changed by shocking. The 2θ values are not altered and are in agreement with calculated values and the relative intensities of the various lines are not altered drastically and are in rough agreement with calculated values.(16,17) In AN the room temperature phase was not changed by the shock.

There are differences in the relative intensities of the diffraction lines between shocked and unshocked material and calculated values. The data for shocked samples tends toward better agreement with calculated values than the data for the unshocked material. This disagreement between relative intensities can be attributed to nonisotropic crystalline shapes and preferred orientation. The better agreement between shocked and calculated patterns can be attributed to grain fracture and particle size decrease as discussed below. For the purposes of this discussion, the term "grain" refers to the macroscopic units which make up the powder while the term "particle" will be reserved for the regions of coherent X-ray scattering which in general are much smaller than the grains.

In addition to the above, there is significant line broadening due to shocking. Line broadening of the type observed can be attributed to a reduction in particle size and/or strain and techniques exist for distinguishing and separating these two effects.(18,19) Unfortunately, very few non-overlapping diffraction lines were observed so that it is difficult to obtain a good measure of line broadening. Thus, a clean separation of the two causes of line broadening could not be made in the usual way. The line width $\Delta(2\theta)_{P.S.}$ due to particle size is given by

$$\Delta(2\theta)_{P.S.} = \frac{\lambda}{L \cos} \qquad (2)$$

where λ is X-ray wave length and L is the linear dimension of the particle perpendicular to the diffracting planes.(18) The line width due to strain, $\frac{\Delta d}{d}$, where d is the interplaner spacing and Δd is the

change because of strain is given by (18)

$$\Delta(2\theta)_S = \frac{\Delta d}{d} \mathrm{Tan}\ \theta \qquad (3)$$

These relationships should allow a clear distinction between the dependence of line broadening due to particle size and strain because of the different dependence on θ and further enable values of L and $\Delta d/d$ to be estimated. While the observed line broadening has no clear cut dependence on θ so as to allow a distinction to be made in this manner, the calculated values of L are of reasonable magnitude while the calculated values of $\Delta d/d$ are much too large to be sustained without relief by plastic deformation and/or fracture. It is, therefore, concluded that the major cause of the observed line broadening is due to a reduction in particle size (regions of coherent X-ray scattering). Strain effects, however, cannot be ruled out; they are only overshadowed by particle size effects for the experimental conditions. Measurements as a function of λ might be of use in separating these effects.

Before discussing the dependence of $\Delta(2\theta)$ on θ, it is expedient to consider the results of another observation. Grains of shocked and unshocked RDX were observed in an optical microscope. The linear dimension of the grains of the shocked sample were decreased by approximately an order of magnitude relative to the unshocked material. Similar observations have been made by others.(20) In addition, polarized light studies indicated that the unshocked grains were polycrystalline. The grains of the shocked material were too small to make similar observations. However, a comparison of the grain size with the particle size indicates that the regions of coherent scattering are much smaller than the grain size. This indicates that the shocked grains are polycrystalline and so contain regions of sufficient distortion to prevent coherent scattering throughout.

It is now possible to explain qualitatively the rather erratic dependence of the line broadening on θ. Preferred crystallographic directions of distortion results in the value of L being dependent on direction, i.e., the dimensions of the regions of coherent scattering are not isotropic. This might be expected if dislocations have well defined slip planes.

In summary, the X-ray line bordering and the optical microscopic observations indicate that there is considerable reduction in grain and particle size due to shocking, and further that the grains contain regions of large lattice distortion or strain.

Lattice distortion may occur by dislocation motion, multiplication and adiabiatic shear.

DISCUSSION: The results of these experiments provide the first direct evidence that a shock of peak pulse less than necessary to cause detonation can break or alter internal molecular bonds of the constituent molecules of an explosive solid. Even more important, the experiments have provided a description of the details of the bond breaking process. It has been shown that in RDX the dominant chemical change induced by the shock pulse is a breaking of the N-N bond between the NO_2 group and the ring. In TNT it has been shown that the shock produces a slight alteration of the bonding of the hydrogen of a CH or CH_3 group with the oxygen of an adjacent NO_2 group. In ammonium nitrate it has been clearly demonstrated that both the NH_4^+ and NO_3^- ions are decomposed by the shock.

These results have important implications concerning the molecular processes involved in the build-up to detonation. It is widely accepted, although without direct evidence, that the rate controlling reactions leading to detonation of secondary explosives are the same as the dominant reactions observed in the slow thermal decomposition of the explosives. In fact, this assumption underlies most of the computer codes that are used to predict explosive behavior. The effect of shock is considered to result in a change of the mechanical energy of deformation to thermal energy, with resulting localized regions of high temperature (hot spots) (2) in which thermal decomposition results. However, detailed slow thermal decomposition studies of RDX in the condensed phase using both XPS and mass spectrographic methods indicate that the dominant decomposition involves a breaking of the C-N bonds of the ring. (21,22) In RDX the dominant shock decomposition is not the C-N bond but the N-N bond. This result raises serious questions concerning the use of slow thermal decomposition reaction kinetics to account for explosive behavior. It is interesting that the major decomposition effect of photolysis in RDX is a breaking of the N-N bond as in shock decomposition. (23) Since the first step in photolytic decomposition is known to involve an electronic excitation of the molecule, the similarity of the dominant bond breaking effects of shock and uv light suggests the possibility that the first step in the shock decomposition is an electronic excitation of the molecule. However, in TNT both photolysis and slow thermal decomposition give results different from shock decomposition. XPS studies of photolyzed and thermally decomposed TNT in both the gas and the condensed phase show a new peak occuring at 401 eV which was definitively shown to be associated with a removal of an oxygen of the nitro group. (24) This new peak was not

seen in the shock decomposed TNT. Thus again the results of slow thermal decomposition differ from shock decomposition. In ammonium nitrate the dominant slow thermal decomposition product is reported to be N_2O while in this study, the dominant effect of the shock seems to be a decomposition of the NH_4^+ ion.(25)

The lack of similarity between reactions produced by slow thermal decomposition and shock decomposition should not be really surprising when it is realized that in the time for a pressure pulse to pass a region of the material (10^{-6} seconds) thermal equilibrium cannot be achieved. The heating associated with mechanical deformation of the lattice will be distributed over excitations of the energy levels of the normal modes of vibration of the lattice. For chemistry to occur with activation energies similar to those of slow decomposition, the internal modes of the molecules would have to come to equilibrium with the lattice modes. It is highly unlikely that there will be sufficient time for this to occur. In fact recent computer molecular dynamic calculations of the effects of shocks on simple solids indicate that equilibrium may not be achieved and in fact question the concept of temperature in a shock front.(26)

It may be that there is a relationship between the bond breaking and the lattice distortion and strain observed by X-ray diffraction. It is known that mechanical deformation can cause bond breaking in polymers, and semi-conductors and can introduce lattice defects.(27,28) There is also evidence that a shock can cause electronic excitations in a solid. It is thus plausible then that the shock induced strain and distortion could be the cause of the bond breaking. If the dislocations in explosive solids have similar properties to dislocations in other materials, the bond breaking may be a direct result of shear during dislocation motion. Alternately, the observed bond breaking may be due to localized heating, (hot spots), produced by fracture and the resultant friction due to the slippage of one surface over another, adiabiatic shear heating or to heating due to dislocation motion.

SUMMARY: Thus important understanding has been gained about the process of shock induced exothermic reactions in solid explosives. The initial step in the process has been shown to involve a breaking of intra molecular bonds or an altering of the bonds of the explosive molecules which make up the lattice of the material and a production of trapped radicals. These trapped radicals are likely candidates for the secondary reactions. It is also shown that this bond breaking is accompanied by considerable permanent distortion in the lattice.

REFERENCES

1. F. E. Walker and R. J. Wasley, Propellants and Explosives 1 73 (1976)
2. F. P. Bowden and A. D. Yoffe in Fast Reactions in Solids (Academic Press, London 1958), P.3
3. J. G. Calvert & J. N. Pitts, Jr. in Photo-Chemistry (Wiley, NY. 1966, P. 478)
4. H. Zelds and R. Livingston, J. Chem. Phys. 35 563 (1961)
5. F. H. Jarke and N. A. Ashford, J. Chem. Phys. 62 2923 (1975)
6. F. J. Owens (Unpublished)
7. S. S. Batsanou, Fizika Goreniya i Vzryua 2 110 (1966)
8. Z. Iqbal, K. Suryanarayanan, S. Bulusu, J. R. Autera, Picatinny Arsenal Technical Report 4401 (1972)
9. M. Rey-Lafon, J. De Chim. Phys. 68 1533, 1573 (1971)
10. D. W. James, M. T. Carrick and W. H. Leong, Chem. Phys. Letters 28 117 (1974)
11. P. jaR. Andrade, A. D. Rao, R. S. Katiyar and S.P.S. Porto, Solid State Communications 12 847 (1973)
12. K. Suryanarayanan and S. Bulusu, J. Phys. Chem, Solids 26 496 (1972)
13. J. Stals, C. G. Barraclough and A. S. Buchanan, Trans Faraday Soc. 68 908 (1969)
14. A. F. Smetana and S. Bulusu, Picatinny Arsenal Technical Report ARCD TR 77039 (1977)
15. C. Ribaudo and V. Hogan (Private Communication)
16. C. S. Choi and E. Prince, Acta Cryst B28 2857 (1972)
17. J. Abel (Unpublished Work)
18. A. Guinier, X-Ray Diffraction (W. H. Freeman and Co, San Francisco, London 1963)
19. B. E. Warren and B. L. Averbach in Imperfections In Nearly Perfect Crystals, W. Shockley Ed. (J. Wiley, New York 1953) P.52
20. E. N. Aleksandrov, V. A. Veretennikov, A. N. Dremin and K. K. Shvedov, Fizika Goreniya i Vzryua 4 400 (1968)
21. J. Sharma, T. Gora, S. Bulusu, D. Wiegand, Proceedings of The Army Science Conference, I West Point, New York (1974)
22. B. Suryanarayana, J. R. Autera and R. J. Graybush, Proceedings Army Science Conference 2 423 (1968)
23. J. Sharma and S. Bulusu, Bull. Am. Phys Soc. 19 283 (1974)
24. J. Sharma (Unpublished)
25. L. Friedman and J. Biegeleisen J. Chem. Phys 18 1325 (1950)
26. D. Tsai (Unpublished)
27. S. N. Zhurkov, A. Y. Savostin and E. E. Tomasnevskii, Soviet Physics 9 986 (1965)
28. W. B. Gager, M. J. Klein and W. H. Jones Appl. Phys. Letters 5 131 (1964)

AD-A056473

DEVELOPMENT OF A SYSTEMATIC AND QUANTITATIVE METHOD FOR EVALUATING INSTRUCTIONAL MATERIAL: INSTRUCTIONAL MATERIAL ADEQUACY GUIDE AND EVALUATION STANDARD (IMAGES)

JAMES C. PERKINS, JR.
HEADQUARTERS, US ARMY TEST AND EVALUATION COMMAND
ABERDEEN PROVING GROUND, MARYLAND 21005

INTRODUCTION

Three essentials to combat readiness are manpower, materiel, and equipment manuals. Equipment manuals provide the information and communication link between the soldier and the equipment he must operate and maintain. These manuals also contribute directly to the reliability, maintainability, and operational effectiveness of the Army's weapon systems. To obtain full advantage of these systems we must provide the soldier with accurate, complete, and understandable equipment manuals.

This presentation describes a recently developed method for evaluating the technical adequacy, accuracy, and readability of Army equipment manuals. The method is entitled the Instructional Material Adequacy Guide and Evaluation Standard (IMAGES). The presentation also includes a brief summary of the results of a 6-month pilot study of IMAGES at four of the Army's proving grounds.

BACKGROUND

In January 1975 an article was published in an Army Materiel Command (AMC) newsletter regarding the large number of complaints from the field about the inadequacies of the Army's technical manuals. As many as 350 complaints were received during one 3-month period.

As the developer's tester and evaluator, the US Army Test and Evaluation Command (TECOM) is responsible for verifying and evaluating the technical adequacy, accuracy, and utility of draft equipment

manuals for all Army equipment and weapon systems submitted for development test and evaluation.

During July-August 1975, TECOM conducted an investigation of the methods employed for evaluating manuals. Based on interviews and discussions with maintenance personnel at each proving ground, it was found that: (1) there was no systematic or standard method for evaluating technical manuals, (2) the techniques employed were dependent upon the subjective judgment and experience of the particular evaluator, and (3) there was no consistent measurement standard for classifying defects or determining overall manual quality. It was also found that in some instances only those portions of manuals necessary for use in performing corrective maintenance were evaluated.

DEVELOPMENT OF IMAGES

Based on the results of the preliminary investigation, TECOM immediately initiated a methodology improvement study with the overall objective of developing a systematic and quantitative method for evaluating technical manuals.

The methodology study was conducted during the period September 1976 through September 1977. The objective of the study was to develop a systematic, quantitative method for evaluating equipment manuals which would: (1) be useable by Army maintenance evaluators, (2) provide for a complete evaluation of manuals, (3) be compatible with the present system for reporting and correcting deficiencies, (4) classify and quantify manual defects, and (5) provide a consistent measurement standard for determining overall manual quality.

IMAGES, as developed by TECOM, is based on the technical specifications to which Army equipment manuals are prepared. It contains a strategy and checklists for evaluating the adequacy of the style, technical contents, and readability of manuals. It also contains criteria for determining the comprehension level to which a manual is written and provides a quantitative measurement system for determining overall manual quality.

IMAGES consists of 11 parts. A summary of the Parts of IMAGES by Category of Equipment is shown in Figure 1. Part I contains the instructions. This part is applicable to all categories of Army equipment and to all types of equipment manuals, Operator -10 through General Support -40. The General Style and Format Requirements are also applicable to all other parts.

Category of Equipment*	Governing Specification	Ref Code	Part Reference
Introduction to IMAGES (Applicable to all Categories)			Part I
General Style and Format Requirements	MIL-M-38784A	A	All Parts
Mechanical and Construction Equipment, Automotive Equipment and Power Tools (Excludes Combat Vehicles)	MIL-M-63009C	B	Part II
Telecommunications Equipment (Except Teletypewriters)	MIL-M-63019	C	Part III
Radar Equipment	MIL-M-63020	D	Part IV
Teletypewriter Equipment	MIL-M-63021	E	Part V
Electronic Test Equipment	MIL-M-63025	F	Part VI
Army Aircraft Equipment	MIL-M-63026A	G	Part VII
Weapons, Combat Vehicles and Fire Control Materiel	MIL-M-63032A	H	Part VIII
Lubrication Orders	MIL-M-63004B	J	Part IX
Equipment Serviceability Criteria	MIL-M-63006B	K	Part X
Commercial Equipment	MIL-M-6298C	L	Part XI

Figure 1. Parts of IMAGES by Category of Equipment

*IMAGES is currently being expanded to include Missile System Equipment and Nonnuclear Explosive Ordnance Disposal manuals.

Parts II through XI are related to specific categories of equipment and the governing specifications. Each of these parts is complete so that the maintenance evaluator only needs to use one part of IMAGES to evaluate all manuals for a given system.

Each part of IMAGES, parts II-XI, contains the following four sections:

a. Section I contains the Introduction which covers the purpose and scope of the evaluation, applicable levels of maintenance, and step-by-step instructions for performing the evaluation.

b. Section II contains a detailed checklist of General Style and Format Requirements. In addition, it contains general technical requirements for engineering drawings, illustrations, and schematics. It also contains requirements and criteria for hazard warnings, security classification markings, and quality assurance provisions, including readability standards.

c. Section III contains a detailed checklist for Specific Technical Requirements by type of manual and covers the type -10 Operator's manual through the type -40 General Support Maintenance manual. This section also includes procedures for evaluating lubrication instructions, preventive maintenance checks and services, troubleshooting provisions, and special tools and equipment.

d. Section IV contains the required Review/Evaluation forms for classifying and recording defects and the criteria for determining the overall quality level of the manual.

IMAGES EVALUATION PROCEDURES

The general procedures which the maintenance evaluator follows in using IMAGES are as follows:

Step 1 - Determine from the Draft Equipment Publication Package the governing specification to which the manual was prepared and determine that a Maintenance Allocation Chart (MAC) is available.

Step 2 - Based on the governing specifications, determine the part of IMAGES applicable for use in the manual evaluation.

Step 3 - Following the detailed review/evaluation procedures in Section I, and using the checksheets provided, conduct a complete evaluation of the manual.

Section I, Introduction to IMAGES, contains instructions for the classification of defects to assist the evaluator in judging the severity of a manual defect. IMAGES provides for three classes of defects as follows: (1) critical, (2) major, and (3) minor. In addition, there are three levels for each category of defect. The definitions and criteria for classifying defects are included on a Classification of Defects card as shown in Figure 2. The defect class and level are assigned code numbers for ease of recording and evaluation purposes. For example, critical defects are indicated by the numbers 1, 2, or 3 and are assigned a defect value of 100; major defects are numbered 101, 102, or 103 and are assigned a defect value of 10.0; and minor defects are numbered 201, 202, or 203 and are assigned a defect value of 0.2.

Checksheets are provided for classifying and recording defects and for determining the overall Quality Index value for the manual. Two different types of checksheets are used for each manual evaluation. The first of these is the Maintenance Requirements by Functional Group Review/Evaluation Checksheet. A sample of this checksheet is shown in Figure 3. This checksheet is used in conjunction with the detailed checklist for specific technical requirements (Section III of IMAGES) to determine the technical adequacy and accuracy of the manual.

The Review/Evaluation of Format Requirements Checksheet is used in conjunction with the General Format and Style checklist (Section II of IMAGES) to evaluate the adequacy of the manual with regard to specified style, format, illustrations, hazard warnings, and readability requirements. A sample of the Review/Evaluation Checksheet is shown in Figure 4. Each requirement in the checklist is compared with the applicable text to determine if the text material complies with the requirements.

The final step in the manual evaluation procedure is completion of the Review/Evaluation Summary Sheet, Figure 5. The total number of defects in each category is transferred from the two checksheets described above to the Summary Sheet. The total number of defects is then multiplied by the weighted value for each category to determine the total value for weighted defects. The "n" value of weighted defects per page is then determined by dividing the number of weighted defects by the number of manual pages evaluated. The overall Quality Index is then determined by entering the Table of Quality Values, which is also shown in Figure 5. The Quality Index Value is used to determine overall manual quality which may also be expressed in adjectival terms: excellent, good, fair, or unacceptable, as shown

CLASSIFICATION OF DEFECTS

This Classification of Defects card is used to assist the evaluator in judging the severity of a manual defect. If a defect exists in the manual, it is selected and rated in accordance with the definition indicated. The defect class code number selected for entry on Form No. 1 and Form No. 2 should define the defect as nearly as possible, based upon the severity of the defect should it remain uncorrected in the manual.

DEFECT CLASS CODE NUMBER	DEFINITION
	CRITICAL DEFECT – Information that is omitted, incorrect, incomplete or confusing in a manual which could result in:
1	hazardous or unsafe conditions for personnel using, maintaining or depending on the equipment described by the manual.
2	destruction or impaired performance of a major tactical end item (missile, tank, vehicle, etc.)
3	access to classified material by unauthorized personnel.
	CRITICAL defect is indicated as 1, 2 or 3 and is assigned a defect value of 100.
	MAJOR DEFECT – Information that is omitted, incorrect, incomplete or confusing in a manual, other than a critical defect, which could result in:
101	immediate or ultimate failure of the equipment or component of the equipment or immediate cessation of operation.
102	reduced usability or inefficient performance of the equipment.
103	unnecessary difficulty or significant loss of time to the user of the manual in performing a particular function.
	MAJOR defect is indicated as 101, 102 or 103 and is assigned a defect value of 10.0.
	MINOR DEFECT – Information that is omitted, incorrect, incomplete or confusing in a manual other than a critical or major defect, which:
201	would not affect the performance of the equipment.
202	deviates from standards having little bearing on the usability of the manual or on the equipment described.
203	does not materially reduce the usability of the manual for its intended purpose.
	MINOR defect is indicated as 201, 202 or 203 and is assigned a defect value of 0.2.

Figure 2. Classification of Defects Card.

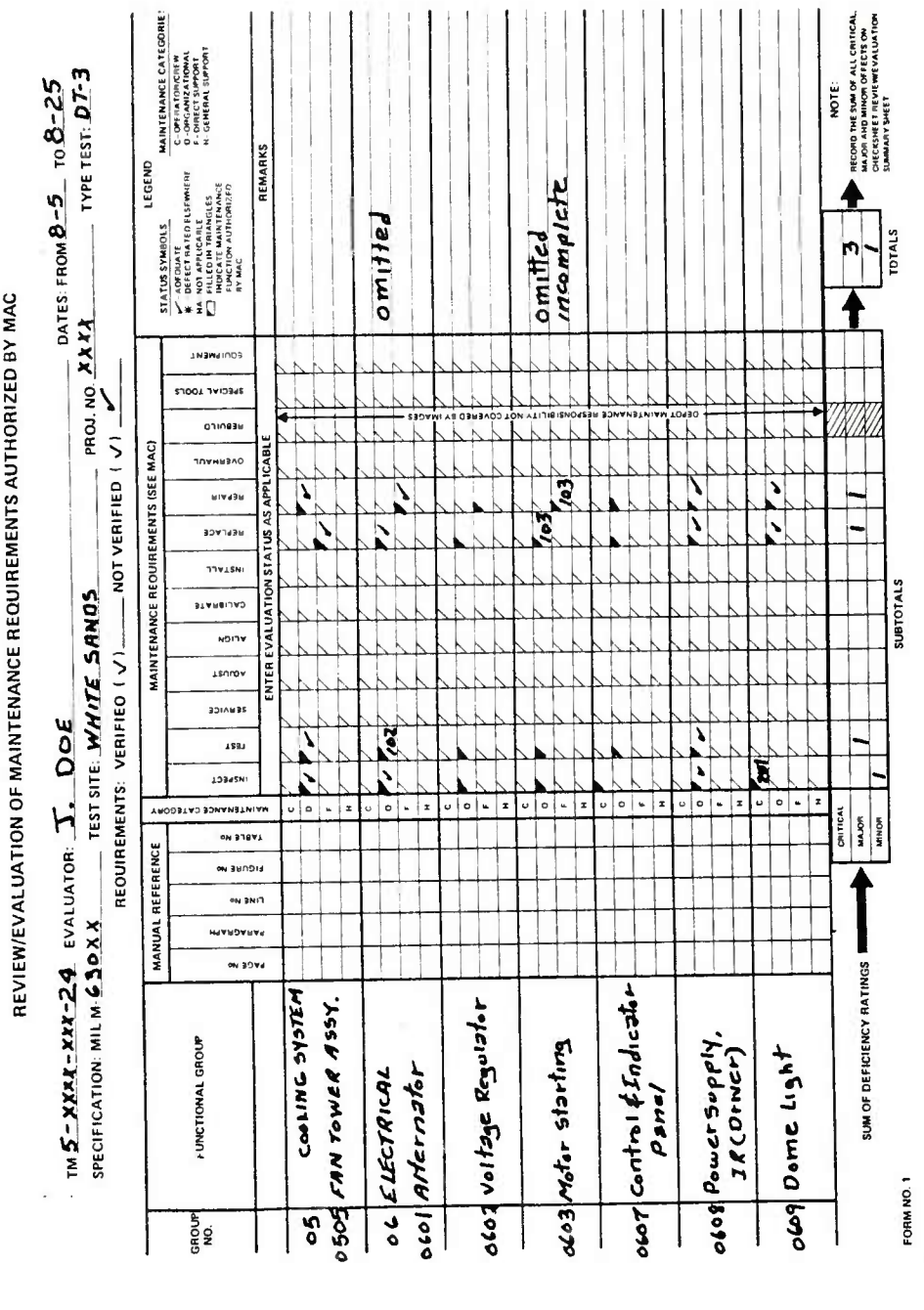

Figure 3. Manual Maintenance Requirements Checksheet.

REVIEW/EVALUATION OF MANUAL FORMAT REQUIREMENTS

TM 5-XXXX-XXX-24 EVALUATOR: J. Doc DATES: FROM 8-5 TO 8-25

SPECIFICATION: MIL-M-63088 TEST SITE: WHITE SANDS PROJ. NO. XXXX TYPE TEST: DT3

REQUIREMENTS: VERIFIED (✓)____ NOT VERIFIED (✓) ✓

REFERENCE CODE	MANUAL REFERENCE					ADEQUATE	NOT APPLICABLE	OMITTED	DEFICIENT	DEFECT CLASS CODE NO.	REMARKS OR RECOMMENDED CHANGES AND REASON
	PAGE NO.	PARA NO.	LINE NO.	TABLE NO.	FIGURE NO.						
A1 THRU A7						✓					
A7.1									✓	203	
A7.2							✓				
A7.3	10								✓	203	Part number not spelled out
	25									*	Part number not spelled out
A7.4						✓					
A7.5									✓	203	
A7.6 THRU A7.10						✓					
A7.11								✓		103	

NOTE: AN ASTERISK (*) IN THE DEFECT CLASS CODE NUMBER COLUMN DENOTES THAT THE DEFICIENCY HAS BEEN CLASSIFIED ELSEWHERE.

FORM NO. 2

TOTAL

CRITICAL	0
MAJOR	1
MINOR	3

NOTE: TOTAL ALL CHECKSHEETS AND ENTER ON SUMMARY SHEET

PAGE 1 OF XX

Figure 4. Manual Style and Format Checksheet.

REVIEW/EVALUATION SUMMARY

TM 5-xxxx-xxx-24 TITLE: Nomenclature of end item
SPECIFICATION: MIL-M-630XX TEST SITE White Sands PROJ. NO: XXXX
TYPE TEST OT-3 REQUIREMENTS: VERIFIED (✓) NOT VERIFIED (✓) ✓

Enter totals of all deficiencies from Review/Evaluation Forms No. 1 and 2 and compute as follows:

Enter Total Number of CRITICAL (1, 2, or 3) DEFECTS: - - - - - - - 0 X 100 = ____
Enter Total Number of MAJOR (101, 102, or 103) DEFECTS: - - - - - 4 X 10 = 40
Enter Total Number of MINOR (201, 202, or 203) DEFECTS: - - - - - 2 X .2 = .4

Total above for number of WEIGHTED DEFECTS: - - - - - - - - - - - - - - - - = 40.4
Enter total number of MANUAL PAGES EVALUATED - - - - - - - - - - - - - - - = 100

Divide total number of WEIGHTED DEFECTS by number of manual pages evaluated to obtain the "n" value or WEIGHTED DEFECTS per page $100\overline{)40.4} = .404$ "n" value

Match the "n" value above with the n value in Table of Quality Values. The QI value in the adjacent column is the value to be entered here:

Quality Index = 67

TABLE OF QUALITY VALUES

QUALITY INDEX FOR n BETWEEN .00 AND 1.99

n	QI	n	QI	n	QI	n	QI	n	QI	n	QI	n	QI	n	QI	n	QI	n	QI
.00	100	.20	82	.40	67	.60	55	.80	45	1.00	37	1.20	30	1.40	25	1.60	20	1.80	17
.01	99	.21	81	.41	66	.61	54	.81	44	1.01	36	1.21	30	1.41	24	1.61	20	1.81	16
.02	98	.22	80	.42	66	.62	54	.82	44	1.02	36	1.22	30	1.42	24	1.62	20	1.82	16
.03	97	.23	79	.43	65	.63	53	.83	44	1.03	36	1.23	29	1.43	24	1.63	20	1.83	16
.04	96	.24	79	.44	64	.64	53	.84	43	1.04	35	1.24	29	1.44	24	1.64	19	1.84	16
.05	95	.25	78	.45	64	.65	52	.85	43	1.05	35	1.25	29	1.45	23	1.65	19	1.85	16
.06	94	.26	77	.46	63	.66	52	.86	42	1.06	35	1.26	28	1.46	23	1.66	19	1.86	16
.07	93	.27	76	.47	63	.67	51	.87	42	1.07	34	1.27	28	1.47	23	1.67	19	1.87	15
.08	92	.28	76	.48	62	.68	51	.88	41	1.08	34	1.28	28	1.48	23	1.68	19	1.88	15
.09	91	.29	75	.49	61	.69	50	.89	41	1.09	34	1.29	28	1.49	23	1.69	18	1.89	15
.10	90	.30	74	.50	61	.70	50	.90	41	1.10	33	1.30	27	1.50	22	1.70	18	1.90	15
.11	90	.31	73	.51	60	.71	49	.91	40	1.11	33	1.31	27	1.51	22	1.71	18	1.91	15
.12	89	.32	73	.52	59	.72	49	.92	40	1.12	33	1.32	27	1.52	22	1.72	18	1.92	15
.13	88	.33	72	.53	59	.73	48	.93	39	1.13	32	1.33	26	1.53	22	1.73	18	1.93	15
.14	87	.34	71	.54	58	.74	48	.94	39	1.14	32	1.34	26	1.54	21	1.74	18	1.94	14
.15	86	.35	70	.55	58	.75	47	.95	39	1.15	32	1.35	26	1.55	21	1.75	17	1.95	14
.16	85	.36	70	.56	57	.76	47	.96	38	1.16	31	1.36	26	1.56	21	1.76	17	1.96	14
.17	84	.37	69	.57	57	.77	46	.97	38	1.17	31	1.37	25	1.57	21	1.77	17	1.97	14
.18	84	.38	68	.58	56	.78	46	.98	38	1.18	31	1.38	25	1.58	21	1.78	17	1.98	14
.19	83	.39	68	.59	55	.79	45	.99	37	1.19	30	1.39	25	1.59	20	1.79	16	1.99	14

QI	Manual Quality
90 – 100	Excellent
80 – 89	Good
70 – 79	Fair
below 70	Unacceptable

J. DOE
Evaluator Name

8-25
Date

FORM NO. 3

Figure 5. Review Evaluation Summary Sheet.

at the bottom of the Summary Sheet. The Acceptable Quality Level for manuals is a Quality Index score of 70 or above. Any score below 70 is considered unacceptable and the manual is considered deficient. The responsible developer is informed of all manual defects, as well as the overall acceptability of the manual. Deficient draft manuals must be corrected before the manuals are considered acceptable for final publication.

PILOT STUDY OF IMAGES

A 6-month pilot study of IMAGES was conducted at US Army Aberdeen Proving Ground, Maryland; US Army Yuma Proving Ground, Arizona; US Army Electronic Proving Ground, Arizona; and US Army White Sands Missile Range, New Mexico, during the period October 1976 through March 1977. The primary objective of this study was to determine the adequacy and usability of IMAGES for evaluating equipment manuals.

Prior to the initiation of the study, a training course in the use of IMAGES was given to maintenance evaluation personnel at each of the participating proving grounds. A total of 24 maintenance personnel, 14 military and 10 civilian, participated in a 5-day training program.

The equipment manuals selected for evaluation at each of the proving grounds were those available at the time of the study. There was no preselection of candidate manuals.

A total of 20 different equipment manuals was evaluated during the study. Of the 20 manuals evaluated, 7 were rated acceptable, with scores of 70 or better, while 13 were rated unacceptable with scores less than 70. A summary of the results of the IMAGES evaluation of the 20 manuals in terms of Quality Index score and overall quality rating is shown in Tables 1 and 2. The data in Table 1 show the results of the evaluation of the seven manuals rated acceptable. The results for the 13 manuals rated unacceptable are shown in Table 2. The types of manuals were varied and representative ranging from the type -12 Operator/Organizational through the type -34 Direct/General Support level. Those manuals designated "P" also included Repair Parts and Special Tool Lists.

TABLE 1

MANUALS RATED ACCEPTABLE
(Total of 20 Manuals Rated)

Manual Title	Manual Type	Quality Index Score*	Quality Rating
Airborne Laser Tracker	-34	98	Excellent
Tank, Fabric Collapsible, 50,000 gal	-12	97	Excellent
Tractor, Universal Engineer, Crawler	-34P	96	Excellent
TD 1065, High Speed Data Buffer	-12	79	Fair
Laser Rangefinder, AN/GVS-5	-34	79	Fair
TD 1069, Digital Multiplexer	-34	76	Fair
Target Designator, Laser, AN/PAQ-1	-20	70	Fair

*A score of 70 or above is acceptable.

TABLE 2

MANUALS RATED UNACCEPTABLE
(Total of 20 Manuals Rated)

Manual Title	Manual Type	Quality Index Score*	Quality Rating
Laser, Rangefinder, AN/GVS-5	-20	67	Unacceptable
Radio Set, AN/ARN 123	-24	66	Unacceptable
MICV, XM723	-20, -34	40, 31	Unacceptable
Doppler Navigation Set	-20	55	Unacceptable
Tractor, Universal Engineer, Crawler	-12P	45	Unacceptable
105MM Gun, M48A5, Turret	-20/1,-20/2	41, 28	Unacceptable
Howitzer, Medium, Towed: 155MM, XM198	-20, -34	40, 29	Unacceptable
TD 1065, High Speed Data Buffer	-12	38	Unacceptable
TD 1069, Digital Multiplexer	-12	29	Unacceptable
Pneumatic Tool & Compressor 250CFM	-14	17	Unacceptable

*A score of 70 or above is acceptable.

A summary of the results of the evaluation of the same 20 manuals set out by classification and category of defect is shown in Table 3. There were 495 defects of format and style and 239 defects of specific technical requirements for a total of 734 defects in the 20 manuals, or an average of 36.7 defects per manual. The number of critical and major defects was fairly evenly distributed between format and style and technical requirements. However, there were substantially more minor defects of format and style, as expected by the nature of the requirements.

TABLE 3

CLASSIFICATION OF MANUAL DEFECTS
(20 Draft Equipment Manuals)

	Manual Defects - IMAGES											
	Format & Style				Specific Reqmts				Total Defects			
	Crit	Maj	Min	Total	Crit	Maj	Min	Total	Crit	Maj	Min	Total
Defects	18	132	345	495	14	121	104	239	32	253	449	734
Avg Per Manual	0.9	6.6	17.3	24.8	0.7	6.0	5.2	11.9	1.6	12.6	22.5	36.7

Critical defects were primarily related to system safety considerations such as the omission of required instruction for grounding of electrical systems, hazard warnings omitted, and the entire safety precautions paragraph omitted from the manual. Examples of major defects include failure to list tools required to perform a job, troubleshooting diagrams which differed from the equipment, and the omission of electrical schematics.

Sixteen of the 20 manuals evaluated using IMAGES had been previously evaluated using the then current method. A comparison of the total number of defects found in these 16 manuals using IMAGES, with those previously reported on DA Form 2028 (Recommended Changes to Publications and Blank Forms) under the existing system, is shown in Table 4.

TABLE 4

COMPARISON OF IMAGES AND CURRENT METHOD
(16 Draft Equipment Manuals)

	Number of Manual Defects					
	IMAGES				Current (2028's)	
	Critical	Major	Minor	Total	Total	Difference
Number of Defects	24	229	345	598	342	(256)
Average Per Manual	1.5	14.3	21.6	37.4	21.4	(16)

In terms of total defects, there were 256 or 43% more defects found using IMAGES than found when using the current method. While the current method did not classify the defects, analysis of the results showed about the same distribution of critical, major, and minor type defects using both methods.

A summary of questionnaire results obtained from 19 of the 20 evaluators who participated in the pilot study is shown in Table 5. One military evaluator was transferred prior to administration of the questionnaire. The responses to question 1 show that there was a reasonably balanced distribution between less experienced and highly experienced maintenance personnel who participated in the study. The responses to questions 2 and 3 show that a substantial majority of the evaluators gave IMAGES a higher rating than the present procedure. The responses to question 4 show that a majority of the evaluators felt that IMAGES required more time than the present method. This response was expected since, with the exception of EPG, the present method did not include a 100% evaluation of each manual. It is noted that at EPG, where the present method included a 100% evaluation of most manuals, all 4 evaluators responded that IMAGES required less time than the present method.

TABLE 5

IMAGES QUESTIONNAIRE RESPONSES
(19 Maintenance Evaluators)

Questions	Responses	APG	YPG	EPG	WSMR	Total
1. Previous manual evaluation experience?	-1 yr	2	1	2	1	6
	1-2 yrs	1	1	1	1	4
	+2 yrs	3	2	1	3	9
2. Rate present procedure for insuring adequacy and accuracy of manuals?	Good	1	2	4	1	8
	Fair	4	2	0	4	10
	Poor	1	0	0	0	1
3. Rate IMAGES for insuring adequacy and accuracy of manuals?	Good	5	3	4	5	17
	Fair	1	1	0	0	2
	Poor	0	0	0	0	0
4. Time required for IMAGES?	Less	0	1	4	0	5
	Same	1	1	0	0	2
	More	5	2	0	5	12

IMAGES is designed to be used in conjunction with "hands-on" performance of actual or simulated maintenance tasks or used strictly for a desk audit of equipment manuals. The "hands-on" experience is of particular value in the evaluation of schematics, illustrations, and troubleshooting procedures. Both techniques were used successfully during the pilot study.

SUMMARY

The results of the pilot study and subsequent use by TECOM in evaluating manuals for a variety of Army systems currently under development have demonstrated the value and utility of IMAGES. IMAGES has been adopted by TECOM as a standard Test Operating Procedure and its use should result in a substantial improvement in the accuracy, readability, and understandability of Army equipment manuals to be sent to the field in the future.

IMAGES is currently being expanded for use in evaluating the Army's "new look" manuals prepared in accordance with Integrated Technical Documentation and Training (ITDT) specifications.

AD-A056474

ARMY HELICOPTER FLIGHT SIMULATION, A RESEARCH AND DEVELOPMENT TOOL FOR THE FUTURE

MR. DALE M. PITT
UNITED STATES ARMY AVIATION RESEARCH AND DEVELOPMENT COMMAND
P.O. BOX 209
ST. LOUIS, MISSOURI 63166

INTRODUCTION

In the last decade, the United States Army has become increasingly interested in flight simulation of its helicopters. In the early 1960's, the Army purchased the 2B24 flight simulator trainer to replace the antiquated 1CA1 "Link Trainer". Subsequently, the Army has purchased flight trainers to simulate the CH-47 and AH-1Q helicopters. However, all these simulators were used primarily for pilot training. It was not until recently that the Army has become interested in piloted simulation as a development tool. Piloted simulations are part of the Army's XV-15 Tilt Rotor Aircraft program and the Rotor System Research Aircraft (RSRA) program. In both of these programs, the simulation was used as a verification tool, i.e., verify handling qualities of the helicopter after design.

This paper presents the results of a piloted simulation that was used as a means of determining the cause of an Army 214 Helicopter accident. The simulation program was also used to augment the design of a flight control monitor system and to investigate the effects of possible control system changes to the 214 helicopter.

ACCIDENT BACKGROUND

In March 1976, the United States Army Aviation Engineering Flight Activity (USAAEFA) was directed by the United States Army Aviation Command (USAVSCOM) to test the Airworthiness and Flight Characteristics of the Iranian Model 214C Helicopter. It was during this testing that the helicopter experienced excessive main rotor flapping, and subsequently, the helicopter disintegrated in flight.

A post crash fire destroyed all in flight data and recordings, thus making it impossible to determine the cause of the accident. However, an observer in the chase helicopter stated that the helicopter was in a nose down and left roll attitude prior to its disintegration. An inspection of the wreckage disclosed that the main rotor shaft, hub, and blades had experienced excessively high main rotor flapping prior to their separation from the helicopter.

During this particular flight, the crew was testing the failure modes of the helicopter's Automatic Flight Control System (AFCS) for compliance with paragraph 3.5.9 of reference 1. The test helicopter was configured so that the flight engineer could induce a hardover failure in a given AFCS channel by depressing the respective button on a special "Hardover Test Box". Upon releasing the button, the hardover was removed and the AFCS resumed its normal function. It was hypothesized that the flight engineer inadvertently released the hardover button coincident with the pilot's corrective input, consequently resulting in a hardover in the other direction.

The primary objectives of the simulation were to duplicate all possible AFCS failures, both inadvertent and advertent, inconjunction with subsequent pilot actions that could have caused the accident. Also, we wanted to try and identify the best pilot technique to use to recover the helicopter from an AFCS hardover.

FACILITY DESCRIPTION

The Flight Simulator for Advanced Aircraft (FSAA) is a piloted simulator at NASA Ames Research Center that has six degrees of freedom. The motion system is capable of $\pm$ 5 feet displacement in the vertical direction, $\pm$ 4 feet in the longitudinal direction, and the unique capability of $\pm$ 50 feet of lateral displacement. The FSAA can achieve velocities of 8.65 ft/sec, 6.32 ft/sec and 17.00 ft/sec in the vertical, longitudinal and lateral directions respectively. Figure one is a comparison of maximum angular rates of the FSAA and maximum rates of the 214C helicopter measured during flight testing. It should be noted that none of the 214C helicopters' rates exceed the capability of the simulator. If the actual helicopter rates exceeds the simulator's capability, false pilot cues would result which would limit/degrade the overall simulation.

The total Flight Simulator for Advanced Aircraft (FSAA) system is depicted in figure two. A Xerox Data System (XDS) Sigma 7 and an XDS Sigma 8 are used to provide driving values for the simulator hardware inconjunction with processing feedback signals from these units. The digital computers communicate with each other via

the XDS 7908 interface hardware. Analog to digital converters, digital to analog converters, and discrete input/output channels are used to process computer generated signals to simulation hardware through the instrument rack. The simulation is conducted from the simulation control room which is the basis for operating/debugging the computer system. Signals are sent to the Visual Flight Attachment, which generates the pilot's visual scene, from the instrument rack. Signals are sent through the Drive Rack to the Motion System Drive which drives the Cockpit to the desired position and attitude.

MAXIMUM RATES (DEG/SEC)		
AXIS	214C	FSAA
DIRECTIONAL	20.4	40.1
LATERAL	28.6	40.1
LONGITUDINAL	16.2	101.4

FIGURE 1. THE FSAA MAXIMUM ALLOWABLE RATES COMPARED TO THE MAXIMUM MEASURED RATES OF THE 214C HELICOPTER

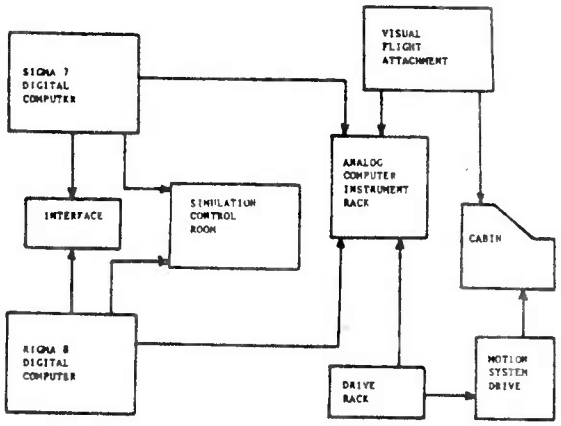

FIGURE 2 THE FSAA DUAL PROCESSOR SYSTEM SCHEMATIC

HELICOPTER MATHEMATICAL MODEL

The requirement to simulate AFCS hardover failures and subsequent recovery techniques demanded that the mathematical model be capable of accurately describing large pertubations from trimmed flight conditions. The mathematical description of the 214 helicopter had to have a high degree of exactness in the calculation of the rotor blade flapping because of the suspected excessively large flapping during the accident. The mathematical model is a non-linear, highly coupled formulation in six degrees of freedom. The math model was a variation of the math model used in the Bell Helicopter Textron/Army/NASA XV-15 Tilt Rotor Program Simulation. The main rotor and tail rotor performance and dynamics were calculated utilizing a lifting disc model. The lift and drag forces for the helicopter fuselage and tail surfaces were calculated from aerodynamic functions stored in the computer program. These aerodyamic functions were derived from wind tunnel test. The math model also represented the engine power and engine governing characteristics. Further description and explanation of the math model can be found in reference 2 and 3.

The Automatic Flight Control System (AFCS) and its associated logic and control authority was also included in the Math Model. The SCAS logic system also included provisions for system failures, i.e., hardovers. In order to perceive the true impact of the simulation program, a brief description of the 214 helicopter's flight control system is in order. The AFCS system of the 214 helicopter consists of a Stability and Control Augmentation System (SCAS) and the Attitude Retention System (ATTD). The SCAS is integrated into the cyclic and anti-torque control systems to automatically provide improved stability and handling qualities of the basic helicopter. SCAS input to the control system is accomplished by an electro-hydraulic servo actuator installed series with the control system. The ATTD mode automatically maintains the desired pitch and roll attitude and heading of the helicopter. The attitude inputs to the control system are accomplished through combined inputs from the SCAS series electro-hydraulic actuators and an electro-mechanical trim actuator connected in parallel.

The complex nature of the nonlinear coupled mathematical equations makes their computation quite lengthy, and could compromise a real-time simulation. The real-time cycle rate has been a considerable problem when doing pilot in the loop simulation in the past. The integrity of the simulation is heavily dependent on the computer program cycle time. Cycle time is the length of time for the computer to integrate all solutions of the differential equations and provide the respective inputs to the simulation hardware, i.e. motion drive, visual system, etc. Generally the solution of the nonlinear equations results in the most significant increase in cycle time.

The unique aspect of this simulation, as opposed to other flight simulations, was that two digital Sigma 7 and Sigma 8 computers functioned in parallel to solve the math model equations. This dual-processor was initiated in the simulation of the RSRA helicopter. (4) The dual-processor was necessary in order to obtain an acceptable cycle time of approximately 40-50 milli seconds. The cycle time would increase by 40 percent if only one Sigma 8 computer was used in lieu of the dual-processor system. This would result in a marginal cycle time.

SIMULATOR CORRELATION AND VERIFICATION

Correlation of the various elements of the helicopter mathematical model were carried out after the completion of the programming of the computers. The primary purpose of the correlation was to determine the degree of fidelity the simulation had with the actual

214 helicopter. The simulator correlation and verification, as required in reference 5 test plan, was done at the airspeed, center of the flight conditions prior to the accident. The evaluation and verification was predicated on comparison of flight test data of references 6, 7, and 8 with the equivalent simulator results. The simulator evaluation consisted of the following test a) Rotor Perform ance, b) Control system characteristics, c) Control positions in trimmed forward flight, d) Dynamic Stability, e) Controllability, and f) Automatic Flight Control System (AFCS) failures.

Rotor thrust and power calculations were obtained by effectively isolating the rotors from the fuselage aerodynamic effects and using these results to compare with the results from BHT AGAJ-7407 (C81) computer program. Any variation in performance between the simulation and C81 was rectified by making slight alternations to the basic aerodynamic functions in the simulator program. This was a performance match of the simulator lifting disc math equations, with the C81 rotorcraft analysis.

The control system characteristics were checked to insure that the breakout forces, trim rates, force gradients, control travel and trim authority matched those of the 214 helicopter. The control positions in trimmed forward flight of the FSAA were checked against flight test results. Figure 3 shows the close correlation of control position locations in trimmed forward flight. The static lateral-directional stability and the dynamic stability of the FSAA were checked against flight test data. The results showed good correlation.

Controllability tests were conducted to evaluate the control power, control response, and control sensitivity of the simulator. Testing was accomplished by applying step control inputs in increasingly equal increments in each direction about the pitch, roll, and yaw axis. Figures 4 and 5 depict the results of the controllability test of the simulator compared to flight test data. The fidelity of the simulator is verified by the close correlation of the controllability plots. This infers that for a given control input, the rotor/airframe coupling is equivalent to that of the actual aircraft.

Automatic Flight Control System (AFCS) failures were conducted to verify that the simulated AFCS logic operated properly and that the simulated hardover failures were representative of the actual helicopter. Figure 6 is a time history plot of comparative hardover failures. Observing the time histories, it should be noted that the cyclic stick's movement is in the right direction. The

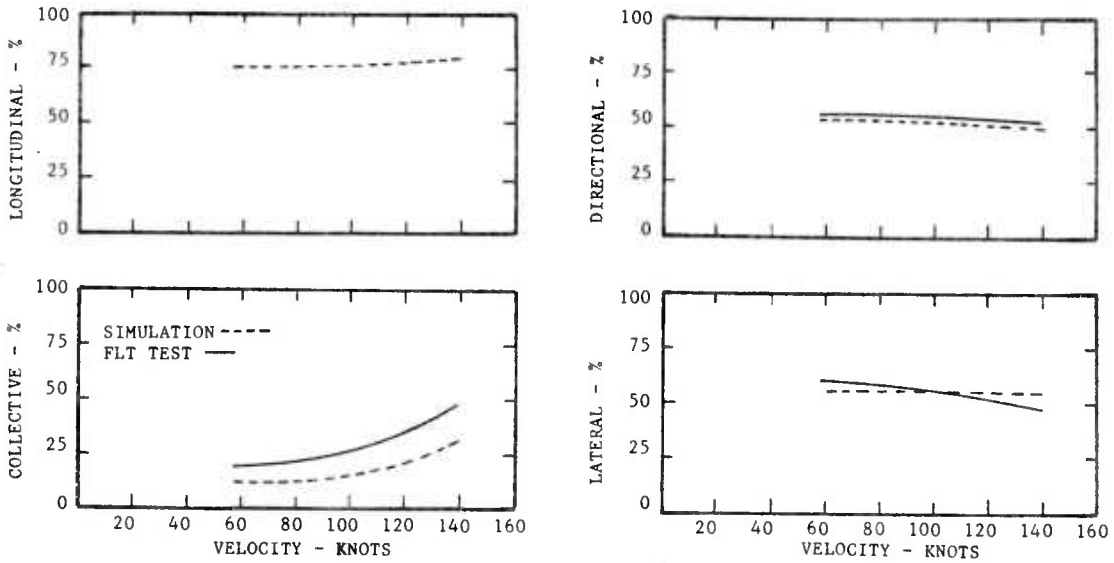

FIGURE 3. CORRELATION OF STATIC TRIM PARAMETERS

pitch rate and attitude show simular trends between flight test and simulator data. It is difficult to match the parameters in a hard-over test because they are all dependent on the pilot delay time. It was almost impossible to have the simulator pilot delay the exact time as on the flight test results. Not shown are other pilot inputs such as lateral cyclic stick, directional and collective stick position which have a slight effect on the parameters displayed. The figure shows minimal discrepancy between actual main rotor flapping and the calculated main rotor flapping of the simulator. With the major discrepancy being credited to diffeence in pilot fore and aft cyclic stick movement as opposed to a shortcoming attributable to the math model. In general, data is strongly influenced by pilot inputs, consequently making simulated hardover verification extremely difficult.

TEST METHODOLOGY

The test consisted of a pilot flying the simulator to accomthe Iranian Helicopter were twofold. The first was to investigate and determine the possible factors and sequence of events leading to high main rotor flapping during maneuvers. The second was to investigate various pilot techniques of preventing flapping and consequently mast bumping during recovery from unusual attitudes.

The test consisted of a pilot flying the simulator to accomplish the above objectives in accordance with the established test

plan. (5) During the simulated flight, hardover failures, both single and dual axis, were induced about each aircraft axis, i.e., pitch, yaw and roll. The majority of the simulator flights were conducted at the flight conditions that were believed to be those of the helicopter at the time of the accident. These flights are referred to as baseline flights. The baseline configuration was 13000 pounds gross weight, with center of gravity at the aft limit of 144 inches, an altitude of 5000 foot and an airspeed of 120 knots.

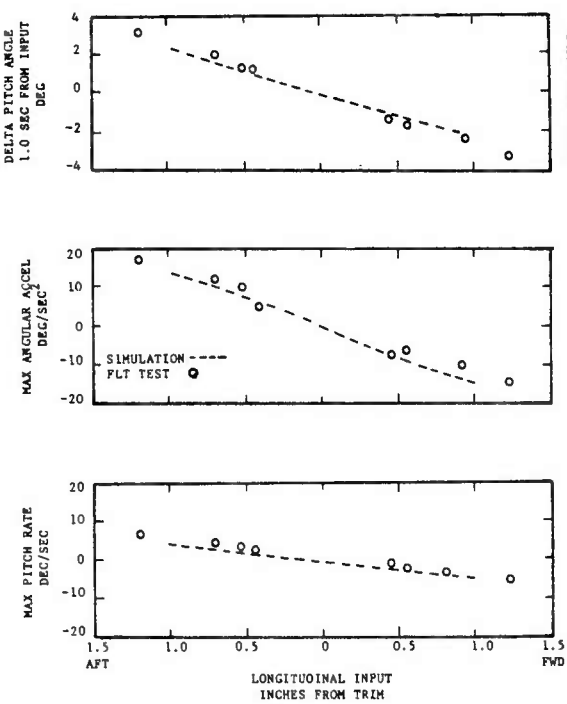

FIGURE 4. LONGITUDINAL CONTROLLABILITY COMPARISON

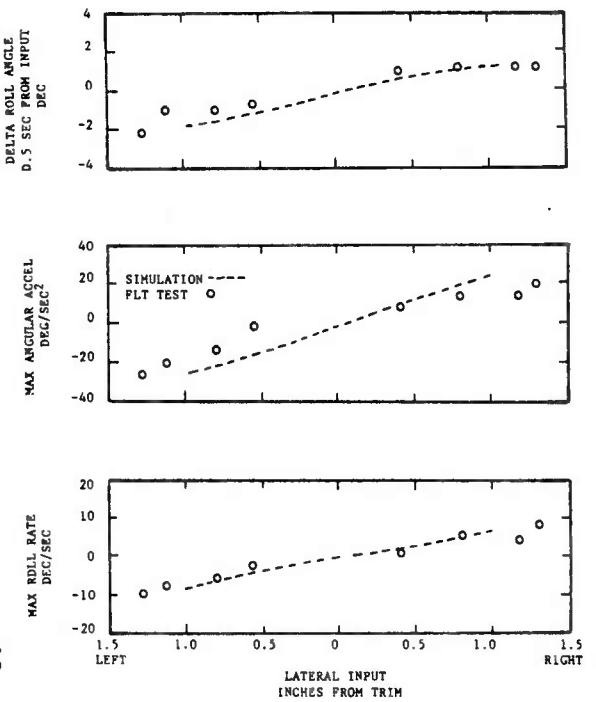

FIGURE 5. LATERAL CONTROLLABILITY COMPARISON

Data was obtained during hardover failures with the pilot delaying his corrective inputs in one second inputs until the maximum delay time was achieved. During flight test programs, hardover delay times are generally built up from a minimum time to a maximum pilot delay time was achieved. During flight test programs, hardover delay times are generally built up to from a minimum time to a maximum delay time. Previous data shows that the maximum pilot delay times in the simulator are in close agreement with results from flight test programs contrary to the thought that the lack of pilot anxiety in a simulator would increase the delay times. (9) However, it is thought that pilot training from flight test experience carried over to the simulator contributing an inhibiting effect. In addition, the pilot has a very low motivation to achieve long delays in an aircraft or simulator. The maximum delay period was determined as being the delay time when

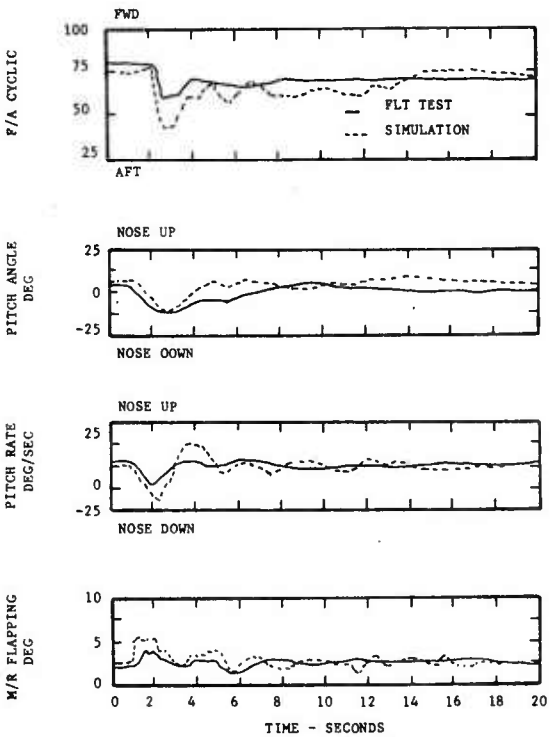

FIGURE 6. PITCH DOWN HARDOVER TIME HISTORY

TABLE I

PILOT RECOVERY TECHNIQUES	
#1	After the initiation of the hardover, the pilot delays the appropriate time and returns helicopter to a level attitude.
#2	Same as technique #1 except that the hardover is removed at the start of recovery.
#3	Same as technique #1 except that the AFCS was disengaged at the beginning of the pilot recovery.
#4	Same as technique #1 except that the collective was dumped during recovery to simulate inadvertent power drop.
#5	After the initiation of the hardover, the pilot delays the appropriate time and arrests the rate/attitude change and then flies out of the attitude in a gentle maneuver.

100 percent main rotor flapping was reached and/or the pilot is still able to regain control of the aircraft.

After the delay, the pilot would use one of five pilot technique (See Table I) to correct for the hardover condition and regain control of the aircraft. One criteria for selecting the pilot techniques investigated were to select those on the basis of being a possible series of events leading to the 214 accident. It was also imperative not only to specify the technique that directly lead to the accident, but also the technique that would result in the minimum main rotor blade flapping during recovery. The latter technique would become the established emergency procedure. Pilot technique number 2 was thought to be the most severe from the aircraft attitude and main rotor flapping aspect. (In technique #2 by removing the simulated hardover at the time of pilot recovery, the AFCS comes back on line and senses the large attitude rate, immediately compensates by moving the actuator just as the pilot is making his inputs. This is in all actuality a hardover in the reversed direction from the original hardover). For each individual pilot technique and time delays, various parameters, e.g., helicopter attitude, control

positions airspeed, etc., were recorded with particular monitoring interest on main rotor flapping.

A total of four test pilots participated in the program. Of the four pilots, three were Army test pilots with a wide background in helicopter testing and one pilot was a Bell Helicopter test pilot with previous simulator experience and 214 helicopter test time. Of the three Army test pilots, none had previous simulator experience other than training flights in the UH-1H Army trainer 2B24. One Army pilot had recently completed a flight test program on te 214C helicopter, and consequently, was quite familar with its performance and handling qualities.

Certain baseline flights were repeated with all pilots utilizing all pilot recovery techniques to insure adequate data overlap. With the comparison of the simulation parameters, one was able to ascertain that the effects of different pilots on the test data was minimal. After completion of the baseline testing, hardover testing was done in a combination of axis concurrently. This required the simulation engineer, who was stationed in the simulation control room, to induce simultaneous failures in two different axis, example: pitch down and left roll. This was performed to determine the pilot effort required to control the dual hardover failures versus single failures.

Upon completion of the above hardover testing, the basic test configuration was varied for the remainder of the test. The airspeed was varied from 100 to 160 knots along with varying the c.g. from aft to forward and varying altitude.

The prepare the simulator to run the different test cases, all that was necessary was to make an input change to the computer program which did not take much time. This is a demonstration of the flexibility that a simulator program has over a flight test program, which would have required extensive work and effort to change the flight conditions.

Testing was also done under simulated IFR conditions. This was accomplished by having the computer generate and project a complete cloud cover over the pilot's visual screen. This required the pilot to completely regain control of his aircraft after a hardover failure by use of the flight instruments only. This test was not performed as part of the accident investigation, but to determine if a pilot could recover the aircraft after a hardover failure while flying IFR, i.e., no outside horizon reference. A flight test of simular magnitude would be dubious, because of the hazard of flying a test under IFR conditions, demonstrating the value of a simulator.

Hardover test were performed with reduced SCAS authority by varying the constants of the SCAS actuators in their respective subroutine package of the computer program. The baseline test were performed with approximately ± 12% pitch authority and was subsequently reduced to ± 10% and eventually to ± 8%.

The test concluded with the incorporation of a SCAS monitor system in the SCAS logic subroutine of the computer program. This was done to demonstrate the benefits of a SCAS monitor into the 214 helicopters. The principle of operation of the monitor is that it has a duplicate SCAS comparator network which in the event of a hardover will only disengage the faulty channel. Thus the hardover is nulified before it can change the helicopter attitude. Thus the remaining SCAS channels are left operating and the helicopter can safely be flown with only one SCAS channel off line.

SIMULATION RESULTS

The results of the baseline hardover simulator test depicting main rotor flapping versus pilot delay time and the respective pilot technique are shown in figures 7 through 10. The data shown in the aforementioned figures are derived from simulator flights that parallels the accident flight conditions. It should be noted that pilot technique number 5, is only applicable to lateral hardovers, i.e., flyout technique is designed for helicopters at high roll attitudes. Pilot technique number 4, was not flown for right roll hardovers because they did not prove effective in controlling previous hardovers.

PILOT DELAY TIME SEC	MAIN ROTOR FLAPPING - PERCENT				
	39 AND BELOW	40 TO 59	60 TO 79	80 TO 89	90 TO 100
1.0		3, 4, 5	1		2
1.5		3			
2.0		3	1, 4, 5		2
2.5			4	2	

FIGURE 7. PITCH UP HARDOVER RESULTS

PILOT DELAY TIME SEC	MAIN ROTOR FLAPPING - PERCENT				
	39 AND BELOW	40 TO 59	60 TO 79	80 TO 89	90 TO 100
.5		1	3		
1.0		4	1	2, 3	
1.5					1, 2

FIGURE 8. PITCH DOWN HARDOVER RESULTS

Figure 7 presents the results of a longitudinal hardover, pitch down, at the basic configuration. It should be noted that the maximum delay time was 1.5 seconds with pilot techniques number 1 and 2 resulting in the largest main rotor flapping. Technique number 2 was specially formulated as the technique which most probably resulted in the accident. Pitch down hardovers resulted in large pitch rates coupled with large roll rates to the right. The roll rate if allowed, built up to such on extent that it could not be controlled by the lateral cyclic stick/lateral rotor control power remaining. An adverse effect of pitch down hardovers is that it results in the aircraft entering a nose low attitude which results in an increase in airspeed and a decrease in altitude. In the event the 214 is engaged in high speed flight at a low altitude and a pitch down hardover is encountered the helicopter may exceed the Vne speed (Velocity Never to Be Exceeded). In addition, a significant loss in altitude may result, thus minimizing the altitude required for a safe recovery of the helicopter.

The data from pitch up hardovers are displayed in figure 8. Pitch up hardovers would result in a nose up altitude of the helicopter, and due to the visual system restrictions the pilot would loses his horizontal reference and would appear to be flying in a thick cloud cover. This made it necessary for the pilots to recover the aircraft by reference to their flight instruments. It is obvious that pilot technique number two resulted in the largest flapping and the minimum pilot delay time, clearly the worse condition.

PILOT DELAY TIME SEC	MAIN ROTOR FLAPPING - PERCENT				
	39 AND BELOW	40 TO 59	60 TO 79	80 TO 89	90 TO 100
1.5	4, 5	1, 2			
2.0		1, 3	2		
2.5		4, 5			
3.0		3	5	2	
3.5			1		

FIGURE 9. LEFT ROLL HARDOVER RESULTS

PILOT DELAY TIME SEC	MAIN ROTOR FLAPPING - PERCENT				
	39 AND BELOW	40 TO 59	60 TO 79	80 TO 89	90 TO 100
1.0	1.				
1.5	3, 5	2			
2.0	1, 3	5	2		
2.5		3	1, 5		2

FIGURE 10. RIGHT ROLL HARDOVER RESULTS

Roll hardovers were generally less severe than the pitch or longitudinal hardovers. Figures 9 and 10 clearly depicts that pilot technique number two resulted in an increase in main rotor flapping

over all other techniques tested. The maximum delay time was approximately 3 seconds for a right roll hardover and 3.5 seconds for a hardover resulting in a left roll. Flight test have shown that yaw hardovers are very mild and due not result in large yaw rates or altitude excursions, and consequently, did not warrant investigation.

The data from the other testing is not shown but will be discussed in general terms. The effects of changing the center of gravity from the baseline aft c.g. to a forward c.g. of 134.6 inches was minimal on the main rotor flapping and delay time. Airspeeds of 100, 120, 140, and 160 knots were tested for all single axis hardover combinations. The results showed that there was no noticeable increase in flapping due to the increased airspeed, except for the case of 160 knots pitch down hardovers which showed a slight increase.

The hardovers that were induced under simulated IFR resulted in no difference in response. This is to say that flapping and maximum time delays are comparable to those of the baseline testing shown in figure 7 through 10.

As previously mentioned, the flight control systems of the 214 helicopter ws mathematically modeled in such a way that the SCAS control gains could be adjusted to investigate their effects on the helicopter handling and stability characteristics during normal flight and hardover failures. During normal trimmed flight, the pilots noted no qualitative difference in helicopter handling qualities with the reduced SCAS pitch authority. The maximum delay times were not effected by varying the SCAS authority, however, the pitch down flapping response was reduced approximately 20 percent when the SCAS authority was reduced to 8 percent.

The results of the SCAS monitor testing showed that the monitor would disengage the failed SCAS channel and center the series actuator. The monitor reduced the main rotor flapping appreciably and made the pilot's job of correcting the hardover minimal.

ACCIDENT DETERMINATION RESULTS

Throughout the testing, it was impossible to achieve a pitch down and left roll altitude from either single or dual hardovers. This is the attitude observed during the accident. The observer was confidient about the pitch down attitude while being hesitant about the left roll attitude. Pitch down hardovers with delays of 1.5 seconds resulted in a nose low attitude and when pilot techniques 1 or 2 were used for recovery excessively high main rotor flapping resulted. However, pitch down hardovers in the simulator would

result in a large roll attitude to the right which was contrary to the observed attitude. This can be explained by the fact that the observer was hesitant about the roll attitude and that the pitch down right rod coupling of the simulator was exaggerated over that of the real helicopter. Predominantly, large flapping would result if the hardover was removed inadvertently at the start of the pilot recovery maneuver, i.e., pilot technique number 2.

Although it was impossible to ascertain conclusively the exact cause of the accident, it is most probable that the accident was caused by a pitch down hardover during flight testing, and its inadvertent release prior to recovery.

CONCLUSIONS

From this program, one can conclude that future Army real-time pilot-in-the loop simulations have considerable merits as a research and development tool. A simulation of the magnitude as outlined in this paper would be extremely costly and time consuming if it had to be performed by flight testing. Also there is considerable pilot risk in flight testing the failure modes of the helicopter control system. Thus simulators are ideal for test that involve a degree of risk during flight testing. A simulator program is cost effective because they require less people to be involved, require less time, and are not affected by weather (can fly 24 hours a day if need be and do not have to wait for good flying weather).

The ability to modify the math equations to represent different test conditions, e.g., gross weight, center gravity, airspeed, etc., and control system configurations of the basic helicopter, as demonstrated by this will result in the simplification of the airworthiness/qualification process of future Army helicopters. This will allow Army assessment of a new/development helicopter's handling qualities and performance, while the helicopter is still in the development phase. The pilot can perform maneuvers in the simulator that are physically prohibited during normal flight testing of development helicopters.

RECOMMENDATIONS

As future follow on, consideration should be given to the following recommendations for piloted simulation as a development tool:

1. Modification of math model to incorporate gust and turbulence inputs into the simulation, thus allowing the pilot to assess the effects of a turbulent environment.

2. Piloted simulation can be used to effectively evaluate simulated night flight and the related effects on pilot workload.

3. Through modification to the basic math model, different configurations of the basic aircraft can be represented and tested. An example would be the effects of a stretched airframe, improved engines, and different control surfaces. Not only can they be evaluated but their design can be optimized without having to build actual hardware.

4. The simulator could be used to effectively evaluate handling quality requirements and military specifications more effectively than previously done in flight test programs. (10 & 11).

5. Piloted simulation could be accomplished with actual flight control hardware interconnected with the simulator to verify and qualify equipment operation (12 & 13).

6. The simulator is an ideal tool to perform helicopter failure analysis, e.g., control system failure, engine failure, loss and center of gravity changes (store jettison), assymetric c.g. effects, etc. Simulator would be used to evaluate the effects of the above failures and to optimize a helicopter design that would minimize the failure.

7. Human factor evaluation of new equipment and its installation location can idealy be accomplished on a simulator with its ease of equipment change.

REFERENCES

1. Military Specification, MIL-H-8501A, Helicopter Flying and Ground Handling Qualities; General Requirements for, 7 Sep 61, with Amendment 1, 3 Apr 62.

2. Harendra, P.B, et al, "A Mathematical Model for the Real Time Simulation of the Bell Model 301 Tilt Rotor Research Aircraft", NASA CR 114614, April 1973.

3. Batra, N.N, "Model 214A Control Hardover Simulation", Bell Helicopter Textron Report No. 214-099-250, April 1977.

4. Mackie, D.B, Alderete, T.S., "A Real-Time, Dual Processor Simulation of The Rotor System Research Aircraft", NASA TN D-8328, January 1977.

5. Pitt, D.M, "Test Plan, Flight Simulation of the 214A Iranian Helicopter Utilizing the NASA/AMES FSAA," USAAVSCOM, January 1977 (Revised).

6. Horton, W.R., et al, "Airworthiness and Flight Characteristics Evaluation Iranian Model 214A Helicopter", USAAEFA Project No. 74-30, July 1975.

7. Blaha, J.T, "Handling Qualities Demonstration of the Iranian Model 214A Helicopter, "Bell Helicopter Textron Report No. 214-099-081, February 1975.

8. Magnuson, R.A, "Results of the Phase I A.P.E. Handling Qualities Test on the Iranian Model 214C Helicopter", Bell Helicopter Textron Report No. 214-099-019, November 1976.

9. Blake, B.B, Abion, N, Radford, R, "Flight Simulation of the CH-46 Helicopter", 25th Annual National Forum Proceedings, May 1969.

10. Harper, H.P, Sardanowsky, W, Schrapf, R., "Development of VTOL Flying and Handling Qualities Requirements Using The Mission Task Performance Oriented Approach", 25th Annual National Forum Proceedings, May 1969.

11. Bryant, W.B, Trueblood, R.B, "Use of Programmable Force Feel For Handling Qualities Improvement in a Helicopter Velocity Flight Control System", 31st Annual National Forum of the American Helicopter Society, May 1975.

12. Townsend, J.L, Blatt, P.E., "New MIL-F-9490D Requirements and Implications on Future Flight Control Design", AIAA Journal of Aircraft, Vol 13, No. 9, Sep 1976.

13. Brown, S.C, et al, "Microwave Landing System Requirements for STOL Operations", AIAA Journal of Aircraft, Vol 13, No. 2, Feb 1976.

AD-A056475

AEROBALLISTICS OF CORKSCREW PROJECTILES

ANDERS S. PLATOU, MR.
U.S. ARMY BALLISTIC RESEARCH LABORATORY
ABERDEEN PROVING GROUND, MARYLAND 21005

1. INTRODUCTION

During the development and exploitation of the BRL Non-Conical Boattail Projectile[1-5], it became evident that a new projectile shape which combines a triangular nose with a triangular boattail (Figure 1) would have low drag and a long wheel base for low balloting in the gun barrel. No aerodynamic data were available on the configuration (nicknamed the corkscrew) at the beginning of this program, so it was deemed advisable to conduct wind tunnel and range tests to determine its drag and stability characteristics.

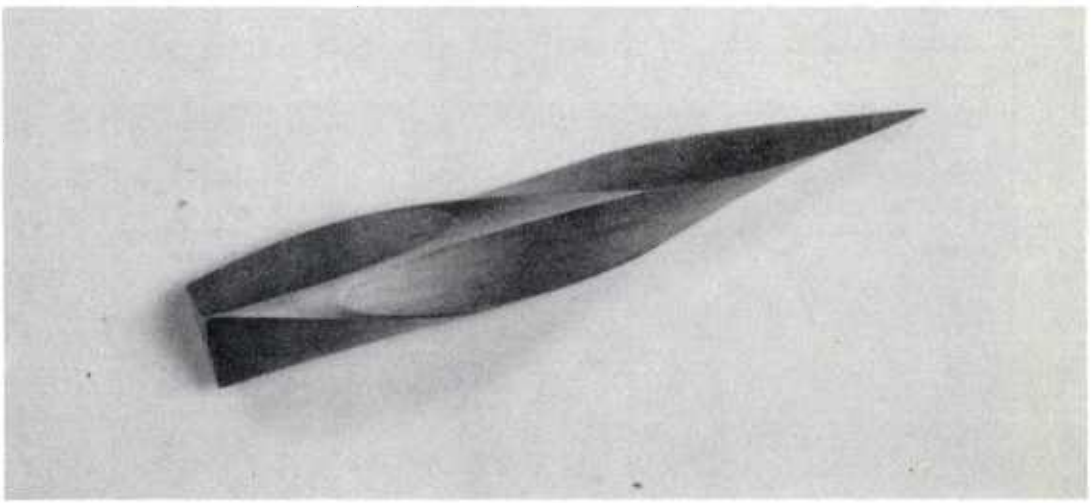

Figure 1. The Corkscrew Projectile

2. THE CORKSCREW GEOMETRY

The basic corkscrew geometric pattern is obtained by cutting a solid cylinder with a series of six skewed planes to obtain the configuration shown in Figure 1. Three skewed planes form the pointed triangular nose and with three skewed planes, sloped the opposite way, to form the boattail. The boattail planes up to now have been terminated when they form an inscribed triangle, but it is possible to terminate them at any desired axial station. The slope or angle of these planes with respect to the cylinder centerline can be varied; however, the angles of the three nose planes must be the same as well as the angles of the three boattail planes. However, the nose plane angles need not be the same as the boattail plane angles. The six planes are usually skewed at a constant twist rate generally near the spin expected at launch.

The corkscrew configuration does not have the usual axial symmetry and, therefore, it can be expected to have non-linear aerodynamic characteristics, especially at spins (pd/V) far from the configuration twist. For this reason, the spin of all of the range flights made to date have been near the twist of the configuration.

3. TEST RESULTS

The first data came from supersonic wind tunnel tests of a 5-caliber long non-interdigitated or non-overlapping configuration (Figure 2). This configuration has a 10° nose angle and a 7° boattail and the model is 5.715 cm in diameter. The significant results from these tests are described below and are compared with results from the 5-caliber Army-Navy Spinner Rocket (ANSR) with a cylindrical tail.

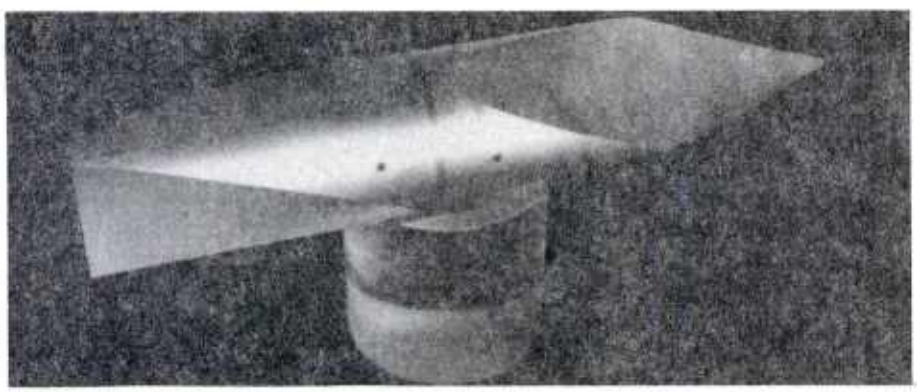

Figure 2. The 5-Caliber Wind Tunnel Model of the Corkscrew Projectile

(a) Even though the normal force on the corkscrew is extremely high (Figure 3), the pitching moments about a center of gravity three-calibers aft of the nose are about the same as those on the 5-caliber ANSR (Figure 4). Therefore, the normal force center of pressure of the corkscrew configuration is located further aft than on the 5-caliber ANSR.

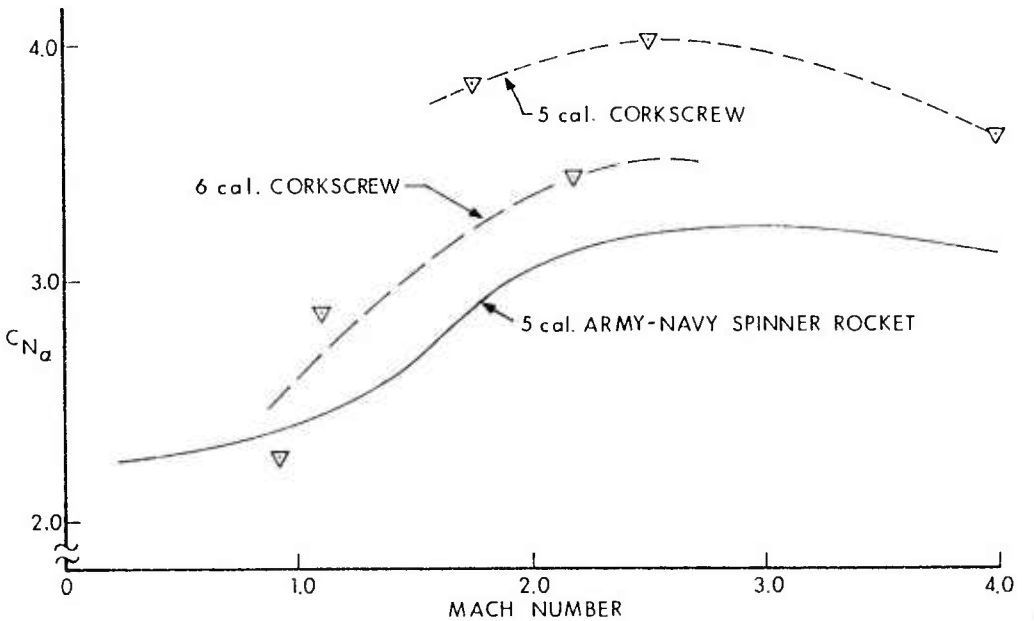

Figure 3. The Normal Force Coefficient of the Corkscrew Projectile

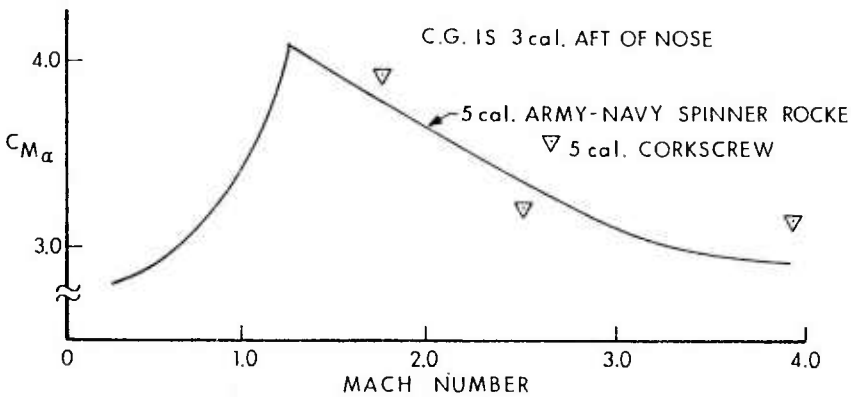

Figure 4. The Pitching Moment Coefficient of the Corkscrew Projectile

(b) At low angles of attack, the Magnus forces and moments are small at all spin rates near the configuration twist. This is due to the zero spin "offsetting" side force and moment characteristic of this configuration[2] (Figure 5).

Because of the difficulty in designing and building the interdigitated wind tunnel version, 20 mm diameter 6-caliber and 8-caliber long models were built for flights in the BRL Aerodynamics Range. The models were made of brass and used drilled base holes to increase the possibility of stable flights in the range. The 6-caliber long models had 7° triangular boattails and 5.71° triangular noses while the 8-caliber long models had 4.76° on both nose and boattail planes. Both the 6-caliber and 8-caliber configuration had one-caliber overlap between the nose and boattail planes. Below, aerodynamic data from several flights up to M = 2.2 are compared with aerodynamic data on the 5.7-caliber long M549 (Figure 6) and the 6.2-caliber long non-conical boattail projectile-A (Figure 7).

(1) Shock waves or flow discontinuities on the corkscrew configuration are virtually non-existent at transonic speeds (Figure 8). This figure can be compared to the shock wave pattern existing on a conventional projectile configuration at the same Mach number (Figure 9). The almost shock free flow pattern is believed to be due to the more uniform area distribution of the corkscrew configuration (Figure 10). Further studies in both ranges and wind tunnels would be necessary to completely understand and explain this phenomenon.

(2) The drag coefficient of the corkscrew configuration is very low compared to that of the two reference projectiles (Figure 11).

(3) The normal force coefficient (Figure 12) is not as large as for the non-interdigitated wind tunnel configuration, but it is larger than for the M549 and the NCB-A projectiles.

(4) Even with the rearward center of gravity of the corkscrews, the pitching moment coefficient is much lower for the 6-caliber corkscrew (Figure 13) than for the M549 and NCB-A projectiles. The pitching moment coefficient of the 8-caliber corkscrew is just slightly higher than the maximum pitching moment coefficient of the M549. The pitching moment coefficient of the corkscrew appears to remain nearly constant with Mach number indicating that the corkscrew configuration does not have the characteristic spike in the pitching moment curve. Additional data above M = 1.05 are required to verify this.

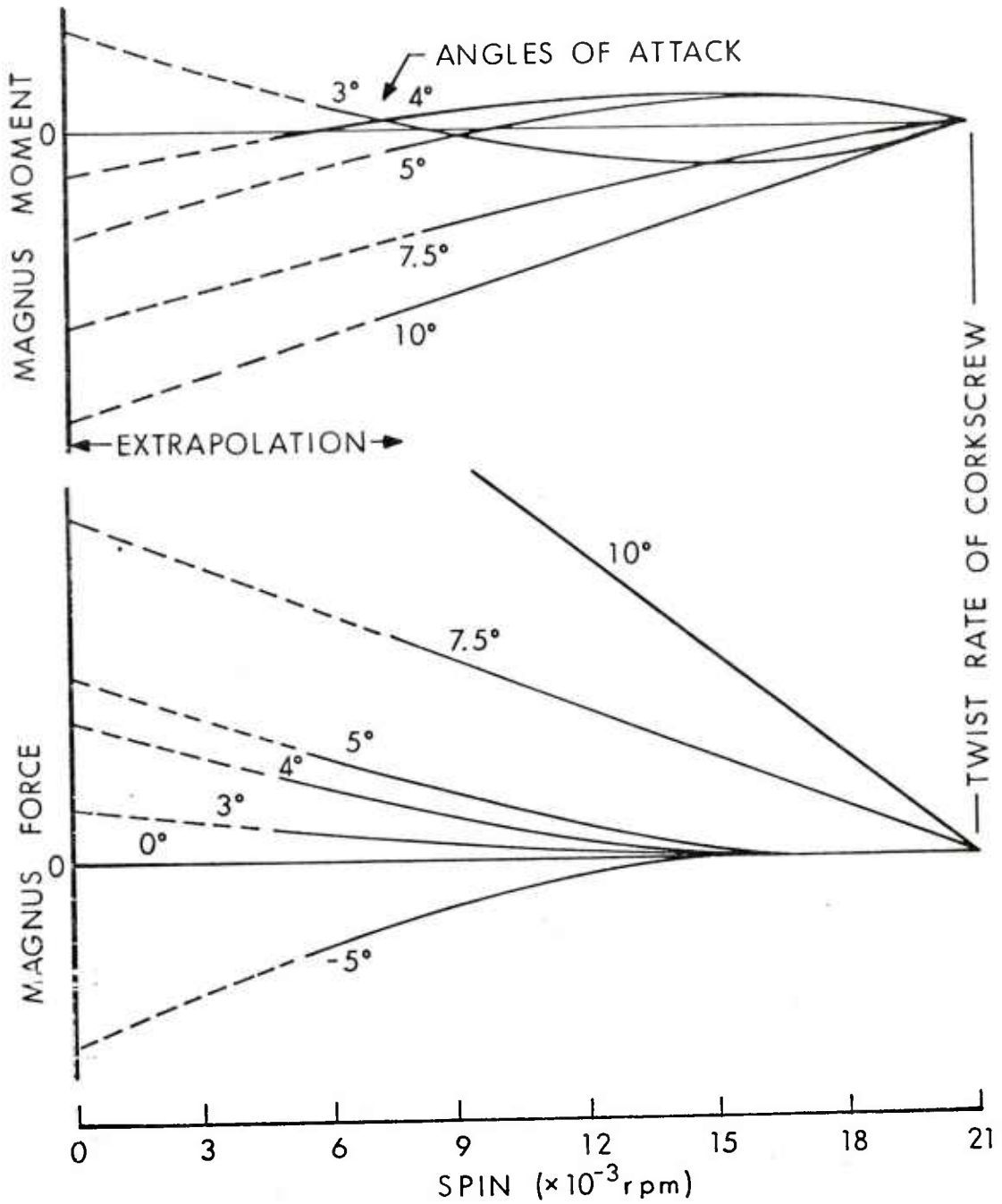

Figure 5. The Approximate Magnus Characteristics of the Corkscrew Projectile

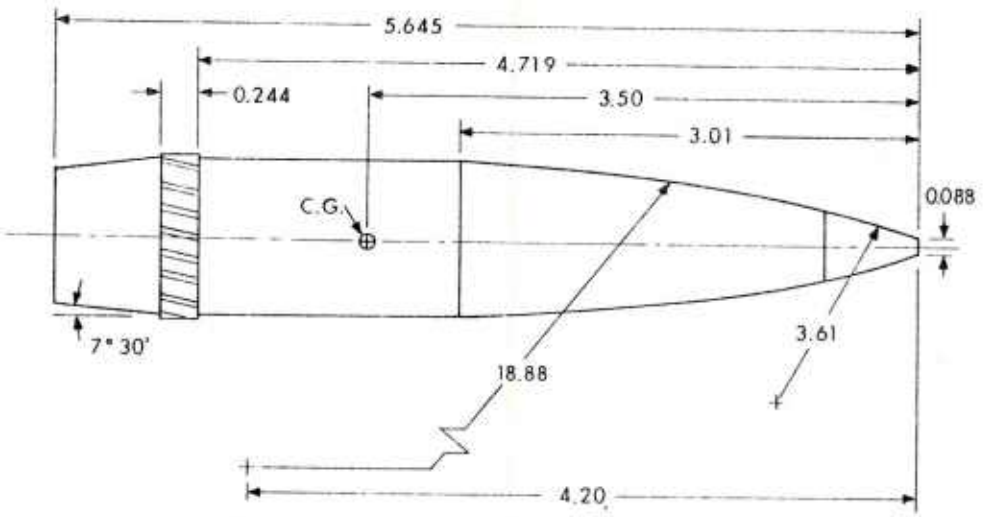

Figure 6. The 155 mm M549 Projectile

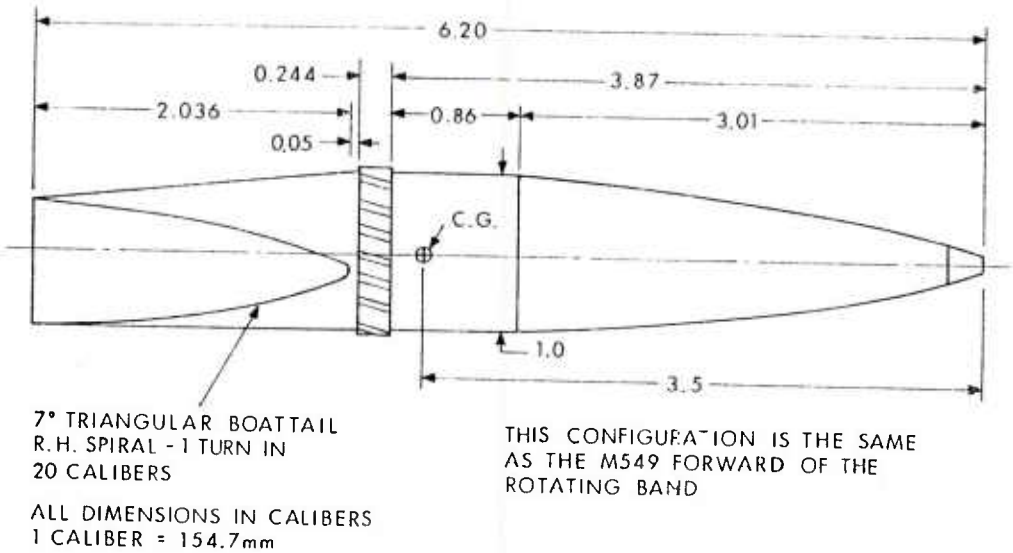

Figure 7. The Non-Conical Boattail Projectile NCB-A

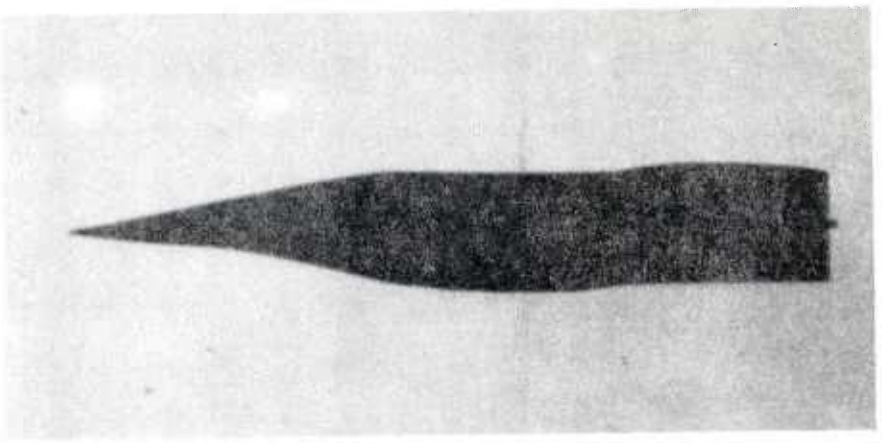

Figure 8. A Shadowgraph of a Corkscrew Projectile Flying at M = .92

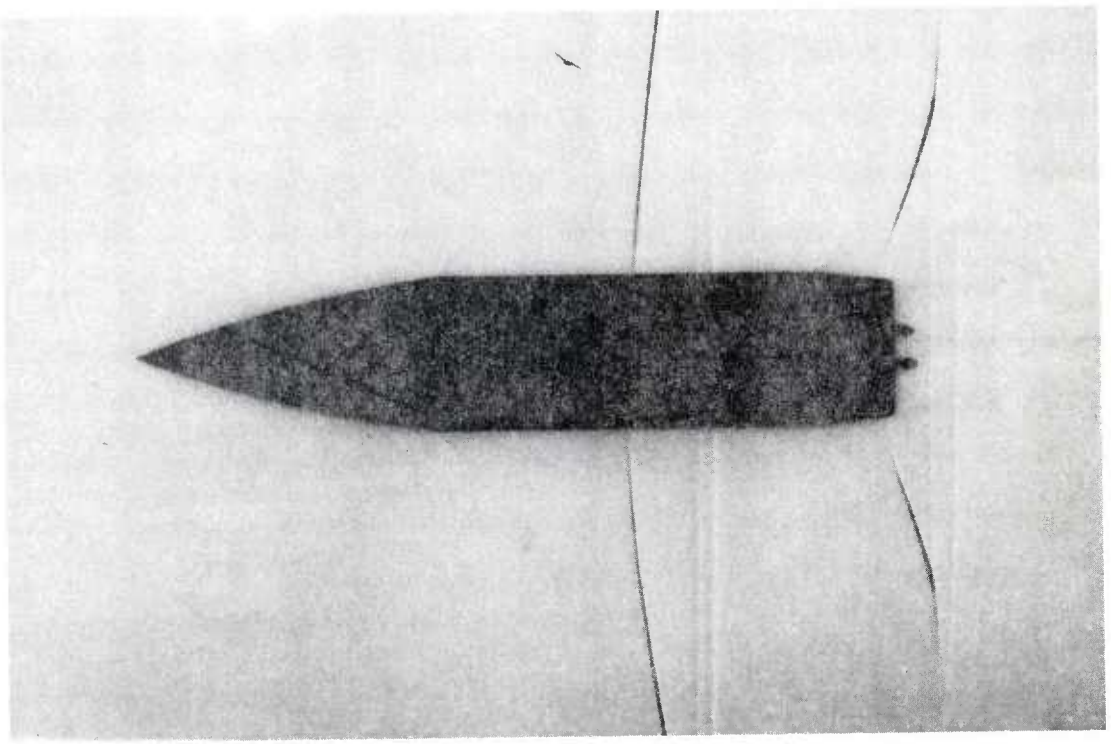

Figure 9. A Shadowgraph of a Conventional Projectile Flying at M = .92

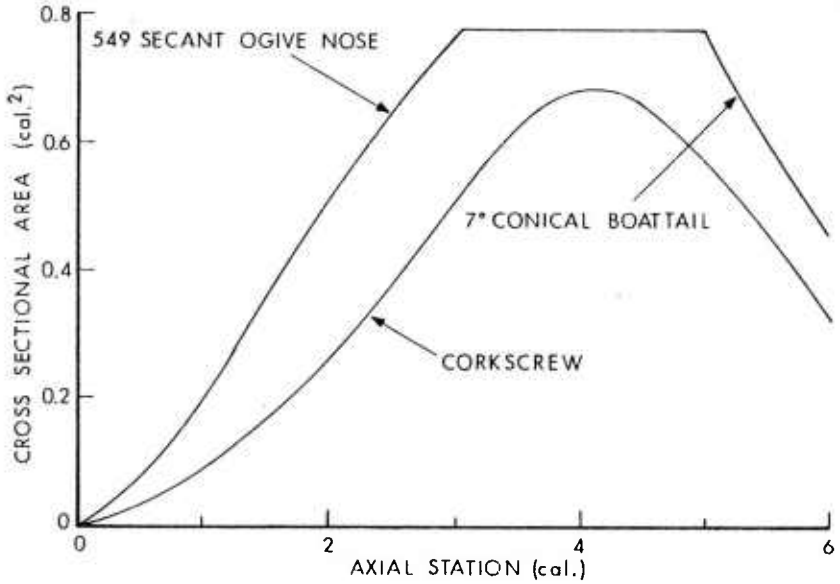

Figure 10. The Area Distribution of a Corkscrew Projectile Compared to a Conventional Projectile

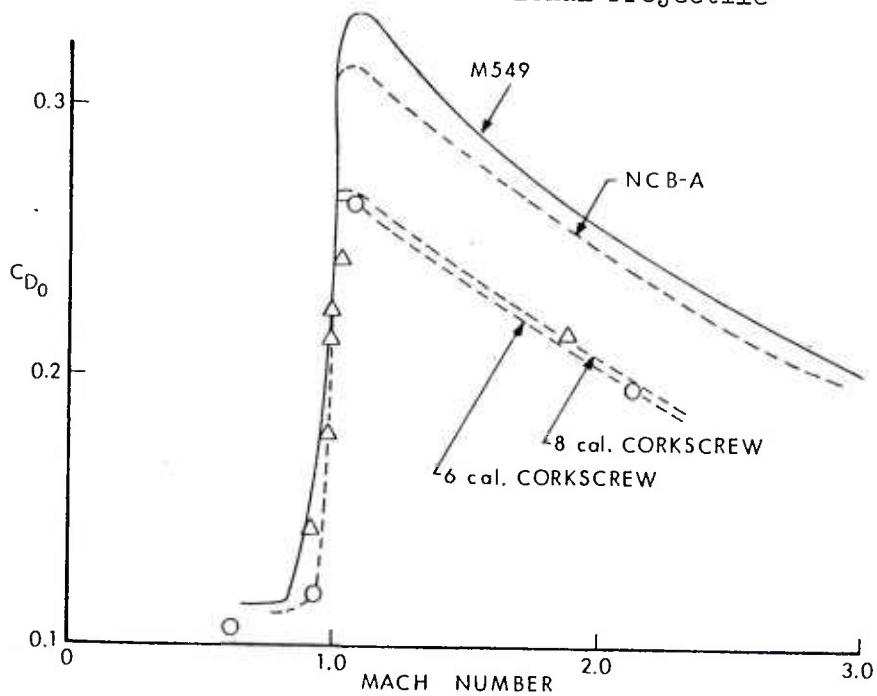

Figure 11. The Drag Coefficient of a Corkscrew Projectile Compared to Other Projectiles

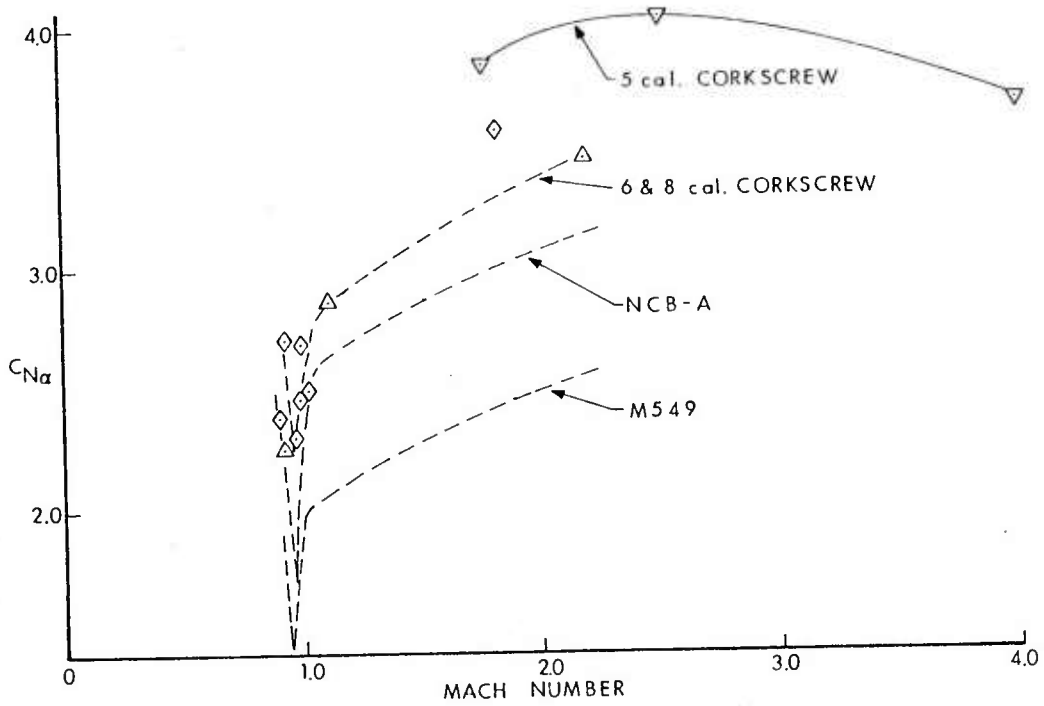

Figure 12. The Normal Force Coefficient of the Corkscrew Projectile Compared to Other Projectiles

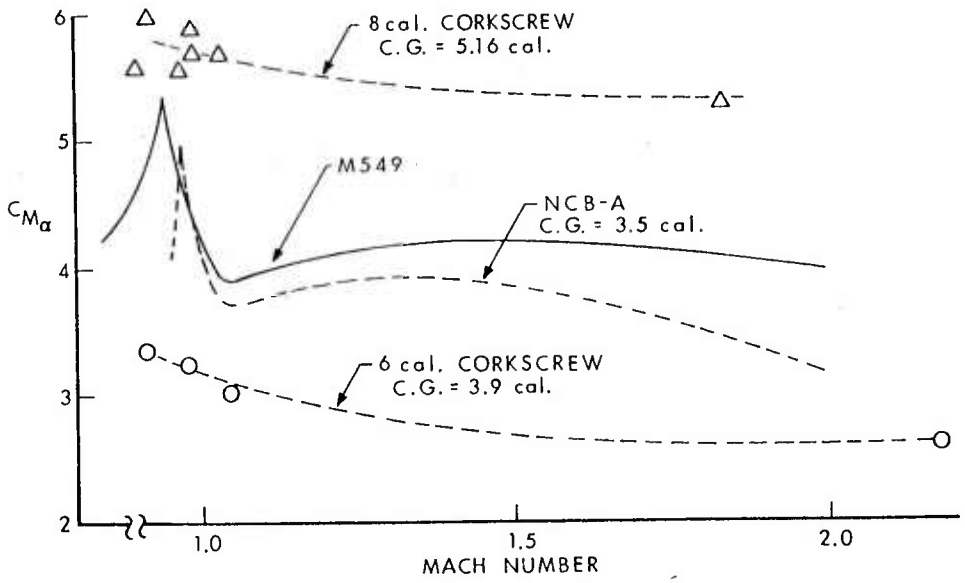

Figure 13. The Pitching Moment Coefficient of the Corkscrew Projectile Compared to Other Projectiles

(5) Efforts to fly corkscrews at higher Mach numbers have so far failed due to excessive loads on the model nose during launch. Various launching techniques are being tried to overcome this problem.

4. EXTRAPOLATION TO LONGER LENGTH PROJECTILES

The aerodynamic data obtained on the corkscrew configurations indicate that longer configurations of this shape can be flown with satisfactory stability. The implication is that the corkscrew will permit the use of much longer, incaliber, spin-stabilized, low drag, projectiles.

Calculation of possible projectile lengths have been made and the results are shown in Table I. For the calculation of the moments of inertia, it was assumed that the corkscrew configuration has equal angles for the nose and tail "flats", that the nose and tail overlap by one-caliber and that the projectile is made of a homogeneous material with a density of 9 gms/cc. Using the obtained values for the 6-caliber and 8-caliber corkscrews, the normal force and pitching moment coefficients for longer configurations have been estimated at Mach 2.1 (Table I).

From these assumptions and calculations, the gyroscopic stability factor has been calculated. This calculation indicates that an 11-caliber corkscrew made of a homogeneous material with a density of 9 gms/cc can be flown with satisfactory stability if the spin is at least one revolution per fifteen calibers of forward travel.

5. APPLICATIONS FOR THE CORKSCREW SHAPE

Besides being an excellent aerodynamic reference shape, the corkscrew configuration may have application as a spin stabilized, kinetic energy penetrator. The corkscrew's low drag will provide low velocity deceleration between the gun and the target, and its' low pitching and Magnus moments will provide good stability for long (ℓ/d) penetrator configurations. In small caliber sizes (20 to 40mm) the whole, high density penetrator might have the corkscrew exterior shape, while in larger calibers (105 to 120mm) the penetrator rod could be submerged in the corkscrew carrier. Both full bore and subcaliber configurations are feasible. A sabot for a corkscrew projectile can be a simpler and lighter weight configuration than the sabots now used on conventional, axisymmetric projectiles. The BRL is presently studying the feasibility of these concepts.

Table I. Physical and Aerodynamic Characteristics

ℓ/d	6	7	8	9	10	11
Vol/r^3	18.0	21.5	24.9	28.4	31.9	35.4
C.G.	3.90	4.53	5.16	5.79	6.43	7.06
$I_{y_{C.G.}}/\rho r^5$	91.2	151.2	233.0	339.9	458.9	624.5
k_y	1.13	1.33	1.53	1.73	1.90	2.10
$I_x/\rho r^5$	6.48	7.85	9.23	10.60	11.97	13.35
k_x	.300	.302	.304	.305	.306	.307
For Mach Number = 2.1 and Spin = 1/15 cal.						
C_{N_α} (estimated)	3.4		3.4		3.2	3.2
C_{m_α} (estimated)	2.58		4.08		5.69	6.28
S_g	3.73		2.27		1.39	1.15

REFERENCES

1. Platou, Anders S., "An Improved Projectile Boattail," Ballistic Research Laboratory Memorandum Report No. 2395, U.S. Army Ballistic Research Laboratory, Aberdeen Proving Ground, Maryland, July 1974. AD 785520.

2. Platou, Anders S., and Nielsen, George I. T., "An Improved Projectile Boattail. Part II," Ballistic Research Laboratory Report No. 1866, U.S. Army Ballistic Research Laboratory, Aberdeen Proving Ground, Maryland, March 1976. AD A024073.

3. Platou, Anders S., "An Improved Projectile Boattail. Part III," Ballistic Research Laboratory Memorandum Report No. 2644, U.S. Army Ballistic Research Laboratory, Aberdeen Proving Ground, Maryland, July 1976. AD B012781L.

4. Whiteside, John H., "Transonic Tests of the 155mm Non-Conical Boattail Projectile A and 8-Inch XM650E4 and EBVP Projectiles at Nicolet, Canada, During January-February 1977," Ballistic Research Laboratory Memorandum Report No. ARBRL-MR-02809, U.S. Army Ballistic Research Laboratory, Aberdeen Proving Ground, Maryland, January 1978.

5. Platou, Anders S., "An Improved Projectile Boattail. Part IV," to be published as a Ballistic Research Laboratory Memorandum Report.

AD-A056476

INTEGRATED AVIONICS CONTROL SYSTEM (IACS)

*CHARLES A. PLECKAITIS, Mr., CARL J. GALANTI, Mr.,
ANTHONY S. SANTANELLI, Mr., and GEORGE STECH, Mr.
US ARMY AVIONICS R&D ACTIVITY
FORT MONMOUTH, NEW JERSEY 07703

The concept of an Integrated Avionics Control System (IACS) in military aircraft has evolved from a significant increase in the number of electronic systems available for use on army aircraft today. A system such as IACS is needed for army aviation because it reduces the crew workload, reduces demands on already crowded cockpits and makes new installation less difficult and less expensive.

Recently, considerable emphasis has been placed on reducing the cost of new avionics systems, thus the IACS program is being pursued under the design-to-cost concept. The design to unit production cost (DTUPC) essential requirement for this program is $22.5K.

Currently Collins Avionics, Cedar Rapids and Grumman Aerospace, New York are under contract to the U.S. Army to develop an IACS for use in Army helicopters. The system weight is expected to be less than 30 pounds and the baseline system consist of five boxes. A primary control panel displays mode and frequency of controlled equipment, a secondary control panel provides a lesser capability for emergency uses, a status panel provides information for heads up viewing and the central control unit provides an interface between the remoted equipments, plus acts as a control for the 1553A data bus.

The following paper will briefly discuss the Army approach to an integrated avionics control system. The background of the program is outlined, followed by a description of the overall IACS and its operation.

*PLECKAITIS, GALANTI, SANTANELLI, & STECH

The U.S. Army Avionics R&D Activity started an internal program in 1972 with a goal to develop a simple low cost integrated cockpit control/display system for use in army helicopters. The program guidelines established at that time were to:

1. provide control of the avionics equipment through a single integrated panel.

2. reduce aircrew workload.

3. increase avionics configuration flexibility.

The first of these guidelines is important because through the use of simple and clearly understood controls the aircrew could control a complement of avionics equipment with a minimum of training. Also, the workload of an aircrew is very high during helicopter missions and very little attention can be given to the avionics not directly involved with the aircraft flight operation. By using preset frequencies for communications equipments, the aircrew's workload is greatly reduced. Avionics flexibility is of particular importance with the introduction into the army inventory of new emerging electronic systems.

In 1974 an experimental model was designed, built, and evaluated. The result of this in-house program was the development of a integrated avionics systems specification in 1976 which served as a nucleus for the present engineering development program. Other guidelines that were included in this program were to minimize production cost, minimize maintenance, reduce weight, and have high reliability. The present program employs the design to cost concept to insure that IACS can be produced and supported economically by the Army. The contract calls for the delivery of eight fully qualified systems in October 1978 for formal flight and operational tests. The qualification test program will be conducted jointly by the contractors and the Army's test command and will include design verification, EMI and environmental tests and reliability, maintainability and human engineering demonstrations. The program will result in a complete production procurement package. One of the competing engineering development contractors will be selected for the initial production contract. Productions systems will be available early in 1982.

The basic IACS, which was recently nomenclatured by the Army as the AN/ASQ-166, consists of five units:

1. Primary Control Unit

2. Secondary Control Unit

3. Status Panel

4. Central Control Unit 1

5. Central Control Unit 2

See figure 1 for a block diagram of a typical IACS interconnection.

The primary control unit performs the following functions:

1. It displays mode and frequency information and other data on its front panel;

2. provides mode controls, display controls, and keyboard entry of data.

Since this panel will control up to ten avionics equipments, these equipments can now be remotely located in the aircraft avionics compartment. Control of such functions as the selection of preset frequencies and tuning to new frequencies is accomplished via the primary control front panel. The primary control unit has the following modes of operation:

1. IFF

2. COMM

3. NAV

4. Status

5. Index

Dedicated switches were retained for important functions as recovery of last frequency, guard, and zeroize of sensitive information.

The secondary control unit provides a minimum capability for emergency situations. The specification requires it to control one FM, one AM radio, and an automatic direction finder as a minimum. This secondary unit is envisioned for use in cockpits for which space or funding does not permit a primary panel for each operator. The primary and secondary control units can be mounted either in the center

console for a side-by-side helicopter or the side pockets for a helicopter with a tandem seating arrangement.

The status panel is a small lightweight one line display which provides frequency and mode status information for the transmitting radio. It is envisioned that the status panel will be installed as a heads-up type display near the brow of the instrument panel.

The central control units provide a means of interfacing the IACS (primary control, secondary control, and status panel) elements with the controlled CNI subsystems. For the initial deployment of this system in the 1982 to 1986 time frame, all subsystem equipments will be controlled through the central control units. However, beyond that time frame, new subsystem equipments will be designed to interface directly onto the data bus. The CCU also provides the function of bus controller for stand alone operation. However, the IACS is capable of operating as a subsystem of a larger bus system or in a dynamic bus allocation mode.

The intra IACS connections are through the use of a 1553A digital data bus. The use of a digital multiplex bus over conventional hard wiring as the means to exchange data between IACS and the controlled CNI equipments is in keeping with the overall goal of reducing aircraft complexity. Less wire and fewer connectors are required with the attendant savings in weight, improvement in reliability, and simpler wire routing in the aircraft. Digital transmission techniques provide a higher data capacity, self check on each transmission and reduced susceptibility to electromagnetic interference.

Human factors engineering (HFE) played a significant role in the design and fabrication of IACS. This involved the analysis of pilot operational procedures, system architecture design, man-machine function allocations, and the matching of operational requirements to available technologies. A basic objective of the HFE effort was to ensure not only that the man-machine interfaces of the system were sufficient for the intended operation and control functions of the equipment, but also that these control functions could be accomplished by the operator.

The human factors approach to accomplish the basic objective entailed the following tasks:

1. Identify all significant man-machine interactions required by the system.

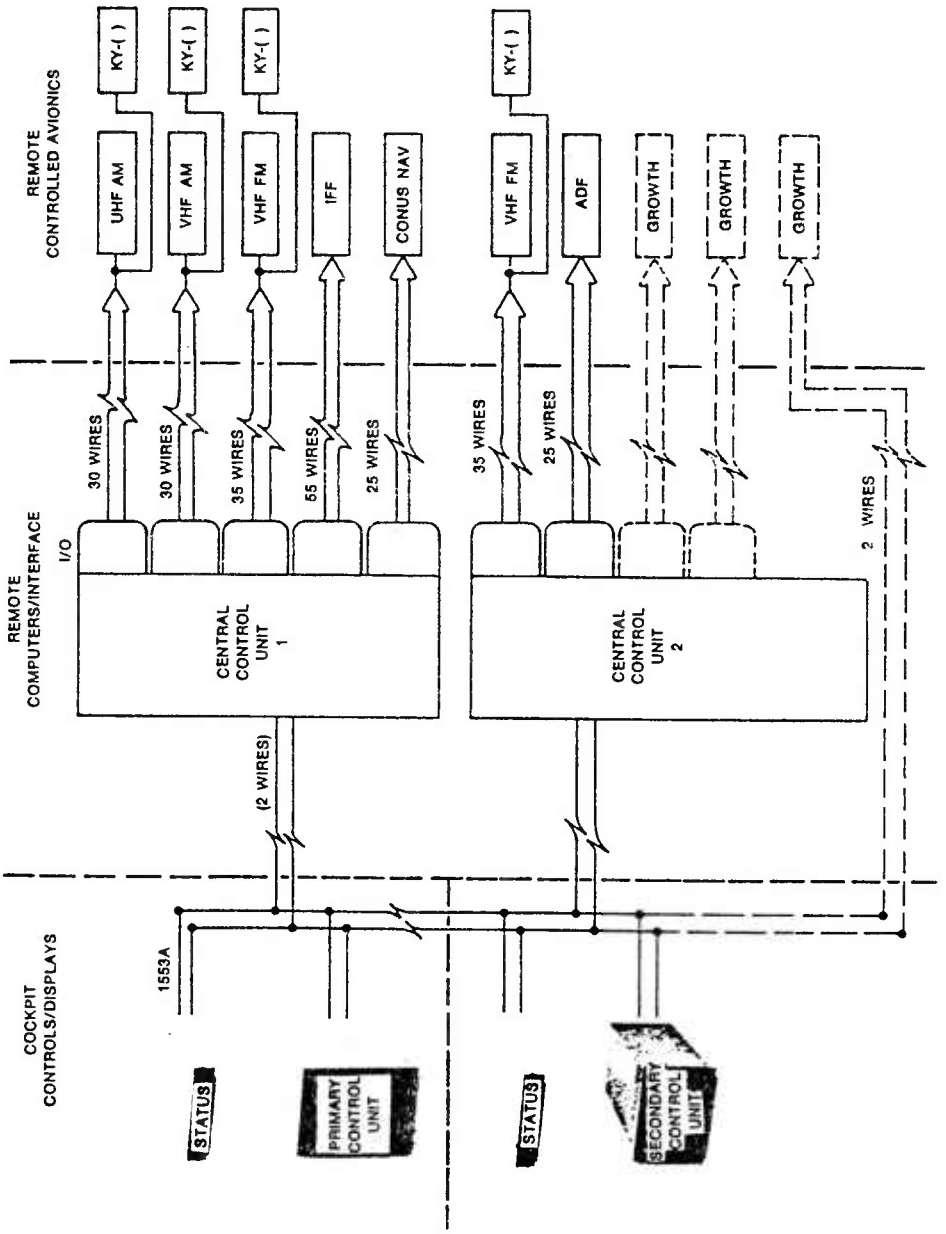

Figure 1. Integrated Avionics Control System AN/ASN-166

2. Determine mission and system characteristics which will influence operator performance during the above interactions.

3. Provide and develop data to support trade studies, concept selection, and detailed design of equipment relating to the man-machine interface.

4. Conduct empirical studies to develop necessary operator performance data to support the above trade studies and design efforts.

5. Conduct empirical studies to verify that chosen equipment designs will permit operator performance consistent with system and mission requirements.

Figure 2 shows the results of this HFE effort. The Primary Control Unit shown in Figure 2A was designed and built by Collins; and the one in Figure 2B, by Grumman. Both panels are multifunction control-display units that permit an operator to control a suite of CNI equipments. The displays (CRT in the Collins design and incandescents in the Grumman) are sun-light readable, are red for night-time viewing, are compatible with Night Vision Goggles, and are readable in a vibratory environment, such as encountered in rotary-wing flight. Both panels can be operated with gloves. In both panels, controls have been placed in close proximity to their related displays. This HFE principle is exemplified by the eight (8) line-select keys on either side of the display. These key switches give the operator direct access to the adjacent label/data lines on the display. It is also exemplified in the packaging of keyboard and display in the same box.

Both designs utilize an interactive or paging technique controlled completely by microcomputer software. In this approach, all available choices (e.g., the mode and frequency choices of a particular equipment) are displayed. Figure 3 shows a typical page. The operator makes a choice and selects, for example, FM 1 by actuating the line-select key to the left of the label. Immediately, a page labeled FM 1 appears, displaying frequency, channel, etc., see Figure 4. The asterisk to the left of SQT and CIP indicates that the pilot has selected these choices Squelch Tone, and Cipher. These actions illustrate another HFE principle: that verification and feedback are a necessary part of any control operation. For every control actuation, there is an immediate display response. Feedback requirements also apply to the actuation characteristics of the controls, themselves. Required actuation forces and switch detent characteristics, are an integral part of feedback information to the

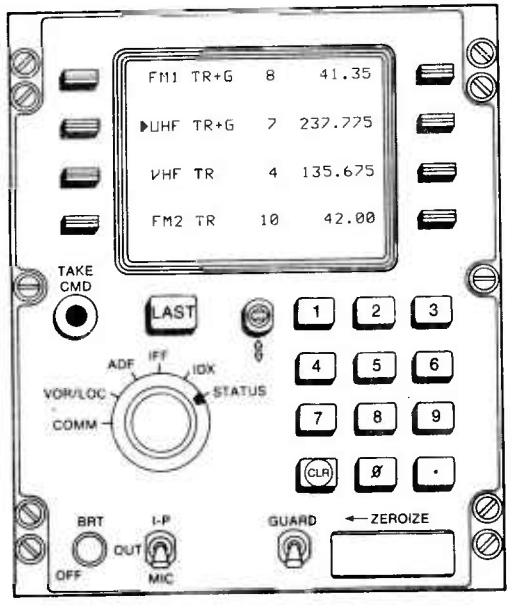

A. Collins

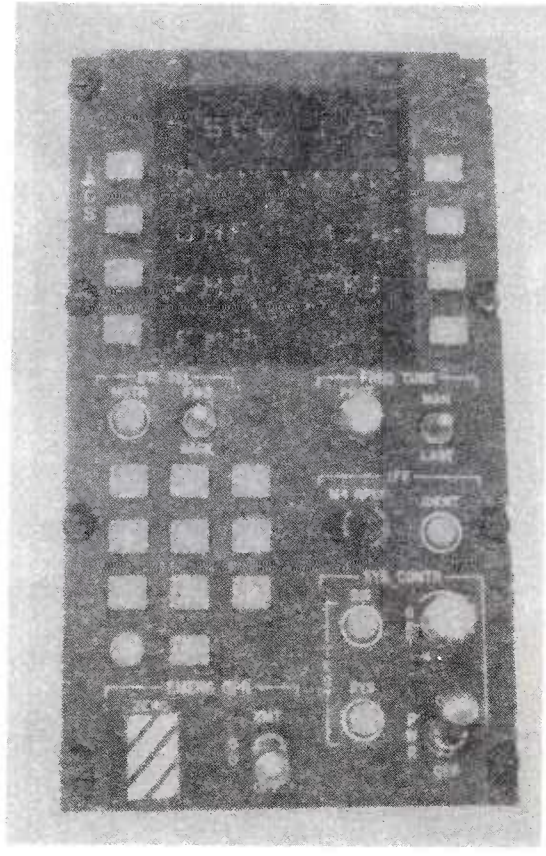

B. Grumman

Figure 2. Primary Control Panels
(not to scale)

pilot, indicating that the switch has been actuated.

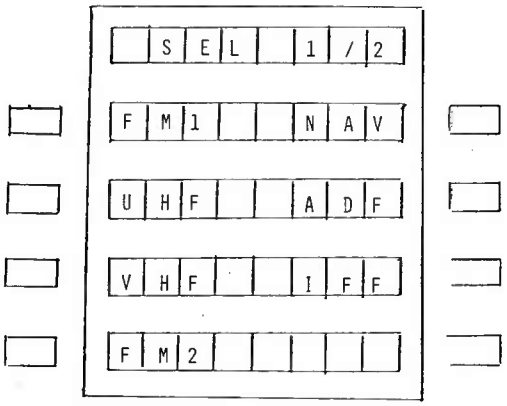

Figure 3. Typical CNI Select Page

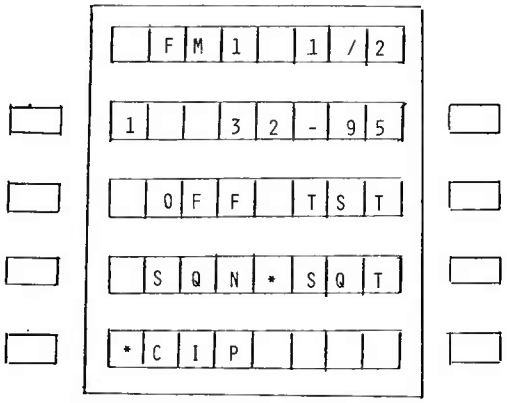

Figure 4. Typical FM 1 Page

Each piece of equipment has one or more pages showing all the control/display functions of the conventional control head. Also, each piece of equipment has been given 10 preset channels in which frequencies can be stored for future use. A control on the PCU allows

the pilot to automatically tune any selected radio to a predetermined channel. For example, look at Figure 5, which shows a VHF control page. Notice the label CH-8 on the first line and the frequency, 141.675 below it. The pilot can select another channel with its associated frequency merely by actuating a rotory switch on the PCU. By rotating the switch to the right, channels are increased and vice versa. To change a frequency, the pilot types in a new frequency with the keyboard. This new frequency appears within the brackets at the bottom of the display. Then he pushes the line key next to the old frequency on the second line. Immediately the new frequency appears, indicating that the VHF radio is tuned to that frequency.

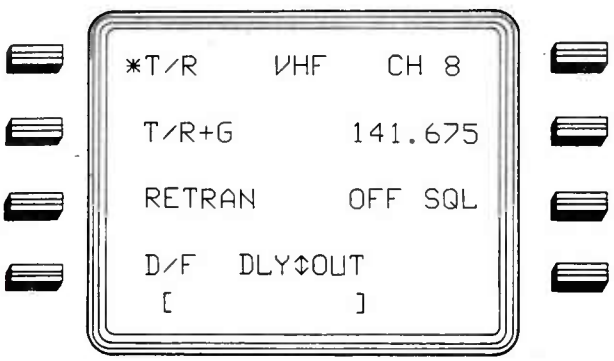

Figure 5. VHF Control Page

The pilot does not have to cycle through different pages to determine the operating frequencies of his radios. Figure 6 shows a Status Page on which his four (4) primary radios and their current operating channels and frequencies are displayed. The asterisk indicates that the ICS is at the FM 1 position, ready for transmission. To transmit on UHF, the ICS is switched to UHF position. The asterisk leaves FM 1 and appears at UHF. Thus, the pilot knows the status of his radios at a glance.

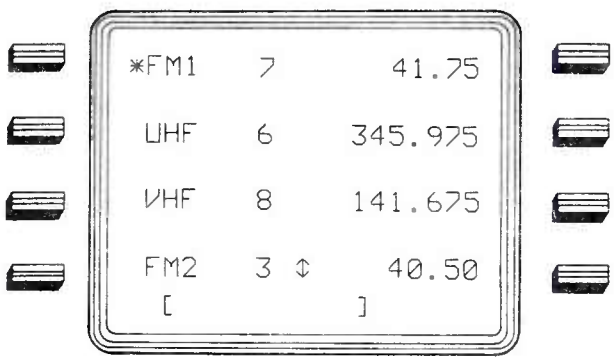

Figure 6. Status Page

As an illustration of a typical IACS aircraft installation (Figure 7) let's look at the AAH pilot station with conventional COMM, NAV, and IDENT control/display units (these are shown crosshatched). We have installed an FM with a security key, an UHF, and a VHF radio with space, weight, and power provisions for additional security keys, an IFF and an ADF.

Now, by way of contrast, let's look at the same station with an IACS installation (Figure 8). The IACS Primary Control Unit not only provides all the control functions of the equipments removed from this cockpit but the pilot also has control over the co-pilot/gunners FM radio and security key and CONUS NAV (VOR/ILS/MARKER BEACON) if the aircraft is so equipped.

In addition, a status panel displaying COMM mode, channel, and frequency is available which can be mounted near the top of the instrument panel so as to provide a nearly heads-up type display.

It can be readily seen that the above examples show how the concept of integrating a control/display unit with a microprocessor provides the pilot with a viable solution to the problems of increased

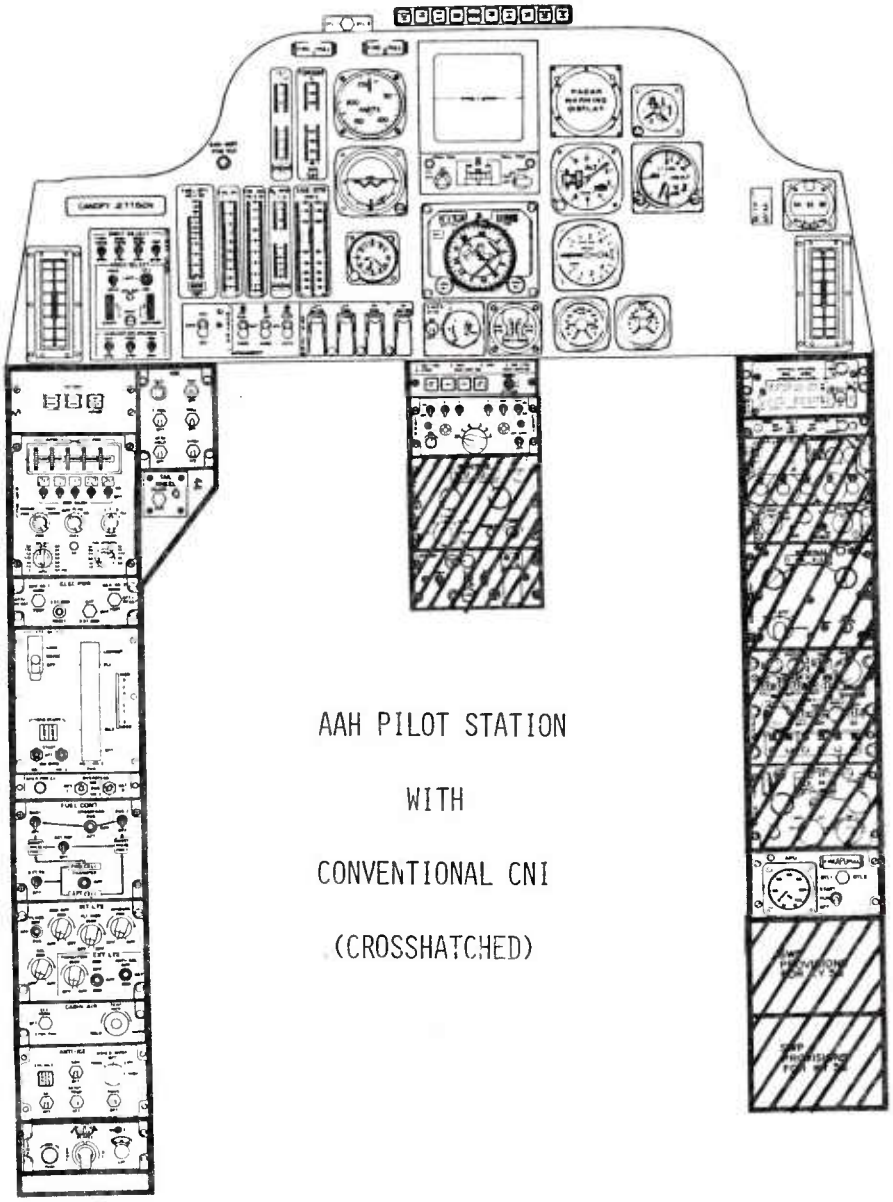

Figure 7. AAH Pilot Station (Conventional)

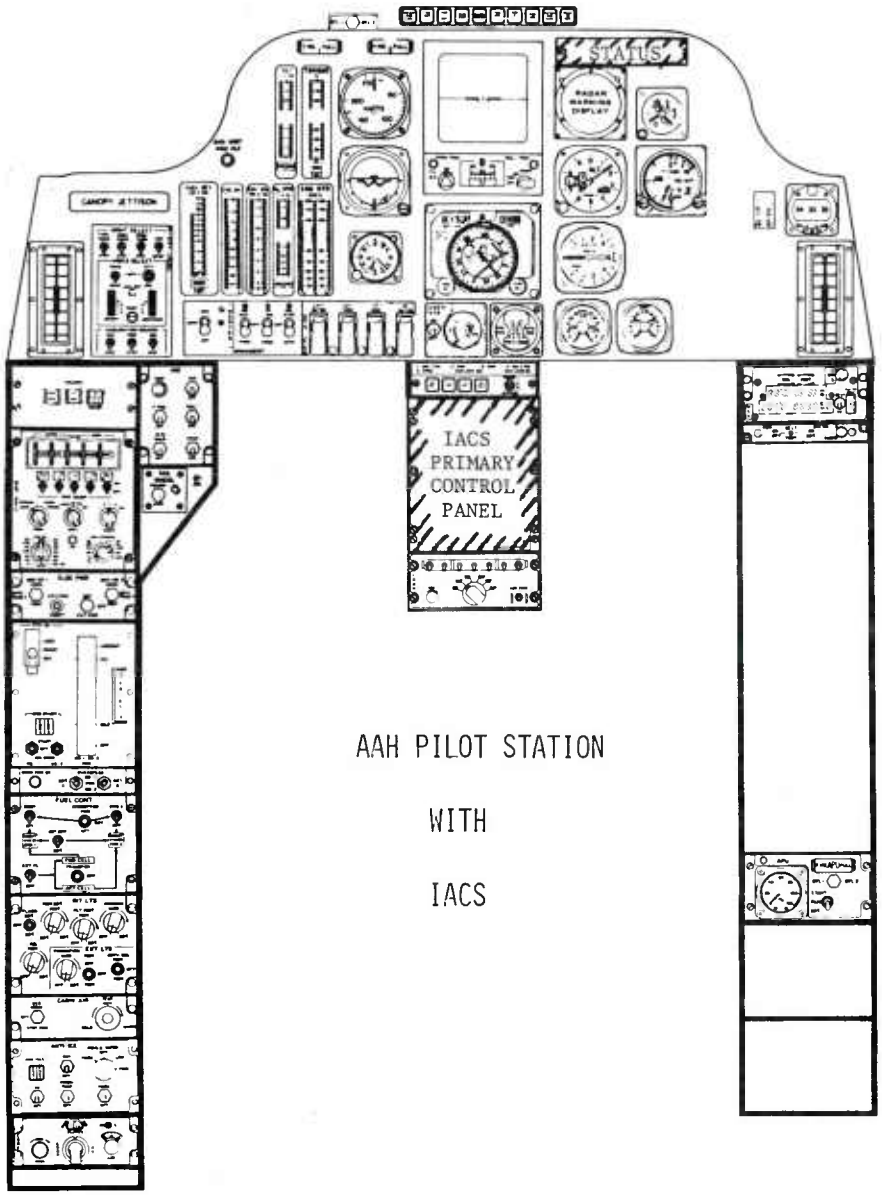

Figure 8. AAH Pilot Station With IACS

workload and decreased cockpit real estate that characterizes modern rotary-wing aircraft today. Through the use of IACS the pilot will be able to operate the helicopter more efficiently while keeping a visual reference on a single integrated control panel for information on the aircrafts avionics posture.

IACS is the Army's first application of the new technologies of digital data buses, microprocessors and integrated controls and displays. It is the first step toward a totally integrated digital aircraft. IACS has been designed to operate as a stand alone system or as part of a total aircraft MIL-STD-1553 multiplex system. A future total aircraft multiplex system could include the avionics, electrical power control and distribution, flight controls, aircraft warning indicators, instruments, fire control and stores management and diagnostics for checkout and maintenance. Such an overall integrated aircraft system would provide for: improved cockpit management; reduced aircrew workload; significant reduction in aircraft wiring weight; considerable flexibility in placement of equipments; intercommunications between various subsystems without costly interface; and more effective and yet simpler diagnostic maintenance. Even though our strategy is evolutionary, so we do not obsolete our inventory of current avionics, the overall result is a revolution in the design of future army cockpits.

Glossary of Terms

AAH - Advanced Attack Helicopter
ADF - Automatic Direction Finder
AM - Amplitude Modulation
CCU - Central Control Unit
CIP - Cipher
CNI - Communication, Navigation, Identification
COMM - Communication
CONUS Nav - Continental US Navigation
CRT - Cathode Ray Tube
D/F - Direction Finder
DTUPC - Design to Unit Production Cost
EMI - Electromagnetic Interference
FM - Frequency Modulation
ICS - Intercommunication System
Ident - Identification
IFF - Identification Friend or Foe
ILS - Instrument Landing System
NAV - Navigation
PCU-Primary Control Unit
Retran - Retransmission
SCU - Secondary Control Unit
SEL - Select
SQN - Squelch Noise
SQT - Squelch Tone
T/R - Transmit-Receive
T/R & G - Transmit-Receive plus Guard
TST - Test
UHF - Ultra High Frequency
VHF - Very High Frequency
VOR - VHF Omnidirectional Range

AD-A056477

NEW ENERGY SAVING TECHNIQUES FOR THE PRODUCTION OF DENSE FOODS

* ABDUL R. RAHMAN, NANCY J. KELLEY,
JOHN A. AYOUB AND DONALD E. WESTCOTT
US ARMY NATICK RESEARCH AND DEVELOPMENT COMMAND
NATICK, MASSACHUSETTS

INTRODUCTION

Dehydration has long been recognized as a successful method of preserving and reducing the weight of foods. Among the many drying methods, freeze-drying has shown to yield a very high quality finished product although with no significant reduction in volume. Therefore, research has been concentrated during the past few years on volume reduction of such dehydrated foods by compression. The use of dehydrated compressed foods compared to non-dried, non-compressed counterparts, results in savings in packaging, transportation and storage costs, since volume and weight are reduced by several fold. Benefits to combat operations are not only realized in military feeding systems but in logistics for the combat soldier, for underwater and surface naval vessels, and for aircraft and space vehicles. Ecological benefits due to reduction of packaging wastes are an added dividend.

THE PROBLEM

The current process for the production of many high quality dense foods requires complete freeze drying, rehumidifying, equilibrating, compressing and re-drying to a low moisture level to provide storage stability. It is time and energy consuming, inefficient and expensive.

THE OBJECTIVE

The objective of current studies reported here is to

develop new techniques for the production of dense (compressed) foods with major emphasis on:

1. Energy savings
2. Increased throughput
3. Optimum use of equipment

REVIEW OF LITERATURE

Freeze drying, also known as sublimation drying or lyophilization, is the removal of water as vapor from a frozen product under vacuum (1). Even though the result is products of high quality, it remains an expensive process. There is little volume reduction from the original food form. However, volume reduction ranging from 4 to 16-fold can be achieved by compressing the freeze dried products without adverse effects on their overall quality (2,3,4). Hamdy, Ishler and Brockman (5,6,7) described the current conventional technique for the production of reversible foods. The product is prepared by blanching, chemical or physical pre-treatment as applicable, freezing, freeze drying, humidifying, equilibrating, compressing, re-drying and packaging. Thermal plasticization of high sugar content freeze dried products has been reported by Rahman, et al (8). The current industrial practices for moisturizing freeze dried foods prior to compression include steaming and water misting to 5 to 20 percent moisture, equilibrating and then compressing (9). MacPhearson (10) indicated that carrot bars of good quality can be produced by spraying with water to about 14% moisture level. Most of the research in the area of dehydration and compression has been with vegetables. Gooding and Rolfe (11) reported that during World War II, the United Kingdom produced dehydrated cabbage and carrots in compressed blocks. Other dehydration techniques which require less energy than freeze drying such as vacuum drying and air drying have also been used in the production of compressed foods (12). A compact shelf stable cabbage product especially suitable for use in cole slaw, was prepared, using air drying at a temperature of 55°C. Addition of a surfactant facilitated rehydration of the compressed cabbage (13, 14). Compressed peas, carrots, green beans and spinach have been successfully produced by: 1 - partial freeze drying (10-30% moisture), 2 - applying microwave energy (1-3 minutes), 3 - compressing, 4 - further drying, and 5 - packaging (15).

EXPERIMENTAL PROCEDURE

1. Partial Freeze-drying and Compression (Fig. 1).

Carrots: Fresh carrots of the variety Emperator, were peeled, cut into 1 cm dice and blast-frozen at -30°C. The frozen diced carrots were placed in trays at about 1 gm/cm^2 and freeze dried for about 5 hours, 3 hours at 120°C and then 2 hours at 80°C to a moisture level ranging from 15-20 percent (Fig. 2). This compares with 12-15 hours for conventional (industrial) freeze drying time, a saving of at least 50%. The partially freeze dried carrots were then placed in polyethylene bags (about 100 gm/bag) and treated with microwave energy either in a stationary unit rated at 0.625 KW and exposure time ranging from 10-60 seconds, or in a conveyorized microwave oven at 1.25 KW and exposure time ranging from 1-3 minutes. The treated carrots which were sufficiently plasticized, were compressed at pressures ranging from 70,000 to 210,000 Pa to form either bars (2.5 x 7.5 x 1 cm) or discs (9 cm in diameter and 1 cm thick). The compressed products were then further dried to about 3 percent moisture by vacuum drying.

Peas: Commercially frozen peas were mechanically slitted and then sulfited by soaking in a solution containing 5 gms of sodium meta bisulfite per liter. The drained peas were then frozen, freeze dried, microwave treated, compressed and further dried as above.

2. Air Drying and Compression

Cabbage: Fresh cabbage was cleaned, cored and sliced into 0.5 cm shreds. The shredded cabbage was sulfited by soaking in a solution containing 5 gms of sodium meta bisulfite per liter. The treated cabbage was then air dried at a starting temperature of 93°C which was lowered within 15 minutes to 55°C. The dehydration was continued until the moisture content reached about 5 percent within about 4 hours. The dehydrated cabbage was re-moistened by spraying with a water solution containing either Tween 60 or 80 as a surfactant, to increase the weight by about 12 percent. The moistened cabbage was then compressed at pressures between 70,000 - 140,000 Pa into discs (9 cm diameter and 1 cm thick). The discs were then re-dried to about 5 percent moisture for stability. For comparison, freeze dried and compressed cabbage treated with calcium as a firming agent was also prepared.

3. Test Procedures

a. Technological panel evaluations were conducted by ten trained judges using a 9-point scale ranging from 1 - Extremely poor to 9 - Excellent.

b. Compression Ratio: A No. 2½ can was filled with compressed discs leaving about 0.5 cm headspace and then weighed. Uncompressed dried product of equivalent weight to the compressed was packed loosely in No. 2½ cans leaving the same headspace. The number of cans utilized to pack the loose product gave the compression or packaging ratio.

c. Rehydration Ratio: A weighed dehydrated and compressed product was placed in boiling water for 10 minutes, drained for 5 minutes and weighed. Rehydration ratio was determined by dividing the rehydrated weight by the dry weight.

d. Fines: The amount of fines was determined by weighing the total sediment after rehydration.

e. Peroxidase: Testing for peroxidase enzyme was performed in accordance with A.O.A.C.

RESULTS AND DISCUSSION

Table 1 indicates that total inactivation of the enzyme peroxidase was achieved by applying microwave energy for one minute to the partially freeze dried carrots at 17 percent moisture. Blanching time is reduced as the microwave power and energy input is increased. This provides a significant advantage since it eliminates the need for water or steam blanching in the production of dehydrated vegetables. Accordingly, a better quality product at a reduced cost is realized. Tables 2 and 3 and Fig. 3 show that time exposure to microwave energy at a given power level determines the amount of fines caused by crushing of the unplasticized portion of the treated product. The optimum time of exposure to microwave energy depends upon the product and its moisture content. The amount of fines in the rehydrated untreated product was so excessive (50-90%) that the product was considered unacceptable. The results of technological panel evaluations of rehydrated compressed peas produced by the conventional technique and by the new partially freeze dried and microwave treated technique, as shown in Table 4, indicate no significant differences in the overall quality of both products. However, a significantly higher rating for texture was received by the product produced by the new technique over that produced by the conventional method.

Air dried cabbage, with a moisture content of 5%, exhibited many of the qualities of fresh cabbage when rehydrated (Table 5). It rehydrated to about 70 percent of its original fresh weight within 35 minutes. Texture of the freeze dried product was mushy, even after the addition of firming agents, such as calcium. Significant savings in volume can be achieved when fresh cabbage is compared with its dehydrated compressed counterpart (Fig. 4).

CONCLUSION:

It is concluded that acceptable compressed products can be produced by partial freeze drying and microwave plasticizing, thereby saving about 50 percent of the freeze-drying time and energy. This new technique enables the producer to make more efficient use of his equipment; namely, several batches of freeze dried compressed product can be produced per day instead of one batch using the current commercial process. There is also the distinct possibility that a semi-continuous process can be developed in which the freeze dried product can be placed on a conveyorized microwave unit and plasticized. The plasticized product can then be fed automatically into a hydraulic press for compression (Fig. 1). These studies have also shown that lower cost air drying can be successfully used for some products such as cabbage that have less sensitive cellular structures.

The microwave process has been covered by a patent which will be issued in the near future, and a patent application has been filed for the dehydrated compressed cabbage process.

REFERENCES:

1. King, C.J. 1971. Freeze drying of Foods, CRC Press, Cleveland, Ohio.
2. Rahman, A.R., Schafer, G., Taylor, G.R. and Westcott, D.E. 1969. Studies on Reversible Compression of Dehydrated Vegetables. Technical Report 70-36-6-FL. US Army Natick Laboratories, Natick, MA.
3. Rahman, A.R., Taylor, G.R., Schafer, G. and Westcott, D.E. 1970. Studies on Reversible Compression of Freeze-dried RTP Cherries and Blueberries. Technical Report No. 70-52-FL. US Army Natick Laboratories, Natick, MA.
4. Emami, S.H., Flink, J.M. and Rahman, A.R. 1976. Compression of Foods During Freeze-drying. In Digest of Papers, 1st International Congress on Food Engineering and Foods, American Society of Agricultural Engineers, Boston, MA.p.56.
5. Hamdy, M.M. 1962. Compression of Dehydrated Foods. Final Report, Contract No. DA 19-QM-1889. Quartermaster Food and Container Institute for the Armed Forces, Chicago, IL.
6. Ishler, N.I. 1965. Methods for Controlling Fragmentation of Dried Foods During Compression. Final Report. Contract No. DA 19-129-AMC-2(X), Technical Report D-13. US Army Natick Laboratories, Natick, MA.
7. Brockmann, Maxwell C. 1966. Compression of foods - Activities Report 18 (2), 173-177.

8. Rahman, A.R. 1974. Method for Making a Compressed Freeze-Vacuum Dehydrated Blueberry Product of Increased Density. US Patent No. 3,806,610.
9. Rahman, A.R. 1973. New Class of Foods - Compressed Foods. In Foods of Tomorrow/Winter. Special Section of Food Processing, 34(1):F4-F7.
10. MacPhearson, B.A. 1973. Compression of Cooked, Freeze-dried Carrots. M.S. Thesis, Texas A&M University, College Station, Texas.
11. Gooding, E.G.B. and Rolfe, E.J. 1957. Some Recent Work on Dehydration in the United Kingdom. J. Food Tech. 11:302.
12. Rahman, A.R., Schafer, G. 1976. Method of Producing Compact and Dehydrated Vegetable Products of Increased Density. US Patent No. 3,950,560.
13. Haralampu, S.G., Rahman, A.R. and Westcott, D.E. 1976. Development of Dehydrated Compressed Cabbage for Cole Slaw. In Digest of Papers, 1st International Congress on Food Engineering and Food. Boston, MA, p. 57.
14. Rahman, A.R. 1977. Compressed Dehydrated Cabbage Has "Fresh" Color and Texture. Food Process. 38(11):93.
15. Rahman, A.R., Kelley, N. and Westcott, D.E. 1977. New Techniques for the Production of Dense Foods. (Abstract) In Program, 37th Annual Meeting, Philadelphia, PA., June 5-8, 1977. Institute of Food Technologists, Chicago, IL. p. 181.

PRODUCT TYPE	BLANCHING TREATMENT	PEROXIDASE ACTIVITY
FRESH 1/2" CUBE	BOILED IN WATER - 30 SEC	POSITIVE
FRESH 1/2" CUBE	BOILED IN WATER - 1 MIN	NEGATIVE
FRESH 1/2" CUBE	MICROWAVE, 1000w, (IN OPEN DISH) - 1 MIN	NEGATIVE
FRESH 1/2" CUBE	MICROWAVE, 500w, (PLASTIC DISH) - 1 MIN	NEGATIVE
FRESH 1/2" CUBE	MICROWAVE, 500w, (PLASTIC DISH) - 30 SEC	POSITIVE
FRESH 1/2" CUBE, FREEZE DRIED TO ABOUT 17% MOISTURE	MICROWAVE, 500w - 30 SEC	NEGATIVE
FRESH 1" SLICE	BOILED IN WATER - 1 MIN	SLIGHT COLOR DEVELOPED AFTER 15 MIN
FRESH 1" SLICE	MICROWAVE, 500w - 1 MIN	NEGATIVE
FRESH 1" SLICE	MICROWAVE, 1000w - 30 SEC	NEGATIVE
FRESH 1" SLICE	MICROWAVE, 1500w - 15 SEC	NEGATIVE

TABLE 1 BLANCHING TREATMENTS TO INACTIVATE PEROXIDASE IN CARROTS

PERCENT MOISTURE	FREEZE DRYING TEMPERATURES	MICROWAVE ENERGY TREATMENT	CONDITION OF REHYDRATED PRODUCT	REHYDRATION RATIO
10	1 HR AT 250°F	0	90% FINES	--
	1 HR AT 200°F	30 SEC	5% "	9.6
	5 1/4 HR AT 150°F	40 SEC	0	9.3
	TOTAL 7 1/4 HRS	60 SEC	5% "	9.2
15	1 HR AT 250°F	0	80% FINES	--
	1 HR AT 200°F	30 SEC	5% "	8.3
		40 SEC	10% "	8.1
	4 HRS AT 150°F	50 SEC	15% "	8.7
	TOTAL 6 HRS	60 SEC	10% "	8.4
17	1 HR AT 250°F	0	50% FINES	--
	1 HR AT 200°F	30 SEC	0	8.6
		40 SEC	20% "	6.7
	4 HRS AT 150°F	50 SEC	10% "	7.2
	TOTAL 6 HRS	60 SEC	20% "	7.3

TABLE 2 . CARROTS FREEZE DRIED TO DIFFERENT LEVELS OF MOISTURE, TREATED WITH MICROWAVE ENERGY AND COMPRESSED

PERCENT MOISTURE	FREEZE DRYING TEMPERATURES	MICROWAVE ENERGY TREATMENT	CONDITION OF REHYDRATED PRODUCT	REHYDRATION RATIO
12.5	1 HR AT 250°F 2 HRS AT 200°F 3 1/2 HRS AT 150°F TOTAL 6 1/2 HRS	0 30 SEC 40 SEC 50 SEC	100% BROKEN & FINES 50% BROKEN 20% BROKEN 20% BROKEN	-- 4.9 4.7 4.7
14.4	2 1/2 HRS AT 260°F 1 1/2 HRS AT 200°F 1/2 HR AT 160°F TOTAL 4 1/2 HRS	0 20 SEC 30 SEC	90% BROKEN & FINES 40% " " 10% " "	-- 4.5 4.5
15.3	1 HR AT 250°F 2 HRS AT 200°F 2 1/2 HRS AT 150°F TOTAL 5 1/2 HRS	0 10 FT/SEC 12 FT/SEC	100% BROKEN & FINES 10% BROKEN 5% BROKEN	-- 4.4 4.0
19.5	2 HRS AT 250°F 1 1/2 HR AT 200°F 1 HR AT 160°F TOTAL 4 1/2 HRS	0 30 SEC 40 SEC	90% BROKEN & FINES 10% " " 5% " "	-- 4.3 4.0

TABLE 3 . PEAS FREEZE DRIED TO DIFFERENT LEVELS OF MOISTURE, TREATED WITH MICROWAVE ENERGY AND COMPRESSED

MICROWAVE TREATMENT	REHYDRATED PRODUCT				
	COLOR	ODOR	FLAVOR	TEXTURE	APPEARANCE
CONTROL (CONVENTIONAL)	6.9	6.9	6.7	5.7*	6.6
20 SEC	7.0	6.5	6.7	6.1	6.6
30 SEC	6.9	6.6	7.0	6.3	6.7
LSD	0.89	0.41	0.42	0.54	0.17

TABLE 4 TECHNOLOGICAL PANEL AVERAGE RATINGS OF PEAS, FREEZE DRIED TO 17% MOISTURE, TREATED WITH MICROWAVE ENERGY AND COMPRESSED

TREATMENT	COLOR	ODOR	FLAVOR	TEXTURE	APPEARANCE
CONTROL (FRESH CABBAGE)	6.7	6.8	7.3	7.2	6.7
FREEZE-DRIED & COMPRESSED	6.5	6.6	6.5	5.8	6.4
FREEZE-DRIED & COMPRESSED CA TREATED	6.7	6.7	6.5	5.8	6.5
AIR-DRIED TWEEN 60	6.8	6.9	6.9	6.8	6.8
AIR-DRIED TWEEN 80	6.8	6.9	6.7	6.8	6.8

TABLE 5 • TECHNOLOGICAL EVALUATION OF DEHYDRATED AND COMPRESSED CABBAGE

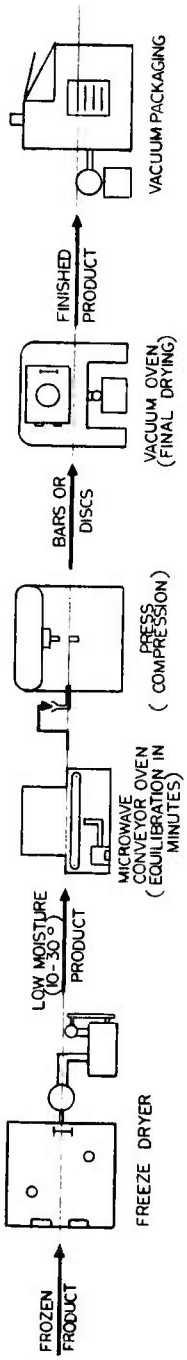

FIG. 1. NEW ENERGY SAVING TECHNIQUE FOR THE PRODUCTION OF DENSE FOOD

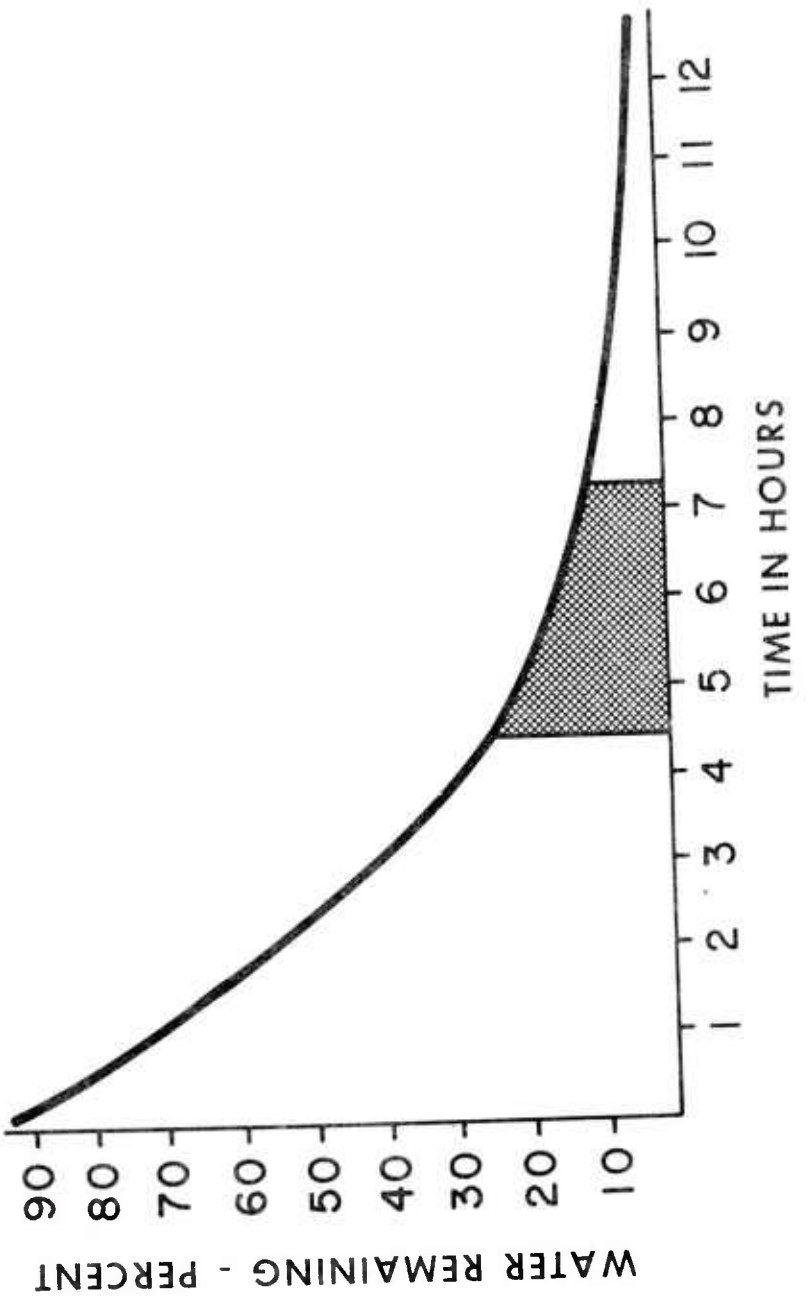

FIG. 2 - TYPICAL FREEZE-DRYING CURVE - SHADED AREA REPRESENTS' THE RANGE OF RESIDUAL MOISTURE IN PARTIAL FREEZE-DRYING

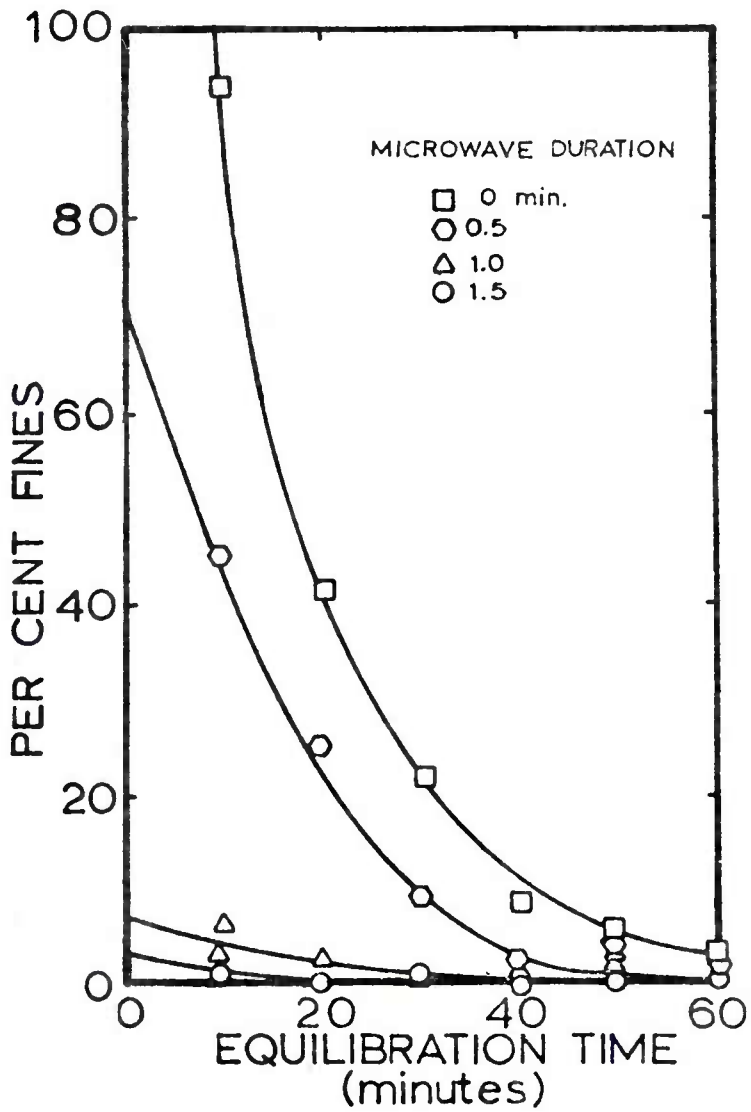

FIG. 3 THE EFFECT OF MICROWAVE DURATION AT 441 WATTS ON FINES PRODUCTION.

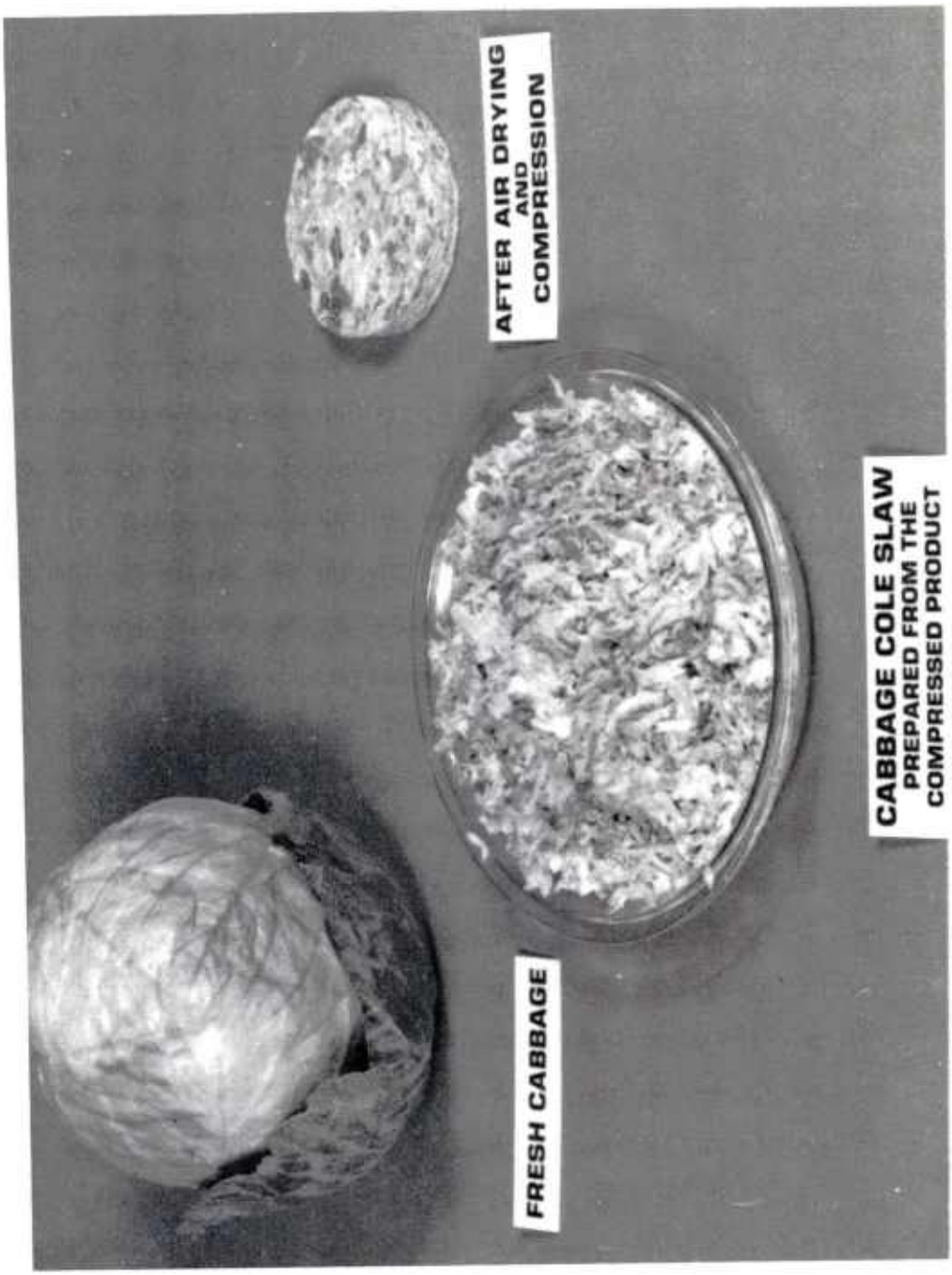

FIG. 4 - VOLUME REDUCTION IN CABBAGE UPON COMPRESSION

AD-A056478

COMPUTER AIDED SELF-FORGING FRAGMENT DESIGN

*GLENN RANDERS-PEHRSON, MR.
I. PETER JURIACO, MR.
LARGE CALIBER WEAPON SYSTEMS LABORATORY
US ARMY ARMAMENT RESEARCH AND DEVELOPMENT COMMAND
DOVER, NEW JERSEY 07801

A number of proposed warhead concepts require an explosive charge which is detonated at a long distance from the target to form a heavy, high velocity fragment which acts as a kinetic energy penetrator to defeat armor. Two such concepts are STAFF (Ref 1) and SADARM (Ref 2), which are envisioned to attack tanks from the top, where the armor is relatively thin. A charge design which can accomplish this task is that known as the "self-forging fragment (SFF)" device or as the "Projectile-forming charge (P-charge)." In contrast to a conventional conical shaped charge which produces a jet having a tip velocity of up to 10 km/s and is capable of perforating very thick armor at short standoff distance, a SFF device forms its liner into a single slug or fragment which remains in one piece as it flies over a trajectory of 100 meters or more at a velocity approaching 3 km/s. While the depth of penetration achievable by a SFF is much less than that of a conventional jet forming shaped charge operating at short standoff distance, its performance at very long standoff is only slightly degraded by its loss of velocity due to air drag. SFF devices are the only chemical energy warheads capable of significant effect at standoff distances exceeding several dozen calibers.

Designing a SFF device is not an easy task, since the liner must be contoured so that the explosive impulse forms it into a slug which has a very low velocity gradient, otherwise it will be pulled apart. Conceptually the job is like forming a cannon ball from a sheet of material with one blow of a hammer, without a die. At ARRADCOM's Large Caliber Weapons Systems Laboratory, the HEMP computer code has been developed to serve as an effective design tool to simplify this task considerably. Using this code, warheads

for the STAFF and SADARM concepts have been designed which successfully form into single compact slugs that are effective against armor at extremely long standoff.

The HEMP Computer Code

The computer code used for modelling the various self-forging fragment configurations is an especially modified version of the HEMP ("Hydrodynamic Elastic Magneto Plastic") program (Ref 3 and 4). This is a general purpose LaGrangian two dimensional finite-difference code developed by Mark Wilkins of the Lawrence Livermore Laboratory and widely used by the Department of Defense for munitions problems. Given a numerical grid representing the initial geometry, together with material and explosive properties (Refs 5 and 6), this code solves the equations of motion iteratively along with the equations of state to determine the deformation of the liner in response to the pressure exerted on it by the detonation products. Figure 1 shows a typical grid describing a SFF device, actually an explosive ordnance disposal item known as a "Ballistic Disc" designed (experimentally) by the late Seymour Kronman of ARRADCOM's Ballistic Research Laboratory. Initially it was not possible to run this or any other SFF problem beyond twenty or thirty microseconds without resorting to very coarse gridding and resultant loss of accuracy. This was due to a thinning out of the liner edge, which resulted in the reduction of the integration time step to an unreasonably small value to preserve computational stability. (See Figure 2.)

A modification was introduced into the code to drop this distorted region out of the problem at the appropriate time (one to three microseconds after the detonation wave strikes the liner edge). This enables the computation to resume with a reasonable time step.

This dropping procedure is performed "on the fly," that is, by including a simple instruction to ignore the distorted liner edge for the remainder of the computation. This replaces an earlier, somewhat timeconsuming method of stopping the program, creating a restart file, operating on the restart file with a rezoning computer program, and then restarting the HEMP calculation from the modified file. In practice, for finely gridded liners, it may be necessary to drop out the liner edge two or three times successively. It should be noted that this part of the liner actually does break off into a ring of fragments in test firings, so that the part that remains in the computation is representative of the part that contributes to the actual fragment or slug. Figure 3 shows a HEMP

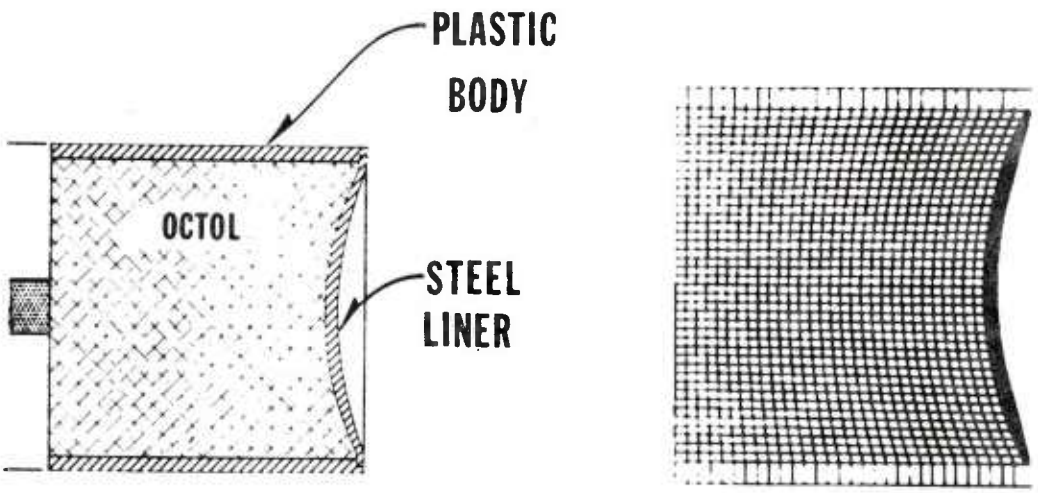

Fig 1 Kronman's ballistic disc device and HEMP numerical grid representing it

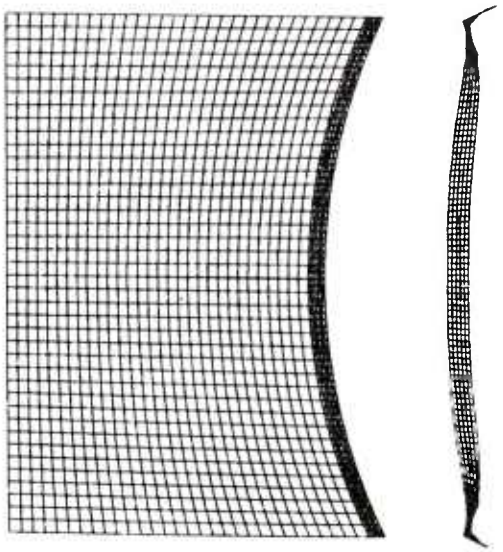

Fig 2 HEMP solution of SFF problem which stopped due to distortion of the liner edge

computation of the Kronman ballistic disc device, together with a flash x-ray of the resulting fragment. The modified code was first used to run a number of SADARM problems in conjunction with an on going experimental program (Ref 7). Extremely good agreement between computed and actual fragment shapes was obtained. With this and other comparisons completed, it was felt that the code could be used as a reliable design tool.

Additional modifications were added to the code to improve its efficiency in execution and its flexibility in use. The slide line routines were modified to improve efficiency by using vector cross products instead of trigonometric functions, and to improve the accuracy of the velocity calculations. Major reorganization of the memory management allowed the code to run fairly large problems (up to 2600 zones) in core on ARRADCOM's CDC 6600 computer, which has 240 000 octal (81 920 decimal) core locations available. Larger problems require the use of disc, which considerably increases the turnaround time for a computation. SFF problems are typically gridded with 40x5 zones in the liner and 20x30 zones in the explosive charge, and run at about one second of central processor time per iteration. On the order of 20 iterations are required for each microsecond of the

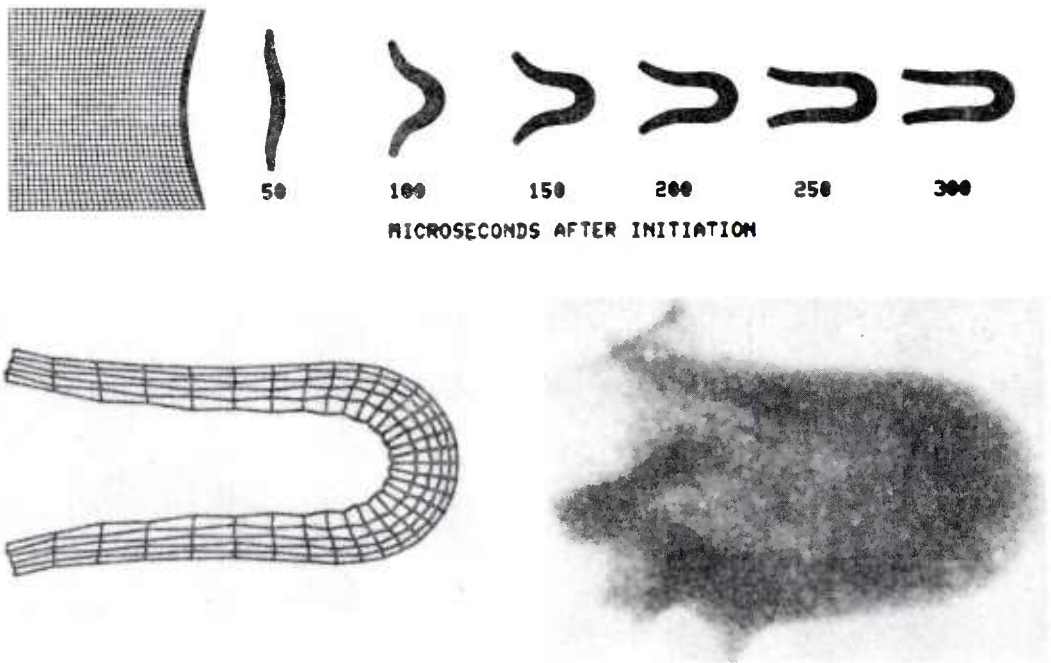

Fig 3 HEMP solution for Kronman's ballistic disc and flash x-ray of fragment

solution. At 40 or 50 microseconds, when the detonation pressure has decreased to a very low value, the explosive region can be dropped from the problem and the liner run alone to its final configuration. This saves a considerable amount of computer time and memory with negligible effect on the calculated fragment shape and velocity. By 300 microseconds the elements of the liner have stopped relative movement if they are going to stop at all. A typical HEMP run to 300 microseconds requires 15 to 40 minutes of computer time on the CDC 6600 machine.

SADARM Liner Design

SADARM ("Sense and Destroy Armor") is a warhead concept in which an artillery round ejects several submunitions in the air above tank targets. Each submunition hangs from a spinning vortex ring parachute. When a sensor detects a target, the explosive warhead detonates, sending a self-forging fragment on its way to (and presumably through) the top of the tank.

The SADARM tests described in Reference 7 were performed using a charge with explosive length to diameter ratio of 1. In the actual system configuration, it has been determined that there is only room for a warhead whose L/D ratio is 0.7. Accordingly, the HEMP code was used to design a liner whose performance would be optimized for this charge configuration. Although the earlier study used steel liners, it was decided to use copper liners here because of its greater density and because of its availability relative to the special steel previously required. Copper is less forgiving of velocity gradients than some very ductile steels, but it was hoped that the HEMP code could be used to design a liner with very little velocity gradient.

Because the hyperbolic liners used in the earlier work had produced tumbling fragments, it was decided to try to design two types of liners: one which produces a spheroidal fragment whose performance should be relatively unaffected by tumbling, and one which produces a rod-shaped fragment, flared at the rear, which might fly stably.

Based on some tests in which charges were deliberately designed to invert their liners without collapsing fully (Fig 4), the required dynamic material properties for copper were deduced. Although the handbook value of the yield strength of the copper is only 70 MPa, work hardening to 220 MPa, the tests indicated that in this dynamic environment a value of 300 MPa is more appropriate.

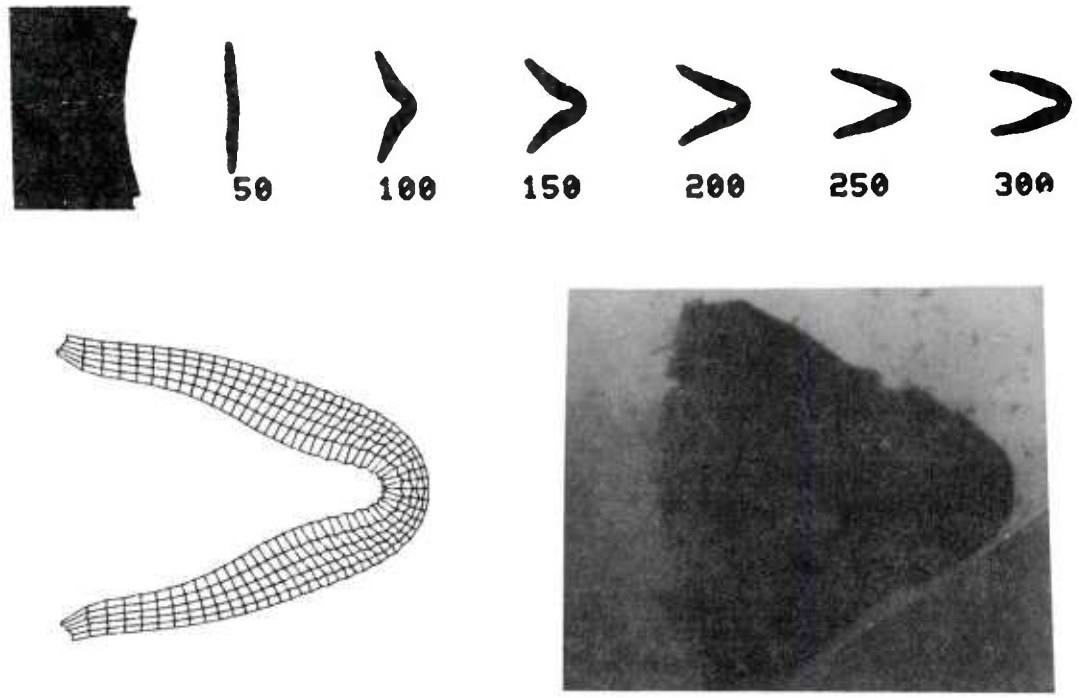

Fig 4 HEMP solution and flash x-ray of copper plate bending test

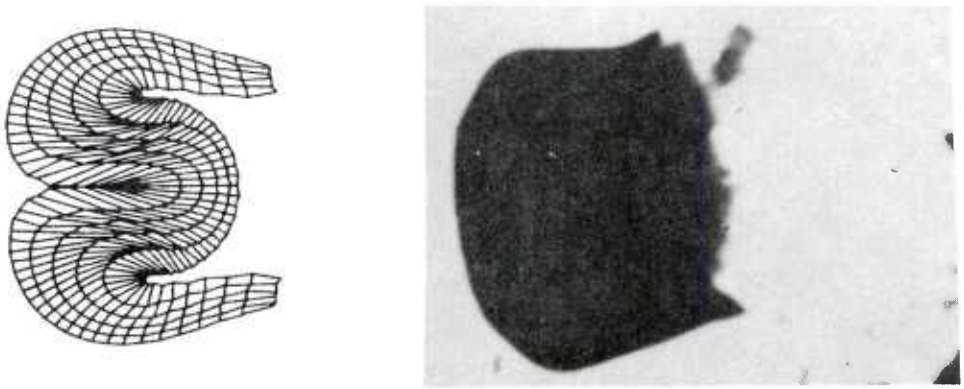

Fig 5 HEMP solution and radiograph of SADARM warhead designed to produce a spheroidal fragment

This value is reached so quickly that HEMP solutions using work hardening and those using only elastic-perfectly plastic formulations are quite similar. The latter formulation was used for the remainder of the study because it consumes less computer resources.

The solution producing a spheroidal fragment is shown in Figure 5, along with a flash x-ray of the actual fragment produced by a test charge. Excellent agreement between prediction and experiment may be noted.

The attempt to produce a flared copper rod was somewhat disappointing, as shown in Figure 6. Although the test charge shown in Figure 4 produced a single copper fragment, the slightly more severe deformation encountered here caused the formed rod to segment into several pieces. It was possible, however, to form a flared rod of steel (Fig 7). ARRADCOM's HEMP code at present has no fracture criteria built in, primarily because of a lack of raw data. It is hoped that, with further experience, it will be possible to predict the occurrence of fracture in a SFF by monitoring the calculated triaxial strain.

STAFF Liner Design

STAFF ("Smart Target Activated Fire and Forget") is another type of target sensing unguided munition. In this 155 mm device, two double ended self-forging fragment warheads will be mounted transversely within a spinning projectile. When the projectile senses that it is above a target, the warheads will be detonated so as to fire the self-forging fragments downward through the top of the target.

HEMP was used as the design tool from the very beginning of this project. The code was used to find the optimum L/D ratio, cylinder wall thickness, and liner thickness, subject only to the constraints that the device had to fit crosswise in a 155 mm munition, and that kinetic energy was to be maximized. Once these were determined, the contour of the liner was designed so as to produce a spheroidal fragment. The resulting warhead configuration is shown in Figure 8. Due to the extremely short time between the receipt of funds for preliminary design work (October 1976) and the proposed concept demonstration (August 1978), there was little time to perform experimental iterations. Fortunately, the first HEMP-designed warhead did produce a spheroidal fragment which performed well against armor. The predicted and actual fragment configurations are shown in Figure 9.

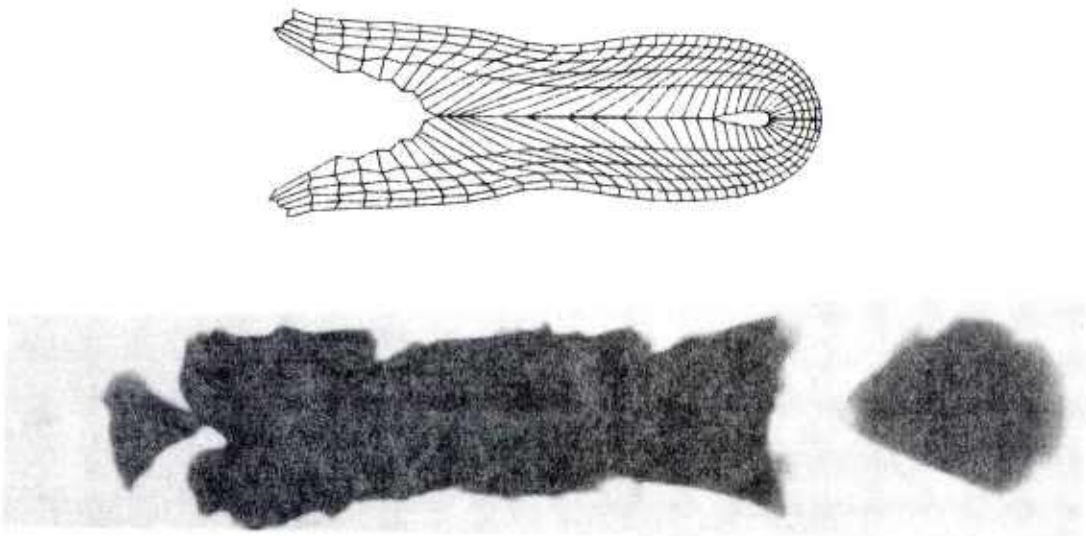

Fig 6 HEMP solution and flash x-ray for SADARM designed to produce a flared copper rod, which fractured in test firing

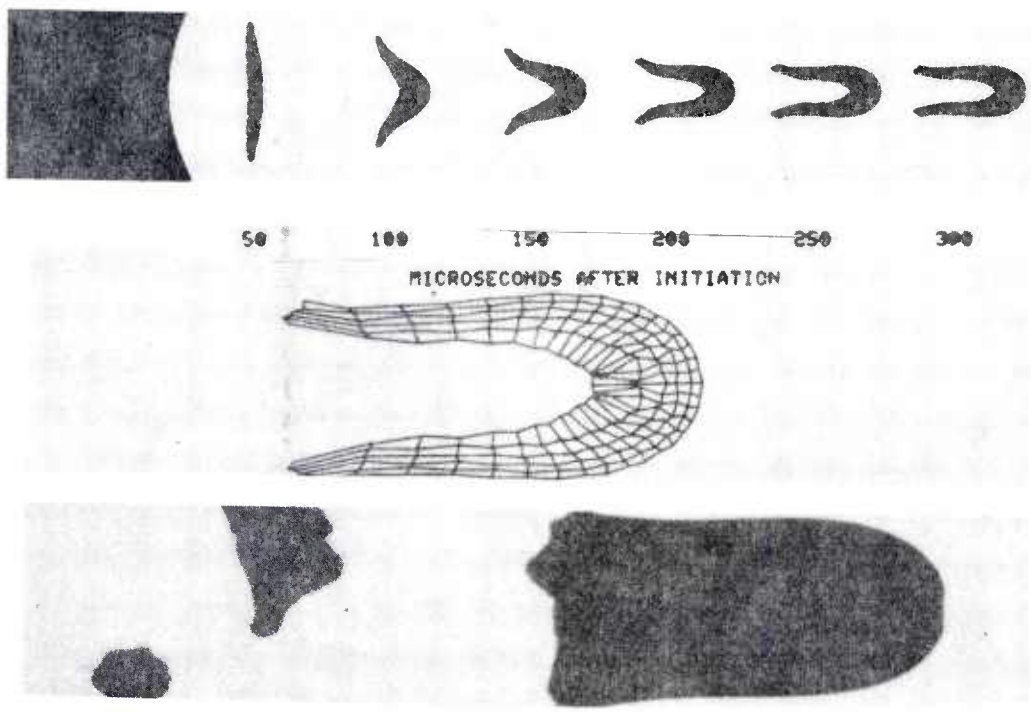

Fig 7 HEMP solution and flash x-ray for SADARM design (L/D=1) which produced a flared steel rod and did not fracture

Conclusions

HEMP has proven to be an invaluable design tool for self-forging fragments, and has been used successfully to design warheads for the STAFF and SADARM weapon concepts.

More needs to be learned about the dynamic fracture behavior of liner materials to ensure that one-piece slugs may be reliably formed.

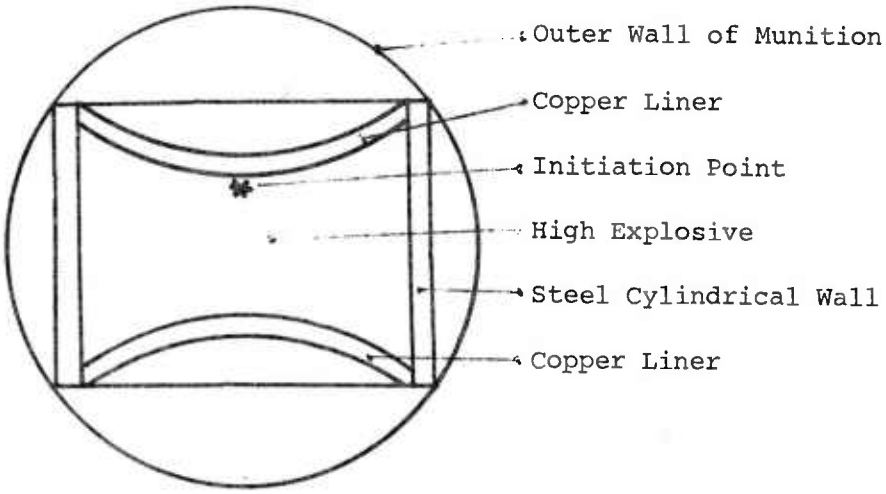

Fig 8 STAFF warhead configuration

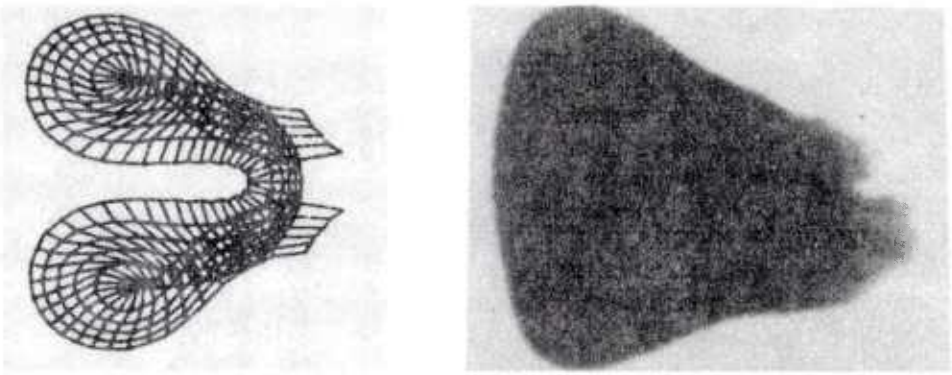

Fig 9 HEMP solution and flash x-ray of fragment from STAFF warhead

References

1. Poisall, Charles, "STAFF Goes After Tanks," Army Research and Development, March-April 1978.

2. Poisall, Charles, "ARRADCOM Continues SADARM Exploratory Development," Army Research and Development, October - November 1977.

3. Wilkins, M. L., Calculation of Elastic-Plastic Flow, UCRL-7322, Lawrence Radiation Laboratory, Livermore, California (1969).

4. Giroux, E. D., HEMP Users Manual, UCRL-51079 (rev. 1), Lawrence Livermore Laboratory, Livermore, California (1973).

5. Rice, M. H., et al, "Compression of Solids by Strong Shock Waves," in Seitz and Turnbull, editors, Solid State Physics, Vol. 6, Academic Press, New York (1958).

6. Dobratz, Brigitta M., Properties of Explosives and Explosive Simulants, UCRL-51319, Lawrence Livermore Laboratory, Livermore, California (1974).

7. Hermann, John W., Jr., Glenn Randers-Pehrson, and Edward R. Berus, "Experimental and Analytical Investigation of Self-forging Fragments for the Defeat of Armor at Extremely Long Standoff," Third International Symposium on Ballistics, Karlsruhe, Germany, March 1977.

Postscript

It is with extreme regret that I must note the accidental death on December 1, 1977, of my dear friend, research partner, and co-author, I. Peter Juriaco. Not only have his many friends at Picatinny suffered a great personal loss, but the Army has suffered a great technical loss. Pete's knowledge of detonation physics and fragmentation and his expertise in instrumentation and ultra-highspeed photography will be sorely missed for a long time.

AD-A056479

COMPUTER AIDED DESIGN, DESIGN AUTOMATION AND LSI; KEYS TO HIGH-PERFORMANCE MILITARY ELECTRONICS

RANDOLPH A. REITMEYER, JR.
US ARMY ELECTRONICS TECHNOLOGY AND DEVICES LABORATORY, ERADCOM
FORT MONMOUTH, NEW JERSEY 07703

INTRODUCTION

The Army is faced with the task of developing new and vastly improved electronic systems to meet the challenge of sophisticated, high-mobility, future battlefields. In general, this challenge requires the use of complex, custom, high-speed, low-power, large scale integrated circuits (LSICs) and very large scale integrated circuits (VLSICs). The successful development of such circuitry is dependent on the availability of advanced integrated circuit (IC) fabrication technologies, e.g., complementary metal oxide semiconductor/silicon on sapphire (CMOS/SOS) and galium arsenide (GaAs) and on the availability of affordable design and design verification capabilities.

SHRINKING ARMY SYSTEMS/EQUIPMENT

The mobility of many Army systems is a function of their size and weight. Multiple-van, multiple-aircraft systems such as QUICKLOOK II-AGTELIS and CEFLY LANCER-TACELIS are examples where advanced IC technology could shrink the system and greatly enhance our ability to see and move on the battlefield.

Shrinking major Army systems requires high-speed, low-power, very complex integrated circuits at affordable cost. For example, current digital signal processors will require a twenty times reduction in size and weight, a five times or more reduction in power consumption and an increase of ten times to one hundred times in operating speed. Most important of all, the cost of developing the hardware must be reduced by at least ten times and turn-around time for custom IC

development must be cut to three months.

ADVANCED ARMY SYSTEM IMPLEMENTATION

Advanced high-density, high-speed integrated circuit technologies are key ingredients for achieving the technical goals. The number of components in an integrated circuit has doubled every year for the past fifteen years. By 1980, chip complexities will be pushed to well beyond 100,000 components. ERADCOM programs in technologies such as CMOS/SOS, SOS, and GaAs will provide the high-speed (5 MHz-5 GHz) low-power performance characteristics needed for electronic counter-countermeasures (ECCM) data links and tactical signal intelligence (SIGINT). Such high-speed IC technology will allow the Army to implement very sophisticated, high-performance, extremely small electronic systems using both off-the-shelf integrated circuits (e.g., microprocessors and associated devices) and custom integrated circuits (e.g., random logic, microprocessors and "systems-on-a-chip").

CUSTOM LSI/VLSI....WHAT IS IT?

Today, the methods for developing custom LSI/VLSI devices fall into three categories:

(1) Handcrafted Approach....High volume (100,000 units) applications.

In the handcrafted design approach, the topological layout design is manually achieved with interactive graphic aids which are utilized extensively. Custom circuits are handcrafted when very large quantities of a device are required. This approach, which focuses on saving silicon area in favor of low initial design cost and turn-around time, is primarily utilized throughout the commercial semiconductor industry. The popular Intel 8080 and Motorola 6800 Microprocessors and random access memory devices are typical examples of handcrafted functions.

(2) Standard Cell Approach....Low to medium (1-100,000 units) quantity applications.

The standard cell approach emphasizes low initial design cost and quick turn-around. It is an automated capability that utilizes a library of design-optimized and performance-proven handcrafted standard logic cells and a placement and routing computer program that automatically generates complete LSI/VLSI topological layouts.

Although standard cell layouts are typically 10 to 20% larger than equivalent handcrafted functions, their design costs and turn-around time (not including processing time) can be from 25% to 40% of a handcrafted approach. The probability of standard cell LSI devices functioning properly the first time is five to ten times greater than for handcrafted designs.

(3) Universal Array Approach....Very low volume (1-1000 units) applications.

The universal array (UA) approach offers the lowest cost and quickest turn-around capability. It is well suited for very low volume applications such as prototyping, feasibility demonstration, and situations where low gate-count (100-300 gates)* is acceptable. UAs are prefabricated circuits comprising alternate rows of transistors for logic, and open areas for aluminum interconnection and feedthrus. All mask levels are defined except the metal mask level. The metal mask level is used to join individual transistors in order to form logic gates as well as to interconnect gates to form complete circuit functions. Topological layout design is typically a manual-planning, interactive-graphics-aided digitizing and editing process. Despite the advantages of fast fabrication cycles using stockpiled UAs, the manual generation and verification of UA layouts, the relatively low gate-count and the general unavailability of UAs, limit their acceptability and ultimate use. This situation will be vastly improved with the planned ERADCOM development of a new high gate-count (500-600 gates) universal array that is designed for optimum compatibility with automatic placement and routing and design verification programs.

CUSTOM LSI & CAD....A MARRIAGE OF TECHNOLOGIES

By the late 1960's, digital logic became the favored approach (over analog circuits) for implementing electronics in military systems. With the advent of the general-purpose digital microprocessor technology, this trend has continued. When off-the-shelf components have not been suitable to satisfy system size, weight, speed or power consumption requirements, then custom LSI has been considered.

*In this paper a gate is equivalent to four transistors.

There have always been many questions concerning custom LSI availability. For example: Will the LSI circuit development cycle meet equipment/system schedules? How much will it cost? Who will fabricate and supply the devices? An early 1970 Electronics Command market survey discovered that custom LSI/VLSI circuits could not, in general, be obtained from large volume-oriented semiconductor vendors. These vendors were, and still are, focused on calculators, watches, games, microprocessors, memories and automotive circuits. It was determined that custom LSI would have to come from the people who build military systems; namely, defense systems contractors. Many of the defense systems contractors that were surveyed were not prepared to develop LSI because of their lack of qualified design personnel, design tools and IC fabrication facilities. For the few vendors who could provide custom LSI for low volume applications, it was determined that relatively simple LSI devices would require at least a one-year, $100K development cycle, For major systems, wherein several custom circuits were required, it became obvious that conventional manual design approaches could not meet system schedules and cost requirements. Clearly, the defense systems industry required an automated design approach to remedy this situation.

EARLY CAD....

Early design automation approaches for custom LSI were evaluated against Army requirements for high-density, high-speed, low-power circuitry. National Aeronautics and Space Administration (NASA) sponsored CAD, based on the utilization of a family of single-side entry, bulk-silicon CMOS standard cells and an automatic placement and routing program called PR2D, was of particular interest. Evaluation of this approach indicated that PR2D-generated LSI topological layouts were about five to ten times larger than handcrafted equivalents. The layouts were large because: (1) the metal gate bulk CMOS standard cells developed for PR2D use were large; (2) the placement and routing algorithms forced a hugh build-up of interconnection metalization on the sides of chips while the areas between cell rows was wasted. The most serious drawback was the speed limitation imposed by the parasitic capacitance and resistance that is inherent with the excessive interconnect metalization. Since the PR2D approach could not provide sufficient high-density, high-speed chip layouts for future Army battlefield requirements, a new approach had to be developed.

MP2D....A BREAKTHRU FOR CUSTOM LSI

New concepts in automated LSI design based on the utilization of double-entry standard cells, feedthru cells and new and improved placement and routing algorithms, have resulted in a new area-efficient, cost-effective and multi-technology useful layout program called MP2D. MP2D is a significant improvement over the early 1970 vintage PR2D program as it provides for a 4:1 reduction in chip area. For example, the 250 gate (1000 transistor) LSI circuit in Figure 1 is 50,284 sq mils using PR2D and 11,700 sq mils with MP2D.

The application of MP2D is based on the placement of box outlines of logic cells which describe the physical size and input/output connections to standard cells, and the interconnection of the cells as prescribed by a user supplied net list. MP2D can, therefore, be utilized for any IC technology that can provide double-entry cells and a two-level interconnection scheme. For this reason, MP2D is utilized for applications that involve the use of CMOS/SOS and radiation-hardened CMOS/SOS, C^2L, I^2L and universal array technologies.

MP2D is also challenging the handcrafted layout approach for higher volume applications. The computer charges for generating the high density layout in Figure 1 was $230 for 30 CPU minutes on an IBM 360/65. Although a handcrafted equivalent of the same function might be 10-20% smaller in area, it is estimated that about 6 to 8 manweeks would be required to manually generate, verify, edit and digitize a handcrafted layout. Should customer requirements change, a new layout via design automation requires only another 30 minute computer run; a manual redesign would require days or weeks, depending on the extent of the changes.

For a custom LSI circuit to be cost-and-time-affordable in military systems, it is critical that the circuit go through only a single very rapid design, fabrication and testing cycle; the chip has to work the first time. The rapid, low-cost development of an LSI chip, therefore, requires more than the automated layout program MP2D. Since the circuit designer cannot realistically breadboard a custom function, fast computer logic simulation is also required. Testing a custom LSI part also requires computer generated test patterns. This means that logic/circuit designers require a total CAD system that can automate all phases of custom LSI design.

ARMY CADDA CENTER FOR CUSTOM LSI

The Electronics Technology and Devices Laboratory, ERADCOM, Fort Monmouth, New Jersey has established an Army computer-aided design and design-automation (CADDA) center for affordable custom LSI. An extensive system of CADDA programs (Figure 2), standard cells and an interactive graphics facility have been developed and implemented during the past several years by ET&DL.

MP2D has been built into the CADDA system which includes a logic simulation program, LOGSIM; a test pattern generation program. AGAT; a common data base system, CDB; and an interface to an Applicon interactive graphic system. In addition, a family of 40, MP2D-compatible, high-density, double-entry CMOS/SOS standard cells was designed, verified and documented. To generate LSI devices using this capability, the designer partitions his logic into standard cells, provides a net list containing cell pattern numbers and their connectivity, and enters the CADDA system via the common data base. Having entered CDB, the designer selects and executes the design programs via control cards. The topological output of the design system is a magnetic tape data file that is loaded into the Applicon interactive graphic system. Once the file is loaded into the Applicon, the LSI/VLSI layout can be edited or modified, for example, to reduce the delay of critical paths, to optimize performance or to relocate or re-orient bonding pads. CALCOMP plots for error checking and general documentation and magnetic tape files for photomask making are also accomplished with the Applicon system.

CADDA TECHNICAL IMPACT

The return on the Army's investment in the advanced CADDA system is in the utilization of the software, standard cells and system-user techniques which are offered to technical groups with a clear U. S. military objective. ERADCOM's ET&D Laboratory has formed a CADDA User's group comprising a continually increasing number of defense systems contractors and other government agencies (Figure 3) who are using the automated LSI/VLSI design software, cells, etc. The use of the Army CADDA software and standard cells is committed to at least six major military programs, such as PATRIOT, REMBASS and PLRS, and is being considered for use in many other systems.

A custom LSI fuze circuit for the PATRIOT missile is a good example of the impact that custom LSI and CAD can have (Figure 4). The one-chip CMOS/SOS circuit provided significant reductions in size,

power consumption, and cost compared to an equivalent TTL implementation. The LSI circuit which contains over 2000 devices was topologically layed out by MP2D at a cost of less than $400.

NEW CADDA FOR THE FUTURE

The trend for Army integrated electronics is toward significantly higher speeds and circuit complexities. Higher operating speed is a function of the speed of the active devices within the standard cells and of the parasitic impedances of the chip interconnections. In the next couple of years, by improving the CMOS/SOS technology and reducing the SOS device channel length, standard cells will operate at frequencies in excess of 200 MHz. Parasitic interconnect impedances will be minimized by improved CMOS/SOS processing and by reducing the physical length of electrical connections. The MP2D program is presently being modified to automatically minimize user-identified critical networks (paths). The program will: control the length of each wire segment, compute and print out actual RC data, and tell the designer if a specified delay limit is exceeded. "System-on-a-chip" custom arrays of VLSI complexity will be accomplished by incorporating, within MP2D, the capability to mix high-density, high-speed, hand-crafted supercells with standard cells. Circuit densities with figures-of-merit below 10 sq mils/device will be achieved using this approach. Linear and digital functions will also be customized together using the supercell MP2D approach.

SUMMARY

A deterrent to the utilization of custom LSI functions has been the lack of an automated design and development system that will allow rapid development of circuits in a single, cost-effective cycle. The manual design of LSI circuits in one year, $100K cycles is too costly for low volume military applications.

ERADCOM's Electronics Technology & Devices Laboratory, Fort Monmouth, N. J., has developed a complete CADDA system for custom LSI that make feasible three-month $35K development cycles. The system is applicable to a wide variety of advanced IC technologies such as CMOS/SOS, radiation-hardened CMOS/SOS, bulk CMOS I^2L and universal arrays.

Key elements of the CADDA system have been widely disseminated to defense systems contractors and are being applied to major Army equipment. Major enhancements are underway to extend the availability of custom LSI to much higher frequencies and levels of complexity.

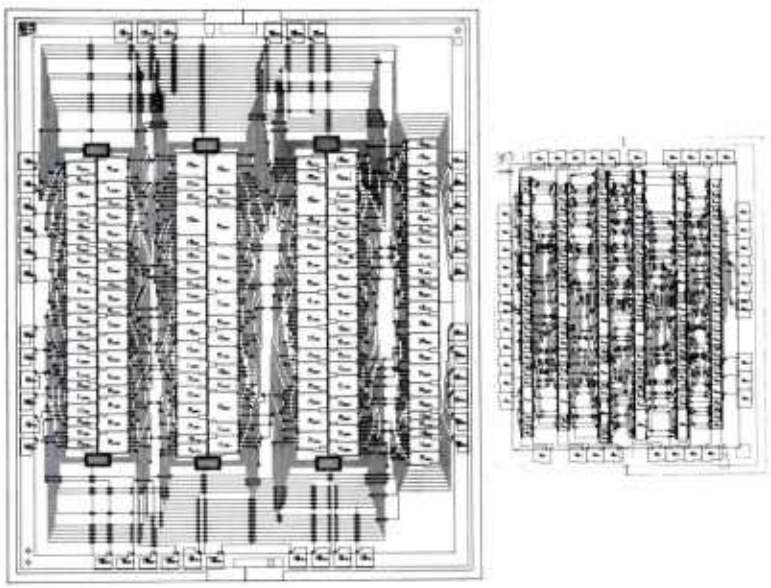

ERADCOM MP2D LAYOUT PROGRAM REDUCES STANDARD CELL LAYOUTS BY 4:1 COMPARED TO PR2D PROGRAM

Figure 1

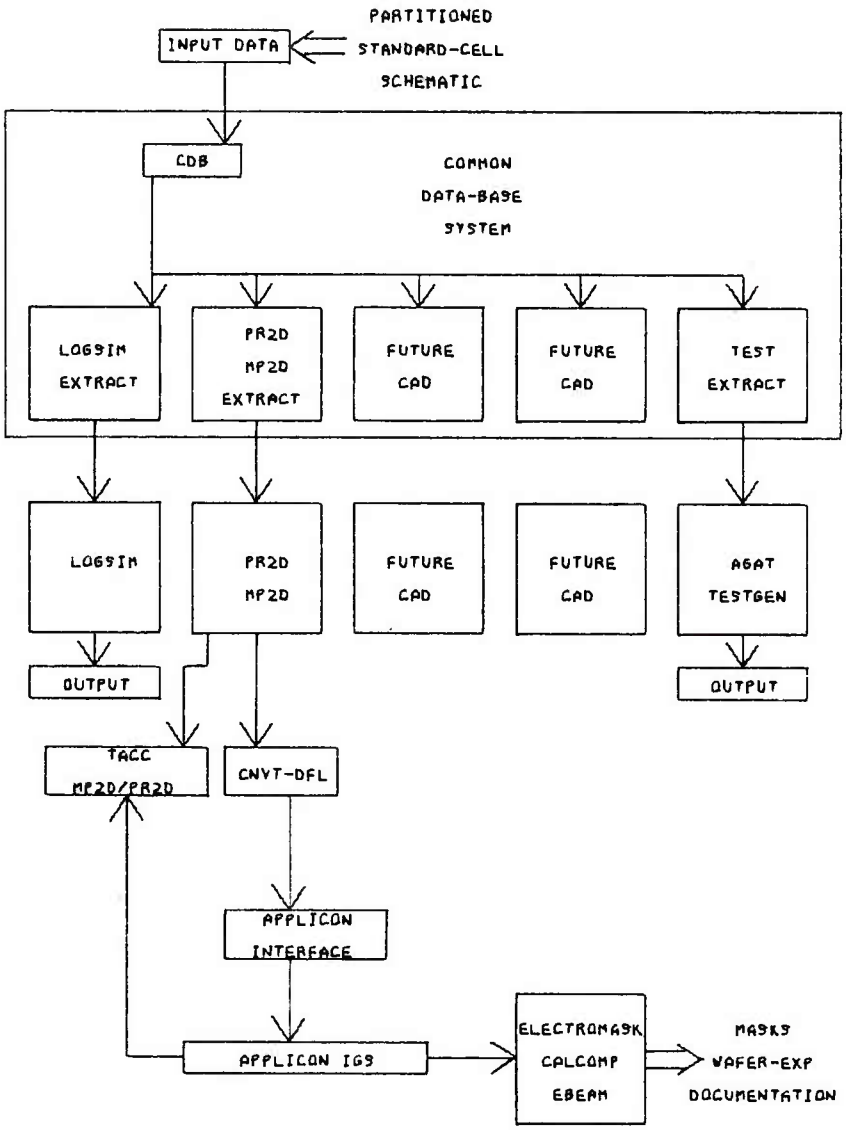

ERADCOM CADDA SYSTEM FOR CUSTOM LSI

Figure 2

REITMEYER

RCA CORPORATION	CAMDEN, SOMERVILLE, NEW JERSEY
RAYTHEON COMPANY	BEDFORD, MASSACHUSETTS
E-SYSTEMS	ST. PETERSBURG, FLORIDA
McDONNELL DOUGLAS	MONROVIA, CALIFORNIA
TRW SYSTEMS	REDONDO BEACH, CALIFORNIA
HARRIS ELECTRONIC SYSTEMS DIVISION	MELBOURNE, FLORIDA
BENDIX CORPORATION	BALTIMORE, MARYLAND
MAGNAVOX CORPORATION	FORT WAYNE, INDIANA
HUGHES AIRCRAFT COMPANY	LOS ANGELES, CALIFORNIA
ROCKWELL INTERNATIONAL	NEWPORT BEACH, CALIFORNIA
SOLID STATE SCIENTIFIC	MONTGOMERYVILLE, PENNSYLVANIA
SPERRY UNIVAC	ST PAUL, MINNESOTA
ITT SEMICONDUCTORS	WEST PALM BEACH, FLORIDA
SANDIA LABORATORIES	ALBUQUERQUE, NEW MEXICO
NASA	HUNTSVILLE, ALABAMA
NAFI	INDIANAPOLIS, INDIANA

USERS OF ERADCOM CADDA PROGRAMS

Figure 3

	IC VERSION	LSI(ERADCOM MP2D LAYOUT)
Technology	TTL	SOS/CMOS
Packages	31	1
External Parts	9	8
Power Consumed	4.5W	1.2 mW
Relative Cost	10	1

IMPACT OF LSI & CAD ON SYSTEM COST/PERFORMANCE
FOR FUZE LOGIC, PATRIOT MISSILE

Figure 4

AD-A056480

THERMAL BLOOMING AND AIR BREAKDOWN INTERACTION FOR PULSED HIGH ENERGY LASERS

*ROBERT S. ROHDE, DR.
RUDOLF G. BUSER, DR.
US ARMY ELECTRONICS RESEARCH & DEVELOPMENT COMMAND
FORT MONMOUTH, NEW JERSEY 07703

1. Introduction and Problem Definition

Laser pulse transmission as related to Army high energy laser systems involves many interacting effects which generally degrade the performance of the laser systems: molecular absorption, scattering, turbulence, wind, non-linear effects including short and long-time thermal blooming, air breakdown, target-plasma interaction, and optical train jitter. There exists extensive literature on the subject (1-4). This paper deals specifically with the combined effects of short-time (as compared to the acoustic transit time, τ_H, across the beam) thermal blooming and air breakdown.

If both phenomena are present, hot spots in the beam output, as well as the need to produce a plasma at the target for enhanced coupling of energy to the target, will, in many cases, produce statistically random situations which will result in an interplay of breakdown and blooming. One can then ask the following questions: first, in a dynamic breakdown-blooming case, what total energy will be delivered to the target as compared to the breakdown only/blooming-only cases? Second, what will be the average intensity profile in this case. Finally, what role does the temporal beam pulse shape play for optimum energy transfer? Answers to these questions cannot yet be predicted by computer modeling.

As far as experiments are concerned, the two effects so far have been studied only separately (1). The thermal blooming occuring during a laser pulse follows a time evolution referred to as "t^3" in which the on-axis intensity falls as $I \sim t^3$ (5). While

there is no loss of energy, there is a loss of intensity as the beam spreads. On the other hand, when air breakdown occurs, the spreading plasma absorbs the beam with resultant loss of energy and, therefore, intensity (2-3). In the following, laboratory simulation experiments combining both effects will be discussed to provide the base line modeling and system prediction.

2. Fundamental Physics Background

A very simple picture of the energy transmission in the presence of both effects can be seen from an examination of the critical times involved in the processes. The on-axis intensity of a pulse beam undergoing thermal blooming will fall to 50% of peak in 1-3 μs for peak intensities of 10^6-10^7 W/cm^2, given the appropriate conditions (absorption, path length, etc.) (see Figures 1 and 2).

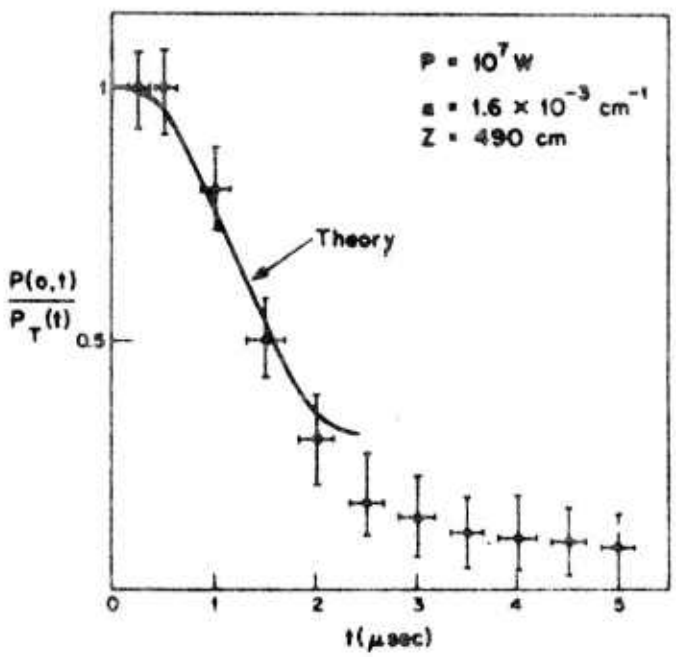

Figure 1. The drop in power due to blooming measured with the aperture located over the peak of the focal distribution has been plotted as a function of time. The theoretical prediction for this case has been plotted for $t < 0.5\ \tau_H$ The length of the absorption cell in the experiments and for the calculation is Z = 490 cm (Ref. 4).

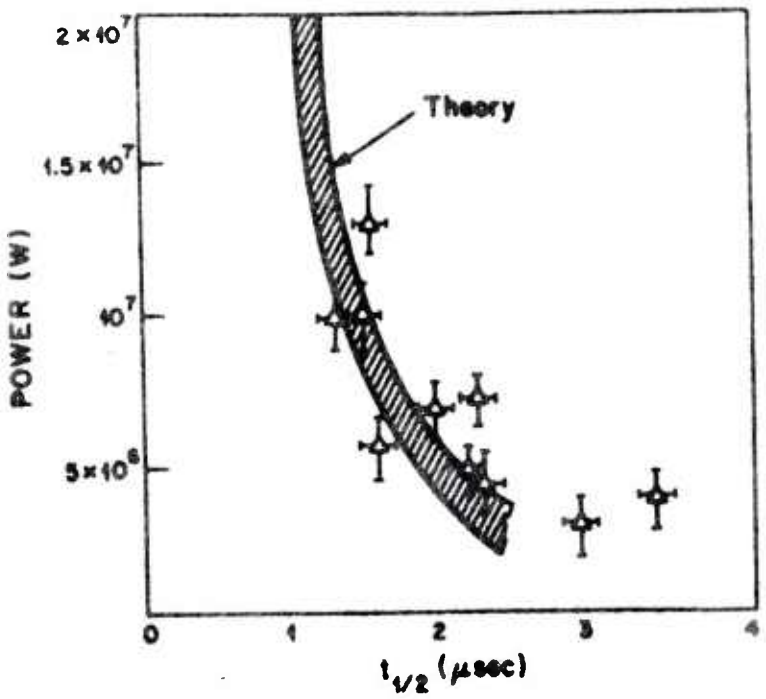

Figure 2. The time for the central aperture power to drop 50% has been plotted as a function of incident power. The cross-hatched area indicates the theoretical predictions for $0.8 \times 10^{-3} \leq \alpha \leq 2.4 \times 10^{-3}$ cm^{-1} and an aperture position uncertainty of $\pm$ 0.05 cm (Ref 4).

On the other hand, the plasma in single point air breakdown will spread 1 mm in 34 μs for intensities of 10^6 W/cm^2 and in 3.4 μs for 10^7 W/cm^2 (Figure 3). In the same time regime that the plasma is spreading, the intensity available to it is being reduced by the blooming. The threshold intensity for breakdown remains constant, so that a plasma is initiated prior to the blooming decay. As the plasma grows, however, the blooming reduces the flux available to it which results in a slower expansion velocity and concomitant lower absorption and reflection. Finally, the intensity is reduced below plasma maintenance with a cut-off time earlier than if the blooming were not present. One may therefore postulate cases where the total energy transmission with both effects present is greater than that with breakdown only, i.e., $E_{Bl + Br} \geq E_{Br}$ (Figure 4).

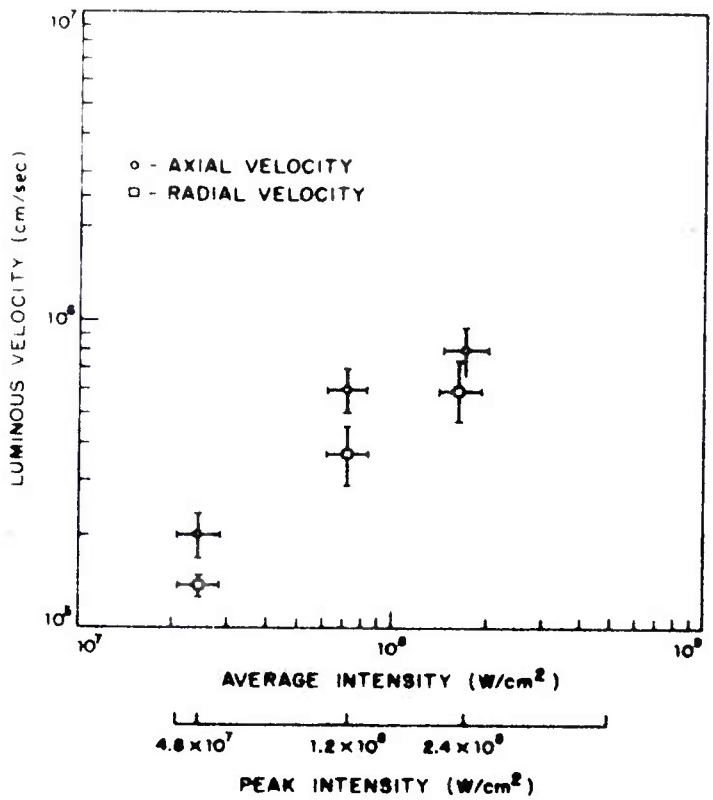

Figure 3. Axial and radial velocities of breakdown plasmas (Ref 3).

For the plasma spread, a simple model assumes a radial growth with a velocity $V_r = \alpha I^k$, where I_o is the beam intensity, and all the radiation is either absorbed or scattered. The transmitted energy for a rectangular pulse of time, t_p, and beam radius, R_o, will simply be

$$E_t = \int_o^{t_c} \left[I_o \pi R_o^2 - I_o \pi (\alpha I_o^k t)^2 \right] dt \qquad (1)$$

where t_c is the time required for the plasma to fill the beam, i.e., $t_c = \frac{R_o}{\alpha I_o^k}$. Integrating, one gets

$$E_t = \frac{2R_o I_o^{-k_{E_o}}}{3\alpha t_p} \quad t_c < t_p \tag{2}$$

$$E_t = E_o \left[1 - \frac{\alpha^2 I_o^{2k} t_p^2}{3R_o^2} \right] \quad t_c > t_p \tag{3}$$

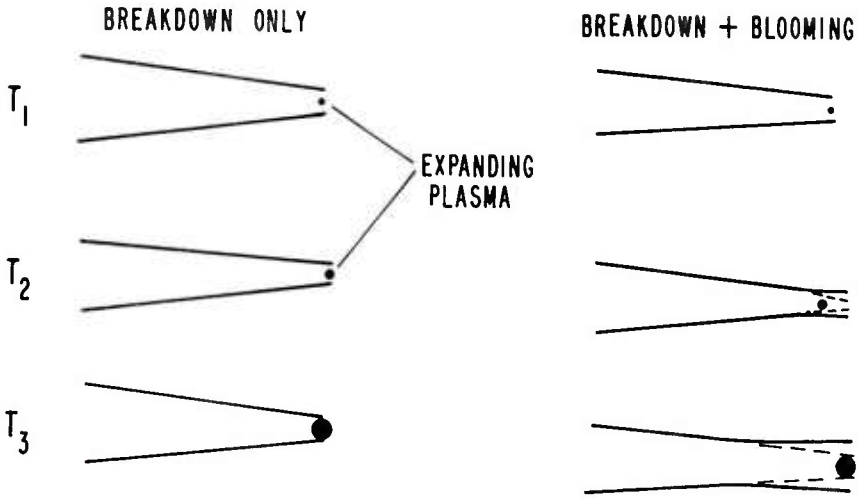

Figure 4. The concept of increased energy transmission due to the interaction of short time thermal blooming upon an air-breakdown induced absorbing plasma. The sequence of events is: (t_1), the plasma is initiated in both cases; (t_2) the plasma expands, but blooming also starts, lowering the available intensity and thus reducing the spreading velocity; (t_3) without blooming, the plasma fills the beam; with blooming, the plasma expansion is reduced and prematurely extinguished with higher total energy transmission.

This model will become increasingly complicated if one assumes that the initial intensity also varies with time due to the blooming. The intensity is then given by (5)

$$\frac{I(r,z,t)}{I_o} = 1 - \beta_o(z)\left[1 - \frac{3r^2}{a^2 D(z)} + \frac{r^4}{a^4 D^2(z)} \exp - \frac{r^2}{a^2 D(z)}\right] \quad (4)$$

$$\beta_o(z) = \delta_o(z)(E/E_f)\ t^3/t_p t_f^2 \quad (5)$$

$$\delta_o(z) = \frac{16}{3} \cdot \frac{f^2}{k^4 a^8} \int_o^z \frac{dz'}{D(z')} \int_o^z dz'' \ \frac{\exp(-\alpha z'')}{D(z'')^2} \quad (6)$$

$$\left[D(z')\right]^{\frac{1}{2}} = 1 - z/f + (z/ka^2) \quad (7)$$

$$t_f = f/kac \quad (8)$$

$$E_f = \pi c^2 / \left[\frac{3}{2} N(\gamma - 1)\ \alpha k^2\right] \quad (9)$$

where E is the total energy, a is the near field e^{-1} beam radius, c the speed of light, $k = 2\pi/\lambda$ where λ is the wavelength, z the path length, f the focus, γ the ratio of specific heats, α the absorption coefficient, and N the refractivity. I_o in Equation (1) is now replaced by Equation (4). Also, the limits of integration must reflect the fact that at some point the intensity will fall below plasma maintenance threshold. At that point, all plasma induced absorption ceases. The beam will propagate further until the plasma shadow is filled by diffraction and threshold is again reached. This process can be seen in the laboratory in the string of "plasma beads" along the propagation path near the focal volume. More generally, the thermal blooming effect is a volume effect, in which a statistical local plasma blackout is embedded. The problem of treating this combined process theoretically has not been solved.

3. Experimental Approach

Figure 5 schematically illustrates the experimental arrangement. A single shot Lumonics 602A CO_2 Transversely Excited Atmospheric (TEA) laser beam, 45 J energy output, with unstable

resonator optics, is focussed through a 5.84 m blooming cell and breakdown is initiated outside the cell exit in the focal volume of the beam in laboratory air (dirty air case).

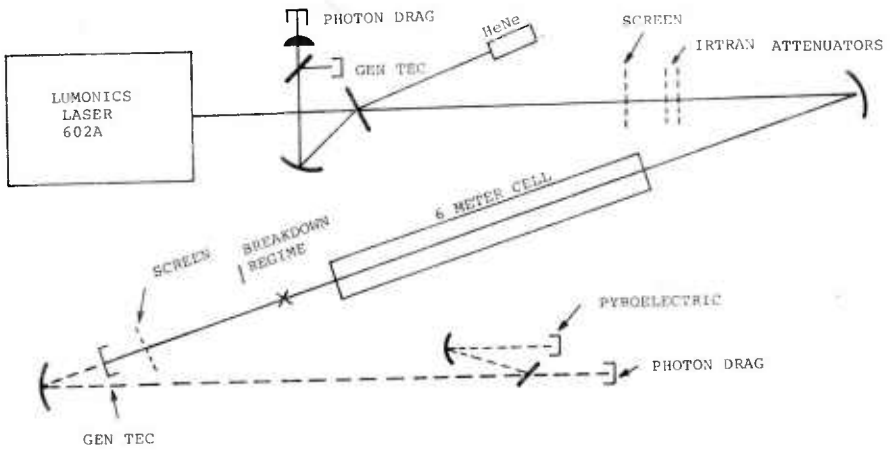

Figure 5. Experimental setup.

There is a need to spatially separate the two effects so that the breakdown with and without thermal blooming may be examined. Alternate experimental approaches, in which blooming and breakdown are spatially not separated, involve significantly more complexity and are in fact unworkable and non-simulating. If the focal volume occurs within the blooming cell, significant linear attenuation occurs in that volume as well. One cannot then separate the two effects of breakdown and blooming. Furthermore, by allowing the breakdown to occur outside the cell, the real atmospheric case is actually better simulated as little linear absorption will occur in the focal volume of a high energy laser beam.

The measurement procedure is as follows: First (A), an attenuating copper screen (9% transmission) and two 10 cm diameter Irtran flats are introduced in front of the cell to reduce the total energy below breakdown. Baseline measurements of the total energy are made with a Gen Tec meter, a photon drag detector (Rofin) is used for observing the on-axis temporal intensity behavior, and for obtaining a one-dimensional integrated energy profile, the focal point of the beam is imaged onto a Laser Precision 32-element pyro-electric array. Representative examples of each of these outputs are shown in Figures 6-8. Next (B), the screen is removed resulting in the breakdown only case. For (C), the Irtrans are removed, the screen replaced, and small amounts of propylene are added until the energy level is identical to that in case (A). Intensity and beam diameter will be the same, then, for breakdown at the cell exit. Finally (D), the screen is removed giving the breakdown and blooming case to be compared with the measurements of (B). It is interesting to note that the energy transmitted in the presence of breakdown is highly repeatable (5% excursions) when multiple breakdowns occurred. A randomness of a few breakdowns occurring in the presence of many will result in a small change in the overall transmission. However, when the intensity is borderline threshold, then large excursions (25-50%) will occur.

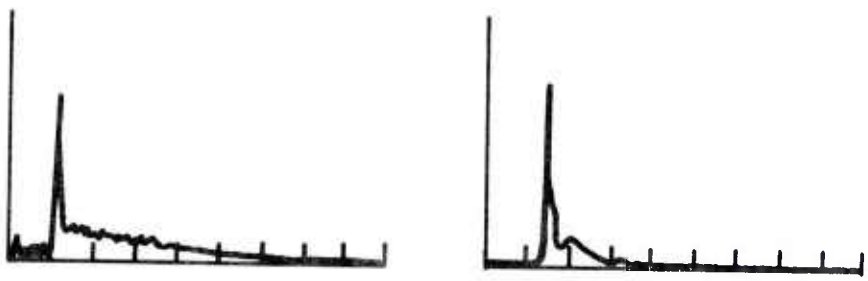

Figure 6. On-axis temporal intensity profile. Left, no blooming; right, blooming. Y scale; arbitrary units. Notice sharply cut-off tail due to blooming effect.

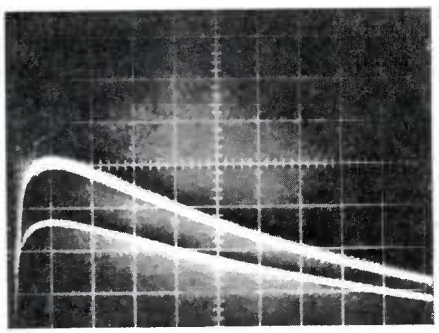

BREAKDOWN; NO BLOOMING

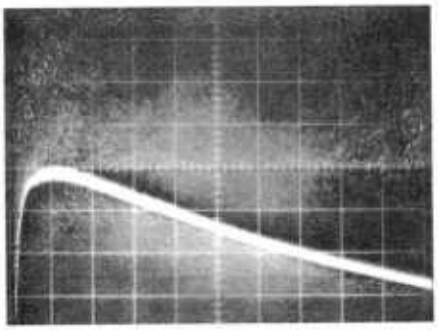

BREAKDOWN; BLOOMING

Figure 7. Integrated energy traces from Gen Tec detector. Each photo has 6 runs; upper traces (3 shots, 0.2 V/cm), transmission at reduced power; lower traces (3 shots, 0.5 V/cm), full power; right photo has traces superimposed showing increased energy (50%) over left photo.

4. Experimental Results

Figure 8 shows the beam profiles of the integrated intensity taken with the pyroelectric array with several shots averaged. The main features show that the beam with and without breakdown and no blooming averages to a similar profile. The blooming, however, results in increased energy in the side lobes of the beam, and a somewhat reduced peak. (In the Figure all curves were normalized to their respective peaks.)

Figure 9 gives the experimental results of the experiment. For the above data, the focal point of the beam was 1.956 meter from the cell exit. The breakdown length was approximately 4.26 m with no absorption and consisted of multiple plasmas. The breakdown data was surprisingly consistent as indicated in the curve. Quite often, one could not distinguish any transmitted energy differences over several separate runs. In all cases, however, the energy transmitted in the blooming case was higher than in the non-blooming cases.

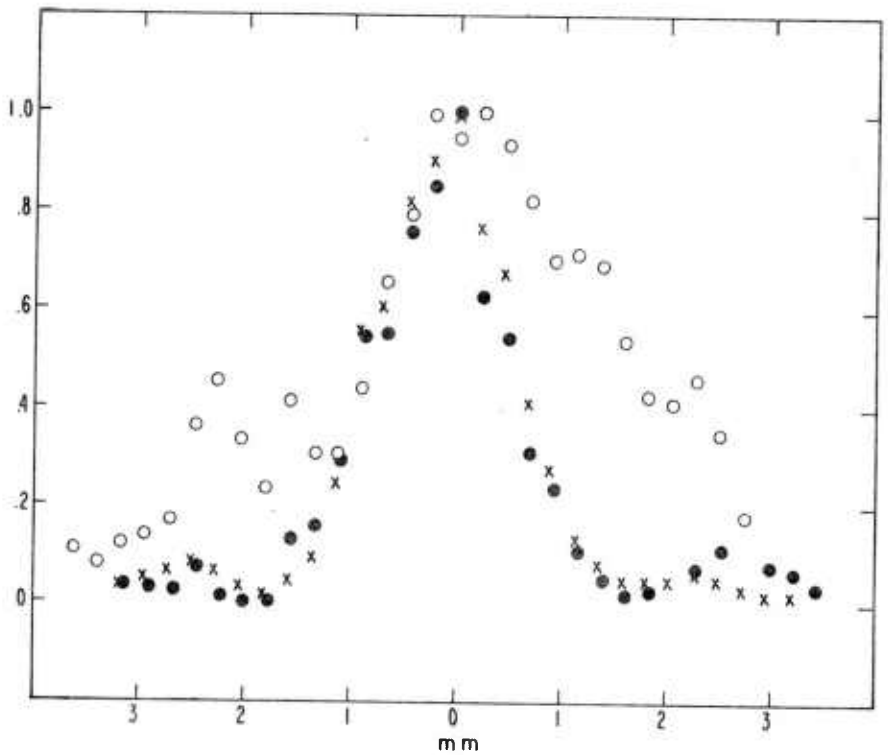

Figure 8. Integrated energy profiles. Each profile is the average of several shots. x - transmission; ● - breakdown-only; o - breakdown and blooming; all curves normalized to unity. Note that the breakdown-only case maintains the same basic profile, while the blooming causes spreading with resulting increased energy transmission.

5. Discussion and Application

As observed in Figure 9, the maximum energy transmitted was 50% higher in the blooming-breakdown case than in the breakdown-only case. This will, of course, be dependent on the beam cross section in the focal volume. A wider beam with commensurate energy increase to achieve identical peak flux intensity, would have higher transmission simply because the plasma would require a longer time to fill the cross section. Therefore, the beam spot size plays a significant role and higher levels of transmission than the 50% achieved in this particular example are expected.

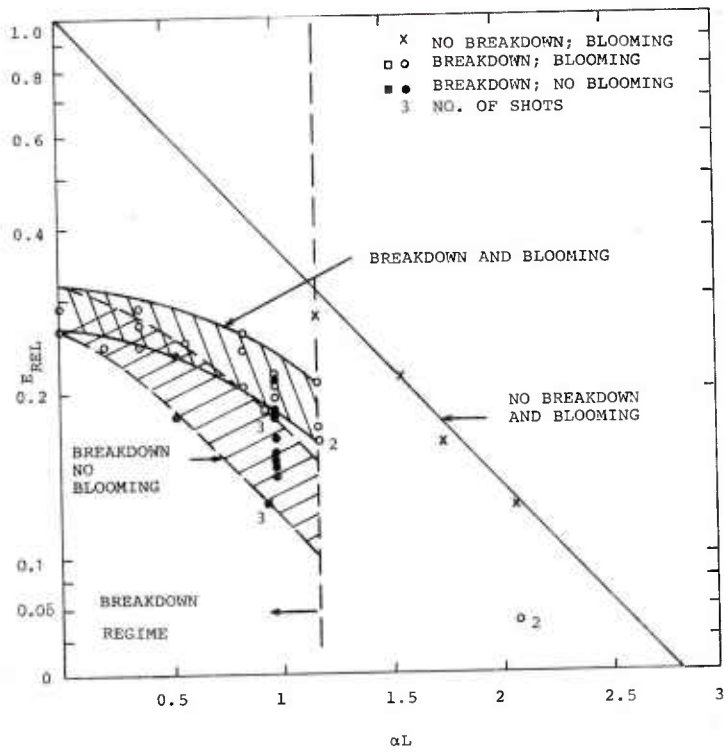

Figure 9. Experimental results: total energy versus the product of absorption coefficient versus path length. The breakdown regime is left of the dashed vertical line; the upper band of data has blooming present, the lower band does not, demonstrating the increased transmission effect.

How applicable will these results be for high energy laser systems? Efficient target interaction phenomena requires the ignition of a laser supported detonation (LSD) wave and the immediate reduction of the intensity to lower levels for enhanced coupling (6). The surface plasma ignition flux levels are roughly 10^7 W/cm^2 and plasma maintenance requires 0.5-8 x 10^6 W/cm^2. For representative short pulses (100-300 ns duration), air breakdown will occur at intensity levels of 10^8-10^9 W/cm^2 (7, 8). Therefore, the ideal pulse shape would be one with a spike of 10^7 W/cm^2 lasting 100-300 ns, followed by a tail of longer duration of 10^6 W/cm^2, thus avoiding air breakdown and allowing thermal blooming which will be partially correctable by adaptive optics.

However, if the beam is spatially inhomogeneous, i.e., hot spots as presently observed with present laser transmitters, then these significantly higher levels of intensity will result in air breakdown near the target. Reducing the average peak intensity to accomodate these peak variations is undesirable because of reduced target coupling. Therefore, the results of this study indicate that the combined effects of thermal blooming and breakdown must be included in detail in the modeling process if optimum energy transfer within operational constraints is to be realized. Preliminary estimates indicate that this optimum energy transfer depends critically on a judicious selection of the pulse structure.

6. Conclusions

An experiment has been performed combining the effects of short-time thermal blooming and air breakdown. The experiments demonstrate that, for the cases investigated, total energy transfer is higher for breakdown with blooming than without. Energy increases up to 50% have been experimentally observed. Breakdown processes are highly sensitive to the thermal blooming structure, and the combination of both effects must be taken into account if optimum energy delivery to the target is to be achieved.

References

1. D. C. Smith, Proc. IEEE 65, 1679 (1973).

2. D. E. Lencioni, Optics Research, Lincoln Laboratory, 1, 19 (1973),

3. D. E. Lencioni, L. C. Pertingill, Optics Research, Lincoln Laboratory, 2, 27 (1973).

4. R. W. O'Neill, H. Kleiman, J. F. Lowder, Appl. Phys. Lett., 24, 118 (1974).

5. A. H. Artken, J. N. Hayes, P. B. Ulrich, Appl. Optics, 12, 193 (1973).

6. R. W. Sepucha, AHELSPO, Huntsville, Alabama, private communication.

7. D. C. Smith, J. of Appl. Phys., 48, 2217 (1977).

8. J. Reilly, P. Singh, G. Weyl, AIAA Fluid and Plasma Dynamics Conference, June 27-29, 1977.

AD-A056481

TRAUMA INDICES AND APPLICATIONS

*WILLIAM J. SACCO, Ph. D., WILLIAM P. ASHMAN, Mr.
CONRAD L. SWANN, Mr.; LARRY M. STURDIVAN, Mr.
CHEMICAL SYSTEMS LABORATORY
ABERDEEN PROVING GROUND, MD 21010

INTRODUCTION

A considerable effort has been devoted to the development of a broad class of trauma indices covering a range of patient conditions. The original work was begun in 1973 in cooperation with the Maryland Institute for Emergency Medicine (MIEM). Efforts have continued in MIEM and also with surgeons at Washington Hospital Center and Monmouth Medical Center.

The focus of the efforts has been to develop a number of different indices based on anatomical diagnosis and physiological and biochemical data and to correlate these indices with mortality.

METHODS

The indices evolved from pattern recognition analyses of over 60 physiological and biochemical variables. Each of the variables and many combinations of variables were evaluated using the concept of information gain. This number, which measures the predictive "power" of an index (or variable), can be interpreted as the average amount by which one could alter the prognosis of each patient of a patient group when provided with a given value of the index for each member of the group. Mathematically, the information gain, E, is written

$$E = \sum_{i=1}^{n} \left| P_D - P_{D,i} \right| P_i ,$$

where P_D is the a priori probability of death, $P_{D,i}$ is the probability that the patient will die given that the index takes on a value in the interval i, and P_i is the probability that the index assumes a value in the interval i. The range of values of the index is divided into n intervals for the calculation. The maximum value of information gain for a patient population is $2P_D(1-P_D)$. If an index were a perfect discriminator in a treatment facility where the death rate was 50%, information gain would be 0.50.

On the basis of these computations, advice from clinicians, and practicality, the indices were derived.

For each of the indices, probability of mortality curves were obtained by fitting the data to a logistic model of the form:

$$P_D(X;B) = \frac{1}{1 + e^{-A}}$$

where

$P_D(X;B)$ = the probability of death,

$A = B_1 + B_2X_2 + \ldots + B_nX_n$,

$(1, X_2, \ldots, X_n)$ is a vector of variables,

and

$(B_1, \ldots, B_n)$ is a vector of weights associated with the variables.

The variables may be physiological or biochemical measurements, indices, age, and may include "indicator" variables; (e.g., for sex, 1 = males and 2 = females). The weights were obtained by the Walker-Duncan regression algorithm (1) which produces approximate maximum likelihood estimates. In the regression calculation, the dependent variable $P_D(X;B)$ used in estimating B was assigned a 0 if the patient lived and a 1 if death ensued. Approximate 95% confidence bounds on the curve were computed by the method of Kendall and Stuart (2).

A further refinement associated with the development of the indices involved calculating the expected misclassification rates associated with the index. A decision rule which predicted survival if the probability of death was less than 0.5 and death otherwise was used as a basis for the prediction of individual survival. Expected misclassification rates were then computed for various patient sets.

Another methodology introduced is known by the acronym PER. P is the a priori probability of death for the study population, E is the information gain described earlier and R is the relative information gain of the index against a perfect predictor. PER is a useful tool for evaluating an index. If P is small, (say .05) then an index must be very good in order to provide better predictions of patient outcome than a random decision rule. PER can be used to characterize any index in terms of its predictive power.

INDICES

A generalized patient status index called the CHOP Index was developed for use as an overall predictor of patient mortality (3). The CHOP Index is based on four variables: serum creatinine (C), hematocrit (H), serum osmolality (O), and systolic blood pressure (P). It is the square root of the sum of the squares of the deviations (measured in standard deviation units) from normal average values of the four variables; that is,

$$\text{CHOP Index} = \sqrt{\left(\frac{C-1.0}{0.5}\right)^2 + \left(\frac{H-37.0}{6.0}\right)^2 + \left(\frac{O-292.0}{15.0}\right)^2 + \left(\frac{P-127.0}{21.0}\right)^2}$$

In mathematics, this quantity is called Euclidean distance and reflects the difference between an actual patient state and a desired patient state. In each of the squared terms in the sum under the radical, the number in the numerator is the estimated normal average value of the variable, and the number in the denominator is the estimated standard deviation of that variable. For example, 37.0 is the average for hematocrit (H) and 6.0 the standard deviation. These estimates of the averages and standard deviations were obtained from final recorded values from 350 survivors.

A Respiratory Index (RI) was developed as an indicator of a trauma patient's respiratory state (4). The purpose of the RI was to (a) compare therapy in patients with respiratory complications in various institutions, (b) compare variations in treatment, and (c) graphically represent a patient's progress or deterioration as an adjunct to patient care. It was computed by the formula:

$$\text{Respiratory Index} = \frac{\left| (P_B - P_{H_2O}T)\, F_{IO_2} - PaCO_2 \right| - PaO_2}{PaO_2}$$

where

P_B = barometric pressure.

$P_{H_2O}T$ = alveolar water vapor pressure at the patient's temperature T (approx. 47 mm Hg).

F_{IO_2} = fractional concentration of O_2 in inspired gas.

$PaCO_2$ = arterial partial pressure of carbon dioxide. In this formula we assume it to be equal to the alveolar partial pressure of the carbon dioxide.

PaO_2 = arterial partial pressure of oxygen.

A Renal Index (REI) was developed as an adjunct method for evaluation of renal failure and indications for hemodialysis in trauma patients (5). The parameters for the study of renal function were the blood urea nitrogen (BUN), the serum creatinine, and the hourly urine volume. Admission and daily measurements were made of the serum creatinine and the BUN. Each patient's 12-hour urine volume was measured and converted to a normalized value called Urine Vol_N. The daily values of the above parameters were used to compute an index of renal function using the formula:

$$\text{Renal Index} = 1/3\ (Cr_N + BUN_N + \text{Urine } Vol_N).$$

Cr_N was calculated from the difference between the measured creatinine value and the mean value for survivors, and dividing this difference by the standard deviation of the creatinine level in the survivors. BUN_N was calculated in the same way.

An Acute Trauma Index (ATI) was developed as a means to characterize patient status at the time of admission to a hospital (6). The Acute Trauma Index, like CHOP, is a Euclidean distance. It is based on admission values of systolic blood pressure (P), hematocrit (H), arterial pH (A), and prothrombin time (T), all of which respond soon after trauma. It has the form:

$$\text{Acute Trauma Index} = \sqrt{\left(\frac{P-127}{21.0}\right)^2 + \left(\frac{H-36.9}{5.96}\right)^2 + \left(\frac{A-7.46}{0.065}\right)^2 + \left(\frac{T-13.0}{2.0}\right)^2}.$$

The Shock Index (SI) uses systolic blood pressure (P), hematocrit (H), and arterial pH. It was derived from retrospective

admission data in 1973 at MIEM. It gives higher weights to shock states (low systolic blood pressure and low hematocrit) and acidotic (low arterial pH) states than to hypertensive and alkalotic states as was reflected by the data on survivors and deaths.

Letting $x_1 = \frac{P-127}{21}$, $x_2 = \frac{H-37.0}{6.0}$, $x_3 = \frac{A-7.46}{0.065}$, and

$$y_1 = \begin{cases} 2|x_1| + 4 \text{ if } x_1 < -2 \\ |x_1^3| \text{ if } -2 \leq x_1 < 0 \\ 2/3\, x_1 \text{ if } x_1 > 0 \end{cases} ; \quad y_2 = \begin{cases} 2|x_2| \text{ if } x_2 \leq 0 \\ x_2 \text{ if } x_2 > 0 \end{cases} ;$$

$$y_3 = \begin{cases} 2|x_3| \text{ if } x_3 \leq 0 \\ x_3 \text{ if } x_3 > 0 \end{cases}$$

The Shock Index is: $SI = y_1 + y_2 + y_3$

The Shock Index appears to be more sensitive than the ATI, in differentiating between patients who are seriously injured and those who are not.

The Blunt Anatomical Index (BAI) was originally developed (7) by reviewing the records of all trauma patients admitted to MIEM over a three year period. Upon death or discharge, a detailed diagnosis was provided by the attending physician and coded according to the Hospital Adaptation of the International Classification for Disease (H-ICDA) system. The coding was validated against the medical record diagnosis and autopsy reports where available. Patients injured by weapons and those without injuries in the H-ICDA code range of 800.0 to 959.9 were excluded. A group of 2135 patients were thus identified and a random sample of 1884 patients were chosen to develop the BAI and the remaining 251 were to be used to test the BAI.

Using the group of 1884 patients, a computed "conditional" probability of survival (P_c) and an "effective" probability of survival (P_e) were developed for each injury code. The P_c is the proportion of survivors associated with each injury code. This reflects the survival associated with a given injury in the presence of other injuries. The conditional probabilities were used to rank the severity of the injury codes. This ranking was used to compute an "effective probability of survival", P_e, for each injury code. The P_e for a given injury code is the proportion of survivors in the subset of patients for whom the injury is the most severe injury sustained, the severity ranking being established by the P_c's.

The effective probabilities were tested by comparing actual mortality rates in randomly generated groups with expected mortality rates as computed from the P_e's.

A Triage Index has been developed (8) which is an objective, non-instrumental clinical evaluative device for use by physicians, nurses or paramedics at the initial encounter between the trauma victim and EMS system resources (pre-hospital or emergency department) to identify patients requiring hospitalization and at risk of dying. The index consists of 10 clinical variables: pulse rate and strength, capillary refill, lip color, respiratory rate and expansion, eye opening, verbal response and motor response, pupillary size and response (to light). Each parameter was evaluated in approximately 1200 patients in three hospital emergency departments in Maryland and Washington, DC to determine their separate and combined ability to predict outcome status.

A new anatomical injury coding system called PEBL, has been developed jointly by personnel from the Biophysics Branch of CSL, and clinicians from MIEM (9).

A basic requirement for PEBL was that it include sufficient detail to discriminate traumatic effects which differ with respect to location, size, mortality, morbidity, and treatment.

RESULTS AND APPLICATIONS

Mortality correlations are available for all of the indices (10,11,12) individually and for combined CHOP and Respiratory Indices, for combined Acute Trauma and Blunt Anatomical Indices, and for combined Triage and Shock Indices.

In Table I we give the PER values for the Indices. The values of P (the a priori probability of death) vary because the

TABLE I

PER Values for the Indices

	P	E	R
CHOP Index (CI)	.17	.16	.57
Respiratory Index (RI)	.34	.23	.51
Renal Index (REI)	.21	.18	.55
Combined CI and RI	.34	.33	.73
Acute Trauma Index (ATI)	.14	.10	.42
	.24	.26	.72
	.33	.23	.52
	.068	.074	.58
Shock Index (SI)	.33	.21	.48
	.068	.073	.58
Triage Index (TI)	.33	.33	.76
	.067	.081	.65
Combined CI and RI	.34	.33	.73
Combined ATI and BAI	.14	.22	.73
	.28	.28	.70
	.35	.40	.89
	.067	.093	.75

results are obtained from several centers and in some instances for select populations (such as intubated patients only in the case of the Respiratory Index).

All of the indices are currently being used in various applications by researchers and clinicans at the MIEM, Washington Hospital Center, Monmouth Medical Center and hospitals in Canada, California, Colorado, Virginia, Pennsylvania, and Maryland.

The applications include patient triage, prognosis (at the time of hospital admission and throughout the patient stay) and tracking; initiation, assessment and communication of therapies; and general evaluation of care.

At the MIEM, the CHOP Index is used as a general predictor of survival for referral patients and for direct admission patients after the first 24 hours (10). A decision rule, based on the CHOP Index, which predicts death or survival, resulted in a misclassification rate of less than 10% for 650 patients in the Unit for more than one day. The misclassifications can be reduced by several percent by comparing the variables which contributes to a large index value to a table of "critical states".

It was also established (3) that the index frequently allows a downward trend to be identified several days before it becomes clinically recognizable.

Results from using Respiratory Index in a study group of 177 consecutive intubated patients showed that a RI of 0.1-0.37 was normal, a value of 2 or greater was an indication for intubation and a value of 6 or above was associated with a .12 probability of survival (4). The RI reflects the presence of pulmonary shunting in a variety of circumstances including atelectasis, pulmonary contusion, or pulmonary emboli.

A nomogram was designed which simplifies the computation of the index, allows one to follow the course of a patient with respiratory problems, and provides a guide for oxygen therapy (4) and for initiation for extracorporeal circulation therapy (13).

Respiratory failure has in the past been responsible for as many as one-third of the deaths in surgical Intensive Care Units. Respiratory Distress Syndrome of trauma will occur as an early complication in some 30% of victims of major blunt trauma with a mortality of up to 50% if not recognized early and aggressively managed. Without such sophisticated assessment as is available in

major centers, many physicians find difficulty in assessing the severity of respiratory problems. In addition, there is the added problem of following the patient's progress. We believe that the Respiratory Index and its associated probability of death chart and nomogram provide the physician with a simple and helpful guide.

A second analysis of the same 177 intubated patients was undertaken to combine the CHOP and Respiratory Indices (11). The overall mortality in the group of patients was 34%. When the indices were combined, it was found that a CHOP Index greater than 5 and a Respiratory Index greater than 6 was associated with a 94% mortality as compared to a 10% mortality when the CHOP Index was less than 5 and the Respiratory Index less than 6.

Our analysis (5) of renal variables and the Renal Index showed that Creatinine levels about 4.0 mg per 100 ml, a BUN over 80.0 mg per 100 ml, and a Renal Index over 3 are all rare in patients who survive trauma. Data for those patients who did have one of the criteria just mentioned were further analyzed to identify which first reached the "critical level". In the majority of cases the sensitive indicator was a Renal Index of 3.

Although acute renal failure after surgery or trauma is recognized as a grave complication, it too seldom provokes the urgent therapeutic response required. The therapeutic approach to acute renal failure in major trauma must be clearly distinguished from that in chronic renal failure where the traditional approach is appropriate. Multiple major trauma is frequently accompanied by hemorrhagic shock, requiring massive blood transfusion under circumstances which sometimes do not allow time for complete cross-matching. Crushed muscle, hematoma formation, and jaundice are commonly components of the primary complicating clinical syndrome. Under aggressive resuscitation, with massive colloid infusion, and the early promotion of diuresis, many patients exhibit only slight or transient impairment of renal function. Once renal failure is established, however, the prognosis is poor, despite full supportive treatment. We believe this accounts for the higher mortality rate in referred patients with an index greater than 2.0.

To reiterate, the results indicated that survival is unlikely when a patient's renal failure deteriorates to the levels earlier defined (e.g., Renal Index > 3), and that aggressive therapy must be directed at preventing deterioration to this level.

The Acute Trauma Index, Triage Index, Blunt Anatomical Index, and the Shock Index were developed to characterize patient status on

arrival at a hospital and are currently in use in several HEW studies focusing on triage and evaluation of patient care. The indices have been used (individually and in various combinations) to predict outcome, prospectively, for over 1,600 patients with excellent results (12, 14). The Triage Index has been surprisingly good considering that all of its data elements can be obtained easily and readily in both prehospital and hospital situations without resorting to invasive techniques.

Several of the indices have been incorporated (15, 16) into clinical algorithms (medical decision trees) for resuscitation of the critically injured patient.

A methodology for medical assessment of soft body armor (17) included correlations of lung damage in goats and humans using the Respiratory Index.

The PEBL Code (9) is part of a new computer man methodology (18) for assessing wound severity and medical workload (19, 20). The methodology consists of simulating missile wounds in a computer man and characterizing the wounds using strings of PEBL codes and associated surgical procedures and medical tasks required for treatment. Also, in process is work which correlates PEBL code strings with mortality using similarly coded data on traumatic injuries from US Army and civilian data bases.

SUMMARY

In the stressful situation of the battleground, it is imperative that rapid evaluation and classification of casualties be made for treatment and evacuation. Trauma indices provide the Army with such a device. For this reason, the work described herein is of importance.

We believe that the Triage Index and Shock Index could be part of a triage rationale for use by military aidmen and clinicians. Also, all of the indices could be applied during a military conflict as a basis for patient prognosis, tracking, and initiation and assessment of therapies.

This research has been supported by funding from the US Army Materiel Systems Analysis Activity, US Army Materiel Development and Readiness Command, US Army Office of the Surgeon General, Joint Technical Coordinating Group, and the Office of the Assistant Secretary of Defense for Health Affairs.

REFERENCES

1. S. Walker and D. Duncan. "Estimation of the Probability of an Event as a Function of Several Independent Variables," Biometrika, 54, 1 (1967).

2. M. Kendall and A. Stuart. "The Advanced Theory of Statistics," Vol. 1, Hafner, NY (1969).

3. R. A. Cowley, W. Sacco, et al. "A Prognostic Index for Severe Trauma", J. Trauma, 14, No. 12 (December 1974).

4. M. Goldfarb, W. Sacco, et al. "Tracking Respiratory Therapy in the Trauma Patient", Am. J. Surg., 129 (March 1975).

5. H. Champion, W. Sacco, et al. "Indications for Early Haemodialysis in Multiple Trauma", Lancet (June 1974).

6. W. Sacco, H. Champion, et al. "An Acute Trauma Index", Edgewood Arsenal Technical Report (EB-TR-76110) (May 1977).

7. W. Sacco, H. Champion, et al. "An Anatomical Index in Blunt Trauma", Edgewood Arsenal Technical Report (EB-TR-76082) (December 1976).

8. S. Hannan, H. Champion, and W. Sacco. "An Objective Triage Index", Paper presented at the 1976 Meeting of American College of Emergency Physicians, New Orleans (October 1976).

9. J. Merkler, A. Milholland, et al. "PEBL: A Code for Penetrating and Blunt Trauma", based on the H-ICDA Index.

10. W. Sacco, R. A. Cowley, et al. "Trauma Indices", Comput. Biol. Med. (February 1977).

11. M. Goldfarb, W. Sacco, et al. "Two Prognostic Indices for the Trauma Patient", Comput. Biol. Med. (February 1977).

12. H. Champion, W. Sacco, et al. "Quantification of Critical Illness and Injury".(In preparation).

13. M. Goldfarb, W. Sacco, et al. "Application of Two Prognostic Indices in Critically Ill Patients". (In preparation).

14. W. Sacco. "Analyses of Trauma Indices for Evaluation of Care", Letter Report (November 1977).

15. W. Gill. "Trauma", J. Roy. Coll. of Surg. of Edinburgh, (January 1977).

16. W. Gill and W. Long. "Manual for Major Trauma", Publication pending, Williams and Wilkins (1978).

17. M. Goldfarb, T. Cuirej, et al. "A Method for Soft Body Armor Evaluations: Medical Assessment", Edgewood Arsenal Technical Report (EB-TR-74073) (January 1975).

18. R. Clare, D. Lamb, et al. "Computer Man", (In preparation).

19. A. Mickiewicz. "Medical Workload Data for TOMSS Study", Letter Report (December 1976).

20. J. Merkler and W. Sacco. "Use of PEBL Code for Encoding WDMET Data", Letter Report (November 1977).

AD-A056482

CHARACTERIZATION OF OBSCURING SMOKES IN THE FIELD (U)

*L. L. SALOMON, DR., E. G. PETERSON, MR.
E. W. BURGESS, MR., W. GOOLEY, JR., MR., F. L. CARTER, MR.
DUGWAY PROVING GROUND
DUGWAY, UTAH 84022

INTRODUCTION: Objective characterization of conventional smokes and other obscurants in the field has become a matter of intense interest during recent years, paralleling the need for evaluating both new smoke munitions and the effectiveness of obscurants in degrading the performance of electro-optical systems and vision. Determination of physical, optical and visual properties of an obscuring cloud involves integrated assessments of the delivery system, of the target, target area, sky and sun or moon, of the cloud itself, and, in some instances, the response of observers. It requires suitable test areas and grids, detailed meteorological and photographic data capabilities, laboratories for chemical analyses and calibration, and systems for automatic acquisition and reduction of the staggering volume of data resulting even from field trials of modest proportions. Dugway Proving Ground has established a stand-alone system for testing of obscurants in the space of about one year, employing in-house developments in instrumentation and methodology which culminated in eminently successful programs conducted during 1977 for the Program Manager, Smoke/Obscurants. Each of the relevant aspects mentioned above could easily serve as the subject of a separate paper. The present report, however, will be limited to a description of certain mathematical procedures, a schematic representation of a section of the test grid with location of instruments and targets to aid in interpretation of the procedures, and presentation of representative test results. (Figures 2-9 and Table 1)

MATHEMATICAL PROCEDURES[+]: Atmospheric particulates may be regarded as constituting a more or less dilute cloud which extends over the

[+]For explanation of instrument locations, see Figure 1.

entire distance between transmitters or targets to the receivers. This atmospheric haze, like clouds of obscurants, exhibits luminance and attenuates electromagnetic radiation. Although frequently negligible, corrections for these effects and for changing light conditions are routinely applied, using the first three procedures.

Transmittance of the Atmosphere (T_A). The transmittance (T_A) of the atmosphere over the line of observation is obtained using

$$T_A = \frac{R_{02} - R_{01}}{R_{03}} \qquad (\lambda = 0.4\text{-}0.7\ \mu m) \tag{1}$$

where R_{01} = average reading of telephotometer No. 1 (Figure 1) when observing the non-reflecting black target located at position (2) prior to arrival of smoke cloud, footlamberts.

R_{02} = average reading of telephotometer No. 1 (Figure 1) observing the white target located at position (2) prior to arrival of smoke cloud, footlamberts.

R_{03} = average reading of telephotometer No. 1 (Figure 1) when observing the white target located at position (8) prior to arrival of smoke cloud, footlamberts.

Luminance of Atmosphere (L_A). The luminance (L_A) of the haze is determined by

$$L_A = R_{01} \qquad (\lambda = 0.4\text{-}0.7\ \mu m) \quad \text{(see Table 1)} \tag{2}$$

Correction Factor (C_f). The observations recorded by telephotometer No. 1 (Figure 1) are corrected by the factor (C_f) to normalize all the readings to the light conditions which existed at the beginning of the test. The correction factor is given by

$$C_f = R_{03}/R_3 \qquad (\lambda = 0.4\text{-}0.7\ \mu m) \tag{3}$$

where R_3 = reading of telephotometer No. 1 (Figure 1) when observing the white target located at position (8) as a function of time, footlamberts.

Luminance of Smoke Cloud (L_c). Cloud luminance (L_c) is given by

$$L_c = C_f R_1 - R_{01} \qquad (\lambda = 0.4\text{-}0.7\ \mu m) \text{ (see Figure 2)} \tag{4}$$

where R_1 = reading of telephotometer No. 1 (Figure 1) when observing the black target located at position (2) as a function of time, footlamberts. Equation (4) assumes L_A is small compared to R_1. Analogous measurements were also made at 1.06 μm, and cloud radiance was determined at longer wavelengths.

Reflectivity of Target (r_t). The reflectivity (r_t) of the target is given by

$$r_t = \frac{R_{05} - R_{01}}{R_{03}} \qquad \text{(see Table 1)} \tag{5}$$

where R_{05} = average reading of telephotometer No. 1 (Figure 1) when observing OD target located at position (2) prior to arrival of the smoke cloud, footlamberts.

Luminance of Any Target (L_t). The luminance of any target can be obtained if the reflectivity (r_t) of the given target is known using

$$L_t = r_t \cdot R_{03} \qquad \text{(see Table 1)} \tag{6}$$

Transmittance of Cloud (T_λ). The transmittance at any given wavelength (λ) is given by

$$T_\lambda = \frac{R_{on} - R_{off}}{\overline{R}_{on} - \overline{R}_{off}} \qquad \text{(see Figure 3)} \tag{7}$$

where R_{on} = reading of the receiver observing a chopped light source of wavelength λ, light "on", units

R_{off} = reading of the receiver observing a chopped light source of wavelength λ, light "off", units

$\overline{R}_{on}$ = average value of R_{on} before the smoke cloud arrives, units

$\overline{R}_{off}$ = average value of R_{off} before the smoke cloud arrives, units

Transmittance measurements were obtained as follows:

Lines 1 & 3: λ = 3.4 μm

Line 2: λ = 8-12, 0.4-0.7, 1.06 and 3.39 μm

Slant range: λ = 1.06 μm

Aerosol Sampling. a. Aerosol photometer. Analog data from APs were digitized and recorded on magnetic tape. In this form, the data were in terms of relative concentration through time. The relative concentrations were converted to "true" concentrations (mg $H_3PO_4 \cdot nH_2O/m^3$ or $ZnCL_2 \cdot nH_2O/m^3$) utilizing ADP software and data from chemical impingers located at the instrument site, i.e., they were individually field calibrated in each trial. Concentrations at one-second intervals were tabulated for each AP position. Plots of the time-concentration relationships at each AP position and CL (concentration-length product) values as function of time were prepared where CL is defined by

$$CL(t) = \int_0^L C(t)dL \qquad \text{(see Figure 4)} \qquad (8)$$

where C(t) = concentration along the line of sight at a given time (t) (see Figure 5), and

L = distance along the line of sight, meters

Equation (8) was numerically integrated to obtain the CL values.

b. Chemical Impinger. The impingers were assayed according to the DPG SOPs for phosphorus or zinc. Assay results were converted to a dosage (mg $H_3PO_4 \cdot nH_2O$ or $ZnCL_2 \cdot nH_2O$ min/m^3) for each trial.

c. Particle Size Analyzer. Analog PSA data were digitized and stored on magnetic tape. The magnetic tape was processed by ADP. These procedures provided, at a given time of cloud history, PSA-derived concentration (particles/m^3), particle size distribution as a proportion from each channel of the PSA to the total number of particles counted across all six channels, log NMD (number median diameter) as determined by probit analysis, probit slope, variance estimates to log NMD and probit slope, NMD and MMD (mass median diameter) for each trial and smoke submunition.

CL Values. CL has been defined above and can also be determined from the Beer-Lambert law $CL = \ln T_\lambda / -\alpha$ (9) (see Figure 4),

where α = extinction coefficient (m^2/g) and can be determined from field data (transmittance and impinger dosage) as seen in the following paragraph, and

where T_λ = transmittance at a given wavelength λ

The CL values obtained using equation (9) were obtained for all lines of sight as a function of time.

CL Values of Two-Component Systems. When dealing with two-component systems, e.g., smoke and dust, determination of CL(t) might appear impossible since the CL values for the components may vary independently of each other as well as with time. However, when the extinction coefficients differ significantly at selected wavelengths (as they do in the case of smoke and dust), CL(t) values can, in fact, be evaluated: Let $d = \alpha(CL)$, so that at two different wavelengths at the same instant for component 1 $d_1 = \alpha_1(CL)_1$ and $d_1' = \alpha_1'(CL)_1$ and, similarly, for component 2 $d_2 = \alpha_2(CL)_2$ and $d_2' = \alpha_2'(CL)_2$. The actual measurements made are $d_1 + d_2 = D$ and $d_1' + d_2' = D'$, respectively. The relationship of $(CL)_1$ and $(CL)_2$ is fixed, and can be established if the extinction coefficients are predetermined. Consider that $D = \alpha_1(CL)_1 + \alpha_2(CL)_2$ and $D' = \alpha_1'(CL)_1 + \alpha_2'(CL)_2$. Since, by rearrangement, $(CL)_2 = (D' - \alpha_1'(CL)_1)/\alpha_2'$, by substitution, $(CL)_1 = (\alpha_2'D - \alpha_2D')/(\alpha_1\alpha_2' - \alpha_2\alpha_1')_1$ which is of the form $(CL)_1 = \omega D - xD'$, or $x\ell nT' - \omega\ell nT$. Using values of $(CL)_1(t)$, one may then solve for $(CL)_2 = D'\{(1 + \alpha_1'x)/\alpha_2'\} - (\alpha_1'\omega D)/\alpha_2')$, which may be represented by $(CL)_2 = yD' - zD$ or $z\ln T - y\ln T'$, where T is the transmittance. Thus, CL(t) for each of the two components in the cloud can be established regardless of dynamic changes in composition of the cloud. Indeed, it is not essential that the two components actually be mixed along the line of sight. Necessary conditions are that the Beer-Lambert law be obeyed for each component, and that the two components do not interact.

Photometric Contrast Ratio. The photometric contrast ratio is defined by $C_t = T(L_T - L_B)/(TL_B + L_C)$ (10).

where T = transmittance in the visual (λ - 0.4-0.7 μm)

L_t = luminance of the target, footlamberts

L_B = luminance at the background, footlamberts

L_c = luminance of the cloud, footlamberts

The reflectance is determined by r = luminance of object/luminance of white target (11). Equation (10) can then be written $C_t = R_{03}T(r_T - r_B)/R_{03}Tr_B + L_c)$ (12).

where R_{03} = luminance of a white target (provided by the tests), footlamberts

where T = transmittance (λ = 0.4-0.7 μm) (provided by the tests)

L_c = luminance of the cloud (provided by the tests)

r_T = reflectance of any target

r_B = reflectance of any background. The luminance of the background was measured by using telephotometer No. 1 (Figure 1) and the background in the field of view along line of sight No. 2 and r_B was determined using equation (11).

The significance of this approach is that the contrast ratio of any desired (actual or hypothetical) target can be computed without the need of physically locating such a target in the test area, provided only that the reflectance of the target is determined, which is simple. Thus, costs, time and effort are saved, without limitation on extent of data acquisition.

Calculated Transmittance. When the readings at a given wavelength (λ_1) approached the noise level of the recorders, the transmittance at these wavelengths was calculated using the following equation:

$$T(\lambda_1) = T(\lambda_2)^K \quad \text{(see Figure 6)} \tag{13}$$

where $T(\lambda_1)$ = transmittance at the given wavelength (λ_1)

$T(\lambda_2)$ = transmittance for some longer wavelength above noise

K = ratio of $\int_{t_1}^{t_2} \ell nT(\lambda_1)dt / \int_{t_1}^{t_2} \ell nT(\lambda_2)dt$ when the readings for $T(\lambda_1)$ and $T(\lambda_2)$ are both above noise

As an example, in this manner, the transmittance of light in the visible range was readily calculated despite millionfold attenuation of light by the clouds.

For a two-component system, e.g., smoke and dust, equation (13) becomes

$$\ell nT(\lambda_1) = K_1 \{\ell nT(\lambda_3) - K_2 \ell nT(\lambda_2)\} + K_3 \ell nT(\lambda_2) \tag{14}$$

Here two wavelengths are used to predict the transmittance in the visible range. The K values are determined using

$$K_1 = \left(\frac{\alpha_S(\lambda_1)}{\alpha_S(\lambda_2)} - \frac{\alpha_D(\lambda_1)}{\alpha_D(\lambda_2)}\right) \Big/ \left(\frac{\alpha_S(\lambda_3)}{\alpha_S(\lambda_2)} - \frac{\alpha_D(\lambda_3)}{\alpha_D(\lambda_2)}\right)$$

$$K_2 = \alpha_S(\lambda_3)/\alpha_S(\lambda_2)$$

$$K_3 = \alpha_S(\lambda_1)/\alpha_S(\lambda_2)$$

In this case K_1, K_2 and K_3 were determined using transmittance values $T(\lambda_1)$, $T(\lambda_2)$, $T(\lambda_3)$ above noise, $\alpha_S(\lambda_X)$ and $\alpha_D(\lambda_Y)$ are extinction coefficients for smoke and dust at wavelength λ_X.

Extinction Coefficient (α). The extinction coefficient for a specified wavelength can be calculated from field data, using the transmittance and chemical impinger data. The theory for this calculation is developed by starting with the Beer-Lambert law.

The attenuation of a plane wave is given by the Beer-Lambert law as follows:

$$I = I_0 e^{-\alpha c x} \qquad (15)$$

where I/I_0 = transmittance (T)

I = transmitted intensity

I_0 = incident intensity

α = extinction coefficient (m^2/g)

c = concentration of droplets (g/m^3)

x = pathlength (m)

The differential form of Eq. (15) is: $\frac{dI}{I} = -\alpha c dx \qquad (16)$

Multiplying both sides of Eq. (16) by (dt) so that $\frac{dI}{I}dt = -\alpha c dx dt \qquad (17)$

and integrating yields $\int_{t_o}^{t_f} \int_{I_o}^{I} \frac{dI}{I} dt = -\alpha \int_{x_o}^{x_f} \int_{t_o}^{t_f} c\,dt\,dx \qquad (18)$

The dosage (D), obtainable from chemical impinger data, is given by

$$D = \int_{t_o}^{t_f} c\,dt \qquad \text{(see Figure 7)} \tag{19}$$

Eq. (19) now becomes $\int_{t_o}^{t_f} \ell n(I/I_o)dt = -\alpha \int_{x_o}^{x_f} D\,dx$ (20)

The extinction coefficient can then be determined from Eq. (20) in the form

$$\alpha = -\int_{t_o}^{t_f} \ell n T dt \Big/ \int_{x_o}^{x_f} D\,dx \qquad \text{(see Figure 8)} \tag{21}$$

Extinction coefficients for unconfined clouds of phosphorus and HC smokes, and for dust, have been successfully obtained by this means.

Submunition Source Parameters. In general when a smoke munition is constructed using submunitions the computer model concept is to utilize parameters defined for the submunition and build up to the full munition. Proper modeling requires knowledge of certain input parameters such as submunition yield fraction, burn rate and cloud geometry. The submunition yield fraction (MYF) was determined in the wind tunnel using $MYF = M_x/M_o$ (22) where M_x is the total mass in grams of P or Zn that passes through the sampling grid in the wind tunnel and M_o is the mass in grams of the submunition.

The amount of aerosol $M_x(t)$ in the air at any time was determined using a load cell to measure the mass loss of the submunition as a function of time and is given by

$$M_x(t) = M_o \cdot MYF \cdot (M_o - M_s(t))/(M_o - M_s(t_b)) \tag{23}$$

where $M_s(t)$ = mass of the submunition as a given time t

$M_s(t_b)$ = mass of the submunition at the burn-out time, t_b

$M_x(t)$ was reduced to

$$M_x(t) = M_o \cdot MYF \cdot \{A + B(t/t_b) + C(t/t_b)^2 + D(t/t_b)^3\} \tag{24}$$

where the coefficient A, B, C and D were determined from experimental burn rate test data. (See Figure 9)

The initial cloud dimensions were determined using photographic methods. Three motion picture cameras (35mm) were used to record the height, width and length of the cloud before the wind disturbed the initial cloud geometry.

DISCUSSION: The mathematical procedures and associated instruments have been found to be powerful tools for characterizing obscuring clouds. Efforts are now in progress to extend the type and applicability of instruments and grids to accommodate tests with obscurants other than conventional smokes, to permit dynamic testing, and to place further emphasis on use of remote sensing devices. Although a small number of chemical impingers has been employed during recent tests, these have principally served as back-up samplers and for calculation of extinction coefficients. In circumstances for which field-validated extinction coefficients are now available (or not needed), and where back-up samplers are not necessary, the impingers are superfluous.

Instrumentation and methodology have permitted collection of a wide range of data essential to evaluation and characterization of smoke, smoke munitions, dust, electro-optical systems and human perception of targets, and have resulted in input data vital to mathematical modeling of obscuration. Among the parameters successfully investigated were:

1. Complete set of munition data, such as hardware evaluation, ballistics performance and similitude, submunition burn time, burn rate and efficiency, and photographic data such as initial cloud dimensions.

2. Optical data, including transmittance of cloud and atmosphere at various wave lengths without resorting to eye-hazardous sources of radiation, luminance of background, targets, smoke clouds and atmosphere.

3. Physical aerosol characteristics including particle size distribution, number density, mass concentration dosages, and extinction coefficients of unconfined clouds.

4. Meteorological and target area data in the great detail necessary for mathematical modeling of cloud behavior and obscuration, and for test design and control.

SUMMARY: In the course of approximately one year following tasking by the Test and Evaluation Command in 1976, a complete capability for field testing and evaluation of obscuring smokes and munitions and,

to a more limited extent, for dust was established. The rugged, reliable, automated system which met a critical need, was employed in full-scale testing during 1977, where it served in one case during 62 essentially consecutive trials without failures or downtime. In these, the first objective field characterizations of a series of inventory and foreign smoke munitions, the new methodologies, grid and associated instrumentation functioned as designed, yielding novel and important information on the performance of munitions and the obscuring properties and characteristics of smokes and dust. Additional field tests are projected. An on-going program of improvement of instruments and methodology will ensure responsiveness to new testing requirements, as well as continued reliability and economy of operations.

FIGURE 1. A TYPICAL BIDIRECTIONAL GRID ARRANGEMENT FOR STATICALLY-FIRED MUNITIONS, WHERE THE NUMBERS HAVE THE FOLLOWING SIGNIFICANCE:

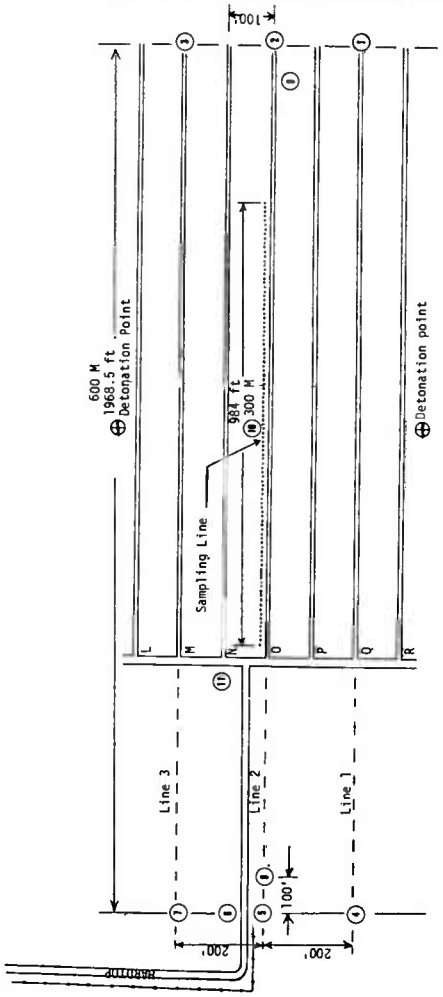

(1), (3) 3.4 μm pulsed sources

(2) 8-12, 3.4, 1.06 and 0.4-0.7 pulsed sources; black, white and OD targets

(4) (7) 3.4 μm receivers

(5) two 0.4-0.7 μm (photopically-corrected) receivers; two 1.06 μm receivers

(6) 3.4 and 8-12 μm receivers

(8) black and white targets (90^0 each on rotating disk, 180^0 open for measurements of black target at (2))

(9) 32-meter meteorological tower, with 1.06 μm elevated slant-range transmissometer source

(10) 300-meter sampling line with 100 chemical impingers, 15 aerosol photometers, and 3 particle-size analyzers and 15 total-dose dust samplers

(11) 1.06 μm slant range receiver at 5-foot level

Not shown because of the scale are location of photographic instruments.

For dynamic firings, a longer line of sight could be required.

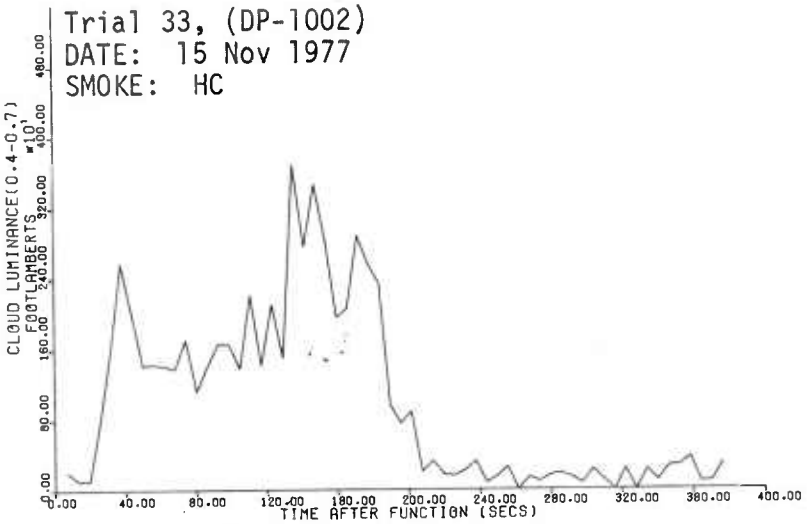

Figure 2. CLOUD LUMINANCE VS TIME FOR WAVE LENGTH BETWEEN 0.4 AND 0.7 MICRONS MEASURED ALONG ROW 0 (Line 2)

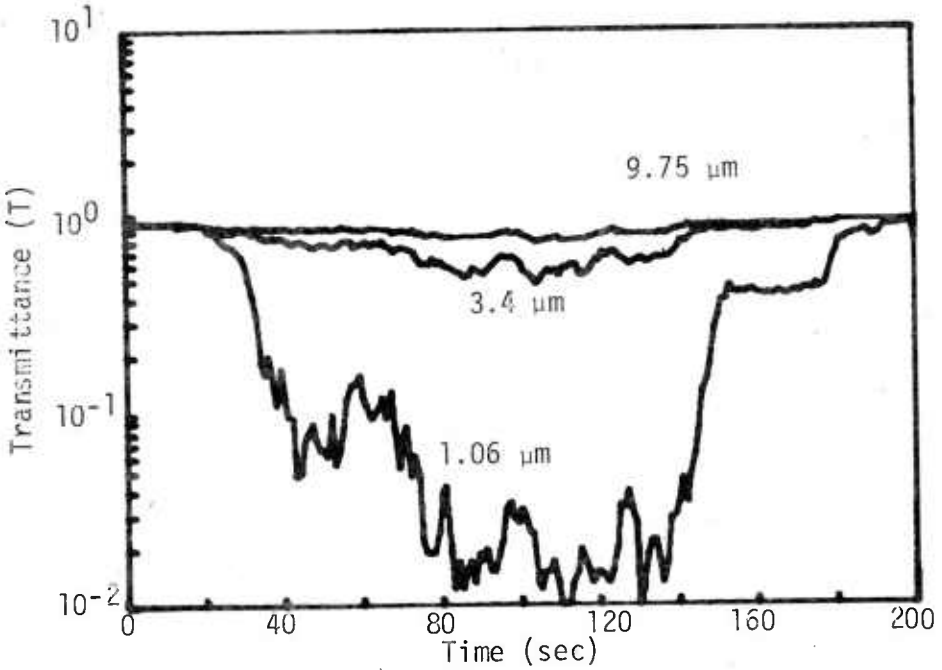

Figure 3. Transmittance at Three Wavelengths Along Line 2, Trial 33 (DP-1002, 15 Nov 77, HC)

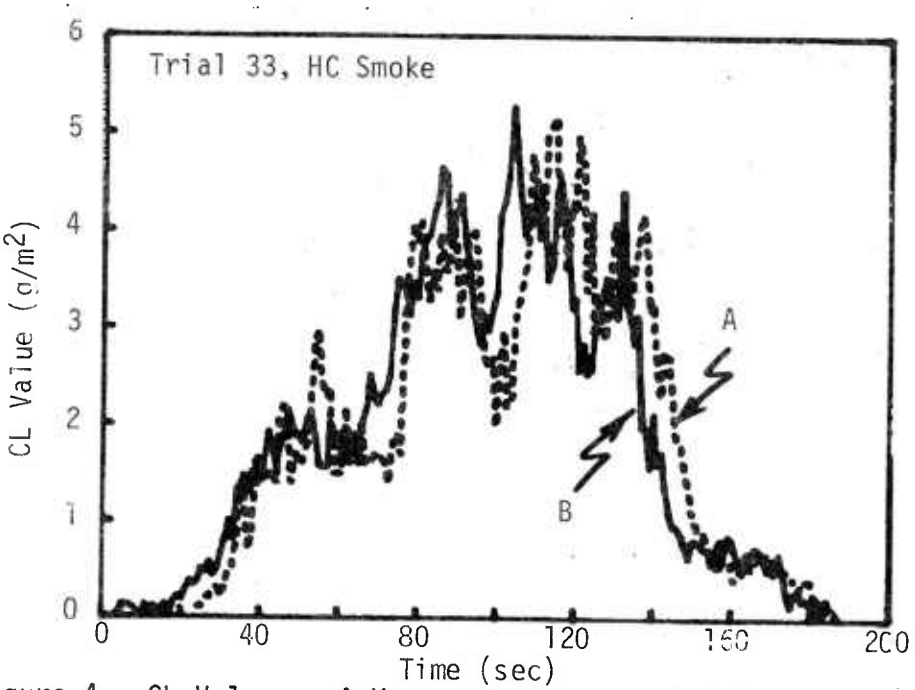

Figure 4. CL Values: A-Measured Using Aerosol Photometers (Eq. 8) B-Calculated from Transmittance at 3.4 μm (Eq. 9). Note time shift due to distance between lines of sight and good agreement of data.

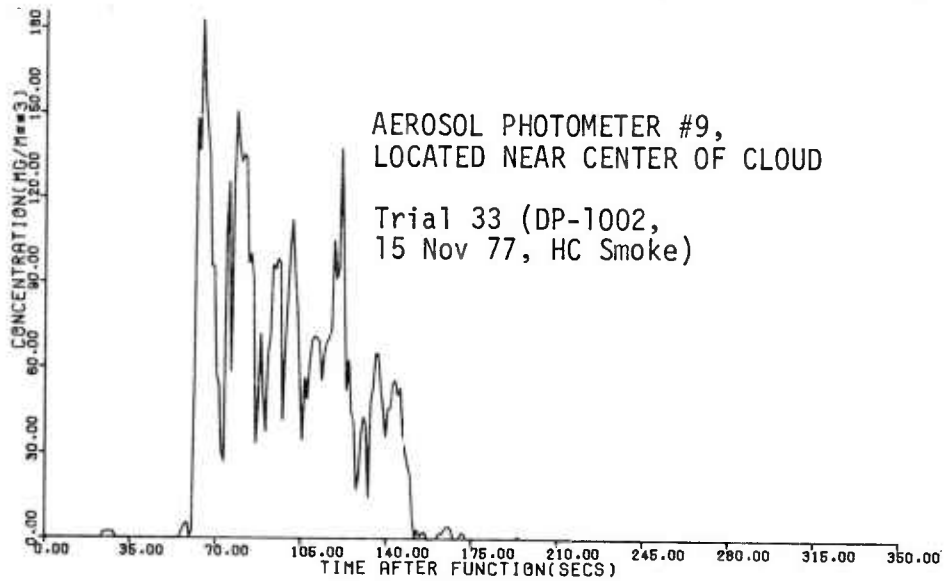

Figure 5. Typical Measured Smoke Concentration Data, Using Aerosol Photometer

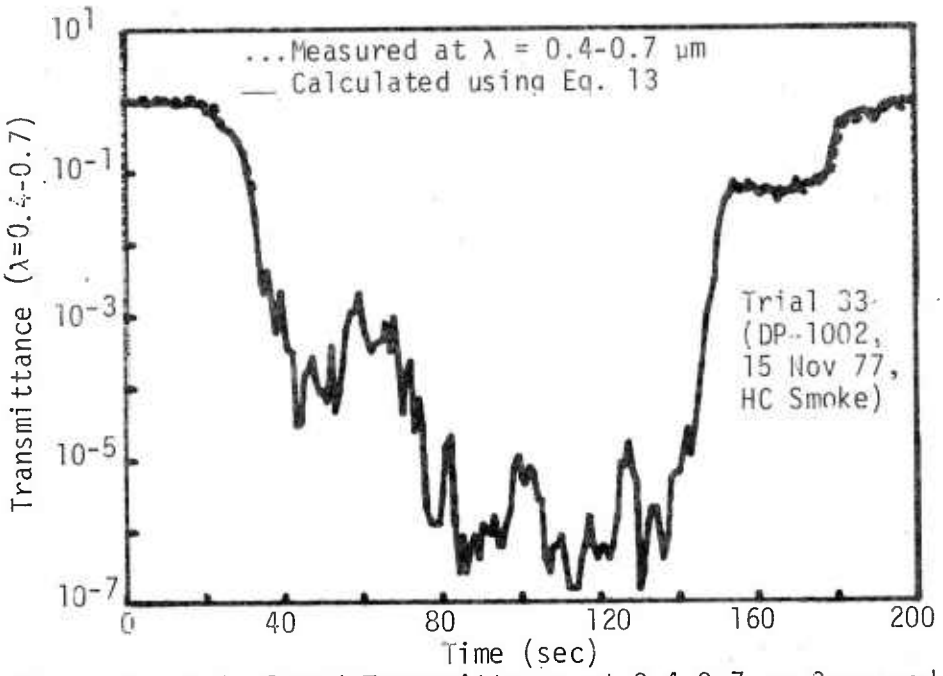

Figure 6. Calculated Transmittance at 0.4-0.7 μm Compared to Measured Values. Excellent agreement is noted down to lower limits (T=.05) of measurements in visible range.

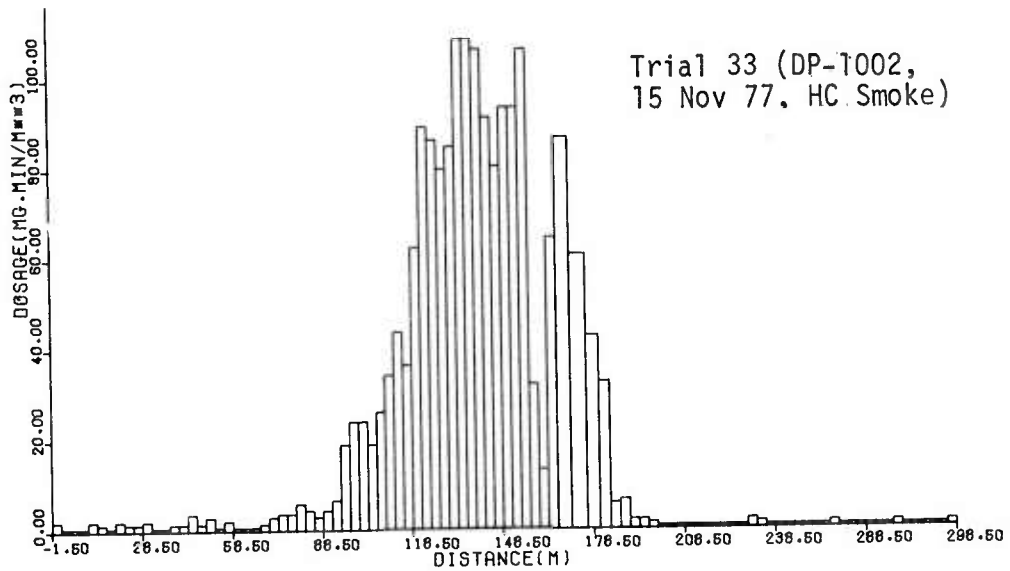

Figure 7. Dosage vs. Distance Along Line 2.

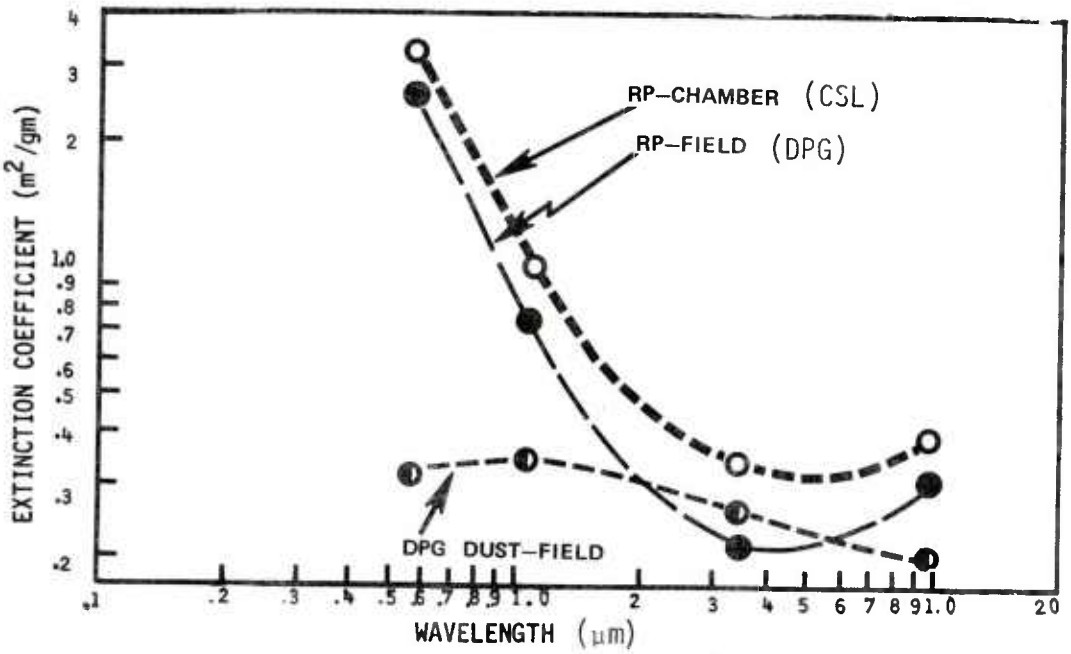

Figure 8. EXAMPLE OF EXTINCTION COEFFICIENTS (m^2/g) DETERMINED FROM EIGHT FIELD TRIALS. VALUES FOR RED PHOSPHORUS (RP) ARE COMPARED WITH CSL CHAMBER DATA.

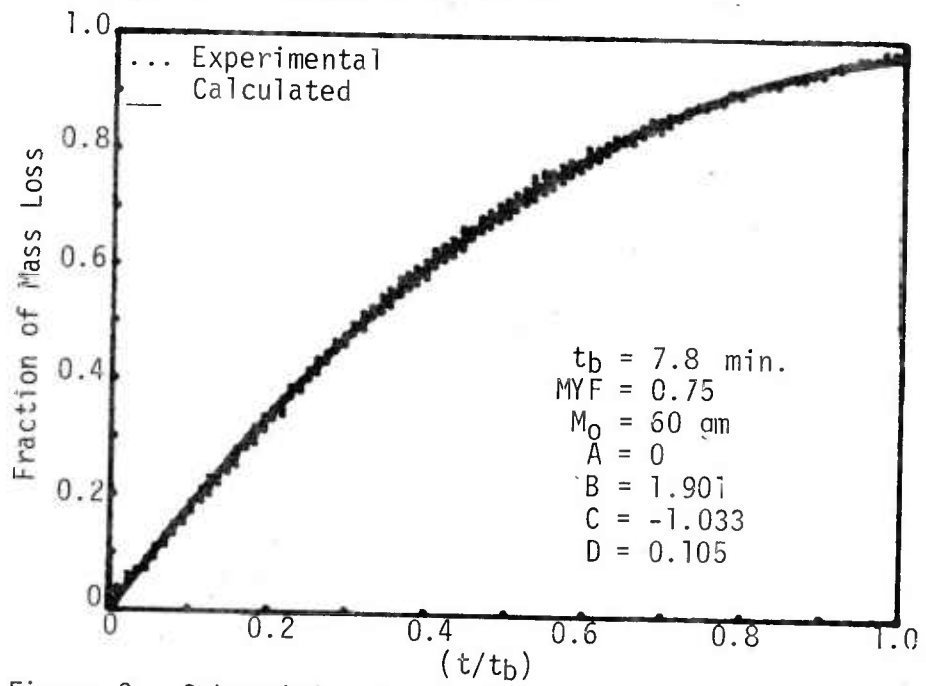

Figure 9. Submunition Source Parameters of Three-Inch WP Wick

Table 1. Typical Test Data from Trial DPI-002-T-33, 15 November 1977, 1201 MST (HC Smoke, 105 mm M116E2, 6 projectiles)

Wind Direction (Transport) (degrees) (4m)			160
Mean Wind Speed (Transport) ($\bar{u}$, m/sec)			2.3
Std. Dev. in Azimuth Wind Angle (σ_a, degrees) (8m)			18.5
Std. Dev. in Elevation Wind Angle (σ_e, degrees) (8m)			7.3
Temperature Gradient, 0.5-8m (ΔT, ^oC)			-1.7
Power-Law Exponent of Vertical Profile of Mean Wind Speed (P) (2m-8m)			0.08
Pasquill Stability Category			C
Relative Humidity (percent) (2m)			26.5
Solar Azimuth (deg)			175.5
Solar Altitude (deg)			31.1
Air Density - ρ(kg m^{-3})			1.055
Solar Radiation (Langleys)			0.88
Barometric Pressure (millibars)			872
Visibility (km)			137
Reflectivity, OD Target			0.11
Haze (footlamberts)			159
Brightness, Background (footlamberts)			1330
Brightness, White Target (footlamberts)			1359
Number of Munitions/Submunitions Used			18
Number of Munitions/Submunitions Functioned			18
Particle Size Range (μm)	(0.3-0.4)	Fraction -	0.19
	(0.4-0.6)		0.22
	(0.6-0.8)		0.20
	(0.8-1.0)		0.16
	(1.0-1.5)		0.16
	(1.5-3.0)		0.06
$Log_{10}NMD$			-0.178
$\sigma Log_{10}NMD$			0.232
NMD			0.66
MMD			1.44

Initial Cloud Dimensions (Meters)

Time	Length	Width	Height
1201:00	4	50	3
1201:30	68	69	11
1202:00	113	59	30
1202:30	154	60	27
1203:00	222	81	36

AD-A056483

METHODOLOGY DEVELOPMENT FOR THE IDENTIFICATION AND ANALYSIS OF TRACE CONTAMINANTS FOUND ON ARMY INSTALLATIONS

EMORY W. SARVER, Ph.D.
WILLIAM J. MAURITS, Ph.D.
MAX KERSCHENSTEINER
CHEMICAL SYSTEMS LABORATORY
ABERDEEN PROVING GROUND, MARYLAND

I. INTRODUCTION

The concepts of modern warfare and associated weaponry requirements have developed primarily during the past four decades. A variety of wastes was produced in association with weapons production. All too frequently, the composition of these wastes was undefined and little was known regarding their composition, toxicities, persistence, and mobility. Then accepted procedures for waste disposal consisted mainly of land filling with little or no consideration given to managing these wastes to prevent their distribution into the environment.

With time, the recognition of external adverse environment effects lead to the realization that these wastes in many cases were highly persistent and were migrating into the ecosystem.

As a result of these circumstances, the Secretary of the Army directed the development and implementation of a comprehensive project to identify the problems associated with these earlier waste disposal practices. In August 1975, the program manager for Chemical Demilitarization was selected to provide program management leadership for this interservice project and was designated as the Project Manager for Chemical Demilitarization and Installation Restoration. Installation restoration technology providing for the containment or elimination of migrating wastes from these numerous land disposal sites is being developed.

The project manager established the Analytical Systems Working Group (ASWG), composed primarily of army scientists with expertise in environmental chemistry. This group, as one of its tasks, reviews the analytical systems research and development program. Also the group provides the project manager advice and

recommendations on current environmental problems relating to Installation Restoration programs. The group oversees a quality control program under which all analytical data is generated. The program employs an onsite Quality Control (QC) coordinator at each participating laboratory and an overall Quality Control coordinator who develops all QC plans, monitors regional QC activities, and reports directly to the working group.

Installations selected for a restoration project are screened initially by a records research team for potential waste migration problems. This screening is accomplished by a multidisciplinary professional team which reviews existing historical records for the installation. This team assesses the potential for migration of contaminants from the installation. If their assessment indicates a potential waste migration problem, a limited sampling and analysis study is scheduled for the installation. This preliminary survey provides sufficient information to either support or refute waste migration. If migration is confirmed, the installation is scheduled for a comprehensive survey which determines the extent and level of waste migration and the sources of the migrating wastes. Based on the results of the comprehensive survey, a restoration program may be developed. The methodology described in this paper is used in the preliminary survey, the comprehensive survey, and during the restoration program.

II. TECHNIQUES FOR THE IDENTIFICATION AND SELECTION OF CONTAMINANTS

During the preliminary and comprehensive surveys, efforts are specifically designed to uncover and identify contaminants. Samples taken from installations are screened for contaminants by several techniques. The most common screening techniques used for water are determinations of the water quality parameters, organic extractables, and the common inorganics. Screening techniques commonly used for soil include organic extractables, water extractable inorganics, and total inorganics.

In the preliminary survey, a major effort is placed on screening water and soil. The sampling locations are based on the geohydrology of the area and other information gained from historical records. The sampling points are selected to provide definitive information on potential or actual migration of contaminated plumes.

Screening during the comprehensive monitoring survey is less intense and is only performed on an as required basis. Most newly identified contaminants in this phase of the project are discovered as interferences to the survey analyses. The intent of the comprehensive survey is the identification and description of sources of contaminants and contamination plumes.

Screening techniques for water soluble inorganics and volatile, extractable organic impurities (1) are well defined, and provide satisfactory data. However, screening techniques for water soluble, unextracted nonvolatile and thermally unstable organics are not well developed. Useful screening techniques for these classes of organics is being actively sought.

III. METHODOLOGY DEVELOPMENT

A systematic method for the development of monitoring techniques for contaminants distributed in the environment has long been needed. In the past, when a method was desired, one or more laboratories would work on parts of it. The end result revealed several well-developed parts of a method but with many unanswered questions. Recognizing this, any comprehensive program for defining environmental contamination must be based on a firm well-tested analytical systems approach. A twelve-step development procedure was devised, tested, and implemented. The stepped procedure and a typical development schedule are represented in the figure.

A. Literature Review

A literature review is conducted to obtain available techniques used for detection, identification, and estimation of quantities of the selected contaminants and related environmental degradation products. The reviews are intended primarily for use by the ASWG and the project methodology developers.

During the literature review, special attention is given to the following subjects: extraction procedure, cleanup procedure, analytical methods, environmental degradation products, and special analytical procedures.

B. Development of Standard Analytical Reference Materials (SARMS)

All of the chemical analyses conducted in support of this program are based on SARMS. These materials are either National Bureau of Standards (NBS) Standard Reference Materials or are traceable to one of these materials. Although NBS offers only a limited selection of standards, it is possible to trace any substance through a series of comparisons or titration to an oxidimetric, basemetric, or some other standard reference material.

Candidate high-purity analyses for SARMS are selected and evaluated on a preliminary basis using known materials. Sufficient analyses are run to document the random and systematic errors in the analyses. The most appropriate high-purity analysis is selected for evaluation of the analytical standard. Those design parameters of the standard which are critical to the survey analysis are identified.

MAJOR TASKS:

1. LITERATURE REVIEW
2. DEVELOPMENT OF STANDARD ANALYTICAL REFERENCE MATERIALS (SARMS)
3. SAMPLING REQUIREMENTS
4. STORAGE REQUIREMENTS
5. SOLVENTS, REAGENT AND STANDARDS CHECKOUTS
6. ISOLATION OF CONTAMINANT
7. SELECTION OF METHOD OF ANALYSIS
8. CONFIRMATION ANALYSIS
9. TEST AND EVALUATION
10. LABORATORY DATA ANALYSIS
11. ANALYTICAL SYSTEMS WORKING GROUP (ASWG) APPROVAL
12. APPLICATION OF METHODS

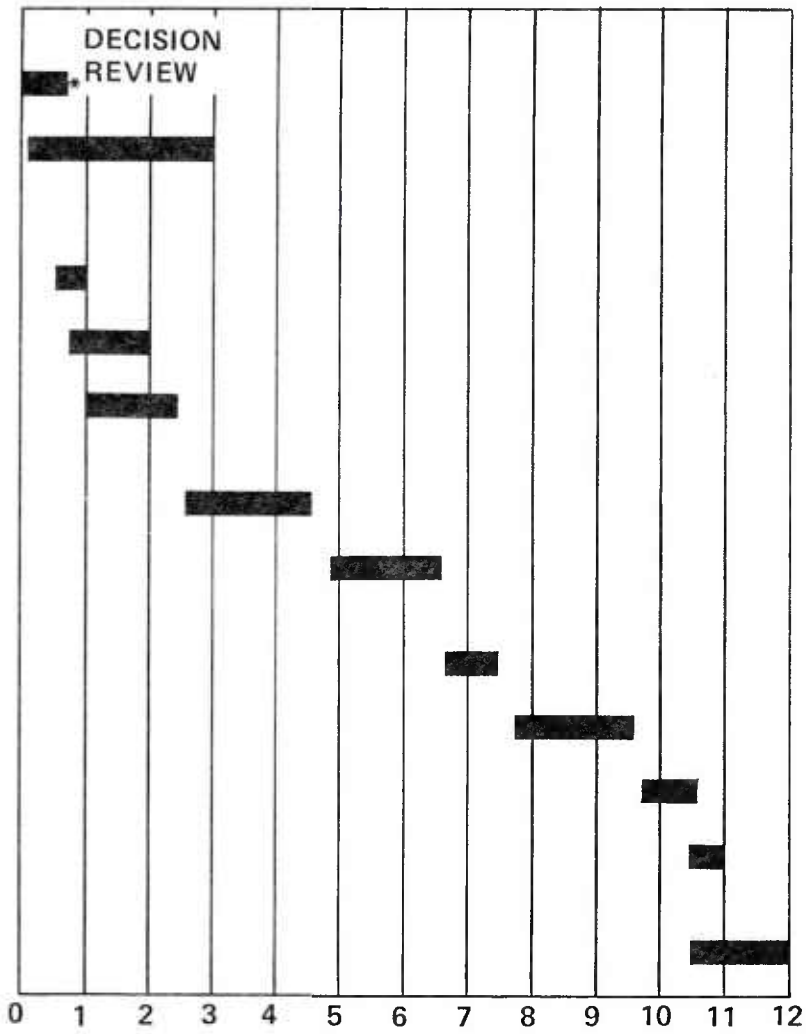

Figure. METHODS DEVELOPMENT PROGRAM

The development of a SARM begins with the synthesis or procurement of the raw material and purification to greater than 98-mole-percent purity. Chromatographic, spectrophotometric, and NMR examinations are routinely used to ensure that each material of certified high purity is indeed the correct compound.

Each SARM is subjected to an aggravated storage period to estimate its stability. Materials showing a propensity for decomposition are repurified and stabilized, if practical. Where not practical an alternate standard is selected. SARMS must emerge from aggravated storage with purities in excess of 98 mole percent.

The SARMS are prepared in sufficient quantity to ensure that enough standard is available for the aggravated storage test, surveillance tests (every six months), and the laboratory QC programs envisioned for two years. The test results are reported to the ASWG. This group approves the suitability of each material and all its supporting data prior to distribution as a SARM. NBS standard reference materials are accepted at face value for use as SARMS; however, care is taken to be sure the standard is being used for the purpose for which it was intended. Commercially available standards may be accepted as SARMS if sufficient supporting data can be obtained from the vendor.

When it is necessary to run preliminary analyses before a SARM is available, the following precautions will be taken.

a. Interim standards are stored at 0°C and a portion retained for a comparison with the approved SARM when available.

b. The following data are recorded as a minimum description of the material.

(1) Infrared spectrum

(2) Melting point, decomposition point, or boiling point

(3) NMR spectrum

(4) Elemental analysis

(5) Gas chromatographic [by difference] analysis

C. Sampling Requirements

The purpose of the sampling requirement task is to ensure that the sample is valid. To accomplish this goal, samples must represent the environmental component being tested. The sampling location, technique, frequencies, duration, and size should be such that the analytical results can be evaluated statistically (2). Special attention is paid to sample integrity and possible cross contamination. Additionally, subsampling is controlled to ensure that samples retain their integrity, and properly represent the initial sample. Analytical results are only as valid as the samples from which they are determined.

D. Storage Requirements

Each contaminant is tested to determine if it is stable in storage. An analysis is made to determine if the sample is degraded by oxidation, visible or ultraviolet radiation, or elevated temperatures. In addition, samples in storage are tested to determine whether contamination occurs by such factors as other sample containers, container seals, or other samples (i.e., through cross contamination). To avoid extensive storage testing, samples are analyzed, as soon as possible, to limit degradation.

E. Solvents, Reagents, and Standards Requirements

Solvents and reagents must be free of substances that interfere with analysis or degrade the sample. To obtain low-background levels and avoid spurious peaks arising from solvent impurities, it is usually necessary to employ specially purified solvents. Solvents and reagents are checked by using them in the specific analytical system. Special methods for uniformly dispersing the standards in soil are studied, tested, and evaluated.

F. Contaminant Isolation Techniques

In order to effectively determine a specific contaminant, it must be isolated from other moieties which could interfere with the determination. Although many methods of contaminant isolation exist, extraction technology is probably the most advanced and is given primary consideration.

Soil extractions are grouped into three classes: batch, column, and continuous. The selection of the method of extraction depends upon the equilibrium constant for partitioning of contaminant between the extraction solvent and the soil. Batch extraction works best when the contaminants strongly partition in the extraction solvent. Continuous extraction works best for all equilibrium conditions and is

ordinarily performed when the partition coefficient is unfavorable. Column extraction works with systems having a wide range of partition coefficients. Also, column extraction affords the analyst use of a mixture of solvents to remove the suspect undesirable substance.

The cleanup procedure should be tested to see that it enhances the detection and determination of the suspect contaminant:

At the desired sensitivity or limit of detection

With reasonable recovery (preferably 85% or better)

With reasonable reduction of background interferences

With adequate separation of the substance sought from interfering substances.

Even though some types of samples are analyzed with little or no cleanup, it may still be advisable to use established cleanup procedures in order to enhance the specificity of the analysis. In any case, details of the cleanup procedures are specified fully by the developers of analytical methods. Any changes or modifications are described explicitly.

An extraction procedure is usually efficient and easily controlled; however, it requires extensive preparation and consumes time. Where less time-consuming procedures have been developed or are feasible, they are pursued and evaluated as alternate methods. The focus of this program is to quantitatively and qualitatively identify environmental contaminants rather than to develop varied methodology for similar environmental systems. Therefore, extensive R&D programs are not funded under this task unless specific guidance from the ASWG is first given.

G. Selection of Methods of Analysis

The quantitative measurement step in determining the analyte, i.e., the substance determined analytically, is the most important step of the analytical system. The method selected for assaying the analyte defines the ultimate sensitivity, precision, accuracy, and detection limit possible. When methods are comparable, the one requiring the least amount of operator skills and time is the most desirable.

H. Confirmation Analysis

Confirmatory tests must support the identity of contaminants. A number of factors dictate the actions needed to confirm the identity of a contaminant.

Essentially all methods and tests regularly employed provide qualitative information which is presumptive in nature, i.e., the behavior of an unknown is compared to that of a known standard material. It is possible in any single test to find one material that masquerades as another. When the behavior of an unknown and standard is the same in a number of tests that measure different chemical or physical properties, the certainty of identification is increased.

Analytical methods are most useful when backed by a bank of data on the behavior of many contaminants, of their metabolites and degradation products when subjected to the various operations that make up the method. The analyst should be familiar with the contaminant's use and the chemistry and metabolism of its residues. The analyst should be aware of available information on the behavior of pesticides and other potential residues when subjected to a specific analytical method, and should consider the possible presence of chemicals that interfere with the analysis. Most importantly, the analyst must use common sense and accepted quality control procedures when drawing analytical conclusions.

I. Test and Evaluation of Trace Analysis

Before any analytical system is employed in the comprehensive survey, the following work is conducted. Sufficient standards and blanks are run to statistically establish the limits of detection. An established confidence level for detection must be met. The methods of Hubaux and Vos (3) are suitable. The percent recoveries of all analytes are determined on control soils of each type encountered in the sample load.

A list of potential interferences is prepared for each analysis. The functional relationship between the concentration of the interference and systematic error caused by this interference is estimated at the detection limit and the upper concentration limit specified for the analyte. An interfering substance is defined as one that causes systematic error in the analytical results for at least one concentration of the analyte within the range of the method.

The bounds of uncertainty due to systematic errors are estimated and reported with the analytical results. This estimate includes the errors which are empirically determined and such additional uncertainties as are known to be inherent in the standard.

J. Laboratory Data Analysis

Upon completion of the methods development and during the test and evaluation subtask, techniques for acquiring raw data are examined. The total amount of raw data per day and the frequency with which the method is required in the

comprehensive survey is the deciding factor in the technique employed to acquire the data. When the data are produced at a high rate and frequently, automatic data acquisition should be considered.

After the data have been acquired, they are used to calculate the results and the QC parameters. Calculation of the results is studied to obtain the best possible results within the allowable limits. The calculated results are validated by an agreed-upon procedure and reported to all appropriate agencies in specified format.

K. ASWG Approval

All the data generated during the development of the specific method are compiled and a summary of results along with the detailed procedure is presented to the ASWG for approval. At the recommendation of the ASWG, the method is either returned for future work, approved or disapproved. All approved methods are cast into a publishable form and submitted to a suitable journal for publication.

L. Application of Methods

Upon approval of the method by the ASWG, it is released to the users, and its application in their laboratories is carefully monitored. If a user has a problem in establishing the procedure, the developer aids in resolving the problem.

IV. RESULTS AND DISCUSSION

A. Contaminant Identification Tasks

During the screening operations conducted at several installations, well over one hundred contaminants in the ground water and surface water have been identified. In addition, two new screening techniques have been developed; one for volatile organics and the other for determination of organic extractables from sediments.

B. Water Methods

Methods for the analysis of ten contaminants in water have been developed and used in field tests. These contaminants are arsenic, thiodiglycol, elemental phosphorus, acetylcholinesterase inhibitors, diisopropyl methylphosphonate, dicyclopentadiene, p-chlorophenyl methyl sulfide, p-chlorophenyl methyl sulfone, p-dithiane, and p-oxathiane. Even though arsenic has been analyzed by many techniques, the method developed under this task has been shown to be free of interferences which have hampered other techniques. The other methods represent

one-of-a-kind procedures unavailable in the open or classified literature. For these methods eight new standard analytical reference materials were developed. These methods have found wide application in both the Government and the private sector.

C. Soil Methods

Analytical methods for five contaminants in soil have been developed. These methods are for the contaminants diisopropyl methylphosphonate, dicyclopentadiene, p-chlorophenyl methyl sulfide, p-chlorophenyl methyl sulfone, and p-dithiane. Since soil is such a complex matrix, a special study to determine the error associated with subsampling was undertaken. Results to date indicate that extremely large errors can occur when soil is improperly subsampled.

V. SUMMARY

This procedure for the development of methodology will allow the user to develop an analytical system with quantitatively defined precision, accuracy, and limits of detection. Treatment of environmental hazards is extremely expensive relative to methodology development and data generation; therefore, the final decision regarding treatment must be founded on data of the highest quality. It should be very clear that any shortcuts in cost or time in the development of methodology or data are not likely to be cost effective. Attention to the generation of quality control parameters in each step is required to meet these stringent conditions. Methodology development for analytical systems is a dynamic process resulting in continuous analytical method modification and validation for varying environmental conditions.

Acknowledgment

The authors would like to recognize the invaluable contribution of Dr. Dean Neptune in the writing and editing of this paper and for the helpful discussions regarding the analytical procedures.

We gratefully acknowledge the cooperation of the following individuals who participated in this program: Ms. Delores Basset and Dr. Henry Nowichi of Calgon Corporation, Pittsburgh, Pennsylvania.

REFERENCES

1. Bellar, T. A., J. J. Lichtenberg, and R. C. Kroner. Occurence of Organohalides in Chlorinated Drinking Waters. J. Am. Water Works Assoc. *66*, 703 (1974).

2. Guidelines On Analytical Methodology for Pesticide Residue Monitoring. Federal Working Group On Pest Management. Council on Environmental Quality. Washington, D.C. June 1975.

3. Hubaux, A., and G. Vos. Decision and Detection Limits for Linear Calibration Curves. Anal. Chem. *42*, 849 (1970).

*SATTLER, WORCHESKY, RITTER,
SIMONIS & RIESSLER

AD-A056484

INFRARED DIAGNOSTICS FOR NEAR-MILLIMETER WAVE SOURCES

JOSEPH P. SATTLER, Ph.D., TERRANCE L. WORCHESKY, KENNETH J. RITTER,
GEORGE J. SIMONIS, Ph.D. and WALTER A. RIESSLER, Ph.D.
U.S. ARMY ELECTRONICS RESEARCH AND DEVELOPMENT COMMAND
HARRY DIAMOND LABORATORIES
ADELPHI, MD 20783

The near-millimeter wave (NMMW) region of the electromagnetic spectrum may be defined as that region between 3.2 and 0.3 mm in wavelength (or equivalently between 94 and 1000 GHz, or between 3.1 and 33.3 cm^{-1}). This region near 1 mm is considered to be a unique region because its components and techniques are hybrids of the microwave and infrared (IR) regions that bracket it and because its atmospheric transmission windows permit reasonable propagation under adverse conditions. The justifications for military consideration of NMMW systems involve complex technical questions (1). Briefly stated, they arise from requirements for various "imaging" and radar systems which can operate under all weather conditions and the environment of battlefield smokes and dust. With a judicious balance of parameters, NMMW systems can combine the propagation advantages of the microwave region with high resolution that is characteristic of IR and optical systems.

This paper reports on new systematic diagnostic procedures developed in part at The Harry Diamond Laboratories (HDL) for obtaining the basic molecular information necessary for modeling and scaling the operation of known photon-pumped NMMW sources and for prediction of new NMMW emission and associated pump frequencies. Our procedures involve the use of tunable IR diode lasers to reveal important details of previously unresolved molecular absorption lines. The sub-Doppler-width resolution achievable with these lasers has permitted us to extend into the IR region a combination of accurate heterodyne and Stark absorption techniques previously employed routinely only in microwave spectroscopy.

First, the basic physics of photon-pumped NMMW sources is explained. Then the instrumental configurations involving the frequency

tunable lead-salt (PbSnSe) diode laser are discussed, with emphasis on heterodyne and Stark spectroscopic techniques used at HDL. The results obtained from studies of CH_3F, D_2O, and CH_3OH are presented, and the relationships to NMMW generation are given. New NMMW frequencies in atmospheric windows are predicted.

Photon-Pumped NMMW Sources

Photon-pumped NMMW sources operate on the principle of obtaining stimulated emission at a NMMW frequency in a gaseous molecular medium. The NMMW output frequency may result from a laser population inversion emission or a Raman emission. In either case, as illustrated in Fig. 1, it is necessary to find an IR emission transition, $h\nu$, which closely matches the molecular absorption energy, $E_2 - E_1$. The frequency separation between pump and absorption should be within about 1 GHz for pulsed NMMW output and within 100 MHz for cw NMMW output.

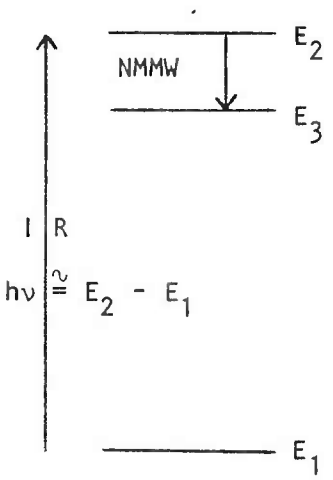

Fig. 1. NMMW Photon pumping scheme.

Conventional grating spectrometers do not have adequate resolution to determine accurately the frequency separation of the pump emission and IR absorption. However, tunable IR diode lasers, with a resolution over 20 times that of conventional spectrometers, can resolve IR spectral lines to less than their Doppler width, which is typically between 50 and 100 MHz for IR molecular transitions near 10 μm (1000 cm^{-1} or 30 x 10^{12} Hz). This is illustrated in Fig. 2. The upper portion shows the survey scan spectrum obtained with a conventional spectrometer for the gas CH_3F at a pressure of a few torr (2). The lower inserted oscillographs give our results obtained with lead-salt diode lasers. In these oscillographs, the upper traces correspond to the CH_3F absorption versus frequency, and the high resolution of the diode laser much detailed absorption structure is displayed where only singlet or blended band structure occurs in the conventional spectrum. The regularly spaced near-sinusoidal lower traces in the oscillographs correspond to periodic transmission maxima spaced by 1475 MHz (0.0492 cm^{-1}); these curves result from the variations with diode laser frequency of transmission through a Ge bar, and are used to calibrate the frequency scale.

A complete understanding of a photon-pumped NMMW source requires (a) identification of the quantum numbers associated with the molecular transitions; (b) measurement of the frequency difference between

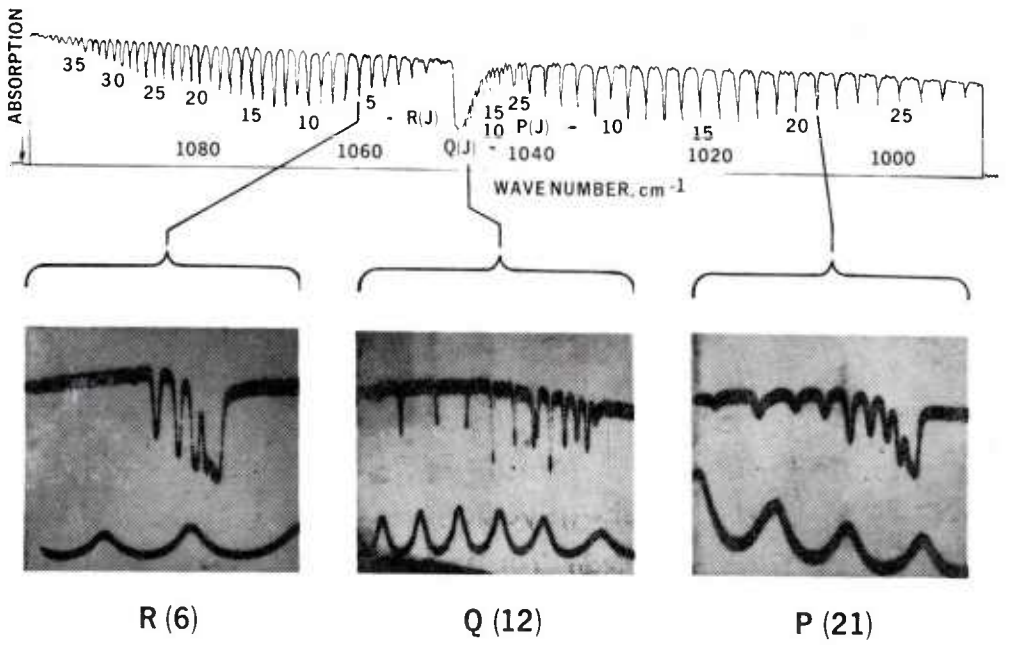

Fig. 2. Comparison of conventional spectrum (upper trace) and tunable diode laser spectra (lower traces) for CH_3F.

photon pump and molecular absorption; (c) measurement of IR line shapes, line strengths, transition rates, and pressure broadening effects; (d) related conventional molecular spectroscopy; (e) related NMMW spectroscopy. Our IR measurements have involved the first three items, and we have drawn from other publications for the other information. The rest of this paper describes our techniques and the application of our results to the molecular transitions of NMMW sources.

Diode Laser Spectrometer

Our first diagnostic step in studying a NMMW gas was to obtain the ultrahigh resolution IR spectrum in the region of interest. This procedure usually revealed important features of previously unresolved absorption line structure. The results of conventional spectroscopy often provide useful experimental and theoretical guides as to what one may expect. Indeed the operation of the diode laser may be compared with the operation of a microscope with very high resolution; without conventional low magnification information, it may be impossible to interpret the high-resolution structure.

The diode laser spectrometer is shown in Fig. 3. The lead-salt diode laser was fabricated by Laser Analytics and typically produced several hundred microwatts of power in each of about six principal

simultaneously oscillating laser modes when operating on a liquid-He cold finger. Varying the injection current between 0.23 and 2.0 A resulted in a piecewise tunability between 1005 and 1020 cm^{-1} at liquid-He temperature. The continuous tuning range of a given mode was about 0.3 cm^{-1} under these conditions. However, the useful diode-laser tuning range was extended by 140 cm^{-1} to higher frequencies by allowing the liquid-He to evaporate and the dewar to warm up slowly, or by mounting the diode in a closed-cycle variable-temperature cryogenic refrigerator. The refrigerator kept the diode laser at temperatures between 10 and 77 K with a short term stability better than 3 x 10^{-4} K. These temperatures allowed the diode laser to be coarsely tuned from 1030 to 1160 cm^{-1}. By adjusting the laser current, the frequency could be fine tuned at the rate of 10 MHz/mA. As the temperature was increased, the threshold current also increased, and fewer modes operated, but the current tuning range of these modes increased to about 1 cm^{-1}.

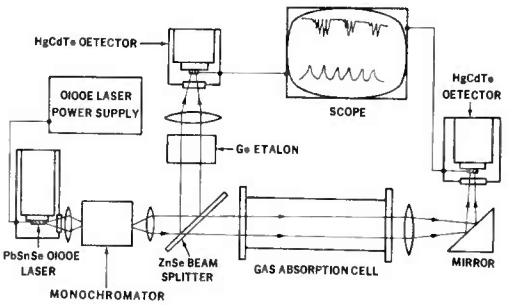

Fig. 3. Schematic diagram of diode laser spectrometer.

The radiation from the diode laser was first passed through a ¼-m monochromator used as a narrow band-pass filter to select a principal laser mode. A beam splitter then passed one portion of the radiation through a Ge bar etalon employed for the calibration of optical frequency differences, while the second portion of the radiation passed through the gas absorption cell (3). Two separate HgCdTe detectors simultaneously received the radiation passed through the etalon and the gas cell. Typically, a sawtooth current ramp of about 0.1-A amplitude with a frequency of about 100 Hz was applied to the diode laser to sweep its output frequency. Direct video presentation of the molecular absorption and the etalon channel spectrum was given simultaneously on a dual-beam oscilloscope for the warm-up exepriments. When the diode was mounted in the cryogenic refrigerator, a chopper and lock-in amplifiers were used to present the molecular and etalon channel spectra versus diode laser current on an X-Y-Y' recorder. Absorption-line separations were measured by comparison with the periodicity (1475 MHz) produced by the etalon. The gas sample cell was 30 cm long. Measurements were made at various pressures between 0.1 and 10 torr.

The search for a particular molecular absorption line proceeded in the following manner. As the diode laser temperature slowly increased, a manual scan of current between 0.2 and 2 A was repeatedly

made. The sawtooth ramp also was applied, and wide spectrometer slits were used during the search. Narrow slits were then inserted to discriminate against unwanted laser modes when it was desired to confirm the appearance of a particular absorption line, and the sawtooth ramp amplitude was decreased for better resolution.

As an example of the results obtainable with the diode laser spectrometer, Fig. 4 shows the tracings obtained from the plotter output of the 12 lines of the Q(J = 12, K) multiplet of CH_3F. This is similar to an oscillograph in Fig. 2, except that in this figure the frequency scale is more linear and increases toward the right.

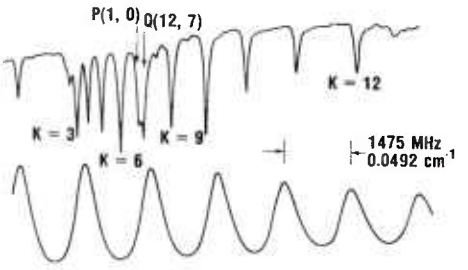

Fig. 4. Absorption spectrum of ν_3, Q(J = 12, K) transitions of CH_3F (upper trace) and etalon channel spectrum (lower trace).

Diode Laser Heterodyne Spectrometer

Although the experimental arrangement discussed above can provide remarkable sub-Doppler IR resolution, it cannot be used to measure the frequency difference between a molecular absorption and the photon-pump laser emission transition which must be obtained for NMMW diagnostics. Since the pumping laser is usually a CO_2 laser, and since the frequencies of this laser have been measured to high accuracy, a beat-note or heterodyne measurement of the pump laser with the diode laser frequency centered at a molecular absorption can determine the absolute frequency of the molecular absorption. Fig. 5 is a schematic of the experimental arrangement used at HDL. Information regarding previous related experimental procedures may be found in Refs. (4) and (5). For heterodyne measurements, the diode laser was mounted in the cryogenic refrigerator. As before, fine tuning was done by adjusting the injection current. The diode laser output was externally chopped and sent to a beamsplitter. Approximately 60% of the radiation passed through a monochromator to eliminate all but one longitudinal mode. The output radiation was made to pass through the gas cell and then onto the HgCdTe detector. The detected absorption signal was

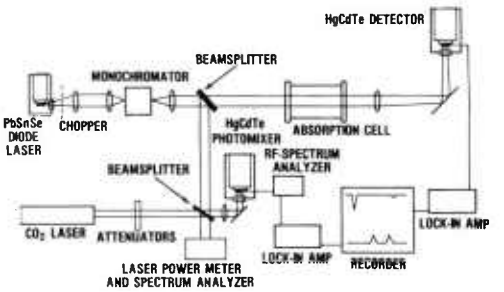

Fig. 5. Schematic diagram of diode laser heterodyne spectrometer.

fed into a lock-in amplifier, and its output was fed into the Y channel of an X-Y-Y' recorder whose X axis was driven as a linear function of the slowly changing diode-laser tuning current. The other portion of the diode-laser radiation was sent to an SAT Model C1 HgCdTe photomixer (3 dB bandwidth of 150 MHz) and heterodyned against a local oscillator.

The local-oscillator laser was a Sylvania Model 950 CO_2 laser whose frequency could be adjusted to be close so that of the molecular absorption line by use of an intracavity diffraction grating. The laser was set to line center maximizing the output power with a piezoelectric transducer. Although the gain profile and thus the absolute laser frequency are uncertain because of the pressure of the lasing gas mixture, this uncertainty is less than 2 MHz (6). The short-term frequency stability of this CO_2 laser was measured to be better than 1 MHz for periods of several minutes.

The rf signal from the photomixer was amplified by a low-noise, wideband amplifier and was detected with an HP model 141T spectrum analyzer system operating as a narrow-band (300-kHz) fixed-frequency receiver, tunable between 0 and 1.2 GHz. Video output at the chopping frequency was detected with a second lock-in amplifier whose output was applied to the Y' channel of the recorder. As the diode-laser frequency was tuned toward the CO_2 laser frequency, the beat note frequency decreased. When this frequency equaled the preset spectrum analyzer detection frequency, a marker was produced in the Y' channel. After the diode-laser frequency passed through the CO_2 laser frequency and their difference again equaled the setting of the spectrum analyzer detection frequency, another marker was generated. Thus we could measure the frequency difference between CO_2 laser line and a molecular absorption line by comparing the absorption and marker traces of the recorder.

Fig. 6 shows the result of one experimental run for D_2O. The upper trace shows the output from the detector that measured the absorption of the diode laser radiation by the D_2O gas; the lower trace shows the frequency markers generated by the heterodyne system. This run was for the absorption $6_6 \rightarrow 5_4$, $6_5 \rightarrow 5_5$ and $7_{-1} \rightarrow 6_{-3}$ near the 9P32 CO_2 laser line. High-resolution grating spectroscopy had placed the $7_{-1} \rightarrow 6_{-3}$ absorption 1770 MHz above the $6_6 \rightarrow 5_4$, $6_5 \rightarrow 5_5$ absorption (7). In Fig. 6, the $6_6 \rightarrow 5_4$, $6_5 \rightarrow 5_5$ absorption is 1177 MHz below the

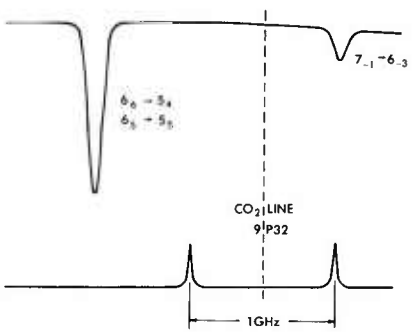

Fig. 6. D_2O absorption (upper trace) and frequency markers (lower trace).

CO_2 laser line, while the $7_{-1} \rightarrow 6_{-3}$ absorption is 565 MHz above this line. To reduce errors arising from the nonlinear tuning of frequency with current, we subsequently produced markers slightly below and slightly above each absorption line by changing the spectrum analyzer detection frequency by 100 MHz during each run. With these 100-MHz markers bracketing each absorption, we interpolated over 100 MHz to find the absorption frequency and thus avoided extrapolations over several hundred megahertz.

We checked the frequency calibration of this system by comparing our data with high resolution data taken by other complex spectroscopic techniques. These included not only the $5_0 \rightarrow 4_0$ transition of D_2O, but also several lines in CH_3F (8). Fig. 7 shows heterodyne results from the Q(12, K) transition of CH_3F. By interpolation, the CO_2 laser 9P20 line lies 53 MHz above the Q(12, 1) and 51 MHz below the Q(12, 2), in agreement with previous results (8). The error in our measurements is ±15 MHz (±0.0005 cm^{-1}). The frequency instability of the diode laser caused by the mechanical and thermal fluctuations of the refrigerator comprises the largest contribution to this uncertainty.

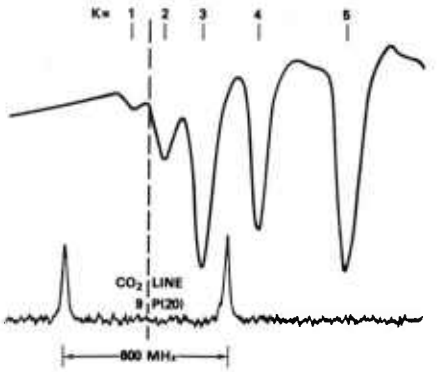

Fig. 7. Heterodyne spectroscopy of ν_3, Q(J = 12, K) transitions in CH_3F.

Diode Laser Stark Spectrometers

The application of external electric fields to gaseous molecules is common in microwave absorption spectroscopy where the high resolution of microwave components permits detection of small changes in transition frequency caused by the Stark effect (9). Although Stark fields have been used to tune IR molecular absorption frequencies through nearby laser line frequencies, until the present work, no publication has reported entire resolved Stark components in IR absorption spectroscopy.

A Stark gas absorption cell was constructed with metal plates 10 cm wide by 36 cm long separated by 0.203 cm. This cell could be substituted for the gas cells in the experimental arrangements depicted in Fig. 3 and 5. The usefulness of the Stark effect arises from the ability to assign directly and unambiguously the quantum numbers corresponding to a molecular transition from the pattern of new absorption lines which result when the electric (E-) field is applied.

*SATTLER, WORCHESKY, RITTER, SIMONIS, & RIESSLER

In Fig. 8 is shown the observed structure obtained when static E-fields were applied to a ν_4, R(J = 2, K = 2) transition in CH_3OH with $\vec{E}$ first parallel, then perpendicular to the linear polarization of the diode laser radiation. The quantum numbers, K, corresponding to the projection of the rotational quantum number, J, on the "symmetry" axis of the molecule, could be readily assigned since K = 0 lines showed no resolvable Stark splittings, whereas other lines showed well-resolved linear or quadratic Stark effects. Stark effects in CH_3OH and CH_3F have been studied and are discussed below.

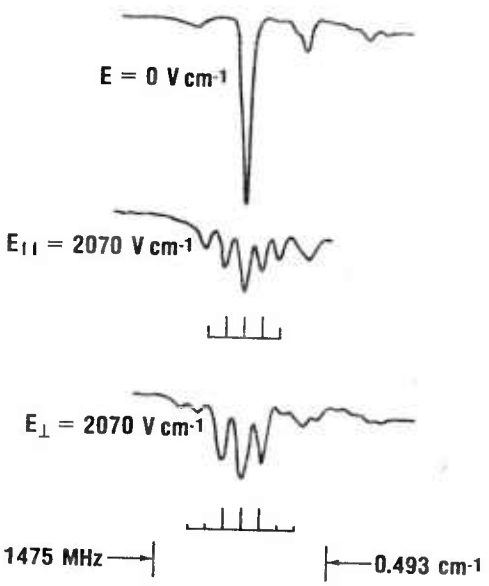

Fig. 8. Linear Stark effect on ν_4, R(J = 2, K = 2) transitions in CH_3OH showing observed and calculated patterns.

Spectroscopy of CH_3F

Methyl fluoride is considered to be an important NMMW and submillimeter wave (SMMW) molecule because strong (13 mW cw and 10 kW pulsed) output power is obtainable at 0.496 mm wavelength. This radiation is given off when the ν_3, Q(12, K = 1,2) transitions depicted in Fig. 2, 4, and 7 are pumped by the 9P20 line of a CO_2 laser (10).

We made a detailed examination of the Q branch of the ν_3 fundamental band of CH_3F (11). Fig. 9 shows typical dual-beam oscilloscope traces. The lower trace contains the regularly spaced maxima and minima of the etalon channel spectrum. The upper trace displays the K-structure of the Q(J, K) absorption lines for J = 3 to 6. These lines are identified according to the symmetric top model where the quantum number J refers to the rotational angular momentum and the axial quantum number K is the projection of J on the C-F symmetry axis. For Fig. 9 and 10, frequency increased toward the right and gas pressure was about 0.5 torr. Some nonlinearity in the diode laser frequency ramp occurred at the start of each application of the sawtooth current ramp (toward the left of the figures); also, there were flyback discontinuities (at the edges of each trace). A better resolved picture of the Q(5, K) quintet appears in Fig. 10, and pictures of the Q(12, K) multiplet appear in Fig. 2, 4 and 7.

The extra line near the Q(12, 7) line is the P(1, 0) line. This has been verified by a Stark measurement. The P(1, 0) line undergoes

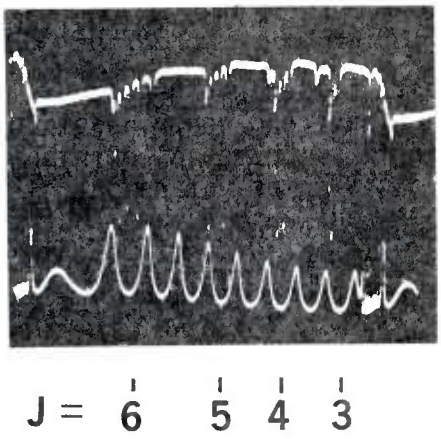

Fig. 9. Diode laser scan over region of several Q(J, K) lines.

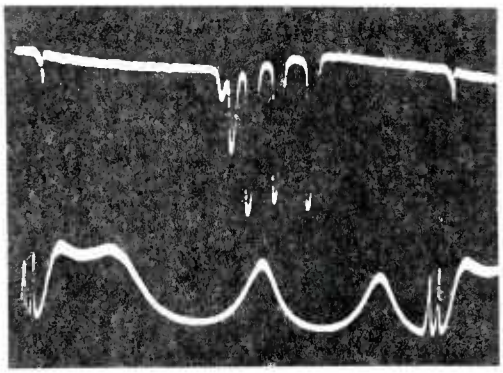

Fig. 10. Diode laser scan of Q(J = 5, K) quintet.

a quadratic Stark shift and has been found to be shifted by -50 MHz with application of a Stark field of 2241 Vcm^{-1}, in excellent agreement with our calculated shift of -48 MHz. Assignment of the symmetric top quantum numbers J and K is particularly easy for lines with $J \leq 12$ in the Q branch because the intensities generally follow the Honl-London intensity rules (12), and most of the lines are well separated with J lines corresponding to the K-values being visible in each multiplet. The K = 1 line is at the lowest frequency of the J multiplet, and lines of increasing K-value appear at correspondingly increasing frequencies. Also, lines with K-values that are evenly divisible by three are stronger than adjacent lines in accordance with the statistics arising from nuclear exchange symmetry (12). As J increases, the strengths of the K = 1 and 2 lines diminish, and the varying intensities help to confirm the line assignments.

We have also obtained spectra of several P- and R-branch lines. In accordance with the Honl-London intensity rules, the lines of low K are of greater intensity than the high-K lines in a J multiplet. It appears that the low-K lines, especially K = 0 and 1, are less than a line width apart, and therefore only J - 1 distinct lines appear for the P branch, and J distinct lines appear for the R branch for J > 0. This behavior is consistent with the spectra calculated from reported values of the vibration-rotation parameters and with line assignments based on the increased strength of lines with K evenly divisible by three. In the P and R branches, as in the Q branch, the frequency increases with increasing value of K.

In Table I are presented the measured and calculated widths of the Q-branch multiplets. The width of each J multiplet has been

*SATTLER, WORCHESKY, RITTER,
SIMONIS, RIESSLER

Table I. Frequency Separation Between Q(J, K = J) and Q(J, K = 1) Lines

J	Measured Separation (MHz)	Calculated Separation[a] (MHz)
2	137 ± 30	133 ± 2
3	386 ± 30	355 ± 10
4	749 ± 40	664 ± 28
5	1081 ± 60	1061 ± 66
6	1581 ± 60	1546 ± 134
7	2204 ± 90	2121 ± 247
8	2836 ± 90	2784 ± 418
9	3636 ± 110	3538 ± 666
10	4543 ± 110	4384 ± 1011
11	5578 ± 110	5324 ± 1475
12	6680 ± 110	6358 ± 2083

Table II. Frequency Separation Between Q(J, K = 1) and Q(J = 1, K = J + 1) Lines

J	Measured Separation (MHz)	Calculated Separation[a] (MHz)
1	1189 ± 100	1221.5 ± 2.5
2	1677 ± 100	1677 ± 9
3	2000 ± 100	2045 ± 29
4	2351 ± 100	2224 ± 67
5	2582 ± 100	2514 ± 135
6	2526 ± 100	2615 ± 248
7	2500 ± 100	2625 ± 419
8	2415 ± 100	2544 ± 667
9	2298 ± 100	2370 ± 1010
10	1983 ± 100	2101 ± 1480
11	1680 ± 100	1736 ± 2080

[a]Calculated with parameters in Ref. (11).

measured as the separation between the K = J and K = 1 components. In a similar manner, Table II gives the separation of adjacent multiplets. No attempt has been made to extract best-fit constants from our data on inter- and intra-multiplet line separations. Our experimental errors of about 100 MHz are caused in part by the low finesse of the etalon, by laser radiation of nearby parasitic modes, and by changes in the laser power output and tuning rate with current. The increasingly large errors in the calculated separations occur because the vibration-rotation parameters that are not well known are multiplied by big integers for large values of J and K, thus increasing the relative error. For example, the calculation of the positions of the P(1, 0) and Q(12, 7) lines, which appear close together in Fig. 4, is not reliable enough to distinguish the lines. Nevertheless, the diode laser spectrum consisting of regularly increasing spacings of the Q(12, K) lines indicate that the Q(12, 7) line should be at a higher frequency than the P(1, 0) line. This information is consistent with our Stark experiment.

The agreement between our measurements and the calculated spectra is within experimental error, except for the Q(4, K) multiple where the measured width seems slightly large. For low values of J and K, the line separations obtained by using the published values of the vibration-rotation parameters are believed to be about two orders of magnitude more accurate than we can measure with the diode laser.

This accuracy is not surprising since the experiments (8) and (13) have encompassed a large number of very accurate data relating to lines of low J- and K-values in the immediate vicinity of available CO_2 laser lines. Nevertheless, the diode laser is very useful for those regions of the spectrum where it is not possible to extrapolate the results of other experiments. Our recent calculations based on such data predict three new NMMW that should result from photon pumping with isotopic CO_2 lasers. The predicted outputs lie in atmospheric windows between 0.7 and 1 mm.

Spectroscopy of D_2O

Heavy water is an important NMMW and SMMW molecule because when the D_2O gas pumped with a TEA CO_2 laser, kilowatts of output power result (10). By using heterodyne techniques, we have measured the frequencies of several D_2O absorption lines that are nearly coincident with CO_2 emission lines.

Table III presents the results of measurements of eight absorption lines in D_2O gas (14). Our measurements were taken with D_2O gas pressures from 0.1 to 0.5 torr. The line $6_6 \rightarrow 5_4$, $6_5 \rightarrow 5_5$ was studied at pressures less than 0.01 torr but was still unresolved. The line assignments are labeled according to the asymmetric top model (9). These results are being used by researchers at two universities in calculations of the efficiency of the D_2O NMMW and SMMW source.

Table III. D_2O Absorption Frequencies

D_2O Absorption[a]	CO_2 Frequency (cm^{-1})[b]	Measured Difference (cm^{-1}) $f(D_2O)-f(CO_2)$	D_2O Frequency (cm^{-1})
$6_6 \rightarrow 5_4; 6_5 \rightarrow 5_5$	1035.4736	−0.0393	1035.4343
$7_{-1} \rightarrow 6_{-3}$	1035.4736	+0.0185	1035.4921
$11_{-6} \rightarrow 10_{-6}$	1048.6608	+0.0399	1048.7007
$12_{-8} \rightarrow 11_{-6}$	1053.9235	+0.0262	1053.9497
$10_{-8} \rightarrow 9_{-6}$	1073.2785	−0.0188	1073.2597
$5_0 \rightarrow 4_0$	1079.8523	+0.0109	1079.8632
$5_0 \rightarrow 4_0$	1079.8523	+0.0106[c]	1079.8629
$10_{-7} \rightarrow 10_{-9}$	1084.6351	+0.0217	1084.6568
$9_{-9} \rightarrow 8_{-7}$	1085.7654	−0.0196	1085.7458

[a] From Ref. (7).

[b] From Ref. (15).

[c] From Ref. (16).

Spectroscopy of CH_3OH

Methyl alcohol provides more NMMW and SMMW transitions than any other molecule (10). Its structure corresponds to a slightly asymmetric top, and the vibrational transition of interest for optical pumping is the ν_4 vibration associated with the C-O stretch. The complexity introduced by the reduced symmetry is compounded by a torsional motion of the O-H group. Fig. 11 shows a comparison of the diffuse structure of the conventional spectrum (insert) and the R(5)-multiplet as obtained with the diode laser. It is also inform-

ative to compare the conventional spectrum in this figure with that of CH_3F in Fig. 2 to see how one extra atom drastically complicates molecular spectra corresponding to similar vibrations.

The identification of R and P multiplets was made only after hundreds of data runs of spectra were taken and fitted together. This piecewise procedure was necessitated because the tuning behavior of the diode laser made it difficult to obtain continuous spectral runs over ranges exceeding 1 cm^{-1}. Multiplets have been identified extending from the R(11) near 1052 cm^{-1} through the Q branch to the P(10) near 1017 cm^{-1}. Assignments of the torsional quantum numbers η and τ and the rotational quantum numbers J and K for certain lines in the P and R multiplets have been made possible because of the constant width of the multiplets, the similarity of the structures of adjacent multiplets, and our Stark measurements. Lines in the P and R branch of the ν_4 band with $J \leq 2$ were identified by direct observation in absorption of the Stark patterns produced when the static E-fields were applied to the gas with $\vec{E}$ either parallel or perpendicular to the linear polarization of the diode laser radiation. The K-values could be unambiguously assigned since the K = 0 lines showed no resolvable Stark splitting, whereas other lines showed well resolved linear or quadratic Stark effects. Fig. 12 shows the quadratic Stark effect on the R(J = 1, η = 0, K = 1, τ = 3) asymmetry-split pair of lines. The agreement between the measured splitting of 214 MHz and our theoretical calculation of 195 MHz is within our experimental uncertainty of 30 MHz. This result allows us to make an unambiguous quantum number assignment for these lines. An example of a linear Stark splitting is shown in Fig. 8. By superimposing the various R(J) multiplets, by using the heterodyne results, and by comparing the similarities of structure, we have given an absolute frequency scale to the CH_3OH spectrum and have established the identifications of the K-values in the multiplet as shown schematically in Fig. 13. The assignments for the J = 0, 1, and 2 multiplets are confirmed by Stark spectra, and the assignments in the higher J multiplets are extrapolations from frequency and intensity considerations.

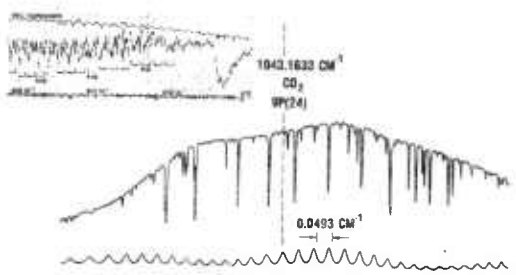

Fig. 11. Diode laser scan of ν_4, R(J = 5) multiplet in CH_3OH.

From our data, it was possible to make definitive tests of two published theoretical calculations (17, 18) which attempted to identi-

*SATTLER, WORCHESKY, RITTER,
SIMONIS, & RIESSLER

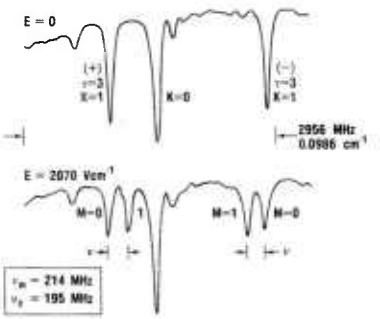

Fig. 12. Quadratic Stark effect on ν_4, R(J = 1, η = 0, τ = 3 K = 1) pair in CH_3OH.

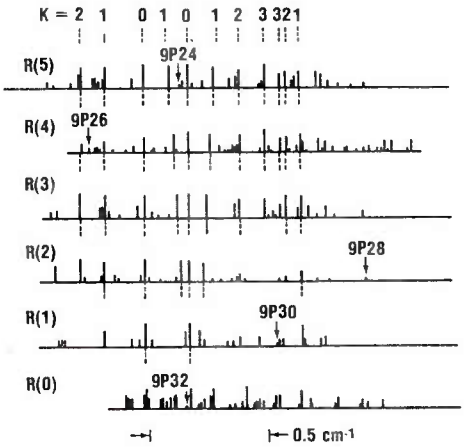

Fig. 13. Schematic spectra of ν_4, R(J)-multiplets.

fy the IR and NMMW-SMMW transition. The results of heterodyne spectroscopy for pumping CH_3OH with the CO_2 9P16 line is shown in Fig. 14. A strong CH_3OH line lies within 105 MHz of the CO_2 laser frequency. This pumping frequency has produced four NMMW transitions and one SMMW transition, including the important line at 1.217 mm (10). Additional measurements place the offset at 73 ± 15 MHz. These data, when combined with the analysis of the structure of the R(J = 10) multiplets, lead to an identification of the strong absorption line as the higher frequency R(J = 10, η = 0, τ, K = 0) transition in partial agreement with Ref. (17) and in disagreement with the conclusion of Ref. (18). Similar methods also show that the assignment as an η = 1 transition (17) for the IR absorption in the Q branch associated with pumping by the 9P34 line may not be correct since a strong n = 0 line lies close to the laser frequency.

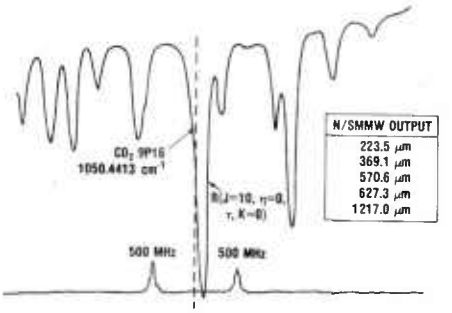

Fig. 14. Heterodyne spectroscopy of ν_4, R(J = 10, K = 0) transition in CH_3OH.

From the etalon and heterodyne spectroscopy and the published frequencies of isotope CO_2 lasers, it has been possible to predict a near-coincidence of an R(J = 6, η = 0, τ, K = 3) line with the IIP48 line of the CO_2^{18} laser. Calculations are proceeding to predict also

the resultant NMMW and SMMW output frequencies.

Conclusions

New IR heterodyne and Stark spectroscopic techniques have been developed and applied to the analysis of molecular NMMW sources. These procedures have revealed previously unresolved molecular IR structure. Quantum number assignments and absolute frequencies of transitions have been tabulated for CH_3F, D_2O, and CH_3OH. New NMMW operating frequencies have been predicted. The results have implications for both fundamental and applied research, since our measurements provide new information regarding molecular structure, as well as important parameters for NMMW source modeling.

Acknowledgements

The authors thank T. DeTemple of the University of Illinois for suggesting D_2O as a gas for study and J. Gallagher of the Georgia Institute of Technology for suggesting the application of Stark fields.

References

1. Near-Millimeter Wave Technology Base Study, S. M. Kulpa and E. A. Brown, eds., U.S. Army Electronics Research and Development Command, Harry Diamond Laboratories (in press).
2. W. L. Smith and I. M. Mills, J. Mol. Spectrosc. II, 11 (1963).
3. W. H. Weber and P. D. Maker, J. Chem. Phys. 64, 2149 (1976).
4. R. S. Eng et al., Mol. Phys. 28, 653 (1974).
5. E. D. Hinkley, Appl. Phys. Lett. 16, 351 (1970).
6. T. W. Meyer, Ph.D. Thesis, U. Cal. Livermore (1974).
7. C. L. Lin and J. H. Shaw, 31st Molecular Spectroscopy Symposium, FC10, Columbus, Ohio (1976).
8. S. M. Freund et al., J. Mol. Spectrosc. 52, 38 (1974).
9. C. H. Townes and A. L. Schawlow, "Microwave Spectroscopy," McGraw-Hill, New York (1955).
10. M. Rosenbluh et al., Appl. Opt. 15, 2635 (1976).
11. J. P. Sattler and G. J. Simonis, J. Quant. Elect. 13, 461 (1977).
12. G. Hertzberg, "Molecular Spectra and Molecular Structure," Vol. II, Van Nostrand, New York (1945).
13. R. S. Winton and W. Gordy, Phys. Lett. 32A, 219 (1970).
14. T. L. Worchesky et al., Opt. Lett. (in press).
15. F. R. Petersen et al., Proceedings on Laser Spectroscopy, Vail, Colorado, 1973, Plenum, New York (1974).
16. F. Keilman et al., Appl. Phys. Lett. 26, 19 (1975).
17. J. O. Henningsen, J. Quant. Elect. 13, 435 (1977).
18. E. J. Danielewicz, Jr., and P. Coleman, J. Quant. Elect. 13, 485 (1977).

AD-A056485

COMPARISON OF THE EFFECT OF STRUCTURAL COUPLING PARAMETERS ON FLAP-LAG FORCED RESPONSE AND STABILITY OF A HELICOPTER ROTOR BLADE IN FORWARD FLIGHT (U)

*DANIEL P. SCHRAGE, MAJ, FA
ARMY AVIATION RESEARCH AND DEVELOPMENT COMMAND
ST. LOUIS, MO. 63166
DAVID A. PETERS, PhD, ASSOCIATE PROFESSOR M.E.
WASHINGTON UNIVERSITY, ST. LOUIS, MO. 63120

INTRODUCTION

Compared to the conventional airplane, the present day helicopter is a modern invention. Although Leonardo da Vinci sketched a man-carrying vehicle with rotating wings around the year 1500, only after World War II has this versatile aircraft come into general use throughout the world. During the last decade the helicopter has become one of man's most useful tools in the air, demonstrating its versatility in both civil and military roles. The reasons for the long delay in realizing Leonardo's dream have not been for want of trying.

If we consider the first flight of de la Cierva's autogyros in 1925-26 as the birth of rotary-wing aviation, then the "childhood diseases" of the helicopter were mainly solved in the first decade (1926-1936). These initial problems were aerodynamic in nature and consisted of balancing, controllability, and stability. More serious deficiencies became apparent, however, when the first series-produced machines appeared and were placed in service. These problems were dynamic in nature such as fatigue due to insufficient dynamic strength of certain structural members and degradation of crew and passenger efficiency due to unacceptable vibration levels (Reference 1). While sufficient control of these deficiencies has been achieved to allow the helicopter to progress to its present state, they remain as a major obstacle in complete maturity phase development of the helicopter.

The loads on the helicopter are quite different from a conventional propeller driven aircraft. The propeller operates practically in an axial flow and, like an engine, sets up no noticeable variable stresses in the structural members. Therefore, it is only during take-off, landing, and maneuvers that appreciable dynamic loads are induced on the aircraft structure. Since these loads usually represent relatively few load cycles during the lifetime of the aircraft, one can generally speak of repeated static loads. The helicopter's main structural members are loaded dynamically, the number of loadings often exceeding tens of millions of cycles during its lifetime. The cause of this dynamic loading is due primarily to the asymmetric airflow past the main rotor as it rotates and simultaneously advances (Reference 1).

In forward flight, when the main rotor provides both lift and propulsive force for the helicopter, the flow over the blades is asymmetric due to the velocity differential over the advancing and retreating blades (Figure 1). Rotor control is obtained by "cyclic pitch" change, which is the name given to the first harmonic variation applied to the blade pitch angle as it rotates. Since the relative air velocity over the blade also has a first harmonic variation and since aerodynamic forces are proportional to the square of the relative velocity, we may expect to find at least three harmonics in the force fluctuations acting on the blades. This would be true if the airflow through the rotor were uniform, however, due to the proximity of the rotor to its own vortex wake, which is swept backwards under the rotor disc, the flow is far from uniform, and velocity fluctuations are induced which give rise to very many harmonics of blade loading. The aerodynamic characteristics of a rotor in forward flight give rise to shear forces and moments at the blade root which are then transmitted to the rotor hub where they are combined and sent through the rotor shaft into the airframe. The dynamics complexity of the helicopter can be ascertained from the cartoon in Figure 2.

During the design of a helicopter, accurate prediction of main rotor blade and hub oscillatory loading is important for fatigue, vibration, and forward flight performance. Critical dynamic components are designed for fatigue based on these predicted loads. Vibration characteristics of the airframe and the need for vibration reduction devices are determined from these loads. Since vibratory response and rotor loads usually determine limiting speed and load factor operational envelopes, the predicted loads greatly influence forward flight performance. Recent Army helicopter development programs, Utility Tactical Transport Aircraft System (UTTAS) and Advanced Attack Helicopter (AAH), have revealed that these loads cannot be predicted accurately (Reference 2). A similar conclusion was

drawn from a comparison study (Reference 3) where the helicopter industry's major state-of-the-art rotor loads analyses were independently exercised on an identical hypothetical helicopter problem. The comparison of results illustrated significant differences, particularly in structural dynamic modeling, between the various analyses. A strong recommendation as a result of this study was to conduct computer experiments to study specific isolated aspects of the solution methods and structural dynamics (Reference 3). It was the results of this study and the UTTAS/AAH Programs that provided the impetus for this research.

ROTOR BLADE AZIMUTHS AND VELOCITIES

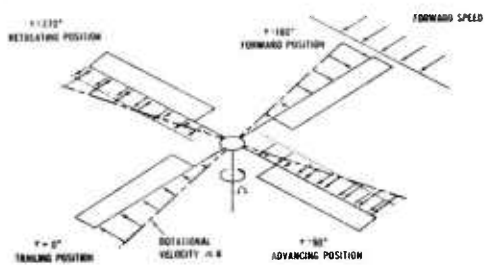

FIGURE 1

DYNAMICS COMPLEXITY

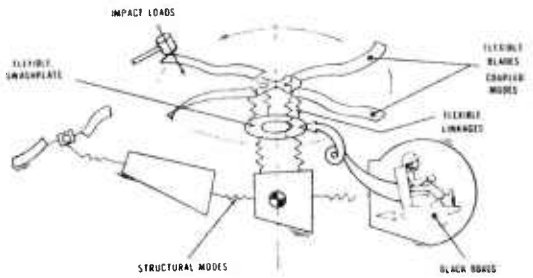

FIGURE 2

THE MATHEMATICAL MODEL

Description

The model is illustrated in Figure 3. It consists of a slender rigid blade, hinged at the center of rotation, with spring restraint at the hinge. The orientation of the flap (out-of-plane) and lag (in plane) restraint springs which are parallel and perpendicular to the blade chord line, respectively, simulate the elastic coupling characteristics of the actual elastic blade. The spring stiffnesses are chosen so that the uncoupled rotating flap and lag natural frequencies coincide with the corresponding first mode rotating natural frequencies of the elastic blade. This allows the model to represent a hingeless rotor treated by virtual hinges or a fully hinged rotor (Reference 4).

The model chosen has been used to evaluate rotor aeroelastic stability and can include the incorporation of flap-lag elastic coupling, pitch-flap and pitch-lag coupling, and a blade lag damper. These were some of the fundamental dynamic mechanisms found important in the stability studies of References 4 and 5. Their importance with regards to forced response is a major objective sought in this research.

CENTRALLY HINGED, SPRING RESTRAINED, RIGID BLADE REPRESENTATION

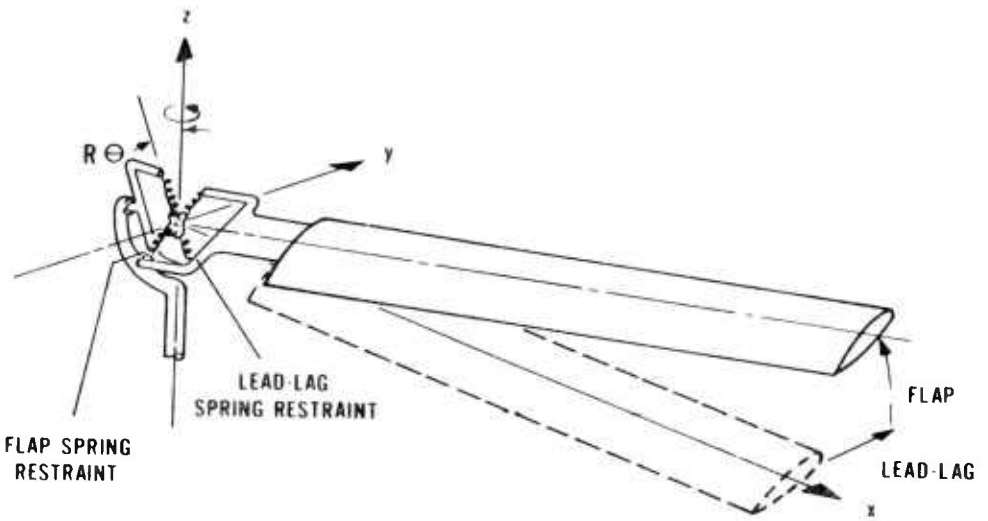

FIGURE 3

To include flap-lag structural coupling and be able to vary it to determine its effect on blade vibrations, the parameter R is defined. Geometrically, it is defined as the ratio of the blade pitch angle inboard and outboard of the pitch bearing. Physically, it represents how the flap-lag structural coupling is dependent on the relative stiffness of the blade segments inboard and outboard of the pitch bearing. This is because the principal elastic axes of the outboard segment rotate through an angle as the blade pitch varies while the inboard segment principal axes do not. The method of implementation is accomplished by replacing θ by $R\theta$ in the structural terms in the flap-lag equations while the mass and inertial terms

are unchanged. Thus, when R=1, the original equations are retained, but as R is reduced to zero, the flap-lag structural coupling terms diminish and eventually vanish (Reference 4).

Torsion is included in a quasi-steady manner as pitch-flap and pitch-lag coupling. This is accomplished by defining the pitch angle, θ, as:

$$\theta = \theta_o + \theta_s \sin\psi + \theta_c \cos\psi + \theta_\beta \delta\beta + \theta_\zeta \delta\zeta$$

Pitch-flap coupling, θ_β, is intentionally built into some rotors to reduce the flapping motion. If negative θ_β is used, then as the blade flaps upwardly the pitch is decreased, which reduces the aerodynamic forces on the blade and the flapping motion is somewhat suppressed. Pitch-lag coupling, θ_ζ, is sometimes used in a similar way to reduce the lagging motion.

As stated previously, the model has been used to evaluate aeroelastic stability. These studies, (References 3 and 5), have shown the model to give quite reasonable accuracy at low advance ratios when compared with more complicated models. Since all pure helicopters currently developed operate at a $\mu < 0.5$ and the aeroelastic stability of a rotor is considered more sensitive to system parameters than forced response the model is believed to be an adequate representation for parametric studies.

Equations of Motion

The general procedure followed was to derive the nonlinear flap-lag equations of a helicopter rotor in forward flight. The left hand side of the equations was made linear by considering small perturbation motions about a periodic equilibrium position (trimmed condition) of the nonlinear system. The nonlinear terms were consolidated on the right hand side to form the following flap-lag perturbation equations of motion:

$$\begin{Bmatrix} \ddot{\delta\beta} \\ \ddot{\delta\zeta} \end{Bmatrix} + \left[C(\psi)\right] \begin{Bmatrix} \dot{\delta\beta} \\ \dot{\delta\zeta} \end{Bmatrix} + \left[K(\psi)\right] \begin{Bmatrix} \delta\beta \\ \delta\zeta \end{Bmatrix} = \left[L(\psi)\right] \begin{Bmatrix} \dot{\bar{\beta}} \\ \bar{\beta} \end{Bmatrix} + \left[M(\psi)\right] \begin{Bmatrix} \bar{\theta} \\ \bar{\Phi} \end{Bmatrix} + \left[N(\psi)\right] \begin{Bmatrix} \ddot{\bar{\beta}} \\ C\frac{do}{a} \end{Bmatrix}$$

There are two forms of periodic coefficients in the equations. The explicit periodic coefficients are of the form $\mu \sin \psi$ or $\mu \cos \psi$. These types are only associated with aerodynamic terms. The second type are implicit periodic coefficients that result from the fact that θ and β may have cyclic components. These types are

found in both structural and aerodynamic terms. A damping term is included in the $C(\psi)$ matrix to account for the lead-lag damper included on many rotors, particularly hinged rotors. These equations are put into state variable format to reduce them to first order so that an efficient computer library differential equation solver can be utilized.

METHOD OF SOLUTION

Eigenvalue and Modal Decoupling Analysis

The method used to solve the linearized flap-lag equations with periodic coefficients is called an eigenvalue and modal decoupling analysis. It takes advantage of Floquet Theory with its application to linear systems with time varying coefficients. It is unique in that it extends the Floquet Transition Matrix (FTM) Method (Reference 6) to include the calculation of forced response. The eigenvalue and modal decoupling method is summarized in Figure 4. Once the flap-lag equations have been put into state variable format, the state transition matrix and FTM are obtained by step-wise integration over one period. This period consists of one rotor revolution from time zero to 2π. Once the FTM, $\Phi(T)$, is obtained it can be shown by application of the Floquet-Liapunov Theorem (Reference 6) that the problem of stability reduces to solution of an eigenvalue problem. Stability is determined from the real part of the complex eigenvalue, $\Lambda = \eta + i\omega$. Therefore, when η is negative the system is stable, with $\eta = 0$ representing the stability limit or boundary.

The extension of the FTM Method to determine forced response requires considerable manipulation although the mathematics are relatively simple. The eigenvectors of the FTM and the state transition matrix at each integration step increment must be obtained and saved. This is necessary in order that the characteristic functions, $A(t)$, can be calculated and used as a variable substitution to decouple the system of equations. This procedure is completely analogous to the modal analysis method (Reference 7) used to uncouple a system of equations with constant coefficients. Hence, the name eigenvalue and modal decoupling analysis is given to the method of solution.

Hub Shears and Moments

The information obtained from the analysis are the flap and lag displacements and velocities. These quantities are combined in the time domain to obtain flap and lag shears and moments in both the rotating and non-rotating systems. Once calculated the shears and

moments are harmonically analyzed through Fourier Series expansion to determine the relative strengths of the rotor harmonics. In the rotating system the primary concern is fatigue of root end and hub components so that the first harmonic (1/REV) is the major oscillatory source. In the fixed system, the rotor acts as a filter and only allows rotor harmonics that are integral multiples of the number of blades to be transmitted. Therefore, for a two bladed helicopter only the even harmonics, 2/REV, 4/REV, etc., are of major concern in the fixed system. The root shears and moments for each blade in the rotating coordinate system are expressed as the integrals of the blade aerodynamic and inertial loading. The single bladed results in the fixed system are valid for rotors with any number of blades so long as the appropriate solution harmonics are set to zero. Therefore, if a three bladed rotor is being analyzed only the 3/REV loads are of interest in the fixed system.

EIGENVALUE AND MODAL DECOUPLING ANALYSIS

Step	Description
1	Put Flap-Lag Equations into State Variable Format: $\dot{X}(t) + D(t)X(t) = f(t)$
2	Determine the State Transition Matrix, $\phi(t)$, and Floquet Transition Matrix, $Q = \phi(T)$, By Numerical Integration Over One Period. The Solution Can Be Written as: $X(t) = \phi(t)\, X(0)$
3	Find Eigenvalues and Eigenvectors of FTM, Q. Floquet's Theorem States that a System of Equations Having Periodic Coefficients Has Transient Solutions of the Form: $X(t) = A(t) \left[e^{\Lambda t}\right] \{\alpha\}$. At t=0: $\{\alpha\} = A(0)^{-1}X(0)$
4	Using 2 and 3 an Eigenvalue Problem is Developed: $A(0)^{-1} Q\, A(0) = \left[e^{\Lambda t}\right]$. The Characteristic Functions, A(t), Can Be Obtained From: $A(t) = \phi(t)A(0) \left[e^{-\Lambda t}\right]$
5	Through Variable Substitution, $X(t) = A(t)Y(t)$, the Equations in 1 Can Be Decoupled to Obtain: $\dot{Y}(t) - [\Lambda]\, Y(t) = g(t)$
6	The Uncoupled Response, Y(t), Can Be Obtained From Complex Fourier Series Expansion. The Coupled Response X(t), Can Be Obtained From Matrix Multiplication.

7 Convert X(t) Information in Time Domain to Vibratory Shears and Moments. Fourier Analyze Shears and Moments to Obtain Various Harmonic Components.

FIGURE 4

RESULTS AND DISCUSSION

As with any new analytical method correlation with other proven analyses or measured data must be obtained for validation. The hypothetical rotor of Reference 3 was used for this purpose. The input parameters for this articulated (hinged) rotor and for a hingeless rotor are presented in Figure 5.

ROTOR BIADE INPUT PARAMETERS

Type	p	ω_ζ	γ	σ	C_T	C_{do}	R	b	c	β_{pc}	θ_β	θ_ζ	Lag Damper
Hinged	1.031	0.25	7.5	.07	.0063	.01	25'	3	1.83	0	0	0	.1536
Hinge-less	1.136	0.75	9.3	.1	.0062	.01	24.5'	4	1.92	.06	.15	0	0

FIGURE 5

The first rotor is typical of hinged rotors on current operational helicopters. It includes a lag damper, as do most hinged rotors, to insure freedom from mechanical instability, usually called ground resonance. Since the rotor has three blades the third harmonic (3/REV) is the largest source of vibration in the fixed system. However, this 3/REV vibration is caused by 2/REV, 3/REV, and 4/REV shears and moments in the rotating system. The 1/REV forces in the rotating system are most important when considering blade and hub component fatigue lives. The second rotor is called hingeless because it does not have a mechanical hinge to allow flapping and lagging motion as does the hinged rotor. The term "soft inplane" hingeless rotor is often applied because the inplane (lag) frequency is less than the rotor speed (1/REV). This rotor includes β_{pc} and θ_β in its baseline configuration. Since the rotor has four blades the first five rotor harmonics can be considered critical in the rotating system. This rotor is very similar to one of the UTTAS candidate helicopters.

Hinged Rotor Results

Calculated hub vertical and horizontal shears are compared in Figures 6 and 7 with the results of Reference 3. While significant differences exist, the eigenvalue and modal decoupling analysis

results, labeled FL for flap-lag, compares favorably with the much more sophisticated methods.

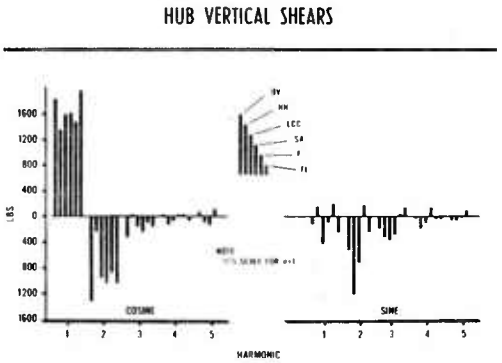

FIGURE 6

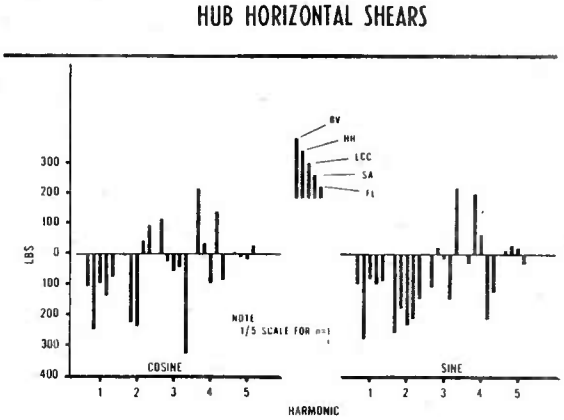

FIGURE 7

Blade lag dampers are considered essential for hinged rotors to insure freedom from mechanical instability. Coalescense between the blade lag motion and the helicopter rolling or pitching motion is the source of this instability. Since the lag motion is lightly damped a mechanical damper is added. Figures 8 and 9 illustrate the effect a mechanical damper setting has on lag damping and lag moments. It is not unusual for an operating hinged helicopter to have a 25% critical damping setting. As can be seen from Figure 9 this damper setting can greatly increase the lag moments.

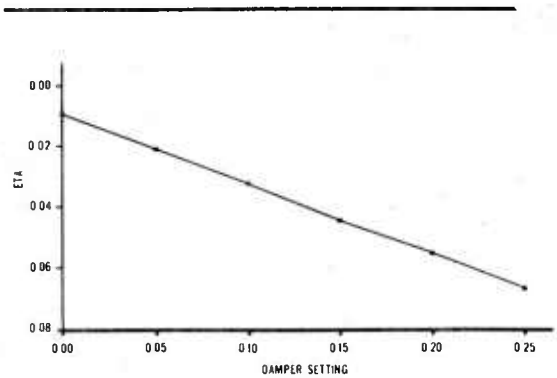

FIGURE 8

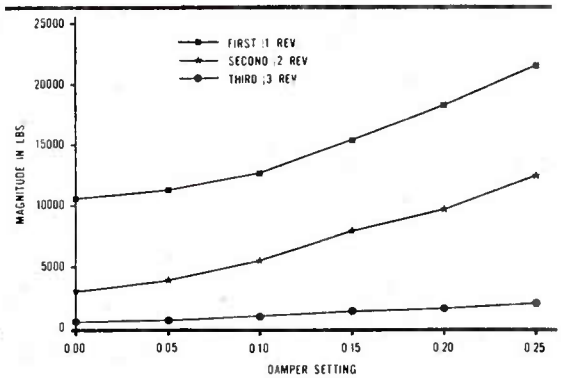

FIGURE 9

On hinged rotors pitch-lag and pitch-flap coupling are due to mechanical linkages which will cause the blade to pitch whenever there is a change in flap or lag angle. The variation of flap and lag damping with pitch-flap coupling is presented in Figure 10. The effect of pitch-flap coupling on lag shears is illustrated in Figure 11. It appears that negative pitch-flap coupling can be used effectively to reduce blade loading and airframe vibration (Figure 11) without jeopardizing stability (Figure 10). The contrary is true for positive pitch-flap coupling which results in a rapid decrease in flap damping above 0.4.

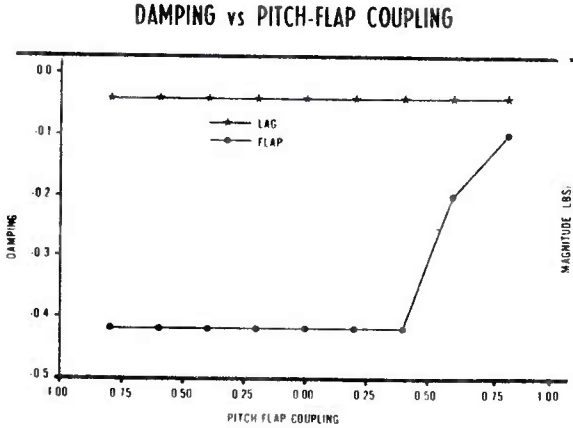

FIGURE 10

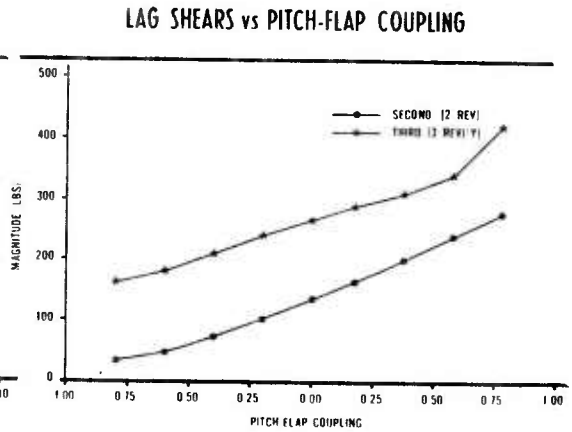

FIGURE 11

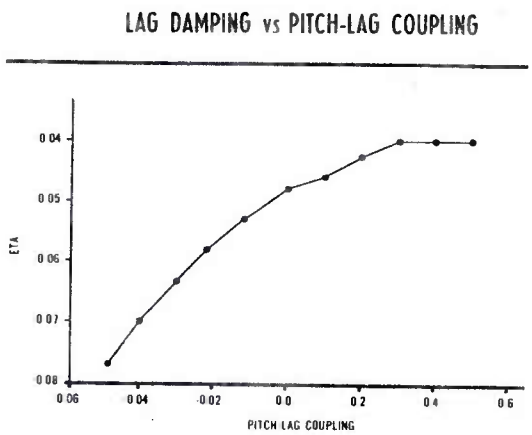

FIGURE 12

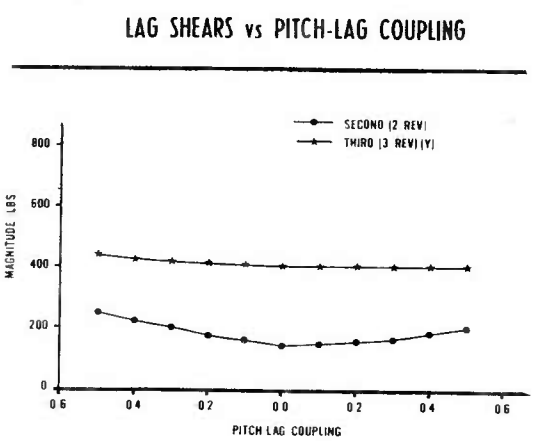

FIGURE 13

Pitch-lag coupling effects are illustrated in Figures 12 and 13. It appears that little benefit is gained with respect to lag

shears. Lag damping varies greatly with pitch-lag coupling. The flattening out of the damping curve in Figure 14 for positive pitch-lag coupling is due to the 15% critical damping setting for the baseline configuration (Figure 5).

Hingeless Rotor Results

Hingeless rotors are attractive because they increase the helicopter's control power, simplify the rotor mechanically, and reduce somewhat the hubweight and aerodynamic drag. With their hub cantilever boundary conditions they do complicate structural dynamic coupling and transmit large vibratory rotor loads into the airframe. Flap-lag elastic coupling is an important consideration on hingeless rotors and an area that is not well understood. Figures 14 and 15 illustrate the effect of flap-lag elastic coupling, R, on lag damping and lag shears, respectively. It can be seen in Figure 14 that small values of R greatly reduce lag damping but that the trend is reversed for larger values of R. With respect to lag shears; the 1/REV shears are greatly increased for small values of R and are relatively constant for larger values.

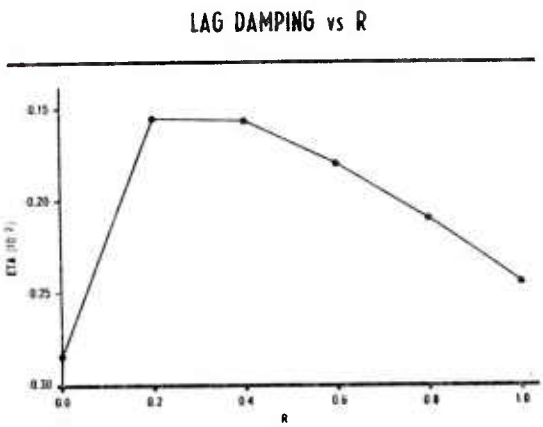

FIGURE 14

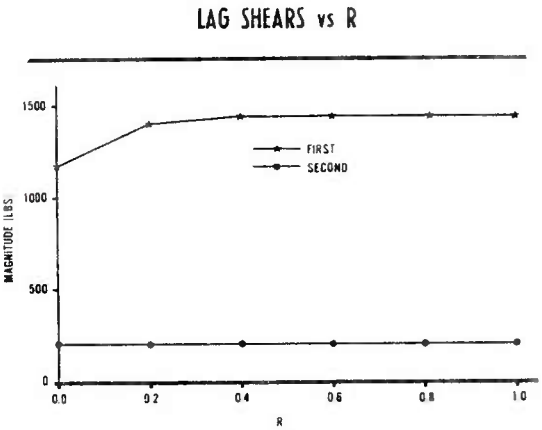

FIGURE 15

The variations with respect to pitch-flap and pitch-lag coupling are similar to the trends found for the hinged rotor. Figure 16 illustrates the reduction in flap damping with positive pitch-flap coupling. For a positive value of 1 the flap damping is reduced to almost zero, the stability boundary. For positive pitch-lag coupling, Figure 17, the lag damping becomes positive, indicating an instability. If no lag damper had been installed on the hinged rotor a similar trend would have been expected.

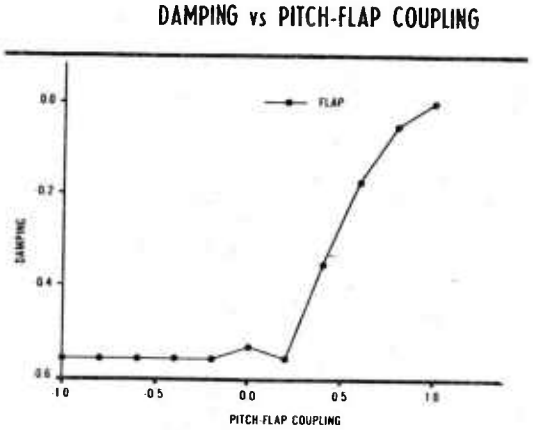

FIGURE 16

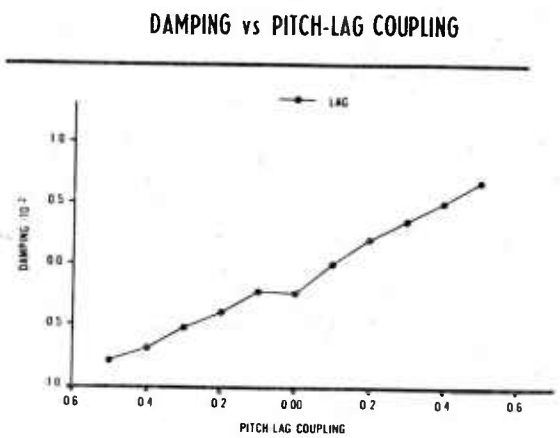

FIGURE 17

CONCLUSIONS AND RECOMMENDATIONS

An eigenvalue and modal decoupling method to predict helicopter rotor stability and forced response has been successfully developed. The advantages of this method are:

1. Stability and forced response are obtained from the same method; thus allowing direct comparison of parametric effects.

2. Only one rotor revolution of numerical integration for an initial condition of unity imposed on each degree of freedom is necessary to define the Floquet Transition Matrix. Therefore, the ambiguous interpretation of time history response data over many rotor revolutions and the separation of transient and forced response is no longer necessary.

3. Additional degrees of freedom such as hub and airframe motions, inflow feedback, etc. in both the fixed and rotating systems can be included since Floquet theory is applicable to equations with periodic coefficients.

The method has been applied to a hinged and hingeless rotor to compare the effect of structural coupling parameters on stability and forced response in forward flight. Significant conclusions drawn from this application are:

1. Pitch-flap coupling has a powerful influence on stability and forced response. Negative coupling reduces lag shears considerably

without jeopardizing stability, while positive coupling produces an opposite effect. This trend was similar for both rotors.

2. Pitch-lag coupling has little influence on forced response but significantly alters lag damping. The use of negative coupling resulted in increased lag damping for both rotors. Positive coupling reduced lag damping for the hinged rotor with lag damper and produced an instability on the hingeless rotor.

3. Variation in lag damper setting on the hinged rotor resulted in significant increases in lag moments and, naturally, increased lag damping.

4. The elastic coupling parameter, R, altered greatly the lag damping on the hingeless rotor. For low values of R the damping decreased drastically but increased again for larger R values. Low values of R also significantly increased the first harmonic lag moments.

The current research has been directed toward developing an alternative solution method to the blade stability and response problem. For this reason a relatively simple mathematical model was used to study the effects of structural coupling parameters. Further research should include:

1. More case studies with the current model to gain a better understanding of the structural coupling parameters in forward flight. Other rotor configurations, such as "stiff inplane" hingeless, should be included.

2. The method should be applied to an elastic blade model to gain a better understanding of higher harmonic interaction.

3. Correlation with wind tunnel and flight measurements should be made to further validate the model and method.

NOTATIONS

a	=	slope of lift curve	β	=	flap angle, pos up, rad
b	=	number of blades	$\bar{\beta}$	=	equilibrium flap angle, $\beta_o + \beta_s S\psi + \beta_c C\psi$, rad
c	=	blade chord, ft.			
c_{do}	=	blade profile drag	β_{pc}	=	precone angle, rad
$C(\psi)$	=	damping matrix	α	=	Locke number, $\rho acR^4/I$
C_T	=	thrust coefficient	$\delta\beta$, $\delta\zeta$	=	perturbation flap and lag angles, rad
$K(\psi)$	=	stiffness matrix			
p	=	nondim. rot. flapping frequency at $\theta=0$, $p=(1+\omega_\beta^2)^{\frac{1}{2}}$	ζ	=	lead-lag angle, pos. fwd, rad
			$\bar{\zeta}$	=	equilibrium lead-lag angle, rad
r	=	blade radial coordinate, ft.	η	=	neg real portion of lead-lag eigenvalue
$\bar{r}$	=	nondim. coordinate r/R	θ	=	pitch angle $\theta + \theta_\beta\delta\beta + \theta_\delta\delta\zeta$
R	=	blade radius, ft., or elastic coupling parameter	$\bar{\theta}$	=	equilibrium pitch angle $\theta_o \pm \theta_s S\psi + \theta_c C\psi + \theta_\beta(\beta-\beta_{pc})$, rad
t	=	time, sec			
T	=	rotor thrust	θ_β, θ_ζ	=	pitch-flap and pitch-lag coupling ratios
V_i	=	uniform induced velocity in negative Z direction, fps	λ	=	inflow ratio $(V_i+V_z)/\Omega R$
			Λ	=	complex eigenvalue, $\Lambda = \eta+i\omega$
V_x, V_z	=	components of helicopter speed in negative X and Z directions, respectively, fps	μ	=	advance ratio, $V_x/\Omega R$
			ρ	=	air density slugs/ft^3
			σ	=	rotor solidity, $bc/\pi R$
X, Y, Z, x, y, z	=	aircraft coordinates and rotating blade coordinates respectively	$\mathcal{T}$	=	period of one revolution, $\mathcal{T} = 2\pi/\Omega$ sec
			$\bar{\Phi}$	=	inflow parameter, $\bar{\Phi} = 4/3\lambda$
$\bar{X}$, $\bar{Y}$	=	Forward and Lateral Shears respectively	ψ	=	rotor azimuth angle, $\psi = 0$ aft, $\psi = \Omega t$, rad, dimensionless time
$L(\psi)$	=	forcing coefficient matrix	ω	=	imaginary portion of lead-lag eigenvalue
$M(\psi)$	=	forcing coefficient matrix	ω_β, ω_ζ	=	dimensionless non-rotating flap and lag frequencies at $\theta = 0$
$N(\psi)$	=	forcing coefficient matrix	Ω	=	rotor angular velocity
			$S\psi$, $C\psi$	=	sine (ψ), cosine (ψ)
			$(\cdot)$	=	$\frac{d}{d\psi}(\ ) = \frac{1}{\Omega}\frac{d}{dt}(\ )$

REFERENCES

1. Mil, M.L., et al, "Helicopter-Calculation and Design Vol. II, Vibrations and Dynamic Stability: NASA TTF-519, May 1968.
2. Schrage, D.P., and Peskar, R., "Helicopter Vibration Requirements," Proceedings, 33rd Annual National Forum of the American Helicopter Society, Washington, D.C., May 1977.
3. Ormiston, Robert A., "Comparison of Several Methods for Predicting Loads on a Hypothetical Helicopter Rotor," Journal of the American Helicopter Society, Vol. 7, No. 4, October 1974.
4. Hodges, D.H., and Ormiston, R.A., "Stability of Elastic Bending and Torsion of Uniform Cantilever Rotor Blades in Hover With Variable Structural Coupling," NASA TN D-8192, April 1976.
5. Peters, D.A., "Flap-Lag Stability of Helicopter Rotor Blades in Forward Flight," Journal of the American Helicopter Society, Vol. 20, No. 4, October 1975.
6. Peters, D.A., and Hohenemser, K.H., "Application of the Floquet Transition Matrix to Problems of Lifting Rotor Stability," Journal of the American Helicopter Society, Vol. 16, No. 2, April 1971.
7. Meirovitch, L., "Elements of Vibration Analysis," McGraw-Hill Inc., 1975.

*SCOVILL, BARTOSEVICH, MASON &
KLAYMAN

AD-A056486

A NEW CLASS OF ANTIMALARIAL AGENTS: 2-ACETYLPYRIDINE THIOSEMICARBAZONES (U)

*JOHN P. SCOVILL, CPT, PhD, JOSEPH F. BARTOSEVICH, BS
CARL J. MASON, AB & DANIEL L. KLAYMAN, PhD
WALTER REED ARMY INSTITUTE OF RESEARCH
WASHINGTON, DC 20012

Malaria remains a formidable global problem in that more than a billion people live in malarious regions and as many as 400 million live in areas where eradication programs have not as yet begun. The continued capability of malaria to disrupt military operations was most recently demonstrated during the Vietnam conflict. The problem has been further complicated by the emergence of highly drug-resistant strains of Plasmodium falciparum--a phenomenon which is being seen increasingly in many other parts of the world. Thus the development of new antimalarial drugs continues to be a high priority project in the Walter Reed Army Institute of Research.

Our investigations into the area of thiosemicarbazone chemistry was prompted by the discovery of the antimalarial activity of 2-acetylpyridine 4-phenyl-3-thiosemicarbazone (WR 190,598). We began a

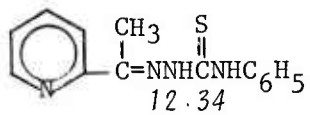

12.34

systematic program of structural modification of this parent compound in an effort to elucidate the molecular features essential for activity.

Examination of the structure of WR 190,598 suggested a myriad of possible variations. 1) The portion of the molecule derived from 2-acetylpyridine might be replaced by any of a large number of aromatic, heteroaromatic, cycloaliphatic aldehydes or ketones. 2) As for the

thiosemicarbazone portion of the molecule, substitution is possible on the nitrogen atom at position 2, while at position 4 a virtually limitless number of mono- and disubstituted analogs can be conceived. 3) The sulfur-containing function at position 3 can be replaced by an oxygen-containing carbonyl group.

The screening of candidate drugs was performed in mice at the University of Miami under a U.S. Army contract.

Results

Initially, a series of 4-substituted thiosemicarbazones was synthesized in which the pyridylethylidene moiety derived from 2-acetylpyridine was replaced by a variety of heterocyclic aldehydes, such as 5-nitrofurfural, 2-thiophenecarboxyaldehyde, and indole-3-carboxyaldehyde; and phenyl ketones and aldehydes, such as p-chloro-acetophenone, m-fluorobenzaldehyde, piperonal, 3,4-dimethoxy benzaldehyde, and cinnamaldehyde. 1-Adamantyl methyl ketone was also tried. In no instance was antimalarial activity observed in the above classes of compounds.

Upon returning to the acetylpyridines, it was found that activity was imparted only by the compound bearing the keto function in the 2-position (Cf. Table 1).

Table 1. Antimalarial Activities of Four Isosteres of WR 190,598 and a 2-Substituted Analog.

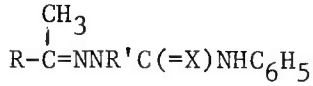

Cmpd No.	R	R'	X	Antimalarial Activity*
WR 190,598	2-Pyr	H	S	C(2/5) 320 mg/kg; C(4/5) 640 mg/kg
WR 232,145	2-Pyr	CH_3	S	Active 320 mg/kg; C(1/5) 640 mg/kg
WR 190,429	3-Pyr	H	S	Inactive
WR 190,612	4-Pyr	H	S	Inactive
WR 210,219	Ph	H	S	Inactive
WR 233,150	2-Pyr	H	O	Inactive

Pyr = pyridine; Ph = phenyl
*C = cures; number of treated mice which survived >60 days.
Active = at least a 100% increase in the mean survival time of treated mice over that of controls.

These data, along with others, led us to believe that the presence of a 2-pyridyl ring at position R is essential, as is the presence of sulfur in the carbonyl group. The greatly diminished activity of WR 232,145 suggested that preparation of 2-substituted derivatives would not be rewarding. Thus our consideration was limited to the study of the effects of replacement of the methyl group in 2-acetylpyridine and effects of mono- and disubstitution of the nitrogen at position 4.

Many ring substituted 4-phenyl-3-thiosemicarbazones were prepared which contained alkyl, hydroxyl, nitro or halo substituents attached to the phenyl ring. Some, such as the 2-fluorophenyl and 3-fluorophenyl analogs, produced cures, but none showed any substantial improvement over the unsubstituted parent compound, WR 190,598.

Substitution of 2-formyl or 2-propionylpyridine for 2-acetylpyridine resulted in a reduction or abolition of activity (Table 2). Thiosemicarbazones containing side chains derived from useful antimalarial drugs were also prepared. Thus the 4-amino-3-diethylamino-o-cresol group from amodiaquine was attached to position 4 to give WR 229,090 as was the 4-diethylamino-1-methylbutyl side chain from chloroquine and pamaquine, producing WR 224,895. Both of these compounds were inactive.

Table 2. Antimalarial Activity of Some Substituted 4-Phenyl Analogs of 2-Acetylpyridine

2-Pyr(R)-C=NNHC(=S)NHR'

Cmpd No.	R	R'	Antimalarial Activity*
WR 32,974	H	C_6H_5	Inactive
WR 190,594	CH_3	C_6H_5	C(2/5) 320 mg/kg; C(4/5) 640 mg/kg
WR 228,397	CH_3	$2\text{-}ClC_6H_4$	Active 320 mg/kg; Active 640 mg/kg
WR 229,090	CH_3	$4\text{-}OH\text{-}3\text{-}CH_2N(C_2H_5)_2C_6H_3$	Inactive
WR 224,895	CH_3	$4\text{-}CH(CH_3)(CH_2)_3N(C_2H_5)_2$	Inactive
WR 227,502	CH_2CH_3	$2\text{-}ClC_6H_4$	Inactive

*See Table 1 for explanation of biological data

*SCOVILL, BARTOSEVICH, MASON &
KLAYMAN

A large number of 4-alkyl and 4-cycloalkyl thiosemicarbazones were prepared of which the 4-benzyl and 4-phenethyl thiosemicarbazones showed some activity. The 4-alkyl compounds, however, were inactive. The medicinally interesting admantyl group when attached in the 4 position gave an active compound (Table 3). This suggested that favorable results might be obtained by the attachment of bulky

Table 3. Antimalarial Activities of Some 4-Alkyl and 4-Cycloalkyl Thiosemicarbazones

$2\text{-Pyr}(CH_3)C{=}NNHC(=S)NHR$

Cmpd No.	R	Antimalarial Activity*
WR 204,584	adamantyl	Active 320 mg/kg, C(1/5) 640 mg/kg
WR 229,805	$-CH\overset{\frown}{(}CH_2)_5$	C(2/5) 160 mg/kg, C(3/5) 320 mg/kg C(2/5) 640 mg/kg, T(3/5) 640 mg/kg**
WR 231,011	$-CH\overset{\frown}{(}CH_2)_7$	Active 640 mg/kg, T(1/5)**
WR 231,534	$-C(CH_3)_2CH_2C(CH_3)_3$	Active 640 mg/kg
WR 227,817	$-CH_2C_6H_5$	Active 320 mg/kg, C(3/5) 640 mg/kg

* See Table 1 for explanation of biological data
**Toxic deaths

groups at this location. To this end a number of derivatives incorporating features of the adamantyl group were prepared. These included the 4-t-butyl and 4-t-octyl thiosemicarbazones, the latter possessing marginal activity (Table 3). However, simplification of the adamantyl ring system gives cyclohexane and 2-acetylpyridine 4-cyclohexyl thiosemicarbazone possessed appreciable antimalarial activity.

A fanciful connection between the adamantyl ring system and that of 3-azabicyclo[3.2.2]nonane suggested the preparation of WR 230,190.

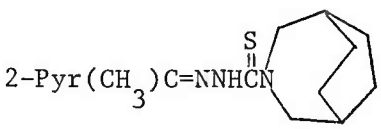

WR 230,190

*SCOVILL, BARTOSEVICH, MASON &
KLAYMAN

This compound possesses excellent antimalarial activity, producing cures at a dosage as low as 20 mg/kg. The ED_{50} was estimated to be 50 mg/kg. Simplification of structure of WR 230,190 by elimination of the two carbon bridge gives WR 231,010, which also exhibited good

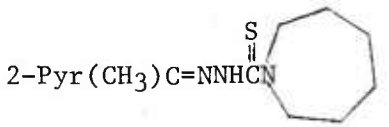

WR 231,010

antimalarial activity. Scission of the carbon bridges of 230,190 yields WR 232,178, which was inactive. Many cyclic amines gave deriv-

WR 232,178

atives with good antimalarial activity (Table 4). Exploitation of this lead led to the synthesis of WR 235,591, which is the most active

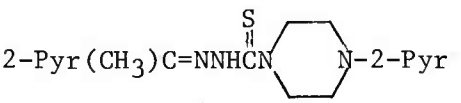

WR 235,591

antimalarial yet produced in this class of compounds.

Consideration of the tuberculostatic property of certain pyridylcarboxaldehyde thiosemicarbazones suggested that antimalarial 2-acetylpyridine thiosemicarbazones might possess useful antibacterial activity. We were able to secure the cooperation of Dr. Arthur Dobek of the Division of Communicable Diseases and Immunology (WRAIR), who established an antibacterial screening system. These compounds were ineffective against Gram negative bacteria, however, they possessed high activity against Gram positive organisms (Table 5). The minimal inhibitory concentration (MIC) of WR 230,190 against 36 recent clinical isolates of Staphylococcus aureus was found to be 1 µg/ml. Further testing of 12 of the testing strains showed that this concentration was also bacteriocidal. Some compounds which are devoid of antimalarial activity are highly bacteriostatic.

Table 4. Antimalarial Activities of Some 4,4-Disubstituted Thiosemicarbazones

2-Pyr(CH_3)C=NNHC(=S)R

Cmpd No.	R	Antimalarial Activity*
WR 231,533	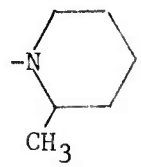	C(2/5) 40 mg/kg
WR 231,010	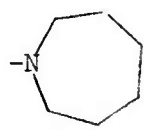	C(3/5) 40 mg/kg; C(4/5) 80 mg/kg
WR 230,190	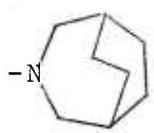	C(1/5) 20 mg/kg; C(3/5) 40 mg/kg; C(5/5) 160 mg/kg
WR 233,545	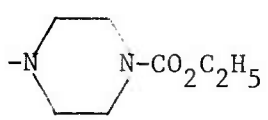	C(2/5) 40 mg/kg
WR 232,706	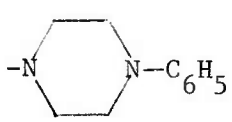	C(4/5) 160 mg/kg
WR 235,591	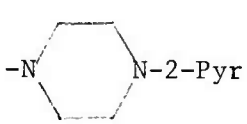	C(3/5) 20 mg/kg; C(4/5) 40 mg/kg; C(5/5) 80 mg/kg

*See Table 1 for an explanation of biological data.

Table 5. Antibacterial Activities* of Some Selected 2-Acetylpyridine Derivatives

2-Pyr(CH_3)C=NNHC(=S)-R

Walter Reed Code Number	WR 223,662	WR 229,805	WR 230,190	WR 232,704
	4-ClC_6H_4-NH	Cyclohexyl-NH	3-(3-azabicyclo [3.2.2]nonyl)	1-(4-methyl-piperidyl)
Bacterial Strain		1	<0.25	
Staph. aureus 15A4 (16 Feb 1944)	3	1	<0.25	
15A5 (1 Jul 1944)	3	1	<0.25	
ATCC 10537 (9 Nov 1949)	1	1	<0.25	
Lafferty	1		<0.25	2
Strep. durans ATCC 9810 (27 Jul 1955)	2		<0.25	2
Strep. pyrogenes 12A2 (22 Feb 1944)	1		<0.25	0.5
ATCC 10100 (8 Aug 1947)	0.25			0.25
Group D Enterococcus**		4		4
Group C Meningococcus**		0.25		<0.25

* Minimal Inhibitory Concentrations given in µg/ml.
**Recent clinical isolates.

*SCOVILL, BARTOSEVICH, MASON &
KLAYMAN

A Possible Mechanism of Action

The biological basis of the antibacterial and antimalarial activity of the compounds described in this paper has not been studied as yet. However, French and coworkers [J. Med. Chem., 13, 1117 (1970)] have proposed a provisional explanation of the antitumor effects of the generic class to which these compounds belong. The following observations may be pertinent: 1) Thiosemicarbazones of this class are strong chelating agents and act as tridentate ligands for suitable metal ions, i.e., Fe, Cu, Zn. 2) Iron stimulates the activity of cytidine diphosphate reductase isolated from Novikoff hepatoma. 3) Ribonucleoside reductases (RDR) isolated from various mammalian tumors have an obligatory requirement for iron. 4) 1-Formylisoquinoline thiosemicarbazone is a very potent inhibitor of DNA synthesis but has little effect upon RNA and protein synthesis by sarcoma 180 cells in vivo. 5) The better tumor inhibitors had $K_i 50$ against a mammalian RDR in the range of 10^{-6} to 10^{-7}M. Related compounds such as 3-formylpyridine thiosemicarbazone which did not contain the proper tridentate ligand orientation were only active at much higher concentrations (10^{-3}M) and were not active against the tumor in vivo.

In view of these observations, French has proposed that heterocyclic formylthiosemicarbazones act by forming a complex with enzyme-bound iron as illustrated below:

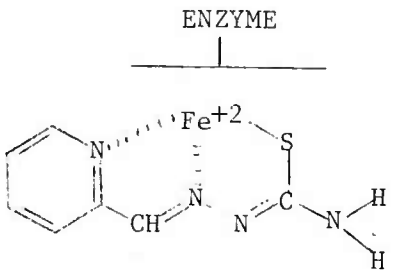

Tenacious binding of the enzymatically-essential iron by the thiosemicarbazone would thus block the active site of the enzyme. This concept also offers an explanation for the lack of antimalarial activities of the isosteres of WR 190,598 (see Table 1); that is, those compounds in which the orientation of nitrogen in the pyridyl ring precludes chelation should be inactive and the compound in which sulfur has been exchanged for the non-chelating oxygen function should also be inactive.

*SCOVILL, BARTOSEVICH, MASON &
KLAYMAN

Organic Chemistry

Three synthetic procedures proved to be useful for the preparation of the thiosemicarbazones required for this study.

In Scheme A, a primary amine was converted to the corresponding isothiocyanate (1), ordinarily by employing thiophosgene. Reaction of 1 with hydrazine afforded a thiosemicarbazide 2. Condensation of this intermediate with 2-acetylpyridine provided the 4-monosubstituted thiosemicarbazone 3. A drawback of this approach is that only thiosemicarbazones monosubstituted at position 4 can be prepared in this manner,

Scheme A

$$RNH_2 + C(=S)Cl_2 \longrightarrow \underset{1}{R\text{-}N=C=S} \xrightarrow{H_2NNH_2} \underset{2}{R\text{-}NHC(=S)NHNH_2} \xrightarrow{2\text{-}Pyr(CH_3)C=O} \underset{3}{2\text{-}Pyr(CH_3)C=NNHC(=S)NHR}$$

as 2-acetylpyridine proved to be usually resistant to condensation with 2,4-disubstituted thiosemicarbazides.

In Scheme B, reaction of hydrazine and carbon disulfide in the presence of sodium hydroxide yielded a dithiocarbazate. Alkylation of this dithiocarbazate with either iodomethane or dimethyl sulfate gave methyl dithiocarbazate (4). Condensation of 4 with 2-acetylpyridine gave the versatile intermediate, 3-[1-(2-pyridyl)ethylidene]-S-methyldithiocarbazate, 5. Reaction of 5 with primary amines gave 4-monosubstituted thiosemicarbazones such as 3 while secondary amines or cyclic amines produced 4,4-disubstituted thiosemicarbazones, 6. In addition, reaction of 5 was not limited to more active nucleophiles, as excellent yields could be obtained with many primary aromatic amines. However, 5 was resistant to reaction with secondary aromatic amines, such as N-methylaniline.

Scheme B

$$\underset{4}{H_2NNHC(=S)SCH_3} + 2\text{-}Pyr(CH_3)C=O \longrightarrow \underset{5}{2\text{-}Pyr(CH_3)C=NNHC(=S)SCH_3} \xrightarrow{HNR'R''} \longrightarrow \underset{6,\ 3(R'=H)}{2\text{-}Pyr(CH_3)C=NNHC(=S)NR'R''}$$

Scheme C involved the reaction of 2-acetylpyridine with hydrazine to yield the hydrazone 7. Reaction of this hydrazone with an isothiocyanate 1 produced a 4-monosubstituted thiosemicarbazone 3. This reaction was especially useful when the required isothiocyanate was commercially available.

Scheme C

$$2\text{-Pyr}(CH_3)C{=}O + H_2NNH_2 \longrightarrow \underset{7}{2\text{-Pyr}(CH_3)C{=}NNH_2} \xrightarrow{1} 3$$

Conclusion

The preparation of WR 231,010 represents an 8-fold improvement in efficacy over that of our initial model, WR 190,598. Now that a clearer understanding of the relationship between structure and activity in this new class of antimalarial agents has been obtained, it is hoped that continued efforts in this area will produce even more fruitful results.

Acknowledgement

We thank Colonel Craig J. Canfield and Dr. Thomas R. Sweeney for interest and encouragement throughout these studies.

AD-A056487

APPLICATIONS OF A GATED IMAGING SYSTEM IN EVALUATION OF LASER DESIGNATOR PERFORMANCE

WILLIAM E. SHAW
ARMY MATERIEL TEST & EVALUATION DIRECTORATE
US ARMY WHITE SANDS MISSILE RANGE

In the early 1970's the Army Materiel Test and Evaluation Directorate, White Sands Missile Range, undertook a multi-year test methodology development program to perfect techniques and develop hardware required to evaluate an anticipated family of Army Laser Designators. Standard laboratory test instruments and procedures were readily available; however, the more complex problems of energy distribution within the laser beam were not resolved. A concurrent development, at this point, was a shift toward acquiring data, wherever possible, in an image format, and subsequently processing the data on a large-scale digital computer. These two ideas led to the development and subsequent procurement of a data acquisition system known as the Laser Spot Scanning System or LS^3.

The LS^3 is a gated, image-intensified silicon vidicon camera with a standard S-1 response. The camera is equipped with a 1.06 micron spike filter mounted on a 15 mm to 150 mm zoom lens. Mounted on top of the camera's environmental container is a YAG 444 series photo-diode with associated optics. The photo-diode controls the gating function of the camera. Control of the camera is remoted, and the output recorded on a standard video tape recorder and/or displayed on a standard closed circuit television monitor. (See Fig. 1, for LS^3 configuration).

The LS^3 is operated in one of two modes. The gated mode is used to provide the greatest system dynamic range, and is required for collecting energy mapping data. In this mode, the photo-diode senses the first two laser energy returns from a device under test, sets a time interval, and gates the image intensifier high voltage on at the time of the next anticipated pulse. The next pulse, and following pulses, must arrive within +8, -2 microseconds of the

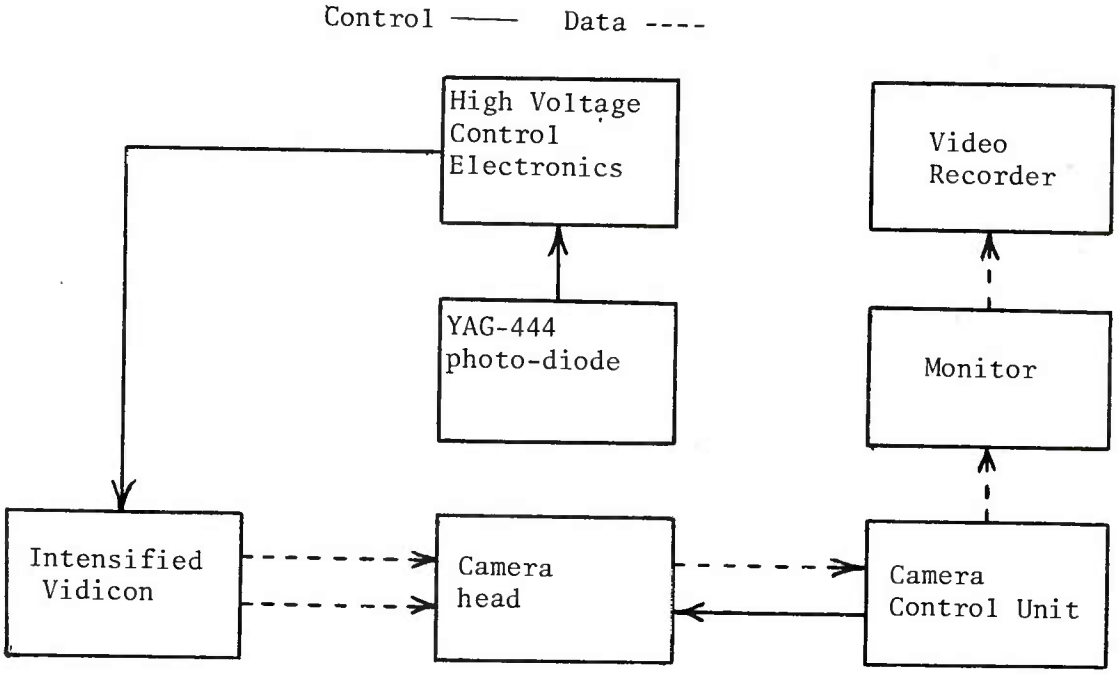

Figure 1 LS^3 Configuration

computed time to retain lock. If the incoming pulse is outside the time limits, two more pulses are required to reset the gating network. Maximum sensitivity of the camera in this mode is 1×10^{-9} w/cm^2; the instantaneous dynamic range of the unit is 48:1 in terms of irradiance at the input aperture. The video voltage output is non-linear, being proportional to the input irradiance to the .74 power. Verification of these operating parameters was achieved using concurrent imaging and radiometric measurements. This same technique was also used to map the surface of the intensifier vidicon for uniformity. A point source was placed in a number of geometric locations, to repeatedly impinge on the major areas of the vidicon surface and the resultant analog voltage of the video waveform was then compared to the measured radiometric value of the input source.

Within the "usable" 80% of the surface area of the vidicon, uniformity is $\pm$ 5%, worst case. There are some areas at the edge of the vidicon with variations of $\pm$ 10%.

An alternate mode of operation for the LS^3 is achieved by "short-circuiting" the high voltage power supply and forcing the unit to operate as a standard image-intensified vidicon camera. In either mode, the spectral response of the unit is S-1 or roughly from .35 to 1.1 microns as shown in Figure 2.

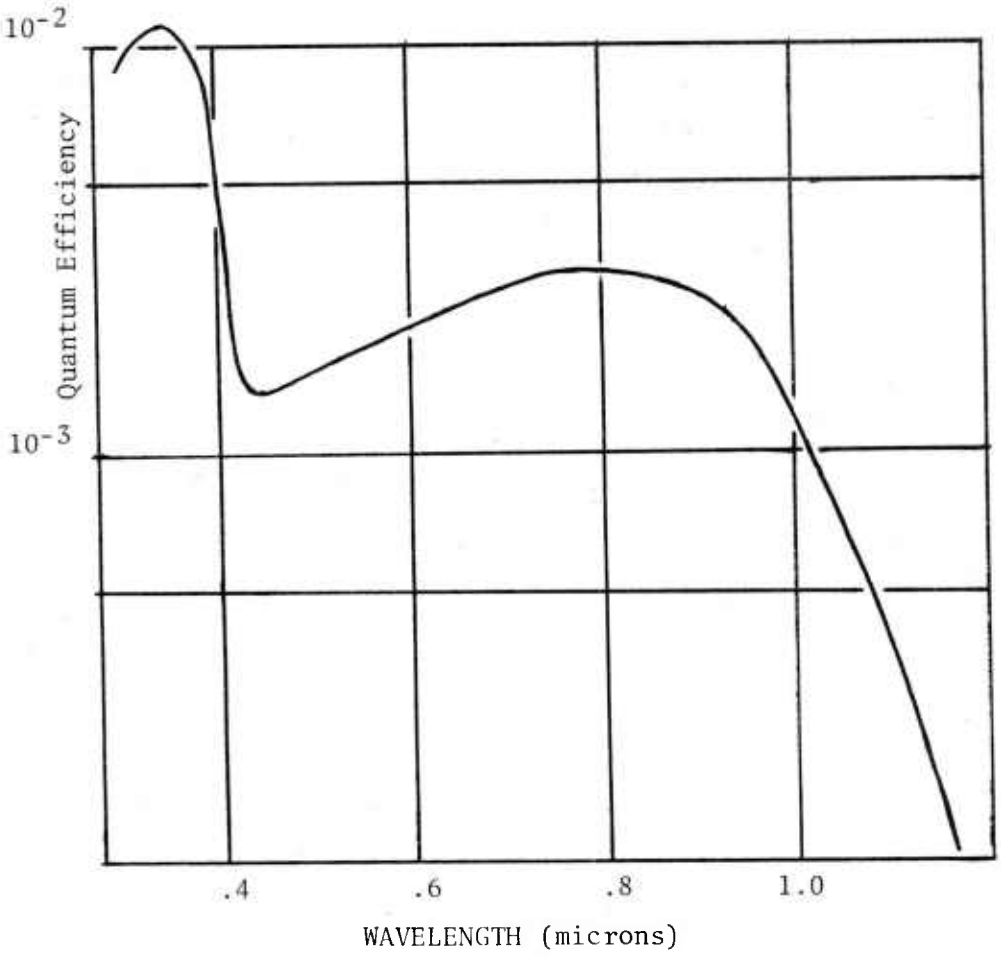

Figure 2 - Image Intensifier Spectral Response

If necessary, the unit could be used to test any type of laser in this spectral band; however, its primary function is in evaluating 1.06 micron laser designators.

The culmination of the LS^3 methodology development came during the recent (summer of 1977) DT-II test of the Ground Laser Locator Designator (GLLD). Three basic categories of data were collected during this test: pointing and tracking data, energy distribution or mapping data, and transmission data through smoke and dust clouds. All data were collected from flat panel targets as sketched in Figure 3.

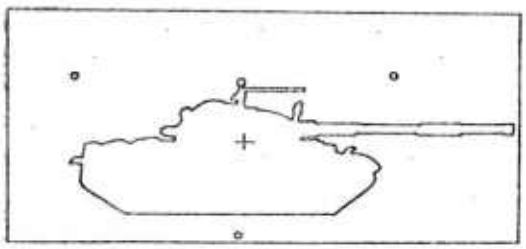

Figure 3a-Test Target, Side Silhouette with Marked Aimpoint

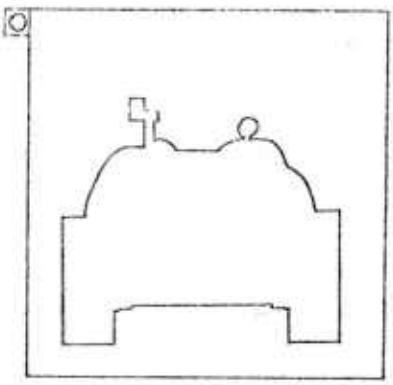

Figure 3b-Test Target Front Silhouette

Figure 3a shows a side silhouette of a full-scale (dimensionally) Soviet T-62 tank. Three beacons (flood lamps) were required to scale data and establish a frame of reference during moving target data collection sequences. The target measures 36 feet (long) by 16 feet (high) and is mounted on a 40 foot long flat bed trailer. The trailer also carries its own motor generator to provide power for the beacons and an inserted steel panel equipped with heater strips to provide for day and night tracking.

The data taken are ultimately used to calculate an energy centroid position for each laser pulse arriving at the target. This necessitated some other design considerations. Specifically, the flatness of the target is important to maintaining the uniformity of reflections. Also the target presented to the GLLD operator must be of high contrast, but the reflectivity of the target at 1.06 microns must be uniform so that the data is not perturbed at the edges of the silhouette. Paint for the target was painstakingly blended in the laboratory until three colors, presenting high visual contrast, within 1% of the same reflectivity at 1.06 micron were developed.

Figure 3b is a frontview silhouette (full-scale) of the T-62 tank. This target is presented on a 12 foot square panel and was used in data collection for stationary "pointing" data runs, energy mapping runs, and transmission tests through smoke and dust.

Stationary runs were done at ranges to 9 Km. Energy maps were gathered at 3 and 5 Km under low, moderate and high scintillation conditions. Tracking or moving target runs, were done at slow, variable and high speeds at ranges to 7 Km. All data taken during the test were collected on video tape. The recorder used was a standard one-inch International Video Corporation (IVC model 800A

recorder). IRIG-B time was encoded on one of the two audio channels of the recorder. The second audio channel was used for voice annotation of the data. Video data tapes were then transferred to the ARMTE Image Analysis System for processing.

As mentioned earlier, concurrent to the development of the LS^3 data acquisition system, emphasis was being placed on utilization of a common processing facility for a wide variety of data collected in, or transformed into, an image format. The system which eventually grew out of this philosophy is shown in Figure 4 below.

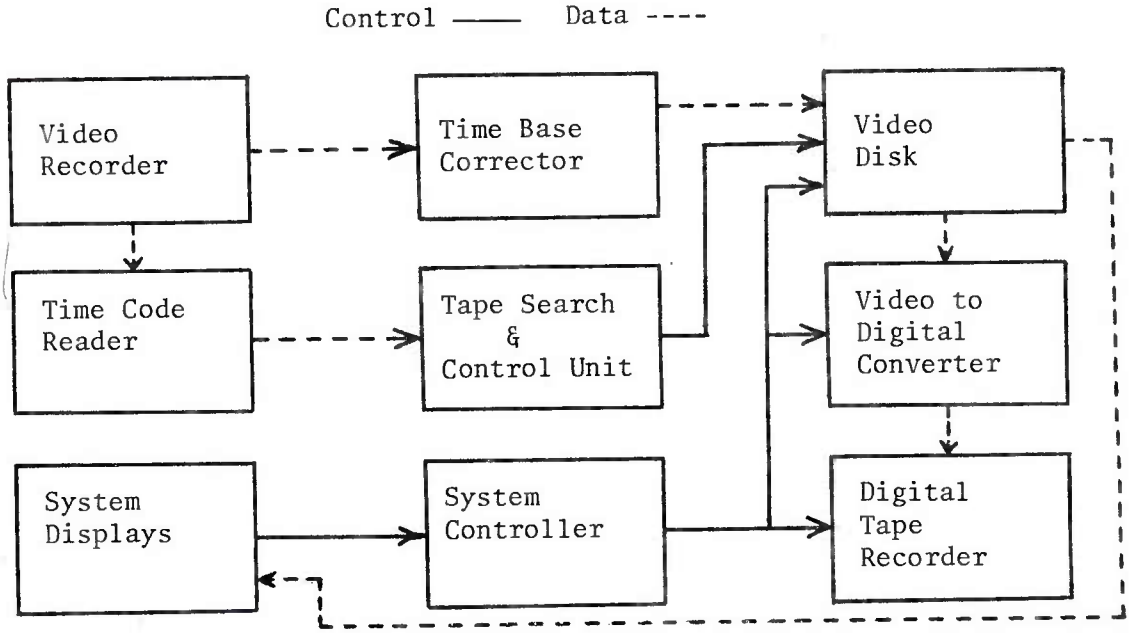

Figure 4 - Data Conversion/Processing System Configuration

The video tape data described above are input to the system through a Time Base Corrector, required to match the recorder and system synchronization. An IVC Model 875 recorder is needed since it is capstan-servoed, a requirement in matching synchronization. The tape is read onto an analog video disk in bursts of 5 seconds. Timing is controlled by a tape search unit, enabling the operator to exactly match four five-second data segments into a complete twenty second data run.

Once the data are stored on the analog video disk, they are then digitized and stored again in 7-tracks on digital tape. Digitizing is done vertically, one field at a time. Figure 5 represents the data format as it would appear on a television monitor.

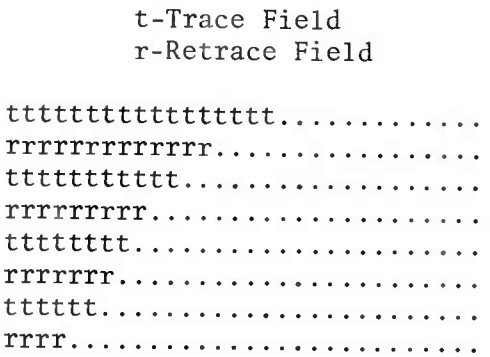

Figure 5 - Television Data Format

For full-frame digitizing, the trace field is first converted as a series of vertical lines; then the retrace field in a similar manner. While this pattern is somewhat inconvenient, it provides the maximum time efficiency for re-recording the digital data on 7-track tapes. Digitizing a full frame (both fields) requires 43 seconds.

In most cases, the actual data exists in a smaller area of the picture. In order to save time and tape space, a series of "windows", controlled by the systems mini-computer, are used. The "windows" are generally 200 X 200 or 100 X 100 matrices which may be positioned on the overall 680 X 512 point matrix of the picture. In the case of data reduction for a pulsed laser designator, the windows used are single field. This is necessary to lend any real credence to the data from the LS^3 system described above. If the pulse repitition frequency (prf) of the laser is an even factor of sixty, dividing into sixty an even number of times, such as 5, 6, 10, 15, or 30 pulses per second, the first, or trace, field of an image will be valid. The gating of the intensifier affects only the input of the image data while the vidicon is read in a free-running mode at 60 fields per second. If, however, the prf is an odd factor of 60, such as 12 or 20, the trace or retrace field may be valid, depending upon the position of the pulse frame in the data sequence.

The subroutines used in digitizing a given data run is then dependent both on the laser device prf for the particular pointing/tracking sequence, the geometry of the data collection system, and the average position of the data on the display screen. The equipment operator selects the appropriate factors and the 5-second quarter segment of the data run is then digitized. Once the operator selections are made, the balance of the work is assumed by the digital system's mini-computer controller. Based upon the pre-programmed guidance of the operator, the analog disk is incremented in the

required steps to maintain the data sequence, and appropriate fields are digitized and stored in 4096 word blocks at eight bits per word. Header records are used with the data to identify all the necessary ancillary information for ultimate processing, including run sequence number, environmental conditions - if appropriate, operator and device identifiers, and the starting address of the digital matrix coordinates - if required. The bulk of the data on a roll of tape consists of intensity of "gray-scale" values of the various picture elements or "pixels". These values are stored in eight bits, providing a range of 256 possible levels. They are the only required values since the geometric coordinates are known from the known sequencing of the digitizer.

Once the operator has a complete data run of 20 seconds stored on 7-track digital tape, the tapes are transferred to the range's large-scale computers for processing. Dependent upon the class of data, i.e. mapping, tracking, or transmission, different reduction programs are applied.

Energy mapping is, of course, the most obvious of applications. No other approach can readily compete with the image camera for the collection of energy mapping data. The only alternative would be a massive array of detectors (348,000)to compete with the camera on a 1 to 1 basis) which would be far too expensive to buy and a nightmare to use.

Energy map data are read into the large-scale computer one frame (field) at a time. Using a pre-determined set of calibration factors for the various intensity levels, the energy contained with the reflected spot is calculated as a weighted sum. This value is then compared to the anticipated energy at the target, considering laser output, range to target, and atmospheric conditions. The result is one data point of the energy versus time data plot for the map run. These plots are expressed as % minimum anticipated energy vs. time, keeping the data unclassified for ease of handling. Ninety-nine more such frames are then processed to produce the plot. The time interval between data points is then .2 seconds. In addition to the energy calculation, the x and y coordinates of the energy centroid are also calculated for each pulse of the data run and appropriate plots are generated.

The primary purpose of energy mapping in the Development Test II (DT-II) of the GLLD system was to acquire data for use in theoretical mathematical models of the effects of the Atmospheric Structure Coefficient (C_n^2) on the transmission of the laser radiation. To this end, in addition to data plots, energy map data were reformatted into 200 X 200 point matrices representative of the spatial distribution of energy levels for direct insertion into digital mathematical models. The in-depth analysis of this data is being done at the Electronics Research and Development Command(ERADCOM)

Fort Monmouth, NJ and by members of the Laser Designator Weapons System Simulation (LDWSS) group at the Missile Research and Development Command (MIRADCOM), Redstone Arsenal, AL. Their results were not available at this writing; however, presented below in Figure 6 are the energy versus time plots for a laser device at 3Km range under low, moderate, and high scintillation conditions.

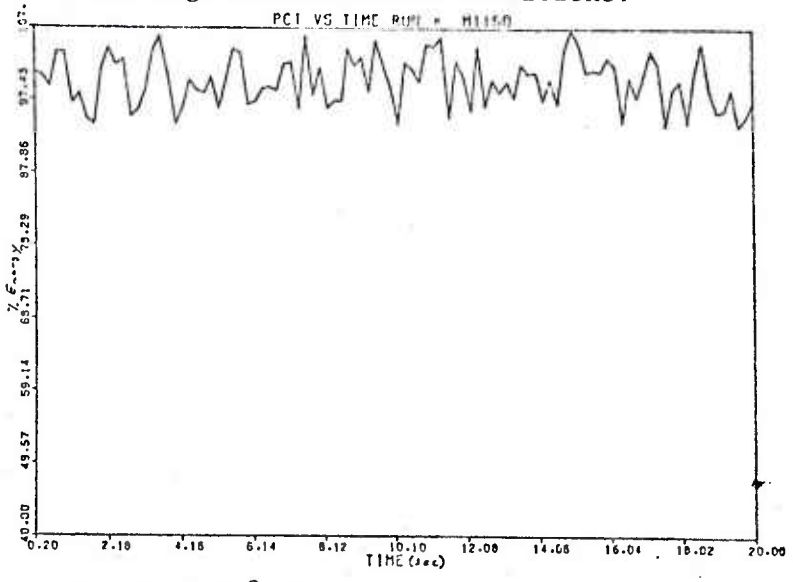

Figure 6a- Weak C_n^2, Percent Energy vs Time

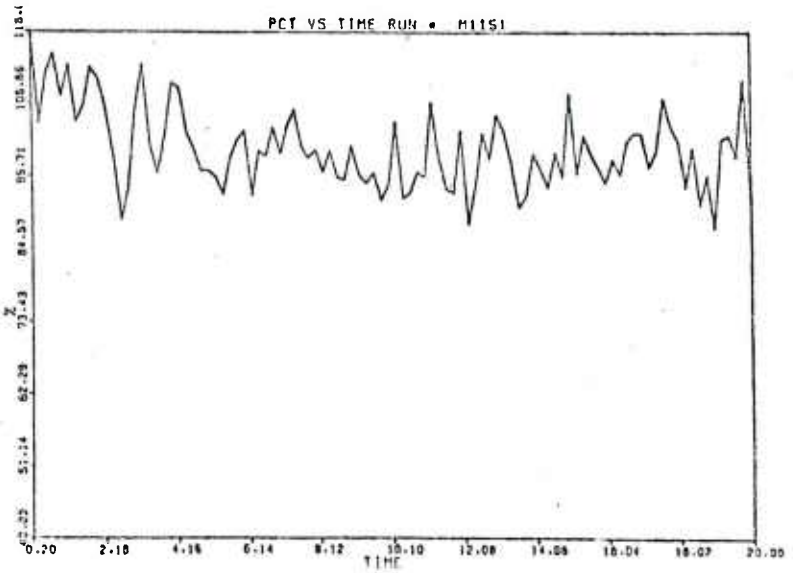

Figure 6b-Moderate C_n^2, Percent Energy vs Time

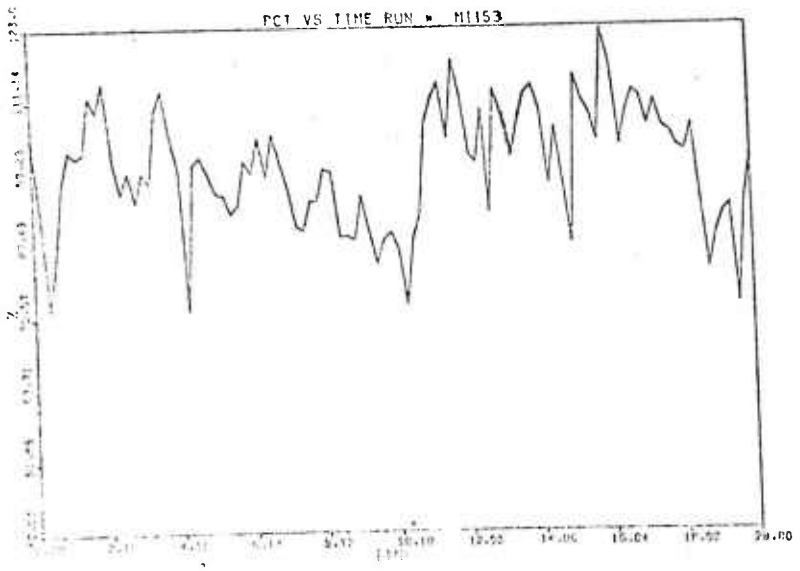

Figure 6c-Strong C_n^2, Percent Energy vs Time

Due to the magnitude of the apparent energy fluctuations, the follow-up test run on a 50 pulse sample of near-field (3 meters) data. The resultant % energy vs time plot is shown below in Figure 7.

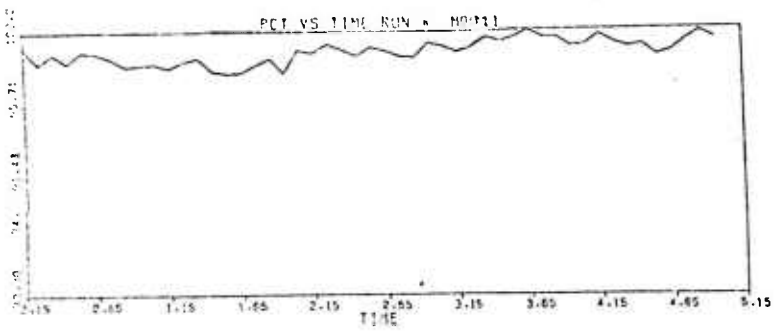

Figure 7-Near Field (3 meters), Percent Energy vs time

Data for laser transmission through smoke and dust are processed in much the same manner as the energy maps and portrayed in similar data plots. Transmission of laser energy through smoke apparently correlated well with previously established laboratory results.

The bulk of the data collection/reduction for GLLD DT-II involved system pointing and tracking accuracy. Nearly two hundred

data runs (twenty seconds each) were processed, representing a variety of target and designator configurations. Use of the gated imaging system was desirable in that the actual energy centroid can be calculated from the image and the energy centroid is the track point of a homing system. Substantial conflict about the adequacy of the LS^3 system and its subsequent reduction hardware and software existed prior to the GLLD DT-II, and a series of experiments were conducted prior to the testing phase to resolve this conflict. Accuracy of the calculations of centroid position was questioned. This was resolved by imaging known sources and carrying the process through to its conclusion. The results showed an uncertainty of 1/2 of a pixel, the predicted uncertainty derived from the data conversion process. A second source of concern was the conversion of coordinates and scaling on the moving target, Figure 3a above. The target was run over a typical course with a fixed source mounted at the aimpoint, then at known coordinates in each "quadrant" of a set of axes zeroed at the aimpoint. The results demonstrated an accuracy limit of 25% of the previously established accuracy requirement.

Processing data for pointing and tracking accuracy requires two major subroutines, coordinate conversion/scaling, and centroid position scaling. For a fixed target, the coordinate set and scale factors are already known; however, each image for a moving target, or tracking, run may have a different frame of reference. Since all target roads were flat, no vertical corrections were required. Horizontal corrections (cosine function) were required, as were scale factors as the target first approached and then receded from the data collection system.

Once these corrections are made, the location of each pixel of a given data frame relative to the target aim point is unknown, and the energy centroid position of the laser spot can be calculated.

Using the representative printed version of a typical laser return as displayed in alphanumeric form below, the energy centroid coordinates are determined, in pixels, using the following expression:

$$X_E = \frac{\sum_i A_i \; E_i \; X_i}{\sum_i A_i \; E_i} \qquad (1)$$

$$Y_E = \frac{\sum_i A_i \; E_i \; Y_i}{\sum_i A_i \; E_i} \qquad (2)$$

Figure 8-Energy Level Distribution in a Reflected Laser Spot

where X_E, Y_E are the X and Y coordinates of the energy centroids, Ai is the number of pixels in i^{th} iso-energy band, and Ei is the intensity scaling factor of the i^{th} iso-energy band.

Plots of centroid position (X and Y) are then generated versus time for each twenty second data run. Subsequent statistical calculations are used to determine the mean and standard deviation in X and Y for the entire data run. A typical output plot is shown below in Figure 9.

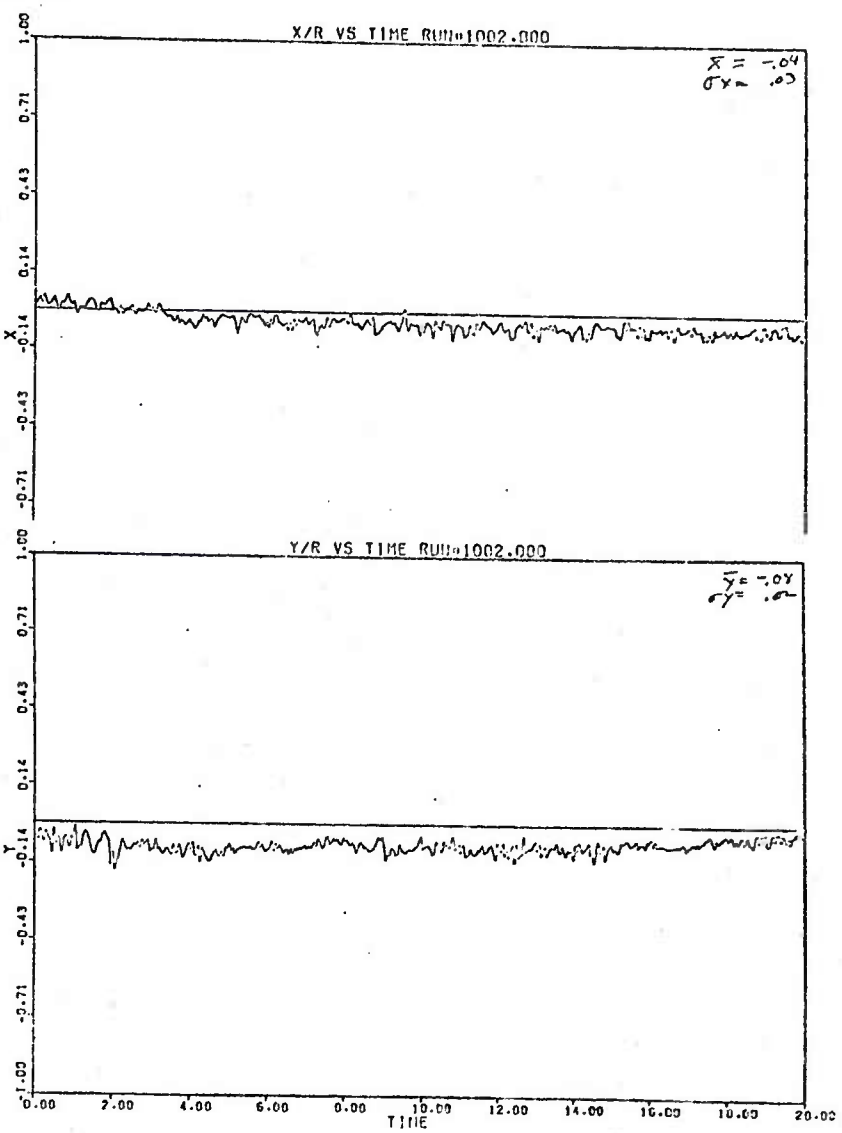

Figure 9-Tracking Accuracy in X and Y

In addition to the plots and calculations referenced above, digital tapes of the X, Y data were forwarded to MIRADCOM for direct insertion into the LDWSS operating model.

Since the GLLD test is now history, let me conclude by discussing a few of the lessons learned from the effort, and resulting plans for system improvement. First, the sensor used, the LS^3 system, proved reliable but the optical limitations imposed by the physical length of a moving target data run suggests addition of at least one more, second-generation LS^3. That action is now in the planning process.

The second lesson learned was in the processing phase. Separate conversion and processing facilities are not practical. Competing requirements on the large-scale range computer creates turnaround time problems, and carrying a floating inventory of over 300 rolls of digital tape is a bookkeeper's nightmare. Data tapes were actually lost in the shuffle and had to be redigitized. Two still haven't turned up. This problem is now being solved by the addition of a dedicated, mid-sized computer system to the existing data conversion system. Once hardware and software interfaces are completed, we will be facing a bright and busy future in the evaluation of pulsed laser performance.

AD-A056488

RADIAL AND TRANSVERSE RESPONSE OF GUN TUBES TO TRAVELING BALLISTIC PRESSURE (U)

*THOMAS E. SIMKINS, PHD, RAYMOND D. SCANLON, MR.
GEORGE A. PFLEGL, MR.
BENET WEAPONS LABORATORY
WATERVLIET ARSENAL, WATERVLIET, NY

INTRODUCTION

The design and analysis of gun tubes presently proceeds on the basis of the static equations of continuum mechanics. Stresses within the tube wall, for example, are calculated by the classical Lame formula (1) - generally viewed as a conservative design criterion. The advent of high speed computation and mathematical modeling, however, has revealed that dynamic bore expansion during the interior ballistic cycle will create significantly higher wall stresses than those on which the tube design is based (2). The analytical and experimental results leading to this conclusion comprise the material in the first section of this work.

The second portion of the work which follows shows how transient bending vibrations may arise during firing due to tube curvature. Tube motions predicted at the muzzle are of sufficient magnitude to explain a portion of the error realized at the target. Three sources of curvature-induced vibration are derived (3) and two are treated in detail.

An appreciable effort has been made in the interest of realism. Highly detailed tube geometries and interior ballistic curves of pressure and projectile travel for specific weapons of interest have been included in the analysis. Wherever possible, use has been made of the large, widely accepted, NASTRAN (NAsa STRuctural ANalysis) finite element computer code. Though NASTRAN is quite versatile, it is not particularly well suited for handling curvature-induced load functions which require special programming.

1. RADIAL VIBRATIONS IN RESPONSE TO TRAVELING BALLISTIC PRESSURE

The 175 mm, M113 gun tube was chosen for analysis. The tube is assumed to be completely free of supports, closed at the breech and subjected to a time-variant internal ballistic pressure which traverses the bore at projectile velocity. Of primary interest is the radial displacement of the bore surface of the tube in time. To this end a 250 degree-of-freedom model of the tube is created by dividing the tube into 62 trapezoidal ring elements as shown in Figure 1. These finite elements allow the true geometry of the tube to be modeled very closely.

Program output in terms of radial or axial displacements, velocities, or accelerations may be requested for any bore station along the tube. As representative output, the radial displacement vs. time at three locations along the tube have been selected for presentation. In all there are 125 points in the model at which program output is computed.

Geometrical information for the NASTRAN program was obtained from tube manufacturing drawings. Tabulations of the pressure-travel curves of Figure 2 provided the input necessary for load specification (4). Traveling loads cannot be prescribed directly for NASTRAN input and require special programming considerations.

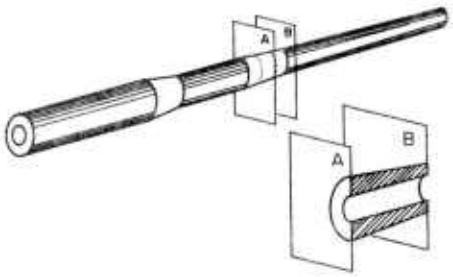

Figure 1 - Section of Trapezoidal Ring Element.

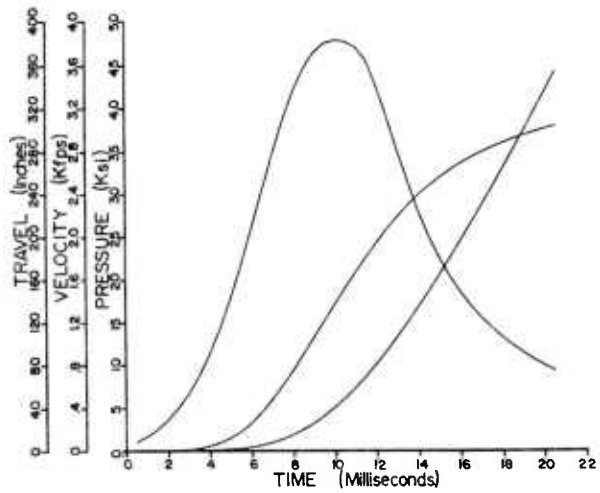

Figure 2 - Ballistic Curves - 175 mm M113 (Zone 3).

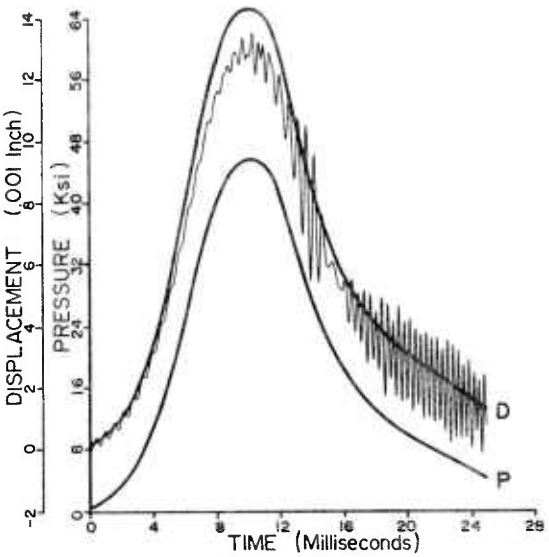

Figure 3 - Theoretical displacement and pressure in the breech section of the tube.

RESULTS

Figure 3 displays the NASTRAN predicted radial displacement of the bore surface at a location in the breech of the gun tube. Superposed for comparison is the displacement as calculated from the Lame design formula and the applied pressure. Owing to its location to the rear of the projectile at all times, this station receives pressure smoothly and continuously from time zero (ignition). Consequently, the loading rate at this point depends only on the rate at which the burning propellant produces pressure and not primarily upon the velocity at which the load follows the projectile.

It may also be observed from figure 3 that there is a steadily increasing amount of natural frequency excitation. These vibrations have a visible tendency to form 'beats' in the classical sense and infer the coexistence of several modes of vibration having nearly equal frequencies. Their importance lies in that the amplitudes of the beat envelopes can attain quite large values, creating an opportunity for overstress and shortened fatigue life.

Finally, it is noted that the Lame-predicted displacement response is conservative in that its maximum value exceeds that predicted by the NASTRAN analysis. This is to be expected since the Lame solution is formed on the assumption that the tube is uniformly pressurized throughout its entire length. In reality - and in the NASTRAN model - the pressure only exists in the region to the rear of the projectile. The unloaded region in front of the projectile tends to assume its unloaded configuration exerting a contractile effort on the pressurized region to the rear. Only when there exists a considerable input of kinetic energy to a given mode of vibration will the Lame prediction be exceeded. It is evident from figure 3 that this condition is not fulfilled in the breech section of the tube. Different behavior will be witnessed further along the bore.

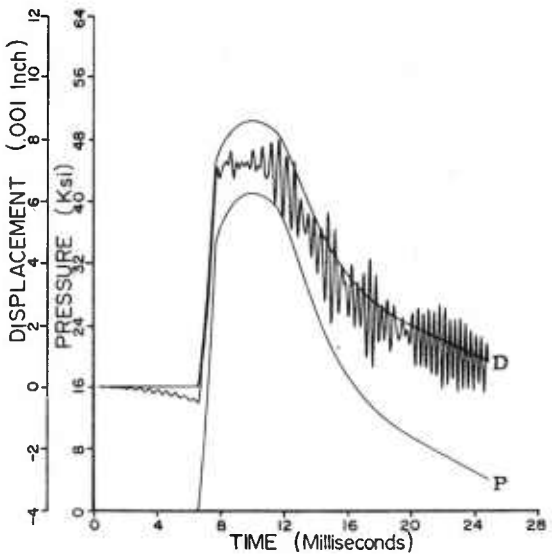

Figure 4 - Theoretical Displacement and Pressure a Short Distance Beyond the Origin of Rifling.

Figure 4 shows the same set of functions, i.e., the NASTRAN and Lame predicted displacements and the applied ballistic pressure, at a station located a short distance in front of the projectile prior to ignition. The distinctive feature as compared with Figure 3 is the time delay prior to the arrival of the projectile. During this delay a negative, that is, an inward radial displacement occurs at this location. This is the 'contractile effect' referred to in the previous paragraph, caused by adjacent regions of pressure and non-pressure. The Lame calculation cannot, of course, account for such an effect since all regions are assumed uniformly pressurized in the Lame problem.

At approximately 6.5 milliseconds following ignition, the projectile passes exposing this portion of the bore surface to the pressure of the propellant gas. Thus the time rate of load application at this station, in contrast with that in the breech, is almost wholly determined by the magnitude of the load velocity at this time. The loading is seen to be much more abrupt than that shown in Figure 3. This notwithstanding, one notes that the Lame-calculated displacement proves once again to be conservative.

While Figures 3 and 4 show the Lame-calculated displacement to err conservatively at bore locations nearer the breech, this is not typical of the behavior at stations further along the bore. Figure 5 represents the response more likely to be realized at least at some down bore locations. The station represented in this figure is approximately midway along the length of the tube. At this point the projectile is moving with a very high velocity and a very abrupt loading condition results. Provided that the vibration of the surface is in phase (i.e., moving outward) with the pressure application, a relatively large radial displacement will result as is the case in Figure 5. One should note that only a short distance forward and aft of this location the surface movement may be completely reversed. A sudden application of pressure at these locations would do negative work on the moving surface and the oscillations may be greatly attenuated. The actual locations along the tube where one can expect overstresses (large

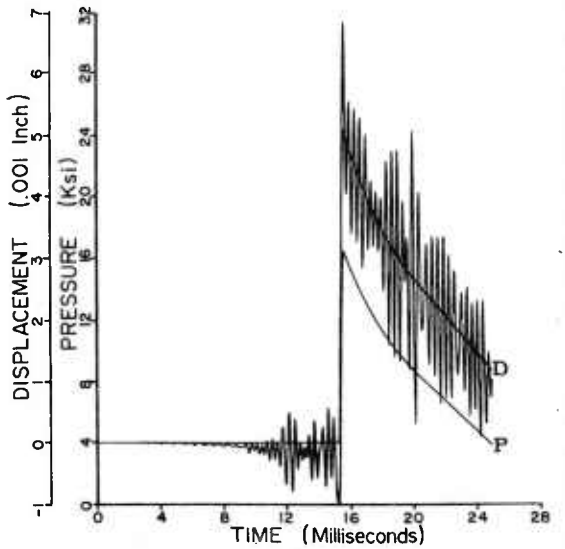

Figure 5 - Displacement and pressure midway along tube

radial displacements beyond the Lame prediction) cannot really be computed accurately owing to the imperfect knowledge of the true boundary conditions and material properties - not to mention the inability of any integration scheme to follow the phase accurately over a great number of cycles of vibration. It is important nonetheless to know that such overstresses are to be expected.

As experimental evidence of the success of the NASTRAN analysis, two representative test records from actual gun firings are offered in figures 6 and 7. Figure 6 shows the displacement at a location midway along the tube and therefore can be compared semi-quantitatively with figure 5. One clearly observes the production of natural oscillations and the formation of beats of large amplitudes. It is mostly due to the absence of damping in the analysis and the greater abundance of modes in the real tube into which energy may flow, that the amplitudes in the test records are lesser than those predicted. It is notable that the time-averaged displacement estimated from figure 6 agrees quite well with that of figure 5. On the other hand the excessively large maximum displacement of figure 5 does not materialize in figure 6. As previously discussed, this is a matter of phase agreement between the surface motion and the applied pressure. In figure 7, however, an overstress condition is clearly in evidence - the peak Lame value being indicated for comparison. This station is located nearer the muzzle. One notes the exceptionally clear oscillation and beat formations which continue after shot ejection which is estimated to occur at t = 21 milliseconds in the figure.

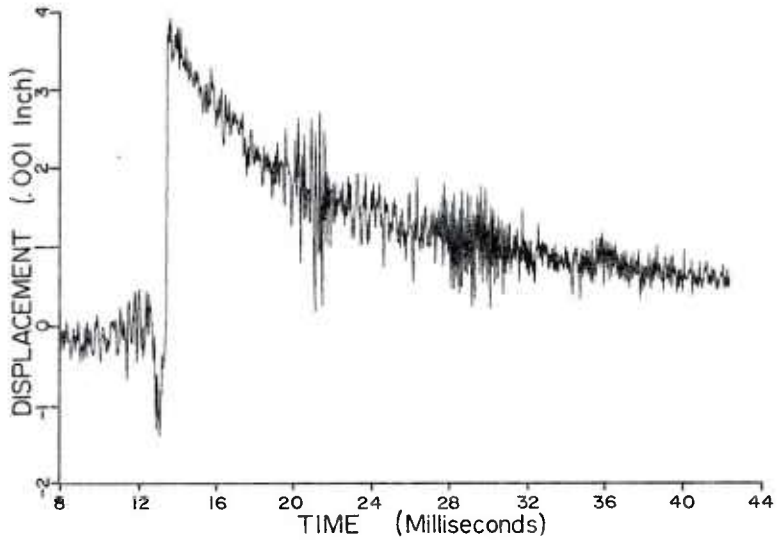

Figure 6 - Displacement Midway Along Tube Length (Actual Test Firing).

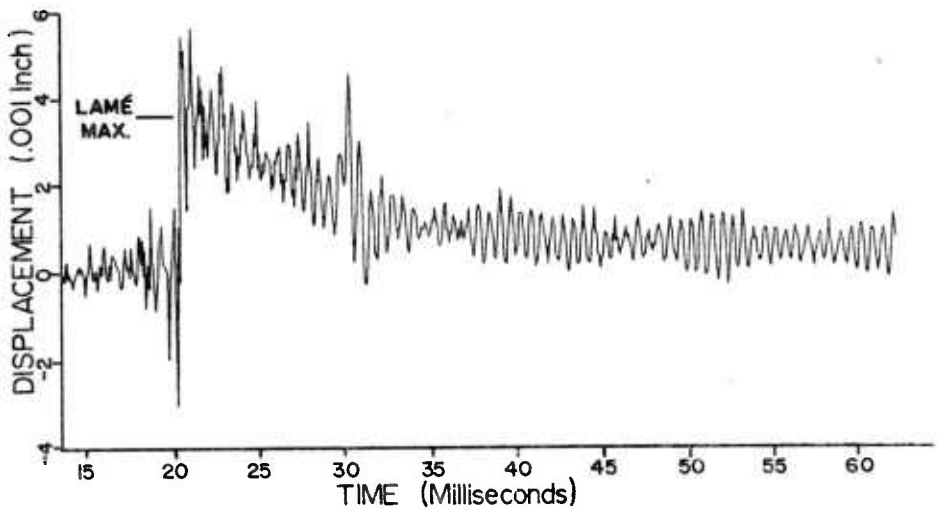

Figure 7 - Displacement a Short Distance From Muzzle (Actual Test Firing)

2. TRANSVERSE (BENDING) MOTION OF GUN TUBES - CURVATURE INDUCED LOADS

In 1959, measurements by Gay and Elder of the US Army Ballistics Laboratory (5) showed that the muzzle motions of a 90 mm tank gun at the time of shot ejection are very small but yet significant in explaining a portion of the error realized at the target. Typical rotations and displacements at the muzzle, for example, were of the order of 10^{-1} milliradians and 10^{-2} inches, respectively. The theory of gun tube motion by which explanations were sought for these observations assumed that the motion was due solely to a mass eccentricity at the breech which produced a sudden inertial moment upon recoil. The theoretically predicted motion, however, was often much smaller in magnitude than that observed. In the work that follows it will be shown that loads resulting from the initial curvature of the M-68, 105 mm gun tube can also produce muzzle motions of these magnitudes and should therefore not be neglected.

Recoil Loads

During the recoil of a gun tube there results an axial load per unit length which is equal to the product of the recoil acceleration, $\alpha(t)$, and the mass per unit length of the tube $\rho(x)$; i.e.,

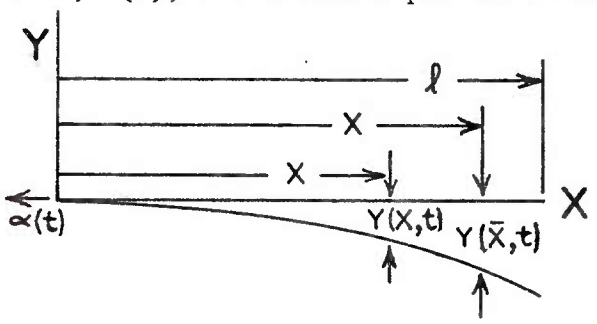

Figure 8 - Inertial Moment Due to Recoil.

$$w(x,t) = -\rho(x)\alpha(t) \tag{1}$$

When the tube is curved, this load creates a moment at any location x, along the tube. Referring to Figure 8, the total moment is given by the integral:

$$M(x,t) = \int_x^{\ell} -w(\bar{x},t)\,[y(\bar{x},t) - y(x,t)]\,d\bar{x} \tag{2}$$

Differentiating twice with respect to the space variable x gives the resultant transverse load intensity due to recoil: [(') = $\partial/\partial x$]

$$f_R(x,y',y'',t) = \alpha(t)\{\rho(x)y'(x,t) - y''(x,t)\int_x^{\ell}\rho(\xi)d\xi\} \tag{3}$$

'Bourdon' Load

If a gun tube is curved, the bore surface area becomes asymmetrically distributed about the central axis owing to the relative extension and contraction of the material. From the geometry of Figure 9 one can verify that the net difference in area is given by the integral:

$$\int_0^{2\pi} (\frac{a}{R} \sin\Theta+1)a\sin\Theta d\Theta dx = -\pi a^2 y'' dx \qquad (4)$$

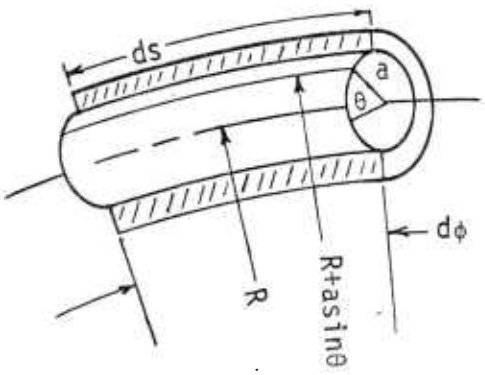

Figure 9 - Curved Section of Tube.

where R^{-1} has been replaced by $-y''$. The applied ballistic pressure therefore produces a resultant transverse load intensity:

$$f_B(x,y'',t) = -p(x,t)\pi a^2 y''(x,t) \qquad (5)$$

$p(x,t)$ is a traveling ballistic pressure function, i.e.,

$$p(x,t) = P_o(t)H(\xi-x)$$

$H(z)$ is the Heaviside unit step function and $\xi(t)$ represents the distance traveled by the projectile along the bore. (f_B has been called the 'Bourdon' Load because of its similarity to a straightening Bourdon tube upon pressurization. Actually, the two effects are completely different and the term 'Bourdon' load is a misnomer.)

Projectile Loads

If the projectile is assumed to be a point mass m_p, traveling a bore path which changes in time, it can be shown (8) that there results a transverse load function containing Coriolis, centrifugal and transverse accelerations, i.e., [$(\cdot) = \partial/\partial t$]

$$f_p = -m_p[\ddot{y} + 2V\dot{y}' + V^2 y'' + g]\delta(x-\xi(t)) \qquad (6)$$

where $\delta(z)$ is the Dirac function and $\xi(t) = \int_0^t V dt$, where V is the projectile velocity. g is the gravitational constant.

Equation of Motion

Using Euler-Bernoulli beam theory, the displacement $y(x,t)$ from the undeformed (straight) neutral axis of the tube must satisfy the partial differential equation:

$$(EIy'')'' + \rho(x)\ddot{y} - f - (EIY'')'' = 0 \tag{7}$$

where $I(x)$ is the area cross section moment of inertia and E is Young's Modulus of Elasticity. The last term on the right hand side of (7) represents the static load intensity corresponding to an initial deformation $Y(x)$.

The initial conditions are: $y(x,0) = Y(x)$ and $\dot{y}(x,0) = 0$ (8)

The load functions $f = f_R$ and $f = f_B$ will be considered in turn. It is to be noted, however, that the beam motions due to each load function may not be superposed as the linear operators involved vary with the particular load function considered.

Taking $Y(x)$ to be the gravitational deformation of the tube prior to firing, and $f = f_R(x,y',y''t)$ it is convenient to first define $\bar{y}(x,t)$ as the displacement as measured from the initial curve $Y(x)$. Thus (7) becomes:

$$(EI\bar{y}'')'' + \rho(x)\ddot{\bar{y}} - f_R(\bar{y},\bar{y}'',x,t) - f(Y',Y'',x,t) = 0 \tag{9}$$

The initial conditions in terms of $\bar{y}$ are homogeneous:

$$\bar{y}(x,0) = \dot{\bar{y}}(x,0) = 0 \tag{10}$$

Static and Dynamic Support Conditions

The support (boundary) conditions which prevail prior to firing may not be appropriate during the ballistic cycle. For the purpose of calculating the initial static gravitational deformation $Y(x)$, the M-68 tube is assumed to be cantilevered from its two mounting points near the breech. Actual vibration records indicate that the mount connections are far from rigid, however. In fact, excellent agreement between calculated and experimentally observed natural frequencies is obtained only if the tube is regarded as virtually unsupported during the ballistic cycle. The dynamic boundary conditions are therefore assumed to be free. This assumption should be valid as long as tube displacements are of the order of the support clearances.

The partial differential equation (9) was transformed into a set of N - ordinary differential equations in time via the Galerkin procedure in which the basis functions were chosen to be the natural modes of vibration of the unsupported M-68 tube. Using once again the NASTRAN finite element program, these mode shapes, $W_i(x)$- as well as the initial gravitational deformation function $Y(x)$ - were determined at nineteen points along the tube. Between these points the shapes were interpolated by cubic spline functions. The approximation for $\bar{y}$ in terms of the mode shapes may be written:

$$\bar{y}(x,t) = \sum_{i=1}^{N} a_i(t)W_i(x) \quad ,$$

the resulting set of differential equations appear as follows:

$$\ddot{a}_i + \omega_i^2 a_i + \sum_{j=1}^{N} (A_{ij}(t)-B_{ij}(t))a_j = C_i(t); \; i=1 \text{ to } N \qquad (11)$$

The initial conditions are homogeneous, i.e., $a_i(0) = \dot{a}_i(0) = 0$ (12)

ω_i represents the natural frequency of the ith vibration mode. $A_{ij}(t)$ derives from the $\bar{y}''$ terms in (9) while $B_{ij}(t)$ reflects the slope dependency, $\bar{y}'$, and vanishes for the case $f = f_B$. $C_i(t)$ is due to terms in the initial deformation function $Y(x)$.

The system represented by (11) and (12) above, was solved numerically using 4th order, variable time step Runge Kutta integration. In practice a value of N = 10 gave satisfactory convergence. This included two rigid body modes (plane rotation and translation) and eight vibration modes of finite frequency.

RESULTS AND DISCUSSION

Figures 10 and 11 represent the response of the M-68 gun tube to recoil and asymmetric ballistic pressure (the 'Bourdon' effect). The magnitudes shown in each of the figures are comparable with those predicted by Gay and Elder (8) in connection with eccentric breech inertia in the T-139 tank gun. This indicates that curvature-induced loads should be included in any theory of gun tube motion during firing.

A fundamental difference is apparent between figures 10 and 11, and is especially obvious in comparing the time histories of the tube shapes, i.e., figures 10a and 11a. Whereas in 10a the motion is well developed along the entire tube length, the motion in 11a is much more wavelike and muzzle displacements remain comparatively small

through shot ejection. This difference is due to the fact that the recoil inertia load acts instantaneously* over the entire tube length whereas development of the 'Bourdon' load proceeds at projectile velocity. Moreover, the recoil loading consists of two parts (cf. equation 3). If evaluated near time zero, these two parts consist of a downward load proportional to the curvature (y'') and therefore stronger near the supports, and an upward load proportional to the slope (y') more intense near the muzzle. The two act in unison to encourage a rotation of the entire tube. The large mass at the breech, however, tends to anchor that end of the tube. The result is the deformation shown in figure 10a. The Bourdon load, on the other hand, consists of only one part (cf. equation 5). This part, being proportional to curvature is greatest near the supports and trails off to practically zero value by mid-length of the tube. Muzzle displacement must therefore await the arrival of a disturbance originating from the support end of the tube.

A similarity is also apparent comparing figures 10 and 11. The time histories of the slopes at the muzzle - probably the most important of all the response curves - show a definite similarity in that little muzzle rotation occurs during the first half of the ballistic cycle. This delay represents the propagation time for a disturbance established near the supports (where y'' is largest) to reach the muzzle.

CONCLUSION

To completely account for the motions of a gun tube prior to shot ejection several effects must be considered, among them the effects of tube curvature. Of particular significance is the muzzle slope at the time the projectile arrives. Slope values are particularly sensitive to sudden disturbances which originate near the support or breech end of the tube and propagate in wavelike fashion reaching the muzzle prior to shot ejection. This is exemplified in the case of the Bourdon load and strongly suggests an opportunity for further study as the supports themselves may create strong forces as clearances are abruptly taken up during the initial phases of recoil. The result may significantly strengthen rotations of the muzzle at shot ejection.

*The tube is assumed axially rigid in the analysis.

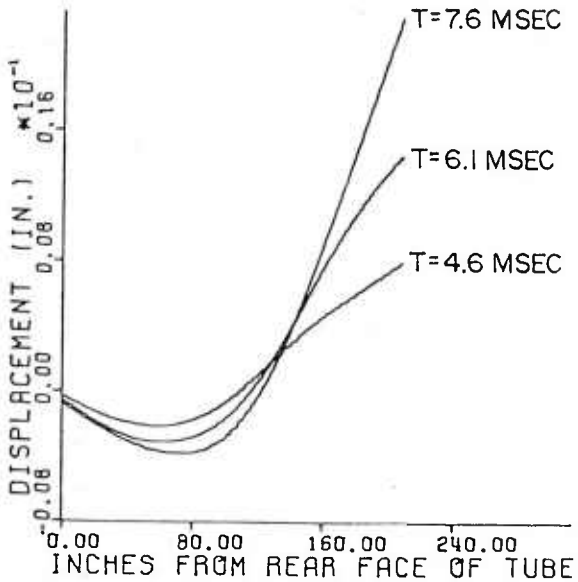

Figure 10a - Displacement of Tube Axis from Initial Position.

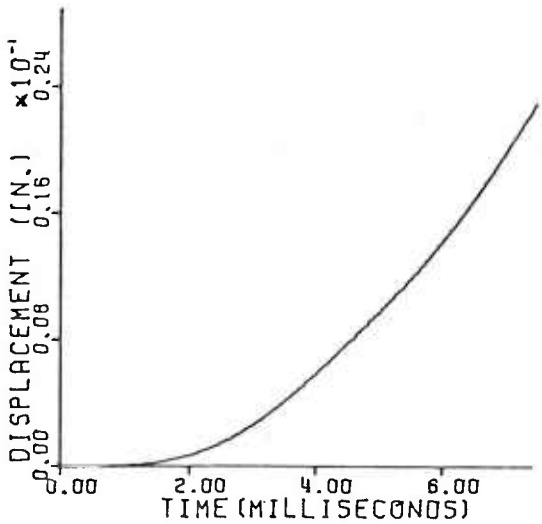

Figure 10b - Muzzle Displacement.

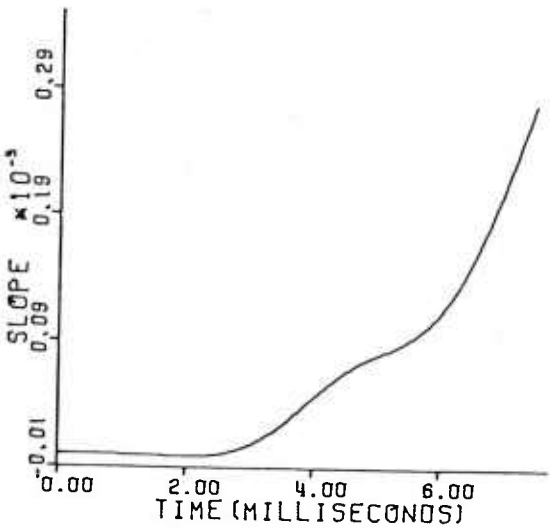

Figure 10c - Muzzle Slope (Rotation).

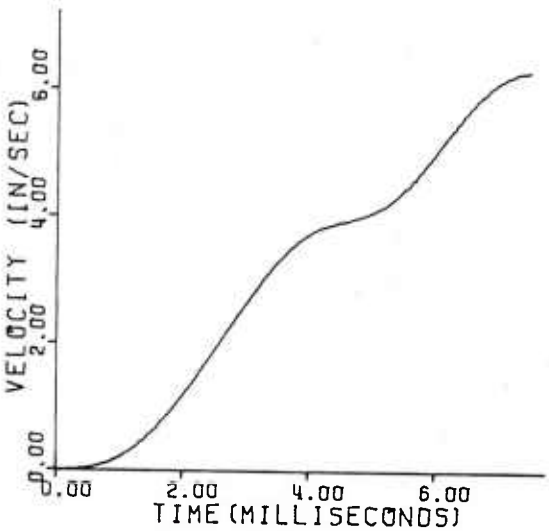

Figure 10d - Transverse Velocity of Muzzle.

Figure 10 - Transverse Response of the M-68 Gun Tube to Recoil Inertia.

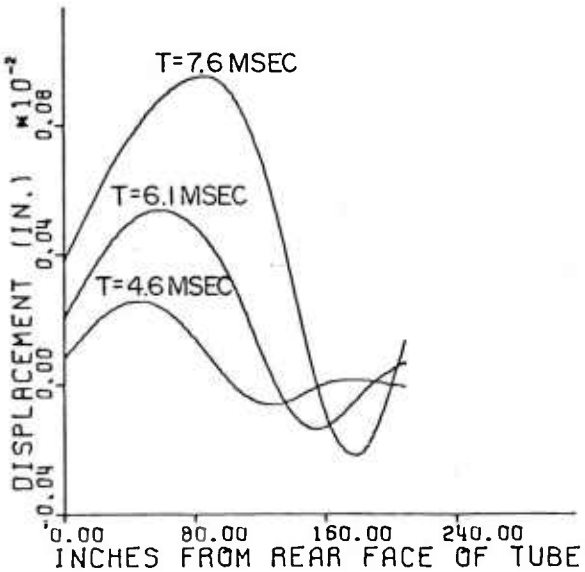

Figure 11a - Displacement of Tube Axis from Initial Position.

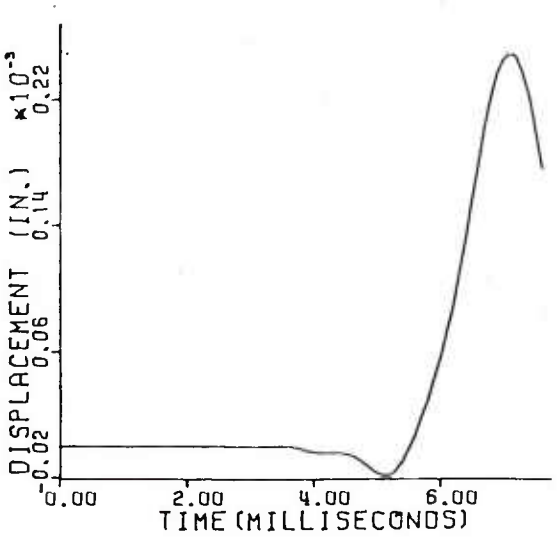

Figure 11b - Muzzle Displacement.

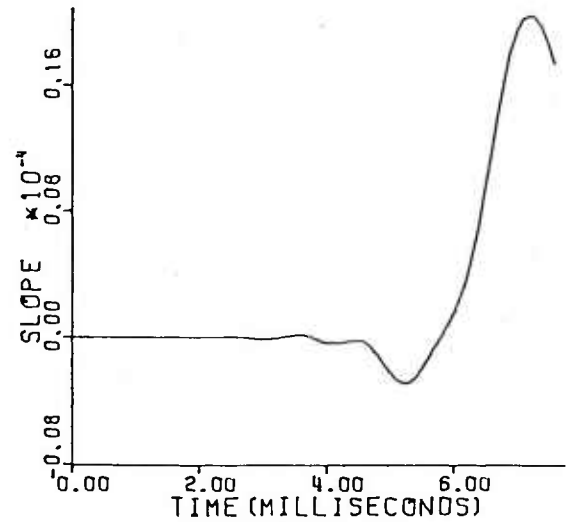

Figure 11c - Muzzle Slope (Rotation).

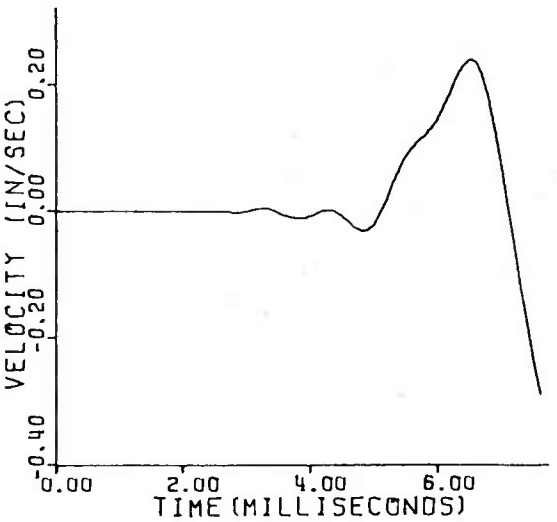

Figure 11d - Transverse Velocity of Muzzle.

Figure 11 - Transverse Response of the M-68 Gun Tube to Traveling Bourdon Pressure.

ACKNOWLEDGMENT:

The authors wish to thank Mr Richard Haggerty of the Benet Weapons Computer Science Laboratory and Miss Ellen Fogarty for their invaluable assistance.

REFERENCES

(1) Seeley, F. and Smith, J., Advanced Mechanics of Materials, 2nd Ed. (Wiley & Sons, NY), pp. 298-99.

(2) Simkins, T., Pflegl, G., and Scanlon, R., "Dynamic Response of the M113 Gun Tube to Travelling Ballistic Pressure and Data Smoothing as Applied to XM150 Acceleration Data" - Benet Weapons Lab Tech Report No. WVT-TR-75015, ADA010662 (1975)

(3) Ref. (2), Appendix B.

(4) Vottis, P., "Digital Computer Simulation of the Interior Ballistic Process in Guns", WVT-6615, (1966).

(5) Gay, H., and Elder, A., "The Lateral Motion of a Tank Gun and Its Effect on the Accuracy of Fire", Ballistic Research Lab Report No. 1070 (1959), AD217657.

(6) Simkins, T., "Structural Response to Moving Projectile Mass by the Finite Element Method," Benet Weapons Lab Tech Report No. WVT-TR-75044, (1975).

(7) Simkins, T., "Unconstrained Variational Statements for Initial and Boundary-Initial Value Problems", (forthcoming, AIAA Journal Structural Dynamics, 1978).

(8) Ref. (5), p.16, Table I.

AD-A056489

INTERNAL COCKPIT REFLECTIONS OF EXTERNAL POINT LIGHT SOURCES FOR THE MODEL YAH-64 ADVANCED ATTACK HELICOPTER

CHRISTOPHER C. SMYTH
US ARMY HUMAN ENGINEERING LABORATORY
ABERDEEN PROVING GROUND, MARYLAND 21005

INTRODUCTION

The US Army Human Engineering Laboratory (HEL) has developed a computer program for computing internal cockpit reflections on the transparent canopy surfaces of external point light sources. This work is part of a three-stage effort to determine optimum canopy designs for the Model 209 AH-1S Cobra Helicopter and the Model YAH-64 Advanced Attack Helicopter (AAH). This work was undertaken at the request of the Project Manager's Office, USA Aircraft Survivability Equipment. The low glare canopy design presently used on both models consists of flat, transparent panels on the front surfaces and simple cylindrical panels on the sides and top. The design is a reasonable choice for reducing both solar glint to outside observers during daytime operations and internal reflections of outside light sources during nighttime operations.

A flat plate canopy (FPC) design was originally developed for the Cobra and AAH to reduce daytime solar glint to a momentary flash at certain observer-aircraft-sun angles. A moving aircraft no longer produced the continual solar glint which was present on the earlier compound-shaped canopy designs. The continual presence of solar glint had increased the range of visual detection by ground observers.

However, in certain lighting situations during nighttime operations, the internal surfaces of the FPC performed as mirrors reflecting virtual images of external light sources that were visible to the pilot. HEL has shown by computer analysis that these reflections are possible on most of the transparent surfaces and for a wide range of source locations (1). These virtual images of ground-level

lights were disorienting to the pilot and he could not easily discriminate between the light sources on the ground and their reflections from the canopy surfaces. This problem was a potential safety hazard during flight.

The present low glare canopy design was developed to reduce these two conflicting problems to manageable levels. The design incorporates front planar transparent surfaces and simple cylindrical surfaces for the sides and top. HEL recommended a similar design with, however, novel features (2). The present work effort is directed toward a closer study of the two problems of glint and reflections, and developing an optimum design for the canopy's transparent surfaces.

METHOD

A ray-tracing program was written to trace in three dimensions the straight-line rays from the nominal position of the pilot's eye backwards to visible points on the internal surfaces of the cockpit. Each ray is traced between transparent surface points until a non-transparent surface is reached. These surfaces are assumed to be diffusive without specular reflectances and the ray is considered absorbed. At each reflection point on a transparent surface, the reflectance and transmittance are computed along with the directional cosines of the corresponding transmitted and reflected rays. In this way, a reflected ray reaching the pilot's eye is traced backwards to all possible external sources that can generate that ray.

The transparent surfaces of the low glare canopy design are specified as a set of planar and cylindrical surfaces and their corresponding edge vertices. Each planar surface is specified by the coordinates of its edge vertices and the consecutive order in which adjacent vertices are listed. A cylindrical surface is specified by cylindrical parameters and the consecutive sequence of the edge vertices and their coordinates. The cylindrical parameters are (1)origin point on the cylindrical axis, (2)directional cosines of the axis, and (3)the radius of the cylinder. The edges of the cylindrical surface are assumed for simplicity to be curvilinear lines which become straightened when the cylinder is transformed into a flat plane.

Given directional cosines and an origin point of a straight-line ray, the program computes, in turn, the intersection point of the ray with each surface. The program tests the intersection point against the surface edges. The reflection point for the ray is that intersection point which is contained within the edges of the corresponding

surface segment. The angle of incidence between the surface normal and the ray at this point is computed along with the corresponding values of reflections and transmittance and the directional cosines of the transmitted and reflected rays. Tracing backwards, the reflected ray becomes the incident ray for the next set of computations. (See Appendix A of reference (1) for ray tracing on planar surfaces and computation of transmittance and reflectance values, and Appendix B of reference (3) for derivation of equations used in ray tracing on cylindrical surfaces.)

The program includes internal and external obstructing surfaces and the internal blast barrier of the YAH-64 between the pilot and copilot, as well as the transparent surfaces of the canopy in the computation. The obstructing surfaces are those that either obstruct the pilot's vision or block incident rays from external sources. The internal surfaces are (1)the pilot's seat, display panel and side armor, (2)the copilot's seat, gunner-sight and side armor, and (3)the sides and floor of the cockpit. The external surfaces are (1)aircraft nose section, (2)gun pods and wheel wells, (3)wing stubs, (4)rocket pods, (5)engine intakes, and (6) rotary housing. These surfaces are specified as planar segments in the same manner as are the canopy surfaces. The intersection computations are performed first for all obstructing surfaces and computation of a reflection point for a ray on an obstructing surface renders the computation complete since the backwards traced ray is considered absorbed.

The transparent blast barrier,which separates the copilot and pilot, is treated first as a reflecting surface and then as a transmitting surface for reflection points on surfaces beyond it.

This computation process is repeated for pilot-viewing directions indexed at equal increments over a quarter sector. The sector is bounded by vision directly to the front, to the side, top and bottom. In this way, a table is constructed which lists at discrete intervals all possible internal reflection points and the corresponding external light directions. This approach generates a large amount of data and a computer-graphics routine is included for output. The primary reflection points and the corresponding incident ray entry points are shown on side, top and front views of the canopy and on perspective drawings of the cockpit as seen from the pilot's position. Similar comments apply to computations for the copilot's position. (See Appendix C of reference (1) for a discussion of perspective drawings.)

DISCUSSION

The results of this application are shown in Figures 1 through 13. These figures are hard copies of the computer graphics output. Figure 1 shows side, top and front views of the canopy frame, blast barrier and obstructing surfaces. The pilot's nominal eye position is shown in each view. The blast barrier and obstructing surfaces are sketched in with broken lines. The aircraft fuselage and tail assembly are not included in this sketch.

Figure 2 shows side, top and front views of the canopy frame and blast barrier, sketched with broken lines, separated from the obstructing surfaces. Figure 3 is a perspective drawing of the cockpit as seen from the pilot's position. The pilot's nominal viewing direction is shown by the small cross near the top center of the upper front canopy surface. The drawing covers a 60-degree field-of-view and shows that the lower portions of the front and forward side canopy surfaces are blocked from view by the pilot's instrument panel.

The frame edges for the canopy sides are drawn as straight lines connecting adjacent corner vertices. This is done for convenience in the computer graphics routines. The computations assume that the frame edges for the cylindrical surfaces are curvilinear lines (see Method).

Figures 4 through 13 show "dots" for the entry positions of external rays generating primary reflections on the right-hand side of the canopy for the pilot's position. Also shown are the corresponding primary reflections spaced at two degrees by two degrees increments. The number shown at each reflection point is equal to the negative value of the logarithm (base 10) of the light reflectance. The numbers are truncated to their integer values by dropping the fractional parts. The numerical "zero" corresponds to those reflectances which are greater than 0.1 in value. The numerical "one" corresponds to those values equal to or less than 0.1 but greater than 0.01.

Figure 4 shows that entry points are possible over much of the lower front panel and the side surfaces. Figure 5 shows that primary reflection points can occur on (1)the upper rear corner of the front side panels, (2)the upper edge of the rear side panels, and (3)the side edges of the top panel. The front side panel reflections have reflectance values in the 0.1 to 1.0 range, while those on the rear side and top are in the 0.01 to 0.1 range.

Figures 6 and 7 are perspective drawings of the cockpit as seen from the pilot's nominal viewing position and direction. Figure 6 shows entry points on the lower front and front side surfaces. Figure 7 shows primary reflections on the right-hand side of the canopy. Figure 8 shows reflection points where the pilot has shifted his viewing direction 20 degrees to the right. (Note that some reflection points are shown on the canopy frame. This is because the structure outline is drawn as straight line members between the corner vertices instead of the curvilinear members used in the computations. See Methods.)

Figure 9 through 13 show reflection points generated on one canopy surface by external rays entering another surface. Figure 9 shows reflection points on the top surface generated by entry points on the right rear side surface. Figure 10 shows reflections on the top surface generated by entry points on the right forward side surface. Figure 11 shows reflections on the right rear side due to entry points on the left rear side. Figure 12 shows reflections on the right forward side due to entry points on the lower front surface. Finally, Figure 13 shows reflections on the right rear side due to entry points on the left forward side.

CONCLUSION

A computer program developed by HEL to show internal cockpit reflections of external point light sources has been applied to the Model YAH-64 Advanced Attack Helicopter (low glare canopy design). The results show that during nighttime operations, ground-light reflections are possible on the transparent surfaces of the canopy. Reflections are possible from the top and side canopy surfaces for the pilot and the front and forward side surfaces for the copilot. The results are an improvement over the flat plate canopy design since reflections are limited to certain portions of these surfaces. Where reflections actually occur depends upon the particular lighting situation and flight scenario.

REFERENCES

1. Smyth, C.C. Computing internal cockpit reflections of external point light sources for the Model 209 AH-1S Cobra Helicopter flat plate canopy design. Technical Memorandum 20-77, US Army Human Engineering Laboratory, Aberdeen Proving, MD, 1977.

2. Stowell, H.R., & Smyth, C.C. Investigation of inside light reflection problem on the flat plate canopy (FPC) for Model 209 AH-1S

helicopter. Technical Memorandum 13-77, US Army Human Engineering Laboratory, Aberdeen Proving Ground,MD, 1977.

3. Smyth, C.C. Computing Internal Cockpit Reflections of External Point Light Sources for the Model YAH-64 Advanced Attack Helicopter (Low Glare Design), Technical Memorandum 24-77, US Army Human Engineering Laboratory, Aberdeen Proving Ground,MD, 1977.

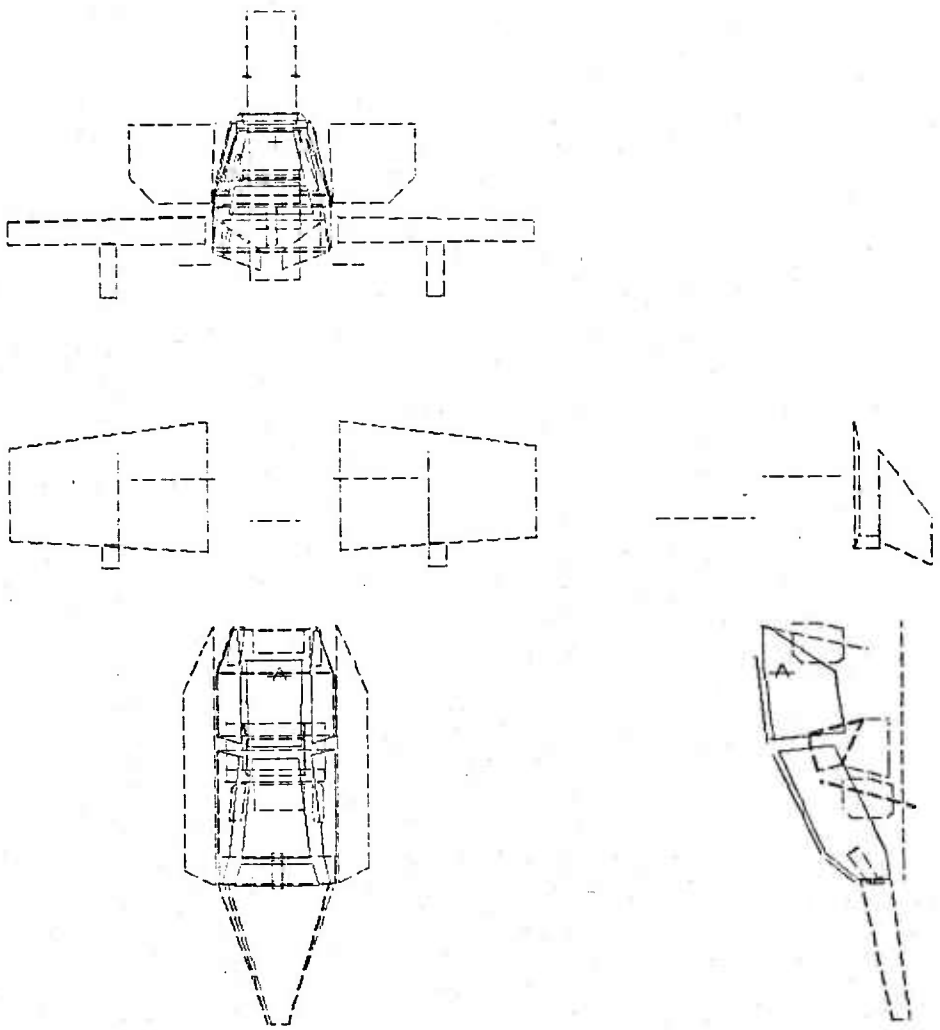

Figure 1. Top, side and front views of canopy frame and obstructing surfaces.

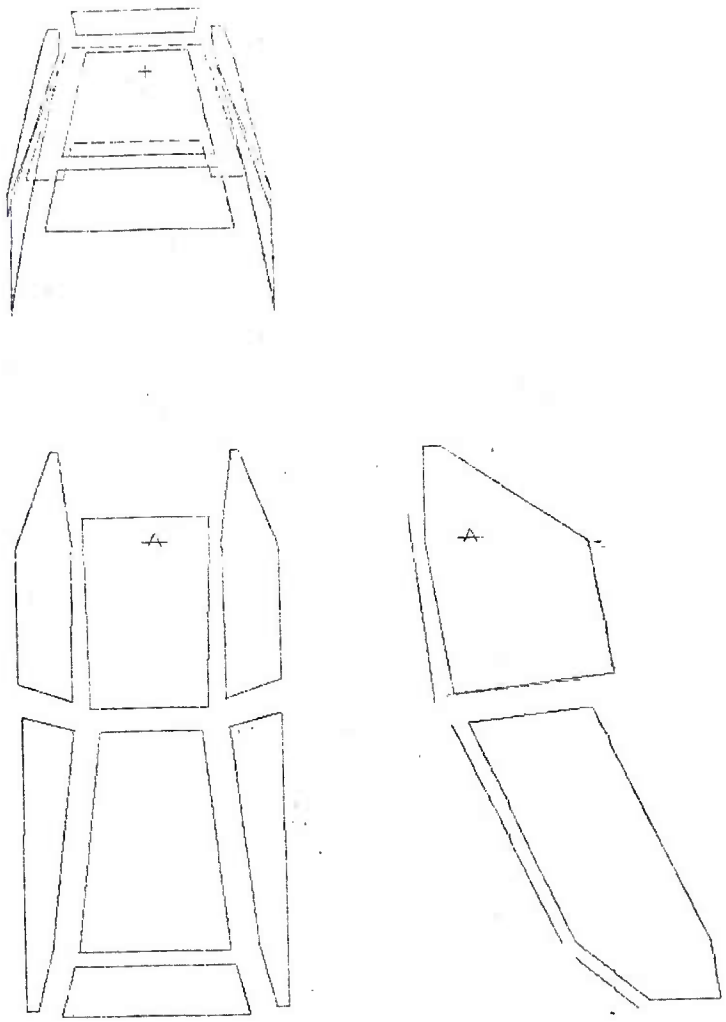

Figure 2. Top, side and front views of canopy frame.

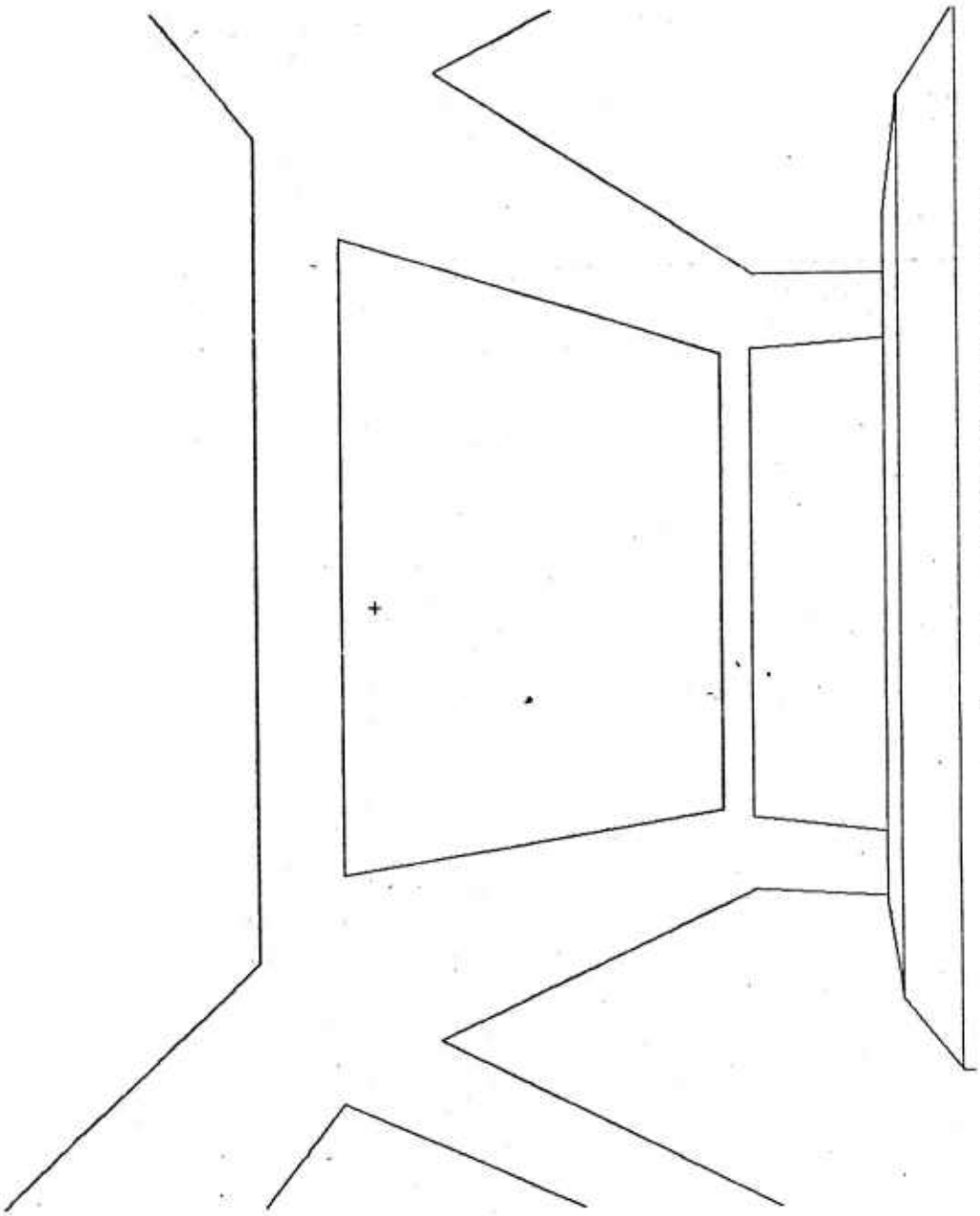

Figure 3. Perspective view of the cockpit interior from the pilot's nominal viewing position and direction.

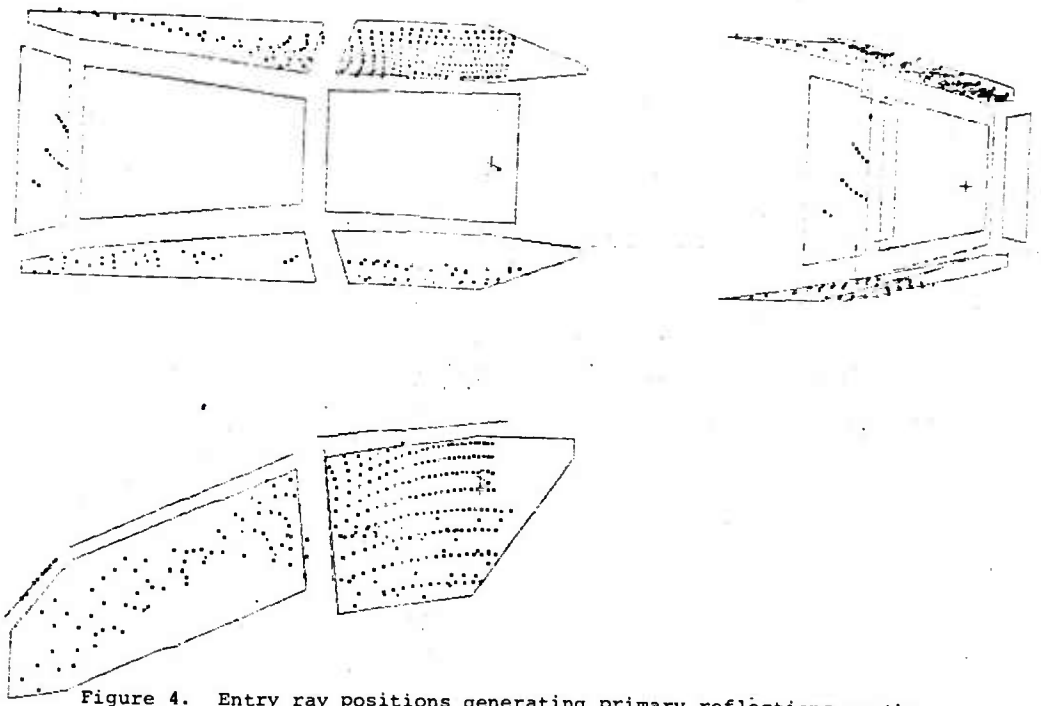

Figure 4. Entry ray positions generating primary reflections on the right-hand side of the canopy as seen from the pilot's position.

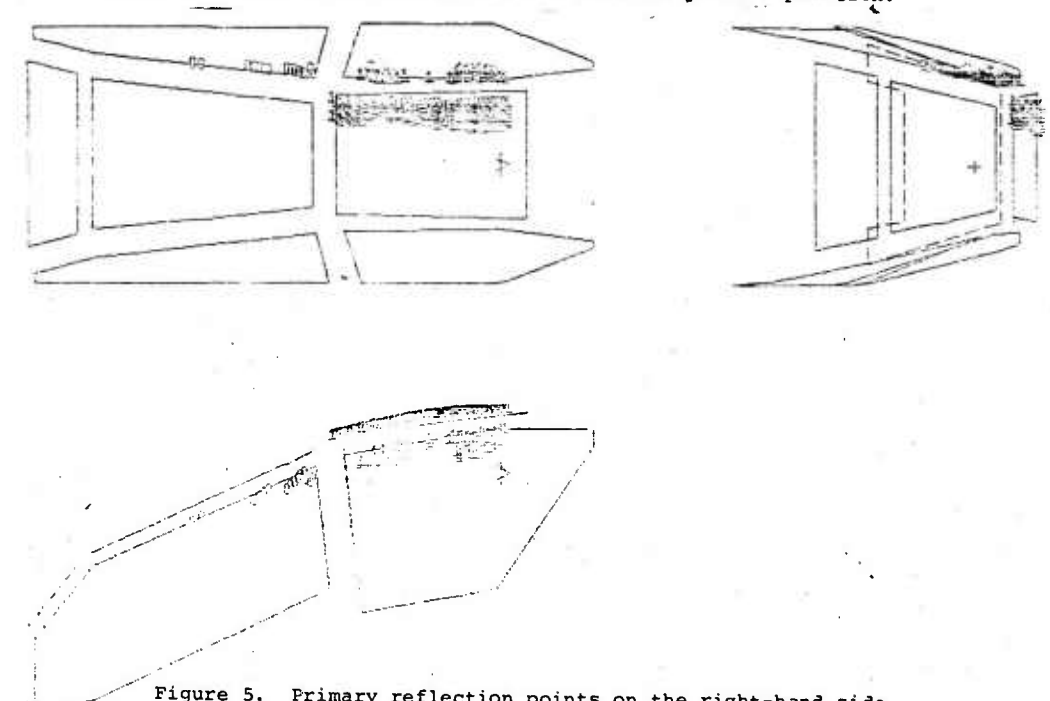

Figure 5. Primary reflection points on the right-hand side of the canopy and their associated reflectance values for the pilot's position.

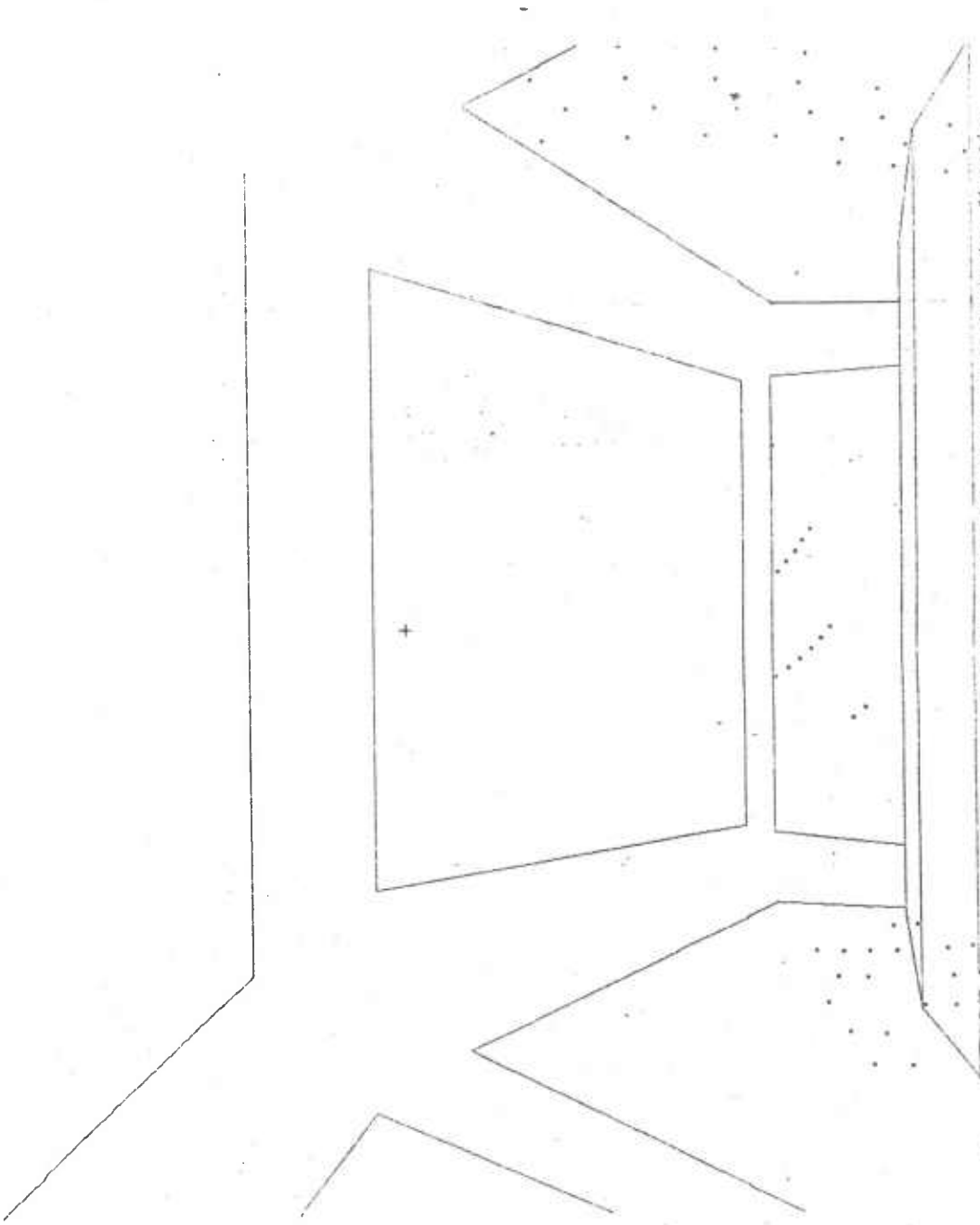

Figure 6. Perspective view of entry ray positions for the pilot's nominal viewing direction and position.

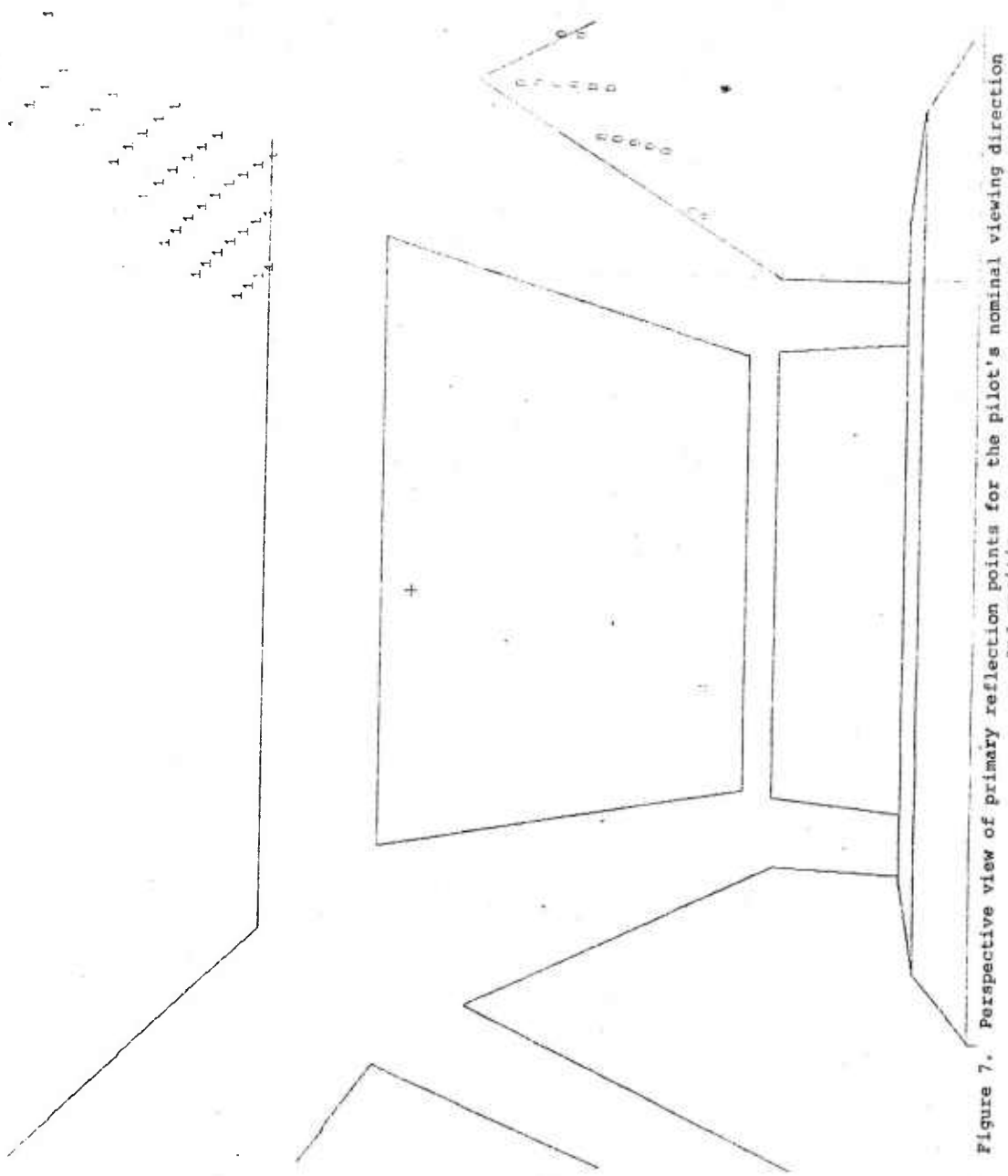

Figure 7. Perspective view of primary reflection points for the pilot's nominal viewing direction and position.

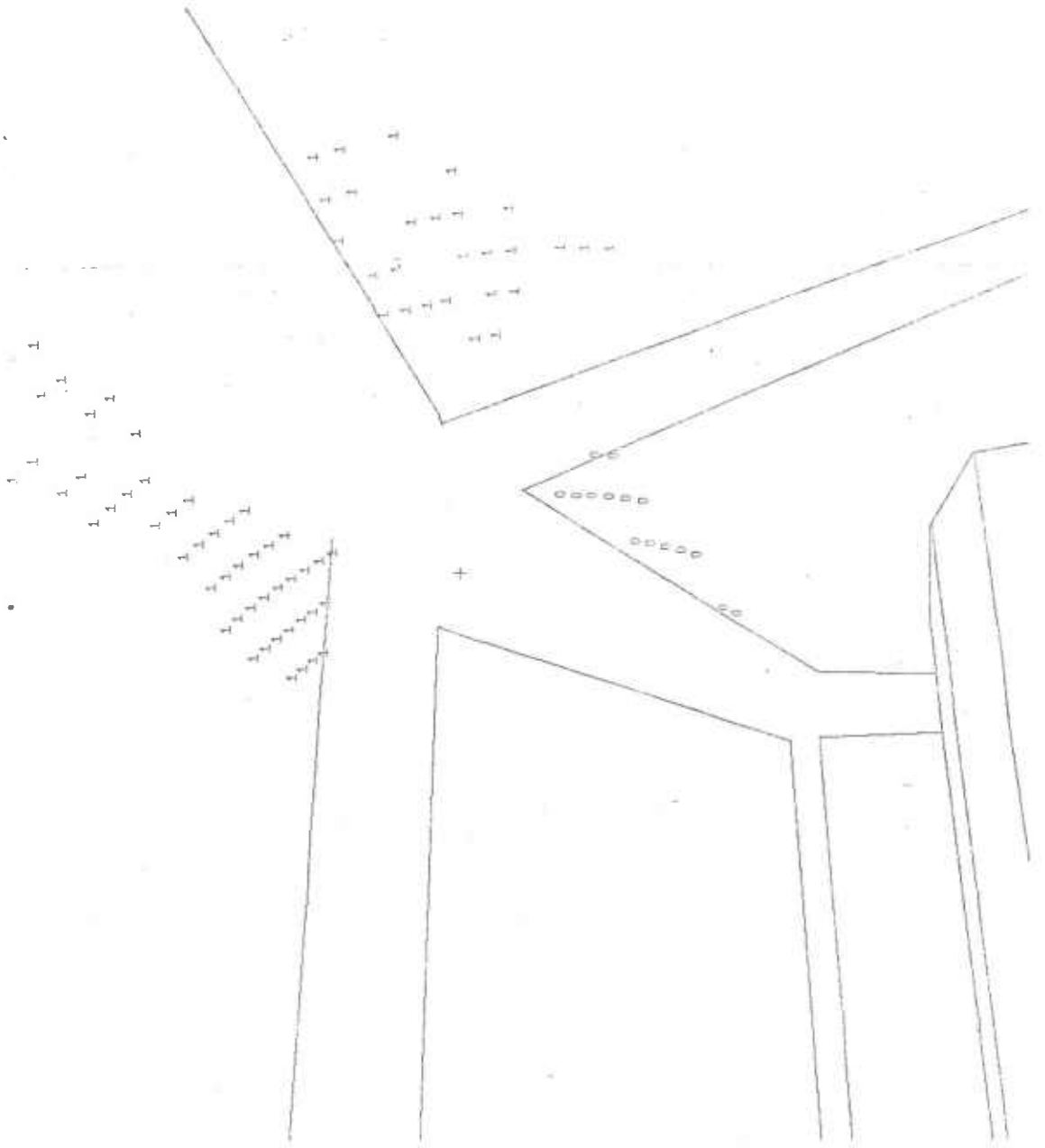

Figure 8. Perspective view of primary reflection points for the pilot viewing 20-degrees to the right side.

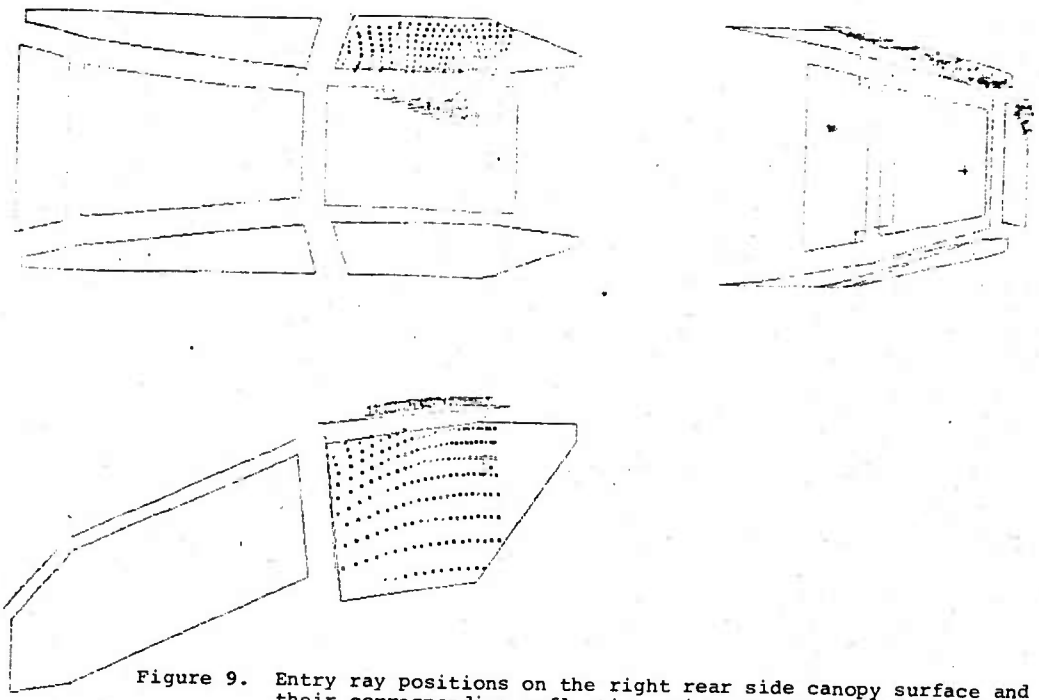

Figure 9. Entry ray positions on the right rear side canopy surface and their corresponding reflection points on the right side of the top surfaces.

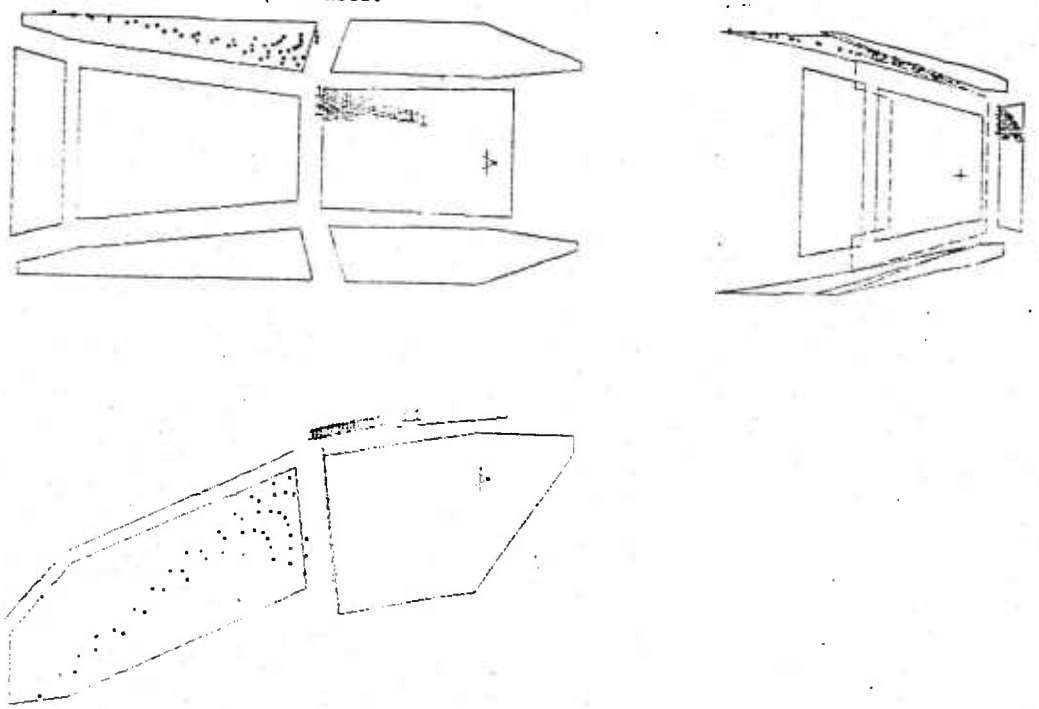

Figure 10. Entry ray positions on the right forward side canopy surface and their corresponding reflection points on the right front of the top surface.

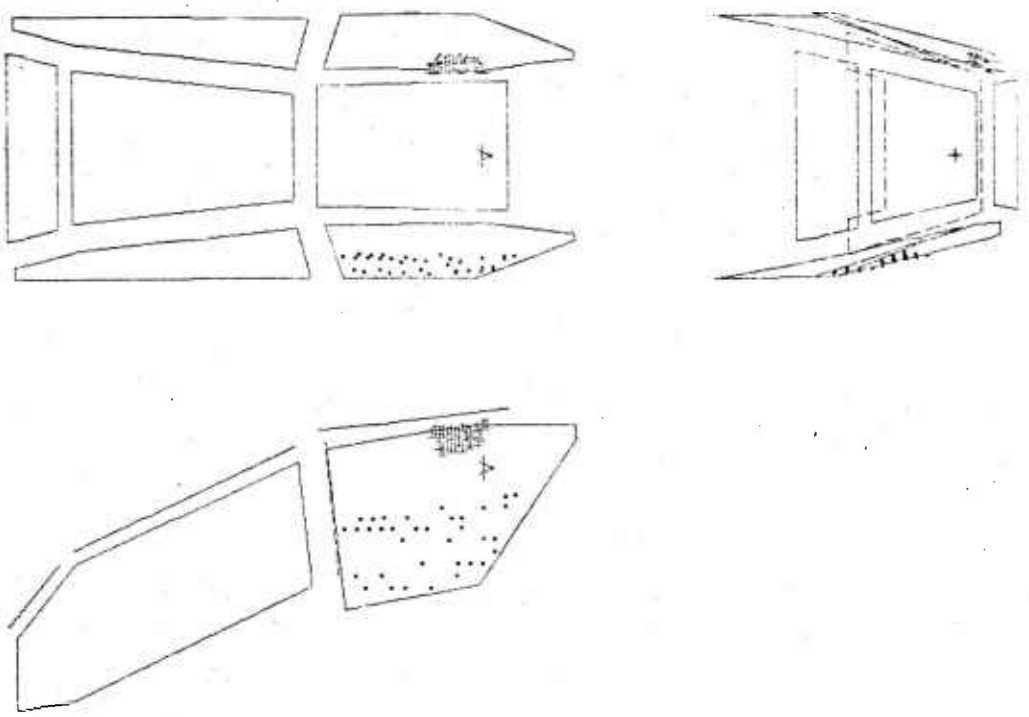

Figure 11. Entry ray positions on the left rear side canopy and their corresponding reflection points on the top edge of the right rear surface.

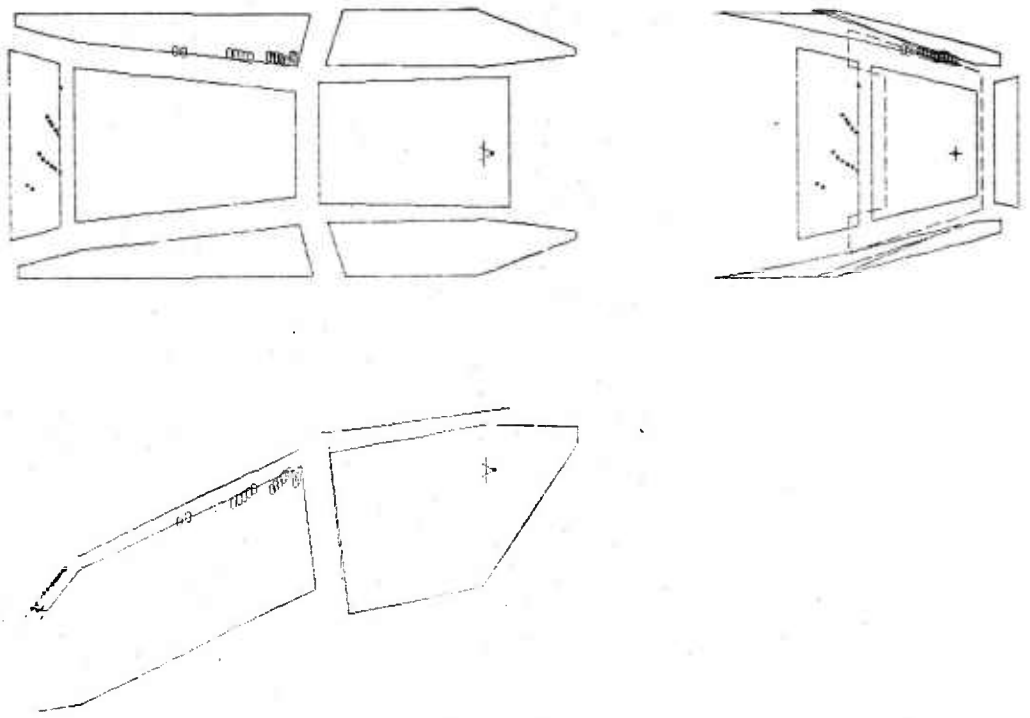

Figure 12. Entry ray positions on the lower front canopy surface and their corresponding reflection points on the upper rear corner of the right forward side surface.

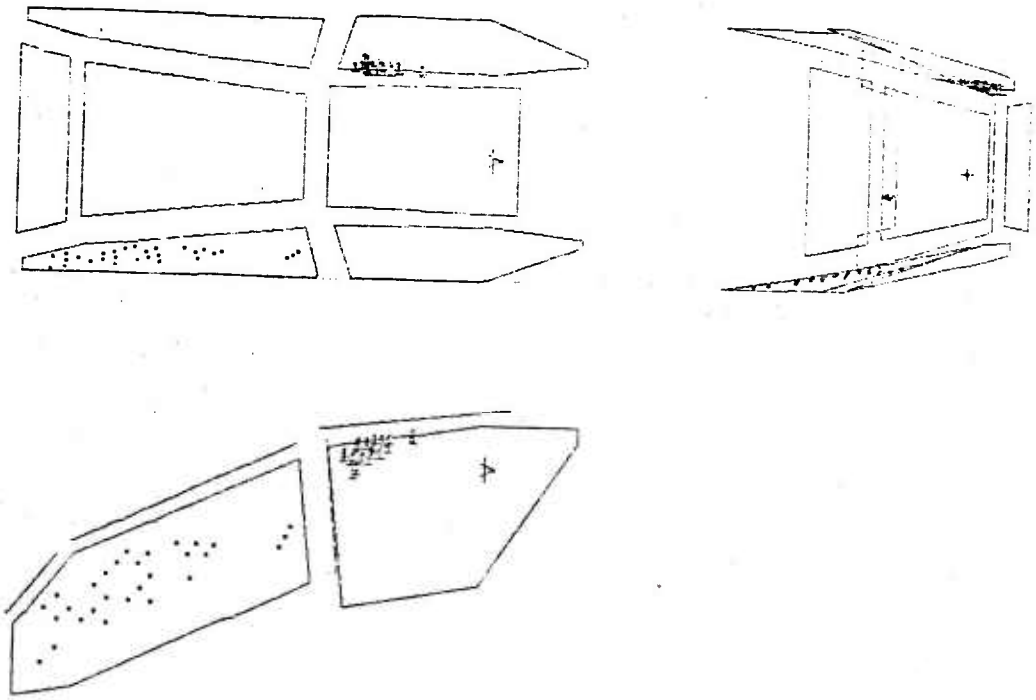

Figure 13. Entry ray positions on the left forward side canopy surface and their corresponding reflection points on the upper front edge of the right rear side surface.

AD-A056490

THE ESSEX PROGRAM: A STUDY OF THE EFFECTS OF UNDERGROUND LOW-YIELD NUCLEAR WEAPONS EMPLOYED IN A TACTICAL WARFARE SCENARIO (U)

*JOHN N. STRANGE, MR.
U. S. ARMY ENGINEER WATERWAYS EXPERIMENT STATION
VICKSBURG, MISSISSIPPI 39180

The possibility of a massive, all-out invasion of Western Europe by Warsaw-Pact forces has made it necessary for the NATO Alliance to prepare for such an eventuality and to develop innovative and effective countermeasures. The initial effort of the NATO forces would be aimed at slowing the enemy's rate of advance, thus buying valuable time in which the NATO forces could mobilize and launch a telling and successful counteroffensive.

One very practical way to slow the enemy's rate of advance would be to deny him the mobility and maneuver options he needs for his armor and mechanized units, particularly along likely invasion corridors. To effect such a denial, the so-called "barrier to mobility" (BATM) concept was introduced late in the decade of the sixties. The concept involves the use of conventional or nuclear underground explosions to produce craters of sufficient size to form a viable obstacle or BATM. The low-yield atomic demolition munition (ADM) was envisioned as the nuclear energy source for producing such craters, while large quantities of conventional explosives could provide a viable alternative as to the explosive type.

In about 1973, a requirement to study the effect of low-yield nuclear explosions on various tactical-type targets was introduced. It was envisioned that such targets, at ranges up to a few hundred kilometers beyond the forward edge of the battle area (FEBA), could be attacked by an aerial- or missile-delivered warhead, i.e., a tactical earth-penetrating warhead (TEPW). It was envisioned that such a warhead would penetrate to depths below the ground surface sufficient to optimize those weapons effects needed to damage or destroy a given target or target complex.

The specific purpose of the ESSEX (Effects of Subsurface

Explosions) Program was to study the effects of low-yield nuclear weapons, the kind envisioned for use in both the BATM and TEPW applications. In essence, the research was aimed at refining the employment doctrine for the ADM and at developing a sufficient data base from which employment doctrines for the TEPW could be formulated.

PROGRAM OBJECTIVES

Major objectives of the ESSEX Program were as follows: (a) develop a means of simulating, with high explosives, the mechanical effects of low-yield nuclear explosions that occur at various depths of burst (DOB), for various stemming conditions, and for various geologies; (b) develop a means of simulating radioactive fallout and of predicting such fallout using a nonradioactive source; (c) assess the barrier effectiveness of craters formed by low-yield nuclear weapons; (d) identify those test geometries that minimize collateral damage without degrading to an objectionable degree the primary effects; and (e) determine the vulnerability of generic classes of targets to the free-field explosion effects (primarily cratering, ground shock/motion, and debris impact). The calculational and experimental programs have provided a data/knowledge base sufficient to develop quantitative conclusions relative to some of the objectives, and definable trends relative to the others.

APPROACH

Simulation of Mechanical Effects. In the ESSEX Program, high explosives (HE) were used to simulate nuclear explosives (NE). In the simulation, two cratering, ground-motion type calculations were conducted, one for NE and one for HE. The NE calculation considered the expansion of the nuclear source through an appropriate equation of state (EOS); this calculation served as input to a medium response calculation which used a field-developed EOS for the host material. The output of the two-phased calculation was a predicted crater profile, predicted stress levels, predicted particle velocities, and a predicted kinetic energy field.

A similar calculation was made for the HE case except that an HE source EOS was used. The NE and HE calculations were then compared, and adjustments were made in the HE yield until the cratering and kinetic energy fields at a given range were in agreement. Thus, proper simulation was tagged to a duplication of crater geometry and a duplication in the ground shock and kinetic energy fields.

Radioactive Fallout Simulation. The fallout of radioactive debris (residual fallout) was simulated by internal seeding of an HE charge using iridium-coated sand particles having a density of about 2.6 gm/cm^3 and diameters smaller than 175 microns, the latter being an appropriate size representation of actual nuclear fallout

particles [1]*.

The HE explosive used in the ESSEX Program was nitromethane, a liquid explosive having properties very similar to TNT. The iridium-coated quartz particles (10 percent of the total charge weight) were added to the nitromethane (87 percent of the total charge weight). The mixture was then stirred while adding a gelling agent (3 percent of the total charge weight). Stirring was continued until the mixture was sufficiently stiff to hold the quartz particles in suspension. Upon detonation, the particles were lofted by the venting phenomena, were carried by the winds, and eventually fell into an area where numerous sampling trays caught the fallout. Appropriate subsamples from each tray were then neutron irradiated, and the radioactivity of each subsample was determined by gamma ray spectrometry. The actual iridium content was determined by its characteristic 0.316-Mev gamma ray. Using this method, it was possible to contour the deposition pattern and through appropriate factors to relate the iridium fallout to the dose rates expected for a nuclear event of roughly equivalent yield.

TEST PROGRAM

The experimental program of ESSEX consisted of nine detonations, each with a nominal yield of 10 tons TNT equivalent. A complete listing of the shots is shown in Table 1; the various experimental programs, conducted on each of the shots, are listed in Table 2. All shots were fired in the Peason Ridge Area of the Fort Polk Military Reservation near Leesville, Louisiana. The near-surface geology was typically sandy-clays and clayey-sands; at one site (12MU), a fairly competent rock layer (about 6 metres thick) was present at a depth of about 2 metres. A major target-response program was conducted in conjunction with the 6MPS Event.

RESULTS OF THE PHENOMENOLOGICAL EXPERIMENTS

Cratering. Dimensions of the nine ESSEX craters are given in Table 1. Omitting the 12MU results (the 12MU Event was the shot with the 6-metre siltstone rock layer), the apparent crater depths ranged from 4 to 9 metres; the radius from 19 to 27 metres; and the volume from 4000 to 6000 cubic metres. The mean dimensions of the craters, excluding 12MU, were: depth, 5.7 metres; radius, 22.7 metres; and volume, 4850 cubic metres. The overall variations reflect a data spread of roughly $\pm$50 percent for depth and $\pm$20 percent for radius and volume. These ranges reflect the variations associated with the insitu geological differences, the variations in the depth of burst, and the variations in the stemming of the charge emplacement

*See comparably numbered entrees in the list of references.

*STRANGE

TABLE 1. LISTING OF ESSEX SHOTS ALONG WITH CRATER DIMENSIONS

Shot	Yield, tons	Apparent Crater Dimensions			True Crater Radius, m
		Radius, m	Depth, m	Volume, m^3	
3MS	11.5	21.5	4.9	4290	24.0
3MU	9.0	20.6	4.6	4400	25.0
6MS	10.0	26.2	4.6	6050	33.5
6MPS	10.0	21.8	5.0	5400	27.0
6MWS	10.0	20.6	9.3	5530	22.0
6MU	8.0	23.6	5.2	5010	27.4
12MS	10.0	18.8	8.5	4750	22.1
12MPS	10.0	26.9	3.7	5360	--
12MU	8.0	14.4	4.0	1200	19.0

TABLE 2. TECHNICAL PROGRAMS OF ESSEX

Technical Program	Title
1	Cratering, Ejecta, and Barrier Effectiveness
2	Ground Shock/Motion Measurements
3	Airblast Measurements
4	Technical Photography
5	Radiation Simulation
6	Detonation Physics
7	Code Calculations for Simulation Design
8	Geologic Exploration and Equation of State Studies
9	Construction and Support

hole.

All nine craters constituted a BATM for the following vehicles: an M60 tank, an M113 armored personnel carrier, and the M175 1-1/4-ton wheeled cargo vehicle. The relative size of the ESSEX craters compared to those that would result from a 1-KT nuclear yield is shown in Figure 1; the 1-KT crater provides a BATM roughly 3.5 times larger than the one associated with the 10-ton HE events.

Ejecta. For the nine ESSEX events, the continuous ejecta field was generally confined to within a range equivalent to 3 apparent crater radii. The thickness of the continuous ejecta blanket at its thickest point was about 1/5 of the crater depth.

The maximum range to which ejecta fragments (clods) were thrown ranged from ~300 metres for the 12M Events to ~800 metres for the 3M Events. Scaled maximum ejecta range (SR_{max}) as a function of scaled DOB (SDOB) is shown in Figure 2. Included in the data set were a number of large HE shots plus several nuclear events. The data are empirically defined as a bilinear upper bound of the data envelope. Appropriate equations for these lines are given, and from them, expected maximum ejecta range can be calculated; however, yields larger than about 1000 tons (TNT equivalent) should not be used.

Ground Shock/Motion. Shock and motion measurements, primarily stress and particle velocity, were made generally at the same depth as the shot, i.e., at shot horizon, and at locations near the ground surface. At the shot horizon, which was generally in a wet soil, the shock propagation velocities for the nine events ranged from 1400 to 2000 metres/sec. In the dryer soil layers (layers well above the water table), the propagation velocity was in the range of 400 metres/sec.

Stress levels and particle velocities as a function of range are shown in Figures 3 and 4, respectively, for gages emplaced at shot depth (wet soil). Stress amplitudes in a significantly dryer soil but still quite moist (the 6MPS Event) were lower than those shown in Figure 3 by a factor of 30 to 40. Excluding the 6MPS results, the particle velocities for the 6M DOB's events were approximately three-fourths those at the 12M DOB; and those at the 3M DOB's were about one-third those at the 12M DOB's. Generally, the stemmed shots tend to define the upper bound of the data and the unstemmed data the lower bound.

Airblast. Results of the airblast measurements close-in and far-out are shown in Figures 5 and 6, respectively. The shallow-buried, unstemmed shots form the upper bound of the observed data and the more deeply buried, stemmed shots form the lower bound. For the long-range airblast, the 3MU overpressure curve is higher than the 12MS curve roughly by a factor of 30. Damage to typical aboveground military targets is not expected to be significant if the overpressure

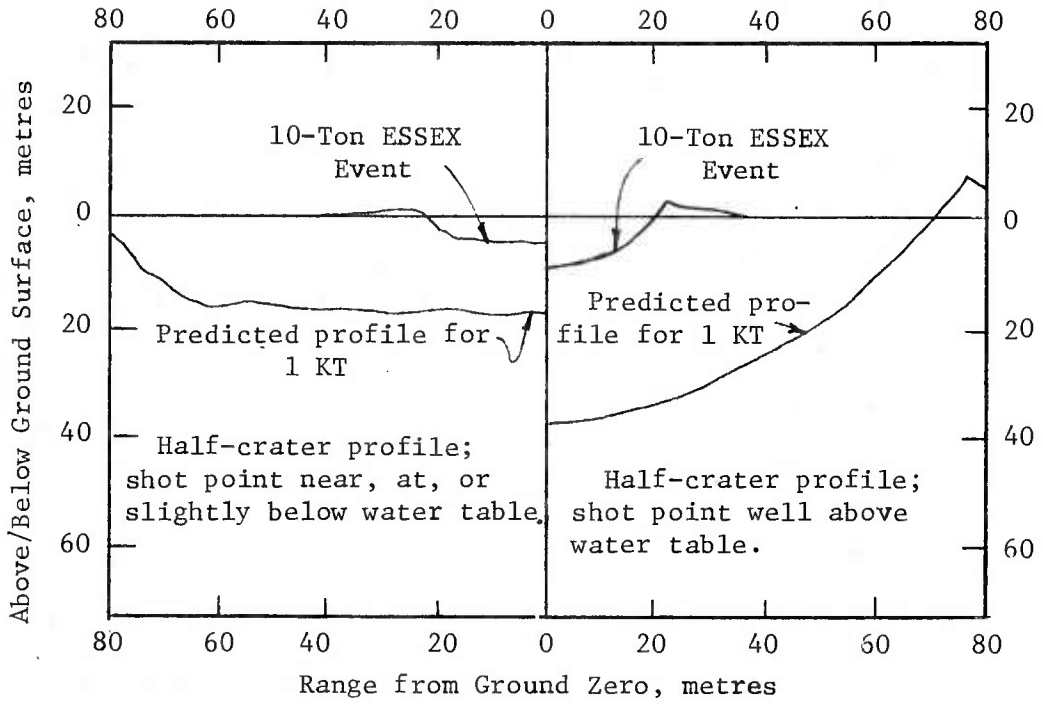

FIGURE 1 Comparison of ESSEX-type crater with the predicted crater for a 1 KT yield at the same scaled depth of burst (20 metres).

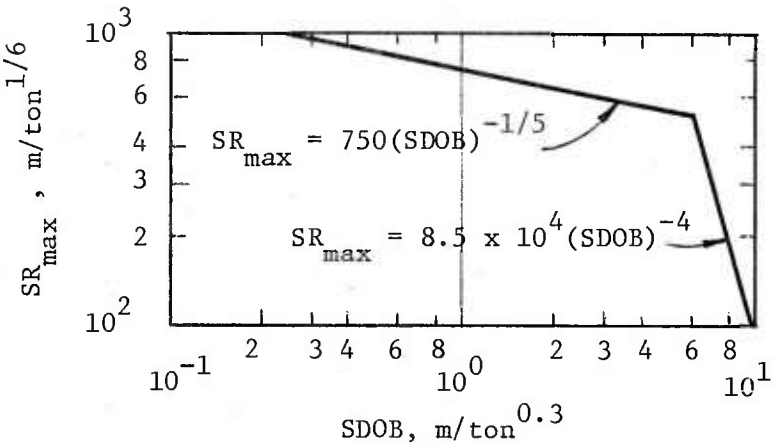

FIGURE 2 Scaled maximum ejecta range as a function of scaled depth of burst.

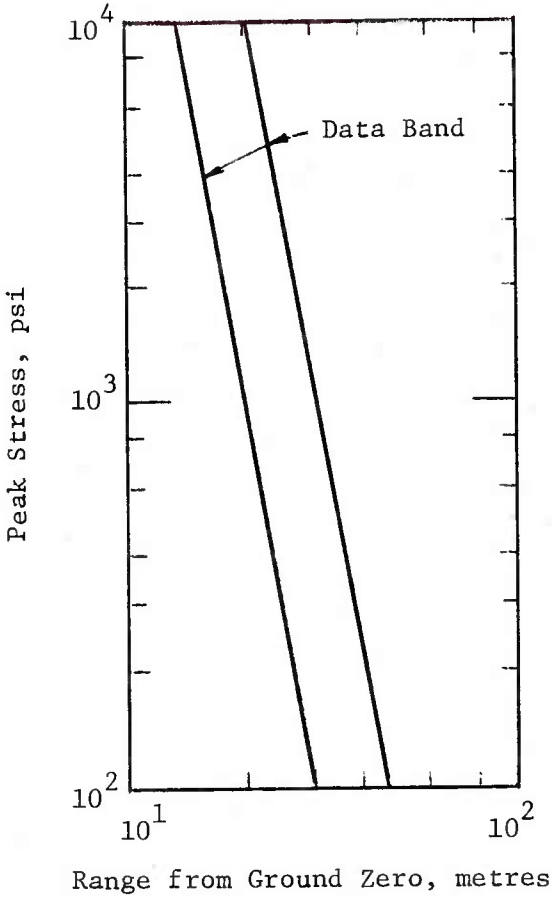

FIGURE 3 Direct induced peak stress as a function of range from ground zero.

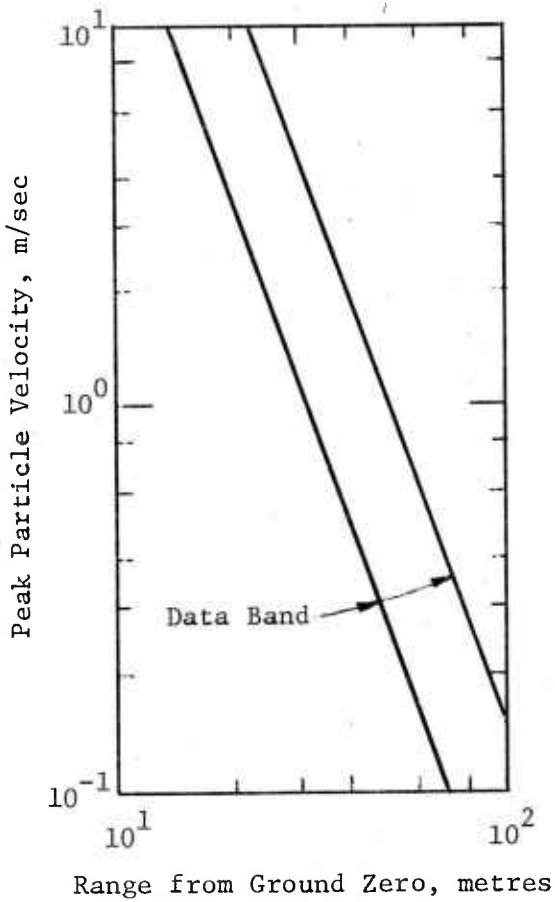

FIGURE 4 Peak particle velocity as a function of range from ground zero.

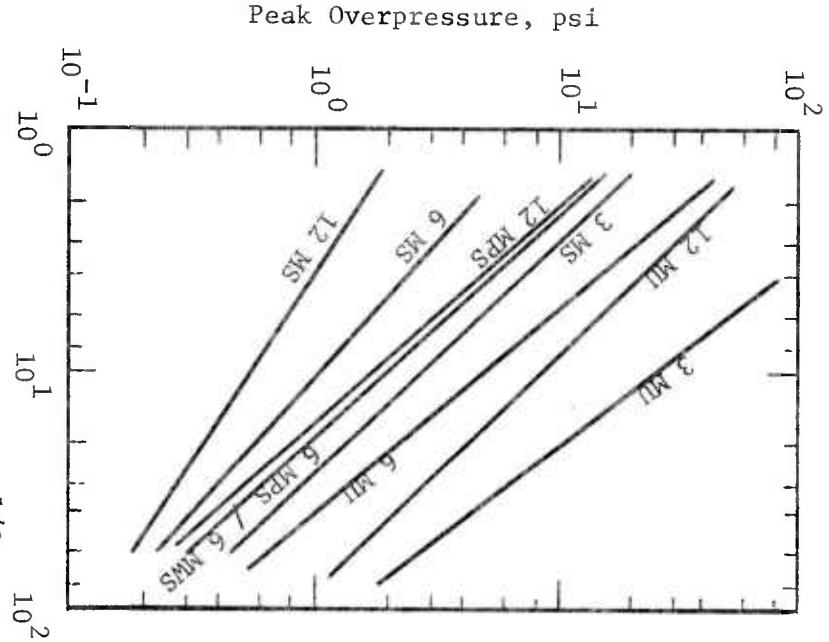

FIGURE 5 Results of close-in airblast measurements.

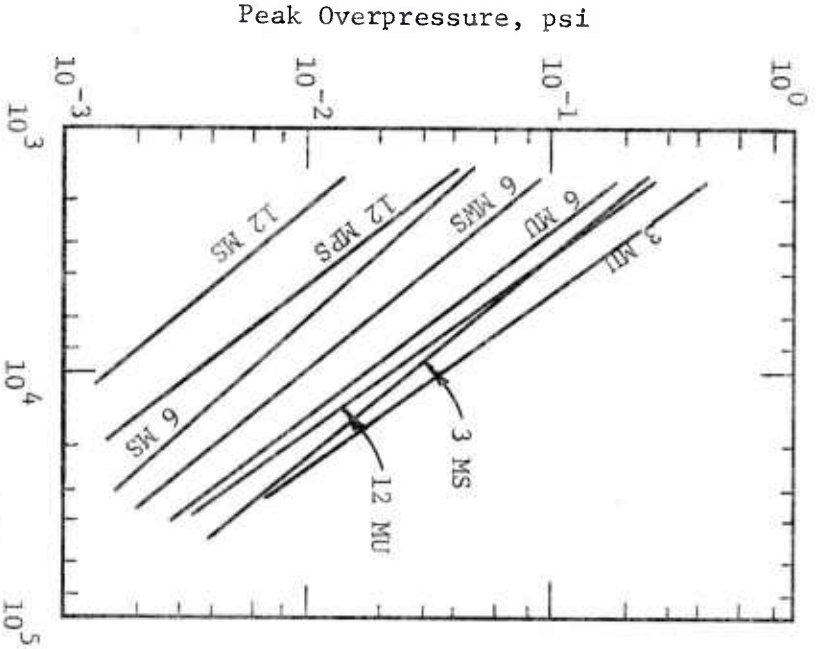

FIGURE 6 Results of far-out airblast measurements.

is less than about 0.03 psi (2 millibars).

Radiation Simulation. The highly significant implications of the radiation simulation experiments, conducted on eight of the nine ESSEX Events, are shown in Figures 7 and 8. The vent fractions* common to the ESSEX shots are much lower, generally an order of magnitude lower, than shots which occurred in dry soils. Prior to ESSEX, an increase in the vent fraction had been predicted for detonations in wet soil; obviously the ESSEX results show just the opposite. Significance of the lower vent fraction means that the dose rates beyond the limit of the continuous ejecta will be less than values obtained from current prediction methods by a factor of 10 or more.

Figure 8 graphically shows the 150 rad envelope as predicted by current state of the art codes and the 150 rad envelope predicted by the NCG method [2] and by ESSEX. As is evident, the residual radiation poses much less of a problem than originally thought assuming the results of the ESSEX simulation technique are valid. An ESSEX-type simulation shot has been proposed for the Nevada Test Site (NTS) to test the validity of the ESSEX results against the results of a nuclear event. Meanwhile, systems designers are cautioned not to make use of these data until the results of the NTS validation tests are available or until analytical studies now underway show the results to be valid.

STRUCTURAL RESPONSE EXPERIMENTS

Various structures, representative of likely theater targets were constructed to a scale of 1 to 3.7**. The structures were exposed to the blast and shock effects of the 6MPS Event. The structural array is shown in Figure 9. In addition, airfield runway response was evaluated on two other shots, viz., the 3MS and 12MS Events. The response of the various structures is described below.

Airfield Runways. Model airfield runways, constructed in the same manner as full-scale Warsaw Pact runways, exhibited considerable damage due to vertical displacement of the articulated slabs out to about 2 crater radii for a detonation occurring at near optimum depth for cratering. Damage due to ejecta debris, sufficient to preclude use of the runways, occurred out to about 5 crater radii. For 1 KT, these damage radii would amount to about 200 metres for damage due to uplift and displacement and about 500 metres due to ejecta debris.

---

*Vent fraction is defined as that fraction of the total radiation vented that falls beyond the limits of continuous ejecta.

**At the scale of 1 to 3.7, the 10-ton events of ESSEX model a nuclear detonation of about 1 KT.

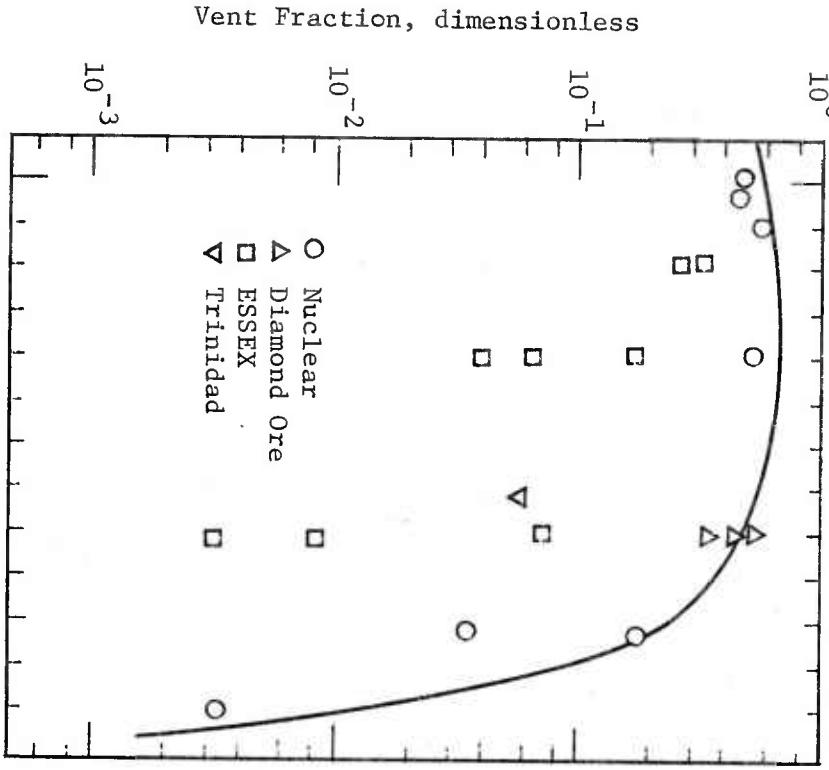

FIGURE 7 Variation of vent fraction with scaled depth of burst.

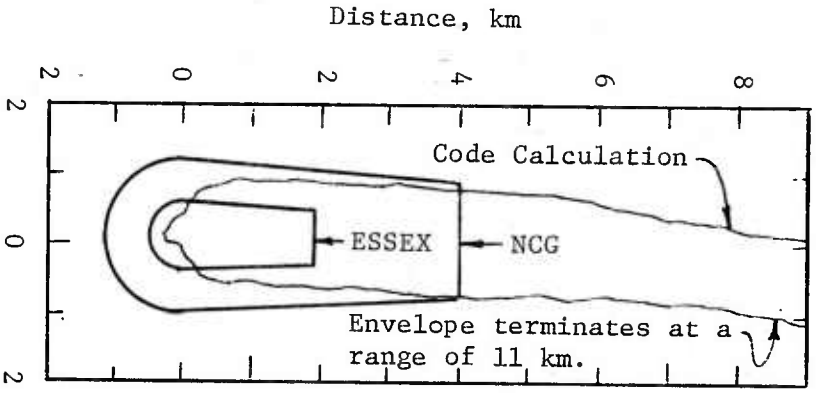

FIGURE 8 Comparison of 150 rad at 50 hours.

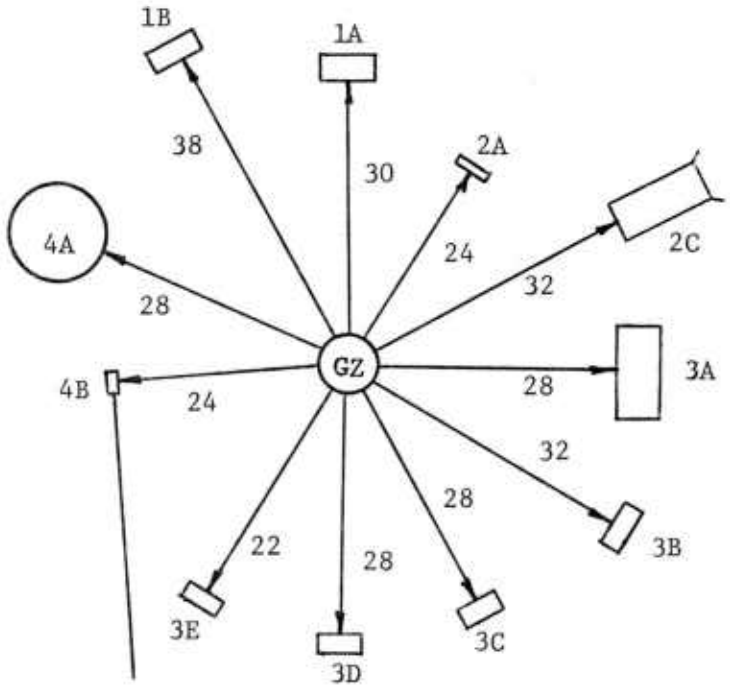

1 Aircraft Shelter
- 1A Structure 1
- 1B Structure 2

2 Bridges
- 2A Bridge Pier on piles
- 2B Bridge Span

3 Buried Hardened Structures
- 3A Arch Structure
- 3B Rectangular Structure (L/d = 10)
- 3C Rectangular Structure (L/d = 10)
- 3D Rectangular Structure (L/d = 4)
- 3E Rectangular Structure (L/d = 4)

4 POL
- 4A Storage Tank
- 4B Pipeline

NOTE: Numbers along the various radials are distances (in metres) from ground zero (GZ) to each structure.

FIGURE 9 Structural array for the Phase 3 Event of ESSEX.

Hangarettes. The aircraft shelters exposed to the 6MPS Event were 1/3.7-scale models of earth-mounded, precast, reinforced concrete shelters made of 90-degree arch segments bolted at the crown and supported by precast strip footings. Both shelters, one at 30 metres and one at 36 metres, apparently were undamaged by either the blast or shock; however, the 30-metre shelter collapsed as a result of the ejecta fallback and the one at 36 metres was severely damaged by ejecta.

Bridging. A typical bridge, typical in the sense that it was representative of the population of bridges within the Warsaw Pact that might be targeted, was constructed at a scale of 1 to 3.7 and exposed to the effects of the 6MPS Event. The single-span bridge, consisting of one pier and an abutment, was aligned along a radial extending from ground zero (GZ); the pier was located 32 metres from GZ and the abutment was 44 metres from GZ (thus the bridge span was 12 metres).

Test results indicate that bridges will be generally undamaged from underground bursts unless a pier or abutment is within one apparent crater radius of GZ. Moreover, the test showed that ejecta fallback of the character present in the Fort Polk tests is not capable of destroying a bridge span even when the 10-ton results are scaled to 1 KT.

Reinforced Concrete Box Structures. Four rectangular box structures, buried 6 decimetres and having interior dimensions of 1.2 metres high, 1.2 metres wide, and 5.5 metres long, were exposed to the effects of the 6MPS Event. Two structures had wall, roof, and floor thicknesses of 12 cm [roof span-to-thickness ratio (RSTR) was 10] while the other two structures had wall, roof, and floor thicknesses of 30 cm (RSTR was 4). The structures were placed at ranges of 22 metres (RSTR=4), 28 metres (RSTR=4), 28 metres (RSTR=10), and 32 metres (RSTR=10).

Preshot predictions, made from two-D finite element codes, indicated structural damage for all structures based on the stress-time histories observed from other ESSEX shots. As pointed out earlier, the stress levels common to the 6MPS Event were lower (by a factor of 30 to 40) than anticipated and consequently no structural damage occurred to any of the structures. They were however severely displaced, moving as a rigid body (the structures were somewhat less massive than the soil they displaced). Had personnel been inside the structures at the 22- and 28-metre ranges, they undoubtedly would have sustained serious injury. Equipment inside these same structures likely would have been damaged and perhaps rendered inoperable.

Reinforced Concrete Arch. A circular arch, buried 6 decimetres with an interior radius of 2.1 metres, thickness of 28 cm, and length of 7.5 metres, was exposed also to the 6MPS Event. The arch

was placed broadside to the event at a range of 28 metres. As was the case with the buried box structures, no structural damage was experienced by the arch. Thus, one would not expect structural damage to similar arches in such a media at a range of 1.3 crater radii or at a scaled range of 14 m/ton$^{1/3}$ (140 m/KT$^{1/3}$).

Shallow-Buried POL Tank and Pipeline. The ESSEX POL storage tank modeled a typical Warsaw Pact type tank. The model tank was fabricated with steel walls; its roof was constructed with reinforced concrete supported by steel beams and columns. Its diameter was 15.5 metres. The tank was surrounded by a circular reinforced concrete retaining wall with a walk space between the tank wall and the retaining wall. The tank was underground and covered with 12 to 15 cm of natural soil.

The tank, located with its nearest point 28 metres from GZ, was destroyed by the blast. The tank, filled with water to simulate fuel, was completely emptied by the net effect of the blast. Principal damage was caused by differential displacements associated with the mass movement of the earth material involved in the crater rim upthrust and by ejecta, which collapsed the roof of the structure.

A model POL pipeline (15 centimetres in diameter) was also exposed to the 6MPS Event and survived with but minor loss in pressurization (500 psi before the shot; 400 psi after the shot). The pipeline was oriented along a tangent to a circle 24 metres in radius and centered on GZ. The simulated pumping plant was located at the point of tangency. The pipeline was 60 metres in length. Peak transient displacements at the simulated pumping plant amounted to about 2.5 metres (horizontal) and 1.7 metres (vertical).

CONCLUSIONS

Results of the ESSEX experiments highlight the following conclusions which should not be generally applied to yields greater than a few KT.

(1) Craters resulting from yields as low as 20 tons nuclear and at scaled DOB's $\geq$ 10 m/KT$^{1/3}$ will definitely constitute a BATM if it is necessary for the vehicle to pass through the crater. Obviously, craters resulting from 1-KT yields will produce barriers of major proportions.

(2) Ejecta definitely must be considered a major cause of damage for shallow-buried structures that have only a thin earth (soil) cover if the range from GZ is less than 1.5 to 2 crater radii; for hardened aboveground structures at ranges less than 2 crater radii; and for airfield runways at ranges less than 5 crater radii.

(3) Airblast effects from underground detonations may be disregarded as a prime source of damage to hardened and/or mounded aboveground structures if located 2 or more crater radii from GZ

provided the burst depth equals or exceeds 1.4 m/ton$^{1/3}$ (HE) and 14 m/KT$^{1/3}$ (NE).

(4) Ground shock/motion phenomena, associated with yields in the range of a few KT or less, are incapable of causing structural damage to most hardened underground structures if they are located at ranges equal to or exceeding (200 KT$^{1/3}$) metres, or about 2 crater radii. However, injury to personnel and damage to equipment inside such structures should be expected.

(5) Assuming that the radiation simulation technique of ESSEX is valid, the residual radiation levels will be much lower at reasonably large distances from GZ than current manuals predict but much higher in the crater area and its immediate environs. The higher radiation levels close-in greatly enhance the barrier effectiveness of ESSEX-type detonations by denying the enemy access to the site for a period of time on the order of days.

FUTURE PLANS

Since there is at present some differences of opinion within the radiation community as to the validity of the ESSEX simulation technique, an ESSEX-type test has been proposed for the NTS. The central purpose of this test is to compare the ESSEX radiation simulation technique with the residual radiation measurements obtained from the TEAPOT ESS Event conducted at NTS in 1955. The ESSEX NTS Event would be a nominal 10-ton gelled nitromethane detonation emplaced 6 metres below ground. This would roughly constitute (assuming a 2 to 1 NE/HE equivalency) a 1 to 3.7 scaled model of the TEAPOT ESS nuclear event with its nominal 1-KT yield. In addition to comparing radiation results, crater, ejecta, ground shock, airblast, cloud dynamics and overall cloud size (all properly scaled) would be compared to the TEAPOT ESS Event.

A two-volume summary report on the ESSEX Program will be published during FY 1978.

*STRANGE

LIST OF REFERENCES

1. Adams, Nolan J. (Major), Lane, William B., and Webster, Lynn C. (Major), A PRELIMINARY ASSESSMENT OF THE RADIATION SIMULATION EXPERIMENTS OF PROJECT ESSEX I, Weapons Effects Laboratory, U. S. Army Engineer Waterways Experiment Station, Vicksburg, Mississippi, August 1977.

2. Burton, Donald E. (Captain), THE NCG FALLOUT SCALING MODEL: A GRAPHIC-NUMERICAL METHOD OF PREDICTING FALLOUT PATTERNS FOR NUCLEAR CRATERING DETONATIONS, U. S. Army Nuclear Cratering Group, Lawrence Radiation Laboratory, Livermore, California, January 1970.

AD-A056491

HIGH ENERGY METAL HYDRIDE FUEL CELL POWER SOURCE

*WALTER G. TASCHEK, MR. AND CORNELIUS E. BAILEY, JR., MR.
US ARMY MOBILITY EQUIPMENT RESEARCH AND DEVELOPMENT COMMAND
FORT BELVOIR, VIRGINIA 22060

INTRODUCTION

A fuel cell is a device which produces electricity cleanly, silently and efficiently. Like the familiar dry cells and lead acid batteries, fuel cells work by virtue of electrochemical reactions in which the energy of a fuel and an oxidant are directly transformed into direct current electricity. Unlike batteries, however, fuel cells do not consume the chemicals that are part of or stored within their structure. The reactant chemicals used by fuel cells are supplied from an external source. This feature, in principle, allows the fuel cell to operate as long as fuel and oxidant are supplied and reaction products removed.

Figure 1 illustrates the operation of a fuel cell. Hydrogen is supplied to the anode where it electrochemically reacts on a catalytic surface in contact with the electrolyte (an acid in this case). Oxygen, or air is supplied to the cathode where it also electrochemically reacts on a catalytic surface in contact with the electrolyte. The anode and cathode reactions occur simultaneously when a load is applied to the external circuit. When the circuit is interrupted or the supply of either reactant is halted, the reaction stops.

The fuel cell's high efficiency, and high energy density, prompted its development for space applications. Fuel cells were successfully developed for GEMINI, and APOLLO missions and today alkaline electrolyte fuel cells are an established technology for space applications.

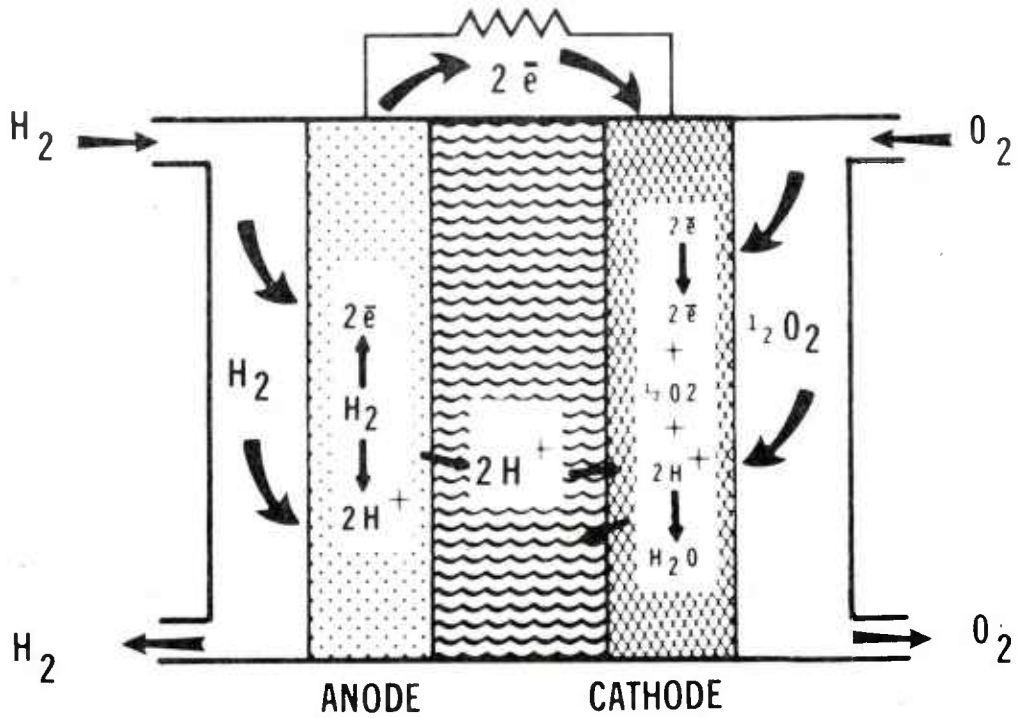

ANODE REACTION $H_2 \rightarrow 2H^+ + 2\bar{e}$

CATHODE REACTION $\frac{1}{2}O_2 + 2H^+ + 2\bar{e} \rightarrow H_2O$

OVERALL

$$H_2 + \frac{1}{2}O_2 \rightarrow H_2O$$

Figure 1. General Construction and Reaction Equations for Fuel Cells

Concurrent to the development of fuel cells for space applications, the US Army Mobility Equipment Research and Development Command (MERADCOM) led development efforts on phosphoric acid fuel cells for terrestrial applications. Phosphoric acid fuel cells typically operate in the range of 150 to 200°C. They can operate on air and hydrogen rich fuel streams derived from liquid fuels such as methanol

and the logistic hydrocarbons. The fuel stream carbon monoxide content must be low, typically less than three percent. Using concentrated phosphoric acid electrolyte at 150 to 200°C temperatures greatly simplifies electrolyte control of water produced by the electrochemical reaction. The water simply evaporates into the reactant fuel and air streams. Aklaline electrolyte fuel cells must use pure oxygen and hydrogen because the electrolyte reacts with carbon dioxide in air and reformed fuel streams.

MERADCOM is currently developing a family of Silent, Lightweight Electrical Energy Plants (SLEEP). The SLEEP power plants will comprise the 0.5 through 5 KW range and will operate on reformed methanol and air. These fuel cell power plants are expected to replace corresponding gasoline engine generator sets now in the field.

Today the phosphoric acid fuel cell is a strong contender for commercial base load electrical power generation and for industrial and residential applications.

LOW POWER APPLICATIONS

The need for smaller, high energy density power sources, in the one to 100 watt range, to power tactical surveillance or communications equipment was recognized several years ago, but development efforts on fuel cells in this realm were unsuccessful for two reasons; a practical fuel cell for low power, low maintenance operation was not available and, hydrogen generators utilizing high energy fuels were complex and required handling and disposing of caustic materials.

Research efforts at MERADCOM have solved both of these shortcomings. First, a hydrogen generator has been developed which utilizes calcium hydride and water.[1] Hydrogen is produced according to the fuel cells demand by utilizing diffusion control principles. Consequently the water source is not contaminated and the reaction product, lime, poses no disposal problems. The hydrogen generator can be sized for any power output and for a wide range in mission lengths.

Secondly, a hydrogen/air fuel cell utilizing a solid polymer electrolyte (SPE) was found to operate well at low temperatures. Since the electrolyte is solid, product water formed simply drains off. Aqueous liquid electrolyte fuel cells will pick up water at normal ambient temperatures. This water accumulation is undesirable and must be removed for extended operation.

MINIATURE HYDROGEN GENERATOR

Pure hydrogen is generated by the reaction of water with some metal hydrides or alkaline earth metals. In the example shown in Figure 2 the reaction of water vapor with calcium hydride supplies hydrogen on demand by the fuel cell. Water from the reservoir flows into the water chamber adjacent to porous hydrophobic membrane. Water vapor diffuses through the membrane and spontaneously reacts with calcium hydride to produce hydrogen.

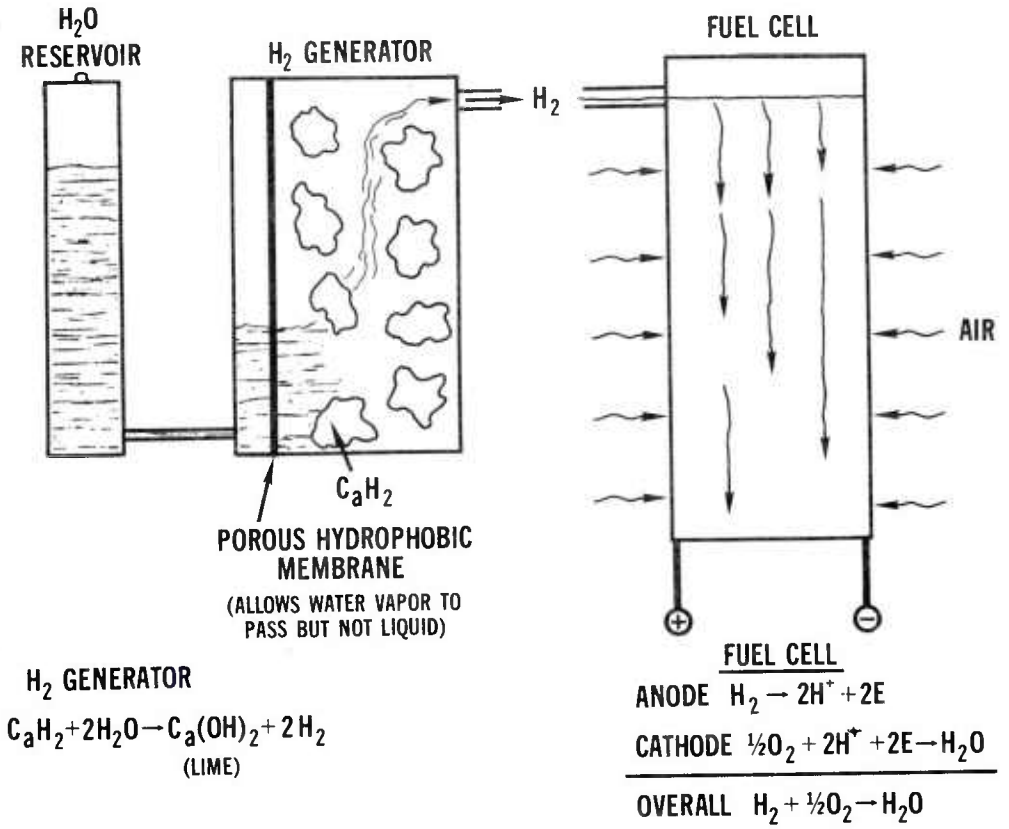

Figure 2. Schematic Diagram of Metal Hydride Fuel Cell Power Sources

At no load, hydrogen is not consumed and the pressure within the reaction chamber increases, thereby forcing water into the reservoir and out of the water chamber. This action reduces hydrogen production. As hydrogen is consumed by the fuel cell, the water level will self-adjust to generate only the required amount of hydrogen. Refueling is easily accomplished by dumping the lime and adding more

fuel and water.

Hydrogen generation rate increases as temperature increases due to higher vapor pressure, but since production is self regulated according to demand it simply means that the water level will drop with increasing temperature for a given demand rate. Conversely, at low temperatures the water level tends to be higher. Below an operating temperature of 0°C., pure water freezes. The hydrogen generation reaction, however, is exothermic. Design calculations indicate that only a moderate amount of insulation would be required to keep the hydrogen generator above freezing while operating in ambient temperature down to -40°C. Also, it appears possible that salt water or antifreeze will allow the hydrogen generator to start up and operate in 0 to -40°C temperatures. For the very cold ambient temperatures, a small portion of the high energy fuel would be converted into heat, this action will promote bootstrapping of the hydrogen production rate.

The hydrogen generator shown on Figure 3 was designed, fabricated and successfully demonstrated for applications where abnormally high hydrogen production rates could occur. The porous hydrophobic membrane will pass liquid water if pressures exceeding 0.25 atm occur across the membrane. To prevent direct contact of fuel and liquid water, a dual membrane approach was used. This generator is identical in principal and function to the one discussed previously (Figure 2) except that it uses a dual membrane. If the excessive demand for hydrogen occurs and the differential pressure of 0.25 atm is exceeded, then water will be pulled through the first membrane and out the hydrogen port. The water will never flow directly into the fuel chamber.

Many prototype hydrogen generators have been developed in-house. Capability of operation at very low power levels (1 watt) and at hydrogen production rates equivalent to 100 watts have been demonstrated. These generators covered a fuel capacity range of 20 grams to 500 grams. This is equivalent to net electrical energy output of 20 to 500 watt hours (WH) respectively. It is significant that larger sized generators could operate efficiently at high and very low loads.

Hydrogen generators using water activated metal hydrides based on the Kipp principle are well known. In most Kipp generators liquid water directly contacts the fuel with the consequence of eventual water and fuel contamination. After each mission, the remaining fuel must be removed and the unit cleaned to remove reaction products. The reaction typically forms an insoluable sludge and lye. The

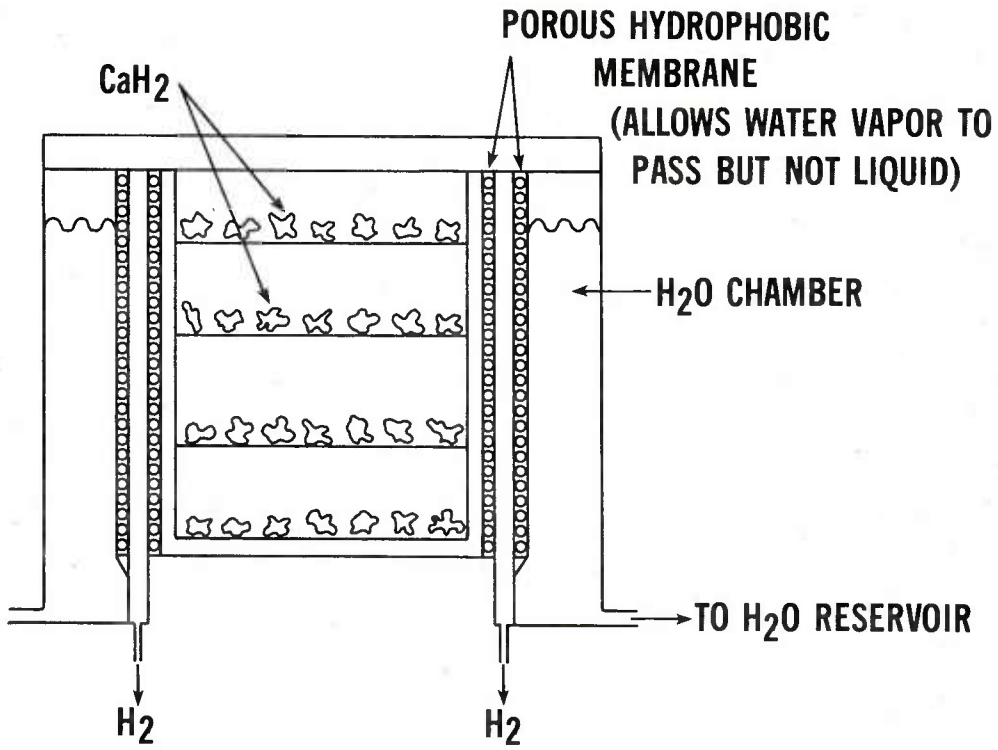

Figure 3. Cross Section of Double Membrane Hydrogen Generator

sludge will solidify and become difficult to remove if the unit is not cleaned. Kipp generators are simple to design, construct, and operate, but they are difficult to maintain and not suited for applications requiring varying periods of standby operation. The miniature hydrogen generators on the other hand will not contaminate the water supply, keep reacted fuel in convenient, disposable paper cartridges and do not require clean out.

SPE FUEL CELL

Figure 4 shows one of MERADCOM's early model hydrogen generators coupled to an SPE fuel cell stack that was purchased from General Electric. The SPE fuel cell operated simply and reliably and provided an excellent match with the miniature hydrogen generators. It, however, utilized costly materials and its design was not amenable to low cost construction. (Components were developed for high power space applications where material costs are secondary to performance.)

For low power applications a less expensive approach geared to more compact assembly of lower power density cells was needed.

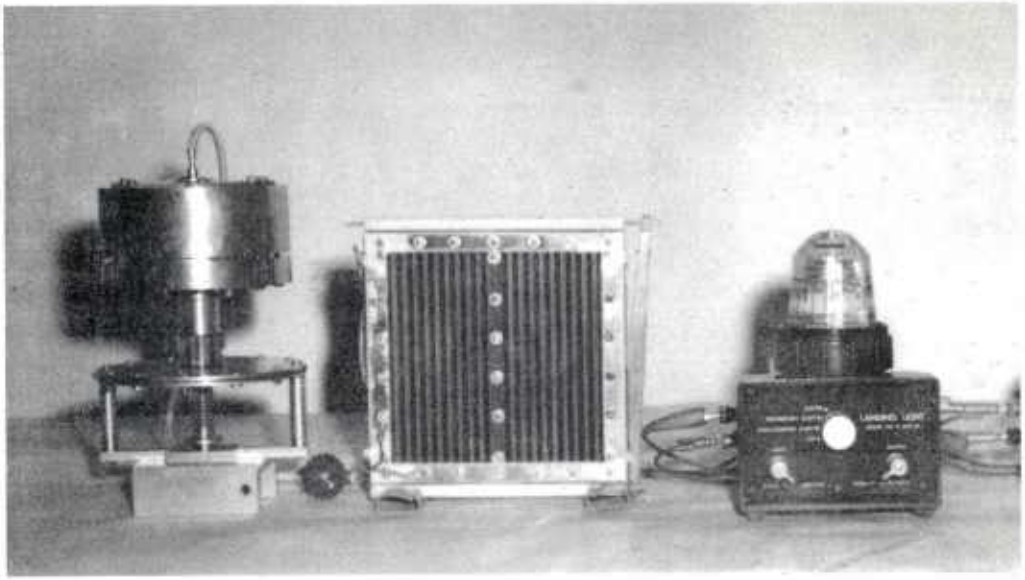

Figure 4. Hydrogen Generator and GE Fuel Cell Stack Powering Landing Lights

Firms experienced with fuel cells were briefed on MERADCOM's results and encouraged to respond to a competitive RFP for the design, development, and fabrication of thirty, 3 watt, 6 V SPE fuel cell stacks. Engelhard Industries won the competition.

A photograph of a 3 watt stack is shown on Figure 5. Electrodes and bipolar separator plates developed for phosphoric acid fuel cell stacks were used with the SPE. The carbon based bipolar separator plates allow compact construction of cells in electrical series. The three watt stacks contain 8 cells to directly provide the nominal 6 V output. This construction technique was easily scaled up to a 24 V DC output at 20 watts. No limitation in power rating is foreseen. A 3 watt stack has been operated for more than 10,000 hours with no appreciable drop in performance.[2]

The SPE 3 watt stacks and in-house developed hydrogen generators were combined into a compact power source for landing/marker lights.

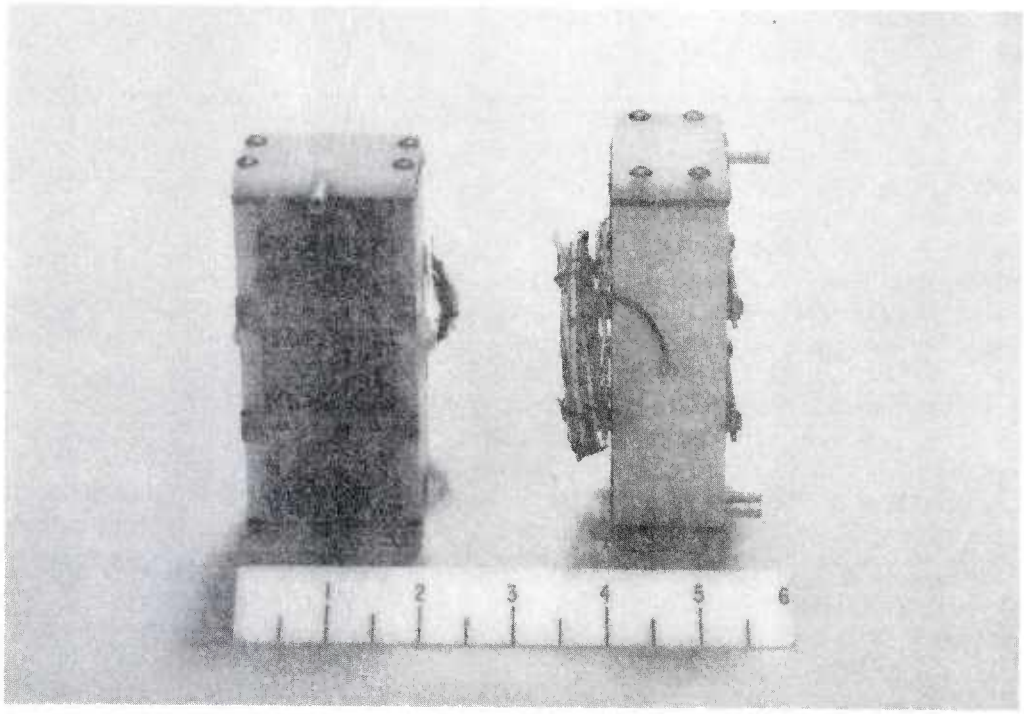

Figure 5. 3 Watt Engelhard Fuel Cell Stack

Ten units were fabricated and frequently demonstrated. Figure 6 is an accurate portrayal of the units. The unit is activated by inserting a paper cartridge containing calcium hydride into the fuel chamber, replacing the cover, and adding water. The power source requires no moving components and once activated requires no maintenance until fuel or water are exhausted. Refueling takes less than one minute on these prototype units. One charge of fuel (70 grams) operated the landing light for over 80 hours compared to 20 hours for the lantern battery power source designated for the light.

Success in this area prompted more serious evaluation of the low power market within the Army. What was found in general was that power requirements less than 1 watt were typically met by primary batteries and tactical requirements from 10 to 100 watts and higher were almost always filled by secondary batteries. For this latter situation the need for better power sources is most evident.

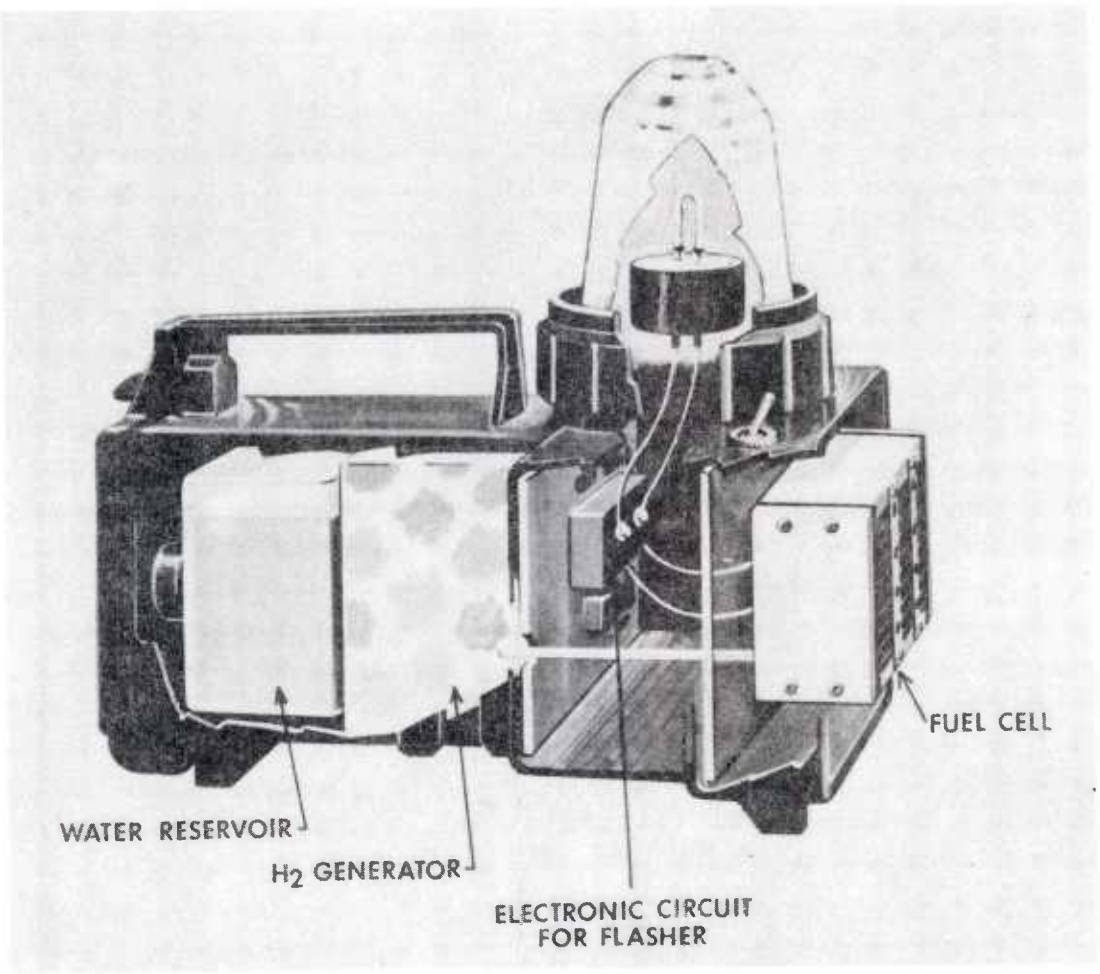

Figure 6. Cutaway of Marker Light Featuring Fuel Cell Power Source

Figure 7 shows what we term the "gray area". In this realm, we feel, that existing power sources are not available. Consequently, operational and mission effectiveness is compromised. The letters noted on the chart are actual battery power sources and these are identified on Table 1. Most of the equipment listed is tactical but several commercial applications are included as a frame of reference. One can extend operational capability into the "gray area" by doubling up on power sources, by running a lengthy power cord, by operating a noisy 0.5 or 1.5 KW generator set at a low load or run the equipment off a vehicle battery with the vehicle operating to charge the battery.

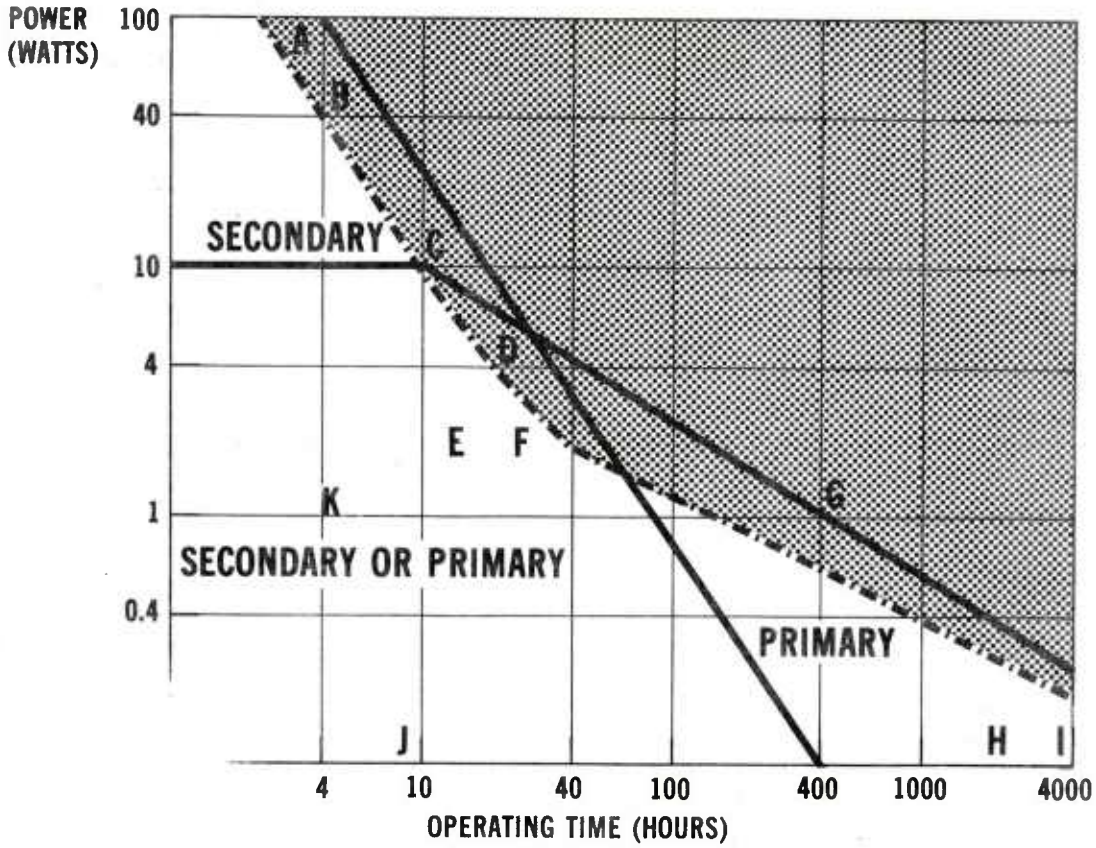

Figure 7. Gray Area Concept of Tactical Missions for Power Sources

Other approaches have been tried but not with widespread success. Thermoelectric generators are feasible but are not efficient, have a high thermal signature, are generally not adaptable to varying loads, and are expensive. The hand crank generator is fine for emergency operations but not for most tactical or remote application.

Military tactical power requirements are much more demanding then those of the civilian sector because utility power is frequently not available. Power and mission time of portable power sources are greater and a high premium is placed on energy density. For example, the silver zinc secondary battery is frequently selected because of its high energy density, (low comparative weight) even though it is more costly, shorter lived, and more difficult to maintain than the

EQUIPMENT	AVE. PWR. WATTS	BATTERY TYPE	BATTERY NUMBER	WEIGHT POUNDS	OPER. LIFE HOURS	REFERENCE
ELECTRIC WATCH	0.0001	DRY		0.02	8000	
ELECTRIC CLOCK	0.001	DRY		0.2	8000	
FLASHLIGHT	1	DRY	2 "D" CELLS	0.5	4	K
LANTERN LIGHT	2	DRY	BA 200	2	12	E
BARRICADE FLASHER	5	DRY		21	72	G
CALCULATOR	0.1	DRY OR NiCd		0.2	10	J
MIL RADIOS/TR						
AN/PRC-25	2	MAG.	BA 4386	4	60	
AN/PRC-77	1.8	MAG.	BA 4386	4	64	
AN/PRC-70	6	NiCd	BB-651	12	20	
AN/PRC-70	6	Sil-Zn	BB-536	8	30	D
AN/PRC-1	18	Sil-Zn		8	12	C
RADAR TRANSP						
SST-119	10	MAG.	BA 4386	4	12	
SST-119	10	Sil-Zn		16	70	
GLLD	6	NiCd		8	15	
RADAR SET						
AN/PPS-5	40	Sil-Zn	BB-622	11	5	B
AN/PPS-5	60	NiCd	BB-422	29	3.5	A
MINISID	0.1	LITHIUM		2	1500	H

Table 1. Power Source Applications

VOLTAGE	24-32 V DC
SIZE	4 x 12 x 12 inch
WEIGHT	15 pounds
FUEL CHARGE	1 pound Calcium Hydride
MISSION CAPABILITIES	360 Watt Hours (30 Watts for 12 Hours)

Table 2. Characteristics of 30 Watt High Energy Fuel Cell Power Source

familiar lead acid or nickel cadmium secondary batteries. For tactical equipments, the battery power source is generally considered a component of the equipment that it powers. While there is merit to this concept, it has fostered a proliferation of specialized batteries.

The portable radar set AN/PPS-5 is a good example of an equipment whose operational capability is limited by the power source. This set can be set up by two men in 10 minutes. It requires from 30-42 watts of power during operation. Power is supplied by a BB-622, silver-zinc secondary battery. Silver zinc does not have a good life (cycle or storage), is expensive, and has poor low temperature performance but it does have the highest energy density characteristics of rechargeable batteries. The training manual recommends "using alternate power sources, when possible, to reduce the burden of charging, maintaining, and replacing Storage Battery BB-622 (U) in the radar set. The alternate power sources will facilitate operation of the radar set if battery boxes containing Storage Battery BB-622 (U) are not available."[3] Optional power sources listed include a 29 lb. nickel cadmium storage battery, BB-422 (U); two 12 V vehicle batteries, 2 HN, connected in series; a 28 V Generator Set, PU-532PPS; and a Power Supply, PP-2953 which converts an alternating current source to 28 V DC. The AN/PPS-5 includes a power converter that adapts an external or internal 24 V DC power supply to 6 V DC. Converter inefficiency requires 60 watts external compared to 40 watt internal. Note reference A&B on Figure 7 and Table 1.

A 30 watt fuel cell power source is currently being developed for demonstration with various tactical communications and other electronic equipment, and as a battery charger. An artist concept of the unit is shown on Figure 8. Design characteristics of the demonstration unit are listed on Table 2. The unit will be available for demonstration this summer. A comparison of the high energy power source with available secondary batteries yields the following for a 24 hour, 30 watt mission: One 20 lb. high energy fuel cell power source complete with fuel and water would satisfy the mission. Each additional 24 hour mission would require an additional 2 lb. of fuel and 2 lb. of water.

The same 24 hour mission would require three battery power sources of the types listed in Table 3. Of course, a repeat mission would require additional batteries or charging equipment.

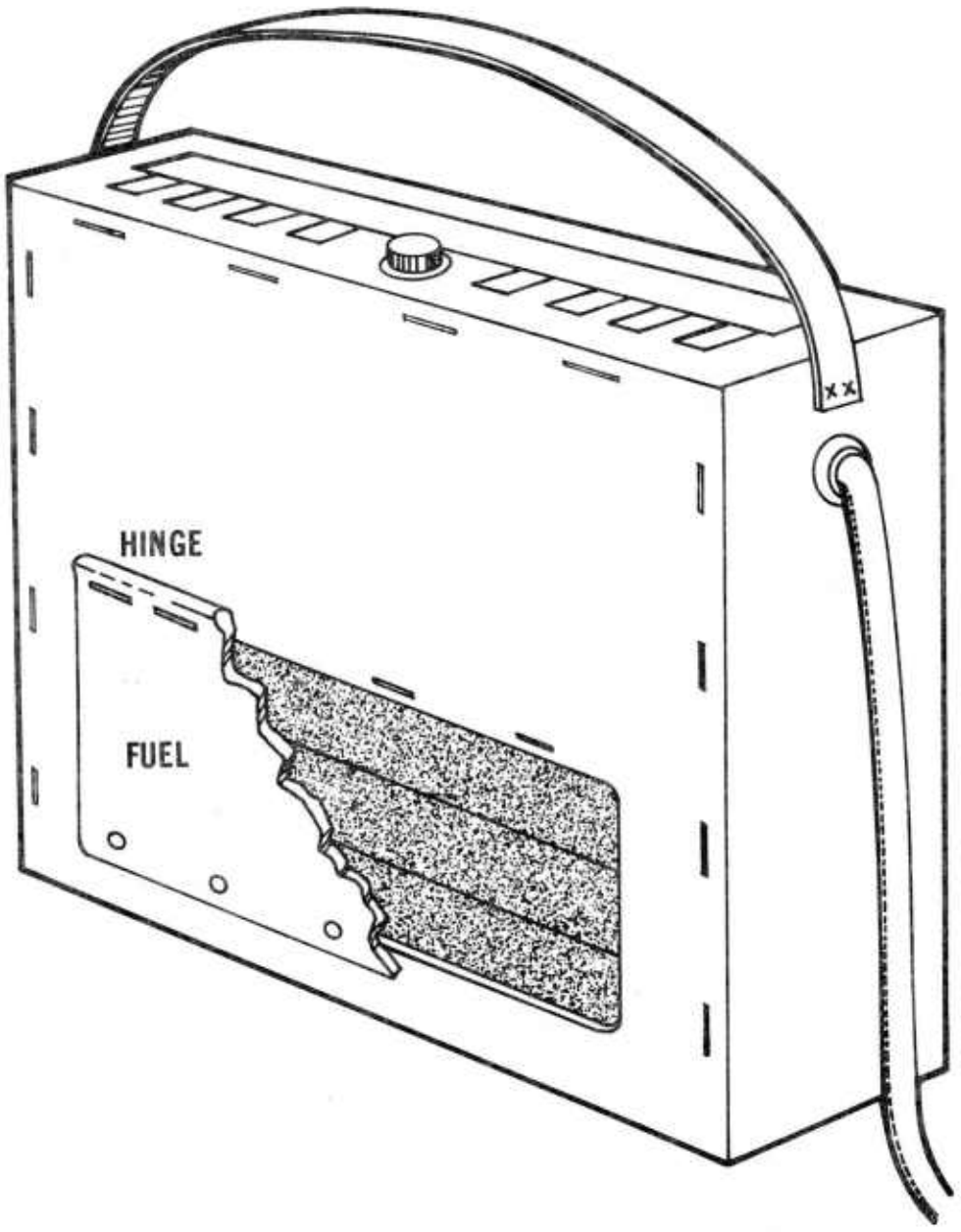

Figure 8. Artist Rendering of 30 Watt Power Source

Battery	Unit Cost[4] $	Weight (lbs)	Capacity at 70°F (WH)
24 V BB501/U	$725	32	308
24 V BB422/U	$231	29	240
6 V BB622/U	$170	11	240

Table 3. Characteristics of A Few Secondary Batteries

Fuel costs for the high energy power source are estimated at 2¢/WH. The logistic burden of storing, maintaining, transporting and charging secondary batteries depends on many factors and the overall costs are likely to be 5 to 20 times greater than those associated with the use of high energy SPE fuel cell power sources.

SUMMARY

The compact, maintenance free miniature hydrogen generator, in conjunction with a solid polymer electrolyte fuel cell represents an attractive electric power source for tactical and remote communications and surveillance equipment. This new electric power source may also be used together with a secondary battery to combine its high energy density feature with the high power density characteristics of secondary batteries. A 30 watt, 28 V power source will be available for demonstration in the near future.

REFERENCES

1. Taschek, W.G., National Fuel Cell Seminar, Boston, Mass, 1977.

2. Adlhart, O. Dr., Engelhard Industries, Metro Park Plaza, Iselin, N.J., Private Communication, Dec 1977.

3. TM 11-5840-298-12, "Organization Maintenance Manual, Radar Set AN/PPS-5," June 1967.

4. Department of the Army Supply Bulletin, SB 700-20, June 1975.

AD-A056492

TOXICITY AND TREATMENT OF SEA SNAKE ENVENOMATION (U)

* JAMES A VICK, LTC MSC
GEORGE V. PICKWELL Ph D.
OFFICE OF THE SURGEON GENERAL
WASHINGTON, D.C. 20310

INTRODUCTION.

In recent years, increasing interest has been directed to the sea snakes of the family Hydrophidae with special attention to their behavior general biology, and the chemical nature of their venoms. Several television features concerning sea snakes, together with newspaper and magazine articles, have generated substantial public interest in these animals (1-3)

Perhaps the greatest current interest in sea snakes lies in the probability of one species, Pelamis platurus (the yellow bellied sea snake), being an early immigrant into the Caribbean Sea from the Pacific Ocean when a Middle American sea-level canal is constructed (4-6). At present no resident, reproducing population of sea snakes of any species has been described from the Caribbean Sea or the Atlantic Ocean.

Concern on the part of members of the scientific community stems from the lack of adequate knowledge with which to judge the probable effect that Pelamis a fish-eating snake, would have on Caribbean pelagic ecology. A second and more immediate problem is the threat to human safety, particularly in regions frequented by tourists. Some scientists have predicted disastrous economic consequences to Caribbean tourist centers (presumed reduction in tourist trade) arising from the presence of this sea snake (6,7). The problem in this latter point of concern seemed to us to center about the following points (1) the actual potency of this sea snake s venom; (2) the quantity of venom available for delivery by individual snakes; (3) the degree of aggressiveness or willingness to bite displayed by

this snake, as well as the total number of snakes; and (4) the degree of fear expressed by people who encounter this snake. In attempting to answer these questions, we hope to shed some light on the true seriousness of the threat to man posed by marine snakes in a new habitat. This paper is a report on our findings, and includes an evaluation of the currently fielded sea snake antivenin

MATERIALS AND METHODS.

A. Sea Snakes.

Our specimens of Pelamis platurus were all collected within the confines of Bahia Banderas, Mexico. This is a deep water bay indenting the Pacific coast some 30 miles and having a mouth 10 to 12 miles across The town of Puerto Vallarta at the foot of the bay (population approximately 25,000) is a tourist resort popular among Mexican and American citizens alike.

The distribution of sea snakes in this area is similar to that which might be expected in the area around the proposed sea way canal.

While our research vessels were hove-to or at anchor during the Naval Undersea Center cruises "MINOX1 (July 1970) PELACAN I (March 1971), and MINOXII (March 1972)", we collected the sea snakes by dip-netting. Captured specimens were held aboard ship in gimbaled aquaria supplied with air bubblers and filters. The snakes were usually milked of their venom and tagged within moments of capture, but some were held for several days before their first milking.

When our holding capacity for live snakes aboard ship were reached (30 to 40 adult specimens), we continued milking newly captured snakes, immediately returning them to the water. Upon the ship s return to San Diego, the captured snakes were placed in aquaria supplied with seawater and filters; aquaria were located in a temperature-controlled room at 80 degrees F. The snakes were fed live goldfish at intervals of 7 to 10 days and were milked every 3 to 4 weeks.

B. Obtaining Venom.

The adult of the sea snake has fangs only 2 mm in length. We therefore followed the method of Barme (8), using capillary tubes of known volume for obtaining the venom. The milking operation involved three operators one restraining and manipulating the snake while the

other two each fitted a capillary over a fang . Frequently, the snake voluntarily expelled venom into the capillaries. Subsequent pressure applied along the venom glands and ducts (maxillary margin) usually extruded an additional quantity of venom (table I). The product from a number of specimens was polled for various tests and analyses. Fresh Pelamis venom was invariably water-clear.

C. Venom Treatment.

Depending on the tests planned, the freshly obtained whole venom was either refrigerated, frozen, or lyophilized. Fresh, unrefrigerated venom was, in some cases, placed on one of our gel filtration columns, submitted to pH determination, or percent solids and specific gravity measurements For whole venom fractionation, we employed Sephadex G75 40 in either a 2 X 300 cm glass column for maximum single pass resolution [9] or a 2 X 150 cm glass column for more rapid separations and use aboard ship. Gel filtration columns were calibrated for molecular weight determinations using primary standards supplied for this purpose in kit form (Pharmacia).

D Test Animals.

All basic toxicity tests were performed on adult male and female albino mice (age 8 to 10 weeks) from the Walter Reed randomly bred ICR/FG strain. Final toxicity assays employed either male mice weighing 30 to 35 grams, or female mice weighing 25 to 30 grams. Male and female mice were never mixed in toxicity tests. The LD50 was estimated using the graphic method of Miller and Tainter [10] and the statistical procedures described by Finney [11].

Stock venom test solutions were made up in cold physiological saline. Dilutions from stock were made so that venom concentration was contained in a standard volume for injection equivalent to approximately 1 percent of mouse body weight. Graded doses of the venom were injected into a tail vein of the mice For each venom dose tested, 10 mice were used. The LD50 evaluation was determined from several pooled assays performed over a 24-hour period. The mice were closely observed for symptomatology and death for 4 hours following injection. Deaths occurring within 48 hours of injection were included in the evaluation of the LD50.

Five lots of sea snake antivenin, batch numbers 549-009(1964) 011 1(1967), 020-1(1969) 23-1(1970) and 25 1(1972), obtained from the Commonwealth Serum Laboratories, Australia were tested for efficacy

against sea snake venom in Walter Reed ICR strain mice (Table IV)

Additional pharmacological tests were performed on adult beagle dogs (Army test stock) weighing 10 ± 2kg. In these animals, the venom was injected into a indwelling catheter in the femoral vein. A single primate test was run on a 6-kg male Rhesus monkey. In all these tests, the dogs and the monkey were anesthesized with sodium pentobarbital (30 mg/kg). Tests for vasoconstrictive and cardiotoxic effects of the venom were performed on the isolated perfused dog heart following the method of Vick and Herman [12].

RESULTS

A. Venom Production.

Bahia Banderas appears to be the northermost site of a year-round population of the Pelamis in the eastern Pacific and in addition, it functions as a nursery area where gravid females congregate to give birth to their free-swimming, precocious young. Consequently, the majority of the specimens listed in table-I were gravid and, therefore, probably heavier than non-gravid specimens of comparable length.

Even when there was no evidence for a broken or unregenerated fang, the venom production from right and left venom glands tended to be unequal by as much as a factor of two or more (table I). Frequently, a varying amount of venom would be voluntarily injected into the capillaries by the snake accompanied by visible contractions of the marginal maxillary musculature. Following this venom expulsion, an additional amount was usually available by milking. Venom production from apparently healthy, vigorous adult snakes ranged from a few lambda to a maximum of 33 lambda, but averaged 15 to 20 lambda per snake (table I; lambda = microliter). The venom was always waterclear and colorless except for the final few lambda expelled by milking which were occasionally cloudy with cellular debris.

B. Whole Venom Toxicity.

Fresh, liquid Pelamis venom (batch 1, refrigerated at 5 degrees C for no more than 4 days from time of milking to time of testing) was found to have an LD50 or 0.092 mg/kg in adult male mice (table II) based on an estimated 15.3 percent solids.* A second pooling of Pelamis whole venom that had been lyophilized (batch 2) showed an LD50 of 0.111 mg/kg in adult female mice (table III). Until

further testing we cannot say whether the apparent difference in toxicity of the two batches may be ascribed to a loss of activity in the freeze dried venom, a possible greater resistance on the part of female mice as has been shown for female over male mice in the Malayan pit viper venom or some other factor.

A limited series of toxicity tests on dogs in conjunction with pharmacological evaluation suggested a somewhat lower LD50 for whole Pelamis venom (fresh, liquid) in dogs than in mice, but insufficient data are available for valid statistical treatment. Using dogs, Vick (13) found the lowest LD50 (0.05 mg/kg) yet reported for any sea snake venom.

C. Toxicity of Major Venom Fractions.

Separation of Pelamis whole venom into its main components on our gel columns produced two major fractions (one a composite) together constituting about 90 percent of the total venom, and a series of minor components* (figure 1).

In the first of two series of tests on lyophilized Pelamis venom fractions, the cuts were obtained and labeled as indicated in figure 1. Although there was subsequent evidence of possible degradation in some of the fractions due to an error in handling during transport, both fractions 2 and 3 were found to be toxic for male albino mice (LD50 of 7.5 and 0.89 mg/kg, respectively) Neither fraction was as toxic as the fresh whole venom, obviously. Fraction 1 was found to be totally nontoxic for mice at concentrations from 50 to 500 mg/kg. Whereas fraction 3 from this batch proved quickly fatal for a single dog at the concentration tested, the same dose of fraction 2 in a second dog of equivalent size was not fatal.

In a second series of tests, cuts were made on the fractionated venom. In this case, some of the minor fraction residues were also tested. Again, only fractions 2 and 3 demonstrated toxic activity, whereas the remaining components were nontoxic at the maximum concentrations tested. Careful assessment of the LD50's for fractions 2 (0.201 mg/kg) and 3 (0.086 mg/kg) in female albino mice indicated that fraction 3 was more toxic than whole Pelamis venom. Fraction 2 is about as toxic as whole venom from the common cobra (Naja naja) (14)

D. Pharmacology.

1. Whole Venom.

The symptoms of envenomation in male and female mice were essentially identical. The dose-response relationship was very steep, typical of highly toxic substances. As the venom dose decreased, survival times increased. Major symptoms observed included deep and rapid respiration, always accompanied by severe mydriasis. At doses greater than the LD50 level, the mice were lethargic or semi-comatose and died almost instantaneously. At doses near the LD50, the symptoms of labored and rapid respiration occured approximately 15 minutes postinjection, accompanied by mydrdriasis. The heart beat seemed to increase. The mice at this stage appeared severely depressed and lethargic, showing impaired reflexes and occasional convulsions. As the effects progressed, respiration decreased and became more shallow until death occurred If the mice remained in this state for more than 2 hours following injection, they usually recovered.

Physiological data obtained from dogs receiving varying doses of Pelamis whole venom (batch 1) paralled results obtained by Vick (13) with dogs receiving venom of the sea snakes Laticauda laticaudata and L. semifasciata. This was particularly apparent for the arterial blood pressure, heart rate, and EKG, all of which remained unchanged for periods of minutes even at the highest venom doses. In common with envenomated mice, the respiration rate in some test dogs was unaffected at first, only gradually increasing in the final preterminal minutes as inspiratory volume declined. In the dogs receiving the highest doses, however, respiration rate remained almost unchanged until time of death.

In animals nearing death, arterial pressure rose simultaneously with a decrease in inspiratory volume while heart rate gradually declined. The abruptness of onset of these latter events and the speed with which they developed seemed directly related to venom dosage. The EKG wave form remained almost unchanged until time of termination.

Physiological events in poisoned monkeys were practically the same as in dogs except that bradycardia developed very abruptly and only in the terminal phase.

A series of graded doses of Pelamis whole venom (batch 1) was tested on the isolated, perfused dog heart. At dose levels equivalent to 0.5, 1.0, 1.5, 2.0, and 2.5 mg/kg of intact animal, no change in rate or force of contraction was shown by the perfused, beating

hearts.

The effectiveness of sea snake antivenin against the venom of 3 sea snake species is shown in Table IV. Results indicate that the antivenin is highly effective against the venoms of Laticauda laticaudata, Laticauda semifasciata, and Pelamis platurus and in addition retains its potency for at least 8 years.

2. Venom Fractions.

Although there were difference in toxicity between fractions 2 and 3 of Pelamis venom, and between these fractions and whole venom, the symptoms produced in mice by each fraction were the same as those elicited by whole venom. That is, the mice envenomated with either fraction in the toxic range showed dyspnea, mydriasis, and impairment of reflexes, particularly the righting reflex. Death, with whole venom, appeared to occur from respiratory failure.

In the dog poisoned with fraction 3, the sequence of events was nearly identical to the sequence seen with high doses of whole venom. In the animals receiving fraction 2, no symptoms directly attributable to the effects of envenomation were observed throughout the 3-hour experiment.

DISCUSSION.

A. Cause of Death from Pelamis Venom.

From the foregoing, it appears that Pelamis venom acts to produce respiratory arrest in animals critically poisoned. No evidence for cardio toxicity was found in whole venom or its toxic fractions. This is essentially in agreement with earlier work indicating respiratory arrest to be a major cause of death in experimental animals [15,16] and in human beings who are victims of sea snake bite. Respiratory failure arising from myoneural junction blockade at the level of the diaphragm was the cause of death in experimental animals injected with whole venom from the sea snakes Laticauda laticaudata and L. semifasciata [13].

B. Hazard to Man from Bites of Pelamis.

The venom of Pelamis is somewhat less toxic than that of other sea snakes studied in recent years [13,16]. In some cases, its

potency is equal to or greater than that of other sea snake species [8,16,18,20]. However, few toxicity studies of sea snake venom published to date have been done with optimal numbers of laboratory animals, particularly mice, from suitably homogeneous populations; or perhaps this important facet has been left undisclosed by the respective authors (exceptions -Vick [13] and Tu and Ganthavorn [20]. Data obtained from test groups of fewer than 30 are frequently not statistically reliable, [21,22] whereas populations of widely divergent size or age, or mixed gender* can all contribute to substantial deviations in LD50 values. Nonetheless, keeping in mind these difficulties, it appears that Pelamis venom toxicities are equal to or greater than those determined by others for this species.

Pelamis produces much less venom than does other species of sea snakes. Even in large specimens (table 1) the quantity available for injection will not be fatal to an adult man if the mouse toxicity data can be extrapolated to mammals, including man. Tests on monkeys suggest that primates may be less susceptible to sea snake venom than are mice. This becomes particularly true considering the work of Reid [16] who was of the opinion that sea snakes infrequently inject venom when biting in defense, and also considering the further probability that a sea snake is unlikely to deliver its total venom supply in a single bite. Under certain circumstances, however, it is possible to visualize how a bite from a large Pelamis might prove serious for a small adult, especially an infirm or elderly person, or a child.

C. Aggressive Behavior of Pelamis Toward Man.

Reid [16] and Barme [19] have documented the incidence of sea snake bites among native fishermen of Southeast Asia. The bites occurred most frequently around the fishermen's hands and arms while they were handling nets and sorting fish, or on their feet and ankles while they were wading in their nets, stepping on or otherwise disturbing unseen snakes in the muddy water. Pelamis was not implicated as the source of envenomation in these reports.

Pickwell [23] has summarized the available information concerning the behavior of sea snakes toward swimmers and divers. The evidence indicates that swimmers on the surface or divers in transit are unmolested by the sea snakes they encounter although a number of instances have been reported of swimmers being followed some distance by sea snakes. Divers working in static situations such as salvage operations have, however, been bitten by sea snakes. There are no verified reports of loss of life under these circumstances, and it is

not clear what attracts the snakes to such relatively large animals as the stationary human divers.

Neither has Pelamis been implicated in any of the diving and swimming encounters reported to us. In contrast to the behavior of other species, Pelamis has not been reported to approach or to bite man.[24] This may be largely because of its life habits and habitat which include spending much of its life at the sea surface where it alone among the 50 species of sea snakes is able to feed on small pelagic fishes. Pelamis thus does not dive for feeding or hunting purposes and is not tied to inshore areas where wading fishermen or divers would most frequently be encountered. Nevertheless, Pelamis does occur in such areas as well as on the open sea, and we have had opportunity to test its possible aggressiveness or curiosity for human divers and swimmers.

In Bahia Banderas, Mexico we have swum with Pelamis where they occurred in some numbers several hundred yards offshore. None of us were ever approached by the sea snakes even when we had been treading water in a stationary position for some time. While in the water, one of our group once attempted to photograph specimens of this species. In two separate instances, the snakes swam away from the diver just rapidly enough to maintain their distance, regardless of how fast the diver swam in pursuit. It seems, on the basis of these experiences, the Pelamis is not among the sea snake species likely to be aggressive or, for that matter, annoyingly curious about people.

There are very few accounts of human deaths from Pelamis envenomation. Such accounts as do exist are impossible to verify and tend to be anecdotal. An example of these is Beck's[25] account of a young diver (working in the Torres Straits, Cape York Peninsula, Australia) who was bitten on the finger by a yellow-bellied sea snake (presumably Pelamis). The man became convulsive and died 48 hours later despite the fact the finger was amputated within an hour of receiving the bite.

Halstead[26] in his monumental treatise on venomous and poisonous marine animals cited a total of four deaths from the bite of Pelamis. He also included more generalized statements from the literature regarding the mortal fear in which this snake is held in such areas as Taiwan. Swaroop and Grab[27] in their summary on worldwide snake bite mortality stated that deaths from Pelamis bite have occured near Mozambique and along the coast of Central America. No data or references were given, however, and we do not know the

source of these statements. Reid and Lim [28] in the course of a survey of Malay fishing villages, learned of the "ular belerang," a mythical sea snake feared more than any other by the natives. The description of this snake (claimed to have been seen by a few of the native people) suggests a young Pelamis (belerang is Malay for sulfur). Fayrer [29] quoted a Mr. Stewart as saying that Indian natives in the region of Puri, in the state of Orissa, on the east coast, believe Pelamis to be the most deadly of all sea snakes. As "kullunder samp," this species figures prominently in local folklore.

d. Pelamis on the Beach.

Although it is able to feed and survive in the open sea and is not committed to shallow water, Pelamis not only occurs near shore in such places as Bahia Banderas, Mexico, and the Bay of Panama, but frequently is washed ashore in thes areas [24,30-32]. Once on the beach, the sea snake is comparatively helpless since it lacks the broad ventral scutes possessed by land snakes. We have reports of large numbers of Pelamis stranded along the beaches of Panama and northrn Peru, and we have observed and counted stranded Pelamis along the beaches at Puerto Vallarta, Bahia Banderas [24]. Many of these snakes were still vigorous in the early morning when we made our counts, and they readily swam away when returned to the water. The possibility of receiving a bite from accidentally treading upon a beached Pelamis seemed real enough since the beaches in this resort area are heavily patronized by Mexican and American tourists alike. Yet our conversations with the town mayor, a local physician, and the port captain for Puerto Vallarta failed to disclose any incidents of sea snake bite within their memory. Evidently, the sea snake fails to intimidate the tourists frequenting the beaches of this popular resort and, at least in this area, has caused no fatalities or serious cases of envenomation.

e. Sea Snake Antivenin.

The currently available antivenin is effective against at least 3 species of sea snake and most probably many more. In addition it retains its potency for at least 8 years which makes it quite useful in actual field situations. Early results in our laboratory further indicate that short term artificial respiration, in addition to antivenin therapy, may increase survivor populations.

LITERATURE CITED

1. Cropp B. Sea Snakes. Oceans Magazine 3(2), 48-54 (1970).

2 Dunson, W. A. The Sea Snakes are Coming. Natural History Magazine 80(9), 52-61 (1971).

3. MacLeish K. Diving with Sea Snakes. National Geographic 141(4), 565 578 (1972).

4. Weathersbee, C. Linking the Oceans. Science News 94(23), 578-581 (1968)

5. Rubinoff I., and Kropach, C. Differential Reactions of Atlantic and Pacific Predators to Sea Snakes. Nature, London 228, 1288-1290 (1970).

6. Gilluly, R. H. Consequences of a Sea-level Canal Science News 99(3) 52-53 (1971).

7. Bailey, D. A Thermal Barrier for Snakes. Biomed News 12-70. December 1970.

8. Barme M. Venomus Sea Snakes (Hydrophiidae) in Venomous Animals and Their Venoms. Vol. 1. Venomous Vertebrates. W. Bucherl E. E. Buckley, and V. Deulofeu, eds., pp 285-308. Academic Press, New York, New York. 1968.

9. Shipman, W. H., and Cole, L. J. A Surfactant Bee Venom Fraction: Separation on a Newly Devised Constant Flow Rate Chromatographic Column and Detection by Changes in Effluent Drop Volume. Anal. Biochem. 29, 490 497 (1969)

10. Miller, L. C. and Tainter, M. L. Estimation of the ED50 and Its Error by Means of Logarithmic-Probit Graph Paper. Proc. Soc. Exp. Biol. Med. 57, 261-264 (1944).

11. Finney, D. J. Probit Analysis. 3d Ed. 333 pp. Cambridge University Press. 1971.

12. Vick, J. A., and Herman, E. H. An Isolated Dog or Monkey Heart Preparation for Studying Cardioactive Compounds. Pharmacology 6, 290-299 (1971).

Table I Venom Production by Newly Captured Adult, Female Sea Snakes (*Pelamis platurus*)[a]

Specimen number	Length[b]	Weight[b]	Venom produced[c]				Total	
			Left fang		Right fang		Liquid venom	Equivalent dry venom[d]
			Voluntary	Milked	Voluntary	Milked		
	cm	gm	lambda				lambda	mg
1	70	160	0	5.8	4.2	1.5	12	1.8
2	75	180	9.6	1.5	5.8	0	17	2.6
3	83	310	8.1	7.7	15.8	1.5	33	5.0
4	75	200	12.7	3.8	13.1	0	30	4.6
5	68	150	1.1	3.8	0	11.1	16	2.4
6	71	160	1.9	1.9	1.9	0.4	6	0.9
7	72	170	4.2	0.8	0.8	2.3	8	1.2
8	80	200	10.0	2.3	4.6	2.7	20	3.1
9	70	160	3.8	2.7	5.8	0	12	1.8
10	77	210	14.6	0.8	6.9	0	22	3.4
11	75	210	5.8	0.8	0.4	3.1	10	1.5
12	73	190	13.1	1.1	8.8	5.0	28	4.3
13	62	110	4.2	2.7	3.8	5.8	17	2.6

[a] Data obtained aboard R/V CAPE on Bahia Banderas, Mexico, 21 to 24 March 1971.

[b] Lengths, ±1 cm, approx; weights, ±10 gm.

[c] 1 lambda = 1 microliter.

[d] Based on 15.3 average percent solids in liquid *Pelamis* venom (Shipman and Pickwell, in preparation).

Table II LD50* Assay – *Pelamis* Liquid Whole Venom in Mice**

Dose group	Dosage	Number of mice	Number dead	Mortality	Mean survival time
	mg dry venom/kg			%	min
1	0.20	5	5	100	27
2	0.12	10	7	70	40
3	0.10	10	6	70	68
4	0.095	10	6	60	68
5	0.086	10	3	30	51
6	0.078	10	2	20	63

*This was fresh, liquid whole venom, batch 1 (see text). Mice were all males, 8 weeks old, 30 to 35 gm of the Walter Reed ICR strain.

**LD50 = 0.092 mg/kg.

Table III LD50* Assay – *Pelamis* Lyophilized Whole Venom in Mice**

Dose group	Dosage	Number of mice	Number dead	Mortality	Mean survival time
	mg dry venom/kg			%	min
1	0.5	5	5	100	5
2	0.2	5	5	100	23
3	0.14	10	10	100	33
4	0.13	30	25	83	40
5	0.12	30	19	63	48
6	0.11	20	11	55	64
7	1.10	20	5	25	64
8	0.075	10	0	–	–

*This was *Pelamis* venom batch 2 (see text). Mice were all females, 9 to 10 weeks old, 25 to 30 gm, of the Walter Reed ICR strain.

**LD50 = 0.111 mg/kg.

Table IV Effectiveness of Sea Snake Antivenin* Against the Venom of Three Heterologous Sea Snake Species

Species	Date of tests	Venom LD50 for mice	Venom LD99 for mice	Antivenin and venom LD50	Potency factor**	Venom (mg) 1 ml antivenin	Neutralized by 1 unit antivenin	Antivenin		
								Batch No.	Date of batch	Strength
		mg/kg								units†/ml
Pelamis platurus	September 1972	0.11	0.15	1.06	9.6	0.1	0.004	25-1	February 1972	26.6
				1.20	10.8	0.1	0.004	23-1	June 1970	27.5
				1.12	10.1	0.1	0.004	020-1	March 1969	23.1
				1.48	13.3	0.1	0.002	011-1	26 June 1967	44.8
				1.17	10.5	0.1	0.003	549-009	24 November 1964	34.4
Laticauda laticaudata	December 1972	0.16	0.26	1.31	8.2	0.3	0.011	25-1	February 1972	26.6
	January 1973			1.03	6.4	0.2	0.007	23-1	June 1970	27.5
				1.10	6.9	0.3	0.013	020-1	March 1969	23.1
				0.90	5.6	0.2	0.004	011-1	26 June 1967	44.8
				0.65	4.1	0.2	0.006	549-009	24 November 1964	34.4
Laticauda semifasciata	April 1973	0.30	0.48	1.90	6.3	0.4	0.015	25-1	February 1972	26.6
	May 1973			1.70	5.7	0.4	0.014	23-1	June 1970	27.5
Laticauda semifasciata				1.65	5.5	0.4	0.017	020-1	March 1969	23.1
				1.30	4.3	0.3	0.007	011-1	26 June 1967	44.8
				1.20	4.0	0.3	0.009	549-009	24 November 1964	34.4

* Commonwealth Serum Laboratories, Australia – equine, liquid, sea snake antivenin (AV) produced from the venom of the common sea snake, *Enhydrina schistosa*, five batches of varying age, all injections IV in mice.

** Potency factor = $\frac{\text{LD50 AV + venom}}{\text{LD50 venom only}}$

† One unit of Commonwealth Serum Laboratories' sea snake antivenin is defined as that quantity which will neutralize 0.01 mg of *Enhydrina schistosa* venom.

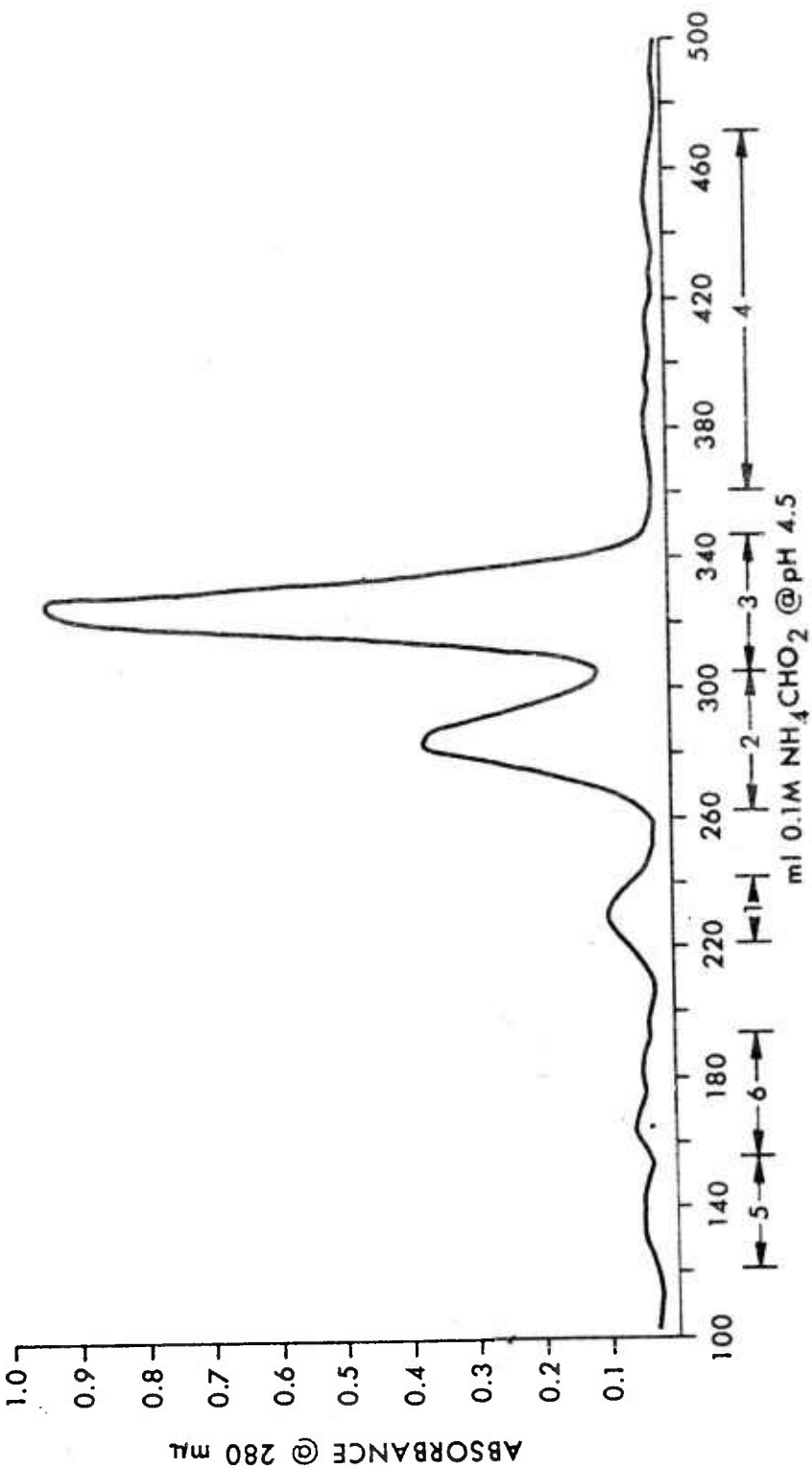

Figure 1 Separation of *Pelamis* Venom Components by Single Pass Gel Filtration on a 2 × 150-cm Column

AD-A056493

THE IMPACT OF FEMALE ANTHROPOMETRY ON THE U. S. ARMY

ROBERT M. WHITE, MR.
*GREGORY DESANTIS, DR.
U. S. ARMY NATICK RESEARCH AND DEVELOPMENT COMMAND
NATICK, MASSACHUSETTS 01760

During the past 30 years, several major anthropometric surveys have been carried out in the U. S. Army. Large numbers of both men and women were measured in 1946, at the end of World War II (1,2,3). Army men were measured again in 1966 (4), while Army aviation personnel were measured in 1959 (5), and again in 1970 (6). The most recent survey of Army women was made in 1977 (7,8,9). A small sample of men also was measured in order to obtain directly comparable data (10). The importance of the latter anthropometric survey of U. S. Army women is the subject of this paper.

An essential element in the effective development of Army clothing, equipment and other materiel is the availability of information on the body sizes, proportions, and distributions of personnel in the Army population. Such information is obtained from anthropometric data. Anthropometry is the measurement of the human body, and the resulting measurements, collected during an anthropometric survey, represent the source of the body size information which is required.

A new anthropometric survey of U. S. Army women was planned and carried out in 1977 in response to the need for current and comprehensive body size data for the women who make up an increasingly large part of the United States Army. The main purpose of the survey was to obtain and develop statistical data on body size and proportions. In addition to conventional anthropometric measurements, measurements also were taken on workspace dimensions and on the static muscle strength of Army women.

During the survey, data for 69 basic body dimensions were obtained on a sample of 1331 women, covering a wide range of age, rank, and military assignment. Additional data were collected on series of between 200 and 300 women for 28 other body measurements, 31 head and face measurements, 14 workspace measurements, and 9 static strength measurements. Many of the measurements made had not been previously reported for any large-scale survey of women, military or civilian. Other measurements were selected to supplement data already available to provide up-to-date information for use in the design of clothing, protective equipment, workspace and industrial equipment which women in the Army wear, use, operate or within which they work.

During the survey, women were measured between November 1976 and February 1977 at four Army installations: Fort Sam Houston, Texas; Fort McClellan, Alabama; Fort Jackson, South Carolina; and Walter Reed Medical Center, Washington D. C. The sample of women measured included Officers (8.7%), Army nurses (17.1%), and enlisted women (74.2%). The measurements were made by a team of six civilian women, who were trained and worked under the supervision of physical anthropologists.

Standard anthropometers, calipers, and steel tapes were used for the measurements. All measurements were made in millimeters, except for weight which was recorded in pounds and tenths. The anthropometric data initially were recorded on data sheets and subsequently transferred to punch cards. The punched cards then were read into a computer where the data were transferred to magnetic tapes. After an editing process with the use of two separate computer programs for the identification and elimination of errors, the data were processed in order to generate statistical values such as means, standard deviations, ranges, and percentiles.

The results of the 1977 anthropometric survey of U. S. Army women have been published in a series of four technical reports (7,8,9,10). A fifth report, containing further analysis of the data, is in preparation. Representative anthropometric data for both Army men and women also are now published in official Department of Defense documents such as the Military Standard: Human Engineering Design Criteria for Military Systems, Equipment and Facilities (MIL-STD-1472B) (11) and the Military Standardization Handbook: Human Factors Engineering Design for Army Materiel (MIL-HDBK-759) (12).

Since 30 years had elapsed between the anthropometric surveys of Army women in 1946 and 1977, the first question concerning the results of these surveys inevitably concerns the amount of change in body size. A comparison of the data from the two surveys indicates that there has been relatively little change in the body size of Army women.

Anthropometric data for selected body measurements of Army women from 1946 and 1977 are given in Table 1. Shown here are the number of women measured (N), the mean value, the standard deviation (S.D.), and the range (represented by the minimum, the maximum, and the difference between them). Also shown are stature ratios, obtained by dividing the mean values of the various dimensions by mean stature.

The 1977 sample of Army women was about four years younger on the average than the 1946 women. On the average, Army women in 1977 were three-quarters of a pound heavier and one-third of an inch taller than in 1946; sitting height was one-half inch higher in 1977. In body girth dimensions, the 1977 women were one-quarter of an inch smaller in bust circumference, one and one-half inches larger in waist circumference, and two-tenths of an inch larger in hip circumference than the 1946 women.

Percentile values for selected body measurements of Army women from 1946 and 1977 are shown in Table 2. At the 50th percentile (median) level, dimensions for the 1977 women are greater than those for the 1946 women, except for bust circumference. However, at the 95th percentile level, values for weight, bust and hip circumferences are lower for 1977 women, but higher for stature, sitting height, and waist circumference.

Body Measurements of Men and Women

In view of the increasing numbers, as well as the emphasis and importance of women in the Army, comparisons of anthropometric data for Army men and women are of even more interest and concern than whether women have increased in body size. In the applications of anthropometric data in research and development programs, two areas are of primary consideration. These are in the design and sizing of clothing and in the human engineering of equipment and materiel.

In military clothing, a distinction is made between dress clothing and field clothing. Army women, of course, have their own dress uniforms, but recently considerable discussion has developed

TABLE 1. STATISTICAL VALUES FOR U. S. ARMY WOMEN

	N	Mean	S.D.	Range Min.	Range Max.	Range Total	Stature Ratio
Weight							
1946 (kg)	8107	59.63	9.00	39.0	111.6	72.6	
1977 (kg)	1331	59.97	8.69	39.9	125.1	85.2	
1946 (lbs)	8107	131.47	19.85	86.0	246.0	160.0	
1977 (lbs)	1331	132.22	19.16	88.0	275.8	187.8	
Stature							
1946 (cm)	8121	162.14	6.00	141.0	184.0	43.0	1.000
1977 (cm)	1331	162.96	6.52	142.6	183.8	41.2	1.000
1946 (in)	8121	63.84	2.36	55.5	72.4	16.9	1.000
1977 (in)	1331	64.16	2.57	56.1	72.4	16.3	1.000
Sitting Height							
1946 (cm)	8119	83.66	3.19	71.0	97.0	26.0	.516
1977 (cm)	1331	85.08	3.59	73.1	96.2	23.1	.522
1946 (in)	8119	32.94	1.26	28.0	38.2	10.2	.516
1977 (in)	1331	33.49	1.41	28.8	37.9	9.1	.521
Bust Circum.							
1946 (cm)	8115	88.91	7.68	68.0	128.0	60.0	.548
1977 (cm)	1331	88.21	6.43	68.9	128.4	59.5	.541
1946 (in)	8115	35.00	3.02	26.8	50.4	23.6	.548
1977 (in)							
Waist Circum.							
1946 (cm)	8115	67.00	6.24	52.0	110.0	58.0	.413
1977 (cm)	1331	71.01	6.90	56.5	117.5	61.0	.436
1946 (in)	8115	26.38	2.46	20.5	43.3	22.8	.413
1977 (in)	1331	27.96	2.72	22.2	46.3	24.1	.436
Hip Circum.							
1946 (cm)	8113	95.09	6.70	74.0	126.0	52.0	.586
1977 (cm)	1331	95.52	6.39	77.4	134.6	57.2	.586
1946 (in)	8113	37.44	2.64	29.1	49.6	20.5	.586
1977 (in)	1331	37.61	2.51	30.5	53.0	22.5	.586
Age							
1946 (yrs)	8118	27.30	5.57	16.0	52.0	36.0	
1977 (yrs)	1331	23.10	5.40	17.0	60.0	43.0	

TABLE 2. PERCENTILE VALUES FOR U. S. ARMY WOMEN

	1st	5th	25th	Median 50th	75th	95th	99th	Range (1st-99th)
Weight								
1946 (kg)	44.0	47.4	53.2	58.3	64.7	76.5	86.6	42.6
1977 (kg)	42.7	46.6	54.1	59.6	65.1	74.5	83.8	41.1
1946 (lbs)	97.0	104.4	117.2	128.6	142.7	168.6	191.0	94.0
1977 (lbs)	94.2	102.8	119.3	131.4	143.6	164.3	184.8	90.6
Stature								
1946 (cm)	148.6	152.4	158.0	162.0	166.2	172.2	176.6	28.0
1977 (cm)	148.2	152.6	158.4	162.8	167.3	174.1	178.4	30.2
1946 (in)	58.5	60.0	62.2	63.8	65.4	67.8	69.5	11.0
1977 (in)	58.3	60.1	62.4	64.1	65.9	68.5	70.2	11.9
Sitting Height								
1946 (cm)	76.2	78.4	81.5	83.7	85.8	88.9	91.1	14.9
1977 (cm)	76.3	79.0	82.7	85.2	87.6	90.8	92.1	16.4
1946 (in)	30.0	30.9	32.1	32.9	33.8	35.0	35.9	5.9
1977 (in)	30.0	31.1	32.6	33.5	34.5	35.8	36.5	6.5
Bust Circum.								
1946 (cm)	74.6	78.2	83.4	87.9	93.4	103.3	110.9	36.3
1977 (cm)	76.2	78.4	83.7	87.9	92.1	99.0	105.8	29.6
1946 (in)	29.4	30.8	32.8	34.6	36.8	40.6	43.7	14.3
1977 (in)	30.0	30.8	33.0	34.6	36.2	39.0	41.7	11.7
Waist Circum.								
1946 (cm)	56.2	58.8	62.6	66.0	70.4	79.0	86.5	30.3
1977 (cm)	59.0	61.7	66.3	70.0	74.6	83.5	92.4	33.4
1946 (in)	22.1	23.1	24.6	26.0	27.7	31.1	34.1	12.0
1977 (in)	23.2	24.3	26.1	27.6	29.4	32.9	36.4	13.2
Hip Circum.								
1946 (cm)	82.3	85.4	90.4	94.4	99.0	107.3	114.7	32.4
1977 (cm)	81.6	85.5	91.3	95.3	99.4	106.1	112.2	30.6
1946 (in)	32.4	33.6	35.6	37.2	39.0	42.2	45.2	12.8
1977 (in)	32.1	33.7	35.9	37.5	39.1	41.8	44.2	12.1
Age								
1946 (yrs)	21.1	22.7	23.7	25.9	30.2	39.7	47.2	26.1
1977 (yrs)	17.2	17.7	19.1	22.0	25.1	33.6	45.7	28.5

over the question of whether women could or should wear men's field clothing, such as fatigues, cold weather clothing, and combat boots. In the area of equipment and materiel, such as wheeled or tracked vehicles, aircraft, control consoles, or other types of workspaces and equipment systems, human engineering considerations with respect to design and sizing usually have been based upon the body sizes of men. Thus a situation now has developed which emphasizes a requirement for the analysis and comparison of body size data for both men and women, whether for clothing or for equipment.

Anthropometric data for selected body measurements of Army men and women are given in Table 3. The data for men are from the anthropometric survey of 1966, while the women's data are from the recent 1977 survey. The statistical values shown in Table 3 are the same as those in Table I.

Average age of the two samples is similar, with the women about one year older. On the average, Army men are about 27 pounds heavier, four and one-half inches taller in stature, and two and one-quarter inches taller in sitting height. In body girth, the men are over two inches larger in chest circumference than the women are in bust circumference. In waist circumference, the men are over three and one-half inchest larger than women, but in hip circumference women are one-half inch larger on the average. Differences in proportions also are indicated by these data. Although chest/bust circumference is about 54 percent of stature for both men and women, differences in proportion are more marked in waist and hip girths. Waist and hip are 46 percent and 54 percent, respectively, of stature for men, but for women they are 44 percent and 59 percent, respectively, of stature. These differences in proportion are a major problem in the consideration of whether women could wear men's field clothing. However, the possibility of developing a sizing system for clothing which would include sizes suitable for both men and women is under investigation.

The differences in body size and proportions between Army men and women also are emphasized in a comparison of the percentile values shown in Table 4. For example, while 50 percent of Army men are heavier than 156 pounds and taller than 68.7 inchest, only 10 percent and 4 percent of women, respectively, are above these median values for men. Men are larger than women in chest and waist circumferences, but above the 5th percentile level, women are larger than men in hip circumference.

TABLE 3. STATISTICAL VALUES FOR U. S. ARMY MEN AND WOMEN

	N	Mean	S.D.	Range Min.	Range Max.	Range Total	Stature ratio
Weight							
Men (kg)	6677	72.23	10.60	45.2	128.7	83.5	
Women (kg)	1331	59.97	8.69	39.9	125.1	85.2	
Men (lbs)	6677	159.10	23.35	99.5	283.5	184.0	
Women (lbs)	1331	132.22	19.16	88.0	275.8	187.8	
Stature							
Men (cm)	6682	174.52	6.61	151.8	199.7	47.9	1.000
Women (cm)	1331	162.96	6.52	142.6	183.8	41.2	1.000
Men (in)	6682	68.71	2.60	59.7	78.6	18.9	1.000
Women (in)	1331	64.16	2.57	56.1	72.4	16.3	1.000
Sitting Height							
Men (cm)	6682	90.69	3.66	77.2	103.2	26.0	.520
Women (cm)	1331	85.08	3.59	73.1	96.2	23.1	.522
Men (in)	6682	35.70	1.44	30.4	40.6	10.2	.520
Women (in)	1331	33.49	1.41	28.8	37.9	9.1	.521
Chest/Bust							
Men (cm)	6682	93.77	6.69	71.8	124.2	52.4	.537
Women (cm)	1331	88.21	6.43	68.9	128.4	59.5	.541
Men (in)	6682	36.92	2.63	28.2	48.9	20.7	.537
Women (in)	1331	34.73	2.53	27.1	50.6	23.5	.541
Waist Circum.							
Men (cm)	6682	80.29	8.18	58.8	127.7	68.9	.460
Women (cm)	1331	71.01	6.90	56.5	117.5	61.0	.436
Men (in)	6682	31.61	3.22	23.1	50.3	27.2	.460
Women (in)	1331	27.96	2.72	22.7	46.3	24.1	.436
Hip Circum.							
Men (cm)	6682	94.21	6.25	77.2	134.2	57.0	.540
Women (cm)	1331	95.52	6.39	77.4	134.6	57.2	.586
Men (in)	6682	37.09	2.46	30.4	52.8	22.4	.540
Women (in)	1331	37.61	2.51	30.5	53.0	22.5	.586
Age							
Men (yrs)	6682	22.17	4.64	17.0	55.0	38.0	
Women (yrs)	1331	23.10	5.40	17.0	60.0	43.0	

TABLE 4. PERCENTILE VALUES FOR U. S. ARMY MEN AND WOMEN

	1st	5th	25th	Median 50th	75th	95th	99th	Range (1st–99th)
Weight								
Men (kg)	52.6	57.4	64.8	71.0	78.4	91.6	103.0	50.4
Women (kg)	42.7	46.6	54.1	59.6	65.1	74.5	83.8	41.1
Men (lbs)	116.0	126.3	142.6	156.3	172.6	201.9	226.9	110.9
Women (lbs)	94.2	102.8	119.3	131.4	143.6	164.3	184.8	90.6
Stature								
Men (cm)	158.9	163.8	170.1	174.4	178.9	185.6	190.3	31.4
Women (cm)	148.2	152.6	158.4	162.8	167.3	174.1	178.4	30.2
Men (in)	62.6	64.5	67.0	68.7	70.4	73.1	74.9	12.3
Women (in)	58.3	60.1	62.4	64.1	65.9	68.5	70.2	11.9
Sitting Height								
Men (cm)	82.0	84.5	88.2	90.8	93.2	96.7	99.2	17.2
Women (cm)	76.3	79.0	82.7	85.2	87.6	90.8	92.7	16.4
Men (in)	32.3	33.3	34.7	35.7	36.7	38.1	39.0	6.7
Women (in)	30.0	31.1	32.6	33.5	34.5	35.8	36.5	6.5
Chest/Bust								
Men (cm)	80.9	84.1	89.1	93.0	97.7	105.9	112.8	31.9
Women (cm)	76.2	78.4	83.7	87.9	92.1	99.0	105.8	29.6
Men (in)	31.8	33.1	35.1	36.6	38.5	41.7	44.4	12.6
Women (in)	30.0	30.8	33.0	34.6	36.2	39.0	41.7	11.7
Waist Circum.								
Men (cm)	66.3	69.7	74.5	78.9	84.7	95.9	105.6	39.3
Women (cm)	59.0	61.7	66.3	70.0	74.6	83.5	92.4	33.4
Men (in)	26.1	27.4	29.3	31.0	33.4	37.8	41.6	15.5
Women (in)	23.2	24.3	26.1	27.6	29.4	32.9	36.4	13.2
Hip Circum.								
Men (cm)	82.0	85.1	89.8	93.6	97.9	105.5	112.0	30.0
Women (cm)	81.6	85.5	91.3	95.3	99.4	106.1	112.2	30.6
Men (in)	32.3	33.5	35.4	36.8	38.6	41.6	44.1	11.8
Women (in)	32.1	33.7	35.9	37.5	39.1	41.8	44.2	12.1
Age								
Men (yrs)	17.4	18.6	19.6	20.6	23.0	31.5	43.0	25.6
Women (yrs)	17.2	17.7	19.1	22.0	25.1	33.6	45.7	28.5

With respect to clothing, women are at a disadvantage in attempting to wear men's field clothing, as, in general, it is too large in girth and too long in length, particularly in sleeve length and trouser length. In the area of vehicles or other equipment designed and sized for men, women are at a disadvantage in sitting height (or eye height), arm reach, and leg reach. These problems of compatibility are accentuated, of course, in the case of short or small women. For example, 44 percent of Army women are below the men's 5th percentile value for sitting height, 80 percent of women are below the men's 5th percentile value in functional arm reach, and 62 percent of women are below the men's 5th percentile in functional leg length. Design criteria for the human engineering of equipment and materiel for Army use obviously should include reference to anthropometric data for both men and women.

Strength of Men and Women

In addition to the collection of data on body size, the recent anthropometric survey of U. S. Army women afforded an opportunity to obtain new and unique data on the static muscle strength of Army women. Strength measurements were made on 349 women in nine different positions. Six of these were two-handed pulls, four of which were made in a standing position and two in a seated position; three other measurements were one-handed pulls. Measurements were made at fixed distances above the floor, using a strain gauge and a force meter with an optical readout which displayed a peak force and an average force during a three-second interval. Each subject performed two trials in each position. Forces were recorded in pounds.

Similar strength data also were obtained on a series of 102 U. S. Army men. Thus some comparable data on the strength capabilities of both Army men and women are now available for direct comparisons of physical performance.

In this series of strength measurements, maximum forces were exerted by men in a standing two-handed pull at a 38cm level. The mean force for this position was 229 pounds, with 5th and 95th percentile values of 166 and 303 pounds, respectively. By comparison, women showed a mean force of 128 pounds under these conditions, with 5th and 95th percentile values of 74 and 184 pounds, respectively. Thus the average strength capability of women in this measurement was about 56 percent of that of men. At waist level (100cm), men could pull an average force of 146 pounds with two hands, while the comparable value for women was 68 pounds or about 47 percent of the

men's value. At shoulder height (150cm), men could push upwards with a force of 150 pounds on the average, but at the same level of 150cm, women could push upwards with a force of 57 pounds, or 38 percent of the men's value.

These comparisons of the strength capabilities of Army men and women emphasize the problems which will be encountered in the area of physical tasks expected to be performed by Army personnel. These data already have been utilized in a review and evaluation of lifting and carrying tasks listed for the MOS categories which are under consideration for assignment to women in the Army.

This brief discussion of the comparative strength capabilities of Army men and women also points up the critical importance of human factors considerations in the design, sizing, configuration, and portability of equipment. Equipment or components which must be lifted, carried, loaded or unloaded obviously must be suitably designed in size, weight, and configuration, and provided with the necessary hand-holds if they are to be handled effectively by individuals or by crews of several people, whether they be men or women.

As the result of a new anthropometric survey of U. S. Army women carried out in 1977, current data now are available on the body sizes, proportions, and distributions of Army women. New information also has been obtained on Army women for workspace measurements and for static muscle strength measurements. The new anthropometric data indicate that there has been relatively little change in the body dimensions of Army women. However, comparisons of data for men and women clearly show that serious design and sizing problems will be encountered in the development of clothing, equipment and materiel intended for use by both Army men and women.

REFERENCES

1. Randall, Francis E., and Melvyn J. Baer; edited and revised by Russell W. Newman and Robert M. White. Survey of Body Size of Army Personnel, Male and Female - Methodology. Environmental Protection Branch Report No. 122 (Revised), U.S. Army Quartermaster Climatic Research Laboratory, Lawrence, Mass., 1951. (AD 149 458)

2. Randall, Francis E., and Ella H. Munro. Reference Anthropometry of Army Women. Environmental Protection Section Report No. 149, U. S. Army Quartermaster Climatic Research Laboratory, Lawrence, Mass., 1949. (AD 209 837)

3. Newman, Russell W., and Robert M. White. Reference Anthropometry of Army Men. Environmental Protection Section Report No. 180, U. S. Army Quartermaster Climatic Research Laboratory, Lawrence, Mass., 1941. (AD 149 451)

4. White, Robert M., and Edmund Churchill. The Body Size of Soldiers: U. S. Army Anthropometry-1966. Technical Report 72-51-CE, U. S. Army Natick Laboratories, Natick, Mass., 1941. (AD 743 465)

5. White, Robert M. Anthropometry of Army Aviators. Environmental Protection Research Division Technical Report EP-150, U. S. Army Quartermaster Research and Engineering Center, Natick, Mass., 1961. (AD 263 357)

6. Churchill, Edmund, John T. McConville, Lloyd L. Laubach, and Robert M. White. Anthropometry of U. S. Army Aviators-1970. Technical Report 72-52-CE, U. S. Army Natick Laboratories, Natick, Mass., 1971. (AD 743 528)

7. Laubach, Lloyd L., John T. McConville, Edmund Churchill, and Robert M. White. Anthropometry of Women of the U. S. Army-1977; Report No. 1 - Methodology and Survey Plan. Technical Report NATICK/TR-77/021, U. S. Army Natick Research and Development Command, Natick, Mass., 1977. (AD A043 715)

8. Churchill, Edmund, Thomas Churchill, John T. McConville, and Robert M. White. Anthropometry of Women of the U. S. Army-1977; Report No. 2 - The Basic Univariate Statistics. Technical Report NATICK/TR-77/024, U. S. Army Natick Research and Development Command, Natick, Mass., 1977. (AD A044 806)

REFERENCES (continued)

9. Churchill, Thomas, Edmund Churchill, John T. McConville, and Robert M. White. Anthropometry of Women of the U. S. Army-1977; Report No. 3 - Bivariate Frequency Tables. Technical Report NATICK/TR-77/028, U. S. Army Natick Research and Development Command, Natick, Mass., 1977. (AD A046 692)

10. McConville, John T., Edmund Churchill, Thomas Churchill, and Robert M. White. Anthropometry of Women of the U. S. Army-1977; Report No. 5 - Comparative Data for U. S. Army Men. Technical Report NATICK/TR-77/029, U. S. Army Natick Research and Development Command, Natick, Mass., 1977. (AD A048 591)

11. Military Standard: Human Engineering Design Criteria for Military Systems, Equipment and Facilities. MIL-STD-1472B (Notice 2), 30 December 1977, Government Printing Office, Washington, D. C.

12. Military Standardization Handbook: Human Factors Engineering Design for Army Materiel. MIL-HDBK-759, 12 March 1975, Government Printing Office, Washington, D. C.

AD-A056494

THE EFFECT OF CERTAIN AROMATIC COMPOUNDS ON ENZYMES INVOLVED IN HEME SYNTHESIS

HAROLD L. WILLIAMS,* M.S., DEADRE J. JOHNSON, B.A.
MICHAEL J. HAUT, LTC, MC & LESLIE B. ALTSTATT, COL, MC
WALTER REED ARMY INSTITUTE OF RESEARCH
WASHINGTON, D.C. 20012

Benzene, toluene and some of their nitro, amino and chloro derivatives often become environmental pollutants during the process of munitions manufacture. The full assessment of the ecological impact made by these compounds inadvertently released into the environment has not been made.

Because of the quantities manufactured, we focused much of our attention on the trinitrotoluenes and dinitrotoluenes. Both trinitrotoluene and dinitrotoluene are found in "pink water," the water soluble effluent from factories making 2,4,6-trinitrotoluene. The 2,4,6-trinitrotoluene is the military high explosive produced in greatest quantity (1-2). This study was undertaken because benzene, trinitrotoluene and several other substituted benzenes and toluenes have been implicated as causative agents for both aplastic anemia (3-5) and leukemia (6-8). Benzene and, in some instances, toluene and xylene, have been shown to inhibit various steps in globin and heme synthesis in in vitro systems (9-10). We have utilized this property to study structure-activity relationships of benzene, toluene and many of their derivatives on two enzymes involved in heme synthesis. The enzymes are delta-aminolevulinic acid synthetase (ALAS) and heme synthetase (HS).

ALAS and HS were chosen for initial studies because they represent the starting and final enzymes in the synthesis of heme. ALAS is the first and presumably rate limiting enzyme in heme synthesis. Delta-aminolevulinic acid, (ALA), is the first stable product formed in the biosynthesis of heme. ALA is synthesized by the action

of ALAS on glycine and succinyl Coenzyme-A with a requirement for pyridoxal-5'-phosphate as a cofactor. Schulman and Richert (11), and Lascelles (12) were the first to demonstrate that pyridoxal-5'-phosphate was a required cofactor for the production of ALA. Observations within our laboratory confirm these earlier findings. In addition to its position in the scheme of the biosynthesis of heme, its short half-life of 1-2 hours makes ALAS ideally suitable to play a regulatory role in heme synthesis.

HS, (ferrochelatase or ferrolyase), E.C.4.99.1.1, is the final enzyme in the production of heme. It catalyzes the insertion of ferrous but not ferric iron into the protoporphyrin-IX ring to produce heme. The incorporation of ferrous iron into the porphyrin ring may occur non-enzymatically under certain mild conditions (13-14); however, the conditions under which we evaluated this system, only the enzymatic incorporation of iron occurred. Some of these conditions include:

1. Maintenance of anaerobic conditions and iron in the ferrous state.

2. A pH optimum near 8; we analyzed at pH 7.5.

3. De-esterification of the porphyrin ester into the corresponding free acid. (15)

Meso- and deuterophorphyrins also allow the incorporation of ferrous iron into their ring systems. Our observations confirmed those of Bonkowsky's (16) in that of the three prophyrin isomers, proto-, meso-, and deutero-, the meso- was the most active in the uptake of ferrous iron.

MATERIALS AND METHODS

The aromatic compounds studied (Figure 1) came from both commercial and "discreet" sources. Many of the compounds tested are available from the Aldrich Chemical Company, Milwaukee, Wisconsin 53233. We tested for impurities by subjecting each compound to thin-layer chromatography using two different solvent systems, benezene-ethyl acetate 1:4, and acetonitrile. Each compound tested showed only a single spot on migration on pre-coated silica gel plates (E.M. Laboratories, 500 Executive Blvd., Elmsford, N.Y. 10523). De-ionized water of at least 7 megohm resistance was used in the preparation of all aqueous reagents (17). All other reagents and solvents were ACS grade or better.

Male rats, Walter Reed strain, 275-400g, were fasted overnight but given water ad libitum. The animals were sacrificed by asphyxiation in a carbon dioxide saturated atmosphere. The livers were quickly excised, blotted with gauze, weighed and placed in ice-cold 0.25 mol/l sucrose - .05 mol/l Tris buffer, pH 7.5, containing 1% Tween-20 (16). All subsequent operations of the tissue prior to incubation at 37°C were carried out in the cold. The tissue samples were homogenized and sonicated to assure disruption of the mitochondrial membrane. After sonication, the volumes were adjusted to provide a 5% w/v suspension of tissue homogenate in the buffer.

The determination for ALAS activity was performed by a modification of the method of Ebert, et al (18). The difference was that we used labeled alpha-ketoglutaric acid instead of labeled succinyl Co-enzyme A. HS was analyzed by a modification of the technique of Bonkowsky, et al (16). The details of this modification are in preparation for publication elsewhere.

Initially, we evaluated some of these compounds at 0.2 mol/l, which was the concentration of the aromatic with respect to the reaction mixture. Recognizing that at higher concentrations, some effect would be manifested, we focused our attention on concentrations which might be reasonably expected to become physiologically achievable. We extensively studied the effects in the 10^{-3} to 10^{-6} mol/l concentration range.

RESULTS

Figure 1 shows the structures of the compounds studied, most of which inhibited ALAS and enhanced HS activities. It is recognized that in mammalian adults, heme acts as an inhibitor or by means of a heme-controlled repressor, controls the additional production of heme by limiting the amount of ALA produced. We have not ascertained through our experiments whether or not the decrease in ALAS activity under the influence of the chemical is due to the presence of the chemical alone, additionally produced heme alone, or a combination of these two factors.

Table 1 gives the relative sensitivity of these enzymes toward the compound studied. The strata of sensitivity to ALAS are the dinitrobenzenes>trinitrotoluenes>dinitrotoluenes>amino-dinitrotoluenes>chlorotoluenes>benzene. For HS, the strata of sensitivity are the dinitrobenzenes>dinitrotoluenes>amino-dinitrotoluenes> trinitrotoluenes>nitrobenzene. As a class of compounds, the monochlorotoluenes had little effect on the enzyme systems. The addition of one nitro group to the benzene ring had little effect on ALAS

and HS activities. The addition of a second nitro group had a marked effect on the activities of both enzymes, especially at 10^{-3} mol/l. At this concentration, the dinitrobenzenes gave an average increase of 48% on HS activity. This effect could be demonstrated at a concentration as low as 10^{-5} mol/l in which one gets an average enhancement of 35% for this enzyme. Conversely, at 10^{-3} mol/l, the activity of ALAS was decreased an average of 44% and at 10^{-5} mol/l, the average was essentially the same as the control value.

The enhancement/inhibition effect of placing the second nitro group on the aromatic ring is also evident with 4-nitrotoluene and the dinitrotoluenes. Toluene and 4-nitrotoluene have little effect on ALAS and HS activities; however, when the second nitro group is introduced to the ring, there is an average decrease of 37% in ALAS activity and an average increase of 26% in HS activity.

One may note in Table 1 that on replacing the nitro group by an amino group, there is a tendency to further inhibit ALAS and enhance HS activities. The reserve trend occurs in the tri-substituted toluenes in which one nitro group has been replaced by an amino group.

Figure 2 shows the comparison of the activities of the dinitrobenzenes on ALAS and HS activities. It may be noted that in concentrations greater than 10^{-5} mol/l, as HS activity increases, ALAS activity decreases. The differences between ALAS and HS activities at 10^{-3} mol/l cannot be solely attributed to aqueous solubilities of the isomers because their rank in water solubilities is m>o>p-isomers respectively, whereas their effect on the enzymes is p>o>m. The effect may be due to steric specificity and/or spatial arrangements of the molecules involved.

Figure 3 shows the comparison of the effect of the dinitrotoluenes on the enzymes studied. At the same concentrations with respect to the dinitrobenzenes, the effect is not as pronounced which suggests that there may be some interaction between the methyl and nitro groups which offsets the enhancement/inhibition effects. A similar trend is noted with the trinitrotoluenes and the amino-dinitrotoluenes which is shown in Figure 4. The addition of an amino group to the aromatic ring appears to lessen the decrease in ALAS activity.

The normal values obtained for rat liver ALAS were 1-3 nmol/g protein/0.5 hr and 8-14 μmol/g protein/0.5 hr for HS.

DISCUSSION

We have utilized the sensitivity of two enzymes involved in heme synthesis to selected organic compounds as a means of assessing pharmacological effects of aromatics of interest on the activity of these enzymes. ALAS and HS were chosen for these studies because they represent the initial and final enzymes in the biosynthetic pathway of heme. In addition, both have regulatory roles in the production of heme.

Several investigators have explored the effect of benzene on heme synthesis. It has been shown by Forte, et al (10) and Wildman, et al (9) that benzene, at a final concentration of 0.113 mol/l, inhibits rabbit reticulocyte heme synthesis in vitro at the ALAS step. Lee, et al (19) have shown that a single subcutaneous dose of benzene in mice decreases the incorporation of ^{59}Fe into erythrocytes, 440 mg/kg body weight produced a 27% and a dosage of 2200 mg/kg producing a 50% inhibition. A smaller dose, 88 mg/kg had no effect on the incorporation of ^{59}Fe and no effect on the hematocrit.

Other groups have examined structure-activity relationships of various classes of compounds with respect to their effect on ALAS and other related enzymes. Marks, et al (20), investigated the porphyrin-inducing activity of 3,5-diethoxycarbonyl-1,4-dihydro-2,4,6-trimethyl pyridine, a compound known to induce porphyria by enhancing the synthesis of ALAS, and several analogues of it and the corresponding pyridines. They determined the porphyria-inducing activity of these compounds by feeding them to guinea pigs and estimating the amount of ALA and porphobilinogen excreted in the urine. Poland and Kende (21) investigated a number of halogenated di-benzo-p-dioxins for their ability to stimulate two hepatic enzymes: (1) ALAS and (2) aryl-hydrocarbon hydroxylase, a cytochrome P-450 mediated microsomal mono-oxygenase. The potency of the halogenated di-benzo-p-dioxins to induce ALAS and aryl-hydrocarbon hydroxylase corresponded precisely with their lethal, teratogenic and acnegenic potency, to the extent that toxicological data were available.

In summary, we have used techniques of measuring two enzymes involved in heme synthesis to study in vitro effects of certain organic chemicals on these enzymes as a means of determining structure activity relationships for in vivo predictions. We have attempted to use physiologically attainable concentrations of the chemicals in question and have demonstrated that an effect can be registered routinely at concentrations as low as 10^{-5} mol/l and in some cases as low as 10^{-6} mol/l.

The utility of these techniques lie in the versatility of measuring the levels of these enzymes not only in liver hemogenates, but also in bone marrow aspirates and reticulocyte rich blood. Bone marrow or whole blood measurements may obviate the need for surgical procedures when monitoring the pharmacological effect of the compounds of interest.

REFERENCES

1. Rosenblatt, D.H., et al., Munitions production products of potential concern as waterborne pollutants - Phase I. USAMEERU Report No. 73-07. U.S. Army Res. and Dev. Command, Washington, D.C., 1973.

2. Small, M.J. and Rosenblatt, D.H. Munitions production products of potential concern as waterborne pollutants - Phase II. Technical Report 7404. U.S. Army Res. and Dev. Command, Washington, D.C., 1974.

3. Alksoy, M., Dincol, K., Erdem, S., et al., Details of blood changes in 32 patients with pancytopenia associated with long-term exposure to benzene. Brit. J. Ind. Med., 29:56, 1972.

4. Kissling, M. and Speck, B., Further studies on experimental benzene induced aplastic anemia. Blut. 25:97, 1972.

5. Scott, J.L., Cartwright, G.D., and Wintrobe, M.M., Acquired aplastic anemia: an analysis of thirty-nine cases and review of the pertinent literature. Medicine. 38:119, 1959.

6. Rejsek, K. and Rejskover, M., Long term observation of chronic benzene poisoning. Acta. Med. Scand. 152:71, 1955.

7. Erf, L.A. and Rhoads, C.P., Hematologic effects of benzene poisoning. Journal of Industrial Hygiene. 21:421, 1939.

8. Beyers, M.R., et al., Hypocellular marrow in acute leukemia. Archives of Internal Medicine. 88:803, 1951.

9. Wildman, J.M., Freedman, M.L., Rosman, J., et al., Benzene and lead inhibition of rabbit reticulocyte heme and protein synthesis: evidence for additive toxicity of these two components of commercial gasoline. Res. Comm. in Chem. Pathol. and Pharmacol. 13: 473, 1976.

10. Forte, F.J., Cohen, H.S., Rosman, J., et al., Hemin reversal of benzene induced inhibition of reticulocyte protein synthesis. Blood 47:145, 1976.

11. Schulman, M.P. and Richert, D.A., Heme synthesis in vitamin B and Pantothenic acid deficiencies. J. Biol. Chem. 226:181, 1957.

12. Lascelles, J., Synthesis of porphyrins by cell suspensions of "Tetrahymena vorax": effect of members of the vitamin B group. Biochem. J. 66:65, 1957.

13. Kassner, R.J. and Walchak, H., Heme formation from Fe(II) and porphyrin in the absence of ferrochelatase activity. Biochim. Biophys. Acta. 304:294, 1973.

14. Tokunaga, A. and Sano, S., Comparative studies on nonenzymic and enzymic protoheme formation. Biochim. Biophys. Acta. 304:294, 1972.

15. Porra, R.J. and Jones, O.T.G., Studies on ferrochelatase: assay and properties of ferrochelatase from a pig-liver mitochondrial extract. Biochem. J. 87:181, 1963.

16. Bonkowsky, H.L., Bloomer, J.R., Ebert, P.S., et al., Heme synthetase deficiency in human protoporphyria. J. Clin. Invest. 56:1139, 1975.

17. Johnson, D.J., Djuh, Y., Bruton, J. and Williams, H.L., Improved colorimetric determination of serum zinc. Clin. Chem. 23(7): 1321, 1977.

18. Ebert, P.S., Tschudy, D.P., Choudry, J.N., et al., Radiochemical assay of ALA synthetase in human bone marrow. Biochim. Biophys. Acta. 208:236, 1970.

19. Lee, E.W., Kocsis, J. and Snyder, R., Dose dependent inhibition of ^{59}Fe incorporation into erythrocytes after a single dose of benzene. Res. Commun. in Chem. Pathol. and Pharmacol. 5:547, 1973.

20. Marks, G.S., Hunter, E.G., Terner, U.K., et al., Studies of the relationship between chemical structure and porphyria inducing activity. Biochemical Pharmacology. 14:1077, 1965.

21. Poland, A. and Kende, A., 2,3,7,8-Tetrachlorodebenzo-p-dioxin: environmental contaminant and molecular probe. Fed. Proc. 3:2404, 1976.

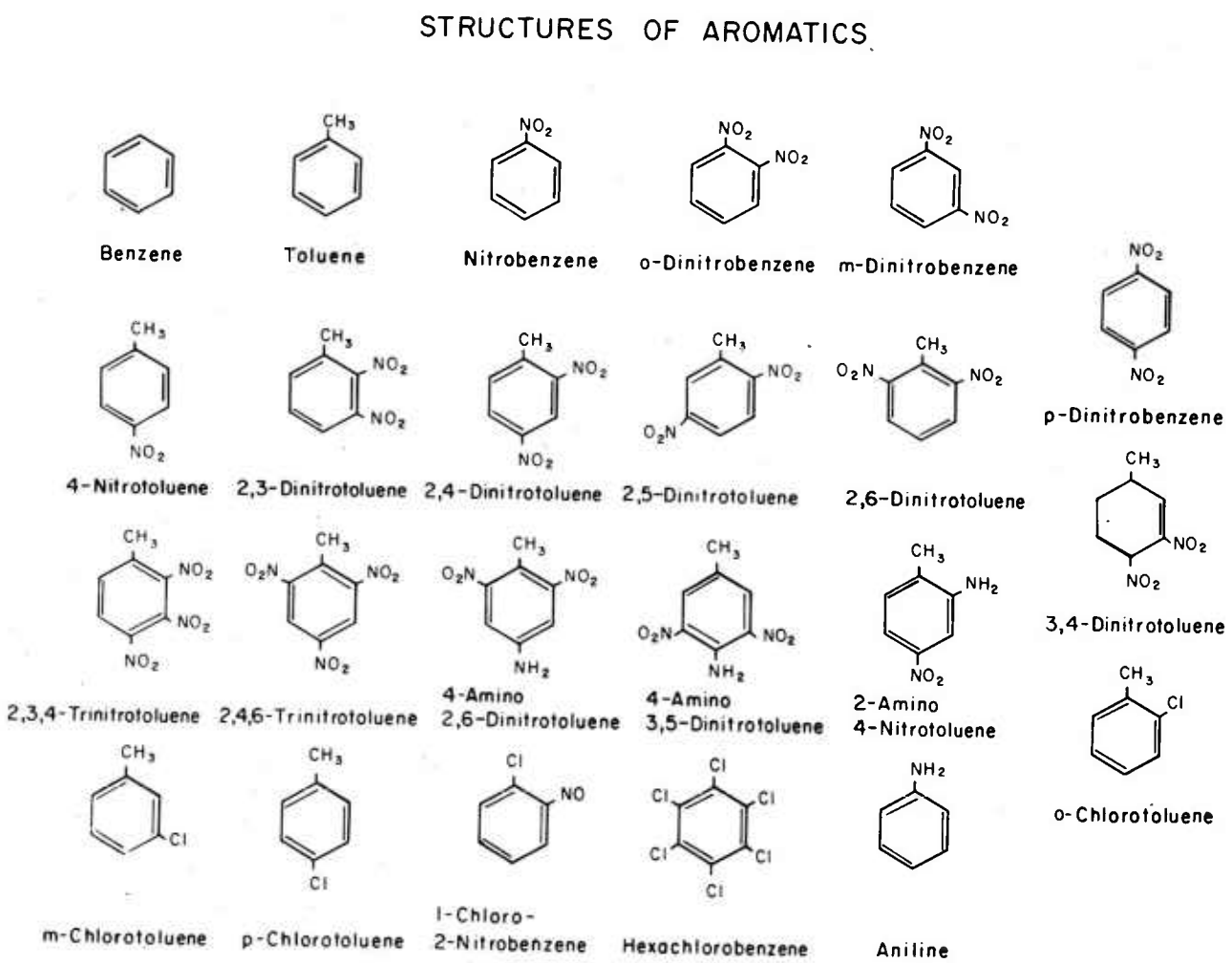

Fig. 1. Structures of the compounds under investigation.

Table 1. The effect of the compounds investigated on the two enzyme systems studied.

	Percentages of Control							
Concentration of Aromatic	10^{-3} mol/1		10^{-4} mol/1		10^{-5} mol/1		10^{-6} mol/1	
Test	ALAS	HS	ALAS	HS	ALAS	HS	ALAS	HS
Aromatic								
Benzene	95	86	104	91	107	94	107	89
Toluene	96	92	104	86	93	91	100	89
Nitrobenzene	86	111	108	104	110	100	81	105
o-Dinitrobenzene	43	143	84	148	104	146	105	105
m-Dinitrobenzene	83	149	94	118	118	119	100	104
p-Dinitrobenzene	41	152	50	180	81	127	93	112
4-Nitrotoluene	84	93	95	99	96	107	96	113
2,3-Dinitrotoluene	55	130	81	103	97	85	104	99
2,4-Dinitrotoluene	92	87	100	80	102	92	99	96
2,5-Dinitrotoluene	43	139	91	102	89	82	90	66
2,6-Dinitrotoluene	77	117	87	96	100	89	97	84
3,4-Dinitrotoluene	56	131	86	119	97	87	99	94
2,3,4-Trinitrotoluene	26	104	69	119	101	96	99	100
2,4,6-Trinitrotoluene	86	150	93	136	103	117	105	119
4-Amino-2,6-Dinitrotoluene	82	137	87	126	93	110	89	109
4-Amino-3,5-Dinitrotoluene	89	152	94	140	107	113	107	105
2-Amino-4-Nitrotoluene	89	97	88	111	87	118	94	103
o-Chlorotoluene	87	101	98	118	99	108	94	111
m-Chlorotoluene	97	107	99	110	101	104	103	104
p-Chlorotoluene	97	108	100	108	102	106	103	104
1-Chloro-2-Nitrobenzene	102	115	88	113	95	109	99	110
Hexachlorobenzene	117	133	94	131	99	116	104	113
Aniline	96	108	91	121	94	104	98	116

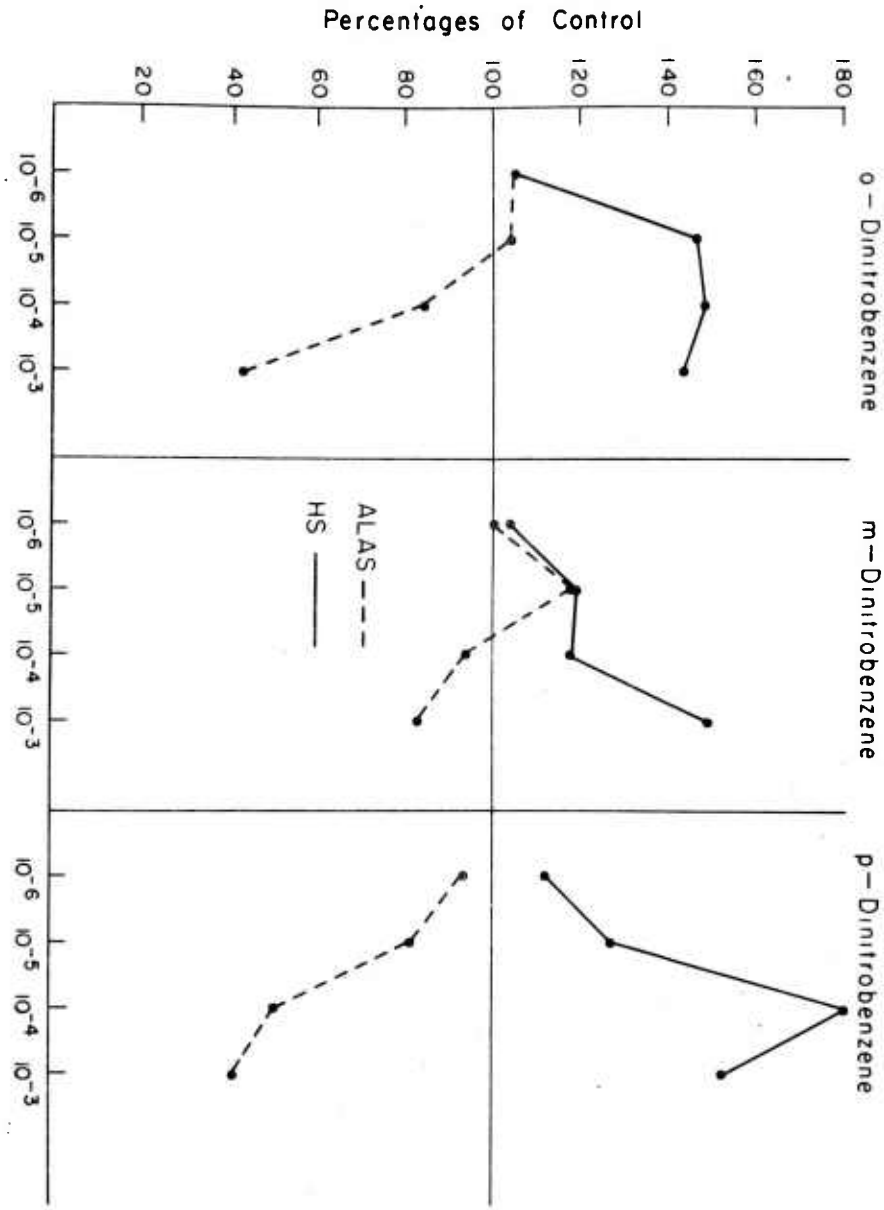

Fig. 2. The effect of the dinitrobenzenes on ALAS and HS activities. Note the inverse relationship at higher concentrations resulting in a "V" shaped curve.

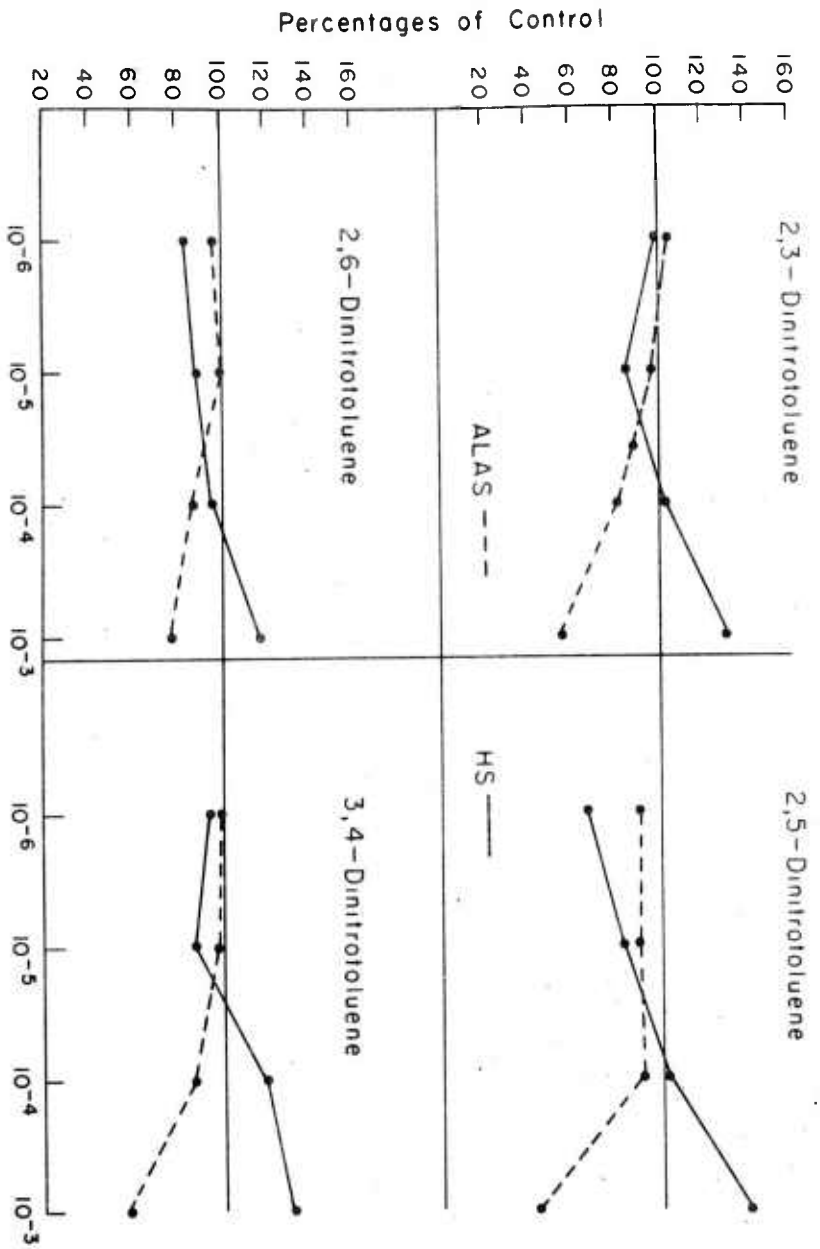

Fig. 3. A comparison of the effect of the dinitrotoluenes on ALAS and HS activities. Note the coincidence of activity in the 10^{-5} to 10^{-4} mol/l concentration range of the aromatic resulting in an "X" shaped curve.

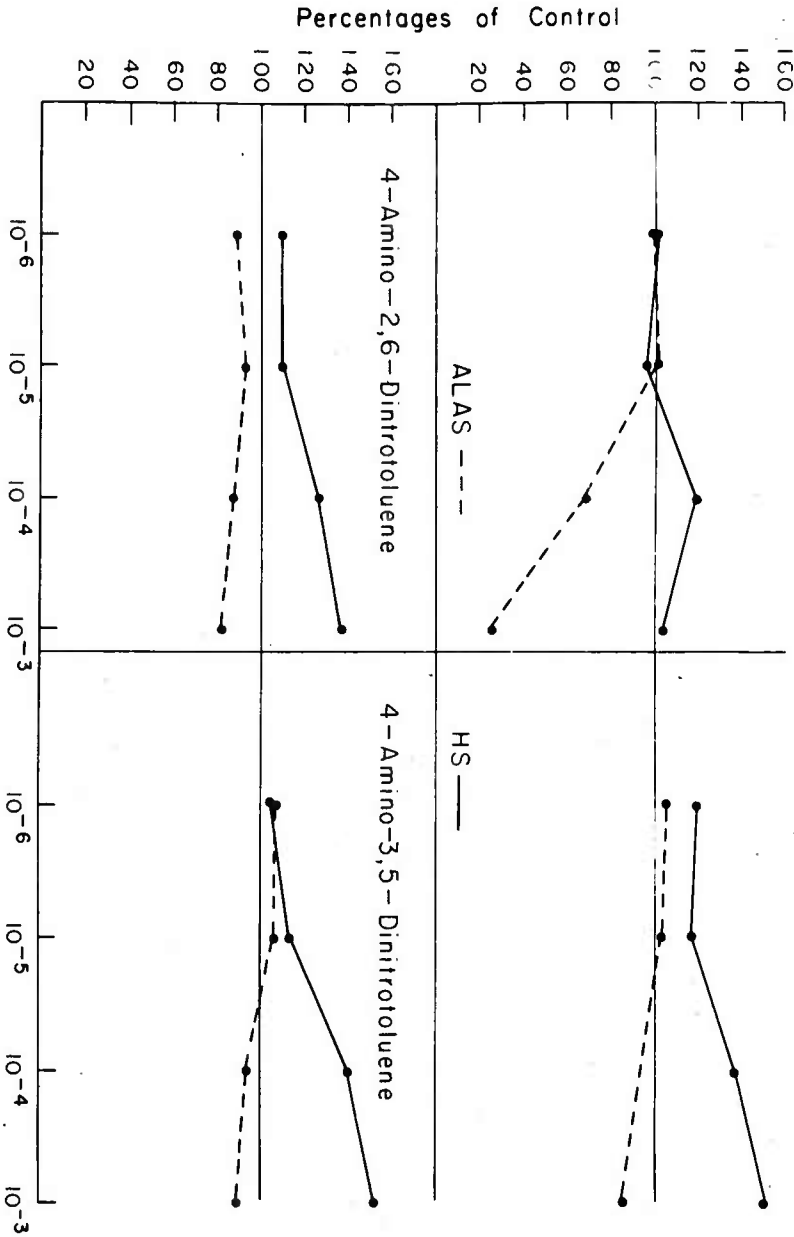

Fig. 4. A comparison of the effect of tri-substituted toluenes on the enzyme systems studied producing a "Y" shaped curve.

AD-A056495

Strong and Specific Interactions of Some Incapacitating Phenothiazines with Nucleic Acids

Charles E. Williamson, Ph.D.
Chemical Systems Laboratory
Aberdeen Proving Ground, MD 21010

In recent years the anti-psychotic and other neurological effects of the tranquilizing phenothiazines have been well described. As a class, they serve a variety of needs and their potent tranquilizing activities render them exceedingly valuable in the treatment of mental disorders. Widespread research[1] has provided an excellent data base for further neuroleptic studies. At Edgewood, such studies have been directed toward the discovery of new and potent neurological incapacitating agents to temporarily render soldiers mentally incapable of waging warfare. Several phenothiazines such as 2-nitro-10-{3-[4-(2-hydroxyethyl)-1-piperazinyl] propyl} phenothiazine dimaleate (I) were found to be sufficiently potent to produce these effects. Their incapacitating activities are described elsewhere[2].

In searching for new biologically active compounds an understanding of the mechanism of biological action is most important, for such information can lead directly to the design of drugs and agents of superior activity. Furthermore, a knowledge of *in vivo* interactions of such compounds with tissues is imperative when considering them for human use. Such is the case for the studies described herein where strong and specific interactions are observed between incapacitating phenothiazines and tissue components.

Binding of phenothiazines to nuclear components is generally, but not universally recognized. For example, phenothiazine dyes such as methylene blue, thionin and toluidine blue have long been used as histological stains[3] for cell nuclei, and the common staining patterns are reported to arise from dye-nucleic acid complexes, but no biological responses have been ascribed to these interactions.

More recently it has been reported that compounds such as chloropromazine, a tranquilizing phenothiazine, do [4-6] and do not[7,8] bind to DNA. A summary of the available literature, however, provides adequate assurance that such binding does, indeed, occur.

The nature of the binding of such compounds to nucleic acids, although partially described for some phenothiazine-type compounds, is still vague and the biological implications of such binding processes are virtually unknown. Numerous interactions of phenothiazines with cellular membranes have been reported to occur and many attempts have been made to relate their tranquilizing activities to these interactions. It is likely that some of the responses elicited by these drugs do arise as a result of such interactions.

In the present study, it is noted that the strongest and most obvious interactions between incapacitating phenothiazines and human cells growing in culture apparently occur with unbound RNA, such as messenger, ribosomal and transfer RNA. Accordingly, such incapacitating phenothiazines might be expected to interfere with the communicative processes that are mediated by these substances. In view of the reports[9] that the quality and quantity of such RNA varies during nervous transmission following stimulation of the cell, interference of these processes might also be expected after treatment with incapacitating phenothiazines.

EXPERIMENTAL

2-Nitro-10{3-[4-(2-hydroxyethyl)-1-piperazinyl] propyl} phenothiazine dimaleate, I; 10-{3-[4- (2-hydroxyethyl)-1-piperazinyl] propyl} phenothiazine-2-carbonitrile dimaleate, II; 2-(2-dicyanoethenyl)-10-{3-[4-(2-hydroxyethyl)-1-piperazinyl] propyl} phenothiazine dimaleate, III; and 2-(2-nitroethenyl)-10{3-[4-(2-hydroxyethyl) -1-piperazinyl] propyl} phenothiazine dimaleate, IV were synthesized in our laboratories. Their synthesis and properties are described by Bossle et al.[2]. All nucleic acids were purchased from Miles Laboratories, Kankakee, IL 60901. All polymers were purchased from Schwartz/Mann, Orangeburg, NY 10962. Nucleic acid and polymer concentrations are expressed as molarity of phosphate groups.

Human dipoid fibroblasts (derived from embryonic skin) were purchased from Microbiological Associates, Inc., Bethesda, MD 20014 after the fourth through the twentieth subcultivations. No primary cultures were performed in our Laboratory. The cells were received in plastic tissue culture bottles and released by the addition of a 0.25% solution of trypsin (Microbiological Associates, Inc., 1:250 trypsin conc.) in Earle's minimum essential medium (MEM) for further

culture. The trypsinized cells were diluted in Hank's MEM with 10% fetal calf serum (Microbiological Associates, Inc.) to approximately 10^5 cells/ml and replanted in 25 cc plastic bottles. The cells were incubated at 37°C. After 2 days and thereafter twice weekly, the medium was replaced with Earle's MEM containing 10% fetal calf serum. In 5 to 7 days the cells were confluent. During culture the pH was monitored by visual observation of the phenol red indicator in the medium.

To all Hank's or Earle's MEM was added 1% of a 200 mM solution of L-glutamine (100 x concentrated) and 1% of a penicillin-streptomycin mixture containing 5000 units each per ml (Microbiological Associates, Inc.).

The association constants between I to IV and salmon sperm DNA were measured by spectroscopy and equilibrium dialysis. Because of the tendency of these compounds to slowly precipitate in the preence of phosphate buffer, equilibrium dialysis experiments were performed in water. The pH in the dialysis cells was approximately 6.3 In these experiments the phenothiazine concentrations were varied from 2.5×10^{-4}M to 10^{-5}M and the concentration of DNA was maintained at 10^{-3}M. The concentration of I in the dialysis cell (reagent side) was monitored by its 325 nm band (E_{max} = 7,000), and II at 320 nm (E_{max} = 2,500). Suitable blanks were employed. Water solutions of compounds I to IV obeyed Beer's Law. Much difficulty was encountered in these measurements, however, because of compound interactions with the dialysis cells and membranes.

To measure association constants of compounds I to IV spectrally, a series of spectra were obtained in various concentrations of the particular nucleic acid or polymer under study. The compounds were dissolved in 0.05 M, pH 7.4 sodium phosphate buffer containing 10^{-3} M salmon sperm DNA and the spectra were determined. Subsequent spectra at lower DNA concentrations were obtained by serially diluting with aqueous solutions of the phenothiazines.

RESULTS

1. Interactions with Nucleic Acids.

The absorption spectra of I in 0.05 M, pH 7.4 sodium phosphate buffer containing various quantities of salmon sperm DNA are illustrated in Fig. 1. The 435 nm band gradually disappears with increasing DNA concentration is is replaced by a new broad band that approaches 525 nm. The latter absorption imparts a bright purple color to the solution.

Essentially the same types of absorption spectra were observed for II, III, and IV. The spectral data together with appropriate association constants are summarized in Table I.

Table I

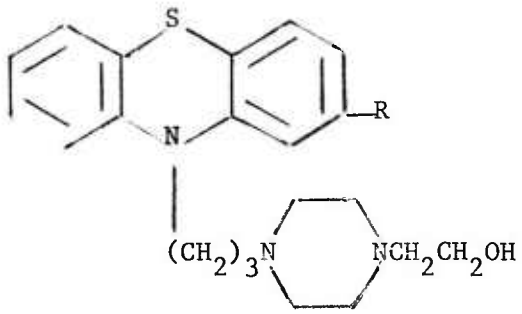

Compound Number	R	λ max (Buffer), nm	λ max (DNA), nm	DNA Association* Constant, 1/mole
I	$-NO_2$	435	525	550
II	-CN	-	358, 430	170
III	$-CH=C(CN)_2$	450	570	3000
IV	$-CH=CHNO_2$	430	530	3100

*Determined by measurement of the DNA-phenothiazine charge-transfer absorption maximum.

In addition to the spectral measurements, association constants were also obtained by equilibrium dialysis measurements. The values for compounds I to IV were all in the range of 3000 1/mole and are considered approximate owing to the experimental difficulties described.

Upon the introduction of sodium chloride (0.1 M to 0.5 M) to solutions of I, II, III, or IV containing DNA or RNA, the λ max (DNA) bands progressively decreased in intensity and were replaced by the λ max (Buffer) bands which correspond to the unbound forms (Table I). Essentially the same behavior was observed when the phenothiazine-nucleic acid solutions were heated above 60°C; the λ max (DNA) bands

progressively disappeared and were replaced by the λ max (Buffer) bands corresponding to the unbound forms.

The λ max values recorded in Table I were also observed when these phenothiazines were treated with a 16s + 23s ribosomal RNA mixture or transfer RNA, both isolated from E. coli K-12 MO (Miles Laboratories, Kankakee, IL). Attempts to reproduce similar bands by the addition of numerous substances to these phenothiazine solutions failed. They were only seen in the presence of double-stranded nucleic acids or double-stranded synthetic polymers.

2. Interactions with Double-Stranded Polymers.

The interaction of I with the following polymers were examined: polyadenylic acid (poly A), polycytidylic acid (poly C), polyguanylic acid (poly G) and polyuridylic acid (poly U). Equimolar quantities (3×10^{-3} M) of poly A and poly U were dissolved in 0.05 M, pH 7.4 sodium phosphate buffer. A similar solution was prepared using poly G and poly C. The solutions were heated to 60°C for 10 min. and then gradually cooled to room temperature to form the respective poly A - poly U and poly G - poly C hybrids. The spectrum of I (2×10^{-4}M) was then measured in polymer solutions ranging from 8.7×10^{-4} M to 7.5×10^{-3} M. In the presence of poly G - poly C, I exhibits bathochromic and hypochromic changes. Although it retained the characteristic yellow color, its absorption maximum shifted from 435 nm to 453 nm with a decrease in molar absorptivity. In the presence of poly A - poly U, however, solutions of I were purple and its spectrum exhibited the same 525 nm band as observed in the presence of nucleic acids (Fig 1). Measurement of absorbance as a function of polymer concentration allowed the calculation of an association constant for this interaction. A value of approximately 330 1/mole was obtained.

Compounds I and II bind strongly to both poly A - poly U and poly G - poly C as evidenced by the spectral changes of both, and by the formation of immediate and intense precipitates when added to either of the double-stranded polymers in buffer.

3. Interactions With Single-Stranded Polymers.

Table 2 contains spectral data of 5×10^{-4} M of I in the presence of 5×10^{-3} M poly A, poly G, and 10^{-3} M poly U and poly C in water, and 2×10^{-4} M of the double-stranded polymers poly A - poly U and poly G - poly C in 0.05 M sodium phosphate buffer. It is noteworthy that the interactions of these polymers with I result in bathochromic

shifts in each instance. None was shifted sufficiently, however, to produce the purple color seen with I in poly A - poly U solutions. Addition of sodium chloride (0.1 M to 0.5 M) to the aqueous (I) - polymer solutions caused precipitation of the phenothiazine complexes with poly A, poly G and poly U. Precipitation did not occur when sodium chloride was added to the (I)-poly C solution and the spectral changes of I caused by poly C were reversed. The spectral changes of I in both poly G - poly C and poly A - poly U were readily reversed by the addition of 0.1 M to 0.5 M sodium chloride.

Table 2

ABSORPTION MAXIMA OF I[a] IN POLYMER SOLUTIONS

Polymer	λ max, nm
Sodium Phosphate Buffer[b]	435
Poly A[c]	455
Poly G[c]	460
Poly U[d]	445
Poly C[d]	460
Poly A - Poly U[e]	525
Poly G - Poly C[e]	453

[a]Conc. of I was 5×10^{-4} M in all experiments; [b]0.05 M, pH 7.4; [c]5×10^{-3} M; [d]10^{-3} M; [e]2×10^{-4} M.

4. Interactions with Human Fibroblasts Growing In Vitro.

Various concentrations of I and II were added to fresh sub-cultivations of human fibroblasts in plastic cell culture bottles and the cells were allowed to divide at 37°C for 3 days before observation. At this time, the tops were removed from the culture bottles and the microscope objective was immersed directly into the nutrient medium. Growth was normal at concentrations of both at and below 5×10^{-6} M, but abnormal at 10^{-5} M (Plate 1).

Compound I could not be visually detected at concentrations lower than 10^{-6} M. As viewed by light microscopy, cells grown in 10^{-5} M of I were weakly stained in granules within the cytoplasm but not within the nucleus. By fluorescence microscopy only a dim

orange field could be seen, nevertheless, extensive uptake of I was observed within the nucleoli. Because of its poor staining properties and low quantum yield, I was not an effective reagent to study the pattern of phenothiazine uptake by fibroblasts in culture.

Upon examination of II by fluorescence microscopy an intense uptake of reagent in granular bodies outside the nuclei was seen. In living cells, II was not observed inside the nuclei. The nucleoli, loci of high RNA concentration , however, were intensely stained. Destruction of the living cells by lysis or drying caused the nuclei to become stained more strongly than any other cell structures.

In aqueous phosphate buffer II fluoresces slightly (λ max = 520 nm). In the presence of 5×10^{-3} M salmon sperm DNA an enhanced yellow-green fluorescence was observed at the same emission maximum. The fluroescent yield of II was neither enhanced nor quenched by the addition of 10^{-2} M poly A - poly U, however, an equivalent quantity of DNA did produce enhancement. Fluorimetric measurement of the increase in fluorescent yield of II in various concentrations of salmon sperm DNA in 0.005 M, pH 7.4 sodium phosphate buffer produced an association constant of approximately 550 1/mole.

In addition to the spectral measurements an association constant between II and salmon sperm DNA was also obtained by equilibrium dialysis. This value, 3000 1/mole at pH 6, 25° C, is considered approximate owing to experimental difficulties described herein.

DISCUSSION

When solutions of nucleic acids are treated with I, a striking purple color forms concurrently with strong and specific binding. This coloration apparently arises from a charge-transfer complex between I and the double-stranded regions of nucleic acids and is readily measured by a newly formed absorption maximum at 525 nm. Corresponding bands arose from II, III, and IV upon interaction with DNA or RNA including microsomal and transfer RNA. In each instance the charge-transfer bands disappeared when the nucleic acids were melted by heating to 60°C or by the addition of organic solvents.

The charge-transfer bands were also produced when I and II interacted with double-stranded poly A - poly U, but not with other combinations studied. Strong interactions were also observed between these compounds and poly G - poly C but without the charge-transfer phenomena. When the double-stranded polymers were melted by heat or by the addition of organic solvents the charge-transfer bands also

disappeared. Throughout these studies such bands were observed only in association with the double-strandedness of nucleic acids or polymer models.

The mechanism by which these phenothiazines bind to nucleic acids and polymers appears similar to that described for several nucleic acid bound acridines and other phenothiazines. Noteworthy are descriptions of the complexes of chloropromazine [4], quinacrine [10], proflavin [11], acriflavin [12], ethidium bromide [8, 13] and others. Two types of proflavin binding have been observed using bromine atoms covalently attached to poly dA - poly dU as spin orbital probes [14]; 1) a strong internal interaction via intercalation involving overlap of the orbitals of the pyrimidine-purine base pairs with those of the reagent, and 2) a weaker external, partially intercalated interaction involving some orbital overlap, and having electrostatic interactions with a nearby phosphate group [13].

Both modes of binding do not appear to operate between these incapacitating phenothiazines and nucleic acids. In each instance, increases in the ionic strength of the media by the addition of sodium chloride resulted in the disappearance of the charge-transfer bands suggesting that electrostatic interactions (probably between the positively charged phenothiazine 10- position side chain and a phosphate group of the nucleic acid) as well as partial intercalation are the main binding forces (type 2 above). Failure to achieve complete intercalation is understandable in view of the bond angle of approximately 139^{o} between the benzene ring planes in phenothiazines of this type[15].

The same behavior was observed when I or II was treated with poly A - poly U, demonstrating that these interactions occur specifically, and in all likelihood arise in DNA from the double-stranded regions rich in dA-dT and in the corresponding A-U rich regions of RNA.

Measurement of the 525 nm complex band of I in various concentrations of salmon sperm DNA yielded an association constant of approximately 550 1/mole. By equilibrium dialysis, however, a value of approximately 3000 1/mole was obtained demonstrating that the 525 nm binding mode contributes only about one-fifth to the overall I - DNA interaction. Other interactions of I with DNA that contribute to the overall association constant are probably similar to those observed between I and various synthetic polymers. Among these, strong interactions were observed between the incapacitating phenothiazines

and poly G - poly C. Binding to poly A, poly G, poly C and poly U was also seen and can contribute to overall association constants. Charge transfer complexes were associated, however, only with interactions of these compounds with double-stranded A-U or dA-dT moieties. The data are recorded in Tables 1 and 2. The large DNA association constants recorded in this table for compounds III and IV are noteworthy. The larger values of these constants correspond to increased conjugation at the 2- positions of the phenothiazine rings.

The large differences in binding strengths at specific sites as reflected by the data in Table I permits speculation with respect to the biological importance of this mode of binding. The cataleptic activities of compounds I to IV together with binding data are presented in Table 3. It is noted that the cataleptic potency in mice is inversely proportional to the apparent binding strength to the dA-dT base pairs of DNA (K_{DNA}). Furthermore, the activity essentially disappears when this binding strength is large as in III and IV.

Table 3

CATALEPTOGENIC POTENCY OF SELECTED PHENOTHIAZINES[a]
CD50 in Mice[b,c]

Compound	μ mol/kg	K_{DNA}, 1/mol
I	2.2 2.3	550
II	0.99 0.41	170
III	28	3000
IV	>57	3100

[a]Data reprinted from ref. (2) by permission of the authors;
[b]CD_{50} dosage to induce 50% of the maximum possible catalepsy score in a group of 6 mice. [c]The cataleptic potency of I was reported to be greater than II in rats(2)

When considering that the overall association constants of these compounds in DNA are approximately equivalent, this data suggests that the cataleptic potency parallels the extent of binding at the dG-dC or G-C base pairs in nucleic acids.

The uptake patterns of the incapacitating phenothiazines in living cells are illustrated in Plate I where human fibroblasts were

grown in sub-lethal concentrations of II. In these dividing cells II was observed to concentrate in granular bodies outside the nuclei in loci corresponding to microsome-rich areas. Uptake of II by the nucleoli is usually seen at higher reagent concentrations. However, detectable uptake by nuclei and cytoplasm did not occur. At cell death (drying or hypotonic lysis) nuclear uptake of II occurred rapidly with intense staining. Since these compounds penetrated the nuclear envelope in living cells to stain the nucleoli, their inability to interact with living nuclear DNA is probably related to the protection afforded by the strong protein-nucleic acid associations in native chromatin.

The patterns of the uptake of II by living cells are compatible with the chemical observations described herein. The strongest interactions apparently occur between these incapacitating phenothiazines and sites associated with microsomal activity - areas of active protein and nucleic acid synthesis in dividing cells and thereby the loci of concentrated unbound RNA.

In view of the observations that unbound nucleic acids bind tightly to these incapacitating phenothiazines in vivo, interference with associated metabolic processes such as protein and nucleic acid synthesis is expected. Simarily, such interference could result in the synthesis of faulty proteins or nucleic acids through strong binding to RNA. Likewise, these compounds should bind strongly to derepressed areas of nuclear DNA, a process known to result in frame-shift mutations.

Neuronal stimulation during nervous transmission is known to alter the nature of the RNA which is produced during this process (9). Incapacitating phenothiazines such as those described in this report would be expected to interact strongly and specifically with these substances and interfere with the nervous processes with which they are associated. The extent of such interference, although unknown, could be sufficient to elicit some of the responses attributed to these compounds.

REFERENCES:

1. Zinkle, C.L. and Kaiser, C., Antipsychotic Agents in Medicinal Chemistry, Burger, A., Ed., p 1410-1469 Wiley - Interscience New York, 1970.

2. Bossle, P.C., Ferguson, C.P., Sultan, W.E., Lennox, W.J., Dudley, G.E., Rea, T.H., and Miller, J.I., J. Med. Chem. 19, 370-373 (1976).

3. Gurr, E. Staining, Practical and Theoretical. p 63. The Williams and Wilkins Co., Baltimore, MD (1962).

4. Kantesaria, P. and Marfey, P., Physiol. Chem. and Physics, 7, 53-67 (1975).

5. Sapin, R., Leterrier, F. and Chambron, J., Biochimie. 57, 127-129 (1975).

6. Legator, M. and Zimmering, Ann. Rev. Pharmacol. 15, 387-408 (1975).

7. Waring, M.J., Humangenetik. 9, 234 (1970).

8. Waring, M.J., J. Mol. Biol. 54, 247 (1970).

9. Hyden, H., Endeavour. 21 144-155 (1962).

10. Weisblum, B. and de Haseth, P.L., Proc. Nat. Acad. Sci. USA 69, 629-632 (1972).

11. Finkestein, T. Weinstein, I.B., J. Biol. Chem. 242, 3763-3768 (1967).

12. Tubbs, R.K., Ditmars, W.E., Jr. and Van Winkle, Q., J. Mol. Biol. 9, 545-557 (1964).

13. Le Pecq, J.B. and Paeletti, C.J., Mol. Biol. 27, 87-106 (1976).

14. Galley- W.C. and Purkey, R.M., Proc. Nat. Acad. Sci. USA, 69, 2198-2202 (1972).

15. McDowell, J.J.H., The Molecular Structures of Phenothiazine Derivatives, p 33-54 in Phenothiazines and Structurally Related Drugs, Forrest, I.S., Carr, C.J. and Usdin, E., Editors, Raven Press, New York, NY, (1974)

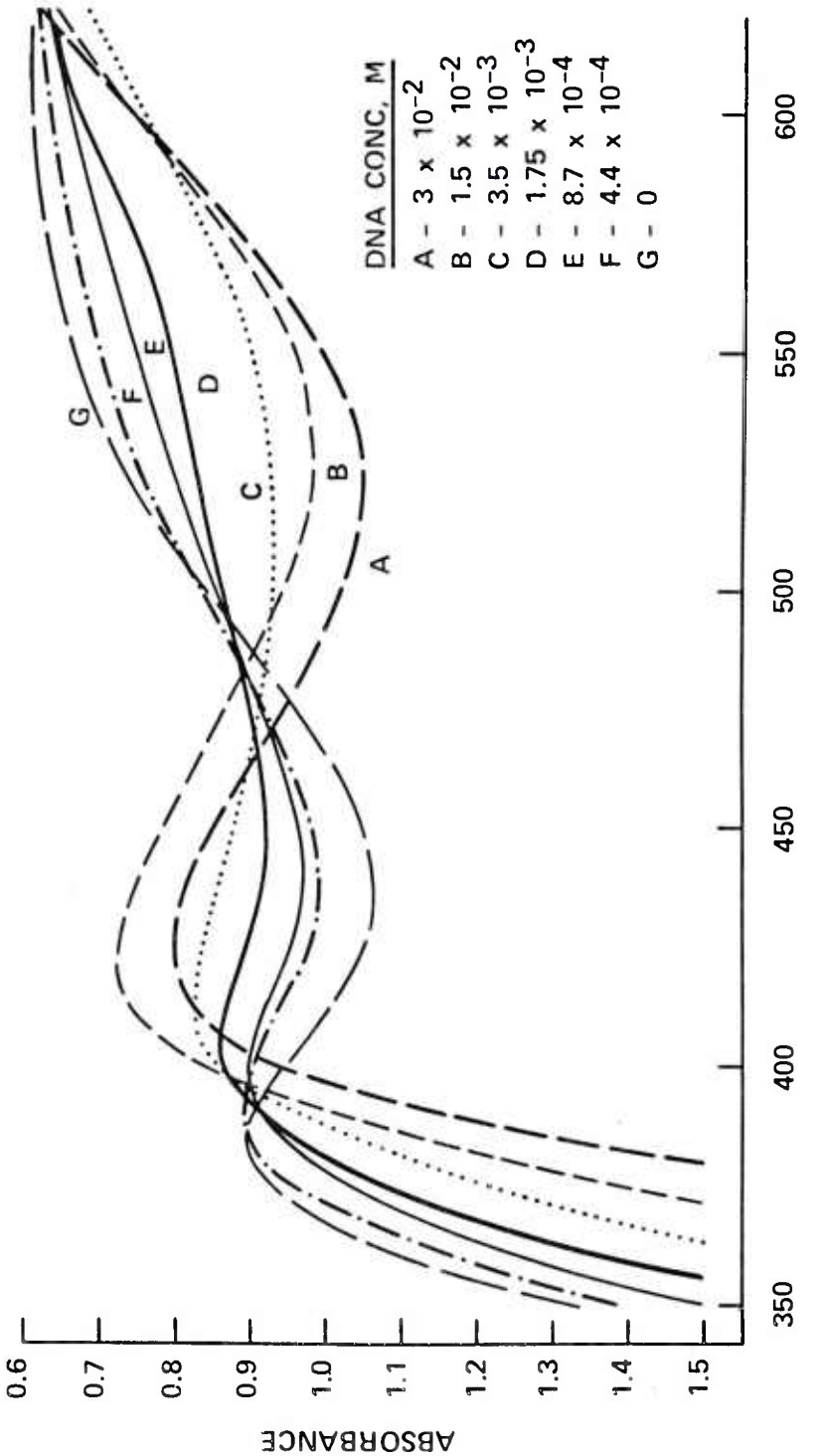

Figure 1. Absorption spectra of 3 x 10^{-4}M 2-Nitro-10- 3- 4-(2-hydroxy-ethyl)-1-piperazinyl propyl phenothiazine dimaleate, I, in 0.05M, pH 7.4 sodium phosphate buffer containing various quantities of salmon sperm DNA, 25°C.

a

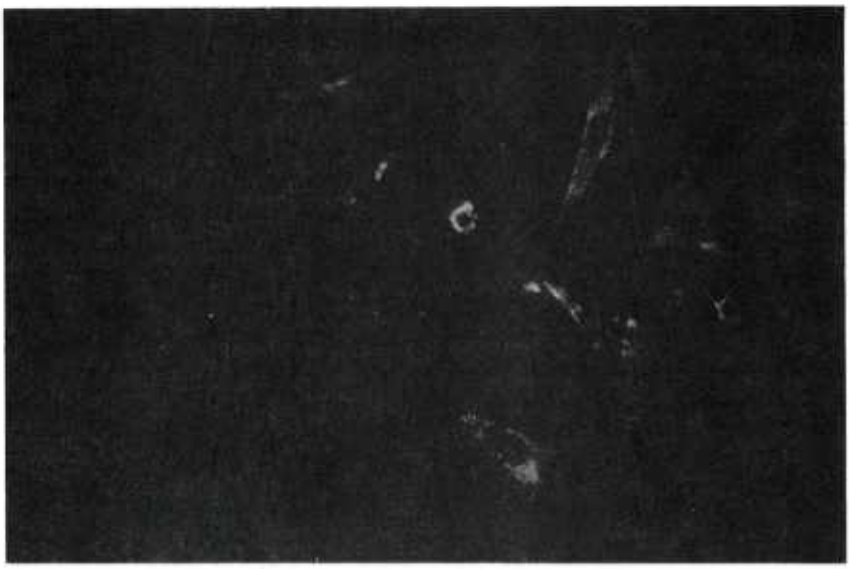

b

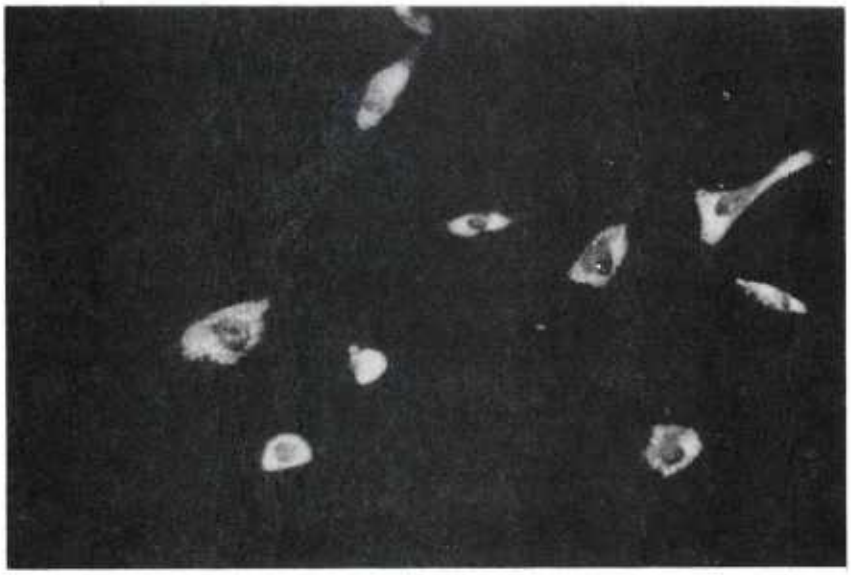

Plate 1. Human fibroblasts growing in 2-Cyano-10-{3-[4-(2-hydroxyethyl)-1-piperazinyl] propyl} phenothiazine dimethanesulfonate, II, three days after treatment. a) 5 x 10^{-6}M of II, b) 10^{-5}M of II. 160x by fluorescence microscopy.

AD-A056496

STEEL FIBERS AS WEB REINFORCEMENT IN REINFORCED CONCRETE (U)

GILBERT R. WILLIAMSON, Ph.D.
U.S. ARMY CONSTRUCTION ENGINEERING RESEARCH LABORATORY
CHAMPAIGN, IL 61820

INTRODUCTION

Background: When steel fibers are randomly dispersed in a concrete or mortar mix, the properties of the basic material are altered. Flexural, compressive and shear strengths are increased, impact resistance and fatigue life are improved, and post cracking behavior is considerably modified. These improved properties have resulted in the widespread use of steel fiber concrete in pavements and pavement overlays, refractories and precast units. However, the use of the material in structural applications has been confined to small scale members. Insufficient research has been accomplished to provide reliable design criteria for large scale structural applications. Henager (1) has demonstrated that steel fibers in beams 8" x 12" x 144" (203 x 304 x 3658 mm) contribute to the ultimate strength of the beam, while Swamy and Al-Noori (2) have shown that steel fibers can be used in large members, 6" x 9" x 90" (152 x 228 x 2286 mm), to produce composite beams. Williamson and Knab (3) demonstrated that steel fibers substituted for shear reinforcing in full scale beams can increase the shear strength of the concrete sufficiently to allow the beam to exceed the ultimate design moment, however the beam did not achieve the desired flexural failure.

Although it has never been proposed that steel fibers replace conventional reinforcing in full-scale structural sections, it has been sufficiently demonstrated that steel fibers can contribute to the overall structural capacity of large members. This study is directed toward a better characterization of the contribution steel fibers can make in structural members.

Objective: the objective of this investigation was to determine the feasibility of replacing shear reinforcement (stirrups) with randomly distributed steel fibers for the prevention of diagonal tension (shear) failure in full-scale conventionally reinforced concrete beams.

Approach: This study was accomplished in two phases. Phase I (3) involved four full-scale conventionally reinforced concrete beams designed in accordance with ACI Code 318-71. Each beam was the same size and contained an equal amount of flexural steel. One beam had no shear reinforcement, one contained stirrups and two were made with straight steel fibers as a replacement for stirrups.

Phase II consisted of two additional fiber concrete beams similar to the first four except that a deformed fiber was used as shear reinforcement rather than the straight fiber. The mix design for Phase I is given in Table 1 together with the strength properties of the concretes. The beam cross-sections and loading arrangements are shown in Fig. 1.

Review of Results of Phase I: The results of the Phase I tests are given in Table 2, where the design moments and shear stresses are compared to the actual values. The beam with no shear reinforcement attained a moment only 72 percent of the design value. The beam with stirrups had reached a value 27 percent greater than the design value and still had not failed, though failure was imminent. The two beams with steel fibers as shear reinforcement attained moments 8 percent and 11 percent in excess of the design moments.

The beam without shear reinforcement developed an average shear strength equal to the design value. At this point the beam failed catastrophically in shear as was expected (Fig. 2). The beam with stirrups reached an average shear stress 61 percent in excess of the design value, and although the beam contained numerous diagonal tension cracks, the beam did not fail; but there is no doubt that it would have failed in flexure, had the capacity of the loading machines not been exceeded. The two beams with fibers as shear reinforcement developed shear stresses 47 percent greater than the design value before the beams failed catastrophically in shear (Fig. 3).

The main conclusion that can be derived from these data is that steel fiber concrete can develop sufficient shear strength for the beam to exceed the ultimate design moment capacity. However, the shear strength was not sufficient to force a flexural failure.

Table 1

Design Mix and Strength Properties,
Phase I

Material	yd^3, lbs	m^3, kg
Cement	572	340
Sand	1485	882
3/8" (10 mm) aggregate	1485	882
Water, plain concrete	352	209
Water, fibrous concrete	393	233
Fibers	220	130
Air	4-6%	4-6%
Water reducer	per mfg. recommendations	

Strength Properties

	Age, days	psi	MPa
	Plain Concrete*		
Compression	29	4660	32.1
Flexural	34	530	3.65
Splitting	30	487	3.36
	Fiber Concrete		
Compression	34	4130	28.5
Flexural	35	694	4.78
Splitting	35	499	3.44

*Compression values are the average of 9 tests. All others are the average of 3.

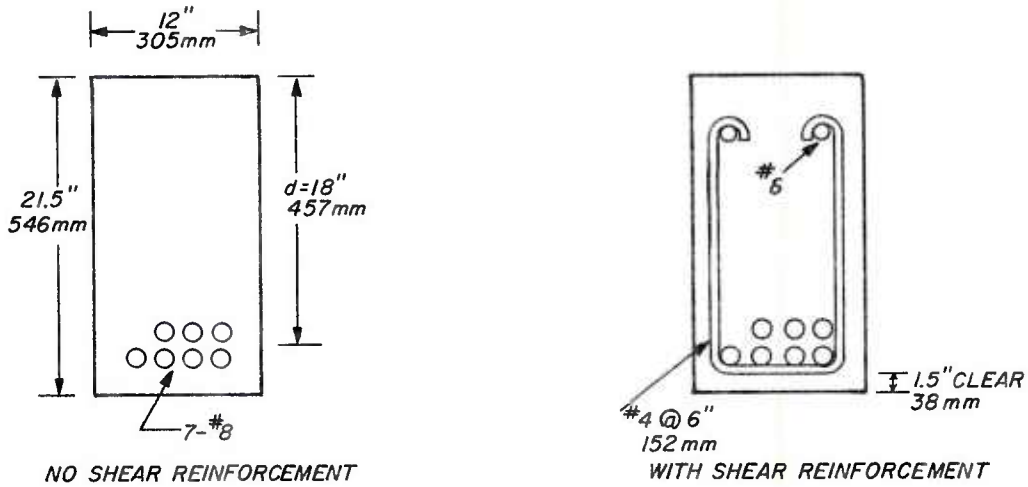

FIG. 1 Beam Cross-Sections and Loading Arrangement

Table 2

Results of Beam Tests, Phase I

Beam[1] No. and Type	Reinforcing Main	Reinforcing Fiber[2] lbs/yd[3]	Steel Ratio, ρ bal	Steel Ratio, ρ act	$\bar{M}u$ design k-ft (kN-m)	$\bar{M}u$ actual k-ft (kN-m)	v^3 design psi (MPa)	v actual psi (MPa)
1. Plain	7-#8[4]	None	.0291	.0256	420.8(570.6)	304.8(413.3)	194.(1.34)	192.(1.32)
2. Stirrups	7-#8	None	.0291	.0256	420.8(570.6)	534.0(724.1)	194.(1.34)	312.(2.15)
3. Fiber	7-#8	220	.0265	.0256	406.9(551.8)	439.5(596.0)	186.(1.28)	271.(1.87)
4. Fiber	7-#8	220	.0265	.0256	406.9(551.8)	450.0(610.2)	186.(1.28)	275.(1.89)

1. All beams were 12" x 21.5" x 23'-0" (.305 x .546 x 7.01 m). d = 18" (457 mm).
2. All fibers were 0.010 x 0.022 x 1.0 inches (0.254 x 0.559 x 25.4 mm).
3. v - average shear stress on cross-section = v/bd.
4. All reinforcing steel was ASTM A615 Grade 60. f_y = 64000 psi (441 MPa).

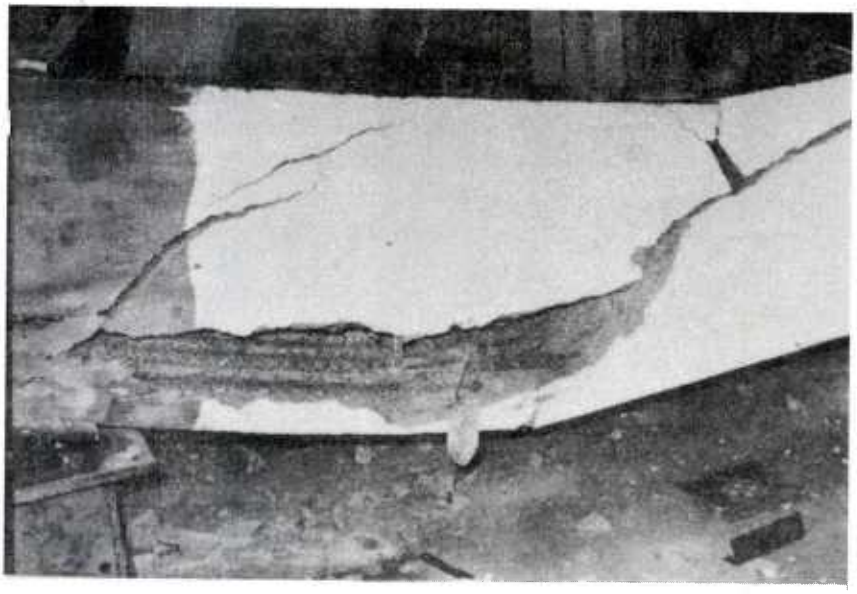

FIG. 2 Diagonal Tension Failure of Beam Without Stirrups or Fibers

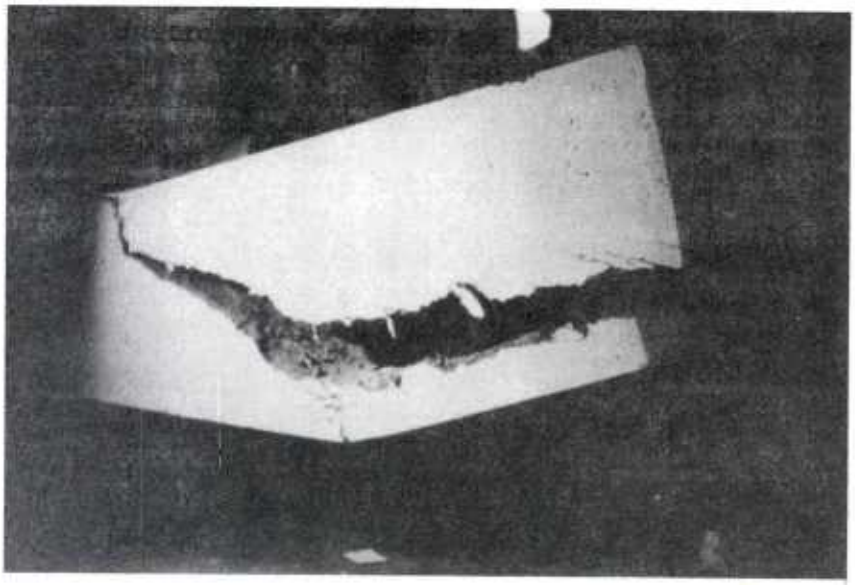

FIG. 3 Diagonal Tension Failure of Fibrous Concrete Beam

All four of the beams developed visible diagonal tension cracks at very low loads, approximately 50 percent of ultimate. It was reasoned that if a greater post cracking strength could be developed by the fibers, then perhaps sufficient shear strength could be developed to force the beams to fail in flexure. Previous work had shown that concrete made with deformed fibers will develop a greater post cracking strength than that made with straight fibers. As a result of these observations, two additional tests were designed using a fiber with deformed ends. These tests constituted Phase II of the study.

PHASE II

Materials and Fabrication: The steel fibers used were Dramix ZC 50/50 manufactured by Bekaert SA. The fibers are 0.02 x 2.0 inches (0.5 x 50 mm) and are deformed at the ends (Fig. 4). The ultimate strength of the fibers is in excess of 200,000 psi (1379 MPa). The main reinforcing steel was ASTM A615 Grade 60 with f_y = 64 ksi (441 MPa) for Beam No. 5 and f_y = 72 ksi (496 MPa) for Beam No. 6. The concrete was specified to be 5000 psi (34.5 MPa) at 28 days, however, poor control at the batch plant caused the concrete strengths to vary for the different beams. The concrete design mix and strength parameters are given in Table 3. The beams were fabricated in oiled plywood forms using primarily external vibration. They were cured at room temperature by coating with a curing compound. Cylinder and beam specimens were cured in the same manner alongside the beams. The concrete strength values shown in Table 3 are those obtained on the same days that the beams were tested.

Testing: The beams of Phase II were tested on a 21'-0" (6.4 m) span with the main loading actuators at the third points as shown in Fig. 1. For these tests, the loading was upward, while for the Phase I tests, the loading was downward; otherwise, there was no difference. A third actuator was placed at the center of the beams for use when the capacity of the main actuators was exceeded. Loading was accomplished with a CGS system. Deflections were obtained by Physitech and dial gages. Readings were taken at 10 kip (44.5 kN) intervals; closer when required. Except for the dial gages, all values were recorded through digital readout equipment. Shear strains at various locations were obtained for Beam No. 6 with SR-4 strain gages.

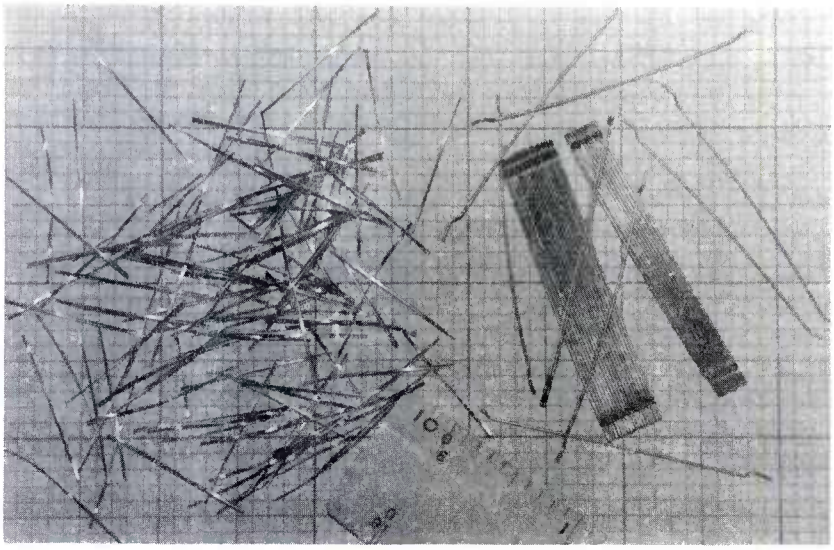

FIG. 4 Left - U.S. Steel "Fibercon" Straight Steel Fibers Used in Beams No. 3 and 4.
Right - NV Bekaert SA "Dramix" Crimped End Steel Fibers Used in Beams No. 5 and 6.

Table 3

Design Mix and Strength Properties,
Phase II

	yd^3, lbs	m^3, kg
Cement	572	340
Sand	1485	882
3/8" (10 mm) aggregate	1485	882
Water	286	154
Fibers-Bekaert ZC 50/50	145	91
Air	4-6%	4-6%
Pozzolith	per mfg. recommendations	

Strength Properties*

	Age, days	psi	MPa
	Fiber Concrete		
	Beam No. 5		
Compression	30	6060	41.80
Flexure	30	1275	8.79
Split tensile	30	1000	6.89
	Beam No. 6		
Compression	43	5860	40.40
Flexure	43	1080	7.45
Split tension	43	700	4.83

*All values average of three tests.

Results: Table 4 compares the design values of the moments and shear stresses with the values obtained from the tests of the two beams. Beam No. 5 achieved 97 percent of the design moment, while Beam No. 6 reached a moment one percent greater than the design moment. Both beams failed in flexure by first yielding of the reinforcing steel followed by crushing of the concrete. Failure was gradual in both cases, extending over several minutes.

The average shearing stresses in Beam No. 5 were 45 percent greater than the design value. This is consistent with the values of Beams No. 3 and 4 of Phase I, except for the fact that they failed as a result of diagonal tension cracks, while Beam No. 5 had only one visible diagonal tension crack even at the point of failure. Beam No. 6 developed an average shear stress 67 percent greater than the design value, with only one hairline diagonal tension crack in the beam. This crack developed at a stress of approximately 245 psi (1.69 MPa) but remained closed through the point of failure. Again, the failure of Beam No. 6 was gradual, with yielding of the tension steel first, followed by gradual crushing of the concrete (Fig. 5).

Fig. 6 shows the load-centerline deflection curve for four of the beams. It can be seen that neither the fibers nor the stirrups influenced the stiffness of the members. The remaining two beams had similar curves.

Strain gages were placed at opposite sides of the beam at mid-depth and at 45° to the long axis, in the theoretical direction of the diagonal tension. The gages were 38" (965 mm) from the support, in the region of constant shear. Measured values for the two gages were .000098 and .000095, respectively.

Discussion: The results shown in Tables 2 and 4 show good agreement with the fiber concrete beam moments theoretically determined by standard ACI Code design procedures and those obtained experimentally. The actual values ranged from 3 percent below to 10 percent above the calculated values. This indicates that no special design procedures are required when using fibers as shear reinforcement.

The average shear stresses developed by the beams with fibers ranged from 40 to 67 percent greater than the shear stress developed by the plain concrete. These stresses were sufficient to force the beams to fail in flexure for those that were made with the crimped end fibers.

Table 4

Results of Beam Tests, Phase II

Beam[1] No. and Type	Reinforcing Main	Fiber[2] lbs/yd[3]	Steel Ratio, ρ bal	act	$\bar{M}u$ design k-ft(kN-m)	$\bar{M}u$ actual k-ft(kN-m)	v[3] design psi (MPa)	v actual psi (MPa)
5. Fiber	7-#8[4]	145	.0293	.0256	445.9(604.6)	431.5(585.1)	194.(1.34)	282(1.94)
6. Fiber	7-#8	145	.0284	.0256	486.1(659.1)	493.0(668.5)	194.(1.34)	324(2.23)

1. All beams were 12" x 21.5" x 23'-0" (.305 x .546 x 7.01 m). d = 18" (457 mm).
2. Fibers were Bekaert ZC-50/50 0.02 x 2.0 inches (0.5 x 50 mm).
3. v = average shear strength on cross-section = v/bd.
4. All reinforcing steel was ASTM A615 Grade 60. For Beam No. 5 f_y = 64000 psi (441 MPa), and for Beam No. 6, f_y = 72000 psi (496 MPa).

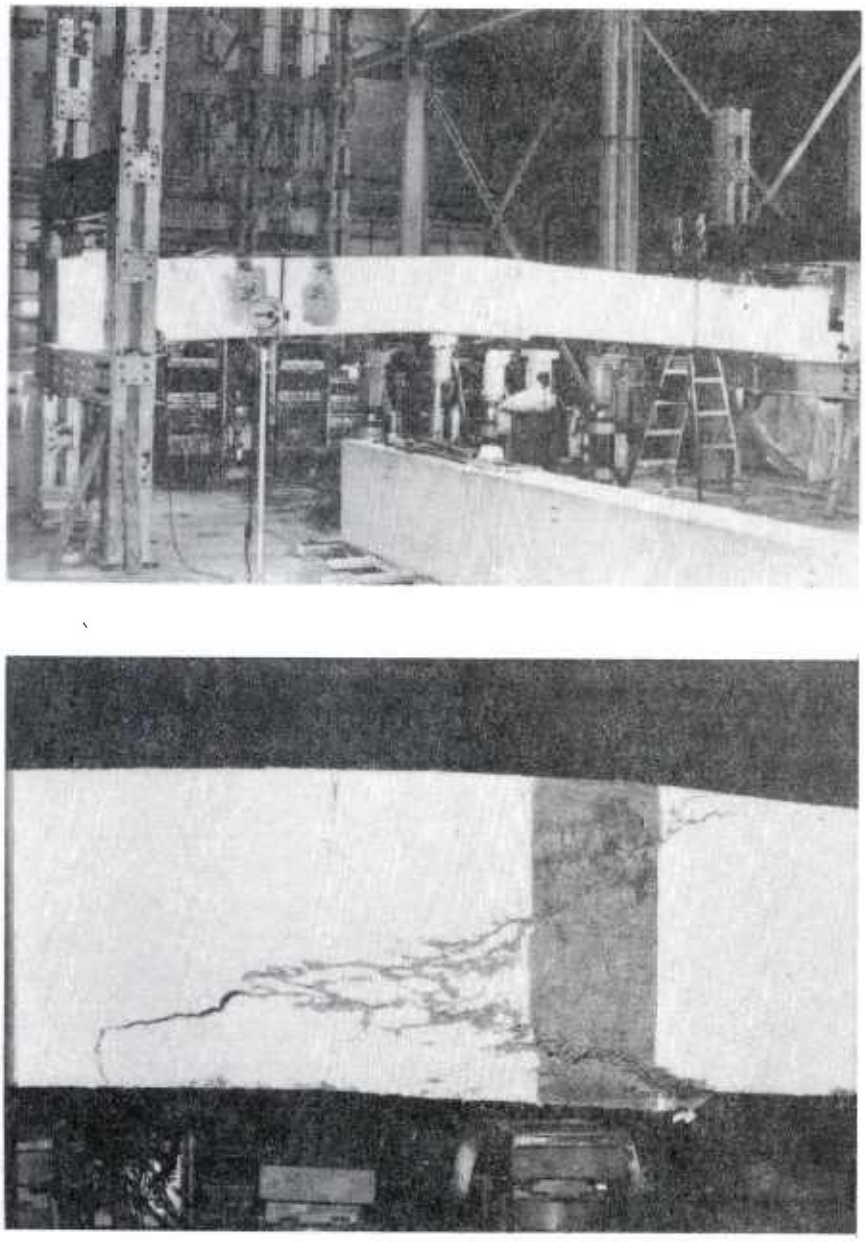

FIG. 5 Top - Overal View of Beam No. 5 at Failure
Bottom - Close-up of the Failure Zone of Beam No. 5

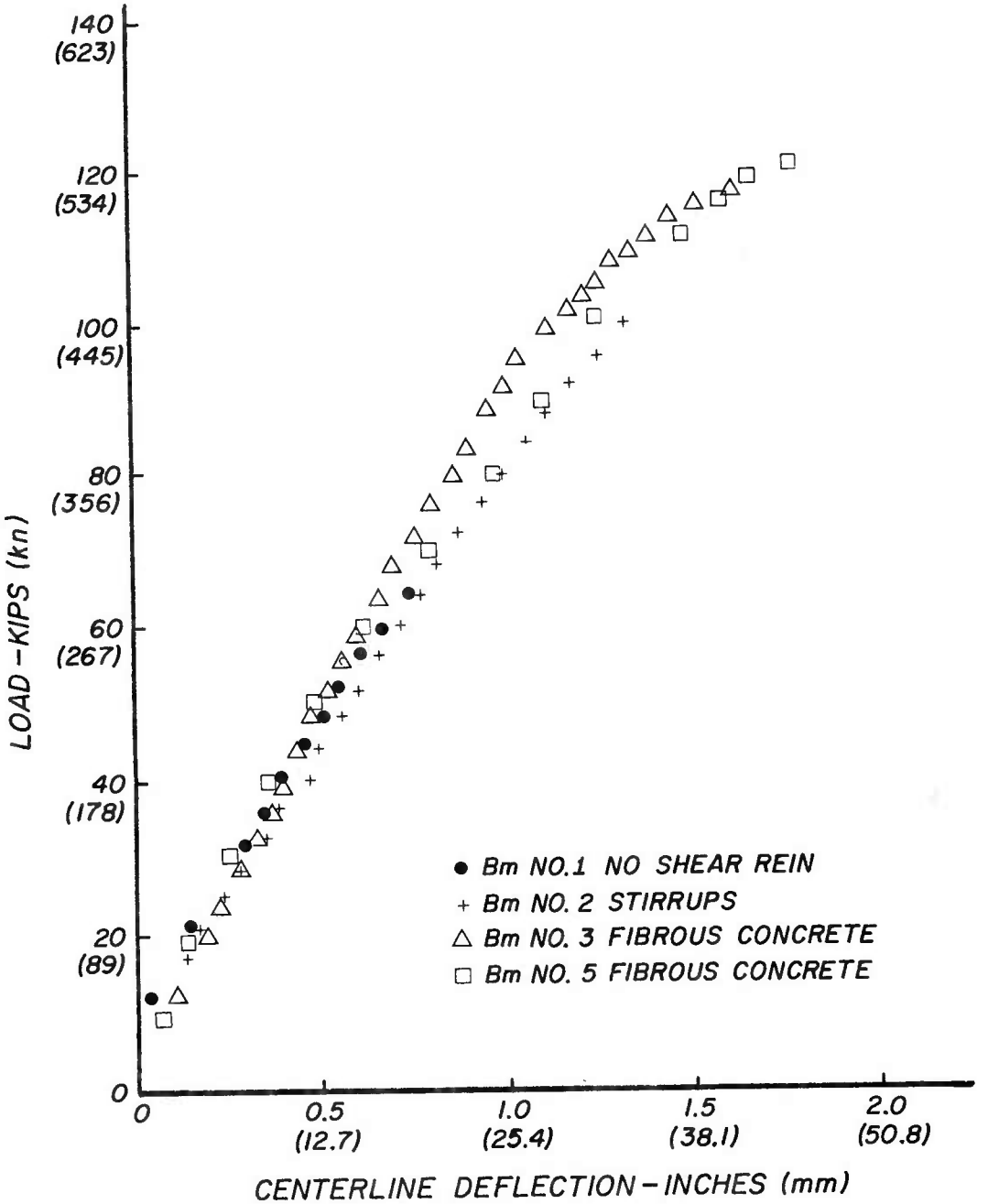

FIG. 6 LOAD - DEFLECTION CURVES

The load-deflection curves of Fig. 6 indicate that the fibers have no effect upon the stiffness of the beams. This is in contrast to what can be expected when steel fibers are used in small members. Both the stiffness and ductility can be considerably affected by the presence of fibers, especially for small beams.

The strains measured by the gages indicate a maximum shear stress 25 percent greater than the average shear stress. This is based upon a Young's modulus derived from the procedure given in the ACI Code, where $E = 57000 (f'_c)^{\frac{1}{2}}$. Although the interaction of stresses due to shear and flexure are not clearly defined in a reinforced concrete beam, it would be expected that the maximum stress would occur at mid-depth as found here.

Conclusions: The following conclusions are based upon the use of steel fibers with deformed ends (Dramix) to replace stirrups in full-scale reinforced concrete beams loaded with concentrated forces.

(1) Steel fibers can be used to replace stirrups in beams with no reduction in the ultimate design moment capacity.

(2) Steel fibers increase the shear strength of concrete beams sufficiently to prevent catastrophic diagonal tension failure, while forcing the beam to fail in flexure.

(3) ACI Code procedures can be used without modification to design reinforced concrete beams that contain steel fibers as shear reinforcement.

(4) Low volume percentages of steel fibers have no effect upon the stiffness of full-scale beams.

(5) This study indicates that steel fibers present a potentially more economic alternative to the use of stirrups in reinforced concrete design.

References

1. Henager, C. H., "Ultimate Strengths of Reinforced Steel Fibrous Concrete Beams," Symposium on Fiber Reinforced Materials, Institution of Civil Engineers, London, 1977.

2. Swamy, R. N. and Al-Noori, K. A., "Flexural Behavior of Fiber Concrete with Conventional Reinforcement," RILEM Symposium on Fiber Reinforced Cement and Concrete, London, Sept. 1975.

3. Williamson, G. R. and Knab, L. I., "Full Scale Fiber Concrete Beam Tests," RILEM Symposium on Fiber Reinforced Cement and Concrete, London, Sept. 1975.

AD-A056497

SIMULATION OF DRIFTING SNOW IN A HYDRAULIC FLUME (U)

JAMES L. WUEBBEN
U.S. ARMY COLD REGIONS RESEARCH AND ENGINEERING LABORATORY
HANOVER, NEW HAMPSHIRE 03755

Introduction

The objective of this investigation was to simulate conditions of drifting snow previously observed in the field in a laboratory hydraulic flume using a sand-water analog. Prototype conditions and model results were evaluated to define modeling parameters that would allow quantitative correlation between actual drift conditions and the model.

Although exact similitude is not feasible, this modeling approach has proven useful in studies of snow conditions which defy theoretical prediction and would be very time consuming or impossible to evaluate in the field. Parameters examined in the model include prototype dimensions, flow velocity, geometric scale effects, structural porosity, and time.

Past Work

Various two-phase systems have been used in the past to investigate the mechanics of blowing snow, including the sand-water analog used here. Theakston (15, 16) took a qualitative approach and developed a model which looked like blowing snow and produced drift patterns resembling those observed in the field. While largely ignoring the quantitative aspects, he was able to use the model as a practical design tool to study the effect of various structural and terrain modifications in the control of snow accumulation.

Isyumov (6), on the other hand, developed theoretical similitude relationships in a study of roof snow loads. Although he did not attempt to correlate the model results to actual field data, he was

able to compare quantitatively the effects of windspeed and wind orientation, roof geometry, snowfall rate and terrain roughness within the model.

Calkins (1, 2, 3) also used a similitude approach in developing models of snow accumulation around various structures. In one study, he used the model to examine possible snow control measures near aircraft instrument landing system antenna facilities in Alaska. The feasible alternatives involved structural, terrain, and site layout modifications that could not be easily addressed in the field. During a study of a radar housing constructed in North Dakota, Calkins developed quantitative relationships within the model to correlate the horizontal drift dimensions resulting from various combinations of windspeed and the geometric scale of the model.

Experimental Design

In designing a model of drifting snow, there are a variety of factors to be considered. On a qualitative basis, the particles should move by a combination of saltation and turbulent diffusion and produce a sand bed that looks like a snow field. While an ideal model would be geometrically, kinematically, and dynamically similar, exact similitude is not practical with the sand-water analog and only the more important factors may be modeled.

A basic assumption made is that drifting occurs in dry, cohesionless snow since the sand used is essentially cohesionless in water. For predicting long-term snow conditions, Isyumov and Davenport (7) suggest an integrated approach in which the physical modelings of specific drifting events are combined with statistical descriptions of meteorological conditions in a mathematical model.

The importance of modeling the wind flow regime is generally accepted. Snyder (10) suggested that complete modeling of a neutral stability atmospheric boundary layer in general terms would result from considering the following criteria:

1) Geometric scaling
2) Reynolds number scaling (viscous effects): VL/v
3) Rossby number scaling (Coriolis effects): $V/L\Omega$
4) Peclet number scaling (heat transfer): Lv/k
5) Densimetric Froude scaling (gravity): $V/[gL(\rho_s-\rho_w/\rho_w)]^{1/2}$

where V is flow velocity, L is a characteristic length, v is kinematic viscosity, Ω is earth's angular velocity, k is thermal conductivity,

ρ is density, and g is acceleration due to gravity. The subscripts s and w denote particle and fluid characteristics respectively.

The assumption of a neutral stability atmosphere should be valid in this model, since drifting normally occurs during periods of high winds and overcast skies. For the short distances considered here, and assuming isothermal conditions during drifting, the Coriolis and heat transfer effects can be neglected.

Besides geometric scaling considerations, this leaves Reynolds and Froude similarity to be dealt with. Although it is feasible to satisfy both of these simultaneously, it is often not practical to do so. Fortunately, however, for fully developed turbulent or "rough" flow, the flow patterns become essentially independent of the Reynolds number. Most natural surfaces are aerodynamically rough even at relatively low windspeeds. A widely used criterion for determining fully rough flow was proposed by Sutton (11) using the roughness Reynold's number: $U_* z_o / \upsilon > 2.5$ where U_* = shear velocity, υ = kinematic viscosity, z_o = terrain roughness length, $\approx \varepsilon/30$ (ε is equivalent sand roughness).

Based on the above assumptions, modeling of the earth's turbulent boundary layer might be approximated by simulation of the terrain roughness (6). This may be stated in terms of the Jensen criterion:

$$\frac{L_m}{L_p} = \frac{z_{o_m}}{z_{o_p}} \qquad (1)$$

where L is a characteristic length, z_o is the terrain roughness length, and m and p denote model and prototype conditions respectively. Since the terrain roughness length z_o was not measured in the field, it will be estimated based on measurements on similar terrain. Using data cited by Isyumov (6), the prototype terrain roughness should be in the range of 0.023 m to 0.09 m. This corresponds to model roughness lengths in the range of 0.023 cm $< z_{o_m} <$ 0.18 cm for geometric scale ratios of 1:50 and 1:100. Because of the appreciable spread in the estimate of z_o, as well as the fact that it is only an estimate, it is not possible to model the terrain roughness accurately. Indeed, there is no clear basis for using different model roughness lengths even between geometric scales of 1:50 and 1:100.

Since the roughness length measured for the bare flume bottom was only 0.001 cm, a system of artificial roughness was developed. By randomly gluing pieces of crushed rock to the flume bottom, the rough-

ness length was increased to approximately 0.084 cm. The resulting boundary layer thickness δ in the model, based on velocity profiles, was estimated to be 8 to 10 cm deep. This is sufficient to just envelop the tallest model (7.6 cm).

Evaluating the roughness Reynolds number for the lowest flow velocity used in the model (mean velocity V_M = 28.1 cm/sec) yields $U_* z_o / \nu$ = 18.1, which is within the rough flow regime defining Reynolds number independence.

Now one of the major problems in using the sand-water analog must be considered. According to Mellor (9), blown snow usually consists of roughly equidimensional grains about 0.01 cm in diameter. It is apparent that it would be difficult to maintain geometric similarity for any significant scale reduction. Strict scaling would result in the very small model particles being transported in a different flow regime unless Reynolds similarity is achieved. Therefore, in order to work under the assumption of Reynolds number independence, it is necessary to distort the model with respect to particle size. Increasing the particle size reduces the significance of viscous effects relative to inertial effects, but provided that the particles used are not too large and that they still respond to the more significant aspects of the flow structure, it may still be possible to achieve adequate similitude.

Velocity scaling will now be examined. Since sand in water is being used to simulate snow in air, density effects become important and the appropriate relationship is the densimetric Froude number cited in the initial list of criteria. Equating the model and prototype Froude numbers yields $\lambda_V = 0.0534\ \lambda_L^{1/2}$, which results in velocity ratios of 1:130 and 1:190 for geometric ratios of 1:50 and 1:100 respectively. The term λ denotes a ratio of model to prototype conditions. For the weighted seasonal mean wind velocity of 16.4 m/sec during drifting cited by Tabler (12) field data, the corresponding mean model velocities would be well below the threshold of movement for the sand being used (V_{th} = 25 cm/sec).

Since modeling based on the the densimetric Froude number is not possible, the velocity scaling will be developed based on gross particle transport and threshold of movement characteristics. According to Isyumov (6), this can be accomplished by maintaining similarity of particle terminal fall velocity W_t and of critical shear velocity U_{*t}. This may be stated in terms of model to prototype ratios as $\lambda_V = \lambda_{W_t} = \lambda_{U_{*t}}$.

The fall velocity for the sand used in the model was not measured, but for a mean sediment diameter of 0.12 cm and a shape factor corresponding to naturally worn quartz, the terminal velocity in water at 20°C would be about 1.2 cm/sec. Corresponding information for snow derived from information given by Mellor (9) gives $W_t = 0.5 \rightarrow 1.0$ m/sec for a diameter on the order of 0.1 mm. This results in a velocity ratio based on terminal fall velocity in the range of $1{:}42 < \lambda_{w_t} < 1{:}83$.

Because of the statistical nature of the entrainment process, it is not possible to pinpoint a threshold of motion, and different observers would likely estimate different thresholds. But, based on observation of a uniform bed of the model sand, the mean flow velocity at the initiation of particle motion is about $V_{th} = 25$ cm/sec, which yields $U_{*t} = 1.22$ cm/sec. Taking the threshold of motion for cohesionless snow to be in the range of 21 cm/sec $< U_{*t} <$ 52 cm/sec gives a velocity ratio based on the threshold of motion in the range of $1{:}18 < \lambda_v < 1{:}43$.

Depending on a combination of geometric and wind structures factors, the dominant form of snow transport may be either saltation or turbulent diffusion. Lacking prototype data, and because of the uncertainty contained in the estimates of the parameters above, a velocity scale will be selected by equating the threshold shear velocity and the fall velocity between model and field conditions. This results in the velocity ratio $\lambda_v = 1{:}42$.

The Model

The objective of this investigation was to simulate conditions of drifting snow and to define modeling parameters that would allow quantitative correlation between actual drift conditions and the model. Due to the complexity of the distortion in the model, it was decided to simplify this correlation by modeling a snow fence which allows a two-dimensional analysis.

The fence modeled is the standard plan snow fence designed by the Wyoming Highway Department and installed along Interstate Highway 80 in 1971. The performance of this system has been documented by the Rocky Mountain Forest and Range Experiment Station of the U.S. Forest Service (12, 13, 14). The fence is of the horizontal slat type with 50% porosity, a bottom gap of about 40 cm, and a leeward inclination of 15°. Fence heights used in the field include 1.8, 2.4, 3.2, and 3.8 m.

The testing was conducted in a hydraulic flume at CRREL. The overall length of the flume is 10.7 m, with a working length of 7.3 m.

The cross section is normally 0.91 m deep and 0.91 m wide, but for these tests the flume width was reduced to 33 cm. The flume is of the recirculating type with a gravity feed sand hopper at the upstream end.

Model Operation

A matrix of the scheme of model run conditions using the standard 50% porosity fences is given in Table 1. These fences were constructed of round metal dowel stock. In addition, runs were made using 2.4-m-high fences at λ_L = 1:100 having densities of 75 and 100%, and a 50% density fence constructed with square doweling. These additional runs were made at a mean velocity of V_M = 50 cm/sec and at a sand feed rate of F_s = 2.8 kg/min.

Table 1. Matrix of model runs.*

Scale	1:100			1:50	
Fence height	2.4 m	3.8 m	7.6 m	2.4 m	3.8 m
F_s (kg/min)	V_M (cm/sec)	V_M (cm/sec)	V_M (cm/sec)	V_M (cm/sec)	V_M (cm/sec)
1.6	30				
	40	40	40	40	
		50			
2.8	50	50	50	50	50
	60				
9.6	50				

*V_M = 50 cm/sec, F_s = 2.8 kg/min.

Ideally, mass flux data would be used to correlate the model results. Originally it was intended to make measurements of sediment flux and concentration profiles using an electro-optical probe, but due to the operational characteristics of the system, the results were unsatisfactory. Because this information was lacking, the model was compared internally based on an open field (no fence in place) accumulation rate for various combinations of flow velocity and sand feed rates. This accumulation rate is defined as the average sand depth D_r divided by elapsed time.

The basis for using this open field accumulation rate dD_r/dt is the assumption that the system approaches a steady state. By feeding in enough sand at the headbox so that the sediment carrying capacity of the flow is substantially exceeded, net deposition occurs in the flume. If a steady state of both horizontal flux and deposition rate

is at least approached, deposition rates should remain more or less constant with respect to distance along the flume. These accumulation rates were calibrated by running the system at various combinations of sand feed rate and water velocity. Keeping the inexactness of these relations in mind, a comparison of drift dimensions based on the reference accumulation rate dD_r/dt gives a relative indication of fence efficiency.

Time scaling in the model might also be best determined on the basis of mass flux, but this information was lacking in both the model and prototype. Alternatively defining the deposition rate ratio as $\lambda_d \, D_r/dt = \lambda_L/\lambda_t = \lambda_V$ yields prototype precipitation rates in the range from 33 to 150 cm/hr. These model accumulation rates correspond to abnormally high values of prototype precipitation rates since most snowfall rates in the U.S.A. would probably be under 6 cm/hr.

Moderate distortion of the precipitation rate was found to have no appreciable effect on the model, and even some of the higher model rates used here appeared to cause only slightly more uniform depth drifts. As a result, it should be possible to reduce the time scale through the use of a distorted precipitation rate. If the rate is increased too greatly, however, drift detail may be obscured and eventually may result in burying the model.

Another basis for model comparison is the saturation value of drift formation. The point at which a fence becomes saturated is subjective since it is approached asymptotically, and in a feed-type flume with net deposition occurring the drift never really stops accumulating. While it appears that there is a vertical limit to drift growth of about 1.2 H, sand continues to be deposited in the tail portion of the drift. As a result, saturation in the model was defined as the point when the fence began to submerge rapidly. Ordinarily the fence would remain relatively clear through most of the run and then the bottom gap would plug and the fence would rapidly submerge. Whether this is the best definition of model saturation or not, it unquestionably signalled the end of a run.

Results

As a first step in evaluation of the model, the results of the various model runs will be correlated internally, and in addition qualitative comparisons will be made to conditions observed in the field. Later, the quantitative correlation of the model results to prototype data will be examined.

Velocity

The data from a series of runs using the 2.4-m at 1:100 scale model demonstrate the influence of velocity on snowdrift formation. Figure 1 gives a plot of dimensionless area A/H^2 versus the reference sand accumulation depth D_r/H. Since this relationship reflects a form of fence efficiency, when differentiated with time it indicates that the trap efficiency of the fence increases with velocity in the range of 30 cm/sec < V_M < 50 cm/sec, but by V_M = 60 cm/sec the trend reverses. An examination of the data for drift length and maximum depth shows a similar trend.

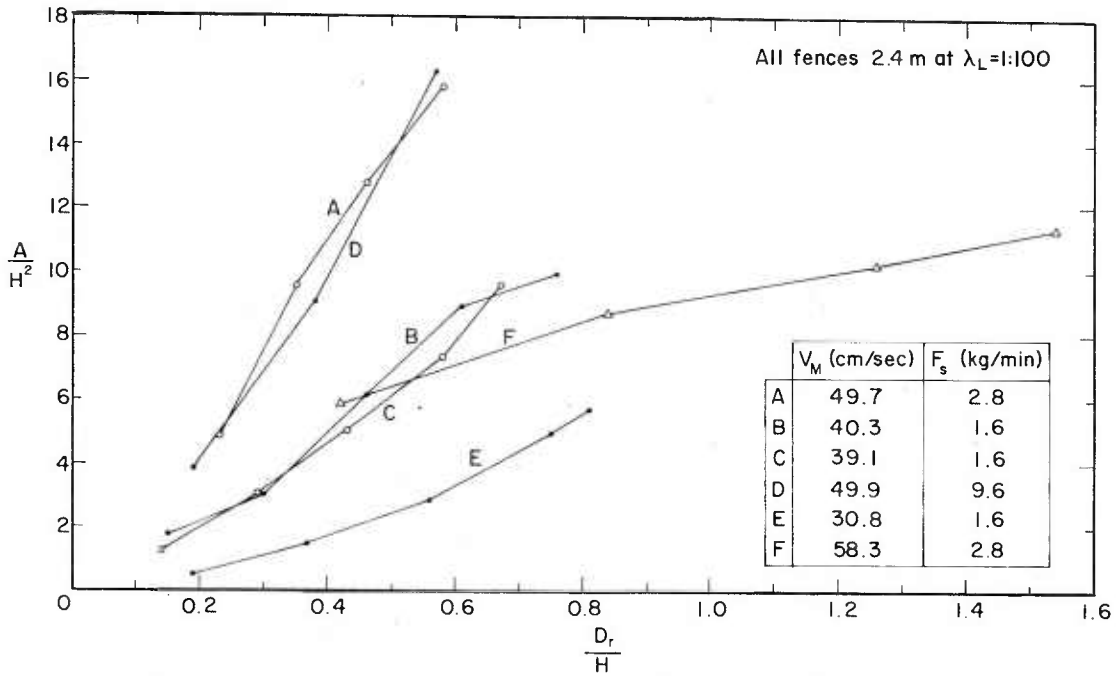

Figure 1. Influence of velocity on fence efficiency.

Examining the dimensions of the drifts for equivalent areas A/H^2, however, shows that as velocity increases, the drift increases in length and becomes shallower. At V_M = 60 cm/sec, the drift becomes both shorter and shallower by approaching a more uniform depth. The dimensions of the leeward drift at saturation for various flow rates are given in Table 2. The term X_{MAX} denotes the distance from the base of the fence to the point of maximum drift depth D_{MAX}, and X_{END} denotes the distance from the base of the fence to the tail of the drift.

Table 2. Variation in drift dimensions with flow velocity (saturation values).*

V_M (cm/sec)	D_{MAX}/H	X_{MAX}/H	X_{END}/H	A/H^2
30	1.19	2.5	8.7	6
40	1.19	3.0	24.0	10
50	1.19	3.55	24.2	16
60	0.93	4.0	26.0	11

*H = 2.4 m, λ_L = 1:100.

Finney (4,5) in his wind tunnel studies, concluded that the length of the eddy area produced by a vertical barrier varies directly with fence height but is independent of wind velocity. However, he noted that the distance from the fence to the position of maximum drift depth is related to windspeed. Kungurtsev (8), on the other hand, claimed evidence of an increase in a drift length with windspeed, and further postulated a linear relationship between drift length and velocity. Finally, Mellor (9) cited data by Nokkentved that indicated a shortening of the drift as velocity increased.

The data from the present study indicate that, for equal drift volumes, the length of the drift increases as velocity increases from the threshold of motion, reaches a somewhat stable value in the range of 40 to 50 cm/sec, and begins to decrease by 60 cm/sec. This would correspond to the prototype drift length increasing with wind velocity up to $V_W \approx 17$ m/sec and starting to decrease with increasing velocity somewhere in the range of 21 to 25 m/sec. Thus, all three trends mentioned in the literature were observed in the model depending on the velocity range.

Figure 1 also shows that two runs at $V_M \approx 50$ cm/sec, which are identical except for sand feed rate, agree very well. This tends to support the contention that precipitation rate is not a dominant factor controlling the characteristics of drift development, an assumption critical to the use of an abnormally high precipitation rate ratio to reduce the time ratio. Data from the runs using the 3.8-m at λ_L = 1:100 fence also support this contention. The drifts do develop more rapidly, however, and there is a tendency towards more uniform depth as the deposition rate increases.

Fence Height

Data in which flow velocity and the sand feed rate are held constant show the expected trend of storage volume increasing with fence

height. However, the 3.8-m at λ_L = 1:50 fence produced a larger drift than the 7.6-m at λ_L = 1:100 fence even though both fences have the same physical height. This difference is attributed to the combined effects of an increased bottom gap and wider openings between slats. In the field, porosity is often considered to be the significant variable rather than slat opening and width, but because of the particle size distortion this may not be true in the model.

The maximum depths obtained for various fence heights became stable before saturation and yielded the values shown in Table 3. These data show that, as fence height increases, the drift becomes relatively shallower and longer, and has its center mass closer to the fence. These effects were not evident in the field data, however, and it is felt that the problem lies in the modeling of the boundary layer. Although the models were contained within the logarithmic portion of the velocity profile, the boundary layer thickness was not modeled, and the height of the largest model fences used approaches the thickness of the boundary layer.

Table 3. Variation in drift dimensions with fence height (saturation values).*

H_p (m)	H_m (cm)	λ_L	D_{MAX}/H	X_{MAX}/H	X_{END}/H
2.4	2.4	1:100	1.19	3.55	24.2
3.8	3.8		1.14	2.7	27.8
7.6	7.6		0.77	1.9	33.4
2.4	4.8	1:50	1.07	3.3	18.7
3.8	7.6		0.64	1.6	30.5

* V_M = 50 cm/sec, F_s = 2.8 kg/min.

Porosity

Another parameter to be examined is fence porosity. Although it is possible to geometrically model the fence porosity, the distortion present in the model makes correlation impossible with the data available.

Runs were made, however, to determine the model's relative response to porosity. Fences were constructed at geometric scales of 1:100 representing a 2.4-m fence having densities of 50, 75, and 100%. In addition, a model was constructed using square doweling to investigate the effect of slat shape.

There is a clear relationship between volumetric accumulation and porosity. At least for porosities less than 50% as studied here, the fence storage efficiency increases as porosity decreases. The effective porosity of the square doweled fence is between 0 and 25%, even though its geometric shadow porosity is 37% and its porosity when not inclined is 50%. This indicates that that shape of the dowels is significant.

The dimensions of the leeward drift at saturation for the various porosity runs are listed in Table 4. Although there is no large difference in the maximum drift depth, the distance from the fence to the position of maximum depth varies greatly. Also, the solid fence produced the longest drift; this is contrary to conditions observed in the field.

Table 4. Variation of drift dimensions with fence porosity* (saturation values).

Porosity (%)	D_{MAX}/H	X_{MAX}/H	X_{END}/H	A/H^2
0	1.22	9.2	35.8	24.0
25	1.2	5.5	24.0	17.5
50	1.19	3.3	24.2	16.0
37†	1.25	4.9	27.0	17.6

*V_M = 50 cm/sec, F_s = 2.8 kg/min.
†Geometric shadow porosity, square doweling.

Model Correlation

From the data discussed in the previous section, it was possible to develop a relationship that would predict the unit storage volume (or cross-sectional area of the drift) at any time, based on the fence height, flow velocity and sand feed rate. This was accomplished by assuming a linear relationship for the central portions of the A/H^2 vs D_r/H plots found in Figure 1. It was further determined that the variation in these relationships due to the velocity was essentially logarithmic in nature. Combining these two trends yields the following relationship:

$$\frac{A}{H^2} = \frac{D_r t}{tH} \times 10^{0.027\ V_M + 0.162} - 2.4 \ . \qquad (2)$$

Equation 2 was evaluated by comparing measured values to those predicted by the equation. Evaluation of data for different fence heights and velocities showed an error of less than 10% for almost all data except those at the lowest values of A/H^2. However, in view of

the inherent inaccuracy of using an open field deposition rate as an indication of sand flux, this relationship appears reasonable.

It was also possible to predict the variation in the distance from the fence to the point of maximum depth of drift. The relationship appears to be linear, at least in the range of $30 < V_M < 60$ cm/sec. Because of sparse data, the variation with fence height was not evaluated, but for the 2.4-m fence at λ_L = 1:100, the variation X_{MAX} with mean velocity may be described as

$$\frac{X_{MAX}}{H} = 0.054\ V_M + 0.86 \qquad (3)$$

where V_M is in units of cm/sec.

The maximum drift depth (D_{MAX}/H) varied with fence height, but no definable relationship was evident. The shortest fences, however, showed more consistent drift depths and, therefore, velocity independence. Although the models were maintained within the logarithmic portion of the velocity profiles, the taller fences were nearly as tall as the boundary layer thickness. The shorter fences, which performed better, more nearly approached the prototype boundary layer proportions. Table 2 listed the relative dimensions for the 2.4-m at λ_L = 1:100 fence, which will be used in further analysis since it is the best documented fence and apparently gave the best results.

An examination of Table 2 shows that the results of the 2.4-m fence are quite similar to the prototype data, except that the cross-sectional area of the drift is slightly smaller and closer to the fence than that of the prototype. Based on the data with the porosity runs and considering the effect of constructing the models from round doweling, it appears that the 2.4-m fence at a geometric scale of 1:100 with a nominal porosity of 25% best represents the field data. This is dubious supposition at best, however, since there are insufficient data to quantitatively evaluate the influence of porosity in this distorted model. Table 5 compares the characteristic prototype drift dimensions with those of the model 2.4-m fences at a geometric scale of 1:100 and porosities of 25 and 50%.

Table 5. Comparison of model and prototype data at saturation.

Fence	D_{MAX}/H	X_{MAX}/H	X_{END}/H	A/H^2
Prototype	1.2	5.7	24.0	18.0
Model 25% porosity	1.2	5.5	24.0	17.5
Model 50% porosity	1.22	3.3	24.2	16.0

In examining the formation of the model drifts relative to the field data, difficulties were encountered, since useful flux measurements were not obtained in the field either. Although a flux gage was installed, it was used more to record the occurrence rather than the magnitude, of drifting. However, it is interesting to note the similarity of drift formation in the model and prototype. In both cases the drift approaches its maximum depth rapidly and then the tail of the drift continues to build.

If the 2.4-m fence at λ_L = 1:100 were taken as a reasonable simulation, the corresponding windspeed would be in the range of 17 m/sec < V_W < 25 m/sec. This would be a reasonable velocity range since, according to Tabler's field data (12), windspeeds greater than 17.5 m/sec occurred during more than 45% of the drifting events, and in fact the mean windspeed during the drifting was 16.4 m/sec. This suggests the concept of a "significant wind" in modeling, that is, a windspeed that is high enough to form the snowdrifts observed in the field and that occurs frequently enough to significantly influence the drift development.

Summary and Conclusions

Although problems with the inadequate modeling of the atmospheric boundary layer were encountered, it was possible to find reasonable quantitative relationships between the results from different model conditions, and a tentative correlation between these results and the prototype data. Specific conclusions from the study are:

1. The modeling of drifting snow using a distorted sand-water analogy appears useful on a practical basis. Because of insufficient prototype and sand flux data, however, some assumptions made are tenuous.

2. The simulation of the atmospheric boundary layer is of primary importance. This may take the form of modeling the terrain roughness and boundary layer thickness. While accurate modeling of the boundary layer thickness may not be possible, the model structure should at least be small in comparison ($H_m \ll \delta_m$).

3. With geometric scaling based on the terrain roughness and boundary layer thickness, velocity scaling based on particle fall velocity and threshold of motion characteristics yields good correlation between model and prototype data.

4. Similarity of the precipitation rate is not essential, and an abnormally high rate may be used in the model to reduce the time

scaling. As the precipitation rate is increased, however, there is a tendency to obscure detail of the model.

5. The response of the model to porosity and dowel shape is significant, indicating a need for detailed model construction.

Literature Cited

1. Calkins, D. (1974) Model studies of drifting snow patterns at Safeguard facilities in North Dakota. USA CRREL Technical Report 256. AD A006018.

2. Calkins, D. (1975) Simulated snowdrift patterns: Evaluation of geometric modeling criteria for a three-dimensional structure. USA CRREL Special Report 219. AD 007735.

3. Calkins, D. (1976) Evaluation and recommendations for snowdrift control at FAA ILS facilities, Barrow and Deadhorse, Alaska. U.S. Department of Transportation, Federal Aviation Administration Report No. FAA-RD-76-139.

4. Finney, E.A. (1934) Snow control on the highway. Michigan State College, Experiment Station Bulletin no. 57.

5. Finney, E.A. (1939) Snow drift control by highway design. Michigan State College Engineering Experiment Station Bulletin no. 86.

6. Isyumov, N. (1971) An approach to the prediction of snow loads. Ph.D. Dissertation to the Faculty of Engineering Science, The University of Western Ontario, London, Ontario, Canada.

7. Isyumov, N. and A.G. Davenport (1974) A probabilistic approach to the prediction of snow loads. Canadian Journal of Civil Engineering, vol. 1, no. 28.

8. Kungurtsev, A.A. (1956) The transfer and deposit of snow. Institut Geograffi Akad Nauk SSSR. USA CRREL Draft Translation. (Unpublished).

9. Mellor, M. (1965) Blowing snow. USA CRREL Cold Regions Science and Engineering Monograph III-A3c. AD 630328.

10. Snyder, W. (1972) Similarity criteria for the application of fluid models to the study of air pollution meteorology. Boundary Layer Meteorology, vol. 3, no. 1, Sept, p. 113-134.

11. Sutton, O.G. (1953) Micrometeorology. New York: McGraw-Hill Book Co., Inc.

12. Tabler, R.D. (1972) Evaluation of the first year performance of the Interstate - 80 snow fence system. Rocky Mountain Forest and Range Experiment Station, U.S. Department of Agriculture (USDA), Forest Service.

13. Tabler, R.D. (1973) Field data from Cooper Cove, Wyoming. Snow profiles behind Wyoming Highway Department Standard Plan fence design. Rocky Mountain Forest and Range Experiment Station, USDA Forest Service, 1971-72 and 1972-73 seasons.

14. Tabler, R.D. (1974) New engineering criteria for snow fence systems. Transportation Research Record 506, p. 65-78.

15. Theakston, F.H. (1969) Instant snow storms. Proceedings of the Eastern Snow Conference, p. 66-75.

16. Theakston, F.H. (1970) Model techniques for controlling snow on roads and runways. Highway Research Board Symposium, Snow Removal and Ice Control Research, Hanover, N.H., Special Report 115.

*ZWICK, BEATRICE & CANHAM

AD-A056498

LASER BIOEFFECTS; LOW LEVEL EFFECTS; IMPACT ON ARMY LASER SYSTEMS (U)

Letterman Army Institute of Research, Presidio of San Francisco, CA

* HARRY ZWICK, Ph.D.
EDWIN S. BEATRICE, M.D., LTC, MC
JOHN E. CANHAM, M.D., COL, MC

INTRODUCTION

Present laser standards are based primarily on a single acute exposure and evaluation of acute gross retinal pathological endpoints. While data obtained under these conditions have been of significant value in answering past immediate needs of military laser safety, they are limited in evaluating long term effects in vision that might be induced by required prolonged repetitive viewing of new laser display systems, holographic investigations and, in general, repeated exposure to very low levels of laser light.

In almost all of these situations, levels of laser radiation are well within present permissible safe limits. Yet refinement of histological retinal criteria by electron microscopy has shown that changes in retinal ultrastructure at the level of the photoreceptor can occur in the absence of a gross "burn." Such changes were observed at the safe level for very acute laser exposure (1) and were persistent to at least 3 years postexposure. It is plausible, therefore, that low level chronic repetitive viewing conditions at even lower laser exposure levels might induce permanent changes in the visual process.

In this investigation we have used rhesus monkeys trained in a behavioral acuity task to evaluate long term changes in visual function at levels many times below current extended source criteria. Correlative retinal electrophysiological measurements in rhesus at slightly higher exposure levels, but still below safe levels, correlate well with our behavioral findings and establish the origin of these effects at the level of the retina.

METHOD

A detailed description of the apparatus and training procedure has been provided previously (2). Spectral sensitivity functions were determined in each session by determining the log threshold background intensity required at each wavelength. These determinations were made by an up-and-down threshold procedure in which Landolt and gapless rings were presented in sets of four rings of equal diameters. Three rings were gapless and the fourth was a Landolt ring whose position was always randomized within the set. Correct responses to Landolt rings decreased background intensity by 0.2 log units, whereas incorrect responses to Landolt rings increased background intensity by 0.2 log units (a log unit is a factor of 10 or 10 times).

Measurements of threshold intensity were made every 20 nm through the spectrum in a quasi-random order. All measurements of background threshold intensity were normalized for quantal flux with the threshold at 600 nm. Spectral sensitivity was measured for various Landolt ring gap sizes from our largest gap at 0.14 min^{-1} to our smallest at 1.85 min^{-1} (1.85 min^{-1} = 0.5 min of arc).

Behavioral data from two mature rhesus monkeys were obtained. Animals were emmetropic (no optical correction was required). Funduscopic examination of both eyes prior to and postexposure revealed no evidence of light-induced funduscopic change. Each animal was chaired and enclosed in a standard primate chamber that attenuated extraneous noise and light. A plexiglass head restraint minimized the ability of the animal to move his head during experimental sessions. The beam from an Argon laser (Spectra Physics Model No. 164) was reflected into the primate cubicle from behind the animal's head and was diffused by a small (5x5 cm) ground glass slide located outside the direct view of the animal (Figure 1). Forward scatter from this diffuser nearly uniformly irradiated a hemisphere painted flat white whose radius was 0.5 m. The location of the animal's head was approximately at the center of the hemisphere. The animal viewed the rear projected stimuli and background through a 5 cm diameter tube protruding 6 cm into the hemisphere. Viewing of the stimuli was binocular. The average of the measured luminance of the hemisphere was 25 nits ± 8 nits. Radiometrically, the average irradiance of the hemisphere was approximately 20 $\mu W/cm^2$ and a corneal irradiance of 20 $\mu W/cm^2$. Retinal irradiance was 0.2 $\mu W/cm^2$ over the entire retina. Retinal illuminance was 2.11 log trolands.

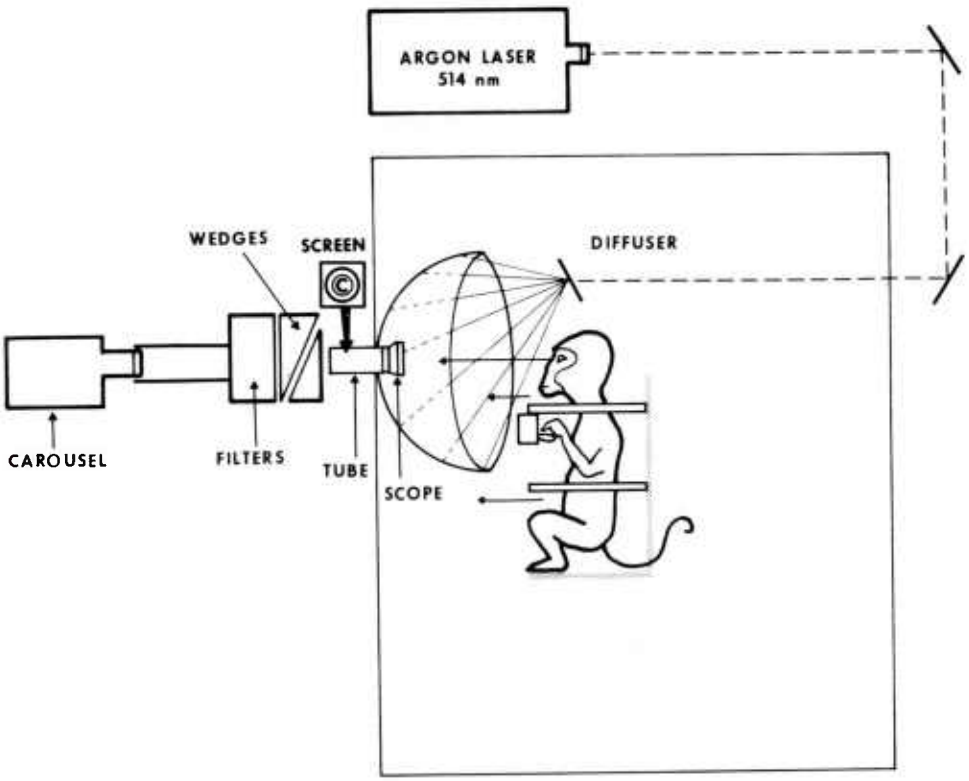

Figure 1. Schematic drawing of a chaired rhesus monkey in the experimental apparatus which was used to test Landolt ring visual acuity as well as to irradiate the animal with the low level forward scatter from the hemisphere. The arrows indicate the position of the animal during test sessions. The carousel, neutral density wedge, and interference filters were located outside the animal's cubicle. The test stimuli (Landolt rings) were projected onto a rear projection screen mounted in a tube that protruded from the center of the hemisphere. The animal's task required titration of the background threshold intensity for detecting a fixed Landolt ring. Spectral sensitivity for a given criterion gap was obtained by plotting the reciprocal of threshold as a function of wavelength through the visible spectrum. Spectral sensitivity curves were obtained for a range of gap sizes from 0.14 to 1.85 min^{-1} (9.0 to 0.50 min of arc) or from very large or coarse acuity criteria to very fine acuity criteria.

Retinal spectral sensitivity measurements were made for a low level ERG (electroretinographic) criterion (0.5 μV_{rms}) using a lock-in amplifier technique (3). Exposure to 514 nm was made in maxwellian view for a visual angle of 55 degrees. The retinal irradiance equalled 12.5 $\mu W/cm^2$. Exposure duration was two hours per session.

RESULTS

Changes in log relative sensitivity over a 14-month period at a single monochromatic background (520 nm) are shown in Figure 2 for a single animal. Arrows on the abscissa indicate exposure days. Each exposure was 2 hours (h) for a total of 38 cumulative h. All measurements made in Figure 2 were obtained after an initial 15 minutes of dark adaptation and prior to the exposure period. The first sign of change during the exposure period occurred at the finest acuity criterion, 1.85 min^{-1} (0.5 min of arc). By the end of 18 h, measurements of sensitivity at 520 nm were no longer obtainable (i.e., sensitivity was depressed by at least 5 log units). Measurements of the entire dark-adapted spectral sensitivity function for this criterion acuity were also unobtainable from this time to about 2½ months postexposure (Figure 3). Sensitivity at coarser but still photopic criteria (1.42 and 0.98 min^{-1} or 0.7 and 1.02 min of arc, respectively), however, showed relatively little change throughout the remaining exposure period at 520 nm. Two weeks after the last exposure, however, sensitivity at the 1.42 min^{-1} criterion (0.7 min of arc) declined sharply and was not obtainable for several weeks. Measurements at the 0.98 min^{-1} (1.0 min of arc) criterion were increased and also reflected a decline in sensitivity. But, corresponding measurements at the 0.14 min^{-1} (7.0 min of arc) criterion increased in sensitivity by almost a log unit (factor of 10). Several weeks later, sensitivity at the 1.42 min^{-1} (0.7 min of arc) criterion returned as did that at the 1.85 min^{-1} criterion. However, long term measurements still indicate that recovery is incomplete one year after the last exposure.

Spectral sensitivity at the 1.85 min^{-1} criterion was obtainable prior to exposure and only after 2½ months postexposure. Comparison of pre- and postexposure data at this time and approximately 9 months later are shown in Figure 3. Postexposure measurements at 2½ months were depressed by a log unit or more through most of the visible spectrum but maximal depression occurred at 540 nm. The smooth curves drawn through the postexposure data points are the cone photopigment nomograms for the 445 and 575 nm primate cones (4). The 445 nm pigment is a poorer fit to our short wavelength data than is that made by the 575 nm pigment to our data.

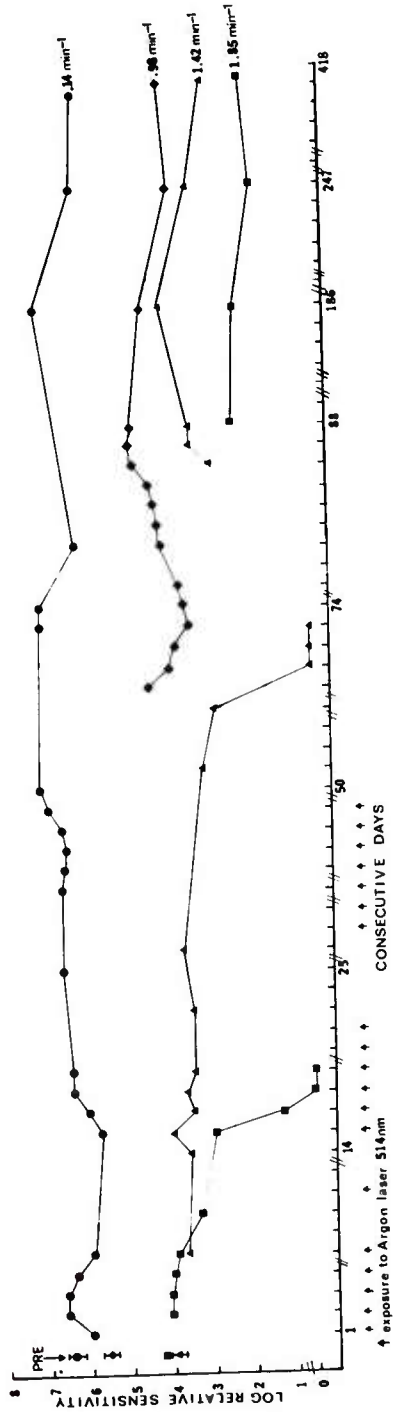

Figure 2. Measurements of sensitivity of the 520 nm background obtained prior to the exposure, during exposure, and postexposure. Each arrow represents a 2-hour exposure for a total cumulative exposure of 38 h. Vertical bars drawn through pre-exposure sensitivity points represents the range across two sessions. Within-session variability was always less than ±0.2 log units about the mean throughout the entire experiment. Measurements at various acuity gap sizes were carried out over a 14-month postexposure period. Similar but less extensive changes were obtained for achromatic (white light) high contrast Landolt ring targets.

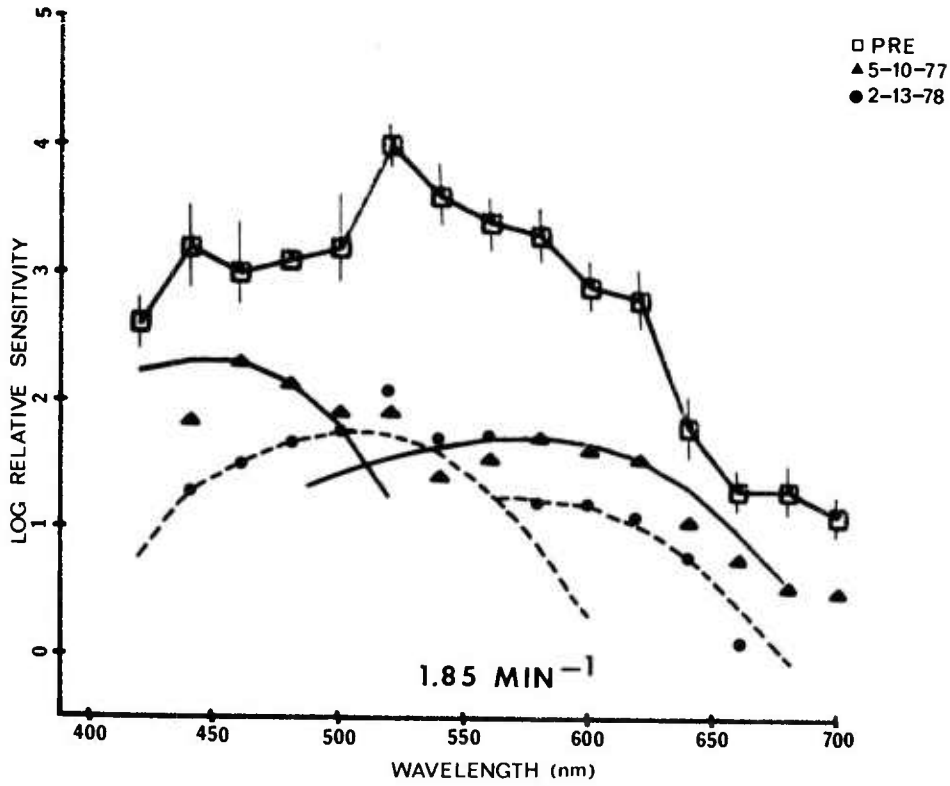

Figure 3. Pre- and postexposure dark adapted spectral sensitivity functions at 1.85 min^{-1}. Pre-exposure function is the mean of two sessions and vertical bars represent the range across two sessions. Postexposure functions were obtained at 2½ months and at 12 months after the exposure. Data obtained 2½ months postexposure were fitted with the 575 and 445 nm photopigment nomogram. Data obtained 12 months postexposure were fitted with the 575 nm photopigment nomogram in the long wavelength region but with the CIE scotopic curve in the shorter wavelength region. (The CIE scotopic curve is a standardized curve representative of the human eye's sensitivity at night; the CIE photopic curve is a standardized curve representative of the human eye's sensitivity during daytime. The nomograms are mammalian cone photopigments derived from standard curves established to reflect current available knowledge of mammalian and vertebrate photoreceptor pigments.)

Postexposure data obtained 9 months after the first postexposure measurements is still depressed by a log unit or more through the visible spectrum. The 575 nm pigment nomogram is still a good fit to the long wavelength data points. In the short and intermediate spectrum, however, we found the scotopic CIE function to provide a more reasonable fit than the short wavelength cone photopigment used to fit the earlier postexposure measurements in this spectral region.

The repetitive effect of the 514 nm exposure on the spectral sensitivity measured for a fine photopic acuity criterion (1.42 min^{-1}) is shown in Figure 4A. These data were obtained during chromatic exposure (514 nm) conditions. The initial chromatic function was measured within the first 10 h of repetitive exposure, whereas the postchromatic function was measured at 32 h of repetitive exposure. Postexposure measurements for the CIE scotopic curve normalized at 520 nm to a better degree than initial measurements normalized to the same wavelength. (Similar findings were obtained for coarser criteria down to 0.14 min^{-1}. The best fitting function was obtained at the 0.98 min^{-1} criterion. Most of the departure from the scotopic function occurred in the long wavelengths, as measured sensitivity tended to be slightly broader than the CIE scotopic curve above 580 nm.) Postexposure measurements made about one year postexposure still fit the scotopic function better than pre-exposure data.

In Figure 4B, ERG spectral sensitivity data for one animal taken before and 2 months postexposure are shown normalized to the CIE scotopic curve at 520 nm. The postexposure fit is considerably closer to the CIE function than pre-exposure data. Measurements of ERG spectral sensitivity that yielded more purely cone receptor system functions for pre-exposure measurements were substantially depressed for postexposure measurements made postexposure at one hour and at two months.

In a second behavioral animal, which has presently been exposed up to a total cumulative dose of 20 h, very similar changes in spectral sensitivity at various acuity criteria have been obtained. As with our first animal, the largest and most extensive depressions in sensitivity have occurred at the finest acuity criterion (1.85 min^{-1}). Relatively little change has occurred for the coarsest acuity criterion (0.14 min^{-1}).

Both animals showed substantial changes in log relative sensitivity for acuity targets measured against white light backgrounds. These changes were somewhat less than that observed at

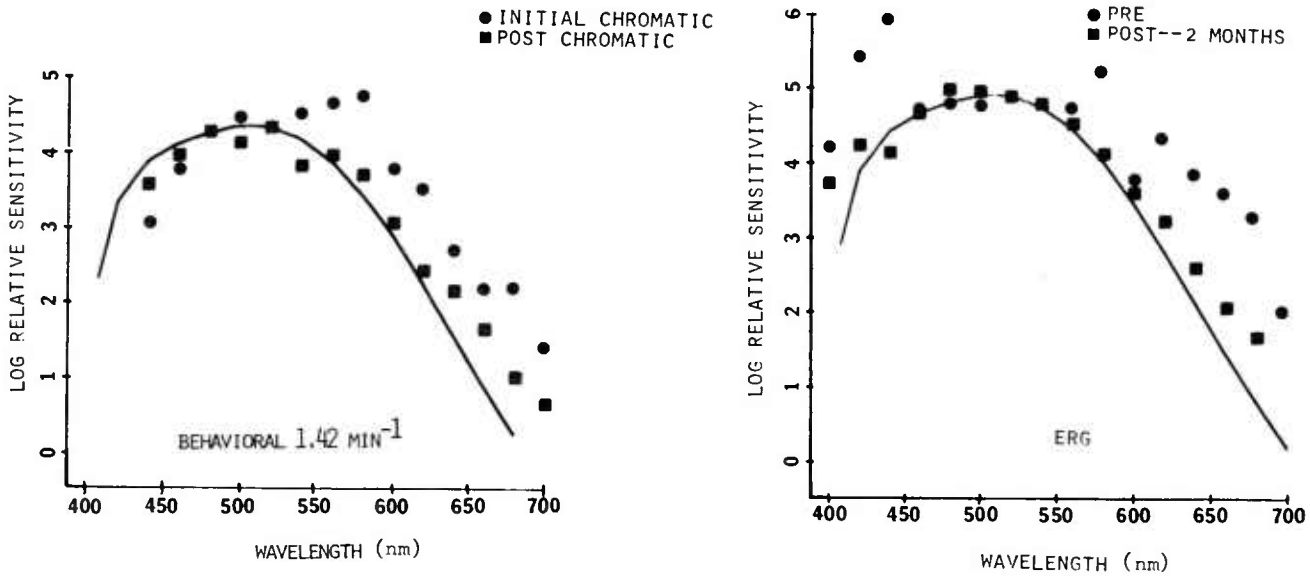

Figure 4. Comparison of behavioral and ERG 514 nm exposure effects. In Figure 4A, the initial and postexposure measurements (30 hour total exposure) at a fine photopic acuity criterion (1.42 min^{-1}) are shown normalized to the CIE scotopic function at 520 nm. After 30 hours of repetitive exposure, data at the 1.42 min^{-1} acuity criterion fit the CIE scotopic curve better than pre-exposure measurements at this acuity criterion. A similar effect was observed in another animal in which ERG spectral sensitivity was measured (Figure 4B). Exposure to 514 nm radiation was a factor of 10 higher than in the behavioral experiment and exposure duration was 2 hours for a visual angle of 55 degrees maxwellian view (test light and laser light are focused in the plane of the animal's pupil). The postexposure fit to the CIE scotopic curve is considerably better than that fit made by the pre-exposure data. Both curves were matched with the CIE scotopic function at the 520 nm points.

520 nm (Figure 2), however. Maximal losses in sensitivity occurred at very fine photopic acuity criterion (1.85 min^{-1}); relatively little change was observed at the coarsest acuity criterion (0.14 min^{-1}).

DISCUSSION

The data presented here indicate that low level, prolonged and repetitive viewing of visible laser radiation at 514 nm can substantially depress photopic visual function. At our finest acuity criterion (1.85 min^{-1}), repetitive exposure produced a general loss in sensitivity of at least one log unit. Postexposure measurements made over a 12 month period suggest that recovery processes are minimal and involve continuous "intrusion" of scotopic function under foveal conditions of measurement (5). Scotopic "intrusion" effects are more evident for measurements that involved both photopic and scotopic contributions as shown in Figure 4 for both behavioral and retinal physiological measurements.

In Figure 5, we have calculated the retinal irradiance received by looking at an extended source irradiated at the current permissible exposure. Our behavioral irradiation level is more than 3 orders of magnitude (1000 times) below the calculated standard at 2 hours; our ERG level is 2 orders of magnitude (100 times) below this line. In addition, our behavioral exposure levels were 3 orders of magnitude lower than those used by Sperling and our induced effects on spectral sensitivity have failed to recover 12 months postexposure. The dichromacy induced by Sperling's group on increment spectral sensitivity required about 30 days for full recovery during postexposure. Our effects have not recovered more than 12 months postexposure. The relationship of our data to other studies where higher levels were used and morphological criteria employed is also shown. These data were obtained at levels much higher than the calculated standard. (Dichromacy refers to the loss of the intermediate cones, leaving a 2- rather than a 3-cone system for vision.)

Our exposure levels are sufficiently low to warrant some preliminary discussion of our source characteristics. The bandwidth of our source was less than 0.1 nm as compared to the 6 nm half maximum bandwidth employed by Sperling's group. Our source was coherent and when diffused gave rise to a speckle pattern with a high spatial frequency distribution. The effects of bandwidth, coherency, and speckle pattern on the inducement of prolonged visual alteration is essentially unknown. Recent experiments, however, in our laboratory suggest that both bandwidth and spatial coherency play a significant role in producing permanent changes in spectral sensitivity (6). Therefore, coherency itself is a contributing factor to our low level effects.

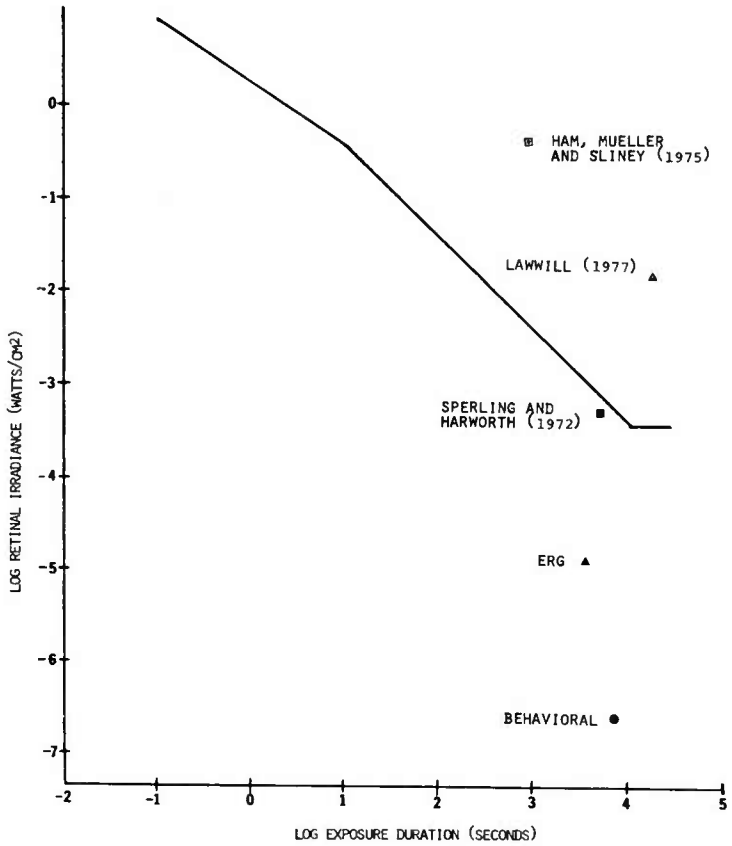

Figure 5. The solid line shows the calculated permissible retinal irradiation for extended source viewing and data from other investigations where higher levels of 514 nm coherent radiation were used to obtain morphological effects. The behavioral data of Sperling and Harworth (6) were obtained with a 520 nm incoherent source at a level a factor of 1000 times higher than that obtained for our behavioral study. Data obtained by Lawwill, Crockett and Courrier (7) and Ham, Mueller and Sliney (8) for a 4-hour and a 1-hour 514 nm coherent exposure, respectively, were obtained at levels at least 10 times above the calculated permissible retinal irradiance. The data point of Ham et al. represent a threshold point for funduscopic opacity. Lawwill's point is a level that produced morphological alteration throughout the various layers of the retina.

Morphologically, recent investigations of light effects on the retina at or below opacity levels have shown that cone outer-segment lamellar structure is more markedly altered than that of rods. Such effects appear to be independent of wavelength (7,8). In our recent investigations, we have found very similar differential effects at levels below those required to produce opacity. The relationship between these differential morphological effects and long-term persistent changes in photopic and scotopic function is currently being determined in our laboratory.

We are specifically concerned with whether cones are exclusively altered and therefore our scotopic (rod) intrusion effects simply mean that normal cone inhibition on rod activity is released, or whether both rods and cones are nonexclusively affected. Both our behavioral and electrophysiological data showed increases in absolute spectral sensitivity under scotopic conditions. Such changes can be interpreted either as a release of neural inhibition or differential alteration to normal rod and cone metabolic processes. If the latter is true, then our effect may involve severe impairment to normal night as well as normal day visual function. This point will be clarified as morphological correlative information is gathered.

In summary, our studies to date indicate that present laser safety criteria are probably not sufficient to deal with prolonged visual changes that might be induced by viewing of laser display systems considered safe by such standards. Our experiments indicate permanent behavioral and electrophysiological retinal changes at many times below levels presently presumed safe. The intended use of laser visible display systems as training devices and the current use of low level laser holographic devices, therefore, pose a potential hazard to human visual function. Our investigations also suggest that altering the coherency characteristics of the laser sources involved in such systems may attenuate these effects. Exploration of interactions of various aspects of coherency with visual processes represents a most promising avenue of investigation for attenuation and/or elimination of the effects reported here.

The impact of these investigations on Army laser systems will not be an easy problem to expedite. On the one hand, the laser has proven its utility in a diversity of military technical situations that render it almost a commonplace in present and future military environments. Yet, the data presented in this paper definitely suggest that present laser safety standards, based in large part on gross morphological change (photocoagulation), are very poor predictors of permanent change in visual function. Our data would suggest

significant lowering of laser safety standards. However, our data base is still not sufficient to indicate the nature of the pathological changes reflected by our long term changes in visual sensitivity. Further correlation with retinal ultrastructure and with human retinal diseases related to incoherent light exposure are required to determine the long term pathological base of our findings. We would recommend strongly, however, that individuals required to work in low level chronic laser environments be closely monitored for changes in visual function and be removed from these situations if such changes are persistent. Simple measurements of visual acuity and dark adaptation made frequently might serve well to provide an early warning of changes in visual function for such workers. Our data strongly suggest that visual function measurements may be the most sensitive indicators presently available to detect the type of visual dysfunction that low level chronic laser exposure has produced in our animal subjects.

In conducting the research described in this report, the investigators adhered to the "Guide for Laboratory Animal Facilities and Care" as promulgated by the Committee on the Guide for Laboratory Animal Facilities and Care of the Institute of Laboratory Animal Resources, National Academy of Sciences - National Research Council.

ACKNOWLEDGEMENTS

We wish to acknowledge Mr. Bruce Stuck for his most significant contributions to this study concerning optical calibration, the comparison of our data with the calculated extended source criteria, and finally for his critical review of this work in regards to its relevance to laser safety standards. The efforts of Mr. Tom Garcia in our behavioral studies and in the data reduction process is similarly greatly acknowledged. Finally, we wish to acknoweldge all of the members of the Division of Non-Ionizing Radiation for their support of this work which presented itself in too many ways to detail here.

REFERENCES

1. Adams, D.O., Beatrice, E.S. and Bedell, R.B.: Retina: Ultrastructural alterations produced by extremely low levels of coherent radiation. Science, 1972, 177, 58-59.

2. Robbins, D.O., Zwick, H. and Holst, G.C.: A method for producing foveal retinal exposures in an awake-task oriented Rhesus monkey. Behav. Res. Methods Instrum., 1973, 5, 457-461.

3. Zwick, H. and Holst, G.C.: Experimental alteration of the red cone photoreceptor process. Mod. Probl. Ophthalmol. 1976, 17, 257-263.

4. Ebrey, T.G. and Honig, B.: New wavelength dependent visual pigment nomograms. Vision Res., 1977, 17, 147-152.

5. Zwick, H. and Beatrice, E.S.: Long-term changes in spectral sensitivity after low-level laser (514 nm) exposure. Mod. Probl. Ophthalmol., 1978, in press.

6. Sperling, H.G. and Harworth, R.S.: Intense light effects on spectral sensitivity. Optica Acta, 1972, suppl., 19, 395-398.

7. Lawwill, T., Crockett, S. and Courrier, G.: Retinal damage secondary to chronic light exposure; thresholds and mechanisms. Doc. Ophthalmol., 1977, 44, 379-402.

8. Ham, W.T., Mueller, H.A. and Sliney, D.H.: Retinal sensitivity to damage from short wavelength light. Nature, 1976, 260, 153-154.

9. Zwick, H. and Jenkins, D.L.: Effects of coherent light on retinal receptor processes of pseudemys. Assoc. for Res. in Vision Ophthalmol., 1978, abstract.

10. Tso, M.O.M., Wallow, H.L. and Powell, J.O.: Differential susceptibility of rod and cone cells to Argon laser. Arch. Ophthalmol., 1973, 89, 228-234.

11. Marshall, J., Hamilton, A.M. and Bird, A.C.: Histopathology of ruby and argon laser lesions in monkey and human retina. Br. J. Ophthalmol. 1975, 59, 610-629.